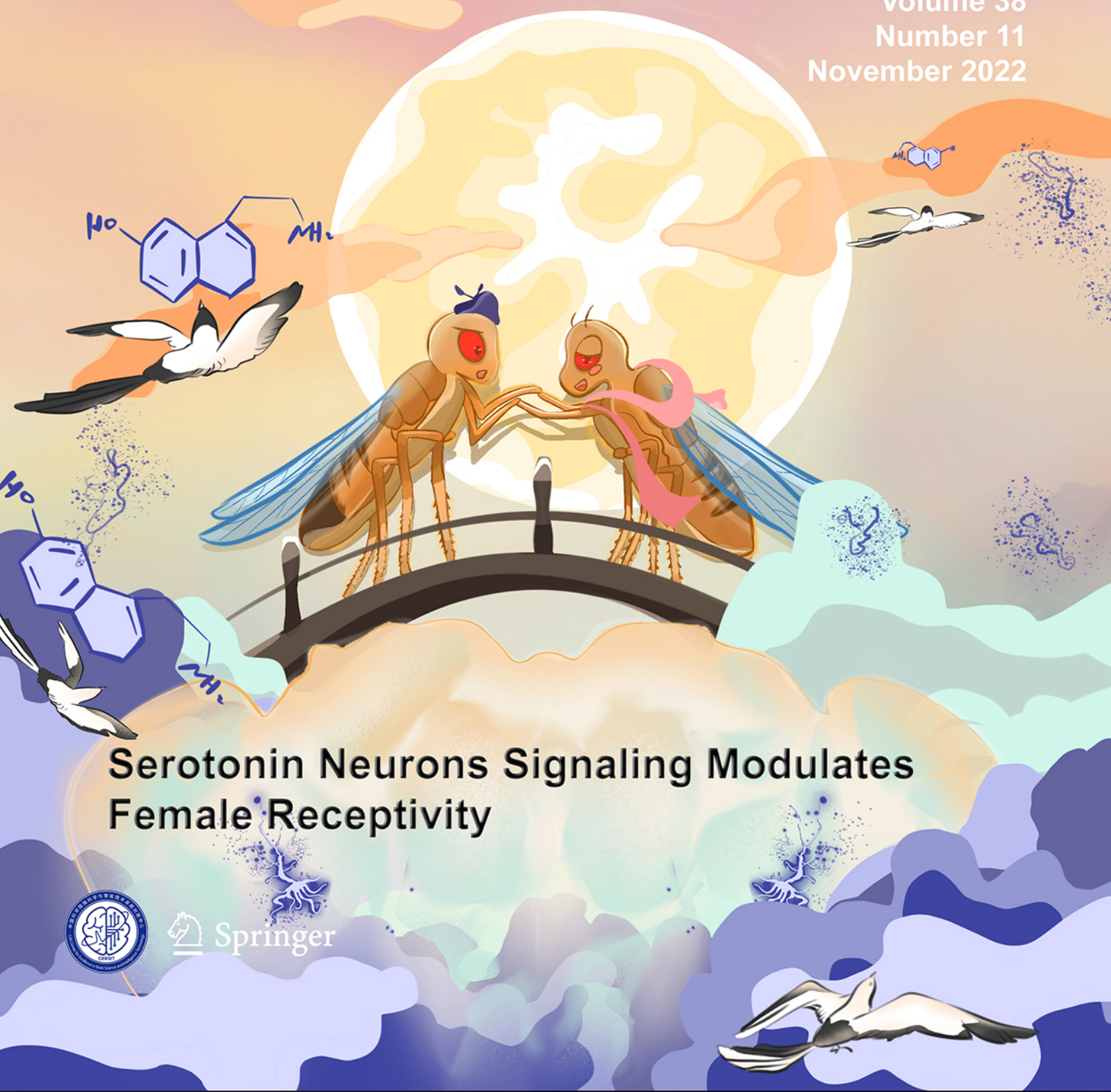


# Neuroscience Bulletin

The Official Journal of the Chinese Neuroscience Society

神经科学通报

Volume 38  
Number 11  
November 2022



**Serotonin Neurons Signaling Modulates  
Female Receptivity**



Springer

## About the Cover

The choice of a female to accept or reject male courtship is a critical decision for animal reproduction. Serotonin (5-hydroxytryptamine) has been found to regulate sexual behavior in many species, but it is unclear how it functions to regulate different aspects of sexual behavior. Ma *et al.* revealed that serotonin signaling plays a critical positive role in modulating the receptivity of female *Drosophila melanogaster*. On the cover, serotonin molecules and a subset of serotonergic neurons in the central brain serve as a bridge of magpies enable a female fly to mate with a courting male fly more easily on Chinese Valentine's Day (also known as the Magpie Festival). See pages 1277–1291. (Cover designed by Baoxu Ma, Rencong Wang, and Li-Chuang Studio)

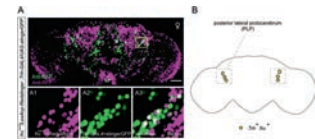


Volume 38 Number 11  
November 2022

## Original Articles

### 1277 Serotonin Signaling Modulates Sexual Receptivity of Virgin Female *Drosophila*

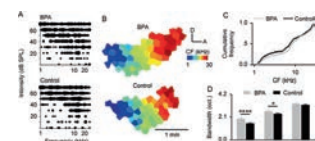
Baoxu Ma · Rencong Wang · Yaohua Liu · Bowen Deng · Tao Wang · Fengming Wu · Chuan Zhou



p 1287

### 1292 Developmental Exposure to Bisphenol a Degrades Auditory Cortical Processing in Rats

Binliang Tang · Kailin Li · Yuan Cheng · Guimin Zhang · Pengying An · Yutian Sun · Yue Fang · Hui Liu · Yang Shen · Yifan Zhang · Ye Shan · Étienne de Villers-Sidani · Xiaoming Zhou



p 1298

### 1303 HMGB1 from Astrocytes Promotes EAE by Influencing the Immune Cell Infiltration-Associated Functions of BMECs in Mice

Junyu Shi · Yifan Xiao · Na Zhang · Mengya Jiao · Xuhuan Tang · Chan Dai · Chenchen Wang · Yong Xu · Zheng Tan · Feili Gong · Fang Zheng



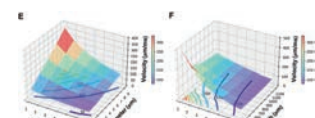
p 1321

### 1315 Whole-Brain Connectome of GABAergic Neurons in the Mouse Zona Incerta

Yang Yang · Tao Jiang · Xueyan Jia · Jing Yuan · Xiangning Li · Hui Gong

### 1330 Dendritic Morphology Affects the Velocity and Amplitude of Back-propagating Action Potentials

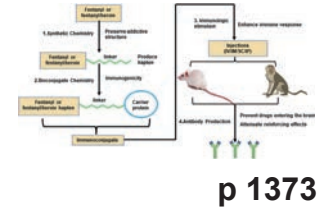
Wu Tian · Luxin Peng · Mengdi Zhao · Louis Tao · Peng Zou · Yan Zhang



p 1342

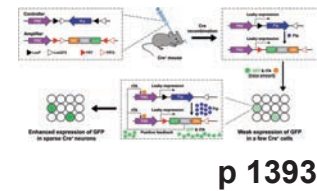


- 1347 Anti-Seizure and Neuronal Protective Effects of Irisin in Kainic Acid-Induced Chronic Epilepsy Model with Spontaneous Seizures**  
Jie Yu · Yao Cheng · Yaru Cui · Yujie Zhai · Wenshen Zhang · Mengdi Zhang · Wenyu Xin · Jia Liang · Xiaohong Pan · Qiaoyun Wang · Hongliu Sun



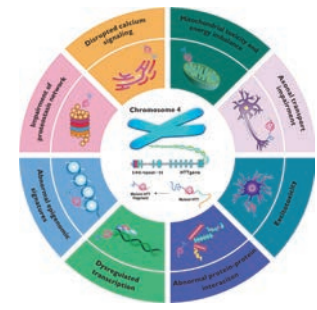
## Reviews

- 1365 Unique Pharmacology, Brain Dysfunction, and Therapeutic Advancements for Fentanyl Misuse and Abuse**  
Ying Han · Lu Cao · Kai Yuan · Jie Shi · Wei Yan · Lin Lu



- 1383 Lighting Up Neural Circuits by Viral Tracing**  
Liyao Qiu · Bin Zhang · Zhihua Gao

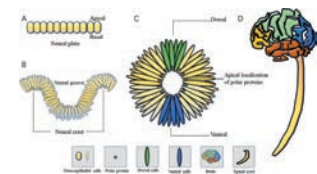
- 1397 CRISPR-Based Genome-Editing Tools for Huntington's Disease Research and Therapy**  
Yiyang Qin · Shihua Li · Xiao-Jiang Li · Su Yang



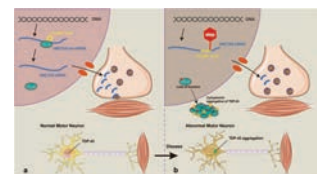
- 1409 Progress in Modeling Neural Tube Development and Defects by Organoid Reconstruction**  
Peng Li · Yongchang Chen

## Letters to the Editor

- 1420 Dual Effects of Light on Regulating *Aedes aegypti* Heat-Seeking Behavior**  
Haonan Zhou · Kai Shi · Fengming Wu · Bingcai Wang · Jing Li · Bowen Deng · Chuan Zhou



- 1425 Release of Endogenous Brain-derived Neurotrophic Factor into the Lateral Entorhinal Cortex from the Paraventricular Thalamus Ameliorates Social Memory Deficits in a Mouse Model of Alzheimer's Disease**  
Yun-Long Xu · Lin Zhu · Zi-Jun Chen · Xiao-Fei Deng · Pei-Dong Liu · Shan Li · Bing-Chun Lin · Chuan-Zhong Yang · Wei Xu · Kui-Kui Zhou · Ying-Jie Zhu



## Research Highlights

- 1431 *UNC13A* Gene Brings New Hope for ALS Disease-Modifying Drugs**  
Xi Chen · Heling Chu · Yi Dong

- 1435 The Lung Microbiome: A Potential Target in Regulating Autoimmune Inflammation of the Brain**  
Luoman Yang · Shu Feng · Chongyun Wu · Luodan Yang

# Neuroscience Bulletin

## Copyright Information

### *For Authors*

As soon as an article is accepted for publication, authors will be requested to assign copyright of the article (or to grant exclusive publication and dissemination rights) to the publisher (respective the owner if other than Springer Nature). This will ensure the widest possible protection and dissemination of information under copyright laws.

More information about copyright regulations for this journal is available at [www.springer.com/12264](http://www.springer.com/12264)

### *For Readers*

While the advice and information in this journal is believed to be true and accurate at the date of its publication, neither the authors, the editors, nor the publisher can accept any legal responsibility for any errors or omissions that may have been made. The publisher makes no warranty, express or implied, with respect to the material contained herein.

All articles published in this journal are protected by copyright, which covers the exclusive rights to reproduce and distribute the article (e.g., as offprints), as well as all translation rights. No material published in this journal may be reproduced photographically or stored on microfilm, in electronic data bases, on video disks, etc., without first obtaining written permission from the publisher (respective the copyright owner if other than Springer Nature). The use of general descriptive names, trade names, trademarks, etc., in this publication, even if not specifically identified, does not imply that these names are not protected by the relevant laws and regulations.

Springer Nature has partnered with Copyright Clearance Center's RightsLink service to offer a variety of options for reusing Springer Nature content. For permission to reuse our content please locate the material that you wish to use on [link.springer.com](http://link.springer.com) or on [springerimages.com](http://springerimages.com) and click on the permissions link or go to [copyright.com](http://copyright.com) and enter the title of the publication that you wish to use. For assistance in placing a permission request, Copyright Clearance Center can be contacted directly via phone: +1-855-239-3415, fax: +1-978-646-8600, or e-mail: [info@copyright.com](mailto:info@copyright.com)

© Center for Excellence in Brain Science  
and Intelligence Technology, CAS 2022

## Journal Website

[www.springer.com/12264](http://www.springer.com/12264)

For the actual version of record please always check the online version of the publication.

## Subscription Information

Volume 38 (12 issues) will be published in 2022.

ISSN: 1673-7067 print  
ISSN: 1995-8218 electronic

For information on subscription rates please contact Springer Nature Customer Service Center: [customerservice@springernature.com](mailto:customerservice@springernature.com)

The Americas (North, South, Central America and the Caribbean)  
Springer Nature Journal Fulfillment,  
Harborside Plaza II,  
200 Hudson Street, Jersey City,  
NJ 07302, USA  
Tel. 800-SPRINGER (777-4643);  
212-460-1500 (outside  
North America)

## Outside the Americas

Springer Nature Customer Service  
Center GmbH, Tiergartenstr. 15,  
69121 Heidelberg, Germany  
Tel.: +49-6221-345-4303

## Advertisements

E-mail contact: [advertising@springer.com](mailto:advertising@springer.com) or [anzeigen@springer.com](mailto:anzeigen@springer.com) (Germany)

## Disclaimer

Springer Nature publishes advertisements in this journal in reliance upon the responsibility of the advertiser to comply with all legal requirements relating to the marketing and sale of products or services advertised. Springer Nature and the editors are not responsible for claims made in the advertisements published in the journal. The appearance of advertisements in Springer Nature publications does not constitute endorsement, implied or intended, of the product advertised or the claims made for it by the advertiser.

## Office of Publication

Springer Nature Singapore Pte Ltd.  
152 Beach Road, #21-01/04  
Gateway East, Singapore 189721,  
Singapore



# Serotonin Signaling Modulates Sexual Receptivity of Virgin Female *Drosophila*

Baoxu Ma<sup>1,2</sup>  · Rencong Wang<sup>1,2</sup> · Yaohua Liu<sup>3</sup> ·  
Bowen Deng<sup>4</sup> · Tao Wang<sup>1</sup> · Fengming Wu<sup>1,2</sup> ·  
Chuan Zhou<sup>1,2,5</sup> 

Received: 7 December 2021 / Accepted: 13 April 2022 / Published online: 5 July 2022  
© The Author(s) 2022

**Abstract** The choice of females to accept or reject male courtship is a critical decision for animal reproduction. Serotonin (5-hydroxytryptamine; 5-HT) has been found to regulate sexual behavior in many species, but it is unclear how 5-HT and its receptors function to regulate different aspects of sexual behavior. Here we used *Drosophila melanogaster* as the model animal to investigate how 5-HT and its receptors modulate female sexual receptivity. We found that knockout of tryptophan hydroxylase (*Trh*), which is involved in the biosynthesis of 5-HT, severely reduced virgin female receptivity without affecting post-mating behaviors. We identified a subset of sexually dimorphic *Trh* neurons that co-expressed fruitless (*fru*), in which the activity was

correlated with sexual receptivity in females. We also found that 5-HT<sub>1A</sub> and 5-HT<sub>7</sub> receptors regulate virgin female receptivity. Our findings demonstrate how 5-HT functions in sexually dimorphic neurons to promote virgin female receptivity through two of its receptors.

**Keywords** Female sexual receptivity · Serotonin · 5-HT · *Fruitless* · Neurochemical · 5-HT receptors · *Drosophila*

## Introduction

Sexual behavior in *Drosophila melanogaster* is an excellent model in which to investigate the neuronal basis underlying social behavior because they are innate and robust [1–3]. Wild-type male and female flies can achieve copulation without social learning experiences during adulthood [4, 5]. *Drosophila* sexual behaviors include stereotypic male courtship rituals such as orienting to a female, extending an ipsilateral wing to produce courtship songs, tapping and licking the female, attempting copulation, and finally copulation [6, 7]. The neural circuit involved in male courtship behavior has been dissected in recent years owing to advances in genetic technology [8–11]. However, studies on female sexual behavior are far fewer than those on males.

Much progress has been made in recent years on how female flies perceive the presence of males and their courtship, and integrate auditory, olfactory, and mechanosensory cues, to decide whether to be receptive or not [12–15]. Such a decision is also dependent on the maturity and mating status of the female. Sexually immature females exhibit rejection behaviors by running away, flicking wings, or kicking the courting male [16, 17]. After sexual maturity, virgin females make the decision to copulate with courting males and exhibit sexual receptivity,

Baoxu Ma, Rencong Wang, and Yaohua Liu contributed equally to this work.

**Supplementary Information** The online version contains supplementary material available at <https://doi.org/10.1007/s12264-022-00908-8>.

✉ Fengming Wu  
wufengming@ioz.ac.cn

✉ Chuan Zhou  
zhouchuan@ioz.ac.cn

<sup>1</sup> State Key Laboratory of Integrated Management of Pest Insects and Rodents, Institute of Zoology, Chinese Academy of Sciences, Beijing 100101, China

<sup>2</sup> University of Chinese Academy of Sciences, Beijing 100101, China

<sup>3</sup> Department of Plant Protection, Shanxi Agricultural University, Jinzhong 30801, China

<sup>4</sup> Chinese Institute for Brain Research, Zhongguancun Life Sciences Park, Beijing 102206, China

<sup>5</sup> Institute of Molecular Physiology, Shenzhen Bay Laboratory, Shenzhen 518132, China

which is a proxy metric to evaluate the willingness of females to mate [18–20]. Recently-mated females display post-mating behaviors by reducing receptivity and increasing egg-laying [8, 21, 22]. Female post-mating behaviors are triggered by the male seminal fluid peptide (sex-peptide, SP) and regulated by SP-responsive neurons which express fruitless (*fru*), doublesex (*dsx*), and pickpocket (*ppk*) [23–26]. Despite this progress in the sensory and integrative circuits for female sexual behavior [26–29], very little is known about how internal factors modulate virgin female receptivity.

Internal factors that modulate the function of neuronal circuits often use neurochemical systems including neuropeptides and neurotransmitters [30]. Serotonin (5-hydroxytryptamine; 5-HT), which is one of the highly-conserved neurotransmitters across species, is involved in a range of behaviors including cognition, reward, learning, and memory, as well as male and female sexual behavior [31–35]. Although 5-HT is known to be involved in mammal sexual behavior, its exact function in regulating sexual behavior is unclear. In *Drosophila*, 5-HT has also been shown to regulate a variety of complex behaviors including aggression, sleep, and feeding [36–38], but whether and how it regulates female sexual receptivity is unknown. Thus, it is of particular importance to investigate the function of 5-HT in female sexual receptivity using the *Drosophila* model.

Sexual behaviors in *Drosophila* are largely controlled by two pivotal regulatory genes, *fru* and *dsx*, that control most aspects of sexual development and behavior [10, 39, 40]. Sex-specific *dsx* transcripts are translated in both sexes to produce the sex-specific proteins Dsx<sup>M</sup> or Dsx<sup>F</sup>, which control male and female differentiation, respectively [15, 41–43]. In contrast, *fru* proteins (Fru<sup>M</sup>) control male courtship and are male-specific [1, 5, 44, 45]. Although Fru<sup>M</sup> proteins are not produced in females, neurons expressing the *fru* transcript (*fru*<sup>+</sup>) are crucial for female sexual receptivity, as silencing these *fru*<sup>+</sup> neurons impairs female receptivity [44, 46]. Recent studies have also revealed the importance of *dsx*<sup>+</sup> neurons in controlling virgin female receptivity and post-mating behaviors in mated females [24, 27, 47, 48].

In this study, we showed that 5-HT signaling modulates female sexual receptivity at both the molecular and the neural circuit levels. Knockout and knockdown of tryptophan hydroxylase (*Trh*), which is involved in the biosynthesis of 5-HT, decreased virgin female receptivity. Activation of the entire population of *Trh*<sup>+</sup> neurons enhanced sexual receptivity in virgin females but had no effect on sexual receptivity in mated females. We identified a group of sexually dimorphic *Trh*<sup>+</sup>*fru*<sup>+</sup> neurons in the posterior lateral protocerebrum (PLP) to be a crucial 5-HT-releasing site in the regulation of female sexual receptivity. Analysis of Ca<sup>2+</sup> activity in 5-HT-PLP neurons revealed stronger activity in virgin flies than in mated flies. Furthermore, we found two 5-HT receptors,

5-HT<sub>1A</sub> and 5-HT<sub>7</sub>, that might be crucial for female sexual receptivity.

## Materials and Methods

### Fly Culture and Strains

All *D. melanogaster* strains were reared on standard medium at 25°C and 60% humidity in a 12-h light/dark photoperiod unless otherwise described. All the knockout lines in this study for screening have been published [49]. The following strains were obtained from Dr. Yi Rao's lab (Peking University, Beijing, China): *isoCS* (wild-type), *Trh-GAL4*, *elav-GAL4*; *UAS-dicer2*, *elav-GAL4*, and *UAS-5-HT1A*. The *UAS-stingerGFP* and *UAS-Redstinger* lines were gifts from Dr. Yufeng Pan's lab (Southeast University, Nanjing, China). *UAS-PACα* was a gift from Dr. Yan Zhu's lab (Institute of Biophysics, Chinese Academy of Sciences). The following strains were from the Bloomington *Drosophila* Stock Center: *UAS-Kir2.1* (BL#6596), *TRIC* (BL#61679), *UAS-mCD8-GFP* (BL#5137), *UAS-shi<sup>ts</sup>* (BL#44222), and *UAS-Trh-RNAi* (BL#33612).

### Behavioral Assays

Female receptivity assays were conducted as previously described [15]. In brief, individual virgin females (8–10 days old) were paired with a naïve wild-type male courter (*isoCS*) (8–10 days old). Before they were paired, females and males were separately introduced into a two-layer courtship chamber (10 mm diameter × 3 mm height per layer), which was divided by a removable transparent strip. The assay was recorded with a resolution of 1280 pixels × 720 pixels (1.78:1) at 30 frames/s for 30 min using cameras (VIXIA HF R500, Canon, Tokyo, Japan). The number of receptive females and the time of receptivity for individual females were analyzed manually.

In the egg-laying assay, 3–4 virgin or mated females (~8 days old) were transferred to a vial with fresh medium left for 48 h at 25°C and 60% humidity under a 12-h light/dark cycle, and the number of eggs laid per female during 48 h was counted manually. To collect mated females, individual females were aspirated into the courtship chamber to allow copulation with a wild-type male before the egg-laying tests.

In the re-mating assay, we obtained mated females by pairing virgin females with wild-type males (both ~8 days old). The mated females were collected as above, transferred to food vials, and left for 48 h before re-mating tests with a new wild-type male of the same age for 1 h. The percentage of re-mating females was analyzed manually.

The locomotion assay was applied at 25°C and 60% humidity. Individual virgin females were transferred to the

courtship chambers without males and recorded for 10 min. The locomotor speed was analyzed using MatLab software (MathWorks Inc., MA, USA) as described previously [50].

All behavioral assays were run from 11:00 to 15:00. The food medium was replaced every 2–3 days to ensure freshness.

### Light-induced Experiments

In *PAC $\alpha$*  (photoactivated adenylyl cyclase  $\alpha$ ) experiments, flies were crossed on standard medium, and the vials were wrapped in aluminum foil to avoid light. Female progeny (<8 h) were isolated in darkness for 8–10 days. Prior to behavioral tests, *PAC $\alpha$* -expression was activated by blue light (420 nm, 1200 mW/cm<sup>2</sup>, 5 s; Denjoy, DY-400-4, Changsha, China).

In *CsChrimson* experiments, flies were crossed on 0.2 mmol/L retinal-containing medium (Sigma-Aldrich, St. Louis, USA) in darkness. Virgin females were immediately transferred to 0.4 mmol/L retinal-containing medium and isolated in darkness for 8–10 days. Female receptivity tests were performed in darkness (control) or with red light activation (620 nm, 0.03 mW/mm<sup>2</sup>; Kemai Vision Technology, Dongguan, China) during a 30-min observation period. The assay was recorded by an industrial camera (Stingray F080B ASG, Allied Vision Technologies, Stadtroda, Germany) equipped with an infrared light source (860-nm IR LED, Kemai Vision Technology) for illumination.

### Temperature-induction Experiments

In *TrpA1* and *UAS-shi<sup>ts</sup>* experiments, virgin females were maintained at 22°C for 8–10 days. Before the behavioral assay, the flies were concurrently introduced into chambers at 30°C or 21°C for 20 min. 30°C was the activation temperature in *TrpA1* activation experiments but a restrictive temperature in *UAS-shi<sup>ts</sup>* inactivation experiment.

### Generation of *UAS-5-HT7*

pJFRC28-5XUAS-IVS-GFP-p10 (# 12073; Fungene Biotechnology, Shanghai, China) was used for the generation of the pJFRC28-*UAS-5-HT7* (*UAS-5-HT7*) construct. pJFRC28-5XUAS-IVS-GFP-p10 plasmid digested within NotI and XbaI was used to excise the coding sequence of GFP. Using the Gibson Assembly, the complementary DNA (cDNA) of 5-HT7 was cloned in the described plasmid. The right upstream of ATG codon added the Kozak sequence, and the *UAS-5-HT7* construct was injected into the attP40 site using phiC31 integrase-mediated transgenesis. The construct was confirmed using DNA sequencing and PCR. The primers used for cloning 5-HT7 cDNA were as follows:

- UAS-5-HT7-forward:

TCTTATCCTTTACTTCAGGCGGCCGCCACCATGGCT  
TTATCTGGACAGGACTG

- UAS-5-HT7-reverse:

GTTATTTTAAAAACGATTCATTCTAGATTAAGAGAA  
AGCTCTCCCTCGC

### Confirmation of Transgenic Flies

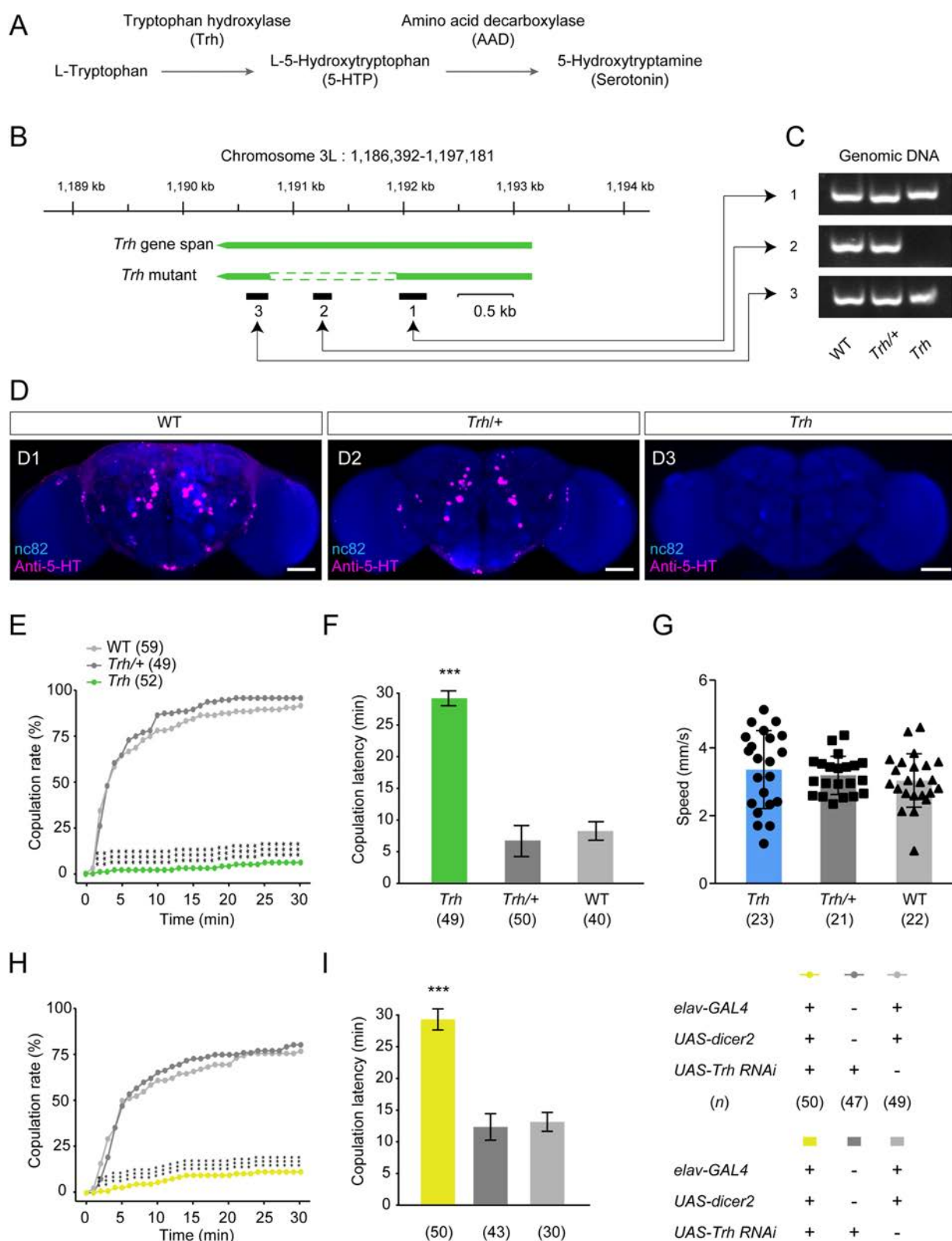
Genomic DNA was extracted from the whole body of adult flies. Individual flies were crushed with a pestle in 50  $\mu$ L DNA extraction reagent. After incubation at 95°C for 10 min, the samples were centrifuged at 12,000 r/min for 10 min at room temperature. The supernatant of DNA was collected and added to the mixing system to conduct PCR, according to the manufacturer's instructions. The mix contained 25  $\mu$ L 2 $\times$  MightyAmp buffer, 1  $\mu$ L MightyAmp DNA polymerase, and 5  $\mu$ L 10 $\times$  Additive for high specificity, and was adjusted to 50  $\mu$ L. Primers used in regions 1–3 (Fig. 1B) were as follows:

- Region 1 forward: GGCTACGGTGGATATTCCAAG
- Region 1 reverse: CATTGAGGCTGTTGTGGAGC
- Region 2 forward: GAGAGGTGGCCTCTGTGAAC
- Region 2 reverse: CGGTGCCCCCTTTGAACG
- Region 3 forward: AGGGAACAGATTCTCGGGAC
- Region 3 reverse: ACTTCTTGGTGCAGTGCCTC

### Immunostaining

Flies were dissected in phosphate-buffered saline (PBS), and then the brains were fixed in 2% (weight/volume) paraformaldehyde (PFA) (Electron Microscopy Sciences, Hangzhou, China) for 55 min at room temperature. Then, the samples were washed five times in PBS with 0.3% Triton (PBST) for 15 min and incubated in blocking solution [5% (volume/volume) goat serum (Sigma-Aldrich) diluted in 0.3% PBST] for 1 h at room temperature. The brains were then incubated with the primary antibody (diluted in blocking solution) for >24 h at 4°C, and washed five times in 0.3% PBST for 15 min before incubation with the secondary antibody (1:500, diluted in blocking solution) overnight at 4°C. The samples were washed five times in 0.3% PBST for 15 min and fixed in 4% PFA for >4 h at room temperature. The brains were washed five times with 0.3% PBST for 15 min at room temperature and were placed on a poly-L-lysine-coated coverslip in 0.3% PBST. The brains were then immersed in 30%, 50%, 75%, 95%, and 100% ethanol. The brains were immersed three times in xylene for 5 min and mounted on glass slides using dibutylphthalate polystyrene xylene (DPX)





(Sigma-Aldrich) for imaging. Images were generated on a Zeiss 710 confocal microscope (Carl Zeiss, Oberkochen,

Germany) and were processed using Fiji software (<https://imagej.net/Fiji>).

**Fig. 1** The *Drosophila Trh* gene is essential for virgin female receptivity. **A** 5-HT biosynthesis process. **B** Schemata of the *Trh* gene locus and mutants generated by *Trh* knockout. Black bars indicate target regions 1–3 in the PCR analysis in **C**. **C** PCR verification of regions 1–3 in **B** from *Trh* mutant genomic DNA samples. **D** Neuropil expression of the *Trh* gene in female adult brains of wild-type (WT) (**D1**), heterozygous (**D2**), and homozygous *Trh* mutant flies (**D3**), immunostained with anti-5-HT antibody (magenta) and nc82 antibody (blue) (scale bars, 50  $\mu$ m). **E**, **F** The copulation rate is decreased (**E**) and the copulation latency is prolonged (**F**) in *Trh*-knockout mutants within a 30 min observation period. **G** *Trh* mutants do not differ in locomotor speed from WT and heterozygous control females. **H**, **I** Knockdown of *Trh* expression reduces virgin female receptivity. The copulation rate is decreased (**H**) and the copulation latency is prolonged (**I**) by knocking down *Trh* expression pan-neuronally. \*\*\* $P < 0.001$ , otherwise no significant difference ( $\chi^2$  test for copulation rate; Kruskal-Wallis with *post hoc* Mann-Whitney *U* test for copulation latency). *n* values are shown in parentheses. Error bars,  $\pm$ SEM.

The antibodies used were mouse anti-nc82 (1:50; Developmental Studies Hybridoma Bank, Iowa City, USA), chicken anti-GFP (1:1000; Life technologies, Carlsbad, USA), rabbit anti-RFP (1:500; Invitrogen, Waltham, USA), and rabbit anti-5-HT (1:500; Life technologies). The secondary antibodies were Alexa Fluor goat anti-chicken 488 (1:500; Life technologies), Alexa Fluor goat anti-rabbit 488 (1:500; Life technologies), Alexa Fluor goat anti-mouse 546 (1:500; Life technologies), and Alexa Fluor goat anti-rabbit 633 (1:500; Invitrogen).

### Drug Treatment in Rescue Experiments

The procedure in the 5-hydroxytryptophan (5-HTP; Sigma-Aldrich) feeding experiment is shown in Fig. 2A. Virgin females were reared on normal food for 8 days after eclosion. Two days before behavioral tests and immunostaining analysis, the flies were divided into two treatment groups. In the control group (5-HTP<sup>-</sup>), females were put on control mock food containing 2% agar and 10% sucrose; in the 5-HTP feeding group (5-HTP<sup>+</sup>), the flies were reared on drug-containing food in which 2 mg/mL 5-HTP was dissolved in the mock food.

### Transcriptional Reporter of Intracellular Ca<sup>2+</sup> (TRIC) Assay

Virgin females with the genotype *10XUAS-mCD8::RFP/13XLexAop2-mCD8::GFP; nSyb-MKII::nlsLexADBD0; UAS-p65AD::CaM/Trh-GAL4* were collected within 8 h after eclosion until TRIC assay. For mated females, 8-days-old virgin females of given genotypes were transferred to courtship chambers and paired with wild-type male flies. The females that copulated successfully within 30 min were collected for further TRIC analysis. Adult female brains from these two groups (virgin and

mated) were dissected, and the whole brain was perfused with a saline solution containing (in mmol/L) 103 NaCl, 3 KCl, 4 MgCl<sub>2</sub>, 1.5 CaCl<sub>2</sub>, 26 NaHCO<sub>3</sub>, 1 NaH<sub>2</sub>PO<sub>4</sub>, 5 N-tri-(hydroxymethyl)-methyl-2-aminoethane-sulfonic acid, 20 glucose, 17 sucrose, and 5 trehalose, adjusted to pH 7.3.

Images were acquired using a confocal microscope (Nikon A1R+, Nikon, Toyko, Japan) with a 40 $\times$  water immersion objective. The Ca<sup>2+</sup> signal was indicated by the fluorescence intensity. 488-nm and 546-nm light was used to excite GFP and RFP, respectively. The regions of interest (ROIs) were manually defined in the PLP cluster area and were analyzed using NIS-Elements D (Nikon; [https://www.microscope.healthcare.nikon.com/en\\_EU/products/software](https://www.microscope.healthcare.nikon.com/en_EU/products/software)). The relative TRIC signal of selected ROIs (GFP signal/RFP signal) was used to compare neural activity in virgin and mated females.

### Statistical Analysis

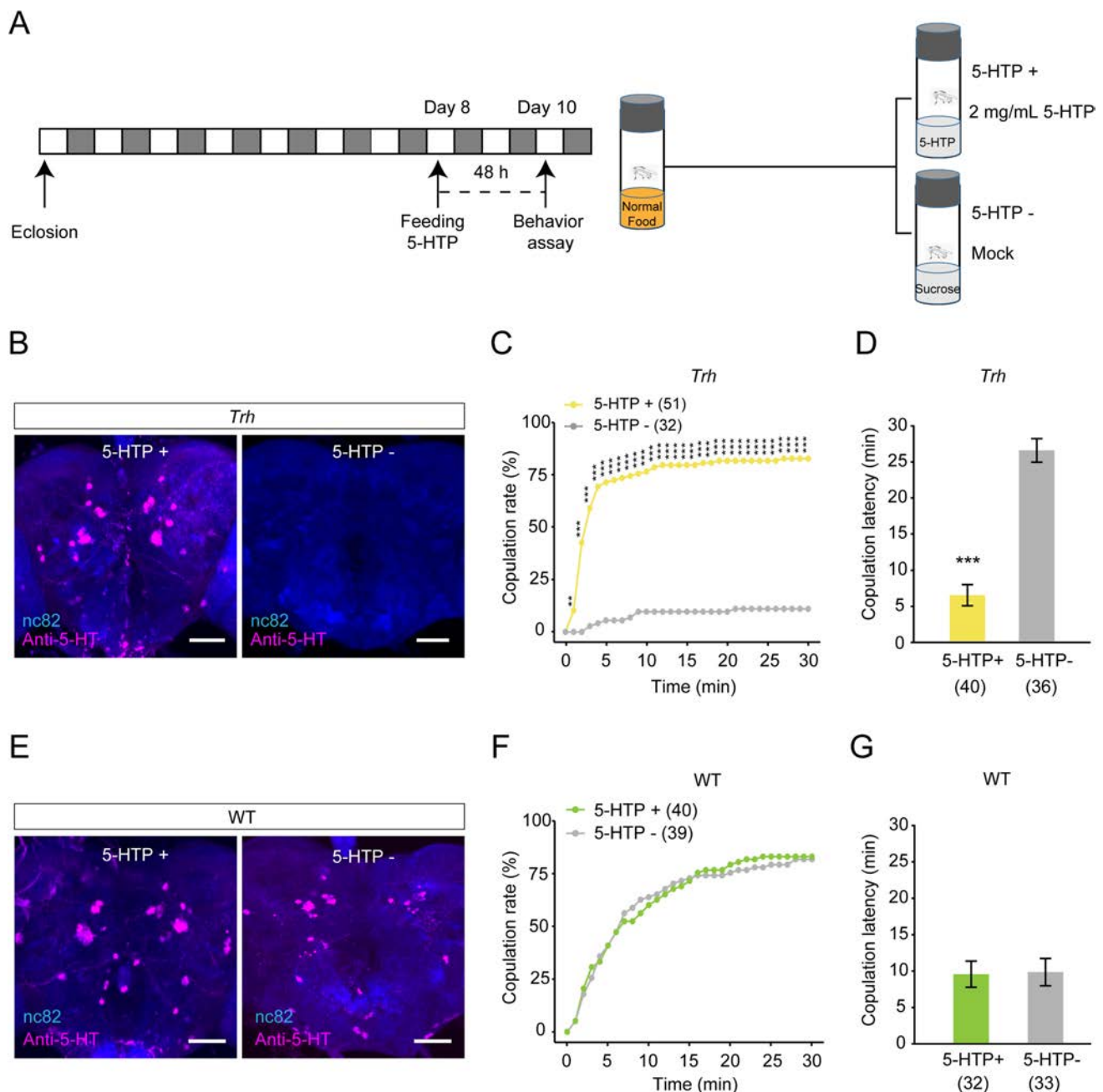
Statistical analysis and graphics were applied with the R system 4.0.2 (<https://www.r-project.org/>), MatLab software (MathWorks Inc., MA, USA), and GraphPad Prism 7 software (GraphPad Software, San Diego, USA). The  $\chi^2$  test was used to compare the copulation rate of different groups at various time points. The Mann-Whitney *U* test was applied for two-group comparisons. Kruskal-Wallis with the *post hoc* Mann-Whitney *U* test was used to compare the differences between multiple groups. All data are shown as the mean  $\pm$  SEM. Sample sizes are indicated in the figures. Statistical significance was set at  $P < 0.01$ .

## Results

### 5-HT Modulates Virgin Female Receptivity

In *Drosophila*, it has been found that virgin female receptivity is associated with the release of dopamine (DA), drosulfakinin (DSK), and SIFamide (SIFa) [51–54]. To identify the role of other neurochemicals involved in regulating virgin female receptivity, we screened 108 chemoconnectome (CCT) knockout lines generated by the CRISPR-Cas9 system [49].

Preliminary screening (unpublished data) showed that virgin female receptivity might be regulated by the *Trh* gene that encodes an enzyme catalyzing the first and rate-limiting step of 5-HT biosynthesis (Fig. 1A) [55, 56]. We confirmed the *Trh* knockout line by using PCR analysis at the *Trh* locus in genomic DNA samples (Fig. 1B, C) and by detecting the immunoreactivity of 5-HT in the central brain (Fig. 1D). 5-HT immunoreactivity was found in the brain of wild-type and heterozygous flies (Figs. 1D), but was absent in homozygous *Trh*-knockout flies (Fig. 1D). We found that knockout



**Fig. 2** Acutely feeding 5-HTP restores 5-HT expression and virgin female receptivity in *Trh*-knockout mutants. **A** The protocol of the feeding assay in the rescue experiment. **B** Immunoreactivity of 5-HT is restored in the brain of *Trh* mutant females after feeding 5-HTP for 48 h (scale bars, 50  $\mu$ m). **C**, **D** Virgin female receptivity is restored by feeding *Trh* mutants with 5-HTP. In *Trh*-knockout mutants, the copulation rate is elevated to the normal level (**C**) and the copulation latency is shortened (**D**). **E** Immunoreactivity of 5-HT in wild-type

females is not significantly affected by feeding 5-HTP (scale bars, 50  $\mu$ m). **F**, **G** Sexual receptivity of wild-type virgin females is not affected by 5-HTP feeding. Wild-type females show a comparable copulation rate (**F**) and copulation latency (**G**) with or without 5-HTP feeding. \*\*\* $P < 0.001$ , \*\* $P < 0.01$ , otherwise no significant difference ( $\chi^2$  test for copulation rate; Mann-Whitney  $U$  test for copulation latency).  $n$  values are shown in parentheses; error bars,  $\pm$ SEM.

of *Trh* reduced the virgin female copulation rate and prolonged the copulation latency compared to heterozygous and wild-type control females (Fig. 1E, F). In contrast, we found that *Trh*-knockout females showed locomotor activity

comparable to control females (Fig. 1G). Furthermore, knocking down *Trh* expression pan-neuronally using the *elav-GAL4* driver reduced the copulation rate and increased



the copulation latency in virgin females (Fig. 1H, I). Given that *Trh* heterozygous and wild-type females displayed similar phenotypes, we mainly used wild-type females as control flies in later experiments.

To determine whether restoration of the 5-HT expression level could rescue the sexual receptivity of *Trh*-knockout females, we performed pharmacological rescue experiments by feeding them with 5-HTP (Fig. 2A). After feeding with 2 mg/mL 5-HTP, 5-HT immunofluorescence was restored in the brain of *Trh* mutant females (Fig. 2B). Furthermore, both copulation rate and copulation latency were rescued to normal levels in *Trh* mutant females (Fig. 2C, D). In contrast, 5-HT immunofluorescence and female sexual receptivity were not significantly affected in wild-type females by feeding with 5-HTP (Fig. 2E–G). These results indicate that 5-HT is crucial for virgin female receptivity in *Drosophila*.

To determine whether 5-HT specifically regulates virgin female receptivity, or affects sexual behavior in both virgin and mated females, we next tested egg-laying and re-mating behaviors in *Trh*-knockout or -knockdown females. We found that *Trh*-knockout virgin females did not show increased egg-laying (Fig. S1A), or any re-mating behavior after mating, like wild-type controls (Fig. S1B). We also observed similar phenotypes in *Trh* RNAi-knockdown females (Fig. S1C, D). Thus, 5-HT specifically regulates virgin female receptivity but not post-mating behaviors.

### *Trh*<sup>+</sup> Neurons Regulate Virgin Female Receptivity

We used a *UAS-mCD8GFP* reporter to visualize the expression pattern of the newly-generated *Trh-GAL4* [36] (Fig. 3A). The *Trh-GAL4* labeled 5-HT clusters in the brain similar to those reported by previous studies [57, 58]. We mapped the distribution of *Trh*<sup>+</sup> neurons in the central brain including the anterior dorsomedial protocerebrum (ADMP), anterior lateral protocerebrum (ALP), anterior medial protocerebrum (AMP), lateral subesophageal ganglion (SEL), lateral protocerebrum (LP), medial subesophageal ganglion (SEM), posterior medial protocerebrum, dorsal (PMPD), medial (PMPM), and ventral (PMPV) posterior medial protocerebrum, and posterior lateral protocerebrum (PLP) (Fig. 3B).

We then analyzed whether *Trh*<sup>+</sup> neurons are involved in the modulation of female sexual receptivity. We activated all *Trh*-expressing neurons by using PACα [59], which specifically enhances intracellular cAMP levels after blue light stimulation, and also has a more moderate activation effect than *CsChrimson* [60] or *dTrpA1* [61], since the *Trh-GAL4* labels a large number of neurons and strong activation of these neurons may have side-effects. We found that

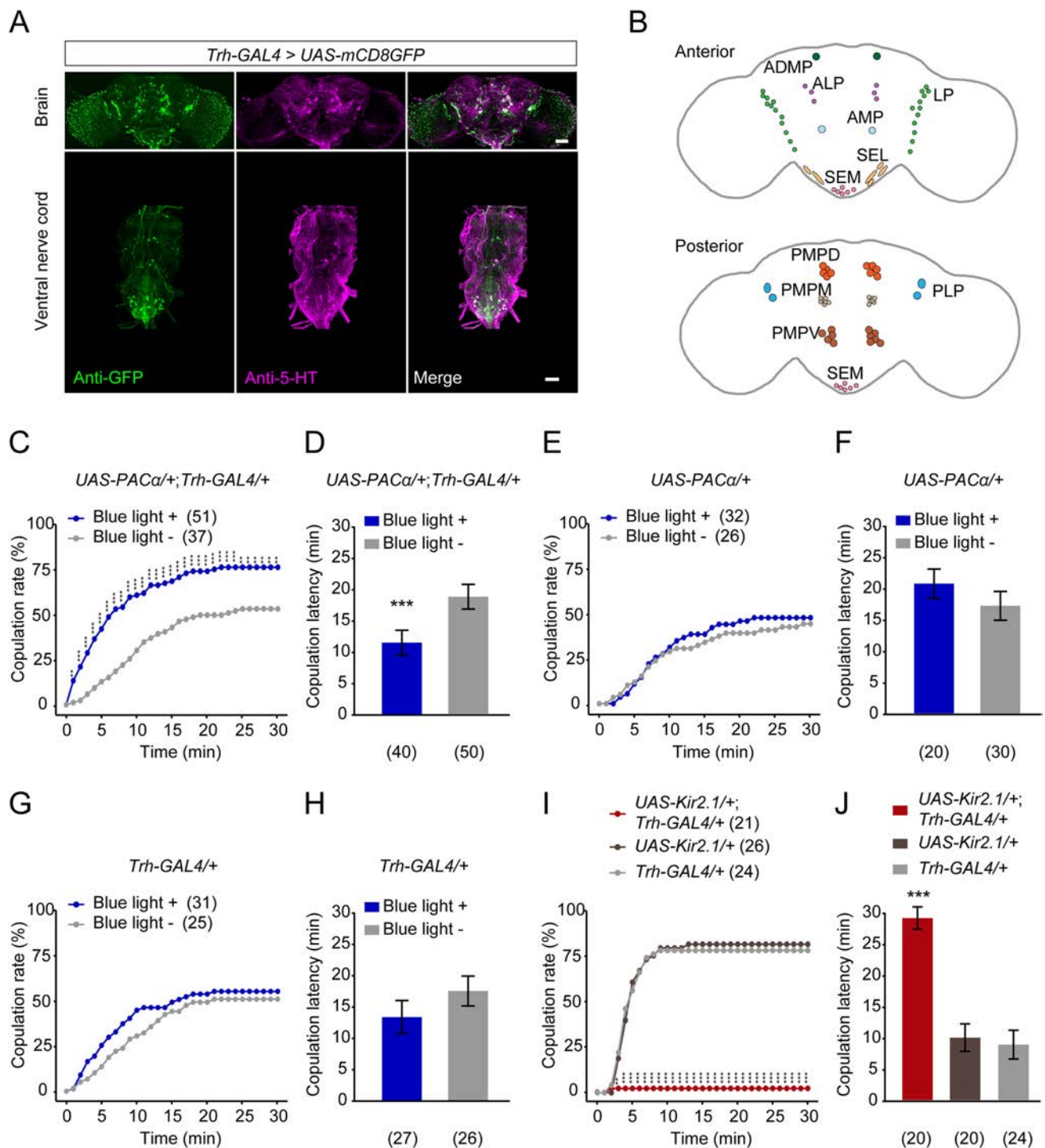
activation of *Trh-GAL4* neurons increased copulation rate and decreased copulation latency in *UAS-PACα/Trh-GAL4* virgin females (Fig. 3C, D). In contrast, there was no significant change in copulation rate and copulation latency after blue light stimulation in *UAS-PACα/+* or *Trh-GAL4/+* control females (Fig. 3E–H).

To further confirm whether *Trh*<sup>+</sup> neurons are necessary for virgin female receptivity, we silenced these neurons by expressing the inwardly-rectifying K<sup>+</sup> channel (*Kir2.1*) [62]. *UAS-Kir2.1/Trh-GAL4* virgin females exhibited a dramatic reduction in copulation rate and a prolonged copulation latency compared to control females (Fig. 3I, J). We also found that blocking neurotransmission from *Trh*<sup>+</sup> neurons expressing the temperature-sensitive *shibire<sup>ts</sup>* (*shi<sup>ts</sup>*) [63] significantly reduced virgin female receptivity (Fig. S2). Furthermore, neither activation nor inactivation of *Trh*<sup>+</sup> neurons affected sexual receptivity in mated females (Tables S1, S2). Taken together, our findings indicate that the activity of *Trh*<sup>+</sup> neurons positively regulates sexual receptivity in virgin, but not mated females.

### *Trh*<sup>+</sup>*fru*<sup>+</sup> neurons Mediate Virgin Female Receptivity

We next set out to narrow down the serotonergic neurons that promote virgin female receptivity. As previous studies revealed crucial roles of *fru* or *dsx* neurons in regulating female receptivity [15, 41, 46], we tried to specifically label and manipulate *Trh*<sup>+</sup>*fru*<sup>+</sup> or *Trh*<sup>+</sup>*dsx*<sup>+</sup> neurons. We first applied the FLP/FRT intersectional strategy [64] to restrict expression in overlapping *Trh*<sup>+</sup> and *fru*<sup>+</sup> neurons (Fig. 4A). *UAS>stop>CsChrimson; fru<sup>LexA</sup> LexAop2-FlpL/Trh-GAL4* virgin females, in which the overlapping *Trh*<sup>+</sup> and *fru*<sup>+</sup> neurons (referred to as *Trh*<sup>+</sup>*fru*<sup>+</sup> neurons hereafter) express the optogenetic effector *CsChrimson* [60], displayed a much higher copulation rate and decreased copulation latency with red light stimulation (Fig. 4B, C). In contrast, control *UAS>stop>CsChrimson; fru<sup>LexA</sup> LexAop2-FlpL/+*, or *Trh-GAL4/+* virgin females did not exhibit red light-induced changes in receptivity (Fig. 4D–G). We also used the thermogenetic effector *TrpA1* [61] to activate the *Trh*<sup>+</sup>*fru*<sup>+</sup> neurons, and found that heat-induced activation of *Trh*<sup>+</sup>*fru*<sup>+</sup> neurons slightly but significantly enhanced virgin female receptivity (Fig. S3). These results indicate that activation of *Trh*<sup>+</sup>*fru*<sup>+</sup> neurons is able to promote virgin female receptivity.

We next tried to silence the *Trh*<sup>+</sup>*fru*<sup>+</sup> neurons using the same intersectional strategy to express the inwardly-rectifying K<sup>+</sup> channel *Kir2.1* [62]. Silencing the *Trh*<sup>+</sup>*fru*<sup>+</sup> neurons dramatically reduced copulation rate and increased copulation latency in virgin females compared with control females (Fig. 4H, I). The reduction of receptivity in these females was not due to locomotor activity as



**Fig. 3** *Trh*<sup>+</sup> neurons regulate virgin female receptivity. **A** Expression pattern of the *Trh* gene and *Trh-GAL4* visualized with anti-5-HT antibody (magenta) and anti-GFP (green) in a *UAS-mCD8-GFP/Trh-GAL4* female brain and VNC (scale bars, 50  $\mu$ m). **B** Anterior (upper) and posterior views (lower) of *Trh*<sup>+</sup> neurons labeled by *Trh-GAL4* in the brain. **C, D** The copulation rate is increased (**C**) and the copulation latency is shortened (**D**) after blue light stimulation in *UAS-PACα/Trh-GAL4* virgin females. **E, F** *UAS-PACα/+* control females do not display a significantly changed copulation rate (**E**) and copulation latency (**F**) after blue light stimulation. **G, H** *Trh-GAL4/+* control females show a comparable copulation rate (**G**) and copulation latency (**H**) with or without blue light stimulation. **I, J**

*UAS-Kir2.1/Trh-GAL4* virgin females exhibit a decreased copulation rate (**I**) and prolonged copulation latency (**J**) relative to control females. \*\*\* $P < 0.001$ , \*\* $P < 0.01$ , otherwise no significant difference ( $\chi^2$  test for copulation rate analysis; Mann-Whitney  $U$  test for **D, F**, and **H**; Kruskal-Wallis with *post hoc* Mann-Whitney  $U$  test for **J**).  $n$  values are shown in parentheses; error bars,  $\pm$ SEM. ADMP, anterior dorsomedial protocerebrum; ALP, anterior lateral protocerebrum; AMP, anterior medial protocerebrum; LP, lateral protocerebrum; PLP, posterior lateral protocerebrum; PMPD, dorsal, PMPM, medial, and PMPV, ventral posterior medial protocerebrum; SEL, lateral and SEM, medial subesophageal ganglion.

they displayed a walking speed comparable with control females (Fig. 4J). We also used the same intersectional strategy to silence the overlapping *Trh*<sup>+</sup> and *dsx*<sup>+</sup> neurons, but did not find any significant change in virgin female receptivity (Fig. S4A, B). Thus, these findings indicate that *Trh*<sup>+</sup>*fru*<sup>+</sup> neurons are crucial for virgin female receptivity.

### Sexually Dimorphic *Trh*<sup>+</sup>*fru*<sup>+</sup> PLP Neurons Promote Virgin Female Receptivity

The above results demonstrated a crucial role of *Trh*<sup>+</sup>*fru*<sup>+</sup> neurons in regulating virgin female receptivity. To visualize the *Trh*<sup>+</sup>*fru*<sup>+</sup> neurons, we first applied double-labeling in *Trh-GAL4/UAS-stingerGFP; fru<sup>LexA</sup>/LexAop-Redstinger* flies, and found that a subset of PLP neurons was co-labeled by *Trh*<sup>+</sup> and *fru*<sup>+</sup> in the brain of females (Fig. 5A, B). In addition, we applied the FLP/FRT intersectional strategy to express GFP in both sexes of *UAS>stop>mCD8-GFP; fru<sup>LexA</sup> LexAop2-FlpL/Trh-GAL4* flies. We observed GFP expression in ~3 pairs of PLP neurons (Fig. 5C) and a few neurons in the ventral nerve cord (VNC) in females (Fig. 5C); in contrast, we observed 1–2 pairs of PLP neurons as well as a few other neurons in the brain (Fig. 5C) and VNC in males (Fig. 5C). Thus, there might be female-specific *Trh*<sup>+</sup>*fru*<sup>+</sup> PLP neurons that regulate virgin female receptivity. We also used the same strategy to visualize *Trh*<sup>+</sup>*dsx*<sup>+</sup> neurons, and observed sparse expression in the brain and VNC (Fig. S4C). Nevertheless, these *Trh*<sup>+</sup>*dsx*<sup>+</sup> neurons were not involved in virgin female receptivity (Fig. S4A, B). In addition, we used the above strategy to express *nsyb-GFP* and *Dscam-GFP* and localized presynaptic and postsynaptic sites of the *Trh*<sup>+</sup>*fru*<sup>+</sup> PLP neurons in females (Fig. S5).

To further test the role of *Trh*<sup>+</sup>*fru*<sup>+</sup> PLP neurons in female receptivity, we monitored the neural activity of PLP neurons by expressing TRIC [65] in virgin and mated females. The TRIC signal in PLP neurons was significantly stronger in virgins than that in mated females (Fig. 5D). Thus, the spontaneous activity of *Trh*<sup>+</sup>*fru*<sup>+</sup> PLP neurons is higher in virgin females, which might reflect an internal state of female receptivity. Together, these results demonstrate that a subset of sexually dimorphic *Trh*<sup>+</sup>*fru*<sup>+</sup> PLP neurons promotes sexual receptivity in virgin females.

### 5-HT<sub>1A</sub> and 5-HT<sub>7</sub> Receptors Regulate Virgin Female Receptivity

There are five types of 5-HT G-protein-coupled receptors (GPCRs): 5-HT<sub>1A</sub>, 5-HT<sub>1B</sub>, 5-HT<sub>2A</sub>, 5-HT<sub>2B</sub>, and 5-HT<sub>7</sub> [36, 66–68]. These receptors, which are mammalian orthologs of the 5-HT receptor family, are expressed widely in the

central nervous system [69] (Fig. S6), and regulate complex behaviors [37, 70–72]. To identify which 5-HT receptors are involved in virgin female receptivity, we used knockout lines of each 5-HT receptor and found that the copulation latency of 5-HT<sub>1A</sub>- and 5-HT<sub>7</sub>-knockout females was significantly longer than in the wild-type control females (Fig. 6A). In addition, knockout of 5-HT<sub>1A</sub> and 5-HT<sub>7</sub>, but not 5-HT<sub>1B</sub>, 5-HT<sub>2A</sub>, or 5-HT<sub>2B</sub>, significantly reduced the copulation rate in virgin females (Fig. 6B–F).

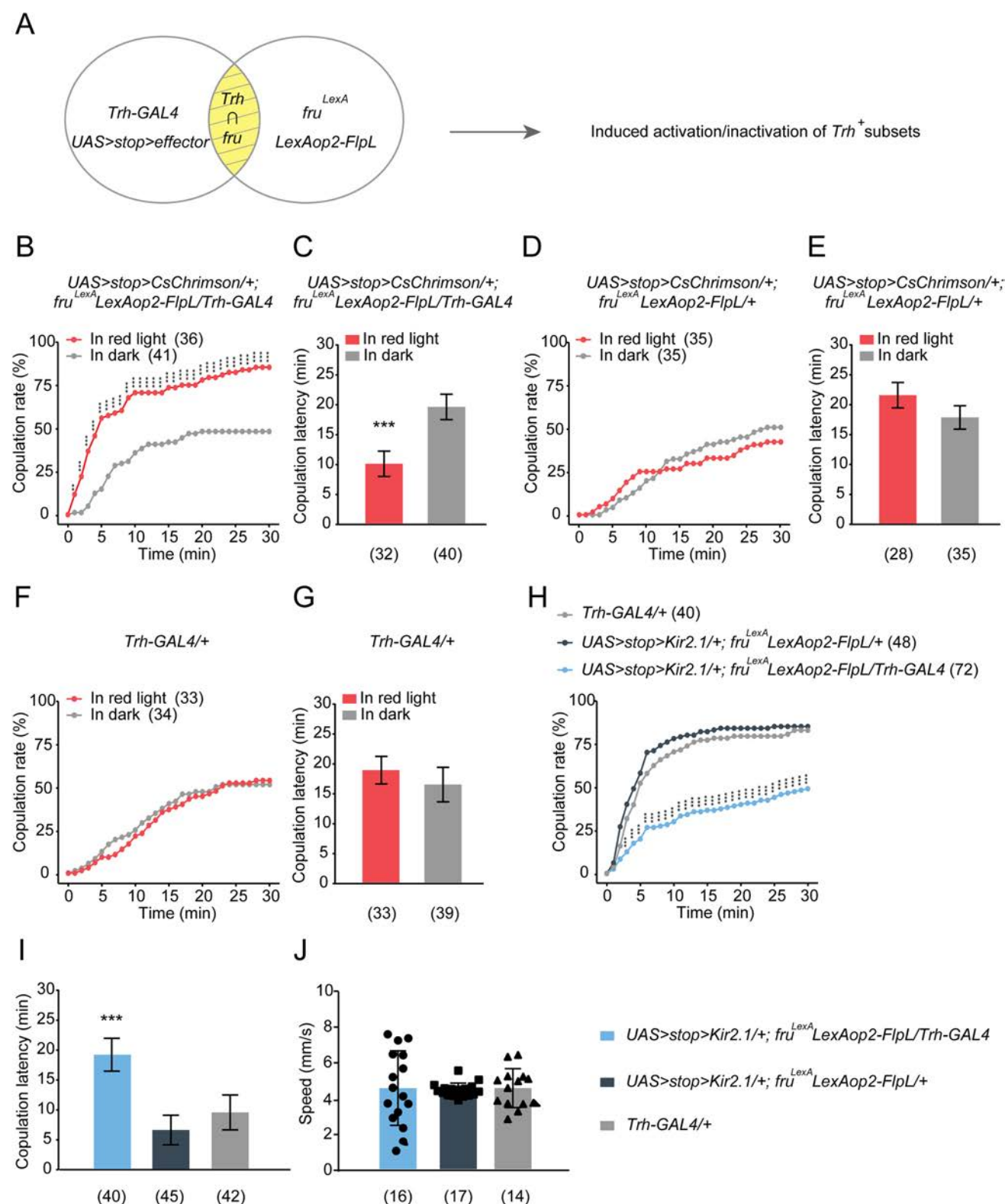
Given that female sexual receptivity was reduced in the 5-HT<sub>1A</sub> and 5-HT<sub>7</sub> mutants, we analyzed whether overexpressing 5-HT<sub>1A</sub> or 5-HT<sub>7</sub> in 5-HT<sub>1A</sub> or 5-HT<sub>7</sub> mutants could restore female receptivity. We used *elav-GAL4* to drive the expression of *UAS-5-HT<sub>1A</sub>* or *UAS-5-HT<sub>7</sub>* in 5-HT<sub>1A</sub> or 5-HT<sub>7</sub> mutant flies, respectively. We found that the copulation rate was increased, and copulation latency was reduced in 5-HT<sub>1A</sub> mutant females with *elav-GAL4*-driven expression of 5-HT<sub>1A</sub> (Fig. 6G, H). Meanwhile, the copulation rate and the copulation latency of 5-HT<sub>7</sub> knockout females were also restored to normal levels with *elav-GAL4*-driven expression of 5-HT<sub>7</sub> (Fig. 6I, J). These results suggest that 5-HT<sub>1A</sub> and 5-HT<sub>7</sub> receptors are involved in virgin female receptivity.

## Discussion

In animals, males often initiate courtship, and females decide whether to accept or reject copulation. Acceptance by females is a prerequisite for reproductive success, which is determined not only by external factors but also by internal sexual motivation. Monoamine neurotransmitters and neuropeptides have been found to regulate female receptivity, such as dopamine [51, 53], octopamine [27], DSK [54], and SIFa [52]. Here, we showed that 5-HT signaling plays a critical role in virgin female receptivity. Both the knockout and *RNAi* knockdown of *Trh* reduced the receptivity. 5-HT may regulate virgin female receptivity through two of the 5-HT receptors, 5-HT<sub>1A</sub> and 5-HT<sub>7</sub>. Furthermore, we identified ~3 pairs of sexually dimorphic *Trh*<sup>+</sup>*fru*<sup>+</sup> PLP neurons in the female brain that promote sexual receptivity in virgin females.

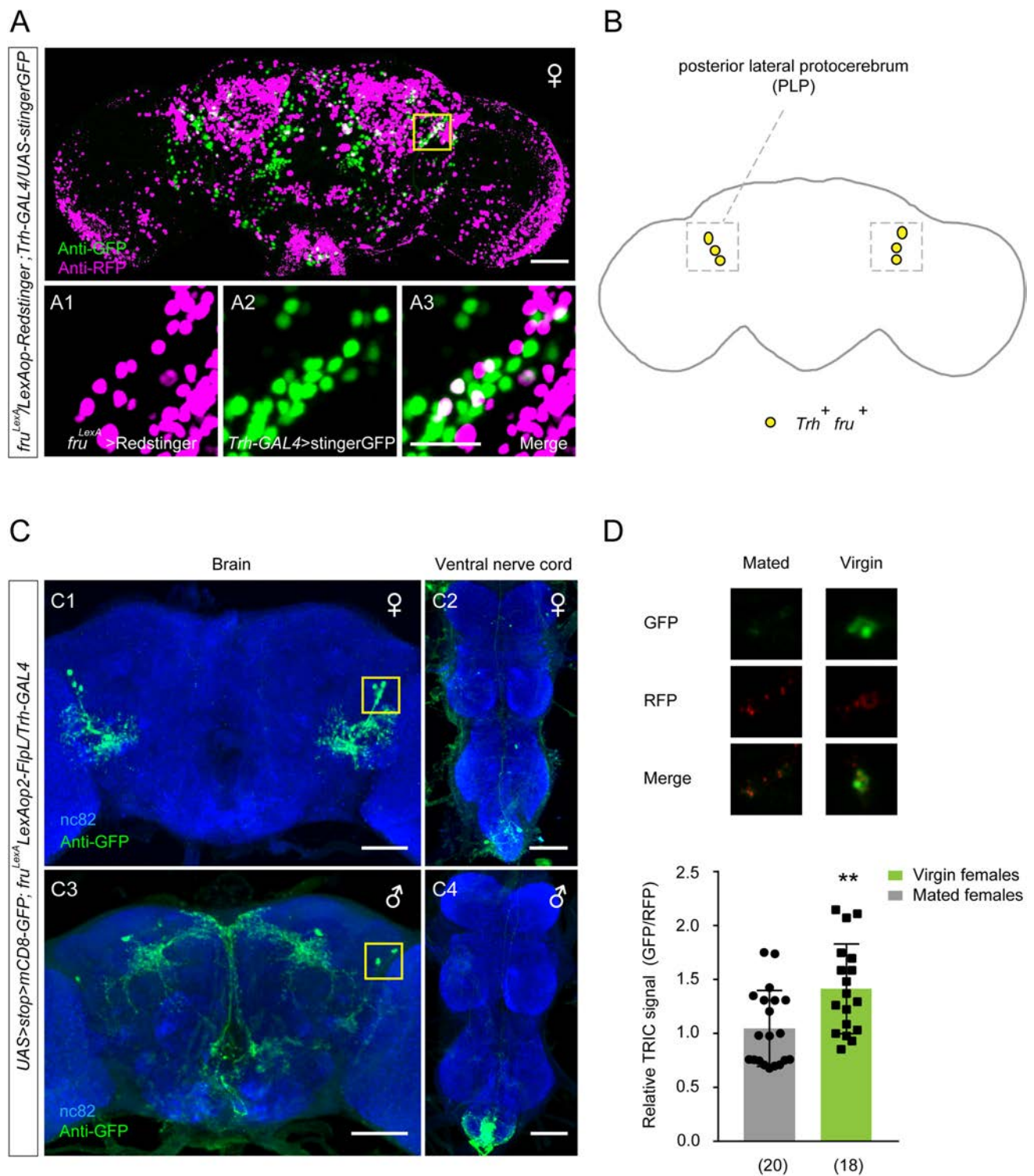
5-HT is a well-known conserved molecule, which participates in regulating sexual behavior in a wide range of species [73]. In mammals, a fraction of 5-HT is produced in the central nervous system to regulate male sexual behavior, such as ejaculation and orgasm [74–77]. Moreover, 5-HT is required for male sexual preference: male mice lacking 5-HT prefer to court males rather than females [78]. Although the role of 5-HT has been





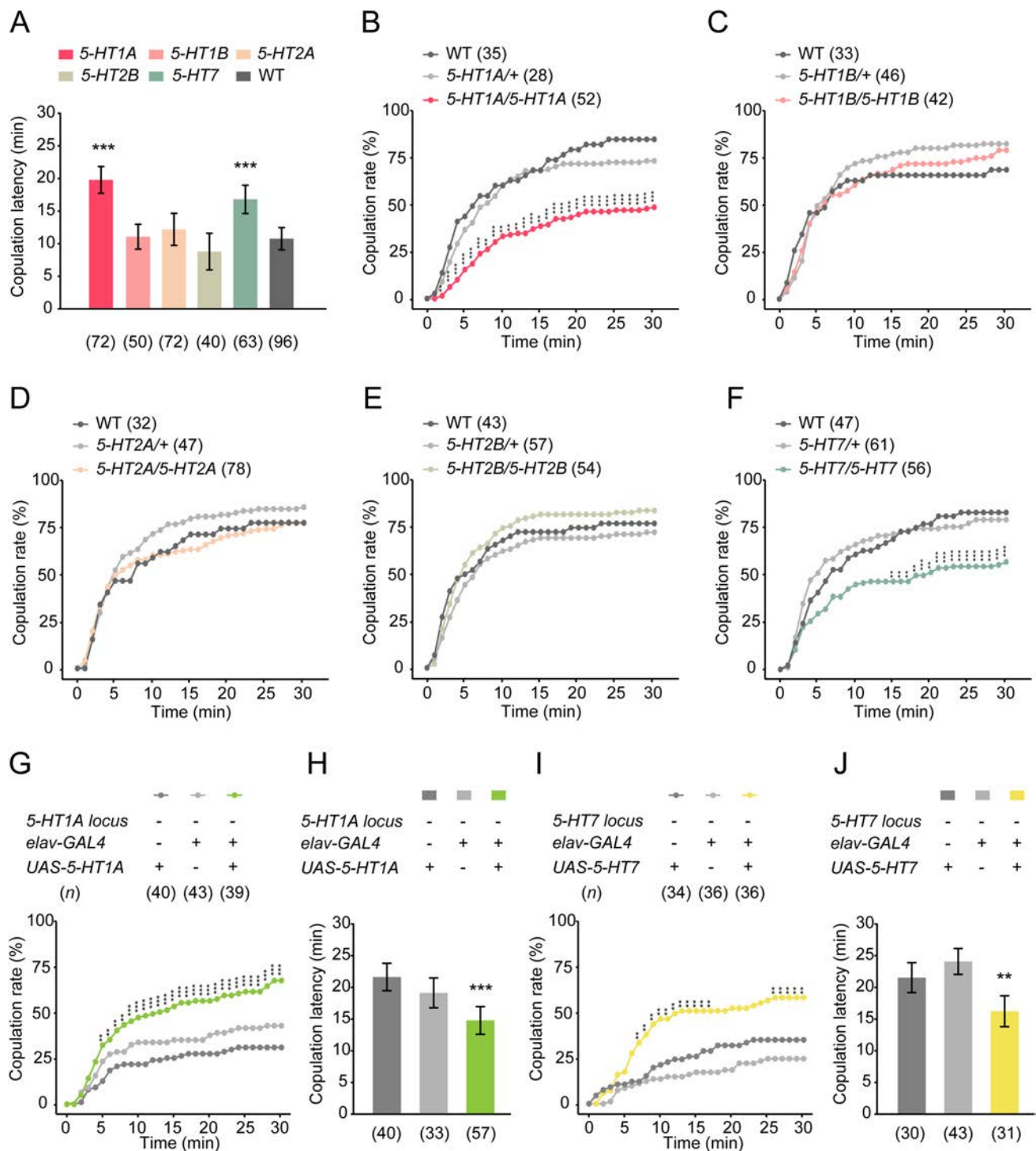
**Fig. 4** *Tth<sup>+</sup>fru<sup>+</sup>* neurons mediate virgin female receptivity. **A** The intersectional strategy used to narrow down the serotonergic neurons. FLP is driven by *fru<sup>LexA</sup>* LexAop2 to excise the transcriptional stop cassette, allowing the expression of specific effectors in intersecting neurons (*Tth<sup>+</sup>fru<sup>+</sup>*). **B, C** Activation of *Tth<sup>+</sup>fru<sup>+</sup>* neurons with red light increases the copulation rate (**B**) and decreases the copulation latency (**C**) in *UAS>stop>CsChrimson; fru<sup>LexA</sup> LexAop2-FlpL/Trh-GAL4* virgin females. **D–G** *UAS>stop>CsChrimson; fru<sup>LexA</sup> LexAop2-FlpL/+* or *Trh-GAL4/+* control

virgin females do not show a red light-induced change in copulation rate or copulation latency. **H, I** Silencing the *Tth<sup>+</sup>fru<sup>+</sup>* neurons decreases copulation rate (**H**) and prolongs copulation latency (**I**) in virgin females compared with control females. **J** Inactivation of *Tth<sup>+</sup>fru<sup>+</sup>* neurons in these females does not affect locomotor speed. \*\*\**P* < 0.001, \*\**P* < 0.01, otherwise no significant difference ( $\chi^2$  test for copulation rate; Mann-Whitney *U* test for **C**, **E**, and **G**; Kruskal-Wallis with *post hoc* Mann-Whitney *U* test for **I** and **J**). *n* values shown in parentheses; error bars,  $\pm$ SEM.



**Fig. 5** Identification of sexually dimorphic *Trh<sup>+</sup>fru<sup>+</sup>* PLP neurons. **A** The cell cluster of PLP neurons (yellow box) is labeled by *Trh-GAL4/UAS-stingerGFP* (green) and *fru<sup>LexA</sup>/LexAop-Redstinger* (magenta) [scale bars, 50  $\mu$ m (upper) and 20  $\mu$ m (lower)]. **B** Schematic of overlapped *Trh<sup>+</sup>fru<sup>+</sup>* PLP neurons (yellow dots) in the brain of females. **C** Neurons co-expressing *Trh<sup>+</sup>* and *fru<sup>+</sup>* visualized with anti-GFP

(green) in females and males. Anti-nc82 (blue) indicates the neuropil of the central nervous system. Yellow boxes indicate cell bodies of the *Trh<sup>+</sup>fru<sup>+</sup>* PLP neurons (scale bars, 50  $\mu$ m). **D** The TRIC signal in PLP neurons is significantly stronger in virgin females than that in mated females. \*\**P* < 0.01 (Mann-Whitney *U* test). *n* values shown in parentheses; error bars,  $\pm$ SEM.



**Fig. 6** 5-HT<sub>1A</sub> and 5-HT<sub>7</sub> receptors are involved in virgin female receptivity. **A** The copulation latency is extended in 5-HT<sub>1A</sub>- and 5-HT<sub>7</sub>-knockout females compared to wild-type control females. **B–F** Copulation rate of females with 5-HT receptor knockout during a 30-min observation period. Knockout of 5-HT<sub>1A</sub> (**B**) and 5-HT<sub>7</sub> (**F**), but not 5-HT<sub>1B</sub> (**C**), 5-HT<sub>2A</sub> (**D**), or 5-HT<sub>2B</sub> (**E**), significantly reduces the copulation rate in virgin females. **G**, **H** The copulation rate (**G**) is increased, and the copulation latency (**H**) is reduced in

5-HT<sub>1A</sub> mutant females with the *elav-GAL4*-driven expression of 5-HT<sub>1A</sub>. **I**, **J** The *elav-GAL4*-driven expression of *UAS-5-HT7* in 5-HT<sub>7</sub>-knockout females also restores the copulation rate (**I**) and copulation latency (**J**) to normal levels. \*\*\* $P < 0.001$ , \*\* $P < 0.01$ , otherwise no significant difference (Kruskal-Wallis with *post hoc* Mann-Whitney *U* test for copulation latency;  $\chi^2$  test for copulation rate). *n* values are shown in parentheses; error bars,  $\pm$ SEM.



unrevealed in the modulation of male sexual behavior, little is known about its role in female sexual behavior. We found that *Trh* knockout females showed a dramatic reduction in receptivity, which was rescued by acutely feeding 5-HTP before the receptivity assay. Loss of 5-HT specifically impaired virgin female receptivity but not post-mating behaviors. Furthermore, the spontaneous activity of a subset of 5-HT-releasing neurons was stronger in receptive virgin females. We speculate that 5-HT is required to maintain proper activity in sex-promoting neurons, and thus serves as a positive regulator for sexual motivation in virgin females.

All 5-HT receptors, 5-HT<sub>1A</sub>, 5-HT<sub>1B</sub>, 5-HT<sub>2A</sub>, 5-HT<sub>2B</sub>, and 5-HT<sub>7</sub>, play coordinated roles in serotonin signaling to modulate diverse complex behaviors including aggression, locomotion, and sleep [36, 79, 80]. Notably, knockout of either *Trh* or individual 5-HT receptors did not result in any evident developmental deficit in flies, which suggests that the role of 5-HT signaling in a variety of behaviors is not due to a developmental deficit. We found that the 5-HT<sub>1A</sub> and 5-HT<sub>7</sub> receptors, but not the 5-HT<sub>1B</sub>, 5-HT<sub>2A</sub>, or 5-HT<sub>2B</sub> receptors, are involved in virgin female receptivity. Knockout of 5-HT<sub>1A</sub> or 5-HT<sub>7</sub> reduced the receptivity, although not as severely as knockout of *Trh*, suggesting that 5-HT receptors might have parallel and redundant roles in virgin female receptivity. We also noted that knockout of 5-HT<sub>2B</sub> induced a slight increase in the female copulation rate. It has been reported that 5-HT<sub>2B</sub> regulates the amount of sleep and sleep homeostasis [36, 81], while sleep significantly influences female mating behaviors. Whether 5-HT<sub>2B</sub> functions to coordinate female sleep and sexual behavior awaits further investigation.

Approximately 90 serotonergic neurons are present in the central brain and are divided into several clusters into distinct brain regions [57, 58]. Distinct clusters of serotonergic neurons modulate various behaviors, such as walking, long-term memory, and feeding [38, 69]. Previous reports have indicated that female sexual receptivity is regulated by *fru*<sup>+</sup> neurons [23, 46, 82], which encouraged us to subdivide the serotonergic neurons involved in sexual receptivity by intersecting with *fru*<sup>+</sup> neurons. We identified *Trh*<sup>+</sup>*fru*<sup>+</sup> neurons in the PLP cluster to be crucial for virgin female receptivity. Interestingly, there were more *Trh*<sup>+</sup>*fru*<sup>+</sup> PLP neurons in females than in males, suggesting the involvement of female-specific *Trh*<sup>+</sup>*fru*<sup>+</sup> PLP neurons in female receptivity. Such dimorphism of *Trh*<sup>+</sup>*fru*<sup>+</sup> PLP neurons might be regulated by the presence/absence of Fru<sup>M</sup> protein in males and females, respectively, as found in other sexually dimorphic *fru*<sup>+</sup> neurons [83–85]. We also found that 5-HT functions in sexually dimorphic neurons to mediate male courtship behavior (unpublished data). Thus, 5-HT signaling regulates both male and female sexual

behavior through sexually dimorphic neural circuits. Future studies may reveal how 5-HT functions in each sex to mediate different aspects of sexual behavior, possibly through distinct 5-HT receptors.

**Acknowledgments** We thank Dr. Yi Rao (Peking University), Dr. Yufeng Pan (Southeast University), Dr. Jue Xie (Chinese Institute for Brain Research), Dr. Pengxiang Wu (Institute of Zoology, Chinese Academy of Sciences), Dr. Yan Zhu (Institute of Biophysics, Chinese Academy of Sciences), and Dr. Yu Mu (Institute of Neuroscience, Chinese Academy of Sciences) for valuable comments on this manuscript. We also thank Shaowei Hu and Yantong Yang for technical guidance and for providing fly stocks, and Bingcai Wang and Na Xiao for editing software. We also thank the members of Chuan Zhou's Laboratory for their comments and discussions. We thank the Bloomington Stock Center for fly stocks. This work was supported by the National Natural Science Foundation of China (Y711181133 and Y711241133) and the State Key Laboratory of Integrated Management of Pest Insects and Rodents at the Institute of Zoology of the Chinese Academy of Sciences (Y652751E03).

**Conflict of interests** The authors claim that there is no conflict of interest.

**Open Access** This article is licensed under a Creative Commons Attribution 4.0 International License, which permits use, sharing, adaptation, distribution and reproduction in any medium or format, as long as you give appropriate credit to the original author(s) and the source, provide a link to the Creative Commons licence, and indicate if changes were made. The images or other third party material in this article are included in the article's Creative Commons licence, unless indicated otherwise in a credit line to the material. If material is not included in the article's Creative Commons licence and your intended use is not permitted by statutory regulation or exceeds the permitted use, you will need to obtain permission directly from the copyright holder. To view a copy of this licence, visit <http://creativecommons.org/licenses/by/4.0/>.

## References

1. Dickson BJ. Wired for sex: the neurobiology of *Drosophila* mating decisions. *Science* 2008, 322: 904–909.
2. Billeter JC, Levine JD. Who is he and what is he to you? Recognition in *Drosophila melanogaster*. *Curr Opin Neurobiol* 2013, 23: 17–23.
3. Pavlou HJ, Goodwin SF. Courtship behavior in *Drosophila melanogaster*: Towards a 'courtship connectome.' *Curr Opin Neurobiol* 2013, 23: 76–83.
4. Ito H, Fujitani K, Usui K, Shimizu-Nishikawa K, Tanaka S, Yamamoto D Sexual orientation in *Drosophila* is altered by the satori mutation in the sex-determination gene *fruitless* that encodes a zinc finger protein with a BTB domain *Proc Natl Acad Sci U S A* 1996, 93: 9687–9692.
5. Peng Q, Chen J, Pan Y. From *fruitless* to sex: On the generation and diversification of an innate behavior. *Genes Brain Behav* 2021, 20: e12772.
6. Greenspan RJ. Understanding the genetic construction of behavior. *Sci Am* 1995, 272: 72–78.
7. Sturtevant AH. Experiments on sex recognition and the problem of sexual selection in *Drosophila*. *J Animal Behav* 1915, 5: 351–366.

8. Greenspan RJ, Ferveur JF. Courtship in *Drosophila*. *Ann Rev Genet* 2000, 34: 205–232.
9. Pan Y, Baker BS. Genetic identification and separation of innate and experience-dependent courtship behaviors in *Drosophila*. *Cell* 2014, 156: 236–248.
10. Villella A, Hall JC. Neurogenetics of courtship and mating in *Drosophila*. *Adv Genet* 2008, 62: 67–184.
11. Gao C, Guo C, Peng Q, Cao J, Shohat-Ophir G, Liu D. Sex and death: Identification of feedback neuromodulation balancing reproduction and survival. *Neurosci Bull* 2020, 36: 1429–1440.
12. Datta SR, Vasconcelos ML, Ruta V, Luo S, Wong A, Demir E, *et al.* The *Drosophila* pheromone cVA activates a sexually dimorphic neural circuit. *Nature* 2008, 452: 473–477.
13. Deutsch D, Clemens J, Thiberge SY, Guan G, Murthy M. Shared song detector neurons in *Drosophila* male and female brains drive sex-specific behaviors. *Curr Biol* 2019, 29: 3200–3215.e5.
14. Liu C, Zhang B, Zhang L, Yang T, Zhang Z, Gao Z, *et al.* A neural circuit encoding mating states tunes defensive behavior in *Drosophila*. *Nat Commun* 2020, 11: 3962.
15. Zhou C, Pan Y, Robinett CC, Meissner GW, Baker BS. Central brain neurons expressing doublesex regulate female receptivity in *Drosophila*. *Neuron* 2014, 83: 149–163.
16. Aranha MM, Vasconcelos ML. Deciphering *Drosophila* female innate behaviors. *Curr Opin Neurobiol* 2018, 52: 139–148.
17. Cook R, Connolly K. Rejection responses by female *Drosophila melanogaster*: Their ontogeny, causality and effects upon the behaviour of the courting male. *Behaviour* 1973, 44: 142–165.
18. Ferveur JF. *Drosophila* female courtship and mating behaviors: Sensory signals, genes, neural structures and evolution. *Curr Opin Neurobiol* 2010, 20: 764–769.
19. Spieth HT. Courtship behavior in *Drosophila*. *Ann Rev Entomol* 1974, 19: 385–405.
20. Manning A. The control of sexual receptivity in female *Drosophila*. *Animal Behav* 1967, 15: 239–250.
21. Kubli E. Sex-peptides: Seminal peptides of the *Drosophila* male. *Cell Mol Life Sci* 2003, 60: 1689–1704.
22. Wolfner MF. Tokens of love: Functions and regulation of *Drosophila* male accessory gland products. *Insect Biochem Mol Biol* 1997, 27: 179–192.
23. Häsemeyer M, Yapici N, Heberlein U, Dickson BJ. Sensory neurons in the *Drosophila* genital tract regulate female reproductive behavior. *Neuron* 2009, 61: 511–518.
24. Rezával C, Pavlou HJ, Dornan AJ, Chan YB, Kravitz EA, Goodwin SF. Neural circuitry underlying *Drosophila* female postmating behavioral responses. *Curr Biol* 2012, 22: 1155–1165.
25. Yang CH, Rumpf S, Xiang Y, Gordon MD, Song W, Jan LY, *et al.* Control of the postmating behavioral switch in *Drosophila* females by internal sensory neurons. *Neuron* 2009, 61: 519–526.
26. Haussmann IU, Hemani Y, Wijesekera T, Dauwalder B, Soller M. Multiple pathways mediate the sex-peptide-regulated switch in female *Drosophila* reproductive behaviours. *Proc Biol Sci* 2013, 280: 20131938.
27. Rezával C, Nojima T, Neville MC, Lin AC, Goodwin SF. Sexually dimorphic octopaminergic neurons modulate female postmating behaviors in *Drosophila*. *Curr Biol* 2014, 24: 725–730.
28. Ding Z, Haussmann I, Ottiger M, Kubli E. Sex-peptides bind to two molecularly different targets in *Drosophila melanogaster* females. *J Neurobiol* 2003, 55: 372–384.
29. Yapici N, Kim YJ, Ribeiro C, Dickson BJ. A receptor that mediates the post-mating switch in *Drosophila* reproductive behaviour. *Nature* 2008, 451: 33–37.
30. Luo L. *Principles of neurobiology*, 2nd edn. Garland Science, New York, 2020, pp 80–87.
31. Ferguson J, Henriksen S, Cohen H, Mitchell G, Barchas J, Dement W. “Hypersexuality” and behavioral changes in cats caused by administration of p-chlorophenylalanine. *Science* 1970, 168: 499–501.
32. Obara Y, Fukano Y, Watanabe K, Ozawa G, Sasaki K. Serotonin-induced mate rejection in the female cabbage butterfly *Pieris rapae crucivora*. *Naturwissenschaften* 2011, 98: 989–993.
33. Soares MC, Paula JR, Bshary R. Serotonin blockade delays learning performance in a cooperative fish. *Animal Cogn* 2016, 19: 1027–1030.
34. Ma Q. Beneficial effects of moderate voluntary physical exercise and its biological mechanisms on brain health. *Neurosci Bull* 2008, 24: 265–270.
35. Zhu Y, Wu X, Zhou R, Sie O, Niu Z, Wang F, *et al.* Hypothalamic-pituitary-end-organ axes: Hormone function in female patients with major depressive disorder. *Neurosci. Bull* 2021, 37: 1176–1187.
36. Qian Y, Cao Y, Deng B, Yang G, Li J, Xu R, *et al.* Sleep homeostasis regulated by 5HT2b receptor in a small subset of neurons in the dorsal fan-shaped body of *Drosophila*. *Elife* 2017, 6: e26519.
37. Alekseyenko OV, Chan YB, Fernandez MP, Bülow T, Pankratz MJ, Kravitz EA. Single serotonergic neurons that modulate aggression in *Drosophila*. *Curr Biol* 2014, 24: 2700–2707.
38. Albin SD, Kaun KR, Knapp JM, Chung P, Heberlein U, Simpson JH. A subset of serotonergic neurons evokes hunger in adult *Drosophila*. *Curr Biol* 2015, 25: 2435–2440.
39. Yamamoto D. The neural and genetic substrates of sexual behavior in *Drosophila*. *Adv Genet* 2007, 59: 39–66.
40. Lee G, Hall JC, Park JH. *Doublesex* gene expression in the central nervous system of *Drosophila melanogaster*. *J Neurogenet* 2002, 16: 229–248.
41. Rideout EJ, Dornan AJ, Neville MC, Eadie S, Goodwin SF. Control of sexual differentiation and behavior by the doublesex gene in *Drosophila melanogaster*. *Nat Neurosci* 2010, 13: 458–466.
42. Waterbury JA, Jackson LL, Schedl P. Analysis of the doublesex female protein in *Drosophila melanogaster*: Role on sexual differentiation and behavior and dependence on intersex. *Genetics* 1999, 152: 1653–1667.
43. Williams TM, Selegue JE, Werner T, Gompel N, Kopp A, Carroll SB. The regulation and evolution of a genetic switch controlling sexually dimorphic traits in *Drosophila*. *Cell* 2008, 134: 610–623.
44. Stockinger P, Kvitsiani D, Rotkopf S, Tirián L, Dickson BJ. Neural circuitry that governs *Drosophila* male courtship behavior. *Cell* 2005, 121: 795–807.
45. Yamamoto D, Koganezawa M. Genes and circuits of courtship behaviour in *Drosophila* males. *Nat Rev Neurosci* 2013, 14: 681–692.
46. Kvitsiani D, Dickson BJ. Shared neural circuitry for female and male sexual behaviours in *Drosophila*. *Curr Biol* 2006, 16: R355–R356.
47. Wang K, Wang F, Forknall N, Yang T, Patrick C, Parekh R, *et al.* Neural circuit mechanisms of sexual receptivity in *Drosophila* females. *Nature* 2021, 589: 577–581.
48. Wang F, Wang K, Forknall N, Parekh R, Dickson BJ. Circuit and behavioral mechanisms of sexual rejection by *Drosophila* females. *Curr Biol* 2020, 30: 3749–3760.e3.
49. Deng B, Li Q, Liu X, Cao Y, Li B, Qian Y, *et al.* Chemoconnectomics: mapping chemical transmission in *Drosophila*. *Neuron* 2019, 101: 876–893.e4.
50. Wu F, Deng B, Xiao N, Wang T, Li Y, Wang R, *et al.* A neuropeptide regulates fighting behavior in *Drosophila melanogaster*. *Elife* 2020, 9: e54229.
51. Ishimoto H, Kamikouchi A. A feedforward circuit regulates action selection of pre-mating courtship behavior in female *Drosophila*. *Curr Biol* 2020, 30: 396–407.e4.
52. Terhzaz S, Rosay P, Goodwin SF, Veenstra JA. The neuropeptide SIFamide modulates sexual behavior in *Drosophila*. *Biochem. Biophys. Res Commun* 2007, 352: 305–310.

53. Neckameyer WS. Dopamine modulates female sexual receptivity in *Drosophila melanogaster*. *J Neurogenet* 1998, 12: 101–114.
54. Wu S, Guo C, Zhao H, Sun M, Chen J, Han C, *et al.* Drosulfakinin signaling in *fruitless* circuitry antagonizes P1 neurons to regulate sexual arousal in *Drosophila*. *Nat Commun* 2019, 10: 4770.
55. Kuhn DM, Rosenberg RC, Lovenberg W. Determination of some molecular parameters of tryptophan hydroxylase from rat mid-brain and murine mast cell. *J Neurochem* 1979, 33: 15–21.
56. Neckameyer WS, White K. A single locus encodes both phenylalanine hydroxylase and tryptophan hydroxylase activities in *Drosophila*. *J Biol Chem* 1992, 267: 4199–4206.
57. Alekseyenko OV, Lee C, Kravitz EA. Targeted manipulation of serotonergic neurotransmission affects the escalation of aggression in adult male *Drosophila melanogaster*. *PLoS One* 2010, 5: e10806.
58. Pooryasin A, Fiala A. Identified serotonin-releasing neurons induce behavioral quiescence and suppress mating in *Drosophila*. *J Neurosci* 2015, 35: 12792–12812.
59. Schröder-Lang S, Schwärzel M, Seifert R, Strücker T, Kateriya S, Looser J, *et al.* Fast manipulation of cellular cAMP level by light *in vivo*. *Nat Methods* 2007, 4: 39–42.
60. Klapoetke NC, Murata Y, Kim SS, Pulver SR, Birdsey-Benson A, Cho YK, *et al.* Independent optical excitation of distinct neural populations. *Nat Methods* 2014, 11: 338–346.
61. Hamada FN, Rosenzweig M, Kang K, Pulver SR, Ghezzi A, Jegla TJ, *et al.* An internal thermal sensor controlling temperature preference in *Drosophila*. *Nature* 2008, 454: 217–220.
62. Baines RA, Uhler JP, Thompson A, Sweeney ST, Bate M. Altered electrical properties in *Drosophila* neurons developing without synaptic transmission. *J Neurosci* 2001, 21: 1523–1531.
63. Kitamoto T. Conditional disruption of synaptic transmission induces male-male courtship behavior in *Drosophila*. *Proc Natl Acad Sci U S A* 2002, 99: 13232–13237.
64. Böhm RA, Welch WP, Goodnight LK, Cox LW, Henry LG, Gunter TC, *et al.* A genetic mosaic approach for neural circuit mapping in *Drosophila*. *Proc Natl Acad Sci U S A* 2010, 107: 16378–16383.
65. Gao XJ, Riabinina O, Li J, Potter CJ, Clandinin TR, Luo L. A transcriptional reporter of intracellular Ca<sup>2+</sup> in *Drosophila*. *Nat Neurosci* 2015, 18: 917–925.
66. Colas JF, Launay JM, Kellermann O, Rosay P, Maroteaux L. *Drosophila* 5-HT<sub>2</sub> serotonin receptor: Coexpression with fushi tarazu during segmentation. *Proc Natl Acad Sci U S A* 1995, 92: 5441–5445.
67. Witz P, Amlaiky N, Plassat JL, Maroteaux L, Borrelli E, Hen R. Cloning and characterization of a *Drosophila* serotonin receptor that activates adenylate cyclase. *Proc Natl Acad Sci U S A* 1990, 87: 8940–8944.
68. Saudou F, Hen R. 5-hydroxytryptamine receptor subtypes in vertebrates and invertebrates. *Neurochem Int* 1994, 25: 503–532.
69. Howard CE, Chen CL, Tabachnik T, Hormigo R, Ramdya P, Mann RS. Serotonergic modulation of walking in *Drosophila*. *Curr Biol* 2019, 29: 4218–4230.e8.
70. Ganguly A, Qi C, Bajaj J, Lee D. Serotonin receptor 5-HT<sub>7</sub> in *Drosophila* mushroom body neurons mediates larval appetitive olfactory learning. *Sci Rep* 2020, 10: 21267.
71. Gasque G, Conway S, Huang J, Rao Y, Vosshall LB. Small molecule drug screening in *Drosophila* identifies the 5HT<sub>2A</sub> receptor as a feeding modulation target. *Sci Rep* 2013, 3: 2120.
72. Siddiqui A, Niazi A, Shaharyar S, Wilson CA. The 5HT<sub>7</sub> receptor subtype is involved in the regulation of female sexual behaviour in the rat. *Pharmacol. Biochem Behav* 2007, 87: 386–392.
73. Berger M, Gray JA, Roth BL. The expanded biology of serotonin. *Annu Rev Med* 2009, 60: 355–366.
74. Dominguez JM, Hull EM. Serotonin impairs copulation and attenuates ejaculation-induced glutamate activity in the medial preoptic area. *Behav Neurosci* 2010, 124: 554–557.
75. Giuliano F. 5-hydroxytryptamine in premature ejaculation: Opportunities for therapeutic intervention. *Trends Neurosci* 2007, 30: 79–84.
76. Gradwell PB, Everitt BJ, Herbert J. 5-hydroxytryptamine in the central nervous system and sexual receptivity of female rhesus monkeys. *Brain Res* 1975, 88: 281–293.
77. Uphouse L. Pharmacology of serotonin and female sexual behavior. *Pharmacol Biochem Behav* 2014, 121: 31–42.
78. Liu Y, Jiang Y, Si Y, Kim JY, Chen ZF, Rao Y. Molecular regulation of sexual preference revealed by genetic studies of 5-HT in the brains of male mice. *Nature* 2011, 472: 95–99.
79. Yuan Q, Joiner WJ, Sehgal A. A sleep-promoting role for the *Drosophila* serotonin receptor 1A. *Curr Biol* 2006, 16: 1051–1062.
80. Alekseyenko OV, Chan YB, Okaty BW, Chang Y, Dymecki SM, Kravitz EA. Serotonergic modulation of aggression in *Drosophila* involves GABAergic and cholinergic opposing pathways. *Curr Biol* 2019, 29: 2145–2156.e5.
81. Xia M, Li Z, Li S, Liang S, Li X, Chen B, *et al.* Sleep deprivation selectively down-regulates astrocytic 5-HT<sub>2B</sub> receptors and triggers depressive-like behaviors via stimulating P2X<sub>7</sub> receptors in mice. *Neurosci Bull* 2020, 36: 1259–1270.
82. Sakurai A, Koganezawa M, Yasunaga K, Emoto K, Yamamoto D. Select interneuron clusters determine female sexual receptivity in *Drosophila*. *Nat Commun* 2013, 4: 1825.
83. Kimura KI, Ote M, Tazawa T, Yamamoto D. Fruitless specifies sexually dimorphic neural circuitry in the *Drosophila* brain. *Nature* 2005, 438: 229–233.
84. Yamamoto D, Sato K, Koganezawa M. Neuroethology of male courtship in *Drosophila*: From the gene to behavior. *J. Comp. Physiol. A Neuroethol. Sens Neural Behav Physiol* 2014, 200: 251–264.
85. Kimura KI, Hachiya T, Koganezawa M, Tazawa T, Yamamoto D. Fruitless and doublesex coordinate to generate male-specific neurons that can initiate courtship. *Neuron* 2008, 59: 759–769.



# Developmental Exposure to Bisphenol a Degrades Auditory Cortical Processing in Rats

Binliang Tang<sup>1,2</sup> · Kailin Li<sup>1,2</sup> · Yuan Cheng<sup>1,2</sup> · Guimin Zhang<sup>1,2</sup> ·  
Pengying An<sup>1,2</sup> · Yutian Sun<sup>1,2</sup> · Yue Fang<sup>1,2</sup> · Hui Liu<sup>1,2</sup> · Yang Shen<sup>1,2</sup> ·  
Yifan Zhang<sup>1,2</sup> · Ye Shan<sup>1</sup> · Étienne de Villers-Sidani<sup>3</sup> · Xiaoming Zhou<sup>1,2</sup>

Received: 11 December 2021 / Accepted: 8 March 2022 / Published online: 7 June 2022  
© Center for Excellence in Brain Science and Intelligence Technology, Chinese Academy of Sciences 2022

**Abstract** Developmental exposure to bisphenol A (BPA), an endocrine-disrupting contaminant, impairs cognitive function in both animals and humans. However, whether BPA affects the development of primary sensory systems, which are the first to mature in the cortex, remains largely unclear. Using the rat as a model, we aimed to record the physiological and structural changes in the primary auditory cortex (A1) following lactational BPA exposure and their possible effects on behavioral outcomes. We found that BPA-exposed rats showed significant behavioral impairments when performing a sound temporal rate discrimination test. A significant alteration in spectral and temporal processing was also recorded in their A1, manifested as degraded frequency selectivity and diminished stimulus rate-following by neurons. These post-exposure effects were accompanied by changes in the density and maturity of dendritic spines in A1. Our findings demonstrated developmental impacts of BPA on auditory cortical processing and auditory-related discrimination, particularly in the temporal domain. Thus, the health

implications for humans associated with early exposure to endocrine disruptors such as BPA merit more careful examination.

**Keywords** Auditory cortex · Auditory behavior · BPA exposure · Cortical processing · Plasticity

## Introduction

The environmental release of substances that interfere with physiological endocrine functions (endocrine disruptors) is one of the inevitable consequences of industrialization. Although these substances do not originate in organisms, they are sufficiently similar in chemical structure to biological hormones that they bind to hormone receptors and interfere with the activity of endogenous hormones. For example, bisphenol A (BPA) is a typical endocrine disruptor with weak estrogen-like activity that causes adverse health effects by interfering with endocrine function [1, 2]. Because BPA is mainly used to synthesize polycarbonate and epoxy resin, it is commonly found in medical equipment, dental sealants, eyeglass lenses, electronics, sporting equipment, and beverage containers. The widespread use of these products makes it very likely that humans are continuously and passively exposed to BPA [3].

To date, the health hazards associated with BPA, including reproductive, developmental, and metabolic dysfunction, have been well documented [1, 2, 4, 5]. In the central nervous system, studies have demonstrated that BPA hinders neurogenesis, impairs synaptic plasticity, and delays function maturation, leading to cognitive deficits in animals and humans [6–12]. However, how BPA exposure might affect the development of primary sensory systems,

Binliang Tang and Kailin Li have contributed equally to this work.

✉ Xiaoming Zhou  
xmzhou@bio.ecnu.edu.cn

<sup>1</sup> Key Laboratory of Brain Functional Genomics of Ministry of Education, Shanghai Key Laboratory of Brain Functional Genomics, School of Life Sciences, East China Normal University, Shanghai 200062, China

<sup>2</sup> New York University-East China Normal University Institute of Brain and Cognitive Science, NYU-Shanghai, Shanghai 200062, China

<sup>3</sup> Department of Neurology and Neurosurgery, Montreal Neurological Institute, McGill University, Montreal, QC H3A 2B4, Canada

which are the first to mature in the cortex, remains largely unknown. Evidence of abnormal sensory development could indicate profound and pervasive effects of exposure. The sensory cortex in particular has a broad range of axonal projections to other areas such as the prefrontal cortex and the hippocampus, participating in the production of higher cognitive behaviors [13–15]. Consequently, it is conceivable that altered information processing in the sensory cortex has profound effects on cognitive functions. Therefore, determining the post-exposure effects of BPA on the sensory cortex is also crucial for understanding the neural basis of BPA-induced cognitive impairments.

More recently, it has been reported in animal models that early BPA exposure inhibits the contrast sensitivity of neurons and decreases dendritic spine density in the visual cortex [10, 16–18]. These studies indicate that BPA adversely affects the development of sensory systems. The auditory cortex plays an important role in the perception of aural speech and other complex acoustic stimuli [19–22]. In humans, language comprehension is correlated with the spectral and temporal responses of auditory cortical neurons; reduced fidelity of the cortical coding of speech impairs auditory-related perceptual abilities [19, 23, 24]. However, no study has yet investigated whether BPA exposure affects information processing in the auditory cortex.

Using the rat as a model, we aimed to investigate the physiological and structural changes in the primary auditory cortex (A1) and their possible effects on behavioral outcomes, as a result of lactational BPA exposure. Because human speech requires significant cortical processing of acoustic inputs, the study may have important implications for understanding the origins of hearing and language-related disabilities in humans induced by endocrine disruptors such as BPA.

## Materials and Methods

All procedures complied with NIH standards and were approved by the Institutional Animal Care and Use Committee of the East China Normal University.

### BPA Administration

Timed-pregnant Sprague-Dawley rats were purchased from the Shanghai Laboratory Animal Center (Shanghai, China). BPA administration was as described previously [18] with slight modifications. Briefly, all offspring were cross-fostered on postnatal day 1 (p1) to achieve groups of 10 pups per litter and were exposed to BPA *via* their dams' milk. The dams were administered 1 mg of BPA (Sigma) per kg body weight daily from gestation day 1 to weaning

at p21. The BPA was dissolved in corn oil and applied to corn flakes that were always consumed within 5 min of administration. The dams of the control groups were fed corn flakes with pure corn oil. A 12-h light/12-h dark cycle and constant humidity and temperature conditions were maintained for each group. After the weaning day (p21), pups from both the BPA-exposed and the control groups were reared under identical housing conditions until the experiments were conducted at ~p49. During experiments and analysis, the researcher was blind to the group identity of the animals.

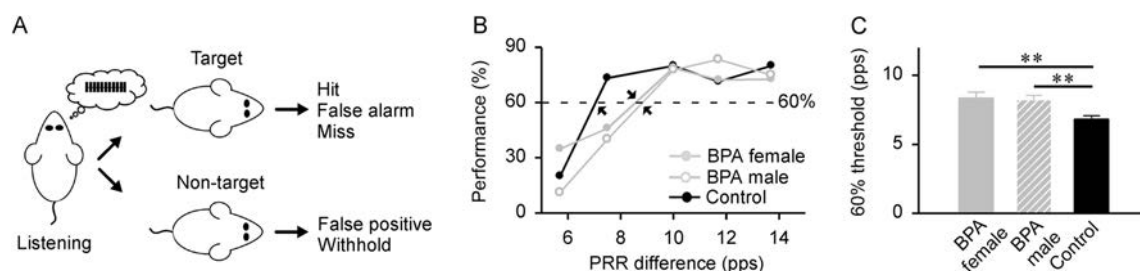
Body weights of the BPA-exposed pups were continuously monitored and were compared with those of age-matched controls. Consistent with earlier studies [18], the exposure protocol did not affect weight gain in the BPA-exposed rats, indicating normal lactation.

### Repetition Rate Discrimination Testing

A total of 15 BPA-exposed rats (7 females and 8 males) and 18 control rats (8 females and 10 males) were used for behavioral testing. The tasks and procedures were similar to those in our previous studies [25–28]. Briefly, the acoustic stimuli used in behavioral testing were pulse trains with a duration of ~520 ms that contained different numbers of noise bursts [30 ms duration with 5 ms linear onset and offset ramps at ~60 dB sound pressure level (SPL)], corresponding to repetition rates of 6.3, 8.3, 10, 12.5, or 14.3 pulses per second (pps). Rats were first trained to discriminate a pulse train of 6.3 pps (the non-target) from one of 20 pps (the target). When animals achieved steady performance scores after ~7 days of training, their temporal rate discrimination was tested on the next day by randomly delivering non-target pulse trains with rates of 6.3, 8.3, 10, 12.5, or 14.3 pps.

The behavioral task was conducted in a wire-mesh cage (20 × 20 × 18 cm<sup>3</sup>) that was enclosed within a sound-attenuating chamber. The rats' behavioral states during the testing were scored as either hit, miss, false positive, withhold, or false alarm (Fig. 1A). While a hit triggered the delivery of a 45-mg food pellet (BioServe) as a reward, a miss, false positive, or false alarm initiated a 9-s time-out during which the lights were turned off and no stimuli were presented). A withhold, however, resulted in neither a reward nor a time-out. Behavioral testing and data acquisition were controlled by an input and output system consisting of a speaker, photo-beam detector, food dispenser, sound card, and lights (Med Associates).

The behavioral discrimination of each rat was quantified as a performance score:  $H-F \times H$  (expressed as a percentage), where H is the number of hits/number of target trials (hit ratio) and F is the number of false positives/number of non-target trials (false-positive ratio) [20, 26, 28, 29].



**Fig. 1** Performance on the sound temporal rate discrimination task. **A** Schematic of the sound temporal rate discrimination task. Acoustic stimuli used in the task are pulse trains of ~520 ms duration that contain different numbers of noise bursts, corresponding to repetition rates of 6.3, 8.3, 10, 12.5, 14.3, or 20 pulses per second (pps). **B** Examples of psychometric curves from a BPA-exposed male rat, a BPA-exposed female rat, and a female control rat. Note that the behavioral testing was conducted on ~postnatal day 49 (p49) for all the rats. Dashed line, 60% of the maximal performance score; arrows,

discrimination thresholds for each psychometric curve; PRR, pulse repetition rate. **C** Average discrimination thresholds of the different groups of rats revealing that discrimination thresholds do not differ between the male and female control rats ( $P > 0.5$ , unpaired Student's  $t$  test). These data therefore were combined as control data to minimize the number of animals used in the study.  $n = 8, 7, 7$ , and 10 rats for BPA-exposed male group, BPA-exposed female group, female control group, and male control group, respectively. Error bars represent the SEM. \*\* $P < 0.01$ .

### Auditory Brainstem Response (ABR) Measurement and Cortical Recording

Ten female BPA-exposed rats and 9 female control rats were anesthetized intraperitoneally with pentobarbital (50 mg per kg body weight). As described in our earlier studies [28, 30, 31], ABRs to tone pips of 3, 10, 15, or 20 kHz at different intensities were recorded by placing three electrodes subdermally at the scalp midline, posterior to the stimulated ear, and on the midline of the back 1–2 cm posterior to the neck. Acoustic stimuli were generated using TDT System III (Tucker-Davis Technologies) and delivered monaurally to the left ear *via* a calibrated earphone with a sound tube. Acoustic calibration was performed with a 1/2-inch Brüel and Kjær microphone. ABR thresholds were defined as the sound intensity that elicited a minimal discernable ABR pattern at each frequency.

For cortical recordings, 5 female BPA-exposed rats and 6 female control rats were anesthetized with pentobarbital (50 mg per kg body weight, intraperitoneally). The auditory cortex was surgically exposed and Parylene-coated tungsten microelectrodes (1–2 M $\Omega$  at 1 kHz; FHC) were lowered orthogonally into the cortex to a depth of 450–550  $\mu$ m (layer IV as shown by earlier studies) [32, 33]. Acoustic stimuli were delivered to the ear contralateral to the recording site *via* the calibrated earphone with a tube. The evoked spikes of a neuron or a small cluster of neurons were recorded using the TDT System III.

The frequency tuning curve of a cortical site was recorded by presenting pure tones (25 ms in duration) of different frequencies and intensities in a random, interleaved sequence. The characteristic frequency (CF) was defined for each tuning curve as the frequency at threshold [28, 34–36]. To document a repetition rate transfer function

(RRTF), cortical responses to trains of six tonal pulses (25 ms in duration with 5-ms ramps) at repetition rates of 2, 4, 7, 10, 12.5, 15, 17.5, and 20 pps were recorded. The tone frequency was set at the CF of each cortical site and the intensity was set at 60 dB SPL. The normalized response for each temporal rate was then calculated as the average response to the last five pulses divided by the response to the first pulse. The RRTF was then defined as the normalized response as a function of the temporal rate [25, 26, 28].

The misclassification rate (MR) was calculated as described in previous studies [28, 30, 37]. Briefly, a filtered function was obtained by convolving each spike train recorded with repeated stimuli of specific pulse rates with an exponential function,  $N(t) = N_0 e^{-t/\tau}$ . The distance between two spike trains was defined as the integral of the squared difference between two functions. A misclassification was then calculated when the distance was less than (for spike trains recorded with different stimuli) or more than (for spike trains recorded with identical stimuli) one standard deviation from the average distance.

The stimulus trains used for cortical recording and behavioral testing were different during the experiments. For example, we recorded cortical responses to stimulus trains of six tonal pulses at 2, 4, 7, 10, 12.5, 15, 17.5, and 20 pps to document a RRTF, as auditory cortical neurons in most mammalian species are not able to follow individual sounds presented at rates faster than 20 pps [25, 26, 28, 30]. During the behavioral testing, however, the discrimination cue used was the temporal rate of a pulse train rather than its duration. We therefore designed pulse trains with a duration of ~520 ms that contained different numbers of noise bursts, corresponding to repetition rates of 6.3, 8.3, 10, 12.5, 14.3, or 20 pps.



## Golgi-Cox Staining

Five female BPA-exposed rats and 5 female control rats were anesthetized with a lethal dose of pentobarbital (85 mg per kg body weight). Brains were then removed and immersed in Golgi-Cox solution for 14 days and then transferred to a tissue-protectant solution for 3 days, according to the directions with the Golgi-Cox kit (Histo-biotec Corp.). Coronal sections were cut at 120  $\mu\text{m}$  on a VT1000 Plus vibratome (Vibratome). The slides were visualized under a Leica DM4000 microscope fitted with a digital camera (DFC 7000 T, Leica Microsystems). Pyramidal (excitatory) neurons in cortical layer IV were chosen at random at low-power magnification and spines were counted *via* a 100 $\times$  objective lens as previously described [38]. Image stacks were analyzed using ImageJ software (<https://rsbweb.nih.gov/ij/>). Spines were traced and counted on a two-dimensional plane, with identification of the spine subtypes as stubby-, mushroom-, or thin-shaped. Stubby spines had a large head closely connected to the dendritic shaft with no clear neck. Mushroom spines also had a large head but with a narrow neck. Thin spines had a small head and a long and thin neck. To determine their density, the spines on two segments of the secondary and tertiary apical or basal dendrites of neurons were analyzed. The number of spines per 10  $\mu\text{m}$  segment was then averaged for each neuron.

## Quantitative Immunoblots

Seven female BPA-exposed rats and 7 female control rats were anesthetized with a lethal dose of pentobarbital (85 mg per kg body weight). Immediately after decapitation, brains were removed and auditory cortices [39] were dissected and homogenized in RIPA buffer (50 mmol/L Tris pH 7.5, 150 mmol/L NaCl, 1% Triton X-100, 0.1% SDS, 2 mmol/L EDTA, 0.5% sodium deoxycholate) containing protease inhibitor cocktail. Cellular debris was removed by centrifugation at 4°C (14,000 rpm for 10 min) and the supernatant was collected for analysis. Tissue lysates were subjected to SDS-PAGE, and transferred to nitrocellulose filter membranes (Millipore). The membranes were blocked with 5% non-fat dry milk in Tris-buffered saline (TBS) (150 mmol/L NaCl, 20 mmol/L Tris-HCl, pH 7.4) for 1 h at room temperature (RT) and then incubated overnight at 4°C with primary antibodies. After three washes with TBST, HRP-labeled secondary antibody was applied for 1 h at RT. After additional washes, the membranes were analyzed by the ChemiDoc XRS+ System (Bio-Rad) and quantified by Quantity One (Bio-Rad). The primary antibodies used included mouse anti-activity-regulated cytoskeleton-associated protein (Arc) (1:500; Santa Cruz Biotechnology) and rabbit anti-

glyceraldehyde 3-phosphate dehydrogenase (GAPDH) (1:5,000; Abways).

## Statistical Analysis

Data are presented as the mean  $\pm$  SEM. Statistical analysis was conducted using unpaired two-tailed Student's *t* test or ANOVA with *post hoc* Student-Newman-Keuls test. In addition, the cumulative distributions of data from different groups were compared with the Kolmogorov-Smirnov test. Differences were considered statistically significant at  $P < 0.05$ .

## Results

As shown by an earlier study that applied a similar exposure protocol [18], BPA exposure resulted in an average blood BPA level of  $\sim 1.15$  ng/mL in the exposed rats, which was significantly higher than that for the control rats ( $\sim 0.04$  ng/mL). This result shows that the rat pups were directly exposed to BPA *via* their dams' milk.

## Performance on the Behavioral Task

We first evaluated the effects of BPA on sound discrimination in BPA-exposed *versus* control rats at  $\sim$  p49 (Fig. 1A). A psychometric curve for each animal during the testing phase was constructed by plotting the performance score as a function of the rate difference between target and non-target (Fig. 1B). The discrimination threshold, defined as the pulse repetition rate difference corresponding to a 60% performance score on the psychometric curve, provided an index of the temporal rate discrimination of each animal (Fig. 1B, arrows). A higher discrimination threshold thus indicated reduced sound discrimination. As shown in Fig. 1C, the average discrimination thresholds of the BPA-exposed male and female rats were significantly higher than those of the controls (both  $P < 0.005$ , one-way ANOVA with Student-Newman-Keuls *post hoc* test). However, the average discrimination thresholds were comparable in the BPA-exposed male and female rats ( $P > 0.5$ , one-way ANOVA with Student-Newman-Keuls *post hoc* test). These results indicated that early BPA exposure sex-independently degrades the ability of animals to discriminate between rates of temporally-modulated sound.

Because BPA-induced behavioral deficits in the sound temporal rate discrimination task were similar between the male and female rats, the following experiments were conducted mainly on female rats, to investigate the neural mechanisms underlying post-exposure behavioral changes due to BPA.

## Thresholds and Wave Latencies of ABRs

To investigate whether the degraded performance on the sound temporal rate discrimination task among the BPA-exposed rats was due simply to changes in hearing sensitivity after BPA exposure, we compared the ABR thresholds recorded in the BPA-exposed rats to those of controls (Fig. 2A).

As shown in Fig. 2C, ABR thresholds (Fig. 2B, arrows) tested at different frequencies were comparable between BPA-exposed and control rats (all  $P > 0.5$ , unpaired Student's  $t$  test). In addition, no significant differences in the ABR latencies of both waves I and V were found between the BPA-exposed and control rats (Fig. 2D; all  $P > 0.1$ , unpaired Student's  $t$  test). These data suggested that BPA exposure has no measurable impact on hearing sensitivity (i.e., thresholds and neural conduction velocities within the brainstem).

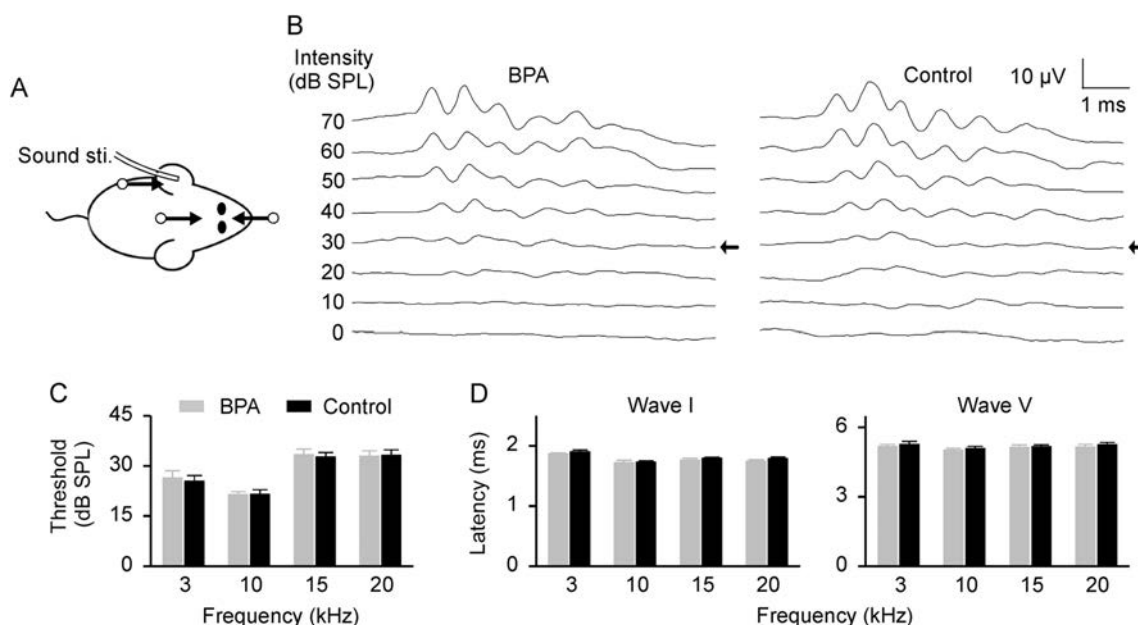
## Cortical Temporal Processing

The response selectivity and reliability of cortical neurons have been argued to underlie the neurological encoding of acoustic inputs and to account for auditory-related behavior [9, 27, 28, 40, 41]. We therefore investigated the potential consequences of BPA exposure on the cortical processing of acoustic stimuli using conventional extracellular unit recording techniques (Fig. 3A). Data were recorded from

neurons in cortical field A1 from 230 sites in five BPA-exposed rats and from 226 sites in six control rats. All subsequent quantitative analyses of electrophysiological data were based on these samples.

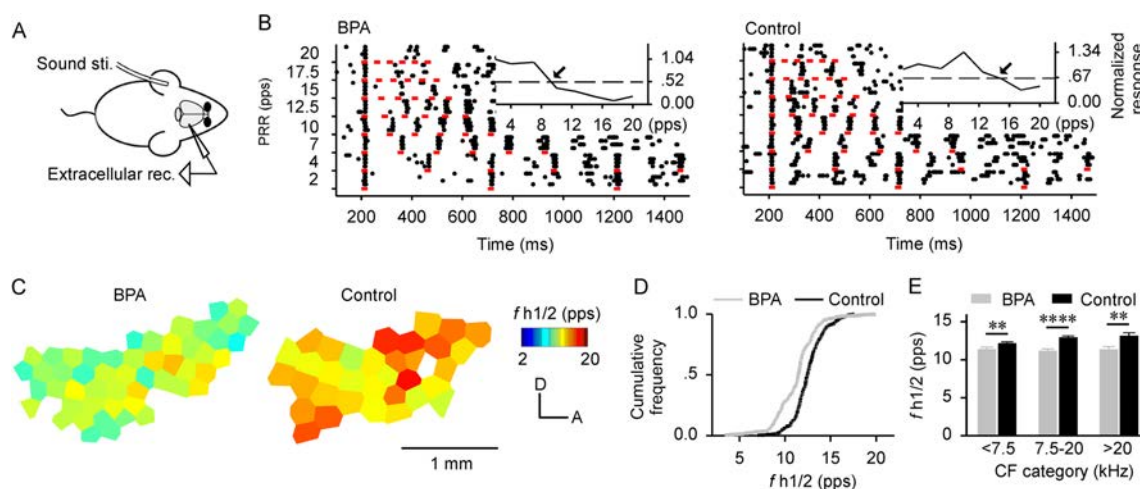
Cortical processing of the temporal modulation rates of sound stimuli in A1 of both BPA-exposed and control rats was first examined by recording cortical responses to repetitive stimuli presented at different repetition rates (Fig. 3B). RRTFs were then derived to characterize the cortical temporal responses for both groups of rats. As shown in Fig. 3B insets, cortical responses recorded in the control group followed identical stimuli at and below 10 pps when tested with CF tonal pulses, each successive tone evoking a number of spikes similar to that to the first tone in the pulse train. In contrast, responses recorded in the BPA-exposed group followed stimuli at or below repetition rates of  $\sim 7$  pps. At higher repetition rates, however, the number of responses per tone for neurons recorded from both groups of rats fell off rapidly.

The cortical capacity for processing repetitive stimuli was assessed by determining the highest temporal rate at which the normalized response was at half of its maximum in the RRTF ( $f_{h1/2}$ ; arrows in Fig. 3B insets). Figure 3C shows representative  $f_{h1/2}$  maps from a BPA-exposed rat and a control rat in which each polygon represents the  $f_{h1/2}$  obtained at that cortical site. In general, the  $f_{h1/2}$  values were lower for the BPA-exposed rats than for the control rats at most cortical sites recorded. This finding was further



**Fig. 2** Thresholds and wave latencies of auditory brainstem responses (ABRs) determined using tone pips of 3, 10, 15, and 20 kHz. **A** Schematic of the experimental setup for ABR recording. Arrows indicate the position of recording electrodes. **B** ABRs of a BPA-exposed and a control rat using 10-kHz tone pips at different

intensities. Arrows, ABR thresholds. **C** ABR thresholds tested at different frequencies in BPA-exposed and control rats.  $n = 10$  rats for the BPA-exposed group and 9 rats for the control group. Error bars represent the SEM. **D** Latencies of waves I and V in BPA-exposed and control rats.



**Fig. 3** Temporal responses of cortical neurons. **A** Schematic of the experimental setup for cortical extracellular recording. **B** Dot rasters showing cortical responses to pulse trains at repetition rates 2, 4, 7, 10, 12.5, 15, 17.5, and 20 pps recorded from a BPA-exposed and a control rat [red lines, pulse durations; insets, repetition rate transfer function (RRTF); dashed lines and arrows, 50% of the maximal response and  $f_{h/2}$  for each RRTF, respectively]. **C** Representative cortical  $f_{h/2}$  maps of a BPA-exposed and a control rat. Voronoi tessellation (a MatLab routine; The MathWorks) was applied to create tessellated polygons, with electrode penetration sites at their centers.

confirmed by a quantitative comparison of the distributions for all  $f_{h/2}$  values from both groups of rats. As shown in Fig. 3D, a significant leftward shift of the  $f_{h/2}$  distribution for the BPA-exposed rats *versus* controls ( $P < 0.0001$ , Kolmogorov-Smirnov test), indicating reduced rate-following as a result of BPA exposure. To determine whether the decrease in  $f_{h/2}$  values was related to the CF at each site, we compared the  $f_{h/2}$  values from cortical sites with different CFs (Fig. 3E). The results showed that the average  $f_{h/2}$  values were significantly lower for the BPA-exposed rats than for controls across the low, middle, and high CF ranges tested (the percentage decreases were  $6.7 \pm 2.2\%$  for low CF,  $13.7 \pm 1.7\%$  for middle CF, and  $13.6 \pm 2.8\%$  for high CF; all  $P < 0.01$ – $0.0001$ , unpaired Student's *t* test).

We next calculated the MR for all combinations of stimulus trains used to construct the RRTFs, in order to examine further the reliability and precision of cortical responses to repetitive stimuli while considering both the number and timing spikes. The MR quantifies the similarity between spike trains responding to different stimulus trains, or the difference between spike trains responding to identical stimulus trains [26, 28, 37]. A lower MR value thus indicates more reliable and precise spike trains representing the temporal structure of acoustic inputs. As shown in Fig. 4A, B, the average MRs of the BPA-exposed rats at most combinations of stimulus rates were significantly higher than those of controls. These results manifest

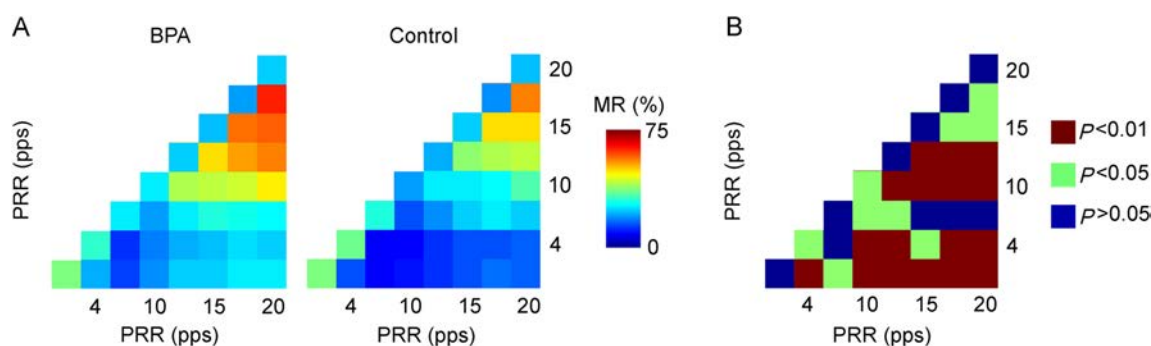
Each polygon was assigned the  $f_{h/2}$  of the corresponding penetration site. In this way, every point on the cortical surface is linked to the  $f_{h/2}$  derived from the sampled cortical site nearest to this point. An unfilled polygon indicates that the RRTF was not recorded at that site. D, dorsal; A, anterior. **D** Cumulative frequency histograms of  $f_{h/2}$  for the BPA-exposed and control rats. **E** Average  $f_{h/2}$  values for all recording sites in the BPA-exposed and control rats, for each of three characteristic frequency (CF) ranges. Error bars represent the SEM.  $**P < 0.01$ ;  $****P < 0.0001$ .

reduced reliability and precision of cortical responses representing repetitive stimuli after BPA exposure.

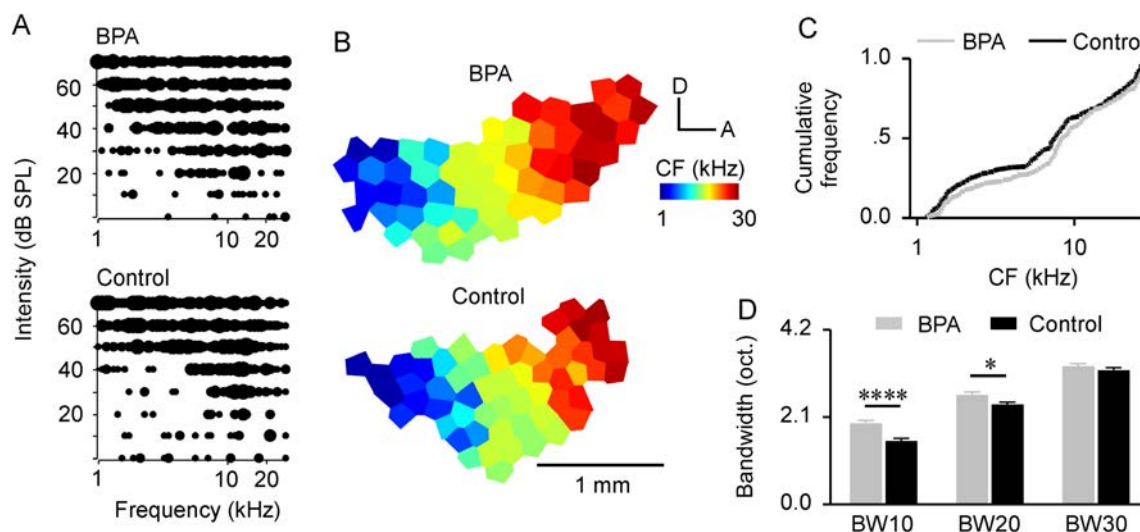
### Cortical Frequency Representations

To evaluate the effects of BPA exposure on cortical frequency representation, we recorded the frequency tuning curve for each cortical site (Fig. 5A). We then compared the CFs, bandwidths of the tuning curves, and response thresholds between the BPA-exposed and control rats. Fig. 5B presents the representative CF maps in A1 of a BPA-exposed rat and a control rat. At first glance, the CF maps of both groups of rats were complete, illustrating orderly tonotopic gradients of sound frequency representation. This was further verified by the finding of no significant difference in the CF distributions between the BPA-exposed and control rats ( $P > 0.1$ , Kolmogorov-Smirnov test; Fig. 5C). However, the bandwidths of cortical tuning curves measured at 10, 20, and 30 dB above threshold (BW10s, BW20s, and BW30s) were larger for the BPA-exposed than for the control rats (Fig. 5D;  $P < 0.0001$  for BW10s,  $P < 0.05$  for BW 20s, but  $P > 0.1$  for BW30s, unpaired Student's *t* test). This predominantly less-selective frequency tuning recorded in the A1 of the BPA-exposed group, particularly at low stimulus intensities, demonstrated degraded spectral processing after BPA exposure.





**Fig. 4** Misclassification rates (MRs) for all combinations of repetition rates, calculated using the van Rossum spike train distance metric. **A** Average MRs for the BPA-exposed and control rats. **B** *t* test results of MR comparisons between the BPA-exposed and control rats.



**Fig. 5** Spectral responses of cortical neurons. **A** Representative examples of frequency tuning curves recorded from a BPA-exposed and a control rat. Note that the frequency tuning curve was recorded by presenting pure tones at different frequencies (1–30 kHz) and intensities (0–70 dB SPL) in a random, interleaved sequence. **B** Representative cortical CF maps from a BPA-exposed and a

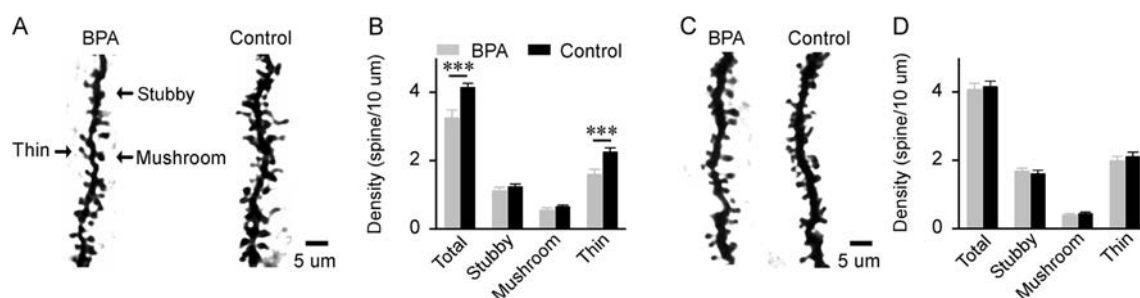
control rat. The color of each polygon indicates the CF of cortical neurons recorded at that site. A, anterior; D, dorsal. **C** CF distributions for the BPA-exposed and control rats. **D** Average frequency tuning bandwidths at 10, 20, and 30 dB above the response threshold for all recording sites in the BPA-exposed and control rats. Error bars represent the SEM. \* $P < 0.05$ ; \*\*\*\* $P < 0.0001$ .

Interestingly, no significant differences were found in the intensity thresholds (BPA,  $25.3 \pm 0.4$  dB SPL; control,  $24.2 \pm 0.4$  dB SPL;  $P > 0.1$ , unpaired Student's *t* test) and response latencies (BPA,  $11.7 \pm 0.9$  ms; control,  $11.5 \pm 0.8$  ms;  $P = 0.1$ , unpaired Student's *t* test) of A1 neurons between the BPA-exposed and control rats.

### Dendritic Spine Density of Cortical Neurons

Previous studies have shown that the spines of the basal dendrites of cortical neurons in the middle layers receive mainly “bottom-up” inputs from sub-cortical areas, while those of the apical dendrites receive mainly “top-down” inputs from higher cortical areas [42]. The electrophysiological data described above were mainly from neurons in layer IV of the A1. Therefore, we quantified the densities of both basal and apical spines of pyramidal neurons in this

middle layer from the BPA-exposed and control rats to dissect the structural basis of altered cortical processing after BPA exposure. A significantly lower density of basal spines was found in the BPA-exposed rats than the control rats (Fig. 6A and B;  $P < 0.001$ , unpaired Student's *t* test). Further analysis revealed that the density of thin-shaped spines in the BPA-exposed group was significantly lower than in the control group ( $P < 0.001$ , unpaired Student's *t* test). No significant changes in the densities of both mushroom- and stubby-shaped spines, however, were found between the groups (both  $P > 0.1$ , unpaired Student's *t* test). Interestingly, the spine density of apical dendrites was comparable in the BPA-exposed and control rats (Fig. 6C and D; all  $P > 0.1$ , unpaired Student's *t* test), indicating that developmental BPA exposure has a region-specific effect on the spine protrusion of dendritic shafts.



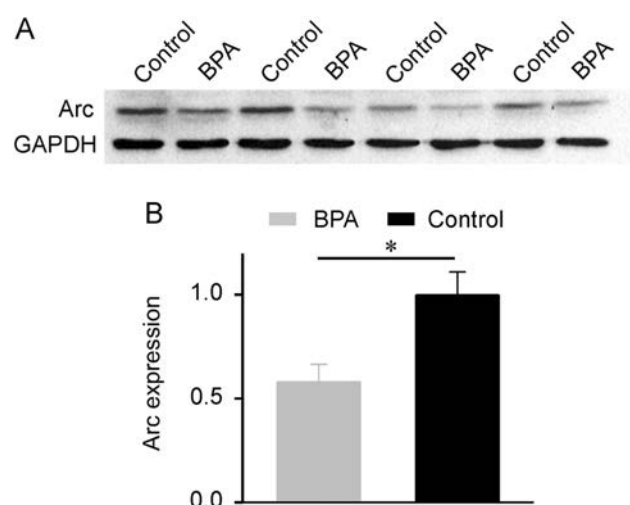
**Fig. 6** Dendritic spine density of cortical neurons. **A** Representative examples of basal spine morphology of neurons from a BPA-exposed and a control rat. Different subtypes of spines (stubby-, mushroom-, or thin-shaped) are indicated by the arrows. **B** Quantitative analysis of basal spine densities in BPA-exposed and control rats.  $n = 29$  neurons from 5 BPA-exposed rats and  $n = 26$  neurons from 5 control rats.

Error bars represent the SEM. \*\*\* $P < 0.001$ . **C** Representative examples of apical spine morphology of neurons from a BPA-exposed and a control rat. **D** Quantitative analysis of apical spine densities in BPA-exposed and control rats.  $n = 23$  neurons from 5 BPA-exposed rats and  $n = 22$  neurons from 5 control rats.

### Cortical Arc Expression

As an activity-driven protein localized at active synapses, Arc has been shown to regulate dendrite development and spine morphology [43, 44]. To begin documenting the molecular changes that paralleled the dynamic changes in dendritic spines induced by BPA exposure, we studied the expression of Arc in cortical field A1 by using quantitative immunoblotting.

As shown in Fig. 7, the expression level of Arc was significantly lower in the BPA-exposed rats than in the controls ( $P < 0.05$ , unpaired Student's  $t$  test). The results suggested that altered Arc expression might contribute to the changes in spine density and morphology in the BPA-exposed group.



**Fig. 7** Cortical Arc expression. **A** Representative immunoblot bands. **B** Expression levels of Arc in BPA-exposed and control rats.  $n = 7$  rats for both groups. Error bars represent the SEM. \* $P < 0.05$ .

### Discussion

In this study, the rats exposed to BPA demonstrated significant behavioral impairments when performing a sound temporal rate discrimination task. A significant degradation in spectral and temporal processing also occurred in their A1, manifested as degraded frequency selectivity and diminished stimulus rate-following by neurons. In addition to these behavioral and cortical physiological changes, we observed alterations in structural aspects of the cortical machinery following BPA exposure: changes in density and maturity of spines. To the best of our knowledge, these results are the first evidence of neurotoxic impacts of developmental BPA exposure on auditory cortical processing and auditory-related discriminative abilities, particularly in the temporal domain. It should be noted that the dose of BPA used for exposure of the dams in this study was 1 mg/kg per day, the same dose as in an earlier study [18]. The blood levels of BPA in such exposed rats are of the same order of magnitude as those in the blood of adult humans without explicit exposure [3]. Significant post-exposure changes were recorded in cortical field A1 of rats that were exposed to BPA *via* their dams' milk between p1 and p21, a critical period for the development of the auditory cortex [45–47]. While breastfeeding is the ideal way to feed an infant, breast milk is also the primary source of abiotic contaminants such as BPA to infants. Importantly, many studies have demonstrated that the developing brain is one of the most sensitive organs disrupted by BPA even at low doses [48]. The current findings, along with the dramatic increase in breastfeeding numbers and duration today, therefore indicate that the breast milk concentrations of potentially harmful substances such as BPA merit careful examination.

We found that BPA exposure significantly decreased the spine density, particularly the basal dendrites, of pyramidal neurons in the middle cortical layer where we made

physiological recordings. The most significant changes occurred in the thin-shaped spines, a type of immature, unstable dendritic spine [49, 50]. Earlier studies have shown that dendritic spines are small membranous protrusions of neuronal dendrites that serve as the first postsynaptic elements to receive excitatory neurotransmission [50–52]. The integrated signals received by numerous spines collectively determine the pattern of neuronal activity of a postsynaptic neuron. The spines thus provide the anatomical basis underlying neuronal function [44, 52, 53]. BPA-induced changes in the density and maturity of spines on cortical pyramidal neurons may weaken the connectivity in neuronal networks, leading to functional alterations in neurons in the spectral and temporal domains. It has been shown that the basal dendritic spines of the neurons we recorded in cortical layer IV typically receive inputs from the thalamus and the apical dendrites receive inputs from other layer II/III neurons [54, 55]. Given that the basal dendritic spines of these neurons receive mainly “bottom-up” inputs from sub-cortical areas, the deficits in cortical neuronal processing are presumably due to interference with feed-forward information in the cortical network, as a result of alterations in the density and maturity of basal dendritic spines following BPA exposure.

Consistent with earlier results from the rat hippocampus, developmental BPA exposure decreased the cortical expression of Arc, an activity-driven protein localized at active synapses [44]. Previous studies have shown that Arc increases spine density and regulates spine morphology by facilitating the endocytosis of AMPA receptors [43]. In addition, a down-regulated expression level of AMPA receptor subtype GluR2 has also been reported in the visual cortex as a result of developmental BPA exposure, while the expression levels of the GluR1 and NMDA receptor subtypes NR1 and NR2 remain unchanged [18]. However, how the altered expression of these synapse-related proteins contributes to the changes in spine density in the auditory cortex after BPA exposure awaits further study.

Sounds in natural environments, including human speech and animal vocalizations, have complex spectral and temporal structures. The auditory cortex has been proposed to play an important role in the perception of aural speech and other complex acoustic stimuli [19–22]. It has been proposed that changes in cortical processing might alter the neurological encoding of the details of acoustic inputs, thereby affecting auditory-related behavior [9, 27, 28, 40, 41]. Thus, BPA-induced deficits in cortical neuronal selectivity, local network coordination, and synaptic plasticity such as spine density and maturity contributed at least in part to the reduced behavioral accuracy in the BPA-exposed rats. In human populations, fundamental deficits in the fidelity of cortical responses to

speech not only affect general hearing but also underlie poor language and reading skills [19, 23, 24]. While our results recorded in a rodent model identified A1 as a novel target for BPA exposure during lactation, they have significant implications for a possible role of early exposure to BPA as a contributor to the ontogeny of hearing and language-related impairments in humans.

The threshold and wave latency of the ABR provide information about the peripheral hearing status and the integrity of brainstem pathways. It has been shown that peripheral hearing alteration also affects cortical responses to amplitude-modulated stimuli in cats [56]. While we found in this study that BPA exposure resulted in a significant degradation in cortical spectral and temporal domain processing, the ABR thresholds and wave latencies remained intact. These data suggest that BPA exposure has little effect on peripheral hearing and neural conduction in the brainstem. Thus, the post-exposure effects of BPA on response properties found in A1 are clearly of central origin. It remains unclear whether cortical processing is more susceptible to early BPA exposure than peripheral hearing and the integrity of auditory brainstem pathways.

With regard to the central nervous system, most studies on the effects of BPA exposure focused on structures such as the prefrontal cortex and the hippocampus, which are associated with emotional and cognitive functions [6–8, 10–12, 44]. These studies have shown that BPA hinders neurogenesis, impairs synaptic plasticity, and delays functional maturation, resulting in cognitive impairments such as anxious and depressed behaviors, working memory deficits, and declines in spatial memory in both humans and animals. However, how BPA exposure affects these higher brain functions remains largely unknown. Earlier anatomical studies demonstrated that sensory cortices, including the auditory cortex, have a broad range of axonal projections to other structures, such as the prefrontal cortex and the hippocampus [13–15, 57]. These extensive inputs from sensory cortices are argued to be necessary for the maturation of emotion and cognition. Because sensory systems are the first to mature in the cortex, disrupted sensory cortical inputs into the prefrontal cortex and hippocampus during development may profoundly affect the formation of higher cognitive functions [31, 57]. While we focused mainly on the auditory cortex when investigating the adverse effects of BPA exposure on auditory discrimination, other studies have reported the effects of BPA on the visual cortex as well [10, 16–18]. It is conceivable that BPA-induced deficits in cortical sensory processing during development disrupt neural inputs into brain structures such as the prefrontal cortex and hippocampus, leading to changes in emotional and cognitive functions. These findings concerning the effects of BPA on cortical processing provide important insights into the



mechanisms potentially underlying early cognitive dysfunction resulting from BPA exposure.

It should be noted that previous studies have shown that BPA exposure has generally sex-specific effects on brain functions. For example, gestational BPA exposure has been found to significantly inhibit spatial learning and memory in female but not in male rats [58]. BPA exposure during adolescence, however, decreases spatial memory in male but not female rats [10]. Because BPA is a typical endocrine disruptor, these sex-specific effects have been attributed to differences in the cortical expression of hormone receptors between the sexes during various exposure periods such as gestation, lactation, or adolescence. In our study, the behavioral deficits induced by BPA exposure during lactation were comparable in the male and female rats. We thus focused mainly on female rats when investigating the cortical mechanisms underlying the post-exposure behavioral changes. A future study could be designed to identify sex-specific effects of developmental BPA exposure on cortical processing. In addition, the sound temporal rate discrimination task used in this study involved significant learning and memory components: it required an animal to identify a remembered target auditory stimulus from a set of distracter stimuli. Therefore, the learning capacity of an animal might also affect its performance on the behavioral task [8, 10–12, 44]. It remains to be studied whether BPA exposure impairs an animal's capacity to learn, and the extent to which changes in this capacity affect its performance accuracy. Lastly, anesthesia has been shown to significantly affect auditory cortical processing [59, 60]. However, due to the identical anesthetic conditions present during recording among both animal cohorts, anesthesia probably would not create a bias in the estimations of the BPA-exposed *vs* the control rats.

**Acknowledgements** This work was supported by the National Natural Science Foundation of China (32171134 and 32161160325), the National Science and Technology Innovation 2030 Major Program (2022ZD0204804), a Project of Shanghai Science and Technology Commission (21490713200), the Program of Introducing Talents of Discipline to Universities (B16018), and a matching fund from the NYU-ECNU Institute of Brain and Cognitive Science at NYU Shanghai.

**Conflict of interest** The authors declare that they have no conflict of interest.

## References

1. Wolstenholme JT, Rissman EF, Connelly JJ. The role of Bisphenol A in shaping the brain, epigenome and behavior. *Horm Behav* 2011, 59: 296–305.
2. Santoro A, Chianese R, Troisi J, Richards S, Nori SL, Fasano S. Neuro-toxic and reproductive effects of BPA. *Curr Neuropharmacol* 2019, 17: 1109–1132.
3. Völkel W, Bittner N, Dekant W. Quantitation of bisphenol A and bisphenol A glucuronide in biological samples by high performance liquid chromatography-tandem mass spectrometry. *Drug Metab Dispos* 2005, 33: 1748–1757.
4. Rochester JR. Bisphenol A and human health: a review of the literature. *Reprod Toxicol* 2013, 42: 132–155.
5. Peretz J, Vrooman L, Ricke WA, Hunt PA, Ehrlich S, Hauser R, *et al.* Bisphenol a and reproductive health: update of experimental and human evidence, 2007–2013. *Environ Health Perspect* 2014, 122: 775–786.
6. Leranath C, Hajszan T, Szigeti-Buck K, Bober J, MacLusky NJ. Bisphenol A prevents the synaptogenic response to estradiol in hippocampus and prefrontal cortex of ovariectomized nonhuman primates. *Proc Natl Acad Sci U S A* 2008, 105: 14187–14191.
7. Hajszan T, Leranath C. Bisphenol A interferes with synaptic remodeling. *Front Neuroendocrinol* 2010, 31: 519–530.
8. Eilam-Stock T, Serrano P, Frankfurt M, Luine V. Bisphenol-A impairs memory and reduces dendritic spine density in adult male rats. *Behav Neurosci* 2012, 126: 175–185.
9. Liu X, Wei F, Cheng Y, Zhang Y, Jia G, Zhou J, *et al.* Auditory training reverses lead (Pb)-toxicity-induced changes in sound-azimuth selectivity of cortical neurons. *Cereb Cortex* 2019, 29: 3294–3304.
10. Chen Z, Li T, Zhang L, Wang H, Hu F. Bisphenol A exposure remodels cognition of male rats attributable to excitatory alterations in the hippocampus and visual cortex. *Toxicology* 2018, 410: 132–141.
11. Bowman RE, Hagedorn J, Madden E, Frankfurt M. Effects of adolescent Bisphenol-A exposure on memory and spine density in ovariectomized female rats: Adolescence vs adulthood. *Horm Behav* 2019, 107: 26–34.
12. Frankfurt M, Luine V, Bowman RE. A potential role for dendritic spines in bisphenol-A induced memory impairments during adolescence and adulthood. *Vitam Horm* 2020, 114: 307–329.
13. Romanski LM, Bates JF, Goldman-Rakic PS. Auditory belt and parabelt projections to the prefrontal cortex in the rhesus monkey. *J Comp Neurol* 1999, 403: 141–157.
14. Aggleton JP, Vann SD, Oswald CJ, Good M. Identifying cortical inputs to the rat hippocampus that subserve allocentric spatial processes: a simple problem with a complex answer. *Hippocampus* 2000, 10: 466–474.
15. Bedwell SA, Billett EE, Crofts JJ, Tinsley CJ. The topology of connections between rat prefrontal, motor and sensory cortices. *Front Syst Neurosci* 2014, 8: 177.
16. Kelly EA, Opanashuk LA, Majewska AK. The effects of postnatal exposure to low-dose bisphenol-A on activity-dependent plasticity in the mouse sensory cortex. *Front Neuroanat* 2014, 8: 117.
17. Hu F, Liu J, Xu G, Wang H, Shen J, Zhou Y. Bisphenol A exposure inhibits contrast sensitivity in cats involving increased response noise and inhibitory synaptic transmission. *Brain Res Bull* 2020, 157: 1–9.
18. Hu F, Zhang L, Li T, Wang H, Liang W, Zhou Y. Bisphenol-A exposure during gestation and lactation causes visual perception deficits in rat pups following a decrease in interleukin 1 $\beta$  expression in the primary visual cortex. *Neuroscience* 2020, 434: 148–160.
19. Ahissar E, Nagarajan S, Ahissar M, Protopapas A, Mahncke H, Merzenich MM. Speech comprehension is correlated with temporal response patterns recorded from auditory cortex. *Proc Natl Acad Sci U S A* 2001, 98: 13367–13372.
20. Rybalko N, Suta D, Popelár J, Syka J. Inactivation of the left auditory cortex impairs temporal discrimination in the rat. *Behav Brain Res* 2010, 209: 123–130.

21. Gaucher Q, Huetz C, Gourévitch B, Laudanski J, Occelli F, Edeline JM. How do auditory cortex neurons represent communication sounds? *Hear Res* 2013, 305: 102–112.
22. Wang X. Cortical coding of auditory features. *Annu Rev Neurosci* 2018, 41: 527–552.
23. Nagarajan S, Mahncke H, Salz T, Tallal P, Roberts T, Merzenich MM. Cortical auditory signal processing in poor readers. *Proc Natl Acad Sci U S A* 1999, 96: 6483–6488.
24. Paterson SJ, Heim S, Friedman JT, Choudhury N, Benasich AA. Development of structure and function in the infant brain: implications for cognition, language and social behaviour. *Neurosci Biobehav Rev* 2006, 30: 1087–1105.
25. Zhou X, Merzenich MM. Developmentally degraded cortical temporal processing restored by training. *Nat Neurosci* 2009, 12: 26–28.
26. Zhu X, Liu X, Wei F, Wang F, Merzenich MM, Schreiner CE, *et al.* Perceptual training restores impaired cortical temporal processing due to lead exposure. *Cereb Cortex* 2016, 26: 334–345.
27. Zhu X, Wang F, Hu H, Sun X, Kilgard MP, Merzenich MM, *et al.* Environmental acoustic enrichment promotes recovery from developmentally degraded auditory cortical processing. *J Neurosci* 2014, 34: 5406–5415.
28. Cheng Y, Jia G, Zhang Y, Hao H, Shan Y, Yu L, *et al.* Positive impacts of early auditory training on cortical processing at an older age. *Proc Natl Acad Sci U S A* 2017, 114: 6364–6369.
29. Han YK, Köver H, Insanally MN, Semerdjian JH, Bao S. Early experience impairs perceptual discrimination. *Nat Neurosci* 2007, 10: 1191–1197.
30. Zhou X, Merzenich MM. Environmental noise exposure degrades normal listening processes. *Nat Commun* 2012, 3: 843.
31. Zhang Y, Zhu M, Sun Y, Tang B, Zhang G, An P, *et al.* Environmental noise degrades hippocampus-related learning and memory. *Proc Natl Acad Sci U S A* 2021, 118: e2017841117.
32. Games KD, Winer JA. Layer V in rat auditory cortex: projections to the inferior colliculus and contralateral cortex. *Hear Res* 1988, 34: 1–25.
33. Roger M, Arnault P. Anatomical study of the connections of the primary auditory area in the rat. *J Comp Neurol* 1989, 287: 339–356.
34. Polley DB, Steinberg EE, Merzenich MM. Perceptual learning directs auditory cortical map reorganization through top-down influences. *J Neurosci* 2006, 26: 4970–4982.
35. Polley DB, Read HL, Storace DA, Merzenich MM. Multiparametric auditory receptive field organization across five cortical fields in the albino rat. *J Neurophysiol* 2007, 97: 3621–3638.
36. Zhou X, Panizzutti R, de Villers-Sidani E, Madeira C, Merzenich MM. Natural restoration of critical period plasticity in the juvenile and adult primary auditory cortex. *J Neurosci* 2011, 31: 5625–5634.
37. van Rossum MC. A novel spike distance. *Neural Comput* 2001, 13: 751–763.
38. Wang HL, Li JT, Wang H, Sun YX, Liu R, Wang XD, *et al.* Prefrontal Nectin3 reduction mediates adolescent stress-induced deficits of social memory, spatial working memory, and dendritic structure in mice. *Neurosci Bull* 2020, 36: 860–874.
39. Paxinos G, Watson C (1988) *The rat brain in stereotaxic coordinate*. Academic Press, New York.
40. Zhou X, Merzenich MM. Intensive training in adults refines A1 representations degraded in an early postnatal critical period. *Proc Natl Acad Sci U S A* 2007, 104: 15935–15940.
41. Cheng Y, Zhang Y, Wang F, Jia G, Zhou J, Shan Y, *et al.* Reversal of age-related changes in cortical sound-azimuth selectivity with training. *Cereb Cortex* 2020, 30: 1768–1778.
42. Harris KD, Mrsic-Flogel TD. Cortical connectivity and sensory coding. *Nature* 2013, 503: 51–58.
43. Peebles CL, Yoo J, Thwin MT, Palop JJ, Noebels JL, Finkbeiner S. Arc regulates spine morphology and maintains network stability *in vivo*. *Proc Natl Acad Sci U S A* 2010, 107: 18173–18178.
44. Liu ZH, Ding JJ, Yang QQ, Song HZ, Chen XT, Xu Y, *et al.* Early developmental bisphenol-A exposure sex-independently impairs spatial memory by remodeling hippocampal dendritic architecture and synaptic transmission in rats. *Sci Rep* 2016, 6: 32492.
45. Zhang LI, Bao S, Merzenich MM. Disruption of primary auditory cortex by synchronous auditory inputs during a critical period. *Proc Natl Acad Sci USA* 2002, 99: 2309–2314.
46. de Villers-Sidani E, Chang EF, Bao S, Merzenich MM. Critical period window for spectral tuning defined in the primary auditory cortex (A1) in the rat. *J Neurosci* 2007, 27: 180–189.
47. Insanally MN, Albanna BF, Bao S. Pulsed noise experience disrupts complex sound representations. *J Neurophysiol* 2010, 103: 2611–2617.
48. Patisaul HB. Achieving CLARITY on bisphenol A, brain and behaviour. *J Neuroendocrinol* 2020, 32: e12730.
49. Koeppen J, Nguyen AQ, Nikolakopoulou AM, Garcia M, Hanna S, Woodruff S, *et al.* Functional consequences of synapse remodeling following astrocyte-specific regulation of ephrin-B1 in the adult hippocampus. *J Neurosci* 2018, 38: 5710–5726.
50. Chidambaram SB, Rathipriya AG, Bolla SR, Bhat A, Ray B, Mahalakshmi AM, *et al.* Dendritic spines: Revisiting the physiological role. *Prog Neuropsychopharmacol Biol Psychiatry* 2019, 92: 161–193.
51. Harris KM, Kater SB. Dendritic spines: cellular specializations imparting both stability and flexibility to synaptic function. *Annu Rev Neurosci* 1994, 17: 341–371.
52. Nimchinsky EA, Sabatini BL, Svoboda K. Structure and function of dendritic spines. *Annu Rev Physiol* 2002, 64: 313–353.
53. Whalley K. Synaptic building blocks. *Nat Rev Neurosci* 2018, 19: 388–389.
54. Smith PH, Populin LC. Fundamental differences between the thalamocortical recipient layers of the cat auditory and visual cortices. *J Comp Neurol* 2001, 436: 508–519.
55. Barbour DL, Callaway EM. Excitatory local connections of superficial neurons in rat auditory cortex. *J Neurosci* 2008, 28: 11174–11185.
56. Aizawa N, Eggermont JJ. Mild noise-induced hearing loss at young age affects temporal modulation transfer functions in adult cat primary auditory cortex. *Hear Res* 2007, 223: 71–82.
57. Zhao H, Wang L, Chen L, Zhang J, Sun W, Salvi RJ, *et al.* Temporary conductive hearing loss in early life impairs spatial memory of rats in adulthood. *Brain Behav* 2018, 8: e01004.
58. Johnson SA, Javurek AB, Painter MS, Ellersieck MR, Welsh TH Jr, Camacho L, *et al.* Effects of developmental exposure to bisphenol A on spatial navigational learning and memory in rats: A CLARITY-BPA study. *Horm Behav* 2016, 80: 139–148.
59. Syka J, Suta D, Popelár J. Responses to species-specific vocalizations in the auditory cortex of awake and anesthetized guinea pigs. *Hear Res* 2005, 206: 177–184.
60. Lu T, Liang L, Wang X. Temporal and rate representations of time-varying signals in the auditory cortex of awake primates. *Nat Neurosci* 2001, 4: 1131–1138.

# HMGB1 from Astrocytes Promotes EAE by Influencing the Immune Cell Infiltration-Associated Functions of BMECs in Mice

Junyu Shi<sup>1</sup> · Yifan Xiao<sup>3</sup> · Na Zhang<sup>1</sup> · Mengya Jiao<sup>1</sup> · Xuhuan Tang<sup>1</sup> · Chan Dai<sup>1</sup> · Chenchen Wang<sup>1</sup> · Yong Xu<sup>1</sup> · Zheng Tan<sup>1,2</sup> · Feili Gong<sup>1</sup> · Fang Zheng<sup>1,2</sup>

Received: 16 January 2022 / Accepted: 16 March 2022 / Published online: 13 June 2022  
© Center for Excellence in Brain Science and Intelligence Technology, Chinese Academy of Sciences 2022

**Abstract** High mobility group box 1 (HMGB1) has been reported to play an important role in experimental autoimmune encephalomyelitis (EAE). Astrocytes are important components of neurovascular units and tightly appose the endothelial cells of microvessels by their perivascular endfeet and directly regulate the functions of the blood-brain barrier. Astrocytes express more HMGB1 during EAE while the exact roles of astrocytic HMGB1 in EAE have not been well elucidated. Here, using conditional-knockout mice, we found that astrocytic HMGB1 depletion decreased morbidity, delayed the onset time, and reduced the disease score and demyelination of EAE. Meanwhile, there were fewer immune cells, especially pathogenic T cells infiltration in the central nervous system of astrocytic HMGB1 conditional-knockout EAE mice, accompanied by up-regulated expression of the tight-junction protein Claudin5 and down-regulated expression of the cell adhesion molecules ICAM1 and VCAM1 *in vivo*. *In vitro*, HMGB1 released from astrocytes decreased Claudin5 while increased ICAM1 and VCAM1 expressed by brain

microvascular endothelial cells (BMECs) through TLR4 or RAGE. Taken together, our results demonstrate that HMGB1 derived from astrocytes aggravates EAE by directly influencing the immune cell infiltration-associated functions of BMECs.

**Keywords** HMGB1 · Astrocytes · Experimental autoimmune encephalomyelitis · Blood-brain barrier

## Introduction

Multiple sclerosis (MS) and its animal model experimental autoimmune encephalomyelitis (EAE) are characterized by inflammation, demyelination, and neurodegeneration in the central nervous system (CNS) [1, 2]. Previous studies have reported that the infiltration of peripheral immune cells into the CNS plays a critical role in the progression of MS, and this is a consequence of destruction of the blood-brain barrier (BBB) [3, 4].

In the brain and spinal cord of mammals, the BBB is constituted mainly of brain microvascular endothelial cells (BMECs) that have tight cell-to-cell contacts [5]. The BMEC monolayer in the BBB is sealed by tight junctions (TJs) and adherens junctions [6]. TJ proteins mainly contribute to the high electrical resistance and low paracellular permeability of the BBB [7]. Claudin5 is one of the most important TJ proteins and the BBB fails to seal in Claudin5<sup>-/-</sup> mice [8]. On the other hand, BMECs also express intercellular adhesion molecule 1 (ICAM1) and vascular cell adhesion molecule 1 (VCAM1), which promote the adhesion and transmigration of leukocytes through the BBB [9].

Other than the central role of endothelial cells, it is now becoming clear that neurons, glia, and microvessel are

**Supplementary Information** The online version contains supplementary material available at <https://doi.org/10.1007/s12264-022-00890-1>.

✉ Fang Zheng  
zhengfangtj@hust.edu.cn

<sup>1</sup> Department of Immunology, School of Basic Medicine, Tongji Medical College, Huazhong University of Science and Technology, Wuhan 430030, China

<sup>2</sup> Key Laboratory of Organ Transplantation, Ministry of Education, NHC Key Laboratory of Organ Transplantation, Key Laboratory of Organ Transplantation, Chinese Academy of Medical Sciences, Wuhan 430030, China

<sup>3</sup> Department of Pathology and Pathophysiology, School of Medicine, Jiangnan University, Wuhan 430056, China

organized into the neurovascular unit (NVU), which takes part in regulating cerebral blood flow and comprehensively modulates the functions of the BBB. Within the NVU, astrocytes release many kinds of agents to induce aspects of BBB phenotype *via* perivascular endfeet closely appose to microvessels under physiological conditions [10–12]. While under pathological conditions, astrocytes release inflammatory molecules that disrupt the BBB by direct action on the endothelium [4, 13, 14]. This disrupts TJ proteins and increases ICAM1 and VCAM1, which facilitate the migration of immune cells through the BBB [15, 16].

High mobility group box 1 (HMGB1) is found in nearly all eukaryotes and promotes chromatin function and gene regulation as a non-histone DNA-binding nuclear protein [17–19]. Under pathological conditions, HMGB1 is translocated from nucleus to cytoplasm or released outside the cells. In the extracellular space, HMGB1 triggers sterile inflammation in various diseases including MS as a damage-associated molecular pattern [20, 21]. Studies have shown that HMGB1 is involved in the damage of the BBB, as treatment with HMGB1 monoclonal antibody (mAb) alleviates the destruction of the BBB in many neurological disorders [22–24]. However, the exact mechanism by which HMGB1 directly acts on the BBB needs to be further explored.

Our past research demonstrated that HMGB1 in the CNS is crucial in the development of EAE, because blockade of local HMGB1 in the CNS clearly suppresses EAE [25]. The CNS has many astrocytes and the expression of HMGB1 in astrocytes increases during EAE but the specific roles of astrocytic HMGB1 in EAE are not well known [25, 26].

Here, we found that depletion of astrocytic HMGB1 alleviated the symptoms of active EAE mice such as decreased morbidity, delayed onset time, reduced disease score, and reduced demyelination, which were accompanied by fewer immune cells especially pathogenic T cell infiltration into the CNS. Meanwhile, conditional knockout of astrocytic HMGB1 enhanced the tight junction protein Claudin5 and decreased the cell adhesion molecules ICAM1 and VCAM1 in the CNS of EAE mice *in vivo*. *In vitro*, HMGB1 secreted by astrocytes reduced Claudin5 while increased ICAM1 and VCAM1 in primary BMECs through TLR4 or RAGE. Overall, HMGB1 derived from astrocytes promotes EAE by influencing the immune cell infiltration-associated functions of BMECs.

## Materials and Methods

### Animals

GFAP-Cre<sup>ERT2</sup> mice were from The Mutant Mouse Resource Center and HMGB1<sup>f/f</sup> mice were custom-

generated by Cyagen (Guangzhou) Bioscience Inc., all on a C57BL/6 genetic background. The two transgenic mouse lines were mated with each other to generate GFAP-Cre<sup>ERT2</sup>-HMGB1<sup>f/f</sup> mice (hereafter G<sup>Cre</sup>-HMGB1<sup>f/f</sup>). The genotyping primers were as follows: Cre (forward, CAGCTAAACATGCTTCATCGTCG; reverse, TCCCA CCGTCAGTACGTGAGATA; band, 295 bp); HMGB1-loxP (forward, ACAGCGAATGCTTGAGTGACCT; reverse, GATCTCCTTTGCCCATGTTTAGT; bands, 308 bp for wild-type and 380 bp for Loxp). PCR conditions: 94°C for 3 min; 35 cycles of 94°C for 30 s, 55°C for 30 s, and 72°C for 30 s; then 72°C for 10 min.

Conditional knockout of HMGB1 in astrocytes was induced by injecting G<sup>Cre</sup>-HMGB1<sup>f/f</sup> mice (postnatal 5 weeks) intraperitoneally with Tamoxifen (Tam, Cat#T5648, Sigma, St. Louis, MO, USA) in corn oil (Oil, Cat#C8267, Sigma) at 75 mg/kg for 5 days.

Animals for experiments were matched for gender and age, and were randomly assigned according to the weight. The different groups of mice were mixed in the same cage and the investigators were blinded to the grouping of animals. The feeding of animals and the performance of experiments were all approved by Tongji Medical College Animal Care and Use Committee (No. S1824).

### Actively-induced EAE

Female G<sup>Cre</sup>-HMGB1<sup>f/f</sup> mice injected with Oil or Tam were used to induce EAE as detailed in our previous reports [26, 27]. In brief, injecting mice subcutaneously with emulsion containing MOG<sub>35–55</sub> (200 µg, ChinaPeptides Co., Ltd, China), Freund's complete adjuvant (Cat#F5881, Sigma) and *Mycobacterium tuberculosis* (5 mg/mL, Cat#231141, strain H37Ra; Difco Laboratories, Detroit, MI, USA). Besides, PTX (200 ng, Cat#2980, Sigma) was given intraperitoneally on days 0 and 2. The severity of EAE was scored daily after its induction based on the criteria described previously [25]: 0 (normal), 0.5 (slight weakness of the tail), 1 (total weakness of the tail), 2 (disability of the back legs), 2.5 (paralysis of one of the back legs), 3 (paralysis of both back legs), 3.5 (disability of the forelegs and paralysis of the back legs), 4 (paralysis of the forelegs and back legs), and 5 (death).

### Sample Preparation and Histological Examination

After anesthesia with 300 µL of 0.5% pentobarbital intraperitoneal and perfusion with saline and 4% paraformaldehyde (Cat#GB1101, Servicebio, Wuhan, China), we isolated the thoracic spinal cord and prepared 20-µm frozen sections for histological, immunohistochemical, and immunofluorescence staining. For histological evaluation, sections were stained with hematoxylin and



eosin (H&E, Cat#G1005, Servicebio) and Luxol Fast Blue (LFB, Cat#2980, Sigma). Infiltrated immune cells were scored after H&E staining as described in our previous report [25]: 0 (no infiltration), 1 (several immune cells), 2 [ $<25\%$  of the white matter (WM) area], 3 ( $>25\%$  and  $<50\%$  of the WM area), and 4 ( $>50\%$  of the WM area). Demyelination was graded by LFB: 0 (without demyelination), 1 (rare foci), 2 ( $<25\%$  of the WM area), 3 ( $>25\%$  and  $<50\%$  of the WM area), and 4 ( $>50\%$  of the WM area).

### Immunohistochemistry

Briefly, spinal cord sections were quenched in  $3\% \text{H}_2\text{O}_2$  for 30 min and incubated with primary antibody (listed in the supplementary methods) overnight at  $4^\circ\text{C}$ , then 3,3'-diaminobenzidine was used as the chromogenic substrate. For the analysis of infiltrated T cells,  $\text{CD3}^+$  cells in the whole spinal cord section were counted and compared. To compare demyelination, the percentage of  $\text{MBP}^+$  area occupied in the white matter of spinal cord sections was calculated using ImageJ software.

### Immunofluorescence

After blockade, incubation with primary antibodies and fluorescein-conjugated secondary antibodies, the sections were visualized with LSM 800 (Carl Zeiss AG., Germany). Negative controls that lacked primary antibodies and with secondary antibodies were conducted for each experiment to exclude the nonspecific fluorescence. For the analysis of immunofluorescence images, the integrated optical density of full spinal cord sections was quantified using ImageJ software.

### Flow Cytometry

Lymph nodes in the axilla and groin were isolated, triturated, and filtered through a  $70\text{-}\mu\text{m}$  molybdenum screen to obtain single cells. Spinal cords and brains were minced and digested in collagenase II (2 mg/mL, Cat#C6885, Sigma) and DNase I (100 ng/mL, Cat#DN25, Sigma) at  $37^\circ\text{C}$  for 45 min. Single cells were obtained by Percoll gradient centrifugation ( $70\%/40\%$ , Cat#P8370, Solarbio, Beijing, China).

To detect cell surface antigens,  $1 \times 10^6$  cells were incubated with antibodies at  $4^\circ\text{C}$  for 0.5 h.

To measure intracellular cytokines,  $2 \times 10^6$  cells were stimulated at  $37^\circ\text{C}$  with a cell stimulation cocktail (plus protein transport inhibitors) (Cat#00-4975-93, eBiosciences, Thermo Fisher Scientific, Carlsbad, CA, USA) for 4 h, then the cells were permeabilized using Perm/Fix solution (Cat#00-5523-00, eBiosciences, Thermo Fisher Scientific) and incubated with anti-IL-17A or anti-IFN- $\gamma$

antibody at  $4^\circ\text{C}$  for 0.5 h. Cells were analyzed with BD LSR Fortessa.

### Western Blotting

After lysing tissues or cells with RIPA buffer (Cat#G2002, Servicebio) containing the proteinase inhibitor phenylmethanesulfonyl fluoride (Cat#G2008, Servicebio) or a phosphorylase inhibitor (Cat#G2007, Servicebio) on ice, the supernatant was collected. The protein concentration was assessed using a protein assay kit (Cat#23225, Thermo Fisher Scientific) and normalized by adding  $1 \times \text{PBS}$ . The samples mixed with sodium dodecyl sulfate (SDS)-loading buffer were denatured in boiling water and separated by  $10\%$  SDS-polyacrylamide gel electrophoresis and blotted onto polyvinylidene fluoride membranes (Cat#05317, Millipore, St. Louis, MO, USA). Different proteins under the same conditions were assessed on the same membrane. After incubation with primary antibody (see supplementary methods) and horseradish peroxidase-conjugated secondary antibody, the blots were imaged using an ECL system (Bio-Rad) and quantified by densitometry using ImageJ software.

### Astrocyte Conditioned Medium Preparation

Primary astrocytes were cultured from  $\text{G}^{\text{Cre}}\text{-HMGB1}^{\text{ff}}$  neonatal mice as previously described [27] and flow cytometry was used to assess the cell purity.  $3 \times 10^5$  astrocytes in 24-well culture plates were stimulated with or without TNF (Cat#AF-315-01A, PeproTech, USA) for 12 h, then the medium was changed to fresh medium with or without neutralizing anti-HMGB1 monoclonal antibody ( $5 \mu\text{g/mL}$ , from the Institute of Biophysics, Chinese Academy of Science, Beijing, China [25, 28, 29]) for another 24 h to harvest the conditioned medium.

### Culture and Treatment of Primary Brain Microvascular Endothelial Cells

Primary mouse BMECs were cultured as previously reported [30]. Briefly, 8–12 week-old mice were sacrificed by cervical dislocation and meninges-free forebrains were collected and minced. The tissue was digested with collagenase 2 (final concentration,  $1 \text{ mg/mL}$ ; Cat#11088807001, Roche) and DNase ( $0.1 \text{ mg/mL}$ ) for 1 h at  $37^\circ\text{C}$  on an orbital shaker at 180 r/min. BSA-DMEM ( $20\% \text{ w/v}$ ) was added to re-suspend the cells and they were centrifuged at  $1,000 \text{ g}$  for 20 min at  $4^\circ\text{C}$  to remove the myelin. The pellet was re-suspended in DMEM with collagenase/dispase (final concentration,  $1 \text{ mg/mL}$ , Cat#10269638001, Roche) and DNase ( $0.1 \text{ mg/mL}$ ) and digested for 1 h at  $37^\circ\text{C}$  on an orbital shaker at 180

r/min and the protein almost. The cells after digestion were maintained in endothelial cell medium containing DMEM with 20% FBS, 20  $\mu\text{g/mL}$  bFGF, 100  $\mu\text{L/mL}$  heparin, and 4 mg/mL puromycin (added only in the first 2 days of culture), plated in wells coated with rat tail collagen, and incubated at 37°C under 5%  $\text{CO}_2$ . The medium was changed every 2–3 days. On days 7–9 of culture, BMECs were used for experiments. They were treated with HMGB1 (100 ng/mL, Cat#H4652, Sigma) or SACM for the indicated time and then the cells were collected for western blot or RT-PCR. TLR4 inhibitor (100 nmol/L TAK-242, Cat#614316, Millipore) or RAGE inhibitor (50 nmol/L FPS-ZM1, Cat#553030, Millipore) was incubated with BMECs for 2 h before HMGB1 or SACM stimulation.

### Real-time PCR Analysis

Total RNA of cells was obtained using TRIzol (Cat#15596018, Thermo Fisher Scientific) and reverse-transcribed into cDNA using a kit (Cat#K1622, Thermo Fisher Scientific). Real-time PCR was performed using CFX96 (Bio-Rad). Primer sequences are listed in supplementary materials and were synthesized by Sangon Biotech. The results are shown as relative expression values normalized to  $\beta$ -actin.

### Statistical Analysis

Experimental data were analyzed using IBM SPSS Statistics 26 and graphed with GraphPad Prism 8.2.1. Comparisons between groups were analyzed by two-tailed Student's *t*-test or one-way analysis of variance (ANOVA) followed by Tukey's test or Mann-Whitney U test as indicated. Data are presented as the mean  $\pm$  SD or median with interquartile range.  $P < 0.05$  was considered statistically significant.

## Results

### Conditional Knockout of HMGB1 in Astrocytes Alleviates EAE

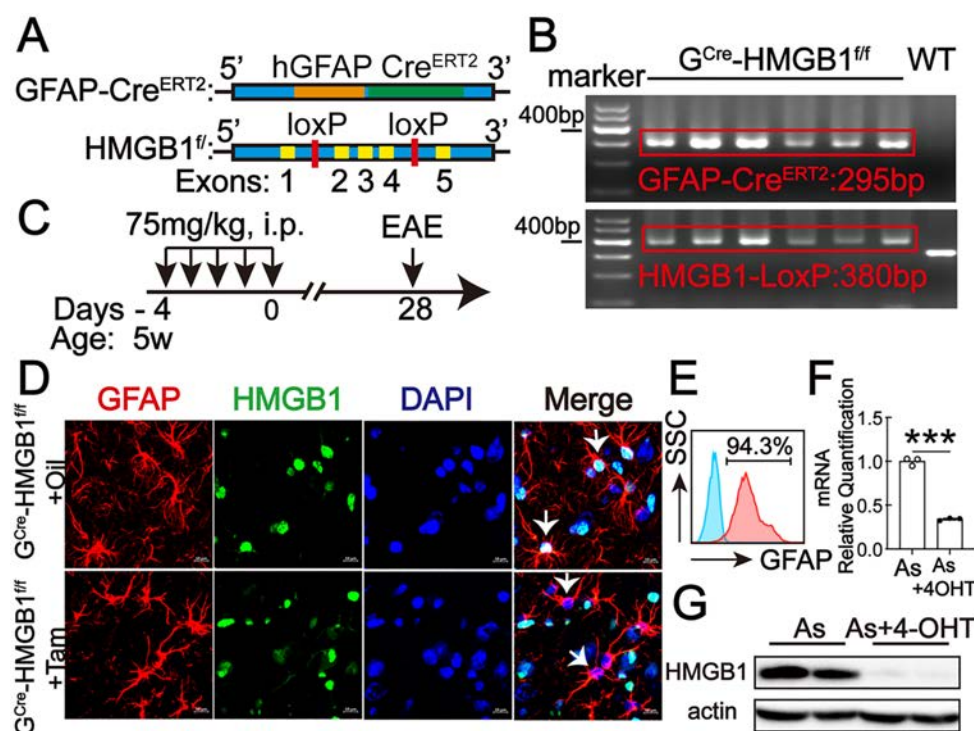
To explore the functions of HMGB1 in astrocytes, HMGB1<sup>fl/f</sup> mice with exon 2–4 of HMGB1 flanked with two loxP sites were crossbred with GFAP-Cre<sup>ERT2</sup> mice, which express Cre<sup>ERT2</sup> under the control of the human glial fibrillary acidic protein promoter (Fig. 1A). PCR genotyping of GFAP-Cre<sup>ERT2</sup>-HMGB1<sup>fl/f</sup> (G<sup>Cre</sup>-HMGB1<sup>fl/f</sup>) mice is shown as Fig. 1B. At postnatal week 5, G<sup>Cre</sup>-HMGB1<sup>fl/f</sup> mice were injected with Tamoxifen (Tam) for 5 days to knock out HMGB1 in astrocytes (Fig. 1C). As shown in Fig. 1D, no HMGB1 was expressed in astrocytes 4 weeks

after injection of Tam and HMGB1 in other resident cells of the CNS was not influenced. Meanwhile, the mice with astrocytic HMGB1 conditional knockout all grew well and had no symptoms of disease under physiological conditions. *In vitro*, when primary astrocytes cultured from G<sup>Cre</sup>-HMGB1<sup>fl/f</sup> mice (Fig. 1E) were treated with 4-OH-Tam (4-OHT), HMGB1 mRNA decreased significantly (Fig. 1F) and the protein almost disappeared (Fig. 1G).

To clarify the roles of astrocytic HMGB1 in EAE, active EAE in female G<sup>Cre</sup>-HMGB1<sup>fl/f</sup> mice was induced 4 weeks after Tam injection, when astrocytic HMGB1 was totally deleted and the effects of Tam on EAE were excluded. As shown in Fig. 2A, astrocytic HMGB1 knockout alleviated the EAE disease score from the onset to chronic stages, and this was accompanied by reduced incidence, delayed onset time, and decreased mean maximal score (Table 1). Astrocytic HMGB1 depletion also decreased the demyelination score, a characteristic pathological manifestation of EAE, as shown by LFB staining (Fig. 2B). Consistent with this, the percentage of MBP<sup>+</sup> area occupied in the white matter of the spinal cord also increased in astrocytic HMGB1 conditional knockout EAE mice (Fig. 2C). These results demonstrate that the knockout of HMGB1 in astrocytes represses the development of EAE and improves demyelination, which suggest that astrocytic HMGB1 plays a harmful role in EAE. As is known that EAE is characterized by the infiltration of immune cells, especially effector T cells in the CNS [31], we next investigated the influence of astrocytic HMGB1 on immune cell infiltration in the CNS.

### Conditional Knockout of HMGB1 in Astrocytes Reduces the Infiltration of Pathogenic Effector T Cells in the CNS During EAE

To uncover the impact of astrocytic HMGB1 knockout on immune cells in the CNS and periphery during EAE, histopathological examination of the spinal cord sections was applied to study the location and number of immune cells. The data showed that many mononuclear cells infiltrated parenchyma of spinal cord during EAE. Astrocytic HMGB1 conditional knockout remarkably reduced the immune cell infiltration in the parenchyma (Fig. 3A, left panel), especially CD3<sup>+</sup> T lymphocytes (Fig. 3A, right panel). Similarly, as illustrated by flow cytometry (Fig. S1), the frequency and absolute number of immune cells (CD45<sup>+</sup>), T cells (CD3<sup>+</sup>), and the subpopulations Th1 (CD3<sup>+</sup>CD4<sup>+</sup>IFN- $\gamma$ <sup>+</sup>) and Th17 (CD3<sup>+</sup>CD4<sup>+</sup>IL-17A<sup>+</sup>) were markedly decreased in the CNS of astrocytic HMGB1 conditional knockout EAE mice (Fig. 3B); however, in the lymph nodes, the frequency and absolute number of T cells and Th1 cells increased in these mice (Fig. 3C). These data suggest that the recruitment of immune cells from



**Fig. 1** Breeding and evaluation of astrocytic HMGB1 conditional knockout mice. **A** HMGB1<sup>fl/fl</sup> mice with exon 2–4 of HMGB1 flanked with two loxP sites are crossbred with GFAP-Cre<sup>ERT2</sup> mice, which express Cre<sup>ERT2</sup> under the control of the human glial fibrillary acidic protein promoter, both on the C57BL/6 background. **B** PCR genotyping of GFAP-Cre<sup>ERT2</sup>-HMGB1<sup>fl/fl</sup> mice (WT, wild-type). **C** Schematic of protocol: GFAP-Cre<sup>ERT2</sup>-HMGB1<sup>fl/fl</sup> mice at postnatal 5 weeks are injected with corn oil or Tamoxifen for 5 days; EAE is induced 4 weeks post-injection. **D** HMGB1 expressed in spinal cord

sections from GFAP-Cre<sup>ERT2</sup>-HMGB1<sup>fl/fl</sup> mice 4 weeks post-injection of Tamoxifen [red, GFAP (indicator of astrocytes); green, HMGB1; blue, DAPI-stained nuclei; arrows, GFAP<sup>+</sup> astrocytes; scale bars, 10  $\mu$ m]. **E** Flow cytometry showing the cell purity of primary astrocytes. **F**, **G** RT-PCR and western blot analysis of HMGB1 in primary astrocytes isolated from GFAP-Cre<sup>ERT2</sup>-HMGB1<sup>fl/fl</sup> pups treated with 4-OH-Tamoxifen (4-OHT; 1  $\mu$ mol/L). Data are shown as the mean  $\pm$  SD. \*\*\* $P$  < 0.001, two-tailed Student's  $t$ -test.

peripheral immune organs to the CNS decreases after astrocytic HMGB1 knockout, and this may influence immune cell infiltration *via* regulating the BBB, especially the functions of endothelial cells.

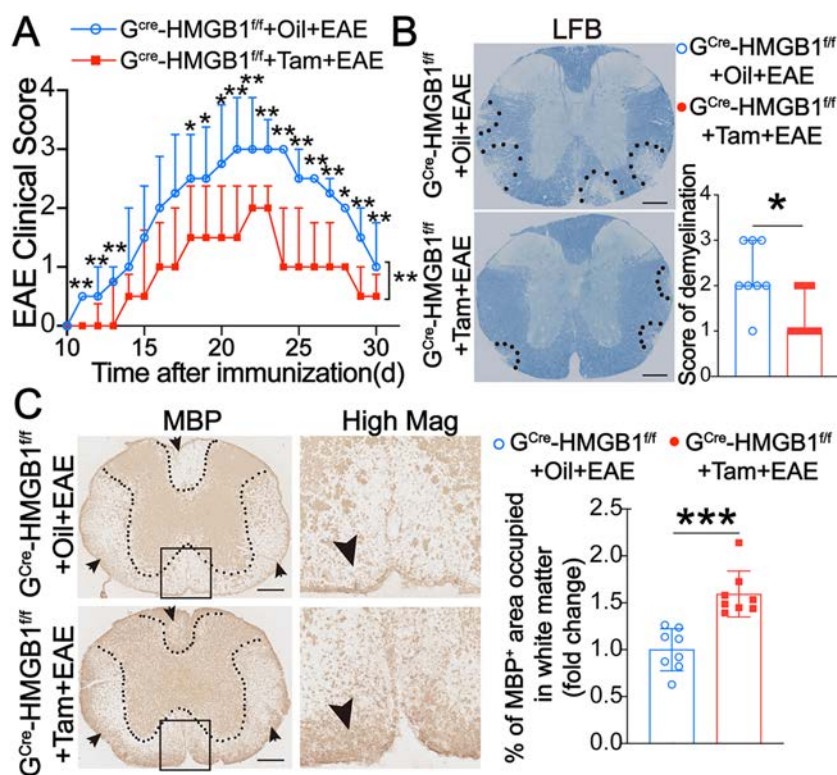
#### Conditional Knockout of HMGB1 in Astrocytes Increases Claudin5 and Decreases Adhesion Molecules in the CNS During EAE

TJ proteins and adhesion molecules expressed on microvessel endothelial cells of the CNS are closely associated with the functions of the BBB. As shown in Fig. 4A, Claudin5 expressed on CD31-positive endothelial cells of microvessels in the spinal cord was lower in EAE mice than under physiological conditions. After astrocytic HMGB1 was deleted, Claudin5 was increased during EAE compared with non-deletion. Similarly, western blots showed that the amount of Claudin5 protein in spinal cord homogenates from astrocytic HMGB1-knockout EAE mice also increased (Fig. 4B). Meanwhile, the critical adhesion molecules ICAM1 and VCAM1 decreased in the spinal

cord homogenates of astrocytic HMGB1-knockout EAE mice (Fig. 4C). These data suggest that knocking out astrocytic HMGB1 avoids the infiltration of immune cells into the CNS by influencing the functions of the BBB.

#### Astrocytes Actively Release HMGB1

The functions of HMGB1 are associated with its location, so the characteristics of HMGB1 expressed in astrocytes were explored to uncover how it influenced the functions of BMECs during EAE. As shown in Fig. 5A (upper panel), astrocytes abundantly expressed HMGB1 in nuclei under physiological conditions. During EAE, astrocytes in the grey matter were hypertrophied and their HMGB1 expression was significantly reduced and mainly located in the cytoplasm (Fig. 5A, middle panel). In astrocytic HMGB1 conditional knockout EAE mice, astrocytes showed normal morphology (Fig. 5A, lower panel). To further confirm the location change of HMGB1, primary astrocytes were stimulated with TNF which is crucial in the development of EAE and could simulate the inflammatory environment



**Fig. 2** Influence of astrocytic HMGB1 conditional knockout on EAE. **A** EAE disease score of GFAP-Cre<sup>ERT2</sup>-HMGB1<sup>fl/fl</sup> mice injected with corn oil or Tamoxifen. Data are representative of three independent experiments and are shown as the median with interquartile range ( $n = 8/\text{group}$ ;  $*P < 0.05$ ,  $**P < 0.01$ , Mann-Whitney U test). **B** LFB staining of thoracic spinal cord sections at the peak stage of EAE (scale bars, 200  $\mu\text{m}$ ;  $n = 8/\text{group}$ ;  $*P < 0.05$ , Mann-Whitney U test;

data are representative of three independent experiments and shown as the median with interquartile range). **C** Left panels, representative images of thoracic spinal cord sections at the peak stage of EAE with immunohistochemical staining for MBP ( $n = 8/\text{group}$ ; squares magnified at right; scale bars, 200  $\mu\text{m}$ ). Right panel, percentage of MBP<sup>+</sup> area in the white matter (mean  $\pm$  SD, two-tailed Student's  $t$ -test).

**Table 1** Disease features of EAE mice

Group	Incidence (No. with EAE/Total)	Mean Maximal Score (Median with interquartile range)	Disease Onset
G <sup>Cre</sup> -HMGB1 <sup>fl/fl</sup> + Oil + EAE	8/8 = 100%	3 (2.625, 3.875)	11 (11, 11)
G <sup>Cre</sup> -HMGB1 <sup>fl/fl</sup> + Tam + EAE	7/8 = 87.5%	2 (1, 2.5) **	14 (12.5, 14) **

Data are representative of three independent experiments ( $n = 8/\text{group}$ ;  $**P < 0.01$ , Mann-Whitney U test).

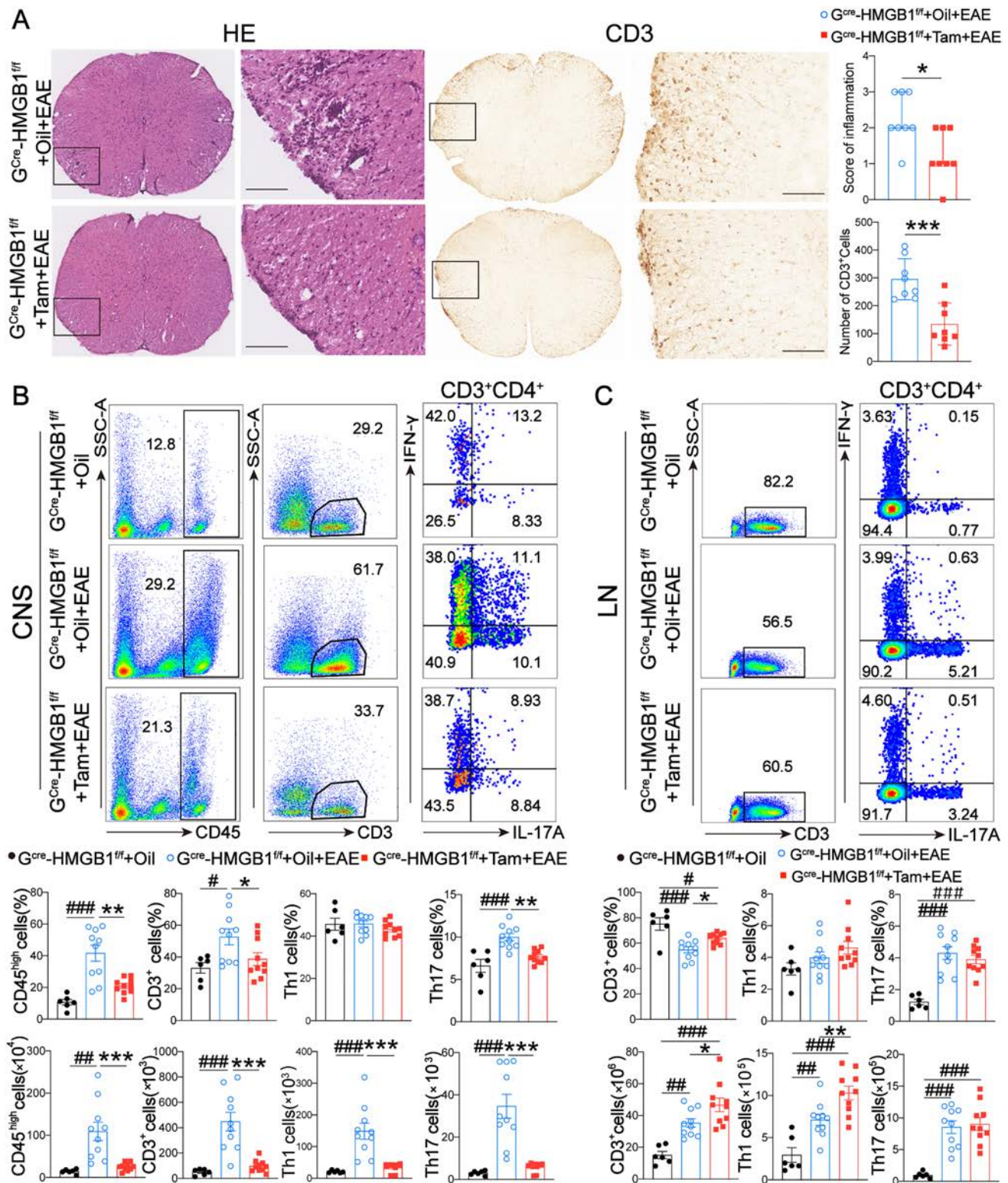
of EAE. As shown in Fig. 5B, abundant HMGB1 was released into the medium of astrocytes after stimulation without affecting their survival. These data indicate that astrocytes actively release HMGB1.

### HMGB1 Released from Astrocytes Influences the Functions of Primary BMECs Associated with Immune Cell Infiltration

To further demonstrate the influence of astrocyte-derived HMGB1 on endothelial cells of the BBB, primary BMECs were cultured (Fig. 6A). Astrocyte-conditioned medium (ACM) from astrocytes primed with TNF (sACM), from

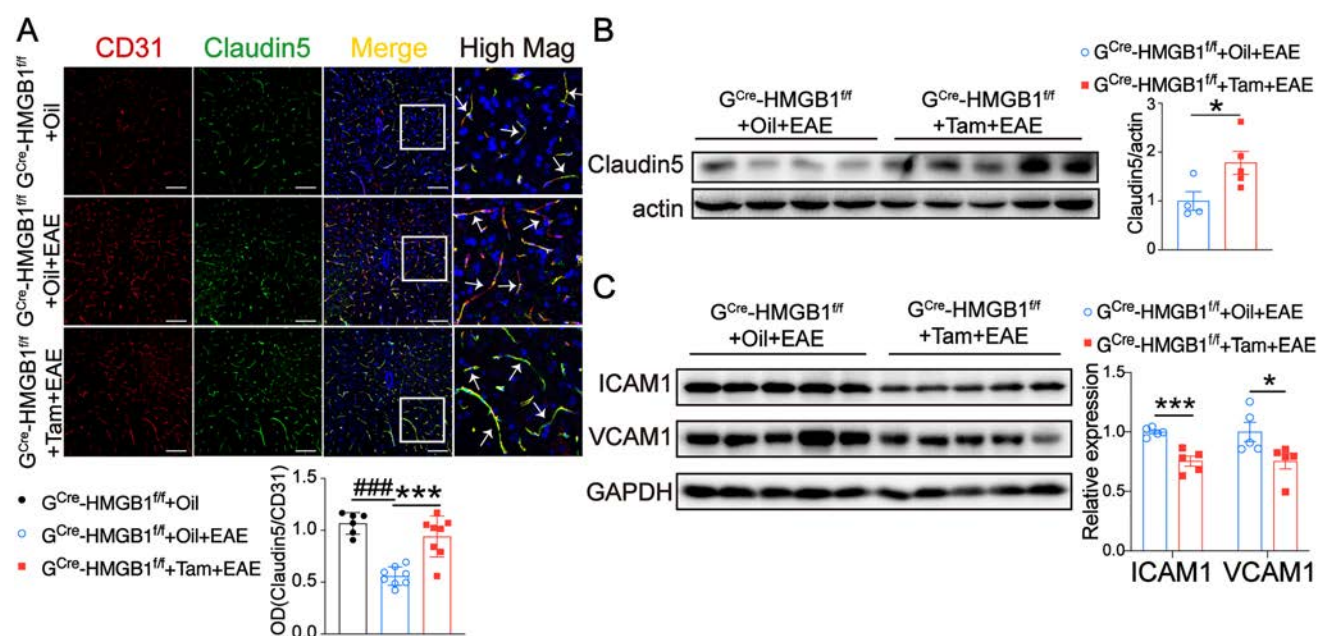
HMGB1-knockout astrocytes primed with TNF (HMGB1-KO sACM), and sACM with anti-HMGB1 neutralizing monoclonal antibody (sACM+HMGB1-mAb) were collected to stimulate BMECs. As shown in Fig. 6B, the survival of BMECs was not influenced by the stimulation. sACM decreased Claudin5 and increased ICAM1 and VCAM1 expressed by BMECs compared with ACM. However, HMGB1-KO sACM upregulated Claudin5 and downregulated ICAM1 and VCAM1 compared with sACM (Fig. 6C). sACM+HMGB1-mAb had the same effects as HMGB1-KO sACM (Fig. 6D). In addition, recombinant HMGB1 decreased Claudin5 and increased ICAM1 and VCAM1 in mRNA and protein without affecting the cell





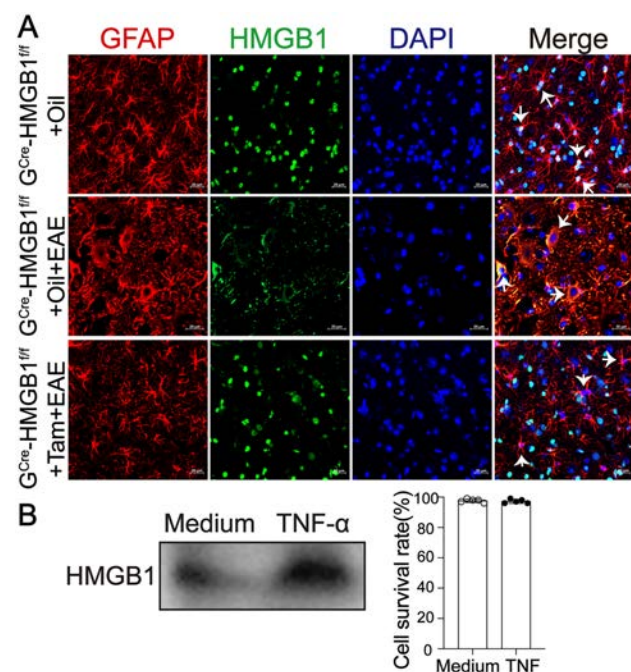
**Fig. 3** Influence of astrocytic HMGB1 conditional knockout on immune cells during EAE. **A** Left and middle panels, representative images of thoracic spinal cord sections at the peak stage of EAE with H&E and immunohistochemical staining for CD3 ( $n = 8$ /group; squares, high magnification; scale bars, 100  $\mu$ m). Right panels, upper, pathological scores (median with interquartile range; \* $P < 0.05$ , Mann-Whitney U test); lower, numbers of CD3<sup>+</sup> cells in whole spinal cord sections (mean  $\pm$  SD; \*\*\* $P < 0.001$ , two-

tailed Student's  $t$ -test). Data are representative of three independent experiments. **B, C** Flow cytometry of immune cells in CNS and lymph nodes from mice at the peak stage of EAE. The upper images are representative of two independent experiments. Data shown below are pooled from two independent experiments and are shown as the mean  $\pm$  SD ( $n = 6$  or 10/group; # $P < 0.05$ , ## $P < 0.01$ , ### $P < 0.001$ , \* $P < 0.05$ , \*\* $P < 0.01$ , \*\*\* $P < 0.001$ , one-way ANOVA followed by Tukey's test).



**Fig. 4** Influence of astrocytic HMGB1 conditional knockout on the BBB during EAE. **A** Upper panels, representative images showing the expression of Claudin5 on CD31<sup>+</sup> microvessels in thoracic spinal cord sections from EAE mice during the peak stage (scale bars, 100  $\mu$ m; red, CD31; green, Claudin5; blue, nuclei stained with DAPI; squares, high magnification; arrows, CD31<sup>+</sup> microvessels). Lower panel, data shown are representative of three independent experiments

( $n = 6$  or  $8$ /group; mean  $\pm$  SD; ### $P < 0.001$ , \*\*\* $P < 0.001$ , one-way ANOVA followed by Tukey's test). **B, C** Left panels, western blots of Claudin5 and ICAM1/VCAM1 in spinal cord homogenates from EAE mice at the peak stage. Right panels, data representative of three independent experiments (mean  $\pm$  SD; \* $P < 0.05$ , \*\*\* $P < 0.001$ , two-tailed Student's  $t$ -test).



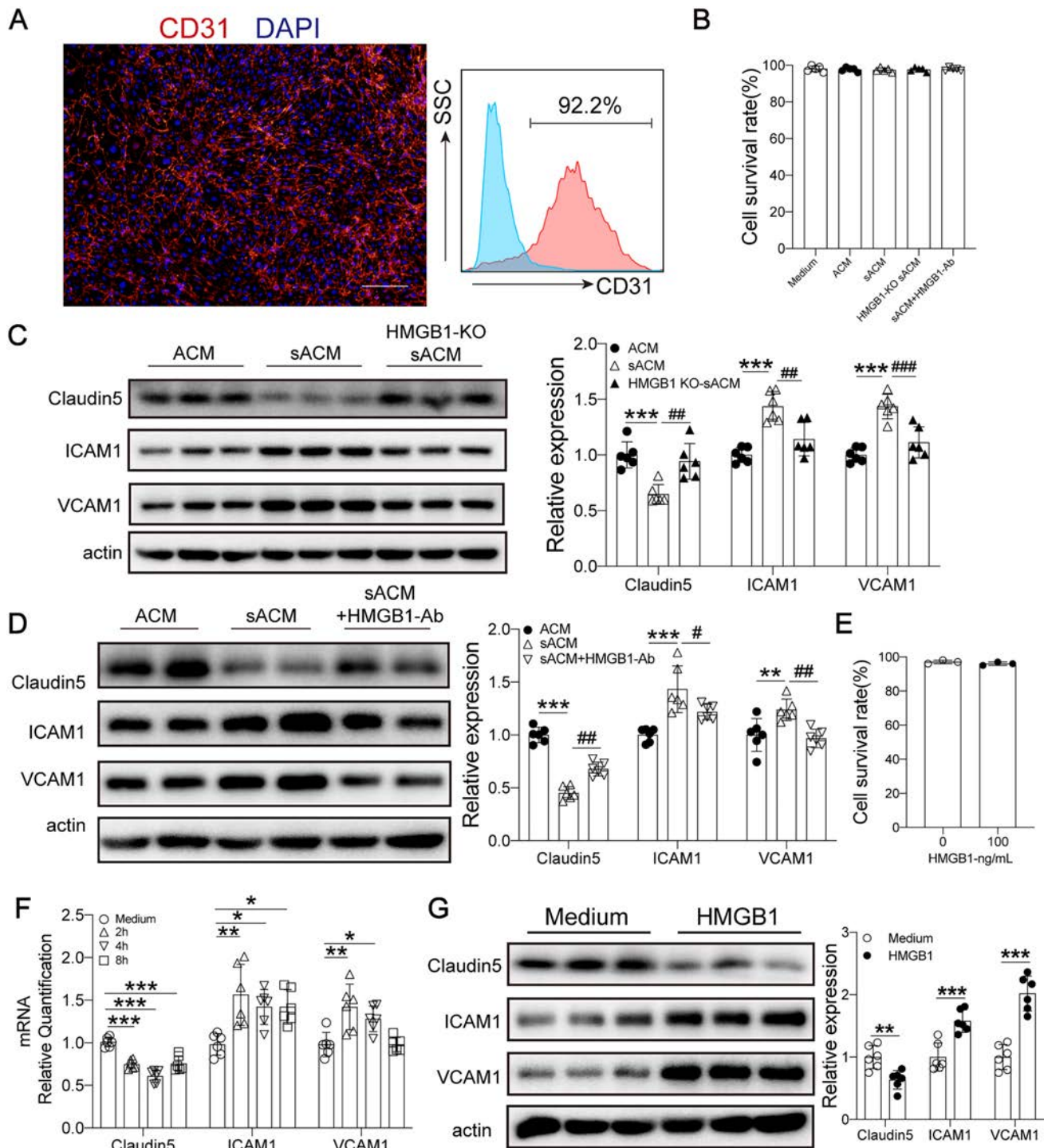
**Fig. 5** Astrocytes actively release HMGB1. **A** Immunofluorescence of HMGB1 and astrocytes in thoracic spinal cord sections (red, GFAP; green, HMGB1; blue, nuclei stained with DAPI; arrows, GFAP<sup>+</sup> astrocytes in the grey matter; scale bars, 20  $\mu$ m). **B** Left, western blots of HMGB1 in astrocyte-conditioned medium and TNF-stimulated astrocyte-conditioned medium (TNF, 10 ng/mL). Right, cell survival rates of astrocytes.

survival (Fig. 6E–G). Taken together, these data indicate that HMGB1 released from astrocytes directly influences the functions of BMECs associated with immune cell infiltration.

### The Effects of Astrocytic HMGB1 on BMECs are Mediated by TLR4 and RAGE

TLR4 and RAGE expressed on BMECs increased significantly after HMGB1 stimulation (Fig. 7A). To address the receptor involved in the effects of HMGB1 on BMECs, the antagonists of advanced glycation end products (RAGE) and toll-like receptor 4 (TLR4) were introduced. The TLR4 antagonist TAK-242 rescued the downregulation of Claudin5 upon HMGB1 stimulation, and did not change the HMGB1-induced upregulation of ICAM1 and VCAM1 (Fig. 7B). FPS-ZM1, a RAGE antagonist, inhibited the HMGB1-induced increase in ICAM1 and VCAM1, and had no effect on the HMGB1-stimulated downregulation of Claudin5 (Fig. 7C). Similarly, the influence of sACM on Claudin5, as well as on ICAM1 and VCAM1, disappeared when TLR4 or RAGE was blocked (Fig. 7D). Taken together, these data indicate that astrocytic HMGB1 decreases Claudin5 through TLR4 and increases ICAM1 and VCAM1 through RAGE.

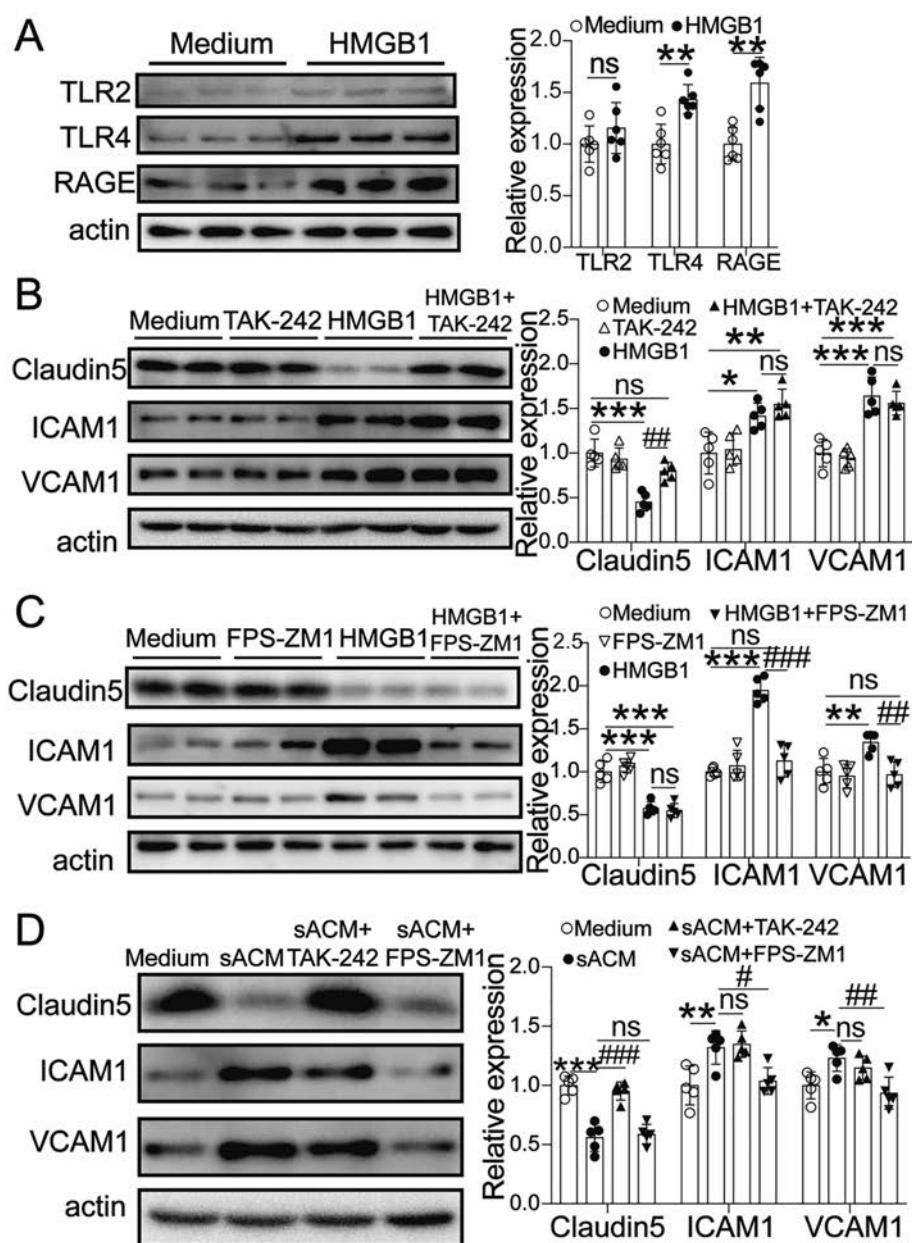




**Fig. 6** Effects of HMGB1 released from astrocytes on BMECs. **A** Left, representative image of immunofluorescence (red, CD31; blue, nuclei stained with DAPI; scale bar, 100  $\mu$ m). Right, flow cytometry showing cell purity of BMECs. **B** Cell survival rates of BMECs after stimulation. **C** Western blots (left) and analysis (right) of Claudin5, ICAM1, and VCAM1 in BMECs stimulated with sACM or HMGB1-KO sACM for 24 h. **D** Western blots (left) and analysis (right) of Claudin5, ICAM1, and VCAM1 in BMECs treated with sACM and sACM with HMGB1-mAb (5  $\mu$ g/mL) for 24 h. **E** Cell survival rate analysis of BMECs after HMGB1 (100 ng/mL)

stimulation for 12 h. **F** RT-PCR analysis of Claudin5, ICAM1, and VCAM1 in BMECs treated with recombinant HMGB1 (100 ng/mL) for different times ( $n = 6$ /group). **G** Left, representative images of western blots of Claudin5, ICAM1, and VCAM1 on BMECs treated with HMGB1 (100 ng/mL) for 12 h. Right, data shown are representative of or pooled from two independent experiments. Mean  $\pm$  SD; \* $P < 0.05$ , \*\* $P < 0.01$ , \*\*\* $P < 0.001$ , # $P < 0.05$ , ## $P < 0.01$ , ### $P < 0.001$ , one-way ANOVA followed by Tukey's test (C, D, F) or two-tailed Student's *t*-test (G).

**Fig. 7** Receptors involved in the influences of astrocytic HMGB1 on BMECs. **A** Western blots (left) and statistics (right) of three receptors (TLR2/TLR4/RAGE) in BMECs after HMGB1 stimulation for 12 h. **B** Western blots (left) and statistics (right) of Claudin5, ICAM1 and VCAM1 under HMGB1 stimulation for 12 h when TLR4 is blocked (TAK-242: 100 nmol/L). **C** Western blots (left) and statistics (right) of Claudin5, ICAM1, and VCAM1 under HMGB1 stimulation for 12 h when RAGE is blocked (FPS-ZM1: 50 nmol/L). **D** Western blots (left) and statistics (right) of Claudin5, ICAM1, and VCAM1 under sACM stimulation for 24 h when TLR4 or RAGE are blocked. Data shown are pooled from two or three independent experiments and shown as the mean  $\pm$  SD. \* $P$  < 0.05, \*\* $P$  < 0.01, \*\*\* $P$  < 0.001, # $P$  < 0.05, ## $P$  < 0.01, ### $P$  < 0.001, two-tailed Student's  $t$ -test (A) or one-way ANOVA followed by Tukey's test (B–D).



The downstream signal pathways for TLR4 and RAGE include MAPKs (ERK, JNK, p38) and NF- $\kappa$ B (p65) [32, 33]. As shown in Fig. S2A, the activated phosphorylation of JNK induced by HMGB1 was inhibited by the RAGE inhibitor FPS-ZM1 and the activated phosphorylation of p65 induced by HMGB1 was inhibited by the TLR4 inhibitor TAK-242, indicating that the effects of HMGB1 on BMECs are through the TLR4-mediated activation of p65 or the RAGE-mediated activation of JNK. TLR4 signaling pathways have two branches: MyD88-dependent and MyD88-independent pathways. As shown in Fig. S2B, the TLR4 inhibitor TAK-242 inhibited the increase of MyD88 stimulated by HMGB1, indicating that MyD88 is involved in the TLR4 signaling pathway of BMECs.

## Discussion

HMGB1 has multiple functions on the basis of expression patterns such as the number, cell location, and sub-cellular location. Our previous studies have demonstrated that HMGB1 in the CNS is detrimental in the development of EAE [25]; carefully exploring the functions of HMGB1 in different cell types is particularly important for research and the prevention of disease. The exact roles of astrocytic HMGB1 in neurological diseases including MS are unknown and there has been no applicable genetically-modified mouse model. HMGB1 mutation causes severe neonatal syndromes as it is essential for the survival of mice [34]. As for gene mutations in astrocytes, the use of



hGFAP-Cre mice has been reported to result in recombination not only in astrocytes, but many neurons and oligodendrocytes are also influenced because of the activity of the hGFAP promoter in progenitor cells during embryonic development [35]. In the present study, astrocytic HMGB1-knockout was achieved by injecting GFAP-Cre<sup>ERT2</sup>-HMGB1<sup>fl/fl</sup> mice with Tam in adulthood to rule out the possible influences on other CNS resident cells or the growth of mice. This study is the first to report the local functions of astrocytic HMGB1 in EAE.

The functions of the BBB mainly depend on microvessel endothelial cells. The TJ protein Claudin5 expressed on these cells in the spinal cord clearly decreases during EAE, indicating destruction of the BBB and it has been reported that BBB fails to seal in Claudin5<sup>-/-</sup> mice [8]. Thus, the increased expression of Claudin5 on the microvessel endothelial cells in astrocytic HMGB1 conditional-knockout EAE mice indicated that the barrier function of BBB was more integrated to avoid the entry of immune cells into the CNS. Meanwhile, the decrease of the adhesion molecules ICAM1 and VCAM1 in the CNS could also reduce the recruitment of immune cells from the periphery to the CNS.

Although HMGB1 has been reported to be involved in the destruction of the BBB as anti-HMGB1 mAb therapies protect the BBB from disruption in diseases such as Parkinson disease, these studies generally applied the systemic administration of HMGB1 mAb and the sources of HMGB1 being neutralized were not determined [22, 23, 36]. Some studies focused on HMGB1 from neurons, but it is passively released from damaged and dead neurons, serious consequences of developed disease [22]. The roles of astrocytes have been overlooked. Here, we found that astrocytes are activated and actively release HMGB1 during EAE.

The reported protective effects of HMGB1-mAb on the damaged BBB are broad and include the improvement of tight junction structures between endothelial cells, the repair of digested basement membrane, and the reduction of activated CNS resident cells and immune cells infiltrated from the circulation [37]. But little was known about how HMGB1 directly acts on the BBB. Some studies showed that recombinant HMGB1 *in vitro* induces upregulation of the adhesion molecules ICAM1 and VCAM1 on vascular endothelial cell lines, but the cell lines used cannot completely replace primary cells because many characteristics are different [24, 30]. Primary BMECs have been reported to better simulate the functions of BBB *in vivo* [30]. Here, the application of HMGB1-KO sACM, HMGB1 monoclonal antibody, and recombinant HMGB1 comprehensively established that HMGB1 released from astrocytes affects the BBB directly by decreasing Claudin5

and increasing ICAM1 and VCAM1 on BMECs, consisted with the results of *in vivo* animal experiments.

Certainly, there are also some limitations in the present study. First, the sulfhydryl in C23, C45, and C106 of HMGB1 are easily oxidized by active oxygen in the external environment and different isoforms of HMGB1 bind to different receptors and have different functions [38, 39]. The increased level of reactive oxygen at the peak stage of EAE [40, 41] indicates that HMGB1 in EAE may have a different redox state but this is not explored here. Second, a growing number of reports have implied that HMGB1 release relies on post-translational modifications; which also have different functions [42, 43]. Here, we find that astrocytes actively release HMGB1 during EAE but the post-translational modifications of HMGB1 are not assessed and how HMGB1 is released from astrocytes is still not clear. Last, we showed that HMGB1 directly influenced the functions of BMECs through TLR4 or RAGE and explored the downstream signaling pathways, but the downstream mediators for TLR4 and RAGE are not entirely clear and need further exploration.

Collectively, using astrocytic HMGB1 conditional knockout mice along with primary astrocytes and BMECs, we found that astrocytes actively released HMGB1 during EAE. The HMGB1 derived from astrocytes directly influenced the functions of BMECs *via* decreasing the junction protein Claudin5 through TLR4 and increasing the adhesion molecules ICAM1 and VCAM1 through RAGE, resulting in the infiltration of pathogenic T cells into the CNS and then leading to the development of EAE.

**Acknowledgements** This work was supported by the National Natural Science Foundation of China (31670876 and 82171761).

**Conflict of interest** All authors claim that there are no conflicts of interest.

## References

1. Keegan BM, Noseworthy JH. Multiple sclerosis. *Annu Rev Med* 2002, 53: 285–302.
2. Long HC, Wu R, Liu CF, Xiong FL, Xu Z, He D. miR-125a-5p regulates vitamin D receptor expression in a mouse model of experimental autoimmune encephalomyelitis. *Neurosci Bull* 2020, 36: 110–120.
3. Lassmann H. Multiple sclerosis: Lessons from molecular neuropathology. *Exp Neurol* 2014, 262 Pt A: 2–7.
4. Minagar A, Alexander JS. Blood-brain barrier disruption in multiple sclerosis. *Mult Scler* 2003, 9: 540–549.
5. Sweeney MD, Sagare AP, Zlokovic BV. Blood-brain barrier breakdown in Alzheimer disease and other neurodegenerative disorders. *Nat Rev Neurol* 2018, 14: 133–150.
6. Hawkins BT, Davis TP. The blood-brain barrier/neurovascular unit in health and disease. *Pharmacol Rev* 2005, 57: 173–185.

7. Bazzoni G, Dejana E. Endothelial cell-to-cell junctions: Molecular organization and role in vascular homeostasis. *Physiol Rev* 2004, 84: 869–901.
8. Nitta T, Hata M, Gotoh S, Seo Y, Sasaki H, Hashimoto N, *et al.* Size-selective loosening of the blood-brain barrier in claudin-5-deficient mice. *J Cell Biol* 2003, 161: 653–660.
9. Daneman R, Prat A. The blood-brain barrier. *Cold Spring Harb Perspect Biol* 2015, 7: a020412.
10. Abbott NJ. Astrocyte-endothelial interactions and blood-brain barrier permeability. *J Anat* 2002, 200: 629–638.
11. Haseloff RF, Blasig IE, Bauer HC, Bauer H. In search of the astrocytic factor(s) modulating blood-brain barrier functions in brain capillary endothelial cells *in vitro*. *Cell Mol Neurobiol* 2005, 25: 25–39.
12. Garcia-Segura LM, McCarthy MM. Minireview: Role of glia in neuroendocrine function. *Endocrinology* 2004, 145: 1082–1086.
13. Zlokovic BV. Neurovascular mechanisms of Alzheimer's neurodegeneration. *Trends Neurosci* 2005, 28: 202–208.
14. Korteas R, Leenders KL, van Oostrom JCH, Vaalburg W, Bart J, Willemsen ATM, *et al.* Blood-brain barrier dysfunction in parkinsonian midbrain *in vivo*. *Ann Neurol* 2005, 57: 176–179.
15. Deli MA, Descamps L, Dehouck MP, Cecchelli R, Joó F, Abrahám CS, *et al.* Exposure of tumor necrosis factor- $\alpha$  to luminal membrane of bovine brain capillary endothelial cells cocultured with astrocytes induces a delayed increase of permeability and cytoplasmic stress fiber formation of actin. *J Neurosci Res* 1995, 41: 717–726.
16. Schwaninger M, Sallmann S, Petersen N, Schneider A, Prinz S, Libermann TA, *et al.* Bradykinin induces interleukin-6 expression in astrocytes through activation of nuclear factor- $\kappa$ B. *J Neurochem* 1999, 73: 1461–1466.
17. Matsuoka N, Itoh T, Watarai H, Sekine-Kondo E, Nagata N, Okamoto K, *et al.* High-mobility group box 1 is involved in the initial events of early loss of transplanted islets in mice. *J Clin Invest* 2010, 120: 735–743.
18. Agresti A, Lupo R, Bianchi ME, Müller S. HMGB1 interacts differentially with members of the Rel family of transcription factors. *Biochem Biophys Res Commun* 2003, 302: 421–426.
19. Goodwin GH, Sanders C, Johns EW. A new group of chromatin-associated proteins with a high content of acidic and basic amino acids. *Eur J Biochem* 1973, 38: 14–19.
20. Kim JH, Kim SJ, Lee IS, Lee MS, Uematsu S, Akira S, *et al.* Bacterial endotoxin induces the release of high mobility group box 1 via the IFN- $\beta$  signaling pathway. *J Immunol* 2009, 182: 2458–2466.
21. Andersson A, Covacu R, Sunnemark D, Danilov AI, dal Bianco A, Khademi M, *et al.* Pivotal advance: HMGB1 expression in active lesions of human and experimental multiple sclerosis. *J Leukoc Biol* 2008, 84: 1248–1255.
22. Zhang JY, Takahashi HK, Liu KY, Wake H, Liu R, Maruo T, *et al.* Anti-high mobility group box-1 monoclonal antibody protects the blood-brain barrier from ischemia-induced disruption in rats. *Stroke* 2011, 42: 1420–1428.
23. Sasaki T, Liu KY, Agari T, Yasuhara T, Morimoto J, Okazaki M, *et al.* Anti-high mobility group box 1 antibody exerts neuroprotection in a rat model of Parkinson's disease. *Exp Neurol* 2016, 275(Pt 1): 220–231.
24. Gao S, Wake H, Sakaguchi M, Wang D, Takahashi Y, Teshigawara K, *et al.* Histidine-rich glycoprotein inhibits high-mobility group box-1-mediated pathways in vascular endothelial cells through CLEC-1A. *iScience* 2020, 23: 101180.
25. Sun Y, Chen HY, Dai JP, Zou HJ, Gao M, Wu H, *et al.* HMGB1 expression patterns during the progression of experimental autoimmune encephalomyelitis. *J Neuroimmunol* 2015, 280: 29–35.
26. Sun Y, Chen HY, Dai JP, Wan ZJ, Xiong P, Xu Y, *et al.* Glycyrrhizin protects mice against experimental autoimmune encephalomyelitis by inhibiting high-mobility group box 1 (HMGB1) expression and neuronal HMGB1 release. *Front Immunol* 2018, 9: 1518.
27. Xiao YF, Lai L, Chen HY, Shi JY, Zeng FF, Li J, *et al.* Interleukin-33 deficiency exacerbated experimental autoimmune encephalomyelitis with an influence on immune cells and *Glia* cells. *Mol Immunol* 2018, 101: 550–563.
28. Zou HJ, Ming BX, Li J, Xiao YF, Lai L, Gao M, *et al.* Extracellular HMGB1 contributes to the chronic cardiac allograft vasculopathy/fibrosis by modulating TGF- $\beta$ 1 signaling. *Front Immunol* 2021, 12: 641973.
29. Zhou HZ, Wang YB, Wang W, Jia JY, Li Y, Wang QY, *et al.* Generation of monoclonal antibodies against highly conserved antigens. *PLoS One* 2009, 4: e6087.
30. Ruck T, Bittner S, Epping L, Herrmann AM, Meuth SG. Isolation of primary murine brain microvascular endothelial cells. *J Vis Exp* 2014, 93: e52204.
31. Rossi B, Constantin G. Live imaging of immune responses in experimental models of multiple sclerosis. *Front Immunol* 2016, 7: 506.
32. Rahimifard M, Maqbool F, Moeini-Nodeh S, Niaz K, Abdollahi M, Braidly N, *et al.* Targeting the TLR4 signaling pathway by polyphenols: a novel therapeutic strategy for neuroinflammation. *Ageing Res Rev* 2017, 36: 11–19.
33. Hudson BI, Lippman ME. Targeting RAGE signaling in inflammatory disease. *Annu Rev Med* 2018, 69: 349–364.
34. Calogero S, Grassi F, Aguzzi A, Voigtländer T, Ferrier P, Ferrari S, *et al.* The lack of chromosomal protein Hmg1 does not disrupt cell growth but causes lethal hypoglycaemia in newborn mice. *Nat Genet* 1999, 22: 276–280.
35. Casper KB, Jones K, McCarthy KD. Characterization of astrocyte-specific conditional knockouts. *Genesis* 2007, 45: 292–299.
36. Nishibori M, Wang DL, Ousaka D, Wake H. High mobility group box-1 and blood-brain barrier disruption. *Cells* 2020, 9: 2650.
37. Okuma Y, Liu KY, Wake H, Zhang JY, Maruo T, Date I, *et al.* Anti-high mobility group box-1 antibody therapy for traumatic brain injury. *Ann Neurol* 2012, 72: 373–384.
38. Vénéreau E, Ceriotti C, Bianchi ME. DAMPs from cell death to new life. *Front Immunol* 2015, 6: 422.
39. Andersson U, Tracey KJ, Yang H. Post-translational modification of HMGB1 disulfide bonds in stimulating and inhibiting inflammation. *Cells* 2021, 10: 3323.
40. Dimitrijević M, Kotur-Stevuljević J, Stojić-Vukanić Z, Vujnović I, Pilipović I, Nacka-Aleksić M, *et al.* Sex difference in oxidative stress parameters in spinal cord of rats with experimental autoimmune encephalomyelitis: Relation to neurological deficit. *Neurochem Res* 2017, 42: 481–492.
41. Wang D, Li SP, Fu JS, Zhang S, Bai L, Guo L. Resveratrol defends blood-brain barrier integrity in experimental autoimmune encephalomyelitis mice. *J Neurophysiol* 2016, 116: 2173–2179.
42. Tang YT, Zhao X, Antoine D, Xiao XZ, Wang HC, Andersson U, *et al.* Regulation of posttranslational modifications of HMGB1 during immune responses. *Antioxid Redox Signal* 2016, 24: 620–634.
43. Lu B, Antoine DJ, Kwan K, Lundbäck P, Wähämaa H, Schierbeck H, *et al.* JAK/STAT1 signaling promotes HMGB1 hyperacetylation and nuclear translocation. *Proc Natl Acad Sci U S A* 2014, 111: 3068–3073.

# Whole-Brain Connectome of GABAergic Neurons in the Mouse Zona Incerta

Yang Yang<sup>1</sup> · Tao Jiang<sup>2</sup> · Xueyan Jia<sup>2</sup> · Jing Yuan<sup>1,2</sup> ·  
Xiangning Li<sup>1,2</sup> · Hui Gong<sup>1,2</sup>

Received: 28 February 2022 / Accepted: 29 April 2022 / Published online: 19 August 2022  
© The Author(s) 2022

**Abstract** The zona incerta (ZI) is involved in various functions and may serve as an integrative node of the circuits for global behavioral modulation. However, the long-range connectivity of different sectors in the mouse ZI has not been comprehensively mapped. Here, we obtained whole-brain images of the input and output connections *via* fluorescence micro-optical sectioning tomography and viral tracing. The principal regions in the input-output circuits of ZI GABAergic neurons were topologically organized. The 3D distribution of cortical inputs showed rostro-caudal correspondence with different ZI sectors, while the projection fibers from ZI sectors were longitudinally organized in the superior colliculus. Clustering results show that the medial and lateral ZI are two different major functional compartments, and they can be further divided into more subdomains based on projection and input connectivity. This study provides a comprehensive anatomical foundation for understanding how the ZI is involved in integrating different information, conveying motivational states, and modulating global behaviors.

**Keywords** Zona incerta · GABAergic neurons · Whole-brain connectome · Input circuit · Output circuit · Topological connection

## Introduction

The zona incerta (ZI) is a large nucleus in the hypothalamic region with extensive connections throughout the brain [1], and is involved in various functions from locomotion to social behavior, including binge-eating [2], sleeping [3], predatory hunting [4, 5], neuropathic pain [6–8], fear memory [9–11], and investigatory and seeking behavior [12, 13]. It is an important target for treating Parkinson's disease by deep-brain stimulation [14]. GABAergic cells, the most abundant inhibitory neurons in the mammalian brain [15], are the majority of neurons in the ZI [1, 16]. GABAergic ZI neurons are essential for cortical neuron development [17], shifting the cortical activity patterns [18–20], and gating signal flow [19, 21, 22]. And it is regarded as a potential integrative node for global behavioral modulation [16, 23]. Comprehensive investigation of its functions and global roles is enlightening to the understanding of brain mechanisms.

The ZI is connected with nearly every neural center of the neuro-axis, from cerebral cortex to spinal cord [1], and even receives projections from the retina [24]. Its principal connections are with the cerebral cortex, diencephalon, and brainstem. Traditionally, the ZI of rodents can be loosely divided into different sectors based on cytoarchitecture. The functions of distinct ZI sectors varies greatly while the connections are topologically organized. Cortical neurons that project to the ZI are confined to layer V and the projections are organized in a topological manner [25, 26]. The ZI projects heavily to the dorsal thalamus, while the projections

**Supplementary Information** The online version contains supplementary material available at <https://doi.org/10.1007/s12264-022-00930-w>.

✉ Xiangning Li  
lixiangning@mail.hust.edu.cn

✉ Hui Gong  
huigong@mail.hust.edu.cn

<sup>1</sup> Britton Chance Center for Biomedical Photonics, Wuhan National Laboratory for Optoelectronics, MoE Key Laboratory for Biomedical Photonics, Huazhong University of Science and Technology, Wuhan 430074, China

<sup>2</sup> Research Unit of Multimodal Cross Scale Neural Signal Detection and Imaging, Chinese Academy of Medical Sciences, HUST-Suzhou Institute for Brainmatics, JITRI, Suzhou 215123, China

to the hypothalamus are mainly from the rostral ZI [27]. The precise connectivity pattern among distinct sectors of the ZI and thalamus is still unclear. As the main connecting region of the ZI, the midbrain has complex circuits with the ZI, such as superior colliculus (SC)–ZI connections that are organized in a topological manner [28–30]. Since the ZI is a potential integrative node, its connectivity map is enlightening to the understanding of its complex functions and global roles and even brain mechanisms. Although the development of transgenic animals and viral tracing has accelerated the investigation of the input and output connections in interesting ZI sectors [2], there is still a lack of comprehensive comparison of the connection patterns of different ZI sectors.

Here, we aimed at providing a comprehensive long-range input-output connectivity map of GABAergic ZI neurons, and obtain the organization patterns of the ZI. To provide a connectivity map of the entire mouse ZI, we selected four injection sites. We applied Cre-dependent monosynaptic rabies virus and Vgat-ires-Cre line mice to characterize afferent connections of GABAergic neurons in the ZI [31], and adeno-associated viral tracing to label GABAergic efferent axons. By quantifying the numbers of labeled neurons and efferent axons, we constructed a long-range input-output connectivity map of GABAergic ZI neurons and analyzed their connection characteristics.

## Materials and Methods

### Animals

This study was approved by the Animal Experimentation Ethics Committee of Huazhong University of Science and Technology, and all animal experiments were conducted in accordance with relevant guidelines. The C57BL/6J mice used in these experiments were purchased from Beijing Vital River (Beijing). The Vgat-ires-Cre (JAX: 028862) mouse line [32] was purchased from the Jackson Laboratory. All mice were housed in an environment with a 12-h light/dark cycle at  $22 \pm 1^\circ\text{C}$  and with food and water ad libitum. The study was gender-neutral and 6- to 12-week-old mice were used.

### Surgery and Stereotaxic Injection

The mice were anesthetized by intraperitoneal injection of 1% pentobarbital sodium in 0.9% saline at 0.1 mL/10 g body weight. The mice were mounted into a stereotaxic frame and eye ointment was applied. Holes were drilled above the target brain regions. For anterograde or retrograde experiments, tracers were delivered *via* glass micropipettes using a pressure injection pump at 35 nL/min. After the injections, incisions were sutured, lidocaine hydrochloride gel

was applied to the wound, and the mice were returned to their home cages for recovery. Monosynaptic rabies virus was used to label the whole-brain inputs of GABAergic neurons in distinct ZI sectors. 150 nL of a 2:1 mixture of rAAV9-EF1 $\alpha$ -DIO-RG-WPRE-pA and rAAV9-EF1 $\alpha$ -DIO-DsRed-TVA-WPRE-pA, all AAV viruses with final titers at  $2 \times 10^{12}$  viral genomes (vg)/mL (virus from BrainVTA) of helper-viruses were injected into target ZI sectors. The following coordinates (mm from bregma) were used: rostral ZI (ZIr): AP:  $-0.95$ , ML:  $+0.75$ , DV:  $-4.5$ ; intermediodorsal ZI (ZIdm): AP:  $-1.95$ , ML:  $+1.0$ , DV:  $-4.45$ ; intermediolateral ZI (ZIlm): AP:  $-2.15$ , ML:  $+1.95$ , DV:  $-3.9$ ; caudal ZI (ZIC): AP:  $-2.55$ , ML:  $+2.0$ , DV:  $-3.9$ . Three weeks later, 300 nL RV- $\Delta$ G-EnVA-eGFP ( $2 \times 10^8$  vg/mL, from BrainVTA) were injected into the same sector, and 7 days later, the mice were sacrificed. For axonal AAV-tracing, 100 nL of rAAV2/5-EF1 $\alpha$ -DIO-eYFP-WPRE-pA ( $2 \times 10^{12}$  vg/mL) was injected into a target ZI sector at the above coordinates. Four weeks later, the mice were sacrificed. To verify the projection pattern of ZIdm, 50 nL red retrobeads (R180–100, Lumafuor) was injected into the periaqueductal gray (PAG; in mm: AP:  $-4.0$ , ML:  $+0.3$ , DV:  $-2.8$ ), and 50 nL fluorescent gold (80014, Biotium) was injected into the SCm (AP:  $-4.0$ , ML:  $+1.5$  m, DV:  $-2.3$ ). Seven days later, the mice were sacrificed. To explore whether single neurons in the ZIr innervated the rostral (AP:  $-3.6$ , ML:  $+0.05$ , DV:  $-2.0$ ) and caudal (AP:  $-4.4$ , ML:  $+0.05$ , DV:  $-1.8$ ) parts of the SC, 50 nL red retrobeads and 50 nL fluorescent gold were injected into the rostral and caudal parts of the medial SC, respectively, and 7 days later, the mice were sacrificed.

### Histology

Anesthetized mice were perfused with 0.01 mol/L phosphate-buffered saline (PBS, Sigma-Aldrich) and then with 4% paraformaldehyde (PFA, Sigma-Aldrich). The brain was removed from the skull, and post-fixed in 4% PFA at  $4^\circ\text{C}$ . Each brain was rinsed 3 times with 0.01 mol/L PBS and embedded in 5% agarose (Sigma-Aldrich). Coronal sections (50  $\mu\text{m}$ ) were cut on a vibratome (VT1000, Leica Microsystems). Every second section was used for whole-brain imaging with an automated slide scanner (VS120 Virtual Slide, Olympus).

### Immunostaining

To verify the type of starter cells, we applied immunofluorescent staining to coronal sections near the injection site. After the sections were rinsed 3 times with 0.1M PBS, the sections were blocked with 5% bovine serum albumin in 0.3% Triton X-100 for 1 h at room temperature. Then the sections were incubated overnight with rabbit anti-GABA (1:800, Sigma) at  $4^\circ\text{C}$ , then rinsed 3 times with 0.01 mol/L



PBS and incubated with goat anti-rabbit 647 (1:500, Thermo Fisher) at room temperature for 2 h. The sections were rinsed 3 times with PBS and then mounted on glass slides. The injection site was imaged by confocal microscopy (LSM 710, Zeiss).

### Embedded Processing

Brains were embedded for whole-brain imaging [33]. After each brain was rinsed 3 times with 0.1 mol/L PBS, it was dehydrated in a graded ethanol series (50%, 70% and 95% ethanol in double distilled water) at 4°C. Then the brains were immersed in a graded glycol methacrylate (GMA) series (70%, 85%, and 100% GMA, with 0.2% Sudan black B in ethanol) at 4°C. The brains were immersed in 100% GMA at 4°C for 3 days. Finally, the samples were embedded.

### Imaging

To obtain the input and output images of the whole brain, we applied dual-channel imaging (output samples were stained with propidium iodide) on the embedded brains [34]. The fluorescence micro-optical sectioning tomography (fMOST) system developed by our group was used to conduct whole-brain imaging at a resolution of  $0.32\ \mu\text{m} \times 0.32\ \mu\text{m} \times 2\ \mu\text{m}$ .

### Data Processing

We used a homemade method to count the numbers of neurons and fiber signals [35]. NeuroGPS was used to obtain the coordinates of the neuron somata. To distinguish the projection signal from background, we used a Gaussian filter to remove the background and images were binarized. Easily distinguishable regions were segmented to obtain the conversion parameters for transforming the whole image stack to Allen CCFv3. All results were checked manually to eliminate errors. To quantify the input and output connections, we transformed the coordinates of the somata of input neurons and image stacks of labeled signals to Allen CCFv3. Then the number of somata or the volume of the projection signal in each area were quantified. Regions with a connection strength of  $<0.03\%$  were set to 0, and the ZI was set to 0. We merged some areas with low connection strength for ease of display. To unify the connection strength between the different samples, we calculated the percentage of connections in different regions.

### Visualization and Statistical Analysis

Amira (v6.1.1, FEI), ImageJ, and Python 3.8.4 were used to visualize the input and output results. To compare the differences in connection strength between different brain regions, we used one-way ANOVA. Pearson correlation coefficients

were used to assess the similarity of connections. Hierarchical cluster analysis and correlation analysis were used to analyze the similarities and variances of the connection strength between different samples or brain regions. These analyses were performed using MatLab (v2017a, MathWorks) and Python 3.8.4. All histograms, scatter diagrams and heat maps were generated by GraphPad Prism (v6.0, GraphPad) and Python 3.8.4.

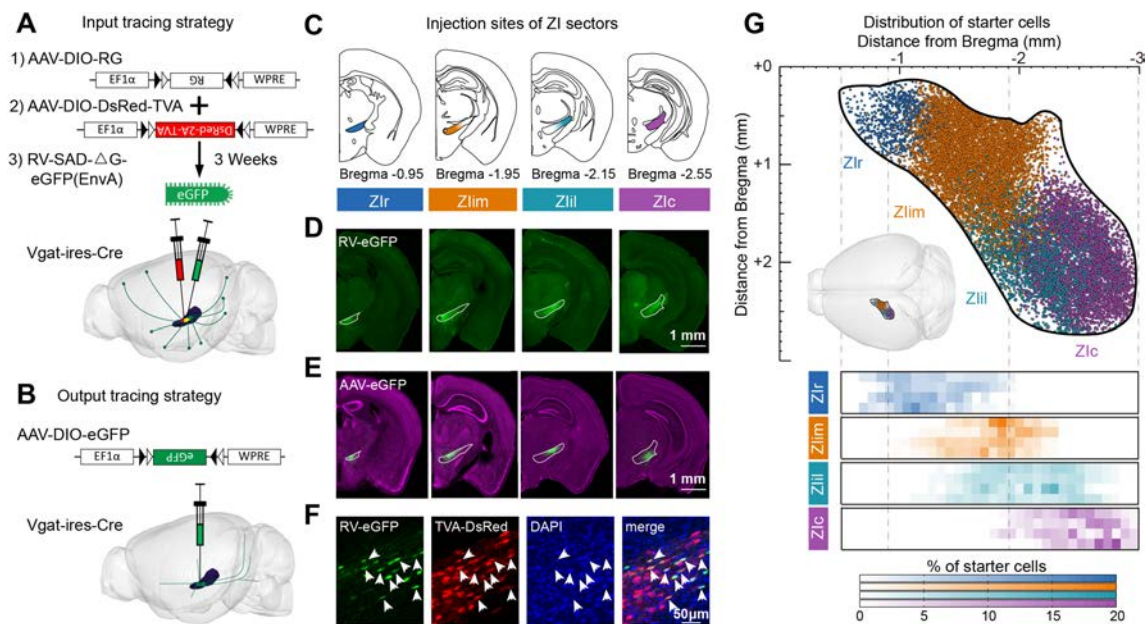
## Results

### Experimental Strategy to Reveal the Connectivity of Distinct ZI Sectors

The ZI is a large elongated string-like structure located in the lateral hypothalamus. To map the connectivity of the entire mouse ZI, we selected four injection sites, and viral tracers were injected into each of these regions. The four sectors were named rostral, intermediodorsal, intermediolateral, and caudal (ZIr, ZLim, ZIil, and ZIc; see Fig. 1C).

To label the GABAergic neurons, we used transgenic mice and cre-dependent viral tools. Vgat-ires-Cre mice, which expressed Cre recombinase directed to GABAergic neuronal cell bodies [32], were used to obtain the whole-brain connectivity map of GABAergic ZI neurons. To demonstrate the monosynaptic inputs of the ZI, we injected two Cre-dependent adeno-associated viruses (AAV9-EF1 $\alpha$ -DIO-DsRed-TVA and AAV9-EF1 $\alpha$ -DIO-RG) into the ZI at the same time. Three weeks later, RV-SAD- $\Delta$ G-eGFP (EnvA) was injected into the same ZI sector (Fig. 1A). The TVA-expressing cells infected with the modified, high specificity, rabies virus (RV), and labeled the presynaptic neurons only with the help of Rabies glycoprotein G (RG). The reliability of the experimental strategy was confirmed by control experiments (Fig. S1). To trace and quantify the efferent axons (outputs) of the ZI, we injected Cre-inducible adeno-associated virus (AAV2/5-EF1 $\alpha$ -DIO-eGFP) into the ZI, and GABAergic neurons infected by AAV virus were labeled with enhanced green fluorescent protein (eGFP) (Fig. 1B). To comprehensively analyze the whole-brain connectivity at single-cell resolution, we obtained the inputome and projectome datasets with fluorescent micro-optical sectioning tomography (fMOST) [34]. As shown in Fig. S2B, the virus-labeled mouse brains were perfused and embedded in resin, then were imaged with fMOST. The datasets were processed and quantified as in our previous reports [35].

To confirm the performance of the virus, we checked coronal sections from monosynaptic retrograde tracing samples, and found that nearly every neural center of the neuraxis had eGFP-positive cells (Fig. S3A). The highest density of eGFP-positive neurons was near the injection sites (Fig. 1D). The coronal sections of anterograde tracing samples were



**Fig. 1** Whole-brain tracing of input and projections of distinct ZI sectors. **A** Schematic of the monosynaptic retrograde tracing strategy. For retrograde tracing, AAV9-EF1 $\alpha$ -DIO-RG (1) and AAV9-EF1 $\alpha$ -DIO-DsRed-TVA (2) are co-injected into the ZI sector of interest. Three weeks later, RV-SAD- $\Delta$ G-eGFP (EnvA) (3) is injected into the same sector. Only with the help of TVA and RG can RV-eGFP spread retrogradely to presynaptic neurons. **B** Schematic of the anterograde tracing strategy. AAV2/5-DIO-eGFP is injected into the ZI sector of interest, and the axons of infected GABAergic neuron are labeled with eGFP. **C** Locations of distinct ZI sectors in this experiment: ZIr (blue), ZLim (orange), ZIil (cyan), and ZIc (purple). **D** RV-

eGFP expression near the injection sites in coronal sections (see Fig. S2A for distribution of starter cells). **E** Coronal sections showing AAV-eGFP expression in the injection sites. **F** Identification of starter cells. Cells co-expressing AAV-DsRed and RV-eGFP are considered to be starter cells. Starter cells of ZLim (see Fig. S2B). Scale bars, 1 mm (**D**), 1 mm (**E**), and 50  $\mu$ m (**F**). **G** Schematic of the dorsal view of retrograde tracing starter cells in distinct ZI sectors and heat map showing the starter cell distribution in each sample at each specific ZI target (lower panels). Center left insert, visual aid representation the location of ZI in the brain. Every row in each ZI sector is from one sample,  $n = 4$  mice per condition in retrograde strategy.

checked too (Fig. S3B). We found that eGFP-positive efferent axons were present in many brain regions, such as the thalamus, hypothalamus, and brainstem. The cell bodies were confined to the ZI (Fig. 1E).

In monosynaptic retrograde tracing experiments, cells co-expressing DsRed and eGFP were counted as starter cells (Fig. 1F). We only analyzed the data with >80% of starter cells located in the ZI to ensure accuracy (Fig. S2D). A few starter cells were located outside of ZI, including in the lateral hypothalamic area (LHA), posterior hypothalamic area (PH), and reticular thalamic nucleus. To compare among distinct ZI sectors, the location of starter cell was certified in the continuous dataset. Most of the starter cells of ZIr were distributed at  $-0.7$  to  $-1.5$  from bregma, while most of those of ZLim, ZIil and ZIc were distributed at  $-1.5$  to  $-2.2$ ,  $-1.6$  to  $-2.5$ , and  $-2.1$  to  $-2.7$  from bregma, respectively (Fig. 1G). Most starter cells of ZLim were located in the medial ZI, and most starter cells of ZIil were located in the lateral ZI. In tracing experiments, we described the distribution of fluorescence (Fig. S2E) and found a similar distribution. Starter cells almost covered the entire ZI in both RV and AAV tracing, and partial regions of distinct ZI sectors were overlapped. Our subsequent analysis also

found that the connectivity patterns of distinct ZI sectors showed significant differences. These data showed that viral labelling samples can reflect the characteristics and variation rules of connectivity of distinct ZI sectors.

To quantitatively analyze the whole-brain input-output connectivity maps, the number of eGFP-labeled cells and the fluorescent signal of efferent fibers were calculated (see Materials and Methods for details).

### Whole-brain Mapping of the Input/Output

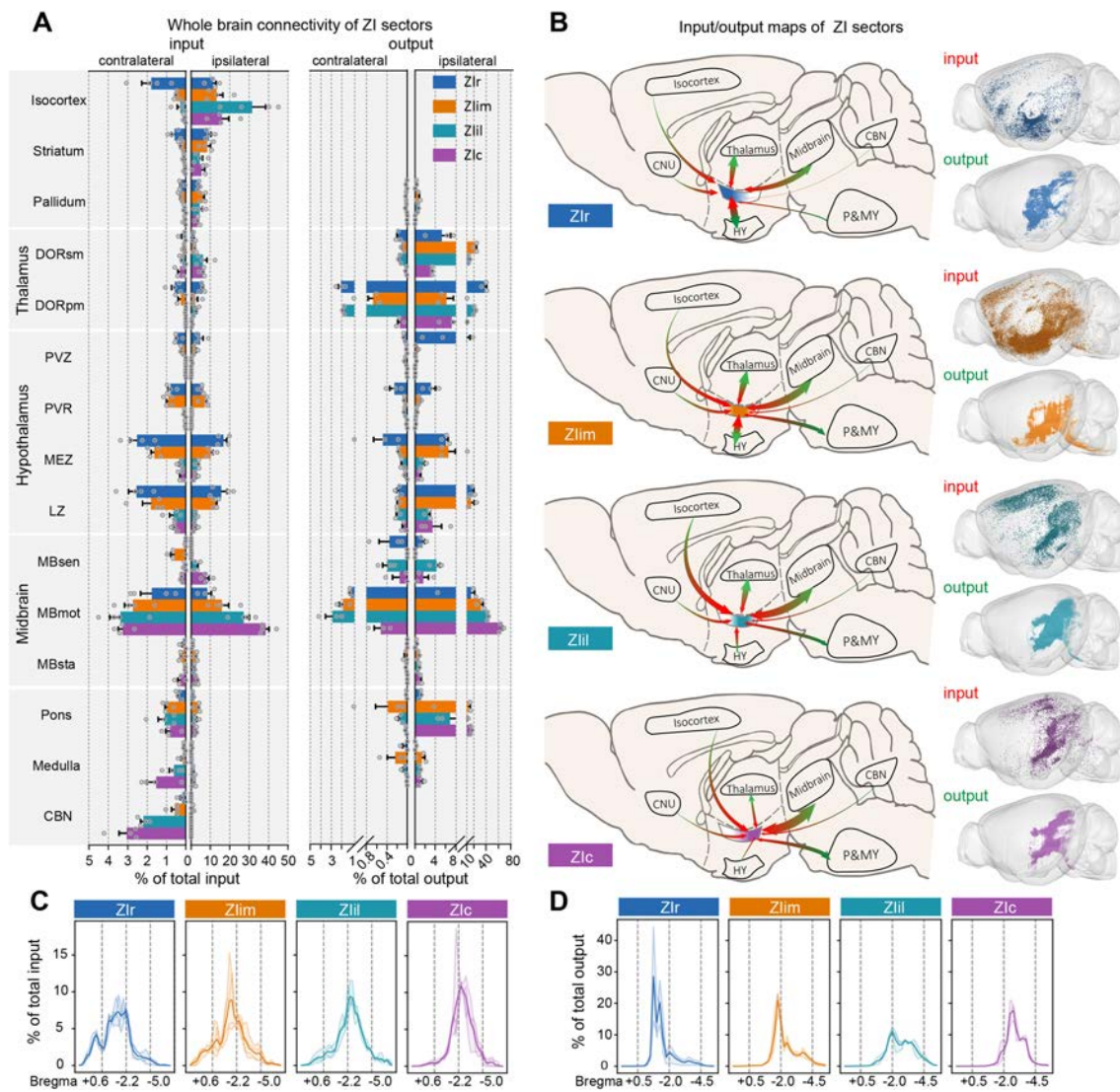
The ZI has widespread connectivity with nearly all neural centers. Here, we analyzed the connections among the ZI and 145 anatomical brain regions (details in Figs S4, S5). Although connecting brain regions were distributed throughout almost the whole brain, the main connections were concentrated in a few regions. The ZI received inputs from 126 regions, and half of the inputs were from  $\sim 10$  regions (9, 13, 11, and 8 regions in ZIr, ZLim, ZIil, and ZIc respectively; Fig. S6A). While its efferent fibers were distributed in 77 regions and half of them were in  $\sim 5$  regions (5, 4, 5, and 4 regions in ZIr, ZLim, ZIil, and ZIc respectively; Fig. S6B). These results indicated that the number of output regions

was less than that of input regions. To overview the whole-brain connectivity, the input-output regions were divided into 15 larger regions.

We compared the input and output of these regions, and generated connection maps for ZI sectors (Fig. 2A, B). The principal connections of the ZI were isocortex, thalamus, hypothalamus, and midbrain. There were differences between the input and output brain regions. ZI neurons received abundant input from the cortex and striatum, but few efferent fibers projected back to these regions. Although there were labeled fibers in isocortex and striatum, their

ratio in the whole output circuit was very low ( $<0.03\%$ ). The ZI also received input from the cerebellar nuclei (CBN), but no labeled fibers were observed in these nuclei. In the remaining regions with interconnections, the output intensity was generally higher than the input, except for the pallidum (input,  $4.61\% \pm 1.91\%$ ; output,  $0.41\% \pm 0.32\%$ ;  $***P = 9.89 \times 10^{-8}$ ). In general, GABAergic ZI neurons received more inputs from the telencephalon cerebrum than projected back.

To further compare the ZI circuit with different brain regions, we analyzed the ipsilateral and contralateral



**Fig. 2** Overview of ZI connectivity. **A** Whole-brain connectivity of ZI sectors. Ipsilateral and contralateral inputs (left) and outputs (right) of the four ZI sectors. Data are shown as the mean  $\pm$  SEM. **B** Individual input-output connectivity patterns of the ZI sectors. Left, schematics of the input-output connection patterns of major brain regions (green arrowheads, outputs; red arrowheads, inputs; area of arrowhead, strength of connection). Right, three-dimensional visuali-

zation of whole-brain inputs to and outputs from the ZI in representative samples. **C** Percentages of inputs plotted along the rostro-caudal axis. **D** Percentages of outputs plotted along the rostro-caudal axis. Bin width, 200  $\mu$ m. Thick lines, mean; thin lines, individual animals.  $n = 4$  mice per condition in (A) (left, input data) and (B).  $n = 3$  mice per condition in (A) (right, output data) and (D). Colors indicate data from each ZI sector: Zlr, blue; Zlim, orange; Zlil, cyan; Zlc, purple.



connectivity (Fig. 2A). All ZI sectors basically received bilateral afferent connectivity from the input regions, and the contralateral input was generally a tenth of that on the ipsilateral (Fig. S6C). The ZI received a higher proportion afferent connectivity from the contralateral pons and medulla. The ZI mainly received input from the contralateral CBN, while eGFP-positive neurons were found in the ipsilateral CBN. Different from the input, the ZI mainly sent efferent fibers to ipsilateral regions, and the ipsilateral output was generally >10 times the contralateral projections (Figs 2A, S6D). In a few regions, the ratios of ipsilateral to contralateral connection were different. For example, the proportion of input from the contralateral isocortex decreased as the injection site was moved backward along the rostro-caudal axis (Figs S6C, S7A).

While there were some quantitative differences, we compared the connections of the four ZI sectors and found that the connections of these regions changed gradually. In general, as the injection site was moved backward along the rostro-caudal axis, the connection centers gradually moved backward too (Fig. 2C, D), and several regions also showed a similar tendency. As the ZI sector was moved backward, the input from motor-related midbrain (MBmot) increased ( $10.21\% \pm 4.44\%$ ,  $18.57\% \pm 6.00\%$ ,  $30.52\% \pm 5.92\%$ , and  $41.69\% \pm 3.43\%$  to ZIr, ZLim, ZIil, and ZIc, respectively). Meanwhile, the efferent fibers from ZI to MBmot also had a same varying tendency ( $15.95\% \pm 8.07\%$ ,  $32.72\% \pm 4.88\%$ ,  $45.39\% \pm 1.77\%$  and  $65.00\% \pm 3.30\%$  from ZIr, ZLim, ZIil and ZIc, respectively). The connectivity of some remaining regions showed a similar tendency, such as input from the CBN ( $0.19\% \pm 0.17\%$ ,  $1.28\% \pm 0.54\%$ ,  $2.19\% \pm 0.24\%$ , and  $3.08\% \pm 0.68\%$  to ZIr, ZLim, ZIil, and ZIc, respectively). Meanwhile, the afferent connectivity from the hypothalamus showed preference too, in that ZIr and ZLim received a large amount but ZIil and ZIc only received a little. Afferent connectivity from the medial zone of the hypothalamus to the ZIr was significantly stronger than that to the ZLim ( $P = 0.0188$ ). Similar to the input, the efferent fibers from ZIr and ZLim to the hypothalamus were much more numerous than those from ZIil and ZIc. The pons, medulla, and CBN also had connections with the entire ZI, while mainly connecting with ZIil and ZIc. These preferred connections were an important source of the circuit differences of ZI sectors (Fig. S6C, D).

Here, we analyzed the connectivity of ZI from the whole-brain perspective, found the principal regions connected with the ZI, and analyzed the tendency of connectivity to vary. However, there were major differences in the connection patterns. To further demonstrate the organizational characteristics of ZI sectors, we showed their detailed connections with the isocortex, diencephalon, and midbrain.

## Connections Between ZI and Isocortex are Topological

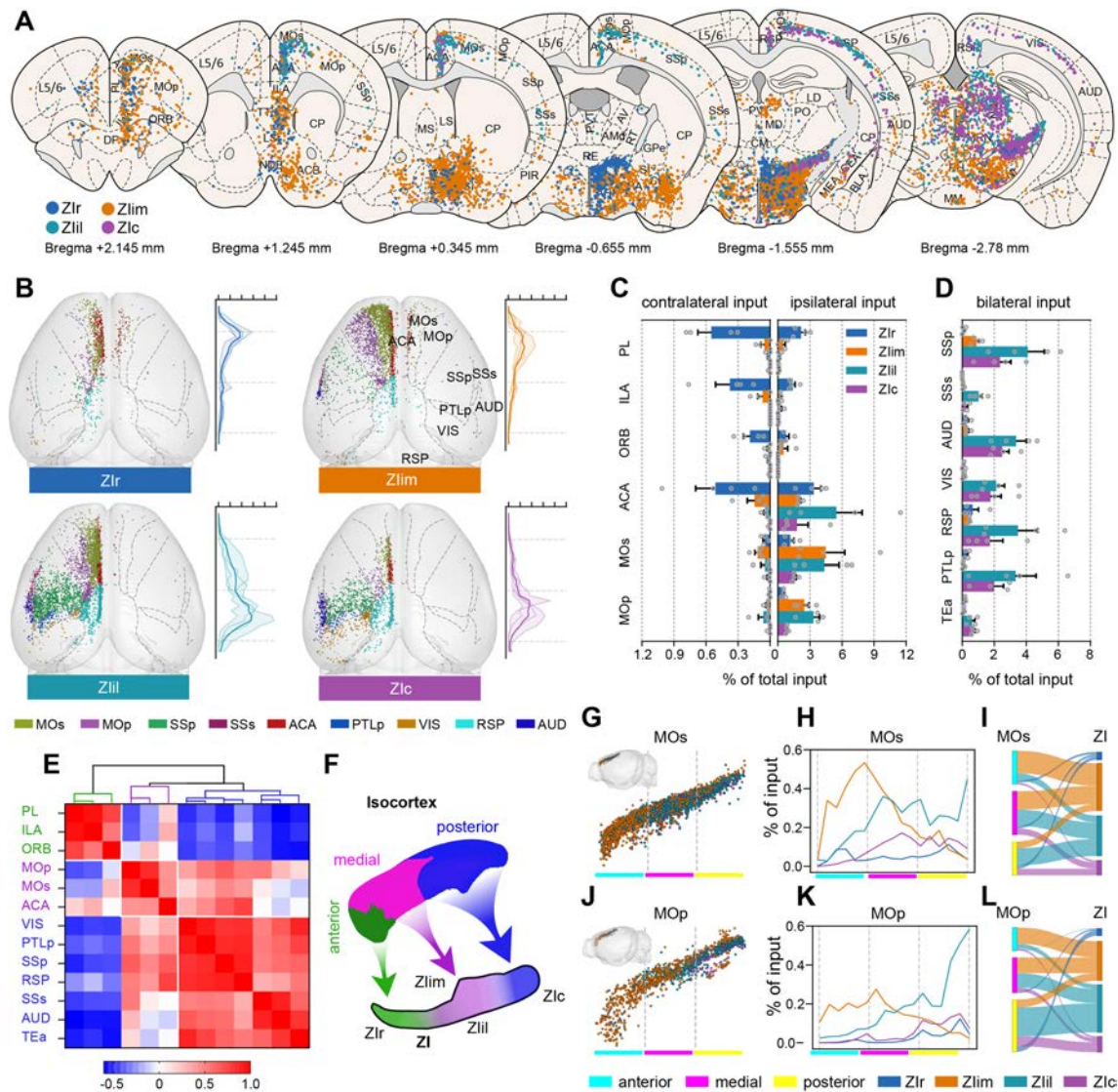
The ZI received projections from most areas of cortex, and the connections were organized topographically. The topology of connection is helpful to understand the functions of ZI. Here, we summarize the projection pattern of the cortical regions to ZI, and further discuss the way cortical input regions change.

The ZI received projections from most regions of the isocortex, and the principal connections were sensory, motor and association cortices (Fig. 3A). We found that the eGFP-positive neurons resided in lamina V of the cortex. All ZI sectors received similar strength of input from cortex (one-way ANOVAs showed no significant difference between the four ZI sectors, except for ZIr vs ZIil,  $P = 0.0421$ ; Fig. S6E), but the eGFP-positive cells in the cortex varied widely (Fig. 3A, B). As the ZI injection sites were moved backward, the connection centers in isocortex moved backward (Fig. 3B). To confirm the source of the difference, we quantitatively compared the main cortical inputs (Fig. 3C, D). We found that the input regions varied greatly, and the proportion of ipsilateral cortical input gradually increased (ratios of ipsilateral isocortical input to whole isocortical inputs: ZIr,  $87.0\% \pm 1.7\%$ ; ZLim,  $95.8\% \pm 1.1\%$ ; ZIil,  $99.3\% \pm 0.3\%$ ; ZIc,  $99.3\% \pm 0.4\%$ ; Fig. S7A). ZIr received the most input from the contralateral cortex, while both ZIil and ZIc received inputs almost entirely from the ipsilateral cortex.

The projections patterns of cortical regions to ZI sectors can be roughly divided into three categories. The first is composed of the bilateral prelimbic, infralimbic, and orbital areas. These regions mainly projected to the ZIr and ZLim, but rarely to ZIil or ZIc. The second category contained the bilateral anterior cingulate, secondary motor (MOs) and primary motor areas (MOp). These regions mainly projected to ZLim and ZIil, and had weaker projections to ZIr and ZIc. Although the input of the second category was also bilateral, the ratio of ipsilateral isocortical input to whole cortical inputs decreased. The last category consisted of remaining cortical regions, which mainly projected to the ipsilateral ZIil and ZIc. To determine whether this classification was reasonable, we used correlation and hierarchical cluster analysis of the cortical inputs (Fig. 3E, F) and this showed that the input regions could be roughly divided into three categories.

The spatial differences in the distribution of cortical eGFP-positive neurons (Fig. 3D) showed topological inputs from cortex to ZI, while the input strength from MOs and MOp did not significantly differ in ZLim and ZIil ( $P > 0.05$ ; Fig. S7B). To determine whether the gradual change in the nature of the input patterns also occurred in these regions, we divided them into anterior, middle, and posterior parts (Fig. 3G, J). Although all parts of the MOs and MOp had afferent connectivity to distinct ZI sectors,





**Fig. 3** Isocortex-ZI connectivity. **A** Schematic coronal sections depicting the distribution of eGFP-positive cells (slice thickness, 100  $\mu$ m). **B** Two-dimensional representation of the isocortex inputs to ZI sectors. Curves on the right corresponds to the isocortical input strength along the rostro-caudal axis (bin width, 200  $\mu$ m; thick lines, mean; thin lines, individual animals). **C** Ipsilateral (right) and contralateral cortical inputs (left) to the four ZI sectors. **D** Bilateral cortical inputs to the four ZI sectors. **E** Heat map of Pearson's correlation coefficient matrix and hierarchical cluster analysis showing that the projections from cortex to ZI can be roughly divided into three categories: anterior, medial, and posterior (pair-wise correlations on the data organized into 16 input samples). **F** Schematic of the connection patterns between cortex and ZI sectors. **G, J** Lateral view of

the distribution of retrogradely-labeled eGFP-positive neurons from distinct ZI sectors in MOs and MOp (upper left inserts, visual aid representation of the location of MOs or MOp). **H, K** Distribution of labeled neurons in MOs and MOp varies with the rostro-caudal axis (bin width, 200  $\mu$ m; data are presented as the mean; MOs and MOp divided into anterior, middle, and posterior parts). **I, L** Schematic of MOs and MOp projections to the ZI (width of the curve represents input strength). The same data sets of representative input samples are used in **A, B, G, and J**.  $n = 4$  mice per condition in **C, D, E, H, and K**. Each dot represents one RV-labeled cell in **A, B, G, and J**. Colors indicate data from each ZI sector: Zlr, blue; Zlim, orange; Zlil, cyan; Zlc, purple.

these regions preferentially targeted different sectors of the ZI (Fig. 3H, K). These findings suggested that Zlr mainly received input from the posterior part of MOp, while anterior and middle MOs and MOp projected to the Zlim, middle and posterior MOs to the Zlil, and middle

and posterior MOs as well as posterior MOp to the Zlc (Fig. 3I, L). Here, we verified that the change in input patterns was gradual, and defined the connection patterns between ZI and motor cortex. These result improve the understanding of the roles of distinct parts of the ZI in motor functions.

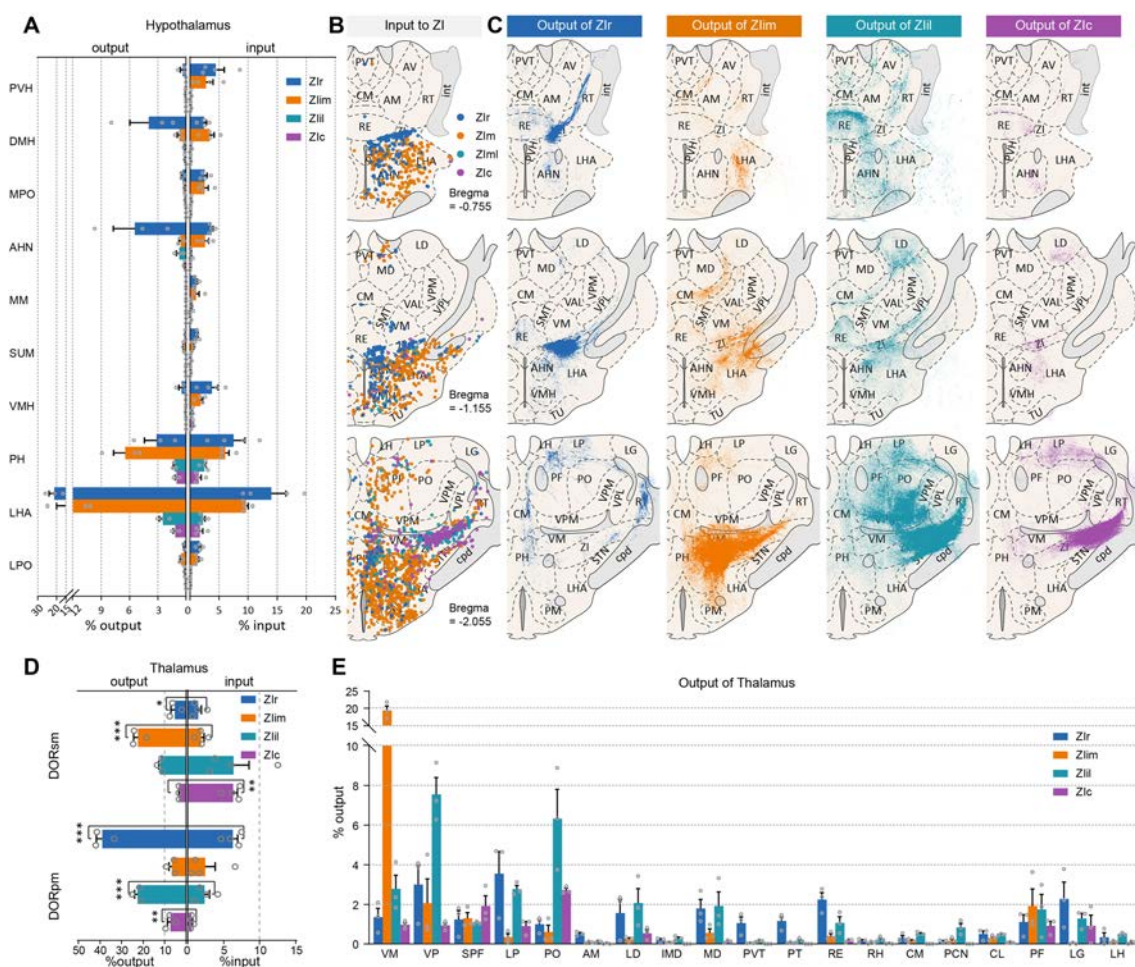
## Connections Between ZI and Diencephalon are Topological

As a part of the lateral hypothalamus, the ZI is located at the junction of the hypothalamus and thalamus, and has strong interconnections with the diencephalon, so we investigated the characteristics of these connections.

The hypothalamus had stronger interconnections with ZIr and ZLim than with ZIil and ZIc (Fig. 4A). ZIr and ZLim had strong interconnections with the PH and LHA, as did both ZIil and ZIc, the latter being rarely mentioned in previous studies (Fig. 4A–C). The connections between ZIr and ZLim did not significantly differ for the hypothalamus, except for the supramammillary nucleus (SUM) (Fig. S8A, B). The afferent connectivity from SUM to ZIr was stronger

( $P = 0.0133$ ) than that to ZLim, while the innervation from ZIil to SUM was stronger ( $P = 0.0037$ ) than that from ZIr. We also observed that in some coronal sections ZIr innervated the medial hypothalamus, and ZLim tended to innervate the lateral hypothalamus (Figs. 4C and S8C, D), but a difference did not show up in the quantitative results.

We found that ZI sent rich efferent fibers to thalamus, but the eGFP-positive cells were only rich in few brain regions (Fig. 4B, C). By comparing the input and output, we found that outputs of the sensory-motor cortex-related thalamus and polymodal association cortex-related thalamus were generally stronger than their inputs (Fig. 4D). The thalamic connections among distinct ZI sectors were significantly different, and the connections were also topological (Fig. S8E). The paraventricular nucleus of the thalamus had a



**Fig. 4** ZI-diencephalon connectivity. **A** Outputs from ZI to the hypothalamus (left) and inputs detected in the hypothalamus (right). **B** Schematic coronal sections depicting the distribution of eGFP-positive cells. Each dot represents one RV-labeled cell. **C** Schematic coronal sections depicting the distribution of eGFP. The eGFP signals represent the output of ZI sectors. **D** Outputs from ZI to the thalamus (left) and inputs detected in the thalamus (right). **E** Outputs from

the four ZI sectors to the thalamus (mean  $\pm$  SEM; \*\*\* $P < 0.001$ , \*\* $P < 0.01$ , \* $P < 0.05$ . Brain slice thickness is 100  $\mu$ m in **B** and **C**.  $n = 3$  mice per condition in **A** (left, output data), **D** (left, output data), and **E**.  $n = 4$  mice per condition in **A** (right, input data) and **D** (right, input data). Colors indicated data from each ZI sector: ZIr, blue; ZLim, orange; ZIil, cyan; ZIc, purple.



strong bidirectional connection with ZIr, and the connection strength was higher than for other ZI sectors (input,  $P < 0.01$ ; output,  $P < 0.05$ . Figures 4E, S8E). The lateral habenula projected heavily to ZIr and ZLim, and the afferent connectivity of ZLim was stronger than that to ZIil and ZIc ( $P < 0.05$ ). Specifically, the ventral medial nucleus of the thalamus (VM) was the main output region of ZLim, while the efferents to the VM were stronger than other ZI sectors ( $P < 0.001$ ). The subparafascicular nucleus (SPF), peripeduncular nucleus (PP), and lateral geniculate complex (LG) were the main afferent connectivity sources of ZIil and ZIc, and the efferent fibers of these sectors to the SPF and PP were stronger than those of ZIr and ZLim ( $P < 0.05$ ). Surprisingly, compared with ZLim, ZIr projected more axons to the LG (ZIr,  $2.38\% \pm 1.08\%$ ; ZLim,  $0.08\% \pm 0.04\%$ ). The posterior complex of the thalamus (PO) mainly received innervation from ZIil and ZIc, and that was significantly stronger than ZIr and ZLim ( $P < 0.05$ ). Efferent fibers from the four ZI sectors were detected in the parafascicular nucleus (PF) and no statistically significant difference was found ( $P > 0.05$ ). But we found that a spatial difference, in that ZIil fibers tended to be distributed in the ventral PF, while the fibers of other ZI sectors mainly projected to the dorsal PF (Fig. 4C). In addition, the projection from the ZI to the thalamus was highly topologically organized. For example, neurons projecting to the ventral or dorsal part of the PO may be two groups of neurons that are distributed differently in the ZI (Fig. S8F–K).

In general, the connection between the ZI and parts of the diencephalon is topological. We found that, in some coronal sections, ZIr innervated the medial hypothalamus, and ZLim tended to innervate the lateral hypothalamus. The projections of distinct ZI sectors to the thalamus not only differ in the strength of connectivity, but also in regional connectivity.

### Connections Between ZI and Midbrain are Topological

The midbrain had strong interconnection with different ZI sectors and the strength increased as the injection sites moved backward along the rostro-caudal axis. Here, we investigated this phenomenon and the topological projections to the SC and PAG.

To determine whether the phenomenon was caused by differences in the regional connectivity or because the main input regions had similar properties, we compared the inputs and outputs of the midbrain (Fig. 5A). All ZI sectors had a heavy interconnection with the midbrain reticular nucleus (MRN), motor-related SC (SCm), PAG, and anterior pretectal nucleus (APN) (Fig. 5A–C). Some regions exhibited increasing connection strength as the injection site moved backward, while other nuclei of the midbrain mainly connected with ZIil and ZIc. Interconnections between ZIr and

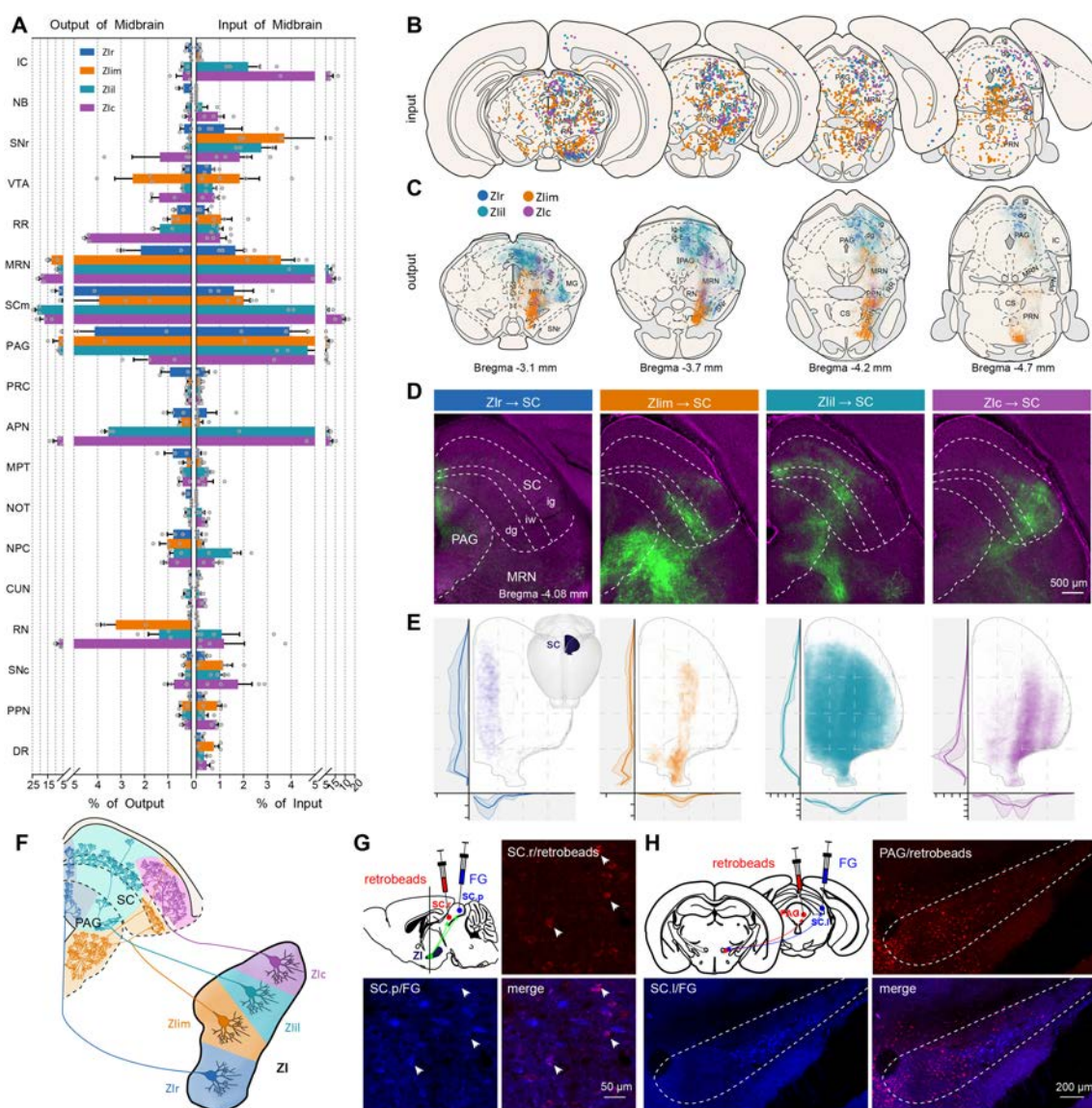
the MRN were weaker than other ZI sectors (input,  $P < 0.05$ ; output,  $P < 0.01$ ). The connections of the SCm with ZIr and ZLim were weaker than those of ZIil and ZIc ( $P < 0.05$ ), and the APN also had a heavier connection with ZIil and ZIc ( $P < 0.05$ ) (Fig. S9A, B).

When comparing the connections of distinct ZI sectors, we found that the efferent fibers in the SC were topologically organized as previously reported, and the distribution of fibers in the PAG also had a certain topology (Fig. 5C, D). We found that the ZIr mainly targeted the medial SCm and dorsomedial PAG while the ZLim preferred the ventral PAG and ventrolateral SCm, the ZIil mainly projected to the intermediate SCm and lateral PAG, while the ZIil focused on the dorsolateral SCm with a few fibers in lateral PAG. In order to further explore the projection patterns from ZI to SC, we investigated the distribution of efferent fibers in the SCm (Fig. 5E). We describe the distribution of fibers along the rostro-caudal axis and medial-lateral axis in the SCm. The topological projection from ZI to SCm was verified, and we found that the projections had a longitudinal-zonal organization. We defined the topological organization of ZI to SC and PAG projections (Fig. 5F).

As shown in Figure 5D, we found that the efferent fibers from any ZI sector, extended to almost the entire SC along the rostro-caudal axis. To determine whether single neurons in the ZI innervated rostral and caudal parts of SC simultaneously, red retrobeads were injected into the rostral part and fluorescent gold (FG) into the caudal part of the medial SC (Fig. 5G). We found that some neurons were co-labeled with retrobeads and FG, thus individual neurons do simultaneously innervate the rostral and caudal parts of the SC. Many of the efferent fibers to the SCm extended to the PAG and the distribution of efferent fibers in PAG and SCm had a roughly corresponding relationship. To explore whether single neurons in the ZI innervated the SCm and PAG simultaneously or separately, we injected red retrobeads and FG into the PAG and SCm in individual mice (Fig. 5H, see Fig. S9C for injection sites). Most of the labeled neurons were divided into two spatially separate groups. Neurons that projected to the ventrolateral PAG were located in the intermediomedial ZI, and neurons that projected to the lateral SC were located in central part of the ZI. Thus, neurons of the ZLim innervate PAG and SCm separately.

### Comparison of Input and Output Distributions

To further investigate whether the distinction among these ZI sectors was meaningful, we compared the correlation coefficients of input or output in a pairwise fashion. The correlation coefficients of inputs and outputs were low, but the correlation coefficients between the outputs of four ZI sectors were slightly higher than the inputs (average correlation coefficient: input,  $0.4677 \pm 0.2736$ ; output,



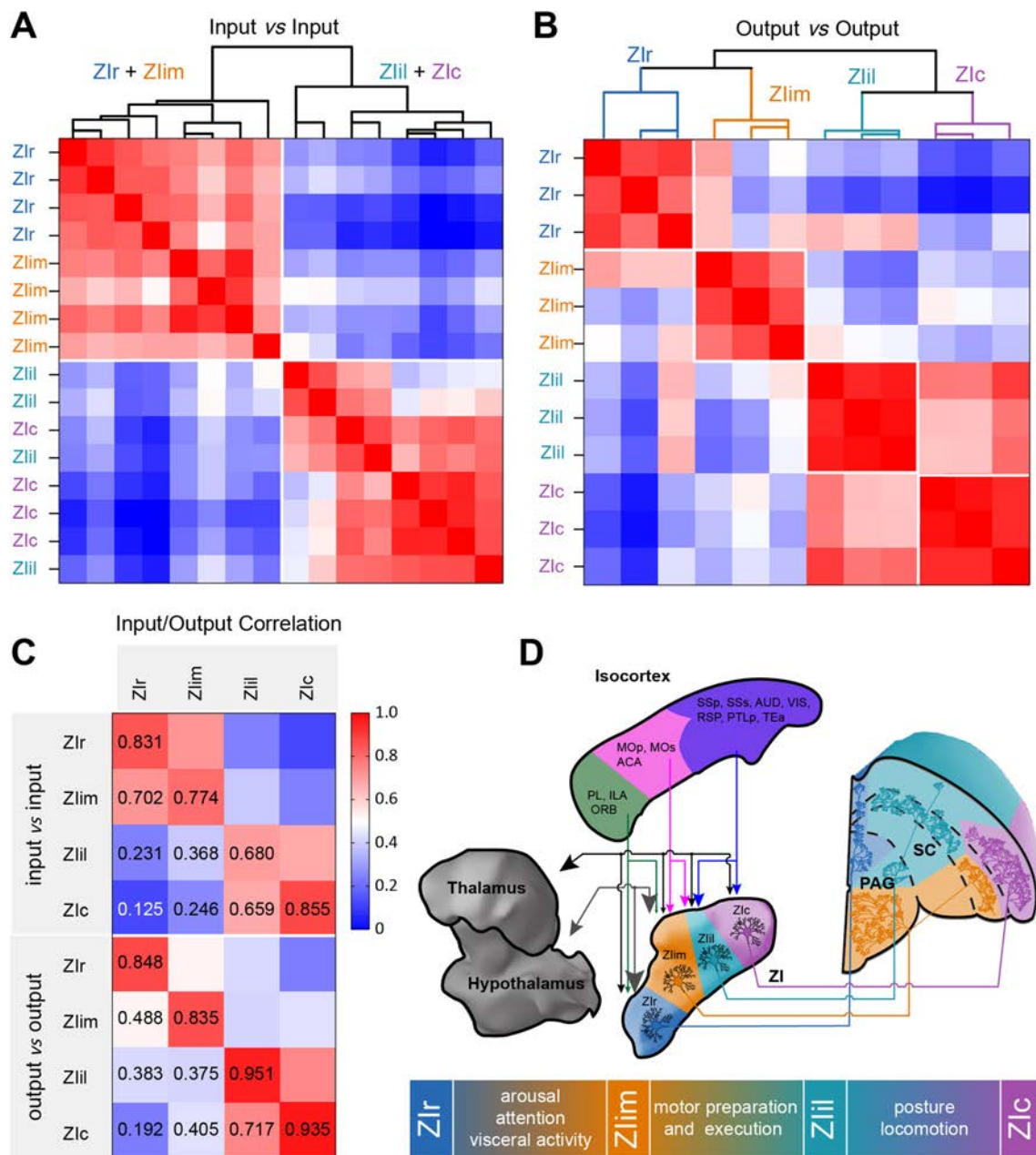
**Fig. 5** ZI-midbrain connectivity. **A** ZI projections to the midbrain (left) and inputs from the midbrain (right). **B** Schematic coronal sections depicting the distribution of eGFP-positive cells. Each dot represents one RV-labeled cell. **C** Schematic coronal sections depicting the distribution of projection fibers. **D** Representative images of projections from four ZI sectors to the midbrain. Scale bar, 500 μm. **E** Two-dimensional representation of the projection fibers in the superior colliculus from the four ZI sectors (upper left, distribution of the eGFP signal in SC along the rostro-caudal axis; lower curves, distribution of projection fibers in the SC along the medial-lateral axis; left insert, visual aid representation the location of the SC; thick lines, mean; thin lines, individual animals). **F** Schematic of ZI sectors pro-

jecting to the SC and PAG. **G** Single ZI neurons simultaneously projecting to the anteromedial and posteromedial SC. Retrobeads (red) are injected into the anteromedial SC, and fluorescent gold (FG, blue) is injected into the posteromedial C. Some neurons in the rostral ZI are co-labeled by retrobeads and FG. Scale bar, 50 μm. **H** Fibers in the PAG and SC from two different groups of neurons. Retrobeads are injected into the PAG and FG is injected into the SC. The labeled neurons are divided into two spatially separate groups. Scale bar, 200 μm. Data shown as the mean ± SEM. Slice thickness is 100 μm in **B**, **C**, **G**, and **H**.  $n = 3$  mice per condition in **A** (left, output data).  $n = 4$  mice per condition in **A** (right, input data) and **C**.

$0.5111 \pm 0.2579$ ). We also hierarchically clustered the input and output regions separately. With both inputs and outputs, two distinct clusters were formed, separating a grouped ZIr/ZIim pool from a grouped ZIil/ZIc pool. The input correlations of ZIr and ZIim tracing were too similar to classify them into separate clusters (average correlation coefficient:

$0.7019 \pm 0.0777$ , Fig. 6A, C). For the same reason, we could not divide the inputs of ZIil and ZIc into separate clusters (average correlation coefficient:  $0.6590 \pm 0.1650$ , Fig. 6A, C). Although the output correlations of tracing the four ZI sectors were also similar, they fell into four separate clusters (average correlation coefficients: ZIr vs ZIim





**Fig. 6** Connectivity characteristics of ZI. **A** Correlation and hierarchical cluster analysis of the inputs ( $n = 16$ ) of the ZI. The pair-wise correlations were calculated for data organized into 126 input regions. **B** Correlation and hierarchical cluster analysis of the outputs ( $n = 12$ ) of the ZI. The pair-wise correlations were calculated for data organized into 77 output regions. The heat maps in **A** and **B** represent Pearson's correlation coefficient matrices. Note for both input and output

correlations, 2 clusters form from the Zlr/Zlim animals and Zlil/Zlc animals. **C** Correlation coefficients of input ( $n = 4$  per condition) and output ( $n = 3$  per condition). **D** Schematic of ZI connectivity characteristics. Lower panel, possible functions of distinct ZI sectors. Similar to the connection results, functions may shift in a progressive manner among different sectors. Area of arrowhead indicates strength of connection.

$0.4882 \pm 0.1352$ , Zlil vs Zlc  $0.7165 \pm 0.0911$ , Fig. 6B, C). Comparing the connection strength between Zlr and Zlim, we found that 31.03% (27/87) of the input areas had significant differences, and 58.33% (28/48) of the output regions had significant differences (Fig. S10A, C). Comparing the connection strength between Zlil and Zlc, we found a

significant difference in 29.63% (24/81) of the input regions and 64.44% (29/45) of the output regions (Fig. S10B, D). These results were consistent with the results of hierarchical clustering. The connectivity patterns of Zlr and Zlim were similar, as were those of Zlil and Zlc. The similarity of the inputs was higher than that of the outputs.

## Discussion

Here, we systematically mapped the input-output connectivity of GABAergic ZI neurons and compared the connectivity of four ZI sectors in the whole brain. From the continuous 3D datasets, we comprehensively mapped the ZI connectivity characteristics (Fig. 6D). The connections of ZI were heterogeneous and topologically organized. Cortical input regions can be divided into three categories. The topology of the connections between ZI and the diencephalon was not only manifested in strength, but also in regions. And the efferent fibers in the SC were longitudinally organized. Clustering results showed that the medial and lateral ZI were two different major functional compartments, and they can be further divided into more subdomains based on output connectivity.

Cortex was the main input region of ZI, and it was also an important source of input differences. We then investigated the connections between ZI and cortex more comprehensively. The cortical projection to ZI could be divided into three categories. These were consistent with the results of previous studies with lentivirus showing that the cortical input of the ZI could be divided into sensory, motor, and anterior limbic cortex [25]. The differences in connectivity may underlie the functional differences. First, prefrontal cortex preferentially projected to the ZIr and ZLim. The projection of the medial prefrontal cortex to ZIr bidirectionally regulates the escape speed of mice [16], and the projection of the prefrontal cortex to ZLim is associated with curiosity in mice [12]. This indicated that emotion and cognition may regulate the behaviors of mice through ZIr and ZLim. Second, the motor cortex (MO) projected primarily to the medial ZI, suggesting that these ZI sectors are closely involved in motor planning and execution. But the functions of ZLim and ZIil are quite different. ZLim is mainly associated with behaviors such as fear [9, 11], predation [4, 5], and curiosity [12], while ZIil is associated with behaviors such as grooming, chewing, incubation, and jumping [36]. We found that ZLim and ZIil preferentially received inputs from the anterior and posterior MO, which control the movement of different parts of the body [37], and the anterior MO is involved in motor preparation [38]. These results can explain the difference in motor-related behaviors between ZLim and ZIil. Finally, sensory cortex preferentially projected to ZIil and ZIc. ZIc is directly associated with movement and is an important region for deep brain stimulation to treat Parkinson-induced tremor [1, 14]. ZIc preferentially received input from the sensory cortex rather than the MO. ZIc also had bidirectional connection with the reticular nucleus that controls trunk movement and posture. Further, lesions of the ZIc result in the loss of stereotyped movements in rats, while not affecting motivation [39]. Combined their connection with MO, we suggest that the ZIc neurons may be involved in the

regulation of stereotyped actions or maintain posture by integrating multisensory information from the cortex. Based on the above information, we speculate that the ZI is involved in emotion and cognition, motivation and motor planning, motor execution and stereotyped actions, and maintaining posture in sequence along the rostro-caudal axis. In addition, cortical neurons that project to the ZI also project to other regions, such as the thalamus, midbrain, and pons [40]. Whether cortical topological output is also present in other regions warrants further investigation.

The projections from ZI to the thalamus were stronger than those from the thalamus. ZI received a lot of input from the cortex, while the output from ZI to the cortex was almost negligible. The thalamus is a "way station" transmitting information to the cerebral cortex [41], and ZI can limit the transmission of ascending sensory information *via* feedforward inhibition of higher order thalamic nuclei [19, 21, 22]. This projection relationship among cortex, ZI, and thalamus is conducive to the cortex to limit the transmission of ascending sensory information *via* ZI. For example, spinal cord injury leads to a significant increase in the activity of PO neurons [8, 42], and this is thought to be caused by a decrease in the activity of GABAergic ZI neurons [43]. And the increased activity of ventral anterior cingulate area (ACAv) neurons increases the activity of GABAergic ZI neurons and significantly improves the symptoms of neuralgia [6, 7]. Therefore, ACAv regulates the intensity of information transmission from PO to cortex by regulating the activity of GABAergic ZI neurons. Once the balance is broken, neuralgia results. In general, the ZI is one of the relay stations through which the cortex regulates thalamic sensory input.

As previously reported, efferent fibers from the ZI were topologically organized in the SC [44]. Moreover, we found that projections from ZI to SC had a longitudinal-zonal organization and the projection of ZI to the lateral SC had a dorsoventral topology, such that the projection of the rostral and caudal ZI to the SC was also topologically organized. Meanwhile, the projection from ZI to PAG was also topological to a certain extent. Neurons of ZLim projected separately to the ventral PAG and ventrolateral SC, which means that ZI can be further divided into more subdomains based on output connectivity to determine its own potential functions. For example, since predation behavior has been reported in the lateral SC and lateral PAG [4, 5, 45], the output from the ZI to the lateral SC may also be associated with predation. It is also worth investigating whether these ZI neurons projecting to the same SC sub-region have the same connecting pattern in other output regions. Analysis of the morphology of single neurons is crucial to understanding the ZI projection patterns.

By applying unbiased cluster analysis, we found that the ZI can be divided into two parts: rostral and

intermediomedial (medial part, including ZIr and ZLim), and intermediolateral and caudal (lateral part, including ZIl and ZIc). This may be due to the fact that afferent fibers were rarely limited to a sector of the ZI and the connections of the medial and lateral ZI are significantly different [1, 25]. Unlike the inputs, although the outputs of ZIr and ZLim were also similar, they grouped into two independent clusters. And ZIl and ZIc also had similar properties. The inputs of ZI sectors changed in a progressive manner, and the outputs were organized in a highly topological form. We speculate that similar functions are distributed in adjacent sectors, but participate in different functions through different circuits. We suggest that, similar to the connection results, functions may shift in a progressive manner among different sectors. This also explains why both ZIr and ZLim are involved in different nutritional status-related behaviors, but the binge-eating and predation cycles are strictly restricted to ZIr and ZLim, respectively [5]. There may be a mutual relationship among ZI sectors in the regulation of similar behaviors, which may reflect how the ZI serves as an integrative node for global behavioral modulation [16, 23].

Due to technical constraints, there were limitations that need to be considered. The ZI is formed of a heterogeneous population of cells, all of which play important roles in various functions. We only studied the input and output of GABAergic neurons, but did not investigate the connections of other types of neurons in the ZI. Numerous studies have shown that chemically different neurons may have similar input regions, and that the location of the injection site determines the input pattern. Therefore, our input results are also valuable for studying other types of neuron. The outputs of various types of neuron in the same region may differ. For example, we found that the inputs from the substantia nigra pars reticulata and pallidum were much stronger than the outputs to them. Previous research found that the neurons that project to the basal ganglia are mainly glutamatergic but not GABAergic [46]. Therefore, it is necessary to more fully study the output patterns of chemically different neurons. And whether other types of neuron also have topological connectivity patterns similar to GABAergic neurons is also worth investigating.

We have shown that the connections of the ZI are topologically organized: as the injection site changed, the input-output connection pattern changed significantly, especially the projections from the ZI to the thalamus. Therefore, special attention should be paid to differences in injection sites when comparing different studies. For example, the distribution patterns of efferent fibers from GABAergic ZIr neurons to the SC and PAG that we found, differed from those of Chou *et al.* [16]. This difference is also due to the different injection sites. Chou *et al.* injected the virus more laterally and caudally than we did. The ZIr outputs of Chou

*et al.* were more similar to our results for ZLim. They both projected to the lateral SC. The results of Chou *et al.* showed that ZIr (corresponding to our ZLim) had very little projection to the PAG, while our results showed a large number of fibers in the PAG. As we show in Figure 5G and H, ZI neurons projecting to the lateral SC were located near the center. Neurons projecting to the PAG were located closer to the medial ZI. So, we suggest that because their injection site was closer to the central ZI, the neurons projecting to the PAG were not infected. And our results may not uniformly reflect the connectivity strengths of all GABAergic neurons in the ZI. For example, the projection from the ZI to the PO is involved in nocifensive behavior [6], whereas our results showed only a few infected fibers in the dorsal PO. Instead, we found that ZIl has substantial projections to the ventral PO. Neurons projecting to the dorsal PO are located in the region between ZLim and ZIl, and only a few were labeled in this experiment. At the same time, we found that the ZI-to-thalamus projections are strongly topologically organized, but it is difficult to obtain the topological projection patterns by analyzing the projections of populations of neuron. Reconstructing the morphology of individual neurons can avoid the above difficulties and further reveal the organization of ZI projections to the thalamus. Readers should note that we used the signals of fibers here to reflect the strength of the output. Besides that, regions with <0.03% connectivity were set to zero, but that does not mean these regions are not connected with the ZI. Given the technical constraints, we could not directly compare the connectivity strength of ZI sectors, but the data still reflect the connectivity trend of the ZI. Furthermore, it does not affect the conclusion that GABAergic ZI neuronal connectivity is topological. Furthermore, some regions are strongly connected with the ZI, which we do not show in detail. They also have important functions (see supplementary materials). For example, there is a rich connection between the ZI and central amygdala nucleus [47], which plays an important role in fear memory.

In conclusion, we comprehensively mapped the input-output connectivity map of GABAergic ZI neurons that showed topographic organization and preferred input/output circuit connections. Connectivity preference provides a structural basis for understanding complex functions. The topological connection of ZI is important for understanding how the ZI integrates multiple kinds of information and modulates global behaviors.

**Acknowledgements** We thank Anan Li, Miao Ren, Mei Yao, Peilin Zhao, and Ahui Xu for help with experiments and data analysis. This work was supported by National Natural Science Foundation of China (61890953 and 31871088), the Chinese Academy of Medical Sciences Innovation Fund for Medical Sciences (2019-12M-5-014), and the Director Fund of Wuhan National Laboratory for Optoelectronics. We thank the Optical Bioimaging Core Facility of HUST for support with data acquisition.



**Open Access** This article is licensed under a Creative Commons Attribution 4.0 International License, which permits use, sharing, adaptation, distribution and reproduction in any medium or format, as long as you give appropriate credit to the original author(s) and the source, provide a link to the Creative Commons licence, and indicate if changes were made. The images or other third party material in this article are included in the article's Creative Commons licence, unless indicated otherwise in a credit line to the material. If material is not included in the article's Creative Commons licence and your intended use is not permitted by statutory regulation or exceeds the permitted use, you will need to obtain permission directly from the copyright holder. To view a copy of this licence, visit <http://creativecommons.org/licenses/by/4.0/>.

## References

- Mitrofanis J. Some certainty for the “zone of uncertainty”? Exploring the function of the zona incerta. *Neuroscience* 2005, 130: 1–15.
- Zhang X, van den Pol AN. Rapid binge-like eating and body weight gain driven by zona incerta GABA neuron activation. *Science* 2017, 356: 853–859.
- Liu K, Kim J, Kim DW, Zhang YS, Bao H, Denaxa M. Lhx6-positive GABA-releasing neurons of the zona incerta promote sleep. *Nature* 2017, 548: 582–587.
- Shang C, Liu A, Li D, Xie Z, Chen Z, Huang M, *et al.* A subcortical excitatory circuit for sensory-triggered predatory hunting in mice. *Nat Neurosci* 2019, 22: 909–920.
- Zhao Z, Chen Z, Xiang X, Hu M, Xie H, Jia X, *et al.* Zona incerta GABAergic neurons integrate prey-related sensory signals and induce an appetitive drive to promote hunting. *Nat Neurosci* 2019, 22: 921–932.
- Wang H, Dong P, He C, Feng XY, Huang Y, Yang WW, *et al.* Incerta-thalamic circuit controls nocifensive behavior via cannabinoid type 1 receptors. *Neuron* 2020, 107: 538–551.e7.
- Hu TT, Wang RR, Du Y, Guo F, Wu YX, Wang Y, *et al.* Activation of the intrinsic pain inhibitory circuit from the midcingulate Cg2 to zona incerta alleviates neuropathic pain. *J Neurosci* 2019, 39: 9130–9144.
- Masri R, Quilton RL, Lucas JM, Murray PD, Thompson SM, Keller A. Zona incerta: A role in central pain. *J Neurophysiol* 2009, 102: 181–191.
- Venkataraman A, Brody N, Reddi P, Guo J, Gordon Rainnie D, Dias BG. Modulation of fear generalization by the zona incerta. *Proc Natl Acad Sci U S A* 2019, 116: 9072–9077.
- Wheeler AL, Teixeira CM, Wang AH, Xiong X, Kovacevic N, Lerch JP, *et al.* Identification of a functional connectome for long-term fear memory in mice. *PLoS Comput Biol* 2013, 9: e1002853.
- Zhou M, Liu Z, Melin MD, Ng YH, Xu W, Südhof TC. A central amygdala to zona incerta projection is required for acquisition and remote recall of conditioned fear memory. *Nat Neurosci* 2018, 21: 1515–1519.
- Ahmadlou M, Houba JHW, van Vierbergen JFM, Giannouli M, Gimenez GA, van Weeghel C, *et al.* A cell type-specific cortico-subcortical brain circuit for investigatory and novelty-seeking behavior. *Science* 2021, 372: eabe9681.
- Ogasawara T, Sogukpinar F, Zhang K, Feng YY, Pai J, Jezzini A, *et al.* A primate temporal cortex-zona incerta pathway for novelty seeking. *Nat Neurosci* 2022, 25: 50–60.
- Ossowska K. Zona incerta as a therapeutic target in Parkinson's disease. *J Neurol* 2020, 267: 591–606.
- Zachmann M, Tocci P, Nyhan WL. The occurrence of gamma-aminobutyric acid in human tissues other than brain. *J Biol Chem* 1966, 241: 1355–1358.
- Chou XL, Wang X, Zhang ZG, Shen L, Zingg B, Huang J, *et al.* Inhibitory gain modulation of defense behaviors by zona incerta. *Nat Commun* 2018, 9: 1151.
- Chen JD, Kriegstein AR. A GABAergic projection from the zona incerta to cortex promotes cortical neuron development. *Science* 2015, 350: 554–558.
- Weitz AJ, Lee HJ, Choy M, Lee JH. Thalamic input to orbito-frontal cortex drives brain-wide, frequency-dependent inhibition mediated by GABA and zona incerta. *Neuron* 2019, 104: 1153–1167.e4.
- Liu J, Lee HJ, Weitz AJ, Fang Z, Lin P, Choy M, *et al.* Frequency-selective control of cortical and subcortical networks by central thalamus. *Elife* 2015, 4: e09215.
- Barthó P, Slézia A, Varga V, Bokor H, Pinault D, Buzsáki G, *et al.* Cortical control of zona incerta. *The J Neurosci* 2007, 27: 1670–1681.
- Trageser JC, Keller A. Reducing the uncertainty: Gating of peripheral inputs by zona incerta. *J Neurosci* 2004, 24: 8911–8915.
- Barthó P, Freund TF, Acsády L. Selective GABAergic innervation of thalamic nuclei from zona incerta. *Eur J Neurosci* 2002, 16: 999–1014.
- Wang X, Chou XL, Zhang LI, Tao HW. Zona incerta: An integrative node for global behavioral modulation. *Trends Neurosci* 2020, 43: 82–87.
- de Góis Morais PLA, de Santana MAD, Cavalcante JC, de Oliveira Costa MSM, Sousa Cavalcante J, do Nascimento ES Jr. Retinal projections into the Zona Incerta of the rock cavy (*Kerodon rupestris*): A CTb study. *Neurosci Res* 2014, 89: 75–80.
- Kita T, Osten P, Kita H. Rat subthalamic nucleus and zona incerta share extensively overlapped representations of cortical functional territories. *J Comp Neurol* 2014, 522: 4043–4056.
- Mitrofanis J, Mikuletic L. Organisation of the Cortical Projection to the Zona Incerta of the Thalamus. *J Comp Neurol* 1999, 412: 173–185.
- Wagner CK, Eaton MJ, Moore KE, Lookingland KJ. Efferent projections from the region of the medial zona incerta containing A13 dopaminergic neurons: A PHA-L anterograde tract-tracing study in the rat. *Brain Res* 1995, 677: 229–237.
- Romanowski CA, Mitchell IJ, Crossman AR. The organisation of the efferent projections of the zona incerta. *J Anat* 1985, 143: 75–95.
- Kim U, Gregory E, Hall WC. Pathway from the zona incerta to the superior colliculus in the rat. *J Comp Neurol* 1992, 321: 555–575.
- Kolmac CI, Power BD, Mitrofanis J. Patterns of connections between zona incerta and brainstem in rats. *J Comp Neurol* 1998, 396: 544–555.
- Callaway EM, Luo L. Monosynaptic circuit tracing with glycoprotein-deleted rabies viruses. *J Neurosci* 2015, 35: 8979–8985.
- Vong L, Ye C, Yang Z, Choi B, Chua S Jr, Lowell BB. Leptin action on GABAergic neurons prevents obesity and reduces inhibitory tone to POMC neurons. *Neuron* 2011, 71: 142–154.
- Ren M, Tian J, Zhao P, Luo J, Feng Z, Gong H, *et al.* Simultaneous acquisition of multicolor information from neural circuits in resin-embedded samples. *Front Neurosci* 2018, 12: 885.
- Gong H, Xu D, Yuan J, Li X, Guo C, Peng J, *et al.* High-throughput dual-colour precision imaging for brain-wide connectome with cytoarchitectonic landmarks at the cellular level. *Nat Commun* 2016, 7: 12142.
- Xu Z, Feng Z, Zhao M, Sun Q, Deng L, Jia X, *et al.* Whole-brain connectivity atlas of glutamatergic and GABAergic neurons in the mouse dorsal and Median raphe nuclei. *Elife* 2021, 10: e65502.
- Rier CIP, Tremblay L, Féger J, Hirsch AEC. Behavioral consequences of bicuculline injection in the subthalamic nucleus and the zona incerta in rat. *J Neurosci* 2002, 22: 8711–8719.



37. Tennant KA, Adkins DL, Donlan NA, Asay AL, Thomas N, Kleim JA, *et al.* The organization of the forelimb representation of the C57BL/6 mouse motor cortex as defined by intracortical microstimulation and cytoarchitecture. *Cereb Cortex* 2011, 21: 865–876.
38. Guo ZV, Li N, Huber D, Ophir E, Gutnisky D, Ting JT, *et al.* Flow of cortical activity underlying a tactile decision in mice. *Neuron* 2014, 81: 179–194.
39. Edwards DA, Isaacs S. Zona incerta lesions: Effects on copulation, partner-preference and other socio-sexual behaviors. *Behav Brain Res* 1991, 44: 145–150.
40. Wang J, Sun P, Lv X, Jin S, Li A, Kuang J, *et al.* Divergent projection patterns revealed by reconstruction of individual neurons in orbitofrontal cortex. *Neurosci Bull* 2021, 37: 461–477.
41. Guillery RW. Anatomical evidence concerning the role of the thalamus in corticocortical communication: A brief review. *J Anat* 1995, 187(Pt 3): 583–592.
42. Mendes-Gomes J, Nunes-de-Souza RL. Anxiolytic-like effects produced by bilateral lesion of the periaqueductal gray in mice: Influence of concurrent nociceptive stimulation. *Behav Brain Res* 2009, 203: 180–187.
43. Moon HC, Park YS. Reduced GABAergic neuronal activity in zona incerta causes neuropathic pain in a rat sciatic nerve chronic constriction injury model. *J Pain Res* 2017, 10: 1125–1134.
44. Benavidez NL, Bienkowski MS, Zhu M, Garcia LH, Fayzullina M, Gao L, *et al.* Organization of the inputs and outputs of the mouse superior colliculus. *Nat Commun* 2021, 12: 4004.
45. Li Y, Zeng J, Zhang J, Yue C, Zhong W, Liu Z, *et al.* Hypothalamic circuits for predation and evasion. *Neuron* 2018, 97: 911–924.e5.
46. Heise CE, Mitrofanis J. Evidence for a glutamatergic projection from the zona incerta to the basal Ganglia of rats. *J Comp Neurol* 2004, 468: 482–495.
47. Fu JY, Yu XD, Zhu Y, Xie SZ, Tang MY, Yu B, *et al.* Whole-brain map of long-range monosynaptic inputs to different cell types in the amygdala of the mouse. *Neurosci Bull* 2020, 36: 1381–1394.

# Dendritic Morphology Affects the Velocity and Amplitude of Back-propagating Action Potentials

Wu Tian<sup>1</sup> · Luxin Peng<sup>2</sup> · Mengdi Zhao<sup>3,8</sup> · Louis Tao<sup>3,5</sup> · Peng Zou<sup>2,4,6,7</sup> · Yan Zhang<sup>1</sup> 

Received: 3 March 2022 / Accepted: 20 May 2022 / Published online: 19 August 2022  
© The Author(s) 2022

**Abstract** The back-propagating action potential (bpAP) is crucial for neuronal signal integration and synaptic plasticity in dendritic trees. Its properties (velocity and amplitude) can be affected by dendritic morphology. Due to limited spatial resolution, it has been difficult to explore the specific propagation process of bpAPs along dendrites and examine the influence of dendritic morphology, such as the dendrite diameter and branching pattern, using patch-clamp recording. By taking advantage of Optopatch, an all-optical electrophysiological method, we made detailed recordings of the real-time propagation of bpAPs in dendritic trees. We found that the velocity of bpAPs was not uniform in a single dendrite, and the bpAP velocity differed among distinct dendrites of the same neuron. The velocity of a bpAP was positively

correlated with the diameter of the dendrite on which it propagated. In addition, when bpAPs passed through a dendritic branch point, their velocity decreased significantly. Similar to velocity, the amplitude of bpAPs was also positively correlated with dendritic diameter, and the attenuation patterns of bpAPs differed among different dendrites. Simulation results from neuron models with different dendritic morphology corresponded well with the experimental results. These findings indicate that the dendritic diameter and branching pattern significantly influence the properties of bpAPs. The diversity among the bpAPs recorded in different neurons was mainly due to differences in dendritic morphology. These results may inspire the construction of neuronal models to predict the propagation of bpAPs in dendrites with enormous variation in morphology, to further illuminate the role of bpAPs in neuronal communication.

Wu Tian, Luxin Peng, and Mengdi Zhao have contributed equally to this work.

**Supplementary Information** The online version contains supplementary material available at <https://doi.org/10.1007/s12264-022-00931-9>.

✉ Louis Tao  
taolt@mail.cbi.pku.edu.cn

✉ Peng Zou  
zoupeng@pku.edu.cn

✉ Yan Zhang  
yanzhang@pku.edu.cn

<sup>1</sup> State Key Laboratory of Membrane Biology, College of Life Sciences, Peking University, Beijing 100871, China

<sup>2</sup> College of Chemistry and Molecular Engineering, Synthetic and Functional Biomolecules Center, Beijing National Laboratory for Molecular Sciences, Key Laboratory of Bioorganic Chemistry and Molecular Engineering of Ministry of Education, Peking University, Beijing 100871, China

**Keywords** Dendrite · Action potential · Back-propagation · Synaptic integration

<sup>3</sup> Center for Quantitative Biology, Academy for Advanced Interdisciplinary Studies, Peking University, Beijing 100871, China

<sup>4</sup> PKU-IDG/McGovern Institute for Brain Research, Peking University, Beijing 100871, China

<sup>5</sup> Center for Bioinformatics, National Laboratory of Protein Engineering and Plant Genetic Engineering, School of Life Sciences, Peking University, Beijing 100871, China

<sup>6</sup> Peking-Tsinghua Center for Life Sciences, Peking University, Beijing 100871, China

<sup>7</sup> Chinese Institute for Brain Research (CIBR), Beijing 102206, China

<sup>8</sup> Beijing Academy of Artificial Intelligence, Beijing 100084, China

## Introduction

In most mammalian central nervous system neurons, the action potential (AP) is initiated at the proximal axon region and propagates forward and backward [1]. The part of the AP invading the soma and the dendritic tree is called a back-propagating AP (bpAP), and active bpAPs have been reported in many types of neurons, both *in vitro* and *in vivo* [2–10].

The most notable role of bpAPs is their participation in spike timing-dependent plasticity (STDP), including long-term potentiation (LTP) and long-term depression (LTD). The induction of STDP requires pre- and postsynaptic activity to occur in a precise temporal order within a window of only tens of milliseconds [11–13], and the invasion of distal dendrites bpAPs is an important source of depolarization [14]. The amplitude of a bpAP may determine the strength of subsequent postsynaptic depolarization and affect the induction of plasticity. The velocity and frequency of bpAPs influence the timing of postsynaptic activity and the chance of potentiation. Therefore, the properties of bpAPs have a critical influence on the integration of synaptic input and the induction of synaptic plasticity [15, 16]. Understanding the ways in which different factors determine the extent of bpAP propagation in dendrites is critical for studies of the functions of bpAPs.

The properties of bpAPs in different types of neurons vary widely. The average velocity of bpAPs in granule cell dendrites is 150  $\mu\text{m}/\text{ms}$  [17], which is slower than their velocity in pyramidal cell apical dendrites (500  $\mu\text{m}/\text{ms}$ ) and basal dendrites (200  $\mu\text{m}/\text{ms}$ ) [18–20]. The marked differences among bpAPs on the dendrites of different neuronal types inspired us to investigate the effect of morphology on bpAPs, with a focus on how the diameter and branch pattern influence bpAP velocity and amplitude.

Most previous studies of bpAPs have used direct dendritic recordings, but their low spatial resolution is a serious drawback. It is extraordinarily difficult to figure out how bpAPs propagate and change between two recording sites using traditional electrophysiological methods, and the reported velocity and amplitude of bpAPs are values obtained from dendrites with lengths of hundreds of micrometers. Without an exhaustive recording and description of bpAPs, it is difficult to reveal how factors influence them and further understand their functions. To overcome this limitation, recent studies have applied optical recording *via* genetically-encoded voltage indicators (GEVIs) or genetically-encoded  $\text{Ca}^{2+}$  indicators [21, 22]. Here we used a previously developed all-optical electrophysiological method using a GEVI [23] to record the membrane voltage in the dendrites of cultured hippocampal neurons. This “Optopatch” method improves spatial resolution to the single-micron level and possesses sub-millisecond

temporal resolution. Previous studies have generally examined only one dendrite in detail, but all-optical voltage imaging allowed us to simultaneously record and study bpAPs in several proximal dendrites from one neuron in detail without perturbation. By comparing the morphology of individual dendrites and the corresponding bpAPs, we were able to understand how the bpAP propagates in the dendrite in detail and study the effect of dendritic diameter and branching on bpAP velocity and amplitude more quantitatively.

We also used computational neuron modeling to simulate the backpropagation of APs in dendrites with various morphological features, to obtain more precise correlations between morphology and bpAP properties. Our models and experimental data together revealed that the varying properties of bpAPs in dendrites are primarily determined by dendritic morphological features. These results have important implications for our understanding of bpAP modulation, and they provide a foundation for the construction of a universal neuron model capable of reproducing the propagation of a bpAP on a dendrite with any given morphology.

## Materials and Methods

### Primary Neuron Culture

Primary neurons were cultured from postnatal day 0 C57BL/6J mice following the rules and regulations of the Peking University Animal Care and Use Committee as described previously [24]. Fresh hippocampal tissue was dissected from the brain and digested with 0.25% trypsin (Gibco, NY, USA) for 15 min in an incubator at 37 °C, followed by inactivation with an equal volume of DMEM/F12 medium (Gibco) with 10% fetal bovine serum (FBS) (Gibco). Next, the mixture was lightly triturated using a pipette. After 2 min of precipitation, the supernatant was collected and centrifuged at 200 $\times$  g for 5 min. The cell sediment was re-suspended in DMEM/F12 medium with 10% FBS and plated on coverslips coated with poly-D-lysine (Sigma, NJ, USA) at a density of  $1 \times 10^5$  neurons/coverslip in a 24-well culture dish. After half an hour, the cells were maintained with Neurobasal medium (Gibco) containing 1% penicillin-streptomycin (Gibco), 2% B27 (Gibco), and 1% GlutaMAX (Gibco). Half of the culture medium was replaced with fresh medium every 2 days.

### $\text{Ca}^{2+}$ -Phosphate Transfection

Neurons were transfected on day 8 *in vitro* (DIV8) with Optopatch2 plasmids *via* the  $\text{Ca}^{2+}$  phosphate transfection

method. FCK-Optopatch2 plasmid was a gift from Prof. Adam. E. Cohen, Harvard University. Generally, 2  $\mu\text{g}$  of plasmid diluted in  $\text{CaCl}_2$ /water solution was mixed with an equal volume of 2 $\times$  HEPES balanced salt solution (HBS) (Clontech, Shiga, Japan) followed by gentle vortexing. The DNA- $\text{Ca}^{2+}$ -phosphate complex was added dropwise to neurons maintained in fresh Neurobasal medium. The neurons were incubated at 37 °C for 1 h and then washed twice with 1 $\times$  HBS (pH 6.8) to completely clear the precipitate. Finally, cells were maintained in their original growth medium in an incubator until DIV12 for imaging as described below.

### Immunocytochemistry

The neurons were fixed in 4% paraformaldehyde for 15 min, permeabilized for 10 min with 0.2% Triton X-100 in phosphate-buffered saline (PBS), and blocked with blocking buffer (5% bovine serum albumin and 0.2% Tween 20 in PBS). The neurons were incubated at 4 °C overnight with primary antibodies diluted in blocking buffer to the appropriate concentration. After washing with PBS, the neurons were incubated with secondary antibodies for 1 h at room temperature. Finally, the coverslips with neurons were mounted on slides with Fluoromount-G (SouthernBiotech, AL, USA). The following antibody dilutions were used: anti-PROX1 (1:500, Abcam, Cambridge, UK), anti-GAD65 (1:500, Abcam), anti-GFP (1:2000, Abcam), and all secondary antibodies (1:500, Invitrogen, NY, USA).

### Imaging Apparatus

Fluorescent images were collected on a spinning disk confocal microscope (Andor Dragonfly, Oxford Instruments, Oxford, UK) equipped with a 40 $\times$  1.3 NA oil immersion objective lens, 4 laser lines (405, 488, 561, and 637 nm), and electron-multiplying charge-coupled device (EMCCD) or scientific complementary metal-oxide-semiconductor (sCMOS) cameras (Andor).

All-optical electrophysiological experiments were conducted on an inverted fluorescence microscope (Nikon-TiE, Nikon, Tokyo, Japan) equipped with a 40 $\times$  1.3 NA oil immersion objective lens (Nikon CFI Plan Fluor), 6 laser lines (Coherent OBIS, 405, 488, 532, 594, 561, and 639 nm), and an sCMOS camera (Hamamatsu ORCA-Flash 4.0 v2, Hamamatsu, Shizuoka, Japan). The microscope, lasers, cameras, and high-precision stage (Marzhauser Wetzlar, Hessian, German) were controlled with customized software programmed in LabVIEW (National Instruments, 15.0 version, TX, USA). Most fluorescent proteins were imaged at illumination intensities of 1–6  $\text{W}/\text{cm}^2$ , while QuasAr2 was imaged at 800–1000  $\text{W}/\text{cm}^2$ .

### Fluorescent Imaging of Neurons

The fixed neurons were imaged on a Dragonfly confocal microscope (Andor). Images were acquired at 1  $\times$  1 camera binning with an exposure time of 100–1000 ms in Z-stack mode with a 0.5- $\mu\text{m}$  step length. In ImageJ/Fiji [25], each image stack was Z-projected with maximum intensity to one image, and new images in several channels were adjusted and merged.

### Whole-cell Patch-clamp with Simultaneous Voltage Imaging

Before imaging and electrophysiology, neurons on coverslips were placed in a glass-bottomed dish filled with customized high-glucose Tyrode's solution containing (in mmol/L) 125 NaCl, 2.5 KCl, 3  $\text{CaCl}_2$ , 1  $\text{MgCl}_2$ , 10 HEPES, and 30 glucose (pH 7.3, adjusted to 305–310 mOsm/kg with sucrose). The synaptic blockers NBQX (10  $\mu\text{mol/L}$ ), AP-5 (25  $\mu\text{mol/L}$ ), and gabazine (20  $\mu\text{mol/L}$ , all from Sigma) were added to the buffer for measurements of single-cell electrophysiology. All experiments were performed at room temperature ( $\sim 22$  °C).

Borosilicate glass electrodes (WPI, FL, USA) were pulled to a tip resistance of 2.5–5  $\text{M}\Omega$ . The electrodes were filled with internal solution containing (in mmol/L) 125 potassium gluconate, 8 NaCl, 0.6  $\text{MgCl}_2$ , 0.1  $\text{CaCl}_2$ , 1 EGTA, 10 HEPES, 4  $\text{Mg-ATP}$ , 0.4  $\text{Na}_2\text{-GTP}$  (adjusted to pH 7.3 with KOH and 290–300 mOsm/kg with 1 mol/L sucrose). Neurons were clamped in the whole-cell current-clamp mode, and the membrane voltage signal recorded from the patch amplifier (Axopatch 200B, Molecular Devices, CA, USA) was filtered with an internal 5-kHz Bessel filter and digitized at 9681.48 Hz with a National Instruments (TX, USA) PCIe-6353 data acquisition board. During the current stimulation, simultaneous voltage images were acquired at a 20 $\times$  down-sampling rate (484.07 Hz, 2.0658 ms/frame).

### All-optical Electrophysiology

Imaging experiments were conducted in the same external solution. We coupled an sCMOS camera and a 488-nm laser, which were controlled by LabVIEW software to achieve simultaneous optogenetic stimulation and imaging. The signal rate of laser control and patch-clamp recording was 4643.60 Hz, with 10 $\times$  up-sampling to camera acquisition (464.36 Hz, 2.1535 ms/frame). We used a 488-nm laser pulse (0.05–0.20  $\text{W}/\text{cm}^2$ ) with a duration of 1.93 ms to illuminate neurons at a rate of 5 Hz, which stimulated neurons to generate 50 APs in 10 s. Meanwhile, we used a 639-nm laser to excite QuasAr2. The two beams were combined and projected onto the neuron through the objective lens. Fluorescent signals were collected by the sCMOS camera under rolling-shutter mode with 2  $\times$  2 binning.



## Quantitative Analysis of Video Data

The relative fluorescence change ( $\Delta F/F$ ) was used to derive the AP signal. To obtain a spike-triggered average movie, the signal of every pixel was averaged over all simulated APs (by peak-finding and alignment) to boost the signal-to-noise ratio (SNR) for the following interpolation and calculation. The camera bias (intensity of 400 in the  $2 \times 2$  binning mode) was subtracted from these average intensities to give the final values. Then we applied photobleaching correction of the fluorescent signal by dividing the raw signal with a reference baseline, which was constructed from processing the sliding minimum filter on the fluorescent signals.

To quantify the bpAP propagation, we processed the video data by a self-developed algorithm with MATLAB (version R2020a, MA, USA). A flowchart of the algorithm is shown in Fig. S1A. First, we drew the center line of the dendrite of interest (Fig. S1B). Next, a 5 pixels  $\times$  5 pixels region centered by each pixel on the center line was set as the whole region of interest (ROI), and the intensity of the whole ROI was smoothed to obtain the photobleaching baseline. The final value we used was the intensity divided by the photobleaching value (Fig. S1C). After that, we found the peaks (local maxima) of periodic APs (Fig. S1D upper) and averaged them to obtain the mean AP trace. To increase the time resolution, we interpolated the mean AP trace with a cubic spline to obtain a green AP trace, which was used as a kernel to revise the APs in each segment. The cubic spline interpolation increased the time resolution of the data from 2 ms to 0.002 ms (Fig. S1D lower).

Next, we calculated the peak time of the AP at each pixel on the center line. The peak time was averaged within an 11-pixel-long window sliding on the center line, which contained 5 pixels before and after the central pixel (Fig. S1E). We first averaged the signals of pixels in this window to obtain the signal on the red point (blue signal) that was the central point. Then, we interpolated the signal of the red point with the cubic spline (red signal) and convolved the splined signal with the kernel (Fig. S1D) to calculate the correlation coefficient (yellow line in Fig. S1E). Then we replaced the splined signal according to the correlation coefficient to obtain the corrected signal (purple signal). After that, we used this corrected, high-precision signal to find the relative peak arrival time of the red point's AP. Finally, we calculated the bpAP propagation velocity in the dendrite (Fig. S1F). The change of the relative fluorescence signal after interpolation was used to calculate the relative amplitude of the bpAP.

## Modeling a Neuron

We created a detailed multi-compartment model of a neuron to explore the characteristics of backpropagating signals. The

model included simplified morphology, ion channel distributions and densities, channel kinetics, and passive properties. The neuronal morphology was modeled with simple stick models consisting of a cylindrical soma (1  $\mu\text{m}$  in length  $\times$  20  $\mu\text{m}$  in diameter) attached to 8 dendrites with different diameters (when simulating how diameter influences velocity) or to a binary tree (when simulating how the branch point influences velocity). We stimulated the model neuron with an AP-shaped voltage stimulus injected directly into the soma, after which the signal backpropagated to the dendrites. The simulation was implemented within the simulation software NEURON (version 7.6.5 running on Microsoft Windows 10). The integration time steps were fixed at 0.001 ms. The length of all segments was 1  $\mu\text{m}$ . The full model is available on ModelDB (<https://senselab.med.yale.edu/modeldb/ShowModel?model=267417>, access code: DendriteSimCode). Analysis of the simulation data was performed with MATLAB (version R2020a).

The parameters used in the simulations are listed in Table 1. Various passive parameter values were explored within physiologically relevant ranges taken from the literature [26–30]. The specific values of the passive parameters were chosen in order to match the experimentally measured input resistance and membrane time constant in mouse hippocampal neurons.

With regard to active properties, the gating kinetics of voltage-dependent  $\text{Na}^+$  and  $\text{K}^+$  channels were modeled after the standard Hodgkin-Huxley model [31, 32]. The kinetics and parameters of the ion channels are listed in Table 2. We adjusted the ion channel densities according to experimentally obtained densities from the literature [26, 29, 31].

According to Rall's study [33], a total of  $k$  dendrites at the same level with arbitrary diameters  $r_k$  are equivalent to one dendrite of diameter  $r_0$  as follows:

$$r_0^{\frac{3}{2}} = \sum_k r_k^{\frac{3}{2}}$$

In simulations of multi-level binary trees, the sum of the diameters of two daughter dendritic cables after the branching point is equivalent to that of the mother dendritic cable, according to this formula.

**Table 1** Parameters used in the simulations

Model parameter	
Passive properties	
Specific membrane capacitance ( $C_m$ )	Default
Specific membrane resistance ( $R_m$ )	0.5 $\mu\text{F}/\text{cm}^2$
Intracellular resistivity ( $R_a$ )	20,000 $\Omega\text{cm}^2$
Leak reversal potential ( $E_L$ )	300 $\Omega\text{cm}$
Active properties	
$\bar{G}_{\text{Na}}$ (maximum $\text{Na}^+$ conductance)	−65 mV
$\bar{G}_{\text{K}}$ (maximum $\text{K}^+$ conductance)	100 pS/ $\mu\text{m}^2$
	100 pS/ $\mu\text{m}^2$

**Table 2** Kinetics of voltage-dependent Na<sup>+</sup> and K<sup>+</sup> channels

Channel type	Gating particle	Dynamics
Na <sup>+</sup> channel	<i>m</i>	$I_{\text{Na}} = G_{\text{Na}}(V_m - E_{\text{Na}})$
		$G_{\text{Na}} = \tau_{\text{adj}} \bar{G}_{\text{Na}} m^3 h$
		$\tau_{\text{adj}} = 2.3 \frac{T-23}{10}$
		$\dot{m} = \frac{m_{\infty} - m}{\tau_m}$
		$\alpha_m = 1.638 \cdot \exp(\frac{-V_m - 35}{9})$
		$\beta_m = 1.116 \cdot \exp(\frac{V_m + 35}{9})$
		$m_{\infty} = \frac{\alpha_m}{\alpha_m + \beta_m}$
		$\tau_m = \frac{1}{\tau_{\text{adj}}(\alpha_m + \beta_m)}$
		$\dot{h} = \frac{h_{\infty} - h}{\tau_h}$
		$\alpha_h = 0.120 \cdot \exp(\frac{-V_m - 50}{5})$
K <sup>+</sup> channel	<i>n</i>	$\beta_h = 0.046 \cdot \exp(\frac{V_m + 75}{9})$
		$h_{\infty} = \frac{1}{1 + \exp(\frac{V_m + 65}{6.2})}$
		$\tau_h = \frac{1}{\tau_{\text{adj}}(\alpha_h + \beta_h)}$
		$I_K = G_K(V_m - E_K)$
		$G_K = \tau_{\text{adj}} \bar{G}_K n$
		$\dot{n} = \frac{n_{\infty} - n}{\tau_n}$
		$\alpha_n = 0.180 \cdot \exp(\frac{-V_m + 25}{9})$
		$\beta_n = 0.018 \cdot \exp(\frac{V_m - 25}{9})$
		$n_{\infty} = \frac{\alpha_n}{\alpha_n + \beta_n}$
		$\tau_n = \frac{1}{\tau_{\text{adj}}(\alpha_n + \beta_n)}$

*I*, current; *G*, channel conductance;  $\bar{G}$ , the maximum channel conductance; *V<sub>m</sub>*, membrane potential; *E*, reversal potential of the ion channel;  $\tau_{\text{adj}}$ , temperature coefficient; *T*, temperature. *x* is the gating parameter (*x* = *m*, *h*, *n*),  $\dot{x}$  is the derivative of *x* with respect to time,  $\alpha_x$  is the opening rate of gate,  $\beta_x$  is the closing rate of gate,  $x_{\infty}$  is the limiting value that *x* approaches, with the time constant  $\tau_x$ .

## Statistical Analysis

We defined the primary dendrite as the dendrite that arose directly from the soma with a length of at least 5  $\mu\text{m}$ , and the secondary dendrites were defined as the dendrites branching from the primary dendrite with a length of at least 5  $\mu\text{m}$ . Diameter and soma area measurements were made on image stacks using Fiji/ImageJ. Data were analyzed using Prism 7.0 (GraphPad, CA, USA). All values are given as the mean  $\pm$  SEM unless otherwise noted. Two-tailed Student's *t*-test and one-way ANOVA with Dunnett's *post hoc* test were used for data analysis. Reported *P*-values indicate statistical significance as follows: \**P* < 0.05, \*\**P* < 0.01, \*\*\**P* < 0.001, and \*\*\*\**P* < 0.0001.

## Results

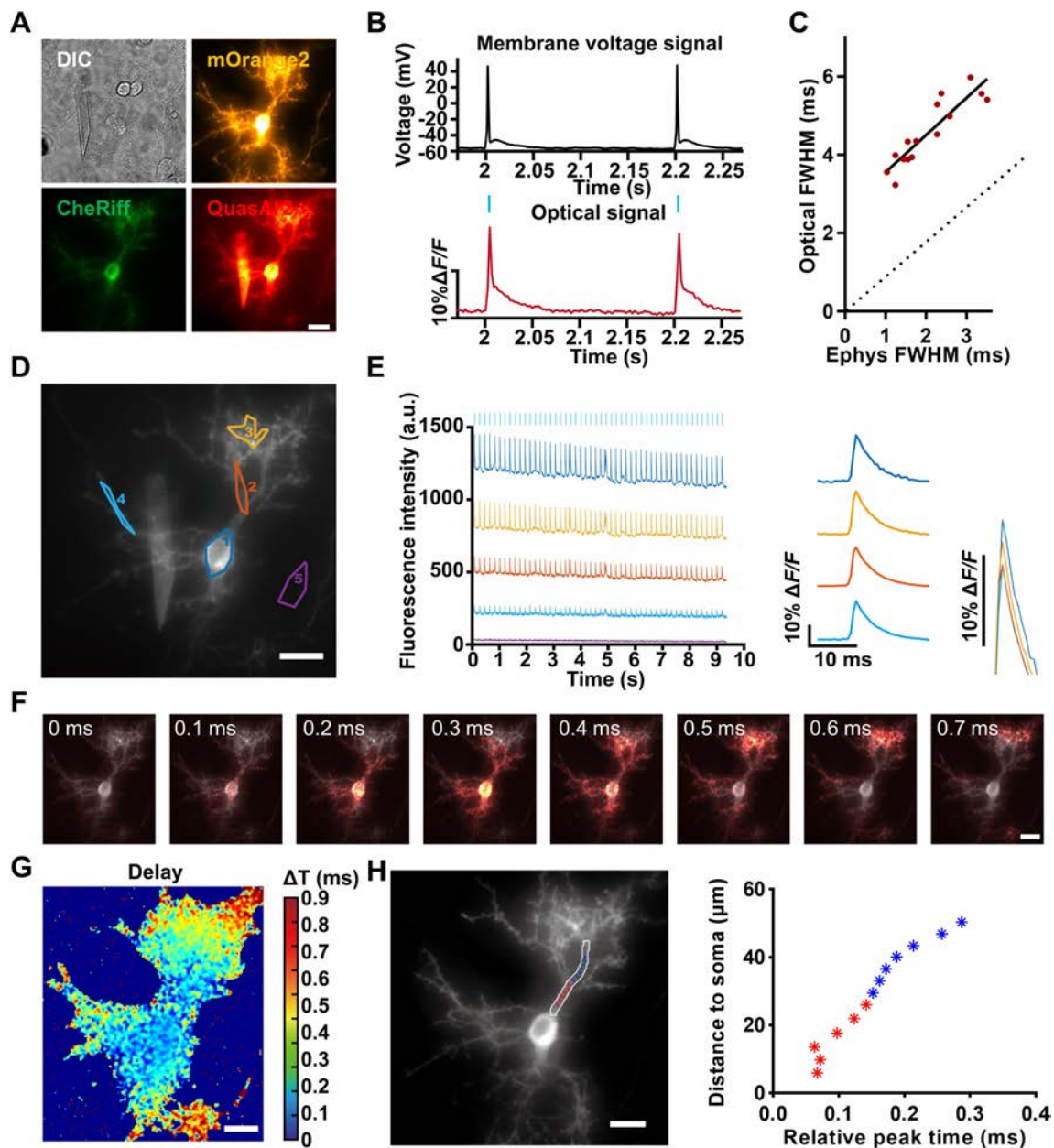
### Sub-millisecond-level All-optical Electrophysiological Techniques Resolve Backpropagating Action Potentials Simultaneously in Several Dendrites

Optical recording using GEVI can, in principle, overcome many of the technical limits encountered in traditional electrophysiological recordings, providing a way to record APs at subcellular regions or at multiple sites with maximum fidelity and millisecond response times. The Optopatch2 construct we used contained CheRiff, a channelrhodopsin, as the AP trigger, as well as QuasAr2, a near-infrared voltage indicator. These two proteins were joined by a self-cleaving 2A peptide sequence to ensure that they were expressed at similar levels. After expression in cultured mouse hippocampal neurons, both proteins showed extensive membrane trafficking in all regions of the neuron, including the soma, axon, proximal dendrites, and distal dendrites (Fig. 1A).

To test whether the fluorescent kinetics of QuasAr2 faithfully reflect the AP waveform, the electrical signal through a patch-clamp and the optical signal after evocation of APs *via* optogenetic stimulation were simultaneously recorded and compared. Imaging data were processed as previously reported [23]. QuasAr2 showed high fluorescent sensitivity and a fast response speed to potential changes, and the synchronization of the traces of the electrical and optical signals was good using the optical stimulation approach (Fig. 1B). We also compared the full width at half maximum (FWHM) of AP waveforms under these two recording methods. The results showed that the FWHM of AP waveforms represented by the optical signal was larger than that of the electrical signal, which was acceptable using a voltage indicator. Moreover, there was still a positive correlation between the FWHM of AP waveforms from the two recording methods, indicating a fast response speed of QuasAr2 and high fidelity of AP waveforms (Fig. 1C).

Next, we used this all-optical electrophysiological method to record and reveal the propagation of bpAPs in the dendritic tree. Subsequent images were recorded at a 484-Hz frame rate for 10 s. Under optical stimulation, membrane voltage dynamics were simultaneously recorded at the soma and dendrites of a single neuron in the field of view. bpAPs were observed in the different regions of the dendrite with perfect synchronization to the somatic APs, but with an attenuated peak (Fig. 1D, E).

Spike-triggered average movies from raw voltage imaging data were generated to improve the SNR and for subsequent analysis. An interpolation algorithm was used to analyze the AP timing with sub-millisecond temporal resolution and pixel-level spatial resolution (see Materials and Methods). The AP propagation heatmap showed that APs occurred



**Fig. 1** Studying backpropagating action potentials in dendrites *via* all-optical electrophysiology. **A** Images of a neuron expressing Opto-patch2 elements. Scale bar, 10  $\mu\text{m}$ . **B** Simultaneous fluorescence and patch-clamp recordings from one neuron. Blue bar, illumination; red trace, whole-cell single-trial fluorescence; black trace, patch-clamp recording. **C** FWHM comparison of AP waveforms from electrical and optical signals. Ephys FWHM, FWHM of the AP signal waveform recorded by the patch clamp. **D** Several regions in the whole view of one sample neuron, including the soma, primary dendrites, secondary dendrites, and background. Scale bar, 10  $\mu\text{m}$ . **E** Fluores-

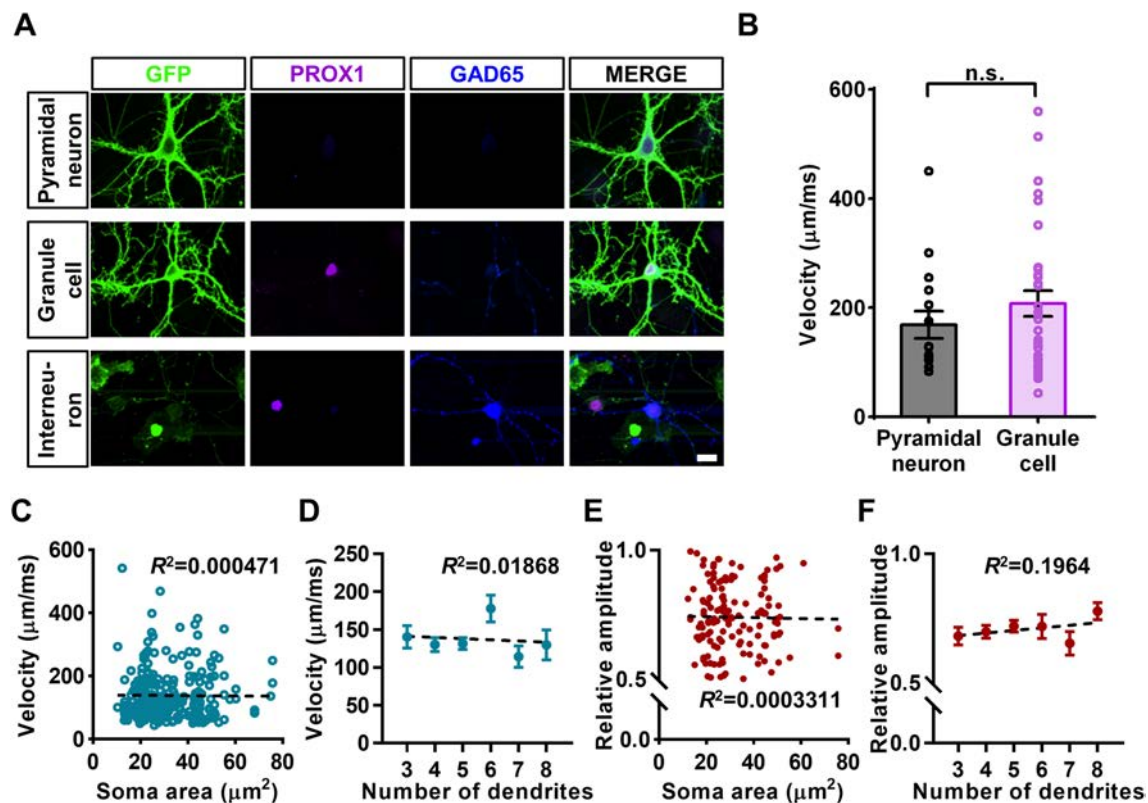
cence signal in several regions marked in **C** during simulation. Left, blue marks at the top of the left panel indicate blue light stimulation. Right, average  $\Delta F/F$  of QuasAr2 fluorescence in several regions (colors of signals represent regions marked by the same colors in **D**). **F** Frames from a propagation video showing the delay of the bpAP on the dendrite relative to the soma. Scale bar, 10  $\mu\text{m}$ . **G** Peak time delay heatmap of a bpAP in the neuron shown in **E**. Scale bar, 10  $\mu\text{m}$ . **H** Image and plot of peak time *versus* distance from the soma of a bpAP propagating along one dendrite (red, propagation on the primary dendrite; blue, propagation on the secondary dendrite). Scale bar, 10  $\mu\text{m}$ .

initially at the soma and were then conducted into the dendrites (Fig. 1F, G, and Video S1).

We obtained information about APs on the whole dendrite within the field of view. This improved the precision

and spatial resolution of bpAP recording and made it possible to analyze the bpAP propagation process in detail. By quantifying this process, we were able to obtain the average bpAP velocity at any given dendrite segment, which could





**Fig. 2** The soma area and the number of primary dendrites are not correlated with bpAP variation among neurons. **A** Immunostaining of different types of neurons. GFP indicates neurons expressing Optopatch2. Scale bar, 10  $\mu\text{m}$ . **B** Velocity of bpAPs in pyramidal neurons ( $n = 26$ ) and granule cells ( $n = 52$ ).  $P = 0.8211$ ; n.s., no significant difference, unpaired  $t$ -test. Error bars, SEM. **C** Plot of the correlation between bpAP velocity on primary dendrites and soma area ( $n = 252$ ). **D** Plot of the correlation between bpAP velocity and the number of primary dendrites. PD, primary dendrite. Column 3:  $n =$

46; column 4:  $n = 49$ ; column 5:  $n = 75$ ; column 6:  $n = 31$ ; column 7:  $n = 20$ ; column 8:  $n = 17$ ; all  $P > 0.05$ , one-way ANOVA. Error bars, SEM. **E** Plot of the correlation between the relative amplitude of bpAPs and soma area.  $n = 143$ . **F** Plot of the correlation between the relative amplitude of bpAPs and the number of primary dendrites. Column 3:  $n = 28$ ; column 4:  $n = 38$ ; column 5:  $n = 51$ ; column 6:  $n = 15$ ; column 7:  $n = 12$ ; column 8:  $n = 11$ ; all  $P > 0.05$ , one-way ANOVA. Error bars, SEM.

consist of the whole primary dendrite or only a part of it. The results clearly showed that the bpAP propagation velocity in dendrites fluctuated (Fig. 1H).

### bpAP Properties Are Mainly Determined by Dendritic Tree Morphology

Previous studies have shown that the propagation velocity of bpAPs differs markedly between pyramidal neurons and granule cells in brain slices, as well as between the apical and basal dendrites of a single pyramidal neuron. To separate recorded neurons into different cell types, we fixed and stained the neurons with several cell markers after acquiring voltage imaging data. Anti-PROX1 antibodies were used to label granule cells, while anti-GAD65 antibodies were used to indicate inhibitory neurons. As neurons transfected with Optopatch2 expressed GFP and mOrange2 at the same time, it was nearly impossible to use another cell marker with an unappropriated fluorescence channel. Therefore, we

considered neurons lacking both the PROX1 and GAD65 signals to be pyramidal neurons (Fig. 2A).

No inhibitory neurons were recorded because the promoter of the plasmid was CamKIIa. After classifying the analyzed neurons into different types, we found that there was no significant difference in the average velocities of bpAPs in pyramidal neurons (190  $\mu\text{m/ms}$ ) and granule cells (202  $\mu\text{m/ms}$ ) (Fig. 2B).

The lack of significant differences between the average velocities of bpAPs in different neuron types might have been a result of differences induced by culturing neurons on coverslips rather than obtaining them from brain slices. The dendritic morphology varied markedly between cultured neurons and neurons in brain slices. The 2D culture conditions might hide the structural and morphological distinctions between different cell types and unique dendrites. These results indicated that the bpAP propagation processes in neurons with similar dendritic tree morphology were identical. This finding inspired us to investigate the basic



principles underlying the effect of dendritic morphology on bpAP propagation that could apply to all types of neuron.

Previous studies considered dendritic morphology to be the main factor that determines the main extent of bpAPs. Besides dendritic morphology, other morphological features of a neuron, like its volume and the number of primary dendrites, may also influence bpAP propagation. Therefore, we designed experiments to determine whether the volume of the cell body and the number of dendrites influences bpAP propagation. In cultured neurons, the soma area was used as a substitute for its volume. We found no direct correlation between the soma area or the number of primary dendrites and bpAP velocity (Fig. 2C, D). Since the fluorescence intensity of QuasAr2 varied among the tested neurons, we posited that the AP amplitudes at the somas of different neurons were nearly equal, and we used the ratio of relative fluorescence change from the dendrites to the soma to represent the relative bpAP amplitude. In addition, we found no correlation between the relative bpAP amplitude and the soma area or the number of primary dendrites (Fig. 2E, F). This finding indicated that the volume of the cell body and the number of primary dendrites have little influence on bpAP propagation.

#### **bpAP Velocity is Positively Correlated with Dendritic Diameter in Individual Neurons**

The diameter of multi-level dendrites is an important morphological characteristic that varies within a relatively large range. The effects of this variation were reflected in the average velocity, as well as the pattern with which the velocity changed (Fig. 3A). We investigated the correlation between bpAP velocity and dendritic diameter. The average bpAP velocity was  $128 \pm 6 \mu\text{m/ms}$  on the primary dendrite and  $81 \pm 5 \mu\text{m/ms}$  on the second dendrite (Fig. 3B). These results were similar to those of previous electrophysiological studies. The average primary dendrite diameter was  $2.08 \pm 0.05 \mu\text{m}$ , and the average secondary dendrite diameter was  $1.51 \pm 0.08 \mu\text{m}$ . We found a trend indicating a positive correlation between bpAP velocity and dendritic diameter (Fig. 3C), although there was no simple and direct relationship. To obtain a more relevant correlation, we divided primary dendrites from the same neuron or secondary dendrites from one primary dendrite into dendrite pairs in which the thinner dendrite was the reference. Then we calculated their velocity ratio and the square root of the diameter ratio based on previous studies of AP propagation simulation [34]. The velocity ratios of 67% of primary dendrite pairs and 85% of secondary dendrite pairs were each  $>1$ , indicating that the bpAP velocity on the thicker dendrite was faster (Fig. 3D). This positive correlation was more significant in secondary dendrites, and might result from a higher level of homogeneity between two secondary dendrites branching from a single

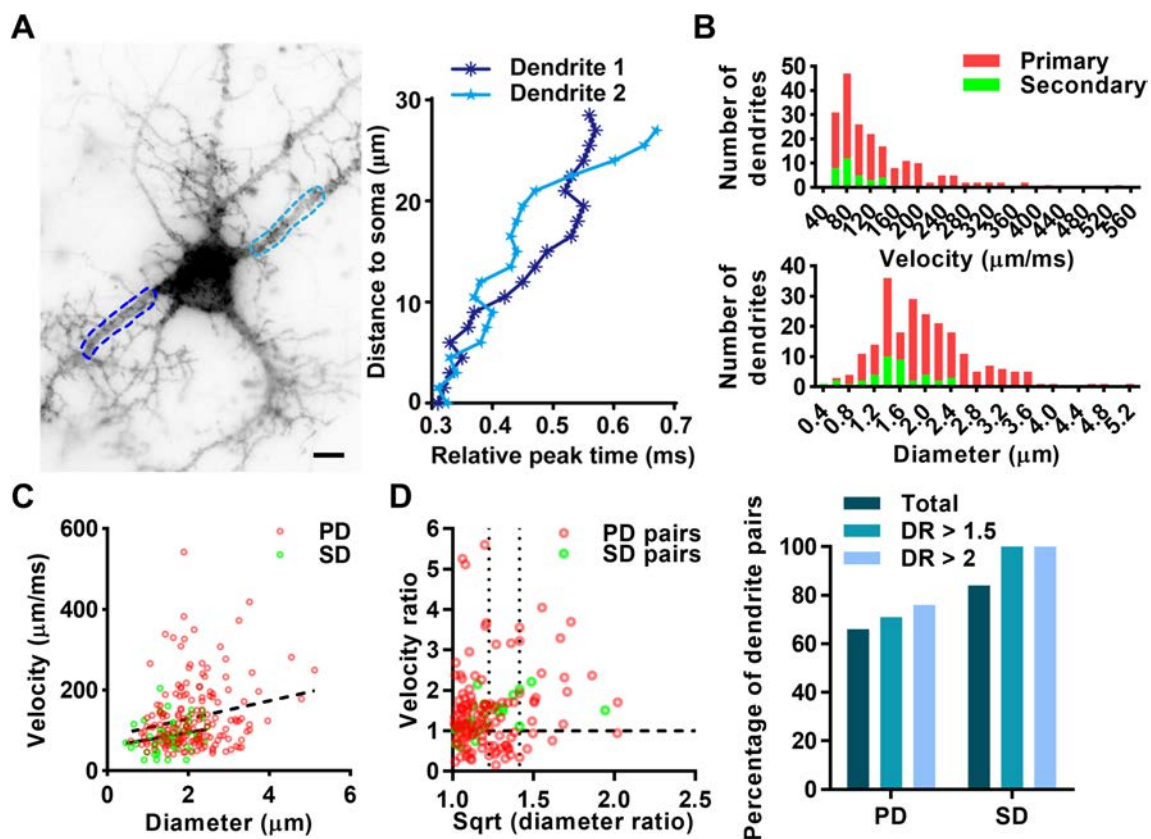
primary dendrite than that between two primary dendrites from the same neuron. As dendrites are relatively small, two dendrites with a small dendritic ratio may not differ markedly; therefore, we examined dendrite pairs with diameter ratios  $>1.5$  and dendrite pairs with diameter ratios  $>2$ . As the diameter ratio increased, the proportion of dendrite pairs with positively correlated bpAP velocities also increased (Fig. 3E). Therefore, for two dendrites from a single neuron, a bpAP is likely to propagate more rapidly on the thicker dendrite. When an AP is initiated at the axon initial segment (AIS) and then backpropagates into dendrites through the cell body, a bpAP on a thick dendrite would be very likely to propagate faster and reach its destination earlier than those on other dendrites.

#### **bpAP Velocity is Negatively Correlated with the Density of Dendritic Spines**

Spines are unique structures in dendrites. Due to the use of synaptic blockers, in our study, dendritic spines did not accept synaptic signal inputs, so the spine could be regarded as the structure that enlarges the volume and membrane area of dendrites to a certain extent. The distributions of spines on the dendrites of the neurons recorded in our experiment were very different, therefore we explored whether the density of spines also affected the velocity of the bpAP. We found that even in one neuron, there were dendrites with similar diameters but quite different spine densities (Fig. S2A). And the velocities of bpAPs on these two dendrites were different as well, not just in the average velocity but also in how the velocity changed. The average velocity of the bpAP on the dendrite with a low density of spines was much higher (Fig. S2B).

Then, we selected dendrite pairs from different neurons with similar dendrite diameters and markedly different spine densities. The diameter ratio of the two selected dendrites was  $\leq 1.1$  (taking the thinner dendrite as reference), and the density ratio of spines was  $\geq 1.5$  (taking the dendrite with fewer spines as reference). Based on the density of spines on two dendrites, we divided every dendrite pair into “sparse” and “dense” groups and compared the velocities of bpAPs on them. The velocity of bpAPs on the dendrites in the sparse group was significantly higher than that in the dense group (Fig. S2C). In order to further confirm this result, we also selected dendrites with similar diameters but different spine densities from the same neuron, and compared the velocities of bpAPs on them. The result showed that the velocity of bpAPs on dendrites with fewer spines from the same neuron was clearly faster (Fig. S2D).

These results indicated that when the diameter of dendrites was similar, the velocity of the bpAP was negatively correlated with the density of dendritic spines. Therefore, the difference in the density of spines may increase the difference between



**Fig. 3** The velocity of bpAPs is positively correlated with dendritic diameter in a single neuron. **A** Plot of the peak time of bpAPs on two dendrites of one neuron *versus* distance to the soma. The data on the dendrite segment marked by a dotted line are shown in the same color in the right panel. Scale bar, 10 μm. **B** Frequency distribution of the velocity of bpAPs and dendritic diameter on primary (PD;  $n = 182$ ) and secondary dendrites (SD;  $n = 40$ ). **C** Plot of the correlation between bpAP velocity and dendritic diameter (red, primary dendrites,  $n = 179$ ; green, secondary dendrites,  $n = 56$ ). **D** Left, Plot of

the correlation between the velocity ratio and the square root (Sqrt) of the dendritic diameter ratio in primary (PD,  $n = 132$ ) and secondary dendrite pairs (SD,  $n = 25$ ). Right, percentage of dendrite pairs showing a positive relationship between bpAP velocity and dendritic diameter in primary and secondary dendrites when the diameter ratio (DR) is in different ranges: total, PD: 67%, SD: 84%; when the diameter ratio >1.5, PD: 71%, SD: 100%; when the diameter ratio >2, PD: 76%, SD: 100%.

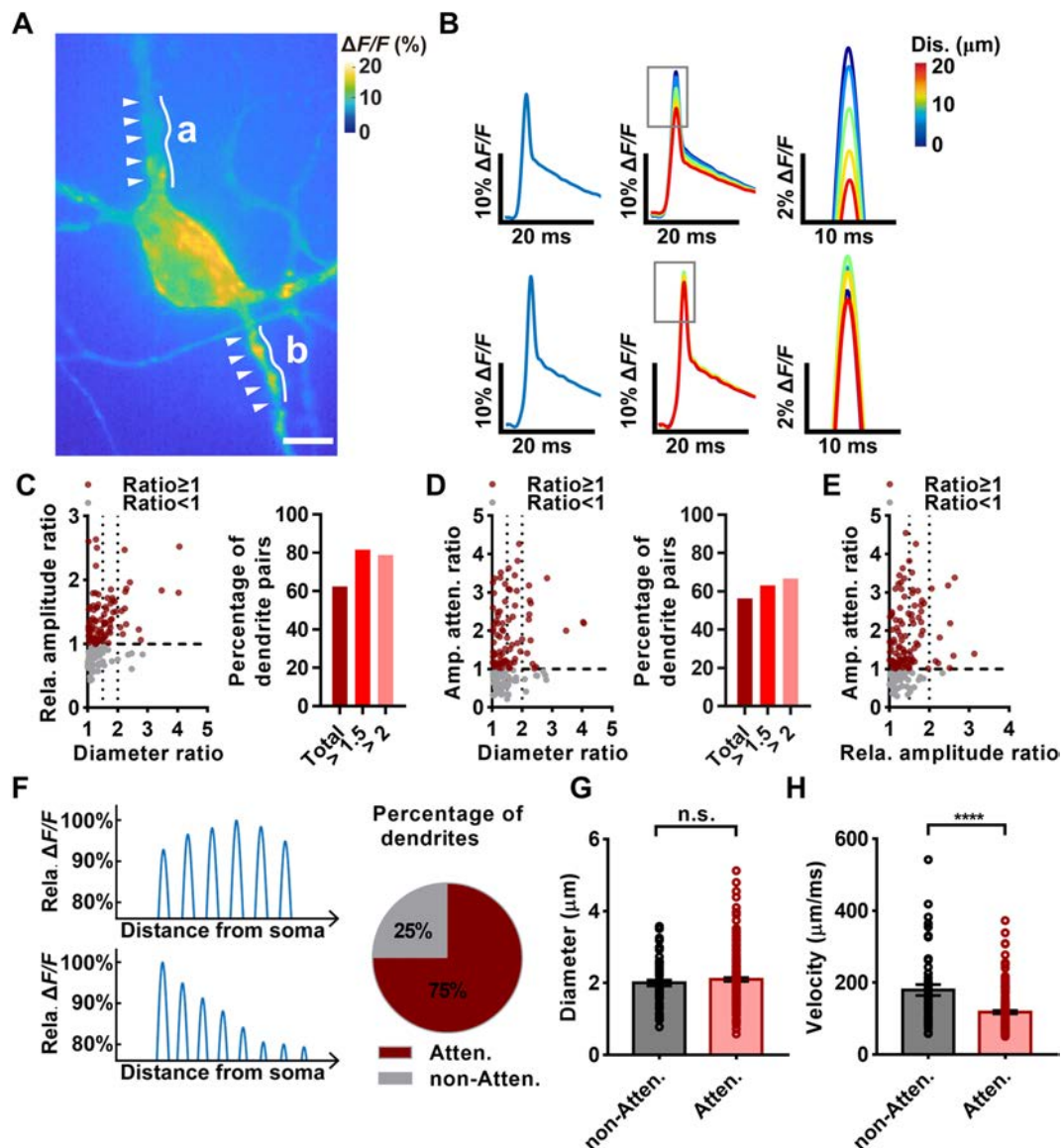
the dendrites of different neurons, and result in an indirect and significant correlation between the velocity of the bpAP and the square root of the diameter of the dendrite.

### bpAP Amplitude, but Not Attenuation, is Positively Correlated with Dendritic Diameter in Individual Neurons

In addition to bpAP velocity, bpAP amplitude is an important parameter reflecting the propagation process. Using an all-optical electrophysiological system, we recorded the relative amplitudes of bpAPs along dendrites and measured bpAP attenuation. Here, the relative fluorescence change was used to indicate the relative bpAP amplitude. The relative initial and average bpAP amplitudes and bpAP attenuation varied largely on different dendrites of the same neuron (Fig. 4B). As bpAP velocity is positively correlated with dendritic diameter, we explored

the relationship between bpAP relative amplitude and dendritic diameter. Therefore, we divided dendrites into dendrite pairs as described above and integrated their relative initial bpAP amplitude ratio with the corresponding diameter ratio, taking the thinner dendrite as a reference. We found that 62% of dendrite pairs showed a positive correlation between the relative initial amplitude ratio and the diameter ratio, and this positive correlation became more significant as the diameter ratio increased (Fig. 4C). This finding indicated that bpAPs on dendrites with relatively large diameters are likely to also have relatively high amplitudes.

Previous *in vivo* studies have shown that the bpAP amplitude attenuates as the distance from the soma increases, and our experiments revealed similar bpAP attenuation dynamics. We investigated the factors that may affect the attenuation of bpAP amplitude. We first assessed the correlation between the attenuation rate and dendritic diameter, which



**Fig. 4** The amplitude and attenuation of bpAPs are correlated with different factors in a single neuron. **A** Representative neuron with different bpAP amplitudes on different dendrites (a and b) (arrowheads, position of bpAP recording). Scale bar, 10  $\mu\text{m}$ . **B** Waveforms of bpAPs on dendrites of **A**. Left, the average waveform of bpAPs on two dendrites. Middle, respective waveforms of bpAPs at different dendrite sites away from the soma. Right, magnification of the waveforms in the middle panels indicated by boxes. **C** Plot of the correlation between the amplitude ratio of bpAPs and the dendritic diameter ratio in dendrite pairs. Left, scatter plot of the relative (Rela.) amplitude ratio and diameter ratio; brown red, dendritic pairs with relative amplitude ratio  $\geq 1$ ,  $n = 99$ ; grey, dendritic pairs with relative amplitude ratio  $< 1$ ,  $n = 59$ . Right panel, percentage of dendrite pairs showing a positive correlation between amplitude and dendritic diameter in groups with different diameter ratio ranges: total, 62%; diameter ratio  $> 1.5$ , 82%; diameter ratio  $> 2$ , 79%. **D** Plot of the correlation between the amplitude attenuation rate ratio of bpAPs and the dendritic diameter ratio in dendrite pairs. Left, scatterplot of the amplitude attenuation rate ratio (Amp. atten. ratio) and the diameter ratio;

brown red, dendritic pairs with amplitude attenuation rate ratio  $\geq 1$ ,  $n = 89$ ; grey, ratio  $< 1$ ,  $n = 69$ . Right, percentage of dendrite pairs showing a positive correlation between amplitude attenuation and dendritic diameter in groups with different diameter ratio ranges: total, 56%; when the diameter ratio  $> 1.5$ , 63%; ratio  $> 2$ , 67%. **E** Plot of the correlation between the amplitude attenuation rate ratio (Amp. atten. ratio) of bpAPs and the relative amplitude ratio in dendrite pairs. Rela. amplitude ratio, relative amplitude ratio. Brown red, dendritic pairs with amplitude attenuation rate ratio  $\geq 1$ ,  $n = 107$ ; grey, ratio  $< 1$ ,  $n = 52$ . **F** A schematic diagram of examples of attenuating (Atten.) and non-attenuating (Non-atten.) bpAPs and the percentage of dendrites showing attenuating or non-attenuating propagation of bpAPs. Left upper, an attenuating bpAP; left lower, a non-attenuating bpAP. Right, brown red, attenuating propagation, 75%; grey, non-attenuating propagation, 25%. **G** Dendritic diameters of attenuating ( $n = 57$ ) and non-attenuating ( $n = 51$ ) bpAPs.  $P = 0.3231$ , unpaired  $t$ -test. Error bars, SEM. **H** Velocity of attenuating ( $n = 57$ ) and non-attenuating ( $n = 45$ ) bpAPs.  $P < 0.0001$ , unpaired  $t$ -test. Error bars, SEM.

revealed that 56% of dendrite pairs showed a positive correlation between the attenuation rate ratio and the diameter ratio. This finding may indicate a weak correlation, although this proportion was larger in the sets of dendrite pairs with diameter ratios  $>1.5$  or 2 (Fig. 4D). Next, we associated the bpAP attenuation rate with the relative amplitude, which revealed that ~68% of dendrite pairs showed a positive correlation between the attenuation ratio and the relative initial amplitude ratio (Fig. 4E). This result indicated that, although the initial bpAP amplitude might be affected by dendritic diameter, the amplitude attenuation rate was more directly positively correlated with the initial amplitude. When bpAPs propagated along different primary dendrites of the same neuron, their initial amplitudes and attenuation rates varied markedly; bpAPs on thicker dendrites tended to have a higher amplitude and to attenuate more rapidly, which would be expected to lead to bpAPs with not much different amplitude at different distal dendrites.

Interestingly, not all bpAPs attenuated on dendrites, or, alternatively, they did not attenuate on the proximal dendrite sections included in our field of view. In total, 25% of bpAPs did not attenuate on the proximal dendrite (Fig. 4F). Therefore, we next explored factors that may control bpAP attenuation. We found no significant difference in diameter between dendrites in which bpAPs did and did not attenuate (Fig. 4G). In addition, we found that the velocity of non-attenuating bpAPs was higher than that of attenuating bpAPs (Fig. 4H). This finding indicated that non-attenuating bpAPs are more robust, and their velocity is more likely to be fast. We hypothesized that one or several dendrites may be responsible for delivering a signal to a distal dendrite as soon as possible, so the bpAP on such primary dendrites would be expected to be strong and non-attenuating.

### bpAPs Decelerate Significantly After Passing Through a Branch Point

Another important morphological feature of dendritic trees is their branching pattern. We found that bpAPs decelerate when they propagate from primary dendrites into secondary dendrites (Fig. 5A). Therefore, we performed experiments to determine how bpAPs change when they travel through a branch point.

First, we compared the velocities of bpAPs in dendrites before and after branch points. Most bpAPs decelerated significantly after a branch point (Fig. 5B). According to previous studies, bpAP amplitude attenuates naturally along dendrites without branch points. To determine whether bpAP self-attenuation influences velocity, we selected long primary dendrites and divided them into proximal and distal parts according to the distance from the soma, with each part 15–20  $\mu\text{m}$  in length (Fig. 5A). In contrast to the bpAPs traveling through branch points, most bpAPs showed only

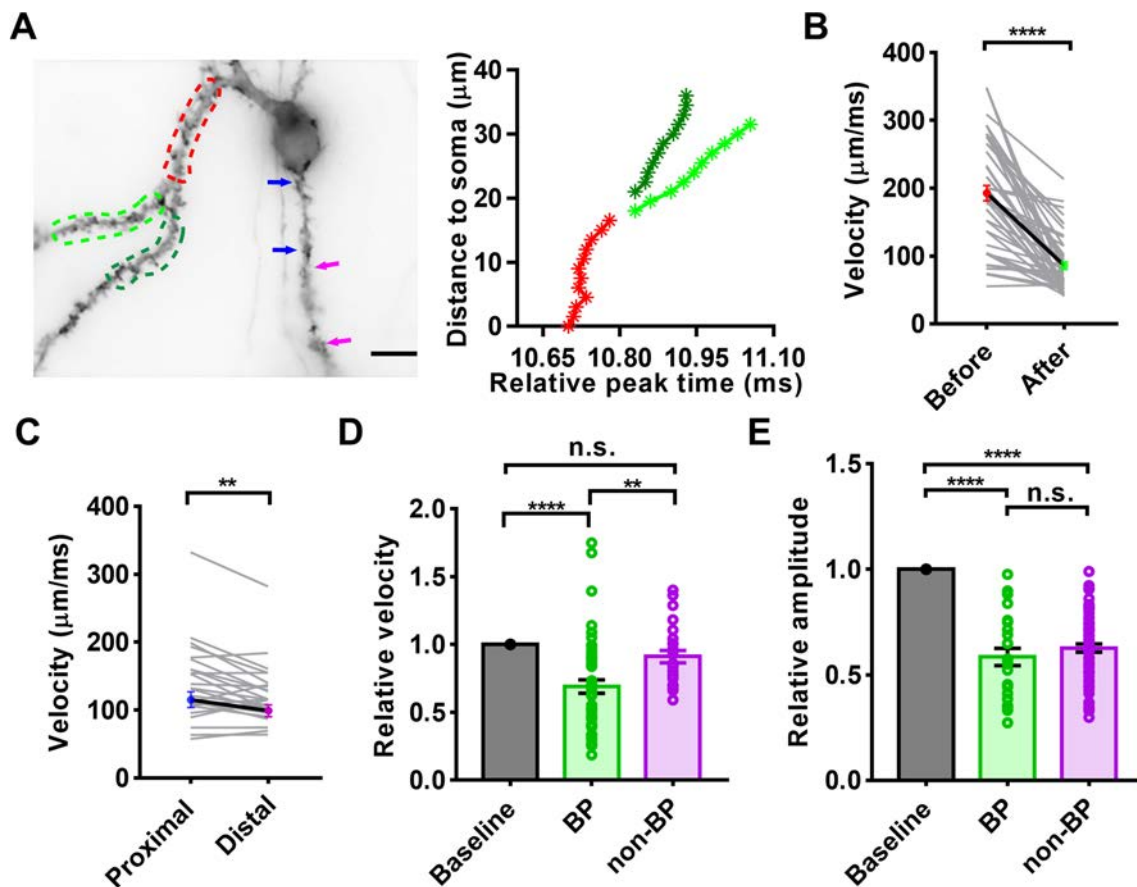
slight changes in velocity at the distal parts of dendrites lacking branch points (Fig. 5C). Although a significant difference was found between the bpAP velocity at each part, the results did not indicate a significant decrease. We also compared the relative change in velocity between these two cases, and this revealed that the decrease in velocity after passing a branch point was significantly greater than that which occurred along a long dendrite (Fig. 5D). These results demonstrated that branch points play a major role in the bpAP velocity decrease that occurs when bpAPs traveled through a dendritic tree. In contrast to the change in velocity, the relative change in bpAP amplitude after a branch point did not differ significantly from that which occurred on a long dendrite (Fig. 5E). This finding indicated that branch points are not primarily involved in the attenuation of bpAP amplitude.

### Simulations Reveal a Significant Correlation Between BpAP Velocity and Dendritic Morphology

We applied modeling to gain a better understanding of how the dendritic morphology influences the velocity and amplitude of bpAPs. The passive parameters and gating kinetics of voltage-dependent  $\text{Na}^+$  and  $\text{K}^+$  channels used in the simulations referred to previous literature [26–30, 32]. First, we tested the influence of dendritic diameter on bpAP velocity. In the model, eight dendrites with diameters increasing from 0.5  $\mu\text{m}$  to 4  $\mu\text{m}$  incrementally were attached to the soma. In the model, the propagation velocity increased as the dendrites became thicker and the velocity of the bpAP was nearly linearly correlated with the square root of diameter ratio (data not shown).

Then, we tested the influence of branch points on bpAP velocity. Eight neuron models with binary dendritic trees were constructed; these dendritic trees had the same total length, but their branching level increased incrementally, ranging from 1 to 8 levels (Fig. 6A). Here a “normal” situation was applied, in which the primary dendrite was 5  $\mu\text{m}$  thick, and the diameters of two daughter dendrites after the branching point were mathematically equivalent to that of their mother dendrite (see Materials and Methods), so the dendritic diameter decreased as the dendritic level increased. All other passive and active parameters were the same in all dendrites. We recorded the AP propagation process, including passage through every branch point, and calculated the average velocity from the soma to the ends of the dendrites. The results showed that the average velocity along an entire dendrite decreased as the branching level of its dendritic tree increased (Fig. 6B); therefore, as the number of branch points passed by the bpAP increased, its velocity decreased (Fig. 6C). To simulate an extreme situation, we modeled a neuron with a binary dendritic tree, while the diameters of the primary dendrite and two secondary dendrites were





**Fig. 5** Branch points (BP) cause attenuation of bpAP velocity. **A** Left, a sample primary dendrite divided into two secondary dendrites. Right, peak time of bpAPs recorded at several points along the dendrite; the colors of lines represented the segments marked by dotted lines in the left panel (red, primary dendrite; light and dark green, secondary dendrite; blue arrows, proximal part; pink arrows, distal part. Scale bar, 10  $\mu\text{m}$ . **B** bpAP velocity before and after a branch point.  $n = 50$ ;  $P < 0.0001$ , paired  $t$ -test. Error bars, SEM. **C** bpAP velocity at the proximal and distal parts of a long dendrite.  $n$

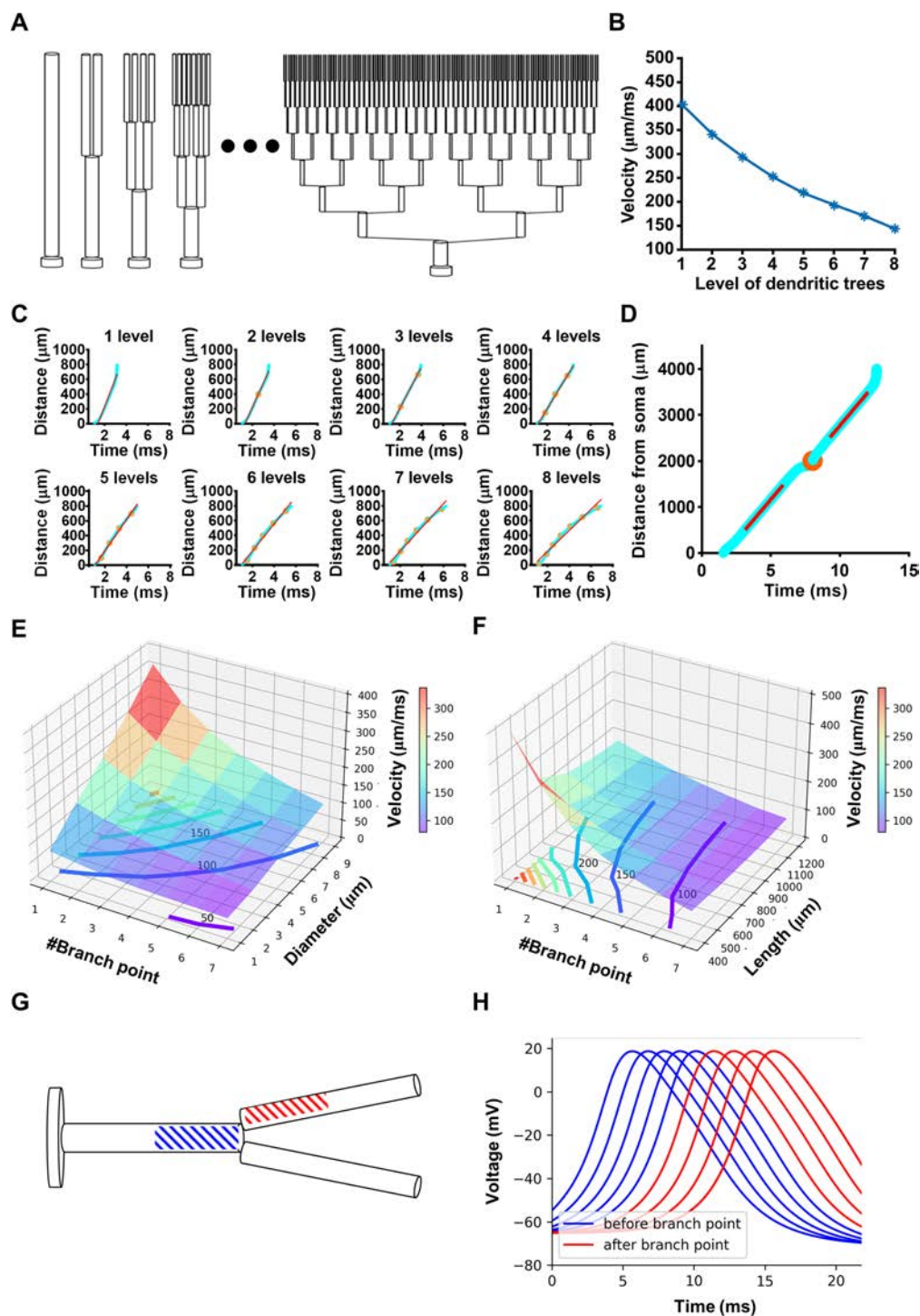
$= 25$ ;  $P = 0.0038$ , paired  $t$ -test. Error bars, SEM. **D** Relative bpAP velocity after passing through a branch point or propagating along a long dendrite. BP, branch point,  $n = 50$ ; non-BP, non-branch point,  $n = 25$ ;  $P < 0.0001$ ,  $P = 0.0034$ ,  $P = 0.4747$ , respectively, one-way ANOVA. Error bars, SEM. **E** Relative amplitude of bpAPs after the branch point or propagation along a long dendrite. BP:  $n = 27$ , non-BP:  $n = 20$ ,  $P < 0.0001$ ,  $P = 0.4900$ ,  $P < 0.0001$ , respectively, one-way ANOVA. Error bars, SEM.

unchanged. We found that the AP propagation velocity on the primary and secondary dendrites was nearly equivalent, except for a small change at the branch point (Fig. 6D). These results corresponded with our experimental findings under relatively conservative conditions. Taken together with the fact that the diameter of a dendrite always decreases after a branch point in actual neurons, this result led us to hypothesize that attenuation of bpAP velocity after a branch point might be the result of a reduction in dendritic diameter.

Next, we changed the number of branch points, dendritic diameter, and dendrite length of neuron models to examine how these parameters interact and regulate bpAP velocities. We first constructed a neuron model in which the total length of the dendritic tree was 800  $\mu\text{m}$ . We adjusted its branch points from 1 to 7 or dendritic diameter from 1  $\mu\text{m}$  to 9  $\mu\text{m}$  (all levels of dendrites) and recorded the velocity

of bpAPs. The results showed that the bpAP velocity was positively correlated with dendritic diameter when the number of branch points was fixed, and the bpAP velocity was negatively correlated with the number of branch points when the dendritic diameter was fixed (Fig. 6E). We then constructed a neuron model with a fixed dendritic diameter (5  $\mu\text{m}$ ) changeable total length and number of branch points. To sum up, the velocity of bpAP was negatively correlated with the density of branch points (Fig. 6F). The bpAP accelerated when it was near the end of the model, because the axial current was bigger. Therefore, in the model, the shorter the dendrite was, the velocity was influenced by the model boundary more and accelerated more.

Then, we tested how the number of branch points influences the attenuation of bpAPs. Here, we also used a neuron model with a binary dendritic tree and the diameters of the



**Fig. 6** Simulations with different dendritic morphology. **A** Eight neuron models with increasing dendritic tree branch levels and the same total dendritic length (800  $\mu\text{m}$ ). **B** The average bpAP velocity on the eight dendritic trees of **A**. **C** The time of the bpAP peak from the soma to the end of the dendrite on the eight dendritic trees. Distance, distance to soma; the orange points mark branch points, and the red lines are linear fits of distance-time curves. **D** Same as **A**, but on one binary tree with one primary dendrite and two secondary dendrites. The three dendrites have the same diameter (5  $\mu\text{m}$ ). **E** The

influence of the number of branch points and the equivalent diameters on the velocity of the bpAP. The step of contours is 50  $\mu\text{m}/\text{ms}$ . **F** The influence of the number of branch points and the lengths of models on the velocity of bpAPs. The step of contours is 50  $\mu\text{m}/\text{ms}$ . **G** A model with two levels of dendrites. The segments with blue and red slashes are located before and after the branch point. **H** The blue/red traces are voltages of blue/red segments in Fig. 5C. The branch point is located at 1000  $\mu\text{m}$ . APs are recorded at 650, 750, 850, 950, 1150, 1250, and 1350  $\mu\text{m}$ .

primary dendrite and two secondary dendrites were the same (5  $\mu\text{m}$ ) (Fig. 6G). We focused on the bpAP on the segments located on the segments before and after the branch points. As the active parameters were set uniformly along the whole dendritic tree, the AP shape (including the amplitude and half-width) was not changed during propagation (Fig. 6H). So under the conditions and parameters of our simulations, the branch point did not attenuate the bpAP.

## Discussion

The extent to which bpAPs invade distal dendrites is influenced in a complex manner by several factors, which include the pattern of excitatory and inhibitory inputs, ion channel distributions, and dendritic morphology. Here we focused on dendritic morphology, which has been considered to be the most decisive factor, to investigate how morphology specifically affects bpAPs. Using an all-optical electrophysiological method, we were able to record and study the propagation of bpAPs in proximal dendrites with relatively high spatial resolution in cultured neurons. By comparing bpAPs in the dendrites of one neuron, we found that the propagation velocity and amplitude of bpAPs were positively correlated with dendritic diameter. Another morphological parameter, the branching pattern, had a repressive effect on propagation. These results, taken together with the results from our computational neuron model, clarified how dendritic morphology affects bpAPs and indicated that dendrites perform distinct functions corresponding with their morphology, especially with regard to their participation in synaptic plasticity. We aimed to reveal a universal rule about the effect of dendritic morphology on bpAPs *in vitro*. And we established a complete process for recording and analyzing the propagation of bpAPs, which could be adapted to study the influence of other factors like ion channel distributions and synaptic inputs.

As a credible method of examining APs, voltage imaging has been used in many studies to measure their velocity and amplitude. However, in previous studies using dual-patch clamp methods, the average velocity along a section of dendrite (usually hundreds of micrometers in length) has been reported, and these data could not reveal the propagation process in detail, because dendrites vary along their lengths and have branch points. Voltage imaging provides a way to overcome such spatial restrictions; for example, bpAPs may be recorded in small dendritic regions such as spines [35]. By taking advantage of the fast response speed of QuasAr2, we were able to measure bpAP velocity in dendrite segments <20  $\mu\text{m}$  in length. On the other hand, due to restrictions associated with technical limitations, it is difficult to record APs on several dendrites using electrophysiological methods, but voltage imaging enabled us to record APs

in the soma and several dendrites at the same time at the micrometer scale. Therefore, we were able to study the entire process of AP propagation on a dendrite, and we compared differences in bpAPs before and after branch points, as well as on two homologous secondary dendrites. In addition, our method provided a way to link AP propagation with morphological parameters and quantitatively analyze their effects. The bpAP velocity recorded *via* patch-clamp was not exactly the same as that reported in previous studies, in which it was generally less than 1 mm/ms. This velocity was slightly faster than that reported in our study, and this change might have been the result of two different factors. First, the brain slices used in electrophysiological experiments provided neurons that more closely resembled cells under normal physiological conditions; such neurons were encircled and supported by glia and other brain tissue. Second, the experimental temperature for brain slice patch-clamp recordings was >30  $^{\circ}\text{C}$  in previous studies, whereas our recordings were performed at room temperature (23–25  $^{\circ}\text{C}$ ). Several studies have found that the experimental temperature has a large influence on bpAPs (~34  $^{\circ}\text{C}$  in [36]; room temperature in [37]).

Theoretical studies have found that AP propagation velocity is directly proportional to neurite diameter [33, 34, 38, 39]. Our research focused on homologous primary dendrites and homologous secondary dendrites as a way of studying the influence of dendritic diameter. This strategy excluded other systematic differences such as different cellular states and fluorescent protein expression. We found that, in a large proportion of primary dendrites, bpAP velocity was positively correlated with dendritic diameter; this proportion was larger among secondary dendrites, indicating that secondary dendrites branching out from the same primary dendrite are more homogeneous in other characteristics. In addition, we were able to shorten the dendritic segments to obtain a more detailed picture of the variation in velocity along a long dendrite. Although this analysis could be improved, the results indicated that bpAPs do not propagate with a steady velocity along dendrites. The underlying mechanisms and functions of this fluctuation remain to be investigated in future studies. The branching pattern is another important morphological feature of dendrites. Previous studies recorded bpAPs between proximal dendrites and distal dendrites after several branching points, making it difficult to discern the influence of each branch point. Using voltage imaging, we recorded the bpAP propagation process in dendrite segments before and after branch points. As expected, the bpAP velocity decreased significantly after each branch point. In addition, further study of long dendrites indicated that self-attenuation has little effect on bpAP velocity.

Previous studies have shown that the velocities of bpAPs are very different not only in different types of neuron, but also in different dendrites of the same neuron, such as the

apical and basal dendrites of pyramidal neurons. In our study, neurons were divided into pyramidal neurons and granulos cells, the major excitatory neurons in the hippocampus. The results showed that the difference in velocities of bpAPs on the dendrites between these two types of neuron was not as large as in previous studies. We thought that this difference might be caused by the *in vitro* conditions. The growth environment plays a central role in the determination of neuronal dendritic morphology. Previous studies have shown that when neurons are isolated from the *in vivo* environment and induced to regenerate in culture dishes, certain specific dendritic morphology of neurons can be preserved, such as Purkinje cells from the cerebellum [40]. But this only happens in neurons with extremely specialized dendritic morphology. Many features of neuronal type-specific complex dendritic morphology depend on local neural signals and specific interactions with matrices and other cells. The dendritic trees of hippocampal pyramidal neurons cultured *in vitro* can become complex and multipole [41, 42], without differentiation into primary (apical) and secondary (basal) dendrites. Therefore, in this study, we suggest that *in vitro* culturing conditions may weaken some of the characteristics of pyramidal neuron dendritic trees and reduce some of the morphological differences in dendritic trees between pyramidal neurons and granule cells, making their morphology tend to become similar. The less significant difference in the bpAP between these two kinds of neuron may demonstrate that the varieties in dendritic morphology largely determine the differences in the properties and propagation of bpAPs in different neurons.

In addition to velocity, the peak amplitude is also an important parameter that partly reflects bpAP strength. Although it was difficult to measure the absolute value of bpAP amplitude using voltage imaging, we were able to compare the relative amplitude in the same neuron to study the effect of dendritic morphology. As with velocity, in most neurons, bpAP amplitude was also positively correlated with dendritic diameter. The bpAP amplitude on primary dendrites of the same neuron varied largely because of morphological and physiological variation. Similar to the results from previous studies, we found that most bpAPs attenuated significantly along dendrites, but ~25% of bpAPs showed nearly unattenuated propagation. In bpAPs attenuating in dendrites, the attenuation rate was also positively correlated with dendritic diameter in most neurons. This finding indicated that the amplitude of a bpAP on a thick dendrite is likely to be high, but it is also likely to attenuate quickly, so the amplitudes of different bpAPs at distal dendrites would be similar. The presence of these two types of bpAP, attenuated and unattenuated, may imply that several kinds of dendrite with distinct properties and functions are present in the brain.

Consistent with our experimental results, in neuron model simulations, the velocity of bpAPs in dendrites increased as the dendritic diameter increased. The velocity ratio and square root of diameter ratio of every dendrite pair showed a linear positive correlation, but the slopes of these correlations in the experimental results varied widely, and this variation did not occur in our simulation. This finding indicated that, under experimental conditions, the dendritic diameter has a large effect on bpAP velocity. Simulations in neuron models with multi-level dendritic trees also demonstrated that the velocity of bpAPs decreased after passing through a branch point when the dendritic diameter decreased after the branch point. However, the bpAP velocity remained almost unchanged when the dendritic diameter was identical before and after the branch point. Combined with the fact that most dendrites became thinner after the branch point, the simulation results indicated that the reduction in velocity after a branch point was mainly due to the decrease in dendritic diameter. The capability of branch points to physically stop propagation remains to be studied. In our simulations with an active propagation neuron model, the amplitude of bpAPs did not attenuate on long unbranched dendrites if the ion channel parameters were constant along the entire dendritic tree. This kind of propagation could be considered as propagation under perfect conditions. Therefore, attenuation of bpAP amplitude was mainly caused by changes in the type and density of ion channels. Combined with our results demonstrating a correlation between dendritic diameter and velocity, these findings allow general predictions to be made regarding the process of bpAP propagation.

In order to study the bpAP in an individual neuron, we used synaptic blockers to block synaptic inputs. But synaptic input also plays a modulatory role in affecting the propagation of bpAPs. The interaction of synaptic inputs and bpAP has been studied both in excitatory and inhibitory synapses. Timely excitatory inputs at the distal dendrites can enhance the bpAP and possibly trigger dendritic spiking and burst firing to support propagation of the active bpAP into more distal dendritic trees [12, 43–46]. In contrast, inhibitory inputs can attenuate the propagation of bpAPs [47–49]. Inhibitory signals through GABA receptors in a single spine attenuates bpAP-induced  $\text{Ca}^{2+}$  influx within the same spine [50]. And the effects of inhibitory inputs on the propagation of bpAPs are likely to be most influential in proximal regions of the dendritic tree in which the bpAP has not attenuated much. Studies of how the AP and the excitatory postsynaptic potential (EPSP) interact initially focused on Ia-type transient  $\text{K}^+$  current [51, 52]. The Ia-type transient  $\text{K}^+$  current attenuates bpAPs in hippocampal CA1 neurons, and Ia-type  $\text{K}^+$  channels that produce this current are deactivated by depolarizing synaptic input signals [53]. This provides an explanation for the mechanism of how timely EPSPs strengthen bpAPs. In general, the complex balance between multiple opposing



synaptic signals determines the integration of synaptic input and bpAPs. The effect of synaptic inputs makes the determination of the extent of the bpAP more complex. So, we blocked synaptic inputs to focus on the effect of dendritic morphology on bpAP. Indeed, it is important and necessary to study the modulation of bpAPs by synaptic inputs in a more detailed way. By using the all-optical electrophysiological method, it will be convenient to compare bpAPs on the same dendrite with or without one or several kinds of synaptic signal and figure out the quantitative effects of synaptic inputs.

The induction of STDP requires the precise temporal order of presynaptic and postsynaptic depolarization in time windows of tens of milliseconds, and the bpAP might be an important source of postsynaptic depolarization. Although AMPA receptor activation is obligatory for STDP induction, the activation of NMDA receptors and bpAPs are necessary as well [54]. The STDP time window can be modulated by interactions between the EPSP and the bpAP [55]. An EPSP can strengthen subsequent bpAPs arriving within tens of milliseconds [12, 56]. And this boosting of bpAP can in turn modulate the magnitude of spike-timing-dependent LTP [11, 12, 57]. The velocity and amplitude of a bpAP directly determined the timing and strength when it reaches the synapse. Considering the effect of dendritic morphology on the velocity of the bpAP, we speculated that among the dendrites of each neuron, one or several dendrites may be primarily responsible for the transmission of neuronal information to distant synapses and the induction of synaptic plasticity. The interactions of EPSPs and bpAPs are more evident on a thick and less-branching dendrite in which the bpAP propagates faster and at a higher amplitude. This functional specialization of different dendrites also allows neurons to integrate and transmit neuronal signals more efficiently, which is crucial for the proper functioning of neuronal circuits.

**Acknowledgements** This work was supported by the National Science and Technology Innovation 2030-Major program of “Brain Science and Brain-Like Research” (2022ZD0211800), the National Natural Science Foundation of China (81971679, 32020103007, 32088101, and 21727806), the Ministry of Science and Technology (2018YFA0507600 and 2017YFA0503600), the Qidong-PKU SLS Innovation Fund (2016000663 and 2017000246), and the National Key R&D Program of China (2020AAA0105200). PZ is sponsored by Bayer Investigator Award. We thank the assistance from the Central Core Facility of the National Center for Protein Sciences at Peking University, and Dr. Siying Qin at the Core Facilities of the School of Life Sciences, Peking University for assistance with optical/confocal imaging.

**Conflict of interest** The authors declare no potential conflict of interest.

**Open Access** This article is licensed under a Creative Commons Attribution 4.0 International License, which permits use, sharing, adaptation, distribution and reproduction in any medium or format, as long as you give appropriate credit to the original author(s) and the source,

provide a link to the Creative Commons licence, and indicate if changes were made. The images or other third party material in this article are included in the article's Creative Commons licence, unless indicated otherwise in a credit line to the material. If material is not included in the article's Creative Commons licence and your intended use is not permitted by statutory regulation or exceeds the permitted use, you will need to obtain permission directly from the copyright holder. To view a copy of this licence, visit <http://creativecommons.org/licenses/by/4.0/>.

## References

1. Stuart G, Spruston N, Sakmann B, Häusser M. Action potential initiation and backpropagation in neurons of the mammalian CNS. *Trends Neurosci* 1997, 20: 125–131.
2. Häusser M, Stuart G, Racca C, Sakmann B. Axonal initiation and active dendritic propagation of action potentials in substantia nigra neurons. *Neuron* 1995, 15: 637–647.
3. Bischofberger J, Jonas P. Action potential propagation into the presynaptic dendrites of rat mitral cells. *J Physiol* 1997, 504(Pt 2): 359–365.
4. Chen WR, Midtgaard J, Shepherd GM. Forward and backward propagation of dendritic impulses and their synaptic control in mitral cells. *Science* 1997, 278: 463–467.
5. Martina M, Vida I, Jonas P. Distal initiation and active propagation of action potentials in interneuron dendrites. *Science* 2000, 287: 295–300.
6. Stuart GJ, Sakmann B. Active propagation of somatic action potentials into neocortical pyramidal cell dendrites. *Nature* 1994, 367: 69–72.
7. Helmchen F, Svoboda K, Denk W, Tank DW. *In vivo* dendritic calcium dynamics in deep-layer cortical pyramidal neurons. *Nat Neurosci* 1999, 2: 989–996.
8. Svoboda K, Denk W, Kleinfeld D, Tank DW. *In vivo* dendritic calcium dynamics in neocortical pyramidal neurons. *Nature* 1997, 385: 161–165.
9. Svoboda K, Helmchen F, Denk W, Tank DW. Spread of dendritic excitation in layer 2/3 pyramidal neurons in rat barrel cortex *in vivo*. *Nat Neurosci* 1999, 2: 65–73.
10. Buzsáki G, Kandel A. Somadendritic backpropagation of action potentials in cortical pyramidal cells of the awake rat. *J Neurophysiol* 1998, 79: 1587–1591.
11. Bi GQ, Poo MM. Synaptic modifications in cultured hippocampal neurons: Dependence on spike timing, synaptic strength, and postsynaptic cell type. *J Neurosci* 1998, 18: 10464–10472.
12. Magee JC, Johnston D. A synaptically controlled, associative signal for Hebbian plasticity in hippocampal neurons. *Science* 1997, 275: 209–213.
13. Markram H, Lübke J, Frotscher M, Sakmann B. Regulation of synaptic efficacy by coincidence of postsynaptic APs and EPSPs. *Science* 1997, 275: 213–215.
14. Sjöström PJ, Häusser M. A cooperative switch determines the sign of synaptic plasticity in distal dendrites of neocortical pyramidal neurons. *Neuron* 2006, 51: 227–238.
15. Johnston D, Magee JC, Colbert CM, Christie BR. Active properties of neuronal dendrites. *Annu Rev Neurosci* 1996, 19: 165–186.
16. Linden DJ. The return of the spike: Postsynaptic action potentials and the induction of LTP and LTD. *Neuron* 1999, 22: 661–666.
17. Krueppel R, Remy S, Beck H. Dendritic integration in hippocampal dentate granule cells. *Neuron* 2011, 71: 512–528.
18. Stuart G, Schiller J, Sakmann B. Action potential initiation and propagation in rat neocortical pyramidal neurons. *J Physiol* 1997, 505(Pt 3): 617–632.

19. Antic SD. Action potentials in basal and oblique dendrites of rat neocortical pyramidal neurons. *J Physiol* 2003, 550: 35–50.
20. Nevian T, Larkum ME, Polsky A, Schiller J. Properties of basal dendrites of layer 5 pyramidal neurons: A direct patch-clamp recording study. *Nat Neurosci* 2007, 10: 206–214.
21. Tang Y, Li L, Sun L, Yu J, Hu Z, Lian K. *In Vivo* two-photon calcium imaging in dendrites of rabies virus-labeled V1 corticothalamic neurons. *Neurosci Bull* 2020, 36: 545–553.
22. Piatkevich KD, Bensussen S, Tseng HA, Shroff SN, Lopez-Huerta VG, Park D, *et al.* Population imaging of neural activity in awake behaving mice. *Nature* 2019, 574: 413–417.
23. Hochbaum DR, Zhao Y, Farhi SL, Klapoetke N, Werley CA, Kapoor V, *et al.* All-optical electrophysiology in mammalian neurons using engineered microbial rhodopsins. *Nat Methods* 2014, 11: 825–833.
24. Sun Z, Wang B, Chen C, Li C, Zhang Y. 5-HT<sub>6</sub>R null mutation induces synaptic and cognitive defects. *Aging Cell* 2021, 20: e13369.
25. Schindelin J, Arganda-Carreras I, Frise E, Kaynig V, Longair M, Pietzsch T, *et al.* Fiji: An open-source platform for biological-image analysis. *Nat Methods* 2012, 9: 676–682.
26. Saraga F, Wu CP, Zhang L, Skinner FK. Active dendrites and spike propagation in multi-compartment models of oriens-lacunosum/moleculare hippocampal interneurons. *J Physiol* 2003, 552: 673–689.
27. Mainen Z, Sejnowski T. Modeling active dendritic processes in pyramidal neurons. *Methods Neuronal Modeling* 1998: 171–209.
28. Mainen ZF, Joerges J, Huguenard JR, Sejnowski TJ. A model of spike initiation in neocortical pyramidal neurons. *Neuron* 1995, 15: 1427–1439.
29. Kim S, Guzman SJ, Hu H, Jonas P. Active dendrites support efficient initiation of dendritic spikes in hippocampal CA3 pyramidal neurons. *Nat Neurosci* 2012, 15: 600–606.
30. McCormick DA, Huguenard JR. A model of the electrophysiological properties of thalamocortical relay neurons. *J Neurophysiol* 1992, 68: 1384–1400.
31. Hu W, Tian C, Li T, Yang M, Hou H, Shu Y. Distinct contributions of Nav1.6 and Nav1.2 in action potential initiation and backpropagation. *Nat Neurosci* 2009, 12: 996–1002.
32. Mainen ZF, Sejnowski TJ. Influence of dendritic structure on firing pattern in model neocortical neurons. *Nature* 1996, 382: 363–366.
33. Goldstein SS, Rall W. Changes of action potential shape and velocity for changing core conductor geometry. *Biophys J* 1974, 14: 731–757.
34. Rall W. Theory of physiological properties of dendrites. *Ann N Y Acad Sci* 1962, 96: 1071–1092.
35. Kwon T, Sakamoto M, Peterka DS, Yuste R. Attenuation of synaptic potentials in dendritic spines. *Cell Rep* 2017, 20: 1100–1110.
36. Golding NL, Kath WL, Spruston N. Dichotomy of action-potential backpropagation in CA1 pyramidal neuron dendrites. *J Neurophysiol* 2001, 86: 2998–3010.
37. Spruston N, Schiller Y, Stuart G, Sakmann B. Activity-dependent action potential invasion and calcium influx into hippocampal CA1 dendrites. *Science* 1995, 268: 297–300.
38. Manor Y, Koch C, Segev I. Effect of geometrical irregularities on propagation delay in axonal trees. *Biophys J* 1991, 60: 1424–1437.
39. Parnas I, Segev I. A mathematical model for conduction of action potentials along bifurcating axons. *J Physiol* 1979, 295: 323–343.
40. Fujishima K, Horie R, Mochizuki A, Kengaku M. Principles of branch dynamics governing shape characteristics of cerebellar Purkinje cell dendrites. *Development* 2012, 139: 3442–3455.
41. Dotti CG, Sullivan CA, Banker GA. The establishment of polarity by hippocampal neurons in culture. *J Neurosci* 1988, 8: 1454–1468.
42. Tahirovic S, Bradke F. Neuronal polarity. *Cold Spring Harb Perspect Biol* 2009, 1: a001644.
43. Larkum ME, Zhu JJ. Signaling of layer 1 and whisker-evoked Ca<sup>2+</sup> and Na<sup>+</sup> action potentials in distal and terminal dendrites of rat neocortical pyramidal neurons *in vitro* and *in vivo*. *J Neurosci* 2002, 22: 6991–7005.
44. Larkum ME, Zhu JJ, Sakmann B. A new cellular mechanism for coupling inputs arriving at different cortical layers. *Nature* 1999, 398: 338–341.
45. Schaefer AT, Larkum ME, Sakmann B, Roth A. Coincidence detection in pyramidal neurons is tuned by their dendritic branching pattern. *J Neurophysiol* 2003, 89: 3143–3154.
46. Stuart GJ, Häusser M. Dendritic coincidence detection of EPSPs and action potentials. *Nat Neurosci* 2001, 4: 63–71.
47. Lowe G. Inhibition of backpropagating action potentials in mitral cell secondary dendrites. *J Neurophysiol* 2002, 88: 64–85.
48. Tsubokawa H, Ross WN. IPSPs modulate spike backpropagation and associated [Ca<sup>2+</sup>]<sub>i</sub> changes in the dendrites of hippocampal CA1 pyramidal neurons. *J Neurophysiol* 1996, 76: 2896–2906.
49. Xiong W, Chen WR. Dynamic gating of spike propagation in the mitral cell lateral dendrites. *Neuron* 2002, 34: 115–126.
50. Chiu CQ, Lur G, Morse TM, Carnevale NT, Ellis-Davies GC, Higley MJ. Compartmentalization of GABAergic inhibition by dendritic spines. *Science* 2013, 340: 759–762.
51. Migliore M, Hoffman DA, Magee JC, Johnston D. Role of an A-type K<sup>+</sup> conductance in the back-propagation of action potentials in the dendrites of hippocampal pyramidal neurons. *J Comput Neurosci* 1999, 7: 5–15.
52. Hoffman DA, Magee JC, Colbert CM, Johnston D. K<sup>+</sup> channel regulation of signal propagation in dendrites of hippocampal pyramidal neurons. *Nature* 1997, 387: 869–875.
53. Goldberg JH, Tamas G, Yuste R. Ca<sup>2+</sup> imaging of mouse neocortical interneurone dendrites: Ia-type K<sup>+</sup> channels control action potential backpropagation. *J Physiol* 2003, 551: 49–65.
54. Fuenzalida M, Fernández de Sevilla D, Couve A, Buño W. Role of AMPA and NMDA receptors and back-propagating action potentials in spike timing-dependent plasticity. *J Neurophysiol* 2010, 103: 47–54.
55. Caporale N, Dan Y. Spike timing-dependent plasticity: A Hebbian learning rule. *Annu Rev Neurosci* 2008, 31: 25–46.
56. Watanabe S, Hoffman DA, Migliore M, Johnston D. Dendritic K<sup>+</sup> channels contribute to spike-timing dependent long-term potentiation in hippocampal pyramidal neurons. *Proc Natl Acad Sci U S A* 2002, 99: 8366–8371.
57. Froemke RC, Tsay IA, Raad M, Long JD, Dan Y. Contribution of individual spikes in burst-induced long-term synaptic modification. *J Neurophysiol* 2006, 95: 1620–1629.

# Anti-Seizure and Neuronal Protective Effects of Irisin in Kainic Acid-Induced Chronic Epilepsy Model with Spontaneous Seizures

Jie Yu<sup>1</sup> · Yao Cheng<sup>1</sup> · Yaru Cui<sup>1</sup> · Yujie Zhai<sup>1</sup> · Wenshen Zhang<sup>2</sup> · Mengdi Zhang<sup>1</sup> · Wenyu Xin<sup>1</sup> · Jia Liang<sup>1</sup> · Xiaohong Pan<sup>1</sup> · Qiaoyun Wang<sup>1</sup> · Hongliu Sun<sup>1</sup>

Received: 26 August 2021 / Accepted: 19 April 2022 / Published online: 12 July 2022

© Center for Excellence in Brain Science and Intelligence Technology, Chinese Academy of Sciences 2022

**Abstract** An increased level of reactive oxygen species is a key factor in neuronal apoptosis and epileptic seizures. Irisin reportedly attenuates the apoptosis and injury induced by oxidative stress. Therefore, we evaluated the effects of exogenous irisin in a kainic acid (KA)-induced chronic spontaneous epilepsy rat model. The results indicated that exogenous irisin significantly attenuated the KA-induced neuronal injury, learning and memory defects, and seizures. Irisin treatment also increased the levels of brain-derived neurotrophic factor (BDNF) and uncoupling protein 2 (UCP2), which were initially reduced following KA administration. Furthermore, the specific inhibitor of UCP2 (genipin) was administered to evaluate the possible protective mechanism of irisin. The reduced apoptosis, neurodegeneration, and spontaneous seizures in rats treated with irisin were significantly reversed by genipin administration. Our findings indicated that neuronal injury in KA-induced chronic epilepsy might be related to reduced levels of BDNF and UCP2. Moreover, our results confirmed the inhibition of neuronal injury and epileptic seizures by exogenous irisin.

The protective effects of irisin may be mediated through the BDNF-mediated UCP2 level. Our results thus highlight irisin as a valuable therapeutic strategy against neuronal injury and epileptic seizures.

**Keywords** Epilepsy · Seizure · Irisin · Genipin · Neuronal injury

## Introduction

Epilepsy is a nervous system disorder that can induce persistent brain injury with serious pathological and psychological consequences [1, 2]. At present, ~50 million people suffer from epilepsy in the world, with an estimated 4–10 per thousand in the general population suffering from active epilepsy [3–5]. Epilepsy is a common chronic disease that affects people across different age groups [6, 7]. To date, the clinical management of epilepsy involves drug therapy, but drug resistance and adverse effects are critical issues that warrant attention [8, 9]. The limitations of drug-based therapy are closely related to the complex and unclear mechanisms underlying epilepsy. Further studies are warranted to better understand the mechanisms underlying the disease and to explore new and effective treatment options.

Increased production of reactive oxygen species (ROS) is an important mechanism in neuronal apoptosis and epileptic seizures [10, 11]. During a seizure, the increase of ROS results in the death of neurons and serious neurological damage [12, 13]. Furthermore, mitochondrial function has been shown to be closely associated with the production of ROS [14–16]. Mitochondria are the main site of ROS accumulation during a seizure and play a significant role in neuronal excitability [17]. Mitochondrial dysfunction and oxidative stress-induced injury are clear

Jie Yu, Yao Cheng, and Yaru Cui have contributed equally to this work.

**Supplementary Information** The online version contains supplementary material available at <https://doi.org/10.1007/s12264-022-00914-w>.

✉ Qiaoyun Wang  
byylwqy@163.com

✉ Hongliu Sun  
sun\_china6@163.com; sunhongliu@bzmc.edu.cn

<sup>1</sup> School of Pharmaceutical Sciences, Binzhou Medical University, Yantai 264003, China

<sup>2</sup> The Sixth Scientific Research Department, Shandong Institute of Nonmetallic Materials, Jinan 250031, China

pathological changes in epilepsy [18]. Active oxygen production associated with mitochondrial dysfunction may affect the occurrence of epilepsy and inhibiting ROS can lead to attenuated seizures [19, 20].

Irisin has been confirmed to reduce the level of ROS as well as mitochondria-dependent apoptosis and injury caused by ischemia/reperfusion [21, 22]. Irisin is a glycosylated protein mainly secreted by skeletal muscle; its expression increases with exercise [23]. Within 30 min of rapid exercise, the irisin level increases in the circulation, which promotes glycolytic degradation and lipolysis in skeletal muscle [24]. Irisin is widely distributed across tissues, including the brain [25]. The cell-protective roles of irisin have garnered increasing attention over recent years [22, 26, 27]. According to Chen *et al.*, irisin participates in mitochondrial biogenic functional activity and oxidative metabolism when the lung is injured by ischemia/reperfusion [21, 22]. Further, irisin reduces ROS production and mitochondria-dependent apoptosis, reducing the cellular injury caused by ischemia/reperfusion [21, 22]. In addition, Wang *et al.* [28] found that irisin reduces the area of cardiac infarction and improves heart function after ischemia by protecting mitochondrial function *via* the inhibition of both mitochondrial permeability transition pore opening and mitochondrial swelling [29]. Moreover, irisin can reduce apoptosis by decreasing the level of active caspase-3 and poly ADP-ribose polymerase, and by increasing the expression of superoxide dismutase and the phosphorylation of p38 [30].

Irisin is a type I membrane protein with 112 amino-acids and a molecular weight of 12 kDa [31]. It is formed after the hydrolyzation of fibronectin domain-containing protein 5 (FNDC5). Under the action of peroxisome proliferator-activated receptor  $\gamma$  coactivator 1 $\alpha$ , FNDC5 is hydrolyzed in the amino-acid sites 30 and 142 to produce irisin [32, 33]. Exercise induces FNDC5 gene expression in skeletal muscle, thus increasing the concentration of irisin in the circulation [34, 35]. and it further induces brain-derived neurotrophic factor (BDNF) expression through the newly-produced irisin. Activation of the FNDC5/irisin/BDNF signaling pathway has been confirmed in the hippocampus through endurance exercise [34, 35]. BDNF is a neurotrophic factor primarily expressed in the central nervous system (CNS) [36, 37]; it promotes neuronal cell survival, differentiation, migration, dendrite growth, synaptogenesis, and synaptic plasticity [38]. Meanwhile, the level of BDNF is closely associated with epileptogenesis and seizures [39]. The expression of BDNF is significantly reduced in FNDC5<sup>-/-</sup> mice [21]. FNDC5 injection, without exercise, increases BDNF gene expression and promotes the growth and survival of brain neurons in mice [40]. Altogether, these results indicate a potential protective role of the FNDC5/irisin/BDNF pathway.

BDNF further promotes the expression of uncoupling proteins (UCPs) [41], which belong to the mitochondrial inner membrane protein family. The UCP family includes five members, which display different distributions and functions. UCP1 is expressed in brown adipose tissue and is responsible for heat production [42]. UCP2, which is expressed in the CNS [43], has been shown to have significant neuroprotective effects [43, 44]. UCP2 reduces mitochondria-mediated ROS production through uncoupling, increases ATP levels, reduces mitochondrial damage caused by free radicals, and helps neuronal cells to consume energy produced by cells and free radicals [45]. Elevated UCP2 levels reduce the seizure-induced death of excitotoxic cells and combat pathological changes in neurodegenerative disorders such as epilepsy and Alzheimer's disease [46]. Altogether, UCP2 emerges as a potentially important contributor to the protective effects regulated by BDNF.

We thus hypothesized that irisin may play neuro-protective and anti-epileptic roles by reducing oxidative stress through BDNF-mediated UCP2 levels. In this study, we investigated the expression of BDNF and UCP2, as well as the levels of oxidative stress and neuronal injury in kainic acid (KA)-induced epilepsy. Furthermore, exogenous irisin treatment and genipin (UCP2 inhibitor) treatment were administered to confirm the protective effects and possible mechanisms of irisin.

## Materials and Methods

### Animals and Surgery

Male Sprague-Dawley rats (8 weeks old; Pengyue Experimental Animal Center, No. SCXK 2017-0002, Jinan, China) weighing 280–310 g were used in experiments. The animals were allowed food and water *ad libitum*. All the experiments complied with the National Institutes of Health Guidelines for the Care and Use of Laboratory Animals (National Institutes of Health Publication No. 80-23, 1996 Revision) and with the Animal Ethics Regulations of the Experimental Animal Center of Binzhou Medical College (approval No. 2017003). All efforts were made to reduce the number of animals used and minimize pain to these animals.

The rats were anaesthetized with sodium pentobarbital (50 mg/kg, *i.p.*; CAS, 57-33-0, Xiya Reagent, China) and fixed in a stereotaxic apparatus (Anhui Zheng Hua Biological Instrument Equipment Co., Ltd., China). A stainless-steel cannula (RSD Life Science, China) was implanted into the left lateral ventricle [anteroposterior (AP): −1.0 mm; lateral (L): 1.8 mm; and ventral (V): −3.6 mm] and the hippocampal CA3 region (AP: −5.3 mm; L: −5 mm; V: −6 mm) of each rat. The recording electrode stripped of insulation (0.5 mm of each tip) was implanted into the right cortex



(AP: −3.2 mm; L: 3.0 mm; and V: −1.8 mm) for electroencephalogram (EEG) recording using the PowerLab system (AD Instruments, Sydney, NSW, Australia). The implanted electrode was connected to a microelectrode socket, which was bonded to the skull with dental cement (Shanghai Zhangjiang Biological Materials Co., Ltd., China). The rats recovered within 7 days after operation.

### Drug Treatment and Seizure Recording

The KA-induced chronic epilepsy model with spontaneous seizures was used. KA (2 µg/µL,  $1.33 \times 10^{-3}$  mg/kg; CAS: 58002-62-3; Sigma, USA) was injected into the hippocampal CA3 region through the implanted cannula 7 days after operation. The rats in the control group were treated with saline instead of KA. In the Irisin+KA group, irisin (3 µg/µL and 50 µg/kg, Xingbao Biotechnology Co., Ltd, China) was delivered into the lateral ventricle 30 min before KA injection through the implanted cannula, and was injected once every three days up to day 15 according to previous studies [47, 48] and our pilot experiments. The Saline+KA group was treated with saline instead of irisin. To evaluate the effects of irisin and guarantee the rigor of our experiment, a control group and an irisin group were added ( $n = 10/\text{group}$ ), and the method of irisin administration was as above.

Genipin (0.5 µg/µL and 8.25 µg/kg, CAS, 6902-77-8, Aladdin, China), the specific inhibitor of UCP2 [46], was delivered into the lateral ventricle 30 min before irisin administration (60 min before KA injection) through a stainless-steel cannula. Genipin and irisin were injected once every three days up to day 15, while the Saline+Irisin+KA group was treated with saline instead of genipin. The details of pharmacological administration are shown in Fig. S1. A total of 289 rats were used in this study, 5 rats in the Saline+KA group died due to severe seizures.

From day 30 after KA administration, spontaneous seizure behavior was observed, and EEGs were recorded for three consecutive days every 10 days, for example on days 30, 31, and 32, then days 40, 41, and 42..., until days 170, 171, and 172. Each rat was placed in a transparent resin observation box (50 cm × 30 cm) and recorded for three consecutive days at each observation time point. EEGs were digitized using filters (1 Hz low-pass and 50 Hz high-pass; PowerLab Biological Recording System, AD Instruments, Australia). The frequency spectrum and the power spectral density of EEGs were analyzed using the PowerLab Biological Recording System (AD Instruments). According to Racine's criteria [49], epileptic behavior was classified into stages 1 to 5. Stages 1–3 indicated focal seizures, with symptoms including squinting, continuous chewing, head-shaking, and unilateral forelimb lifting. Stages 4–5 indicated generalized seizures, including bilateral forelimb lifting, wet

dog-like shaking, generalized convulsions, and prostration. An electroclinical seizure was defined as polyspike discharges >5 Hz, >2 times baseline EEG amplitude lasting >3 s [50].

### Immunohistochemistry

As in our previous report [51], at the 24 h, and days 3, 15, and 170 time points after KA administration, 5 rats in each group were anesthetized with sodium pentobarbital (50 mg/kg, i.p.; CAS, 57-33-0, Xiya Reagent, China), perfused through the heart with 250 mL saline for 20–30 min until the liver became white, and then perfused with 250 mL of 4% paraformaldehyde. The brain was removed and immersed in 4% paraformaldehyde for 24 h followed by 30% sucrose. When the brain sank to the bottom, it was cut at ~2.3 mm to ~5 mm from posterior to the bregma (The Rat Brain in Stereotaxic Coordinates, Third Edition) into 12-µm sections on a cryomicrotome (CM1850, Leica, Germany). The sections were washed with 0.01 mol/L phosphate-buffered saline (PBS) and incubated at 37°C for 1 h with 10% bovine serum albumin. After blocking, 50 µL of the primary antibody mouse monoclonal anti-mouse BDNF (1:200, Abcam, ab205067) was added to each section, which were washed three times with 0.01 mol/L PBS and then kept overnight at 4°C. Fluorescein isothiocyanate goat anti-rabbit IgG (50 µL; FITC, 1:200, A0562, Beyotime, China) was added to each section, which were then incubated at 37 °C for 1 h. After three washes, 50 µL of DAPI (C1005, Beyotime, China) per section was added and the sections were incubated at 20 °C for 15 min. After washing with 0.01 mol/L PBS, each section was sealed with a coverslip. The fluorescence intensity of brain sub-regions was assessed by confocal microscopy (LSM 880, Zeiss, Germany). All samples were repeated three times and averaged under the same conditions. The images were observed and acquired at the same brightness level. Fluorescence intensity was analyzed using ImageJ 1.37 (National Institutes of Health, Bethesda, USA).

### Fluoro-Jade B Staining

Fluoro-Jade B (FJB) is a fluorescein derivative dye that specifically binds to degenerating neurons [51–53]. Slides with adherent brain tissue were immersed in 1% NaOH/80% ethanol for 5 min and in 70% ethanol for 2 min [52, 53]. The following steps were followed: the slides were rinsed with distilled water for 2 min; wiped and immersed in 0.06% potassium permanganate for 15 min to maintain a constant background; and rinsed with distilled water for 2 min. A 0.0004% FJB staining solution was prepared with 4 mL of 0.01% FJB stock solution (AG310-30MG; Millipore, Burlington, MA, USA) and 96 mL of 0.1% glacial acetic acid. The slides were incubated in the 0.0004% FJB staining

solution for 20 min in the dark, rinsed with distilled water for 1 min, dried at 50°C for 10 min, cleared in xylene for 10 min, and sealed with neutral resin. The slides were observed under a fluorescence microscope (Olympus, IX73, Japan) with blue (450 nm) excitation light. FJB-positive signals were manually counted for analysis.

### Oxidative Stress Detection

2',7'-dichlorofluorescein (DCF) level changes were measured in each group to assess the level of oxidative stress, as described in our previous studies [53, 54]. Briefly, after KA treatment, 5 rats in each group were sacrificed at two time points (24 h and 3 days) after anesthesia. The brains were quickly extracted, and the cortices and hippocampi were separated on ice, then filtered into single-cell suspensions with 0.01 mol/L PBS (10 µL/mg). 250 µL from each sample was added to 500 µL of DCF diacetate (10 µmol/L, Beyotime, S0033, China) and incubated at 37°C for 40 min without light [53]. Centrifugation was repeated to remove the supernatant and wash the cells. Using excitation at 488 nm and emission at 525 nm, fluorescence intensity was measured in each group using a fluorescence microplate reader (Thermo, USA) [52]. The DCF levels are presented as ratios relative to the values measured in the control group.

### Evaluation of Mitochondrial Reactive Oxygen Species by Mito-SOX Fluorescence and Flow Cytometry

As in our previous studies [52, 53], following KA treatment, 5 rats from each group were sacrificed after anesthesia at 24 h and 3 days. Their brains were quickly extracted, and the cortices and hippocampi were separated. Mitochondrial ROS were detected using Mito-SOX™ (M36008, Thermo Fisher, USA). Similar to the method of DCF assessment, after immersion in 0.01 mol/L PBS, single-cell suspensions of cortices and hippocampi were separately prepared. 1 mL of 5 µmol/L Mito-SOX working solution was added to each cell suspension for incubation in the dark in a 37°C cell incubator for 10 min [54]. After washing, fluorescence intensity was measured at 510 nm excitation and 580 nm emission, using a fluorescence microplate reader (Thermo, USA) and flow cytometer (Becton, Dickinson and Co., USA).

### Learning and Memory Tests

As previously described [54], the Morris water maze (ZS-001, Beijing Zhongshi Di Chuang Technology Development Co., Ltd, China) was used to evaluate the learning and memory of rats on day 170 after KA administration [55]. These experiments consisted of two parts: positioning navigation and spatial exploration [56]. Before the experiment, each rat was placed in the pool to swim freely for 2 min to familiarize with the

environment. In the 4-day positioning navigation experiment, each rat was returned to the pool wall in any quadrant, and the time needed to find the platform was recorded. The space exploration experiment was carried out on day 5 [57]. The platform was removed, each rat was allowed to swim freely for 60 s, and the number of crossings was recorded. All rats performed the above tasks. The evaluation was latency to the platform, number of times through the platform, and time spent in the target quadrant and in the contralateral quadrant [58].

Simultaneously, the novel object recognition (NOR) test was applied at day 30 ( $n = 10/\text{group}$ ). NOR is a common means of assessment of memory in rodent models such as rats [59]. This experiment was divided into three periods: adaptive, training, and testing periods [60]. The rats were handled gently daily for 2 days before the experiment in order to familiarize them to the testers [61]. In the habituation period, rats were allowed move freely for 10 min in the apparatus (50 cm × 60 cm × 60 cm box and no object was present). During the training period, two identical, firm and scentless objects A and B were placed equidistant away from the side walls. The rats were placed in the box equidistant from and facing away from the objects, and the duration of exploring the objects was recorded. After 14–16 h from the training session [62], object A was replaced with a new object C, which had a different color and shape from the previous two, and the rats were put in the box as in the training session. The duration of testing was 5 min. Finally, the learning and memory was evaluated by measuring the time spent on exploring the new object and by calculating the identification index (Identification index = Time exploring new object/Total time exploring both objects) [60]. The experimental environment was always quiet and kept at the same light intensity. Rats that were born with abnormal horizontal or vertical movements were excluded.

### Western Blotting

For western blotting, the brain was micro-dissected into cortex and hippocampus on ice. After treatment with RIPA lysis buffer (Meilunbio, MA0151) and PMSF (Beyotime, ST506), 10 µL lysis buffer per mg of brain tissue was added. The tissue was then sonicated on ice and the protein concentration was determined using the BCA Protein Kit (P0012; Beyotime, China). The proteins from tissue samples were separated on 12% sodium dodecyl sulfate polyacrylamide gels and electro-transferred. After blocking with 5% skim milk for 3 h, the membranes were incubated with mouse monoclonal antibodies against BDNF (1:1000, ab205067, Abcam, UK), anti-rabbit UCP2 (1:2000, ab97931, Abcam, UK), anti-rabbit caspase-3 (1:1000, 9662, Cell Signaling Technology, USA), anti-rabbit activated caspase-3 (1:1000, ab2302, Abcam, UK), or glyceraldehyde-3-phosphate dehydrogenase (GAPDH, 1:1000, AB-P-R 001, Kangchen, China) at 4°C overnight. The bands

were incubated with horseradish peroxidase-conjugated IgG secondary antibodies. Images were acquired from different gels under the same electrophoresis conditions using an image analyzer (Odyssey, LI-COR Biosciences, USA). The results were the gray values of the target strips compared to the GAPDH band.

## Statistical Analysis

The sample size was estimated based on our preliminary experiments and balanced one-way analysis of variance (ANOVA). All the data are shown as the mean  $\pm$  SEM. Statistical analyses were carried out with SPSS 25.0 (IBM, USA). The cumulative number and duration in stages 1–3 between the Saline+KA and Irisin+KA groups were analyzed using the nonparametric Mann-Whitney U test. Cumulative seizure duration and latency to platform were analyzed by two-way ANOVA for repeated measures. The other parameters were analyzed by one-way ANOVA followed by a Dunnett's T3 *post-hoc* test. For all analyses, differences were considered significant at  $P < 0.05$ .

## Results

### Irisin Treatment has No Significant Toxic Side-effects

On day 30 after KA treatment, the heart, liver, spleen, lung, and kidney from rats treated with irisin were stained with hematoxylin-eosin (HE), and their weight and hair were assessed for 30 days ( $n = 8$ /group). Likewise, the novel object recognition test (day 30,  $n = 10$ /group), oxidative stress (24 h,  $n = 5$ /group), FJB staining (24 h,  $n = 5$ /group), and western blotting (24 h,  $n = 5$ /group) were also performed. The results of HE analogously showed no significant lesions in the organizational structure of the heart, liver, spleen, lung, and kidney (Fig. S4A), as well as no significant changes in body weight or hair color and texture due to irisin treatment (Fig. S4D). Meanwhile, the levels of caspase-3 increased slightly (cortex,  $P = 0.041$ ; hippocampus,  $P = 0.045$ ; Fig. S3A, B), accompanied by slightly decreased levels of activated caspase-3 (cortex,  $P = 0.018$ ; hippocampus,  $P = 0.033$ ; Fig. S3A, C), neuronal injury (CA2,  $P = 0.032$ ; EC,  $P = 0.025$ ; Fig. S3D, E), and oxidative stress (Fig. S3F, G) in irisin-treated rats compared to controls. Therefore, these results confirmed that no significant toxic side-effects occur after irisin treatment.

### Exogenous Irisin Treatment Attenuates KA-induced Spontaneous Seizures

The spontaneous seizure behavior and EEGs were recorded in each group up to day 170 after KA treatment. In the

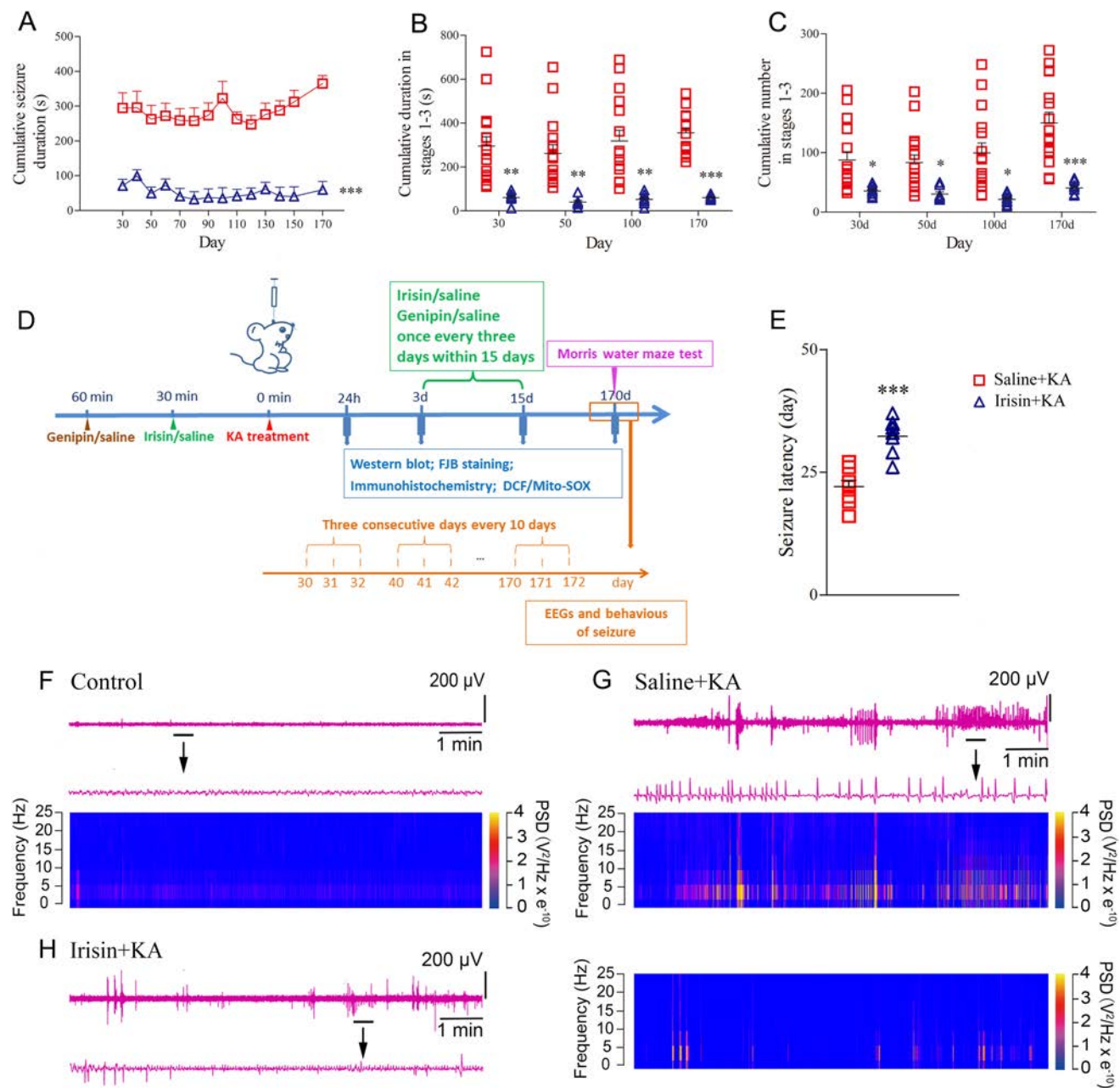
Irisin+KA group ( $n = 8$ ), the cumulative seizure duration was significantly shorter than that in the Saline+KA group ( $n = 16$ ) at all time points from day 30 to day 170 ( $P < 0.001$ ; Fig. 1A). Because the spontaneous seizures corresponded mainly to stages 1–3, the cumulative seizure number and the duration in these stages were further analyzed in each group. The results showed that irisin-treated rats had fewer seizures of shorter duration than rats treated with saline (Saline+KA; Fig. 1B, C). For example, on day 170, the cumulative duration ( $60.56 \pm 3.36$  s) and the number of stage 1–3 seizures ( $40.64 \pm 3.86$ ) in the Irisin+KA group were significantly lower than those in the Saline+KA group ( $359.30 \pm 28.94$  s,  $P < 0.001$ , Fig. 1B;  $150.23 \pm 17.70$ ,  $P < 0.001$ ; Fig. 1C). Representative EEGs and their power spectra analyses are presented in Fig. 1F–H. In addition, irisin treatment resulted in a longer latency of spontaneous seizures (Fig. 1E). Seizure and EEG results showed that exogenous irisin has a significant inhibitory effect on KA-induced chronic epileptic seizures. The detailed pharmacological manipulations and animal groups are presented in Fig. 1D.

### Effect of Irisin Treatment on the KA-induced Learning and Memory Defect

The differences in learning and memory after KA administration were evaluated with the water maze test. The results showed that the latency to reach the platform was significantly prolonged in KA-treated rats ( $n = 12$ ) compared with control rats treated with saline ( $n = 10$ ,  $P < 0.001$ , Fig. 2A). Moreover, KA-treated rats displayed a reduced target quadrant time ( $P = 0.005$ , Fig. 2B), longer opposite quadrant time ( $P < 0.001$ , Fig. 2C), and reduced target zone frequency ( $P = 0.005$ , Fig. 2D). Irisin treatment partly reversed the KA-induced learning and memory defect. In rats treated with irisin ( $n = 8$ ), the latency to reach the platform ( $P < 0.001$ , Fig. 2A) and the time spent in the opposite quadrant ( $P = 0.001$ , Fig. 2C) were significantly shorter. Moreover, the time spent in the target quadrant ( $P = 0.008$ , Fig. 2B) and frequency of crossing the target zone ( $P = 0.035$ , Fig. 2D) significantly increased. Representative tracks of rats from each group searching for the platform are shown in Fig. 2E.

In addition, NOR testing showed that the identification index was lower in the Saline+KA group ( $n = 10$ ;  $P < 0.001$ , Fig. 3K, L) than in controls. However, the rats had a higher identification index due to irisin administration ( $n = 10$ , Irisin+KA group;  $P < 0.001$ , Fig. 3L). Our results suggested that irisin treatment partly reverses the learning and memory impairment in KA-induced epilepsy.





**Fig. 1** Exogenous irisin treatment attenuates KA-induced spontaneous seizure severity and the learning and memory defect in rats. **A** Cumulative seizure duration of stage 1–5 seizures in each group from day 30 to day 170 following KA injection (Saline+KA group,  $n = 16$ ; Irisin+KA group,  $n = 8$ ). **B** Cumulative time of stage 1–3 seizures in each group. **C** Cumulative number of stage 1–3 seizures.

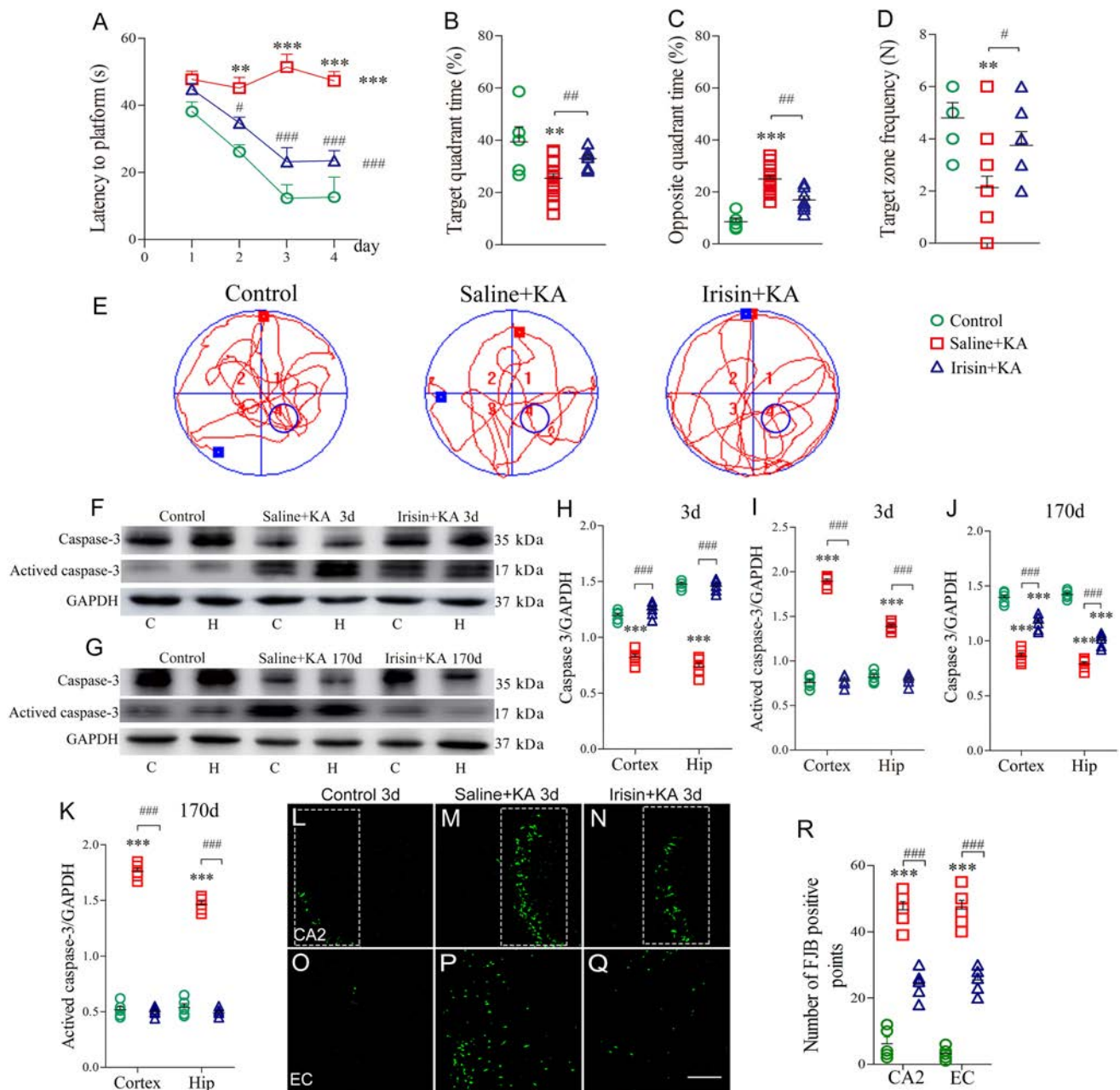
**D** Schematic of the experimental design. **E** Latency of spontaneous seizures. **F–H** Representative electroencephalograms (EEGs) and corresponding analysis of frequency spectrum and power spectrum for each group on day 170. \* $P < 0.05$ , \*\* $P < 0.01$ , \*\*\* $P < 0.001$  vs Saline+KA group. KA, kainic acid.

### Irisin Treatment Attenuates the Elevated Levels of Apoptosis and Neuronal Degeneration Induced by KA

Western blotting was used to analyze changes in the apoptosis-related proteins caspase-3 and activated caspase-3 on

days 3 and 170 after KA administration ( $n = 5$ /group) to evaluate the effects of irisin on apoptosis. The results showed that KA administration significantly increased the level of activated caspase-3 in both cortex and hippocampus (day 3, cortex,  $P < 0.001$ ; hippocampus,  $P < 0.001$ ; Fig. 2F, I; day 170, cortex,  $P < 0.001$ ; hippocampus,  $P < 0.001$ ; Fig. 2G,





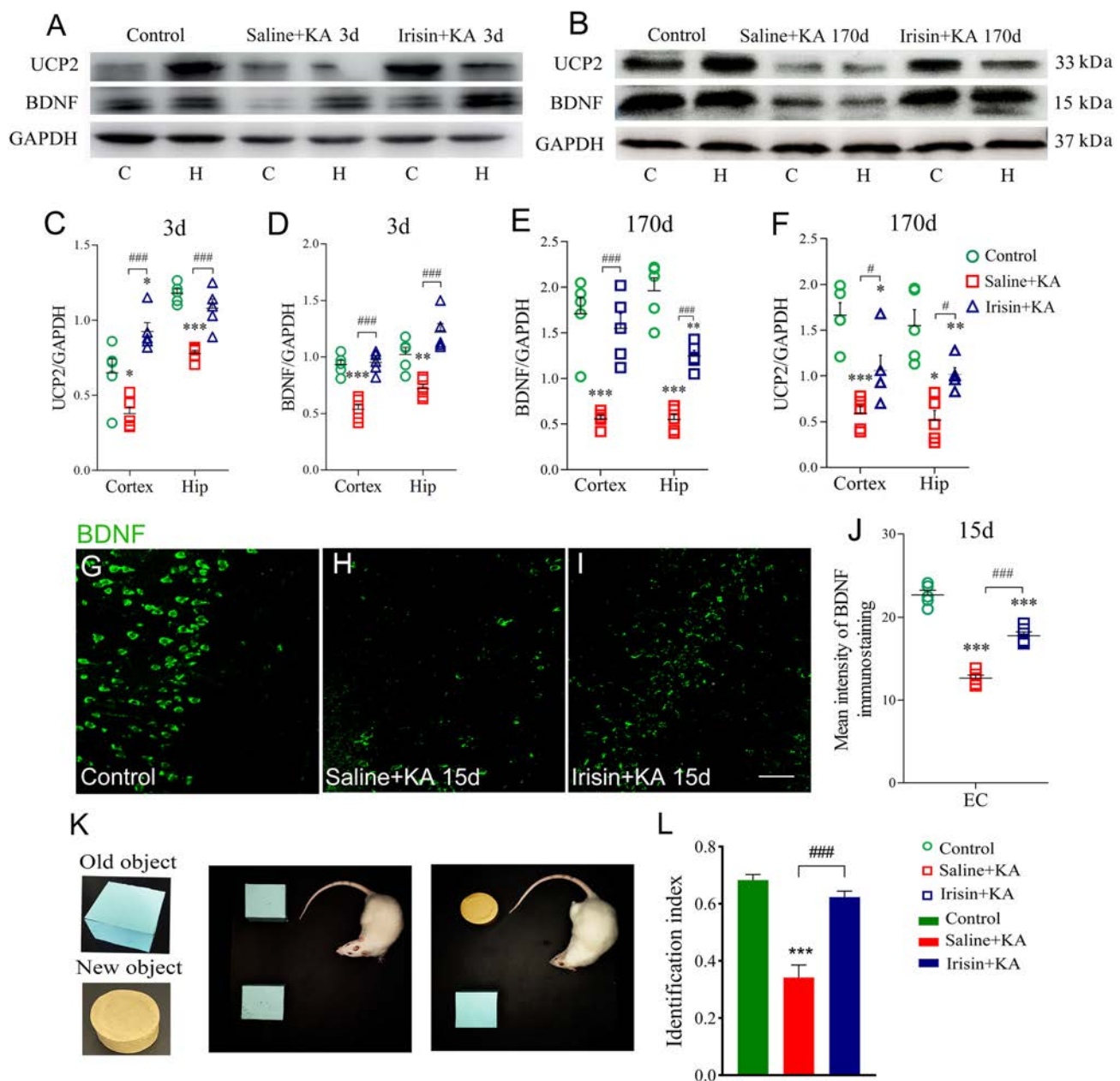
**Fig. 2** Exogenous irisin treatment attenuates the elevated levels of apoptosis and neuronal degeneration induced by KA. **A** Latency to find platform (Control group,  $n = 10$ ; Saline+KA group,  $n = 16$ ; Irisin+KA group,  $n = 8$ ). **B** Percentage of time in target quadrant. **C** Percentage of time in opposite quadrant. **D** Platform crossing times. **E** Trajectories in Morris water maze. **F, G** Immunoreactivity of caspase-3 and activated caspase-3 on days 3 and 170 after KA treat-

ment ( $n = 5$ /group). **H–K** Normalized intensity of caspase-3 and activated caspase-3 relative to GAPDH. **L–R** FJB-positive signals in CA2 and EC ( $n = 5$ /group; scale bar, 50  $\mu$ m) on day 3.  $**P < 0.01$ ,  $***P < 0.001$  vs control group;  $\#P < 0.05$ ,  $\#\#P < 0.01$ ,  $\#\#\#P < 0.001$  vs Saline+KA group (one-way ANOVA with Dunnett's T3 *post-hoc* test). KA, kainic acid; C, cortex; EC, entorhinal cortex; CA2, cornu ammonis 2; H/Hip, hippocampus; FJB, Fluoro-Jade B.

K), with a reduced caspase-3 level (Fig. 2F–H, J). However, the Irisin+KA group presented significantly lower levels of activated caspase-3 than those of the Saline+KA group (day 3, cortex,  $P < 0.001$ ; hippocampus,  $P < 0.001$ ; Fig. 2F, I; day 170, cortex,  $P < 0.001$ ; hippocampus,  $P < 0.001$ ;

Fig. 2G, K). The results supported a strong anti-apoptosis effect of irisin on KA-induced apoptosis.

FJB staining was used to further analyze the degeneration of neurons ( $n = 5$ /group). FJB-positive signals in rats were counted 24 h and 3 days following KA administration.



**Fig. 3** Exogenous irisin treatment increases BDNF and UCP2 expression in cortex and hippocampus in KA-induced epilepsy. **A, B** Expression of UCP2 and BDNF on day 3 (**A**) and day 170 (**B**) after KA treatment ( $n = 5/\text{group}$ ). **C–F** Normalized intensity of UCP2 and BDNF relative to GAPDH. **G–J** Mean fluorescence intensity of BDNF (green) ( $n = 5/\text{group}$ ; scale bar, 30  $\mu\text{m}$ ). **K, L** The novel object

recognition test (**K**) and the identification index (**L**) in each group ( $n = 10/\text{group}$ , on day 30).  $*P < 0.05$ ,  $**P < 0.01$ ,  $***P < 0.001$  vs controls;  $\#P < 0.05$ ,  $###P < 0.001$  vs each other (one-way ANOVA with Dunnett's T3 *post-hoc* test). BDNF, brain-derived neurotrophic factor; UCP2, uncoupling protein 2; C, cortex; EC, entorhinal cortex; H/Hip, hippocampus; KA, kainic acid.

Significantly increased FJB-positive signals were observed in the hippocampus (CA2,  $P < 0.001$ , Fig. 2M, R) and entorhinal cortex (EC,  $P < 0.001$ , Fig. 2P, R) on day 3 after KA administration compared with those in the control group (Fig. 2L, O, R). Irisin treatment significantly reduced the number of FJB-positive signals in both the hippocampus ( $P < 0.001$ , Fig. 2N, R) and the EC ( $P < 0.001$ , Fig. 2Q, R) compared with those

in the Saline+KA group. Similar changes in FJB signals were observed at 24 h (data not shown). The FJB staining results showed that KA induces significant neurodegeneration in the hippocampus and EC, and that irisin partly reverses this neuronal injury. Combined with the anti-apoptosis effects of irisin, the results showed a remarkable neuroprotective role of exogenous irisin treatment in KA-induced epilepsy.

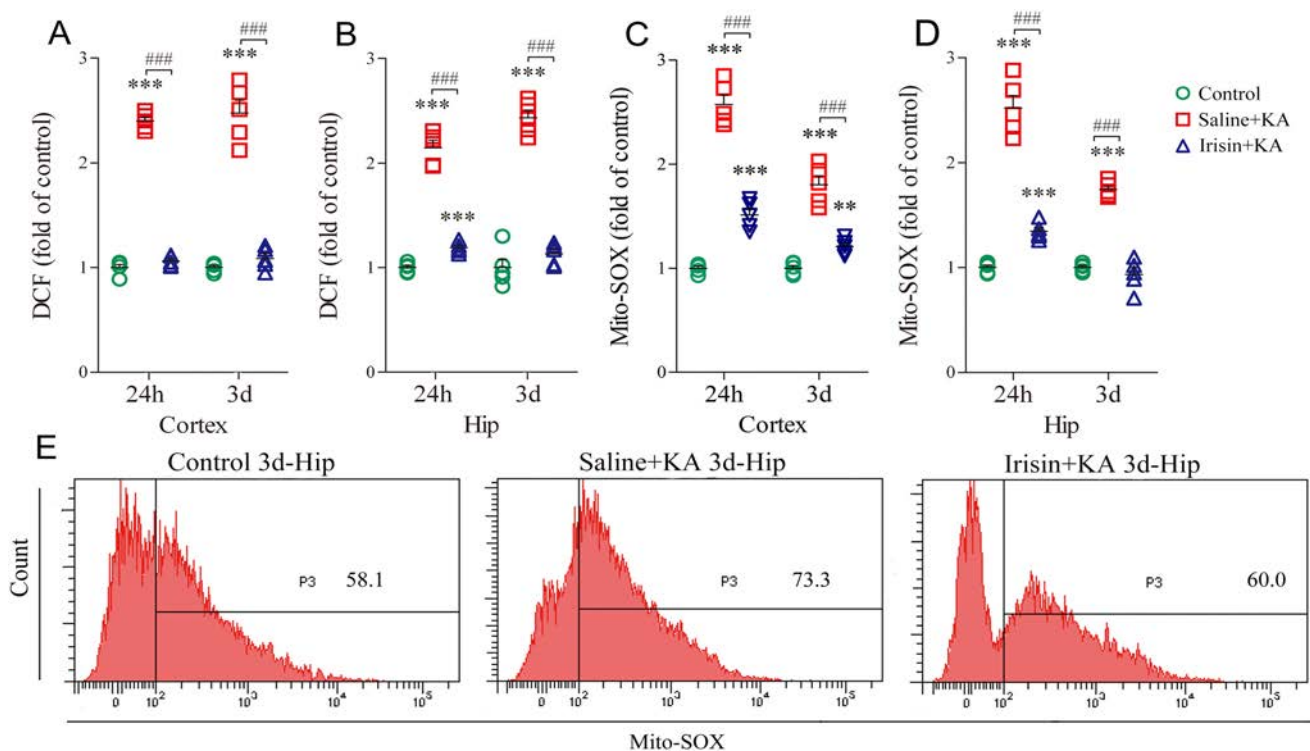
### Exogenous Irisin Treatment Increases BDNF and UCP2 Expression in the Hippocampus and Cortex in KA-Induced Epilepsy

The expression of BDNF and UCP2 in brain sub-regions was evaluated on days 3 and 170 in each group ( $n = 5/\text{group}$ ). Western blotting showed decreased BDNF and UCP2 expression in the hippocampus and cortex on both day 3 (Fig. 3A, C, D) and day 170 (Fig. 3B, E, F) following KA administration. Immunohistochemistry also showed reduced levels of BDNF after KA administration (representative images in EC are shown in Fig. 3H,  $P < 0.001$ ).

Exogenous irisin treatment significantly increased the level of BDNF as assessed by both western blotting (cortex and hippocampus, day 3, Fig. 3A, D; day 170, Fig. 3B, E) and immunohistochemistry ( $n = 5/\text{group}$ , EC, Fig. 3G–J) compared with the Saline+KA group. Synchronously, the elevated levels of UCP2 in the hippocampus and cortex were confirmed by western blots on both day 3 (Fig. 3A, C) and day 170 (Fig. 3B, F). Altogether, the results suggested that, in KA-induced chronic epilepsy, exogenous irisin treatment increases the expression of BDNF and UCP2 in the hippocampus and cortex.

### Exogenous Irisin Treatment Reduces High KA-induced DCF/Mito-SOX Levels

The levels of oxidative stress were evaluated by measuring DCF/Mito-SOX [43] in the hippocampus and cortex 24 h and 3 days after KA administration ( $n = 5/\text{group}$ ). KA administration led to a remarkable increase in the DCF level in both the cortex (Fig. 4A) and the hippocampus (Fig. 4B). Synchronously, the level of Mito-SOX was increased in the cortex (Fig. 4C) and the hippocampus (Fig. 4D) after KA administration. Conversely, in the Irisin+KA group, the DCF levels significantly decreased in the cortex (24 h,  $P < 0.001$ ; day 3,  $P < 0.001$ , Fig. 4A) and in the hippocampus (24 h,  $P < 0.001$ ; day 3,  $P < 0.001$ , Fig. 4B) compared with those in the Saline+KA group. Similarly, Mito-SOX showed decreased levels in rats treated with irisin in both the cortex (24 h,  $P < 0.001$ ; day 3,  $P < 0.001$ , Fig. 4C) and the hippocampus (24 h,  $P < 0.001$ ; day 3,  $P < 0.001$ , Fig. 4D). Representative Mito-SOX flow cytometry results for each group are shown in Fig. 4E. The results indicated that the increased levels of oxidative stress induced by KA are partly reversed by exogenous irisin treatment.



**Fig. 4** Effects of exogenous irisin treatment on oxidative stress. **A**, **B** DCF levels in cortex and hippocampus ( $n = 5/\text{group}$ ). **C**, **D** Mito-SOX levels in cortex and hippocampus ( $n = 5/\text{group}$ ). **E** Representative Mito-SOX changes as measured by flow cytometry on day

3. \*\*\* $P < 0.001$  vs controls; ### $P < 0.001$  vs each other (one-way ANOVA with Dunnett's T3 *post-hoc* test). Hip, hippocampus; KA, kainic acid; DCF, 2',7'-dichlorofluorescein.



### Genipin Administration Reverses the Increased UCP2 and Reduced DCF and Mito-SOX Levels Due to Irisin Treatment

The expression of BDNF and UCP2 in brain sub-regions was measured in each group ( $n = 5/\text{group}$ ) using western blotting on days 3 and 170 following KA administration. The results showed that their expression was significantly higher in irisin-treated rats (Saline+Irisin+KA) than in the Saline+KA group (Fig. 5A–F), while genipin administration (Genipin+Irisin+KA) decreased UCP2 expression in the hippocampus and cortex on both day 3 ( $P < 0.001$ , Fig. 5A, C) and day 170 ( $P = 0.02$ , cortex;  $P = 0.03$ , hippocampus, Fig. 5B, F) compared with the Saline+Irisin+KA group. However, the BDNF level showed almost no change after genipin treatment (Fig. 5A, B, D, E).

The levels of oxidative stress were assessed in the hippocampus and cortex at 24 h and 3 days after KA administration ( $n = 5/\text{group}$ ). The results showed that genipin administration led to an increased level of DCF in both the cortex (24 h,  $P < 0.001$ ; day 3,  $P < 0.001$ , Fig. 5G) and the hippocampus (24 h,  $P < 0.001$ ; day 3,  $P < 0.001$ , Fig. 5H). Moreover, there was a similar increase in Mito-SOX levels in the cortex (Fig. 5I) and hippocampus (Fig. 5J) at 24 h and day 3 compared with those in the rats treated with saline (Saline+Irisin+KA group). Representative Mito-SOX flow cytometry results are shown in Fig. 5K. The results indicated that genipin reverses the reduction of oxidative stress by irisin as measured by DCF and Mito-SOX levels.

### Genipin Administration Reverses the Attenuating Effect of Exogenous Irisin on KA-induced Epilepsy

Spontaneous seizure behavior and EEGs were recorded in each group at preset time points between days 30 and 170. In the Genipin+Irisin+KA group ( $n = 10$ ), the cumulative seizure duration in stages 1–5 was significantly longer than that in the Saline+Irisin+KA group ( $n = 8$ ) at all time points ( $P < 0.001$ , Fig. 6A). Because the spontaneous seizures mainly corresponded to stages 1–3, the cumulative number and the duration of stage 1–3 seizures were further analyzed in each group. The number and duration of seizures were greater in the genipin-treated rats than those in the Saline+Irisin+KA group (Fig. 6B, C). For example, at day 170, the cumulative duration ( $317.04 \pm 50.14$  s) and number ( $96.87 \pm 19.11$ ) of stages 1–3 seizures in the Genipin+Irisin+KA group were significantly higher than those in the Saline+Irisin+KA group ( $58.38 \pm 5.78$  s and  $38.42 \pm 8.64$ ;  $P < 0.001$ , Fig. 6B, C). Representative EEGs and their power spectral analyses are shown in Fig. 6D–F. The behavioral and EEG results showed that genipin reverses the inhibition of KA-induced chronic epilepsy by exogenous irisin.

### Genipin Administration Reverses the Irisin-mediated Enhancement of Learning and Memory in KA-induced Epilepsy

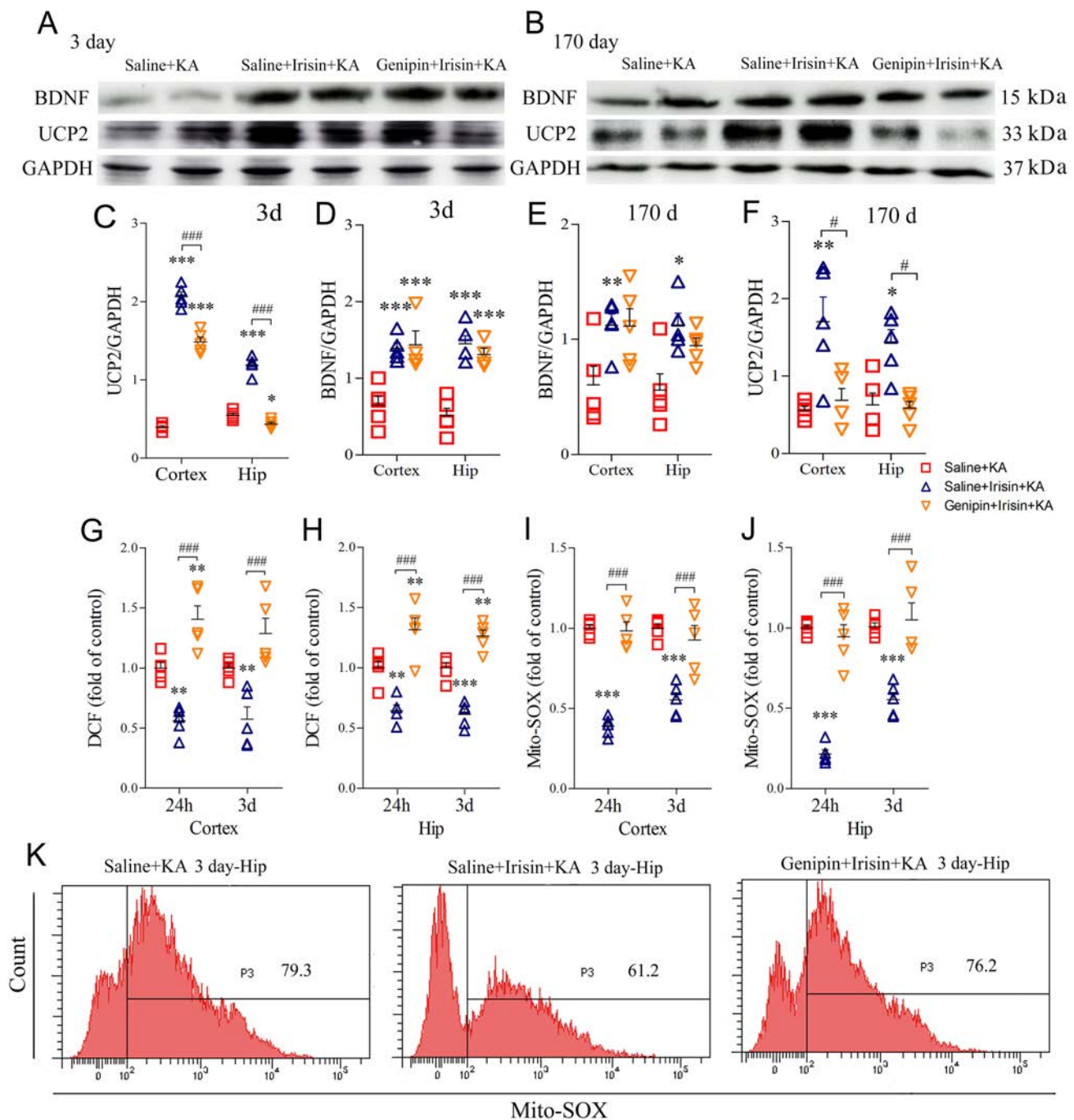
The differences in learning and memory were evaluated with the water maze test. The results showed that latency to reach the platform was significantly prolonged in genipin-treated rats ( $n = 10$ ) compared with Saline+Irisin+KA rats ( $n = 8$ ,  $P < 0.001$ , Fig. 6G). Moreover, there was a decrease in target quadrant time ( $P = 0.002$ , Fig. 6H) and target zone frequency ( $P = 0.012$ , Fig. 6J), together with a longer opposite quadrant time ( $P < 0.001$ , Fig. 6I). Meanwhile, the results of the NOR test showed that the elevated level of interaction with the new object in irisin-treated rats was reversed by genipin administration ( $n = 10$ , Genipin+Irisin+KA group, Fig. 7K, L). The results indicated that genipin partly reverses the protective effect of irisin against the learning and memory defect induced by KA. Representative tracks of rats searching for the platform are shown for each group in Fig. 6K.

### Genipin Administration Reverses the Inhibitory Effect of Irisin on KA-induced Apoptosis and Neuronal Degeneration

Changes in the apoptosis-related proteins caspase-3 and activated caspase-3 were assessed by western blots on day 3 after KA administration to evaluate the effect of genipin on the anti-apoptosis effect of irisin. As described above, irisin significantly reduced the level of activated caspase-3 in both the cortex and hippocampus (day 3, cortex,  $P < 0.001$ ; hippocampus,  $P < 0.001$ ; Fig. 7A, C), with an increased caspase-3 level (Fig. 7A, B). The brain sub-regions of rats treated with genipin (Genipin+Irisin+KA group), however, showed a significantly higher level of activated caspase-3 than that in Saline+Irisin+KA rats (day 3, cortex,  $P < 0.001$ ; hippocampus,  $P < 0.001$ ; Fig. 7A, C). The results indicated that genipin reverses the anti-apoptosis effect of irisin on KA-induced apoptosis.

To analyze the degeneration of neurons further, FJB-positive signals were counted in each group of rats after KA administration (Fig. 7D–J). Significantly increased FJB-positive signals on day 3 were observed in both the hippocampus (CA2,  $P < 0.001$ , Fig. 7F, J) and EC ( $P < 0.001$ , Fig. 7I, J) in the Genipin+Irisin+KA group compared with those in the Saline+Irisin+KA group (CA2, Fig. 7E, J; EC, Fig. 7H, J). Similar changes in FJB signals were observed at 24 h (data not shown). The FJB staining results showed that the irisin-mediated inhibition of neuronal injury is reversed after genipin treatment. The results highlighted the potential contribution of UCP2 to the strong neuroprotective effect of irisin treatment in KA-induced epilepsy.





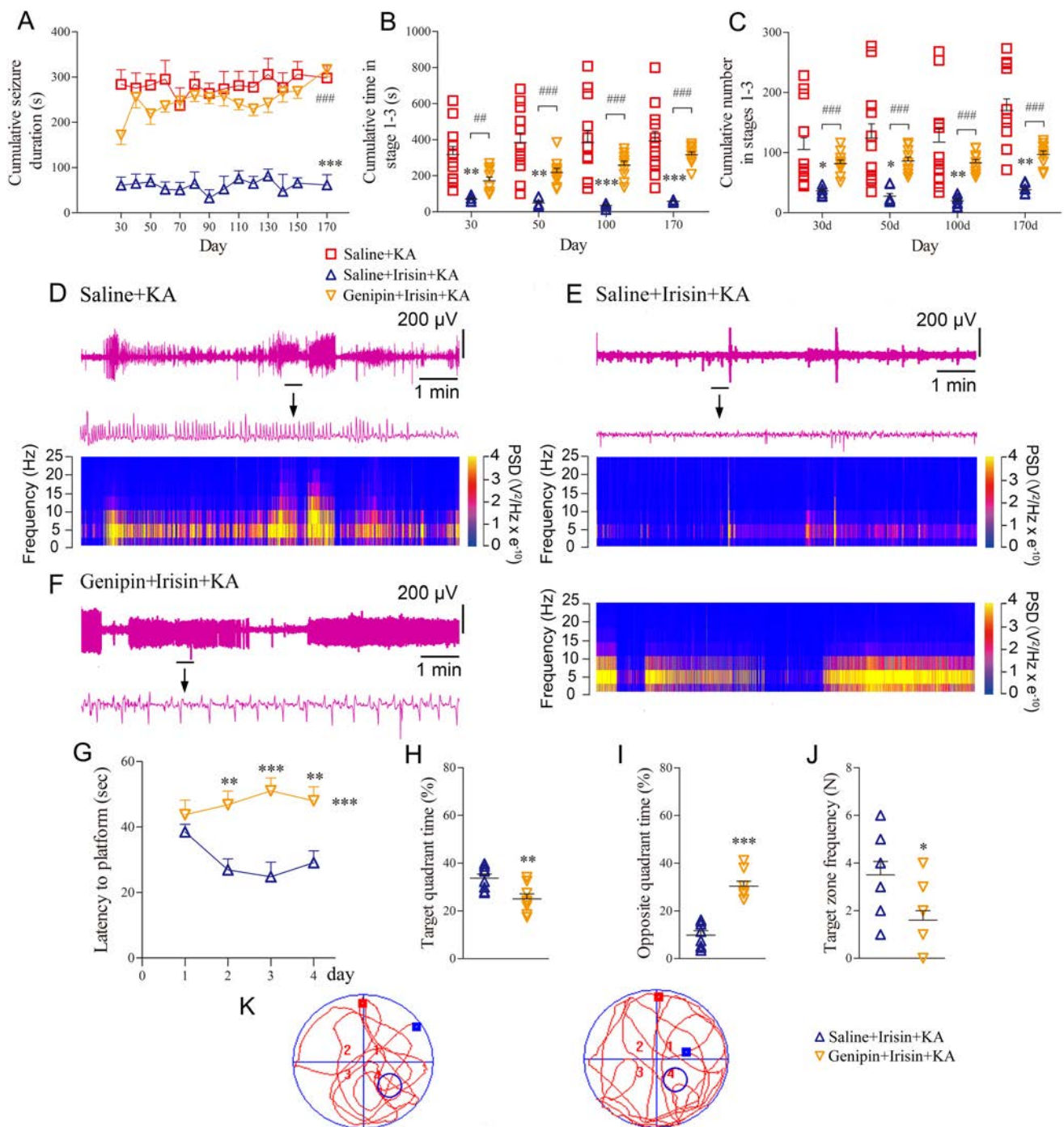
**Fig. 5** Genipin administration reverses the increased level of UCP2 and oxidative stress reduction due to exogenous irisin treatment. **A, B** Levels of UCP2 and BDNF on day 3 (**A**) and day 170 (**B**) after KA treatment ( $n = 5/\text{group}$ ). **C, F** Normalized intensity of UCP2 relative to GAPDH. **D, E** Normalized intensity of BDNF relative to GAPDH. **G, H** DCF levels in cortex and hippocampus ( $n = 5/\text{group}$ ). **I, J** Mito-SOX levels

in cortex and hippocampus ( $n = 5/\text{group}$ ). **K** Representative Mito-SOX changes assessed by flow cytometry on day 3.  $*P < 0.05$ ,  $**P < 0.01$ ,  $***P < 0.001$  vs Saline+KA group;  $\#P < 0.05$ ,  $###P < 0.001$  vs each other (one-way ANOVA with Dunnett's T3 *post-hoc* test). C, cortex; H/ Hip, hippocampus; KA, kainic acid; BDNF, brain-derived neurotrophic factor; UCP2, uncoupling protein 2; DCF, 2',7'-dichlorofluorescein.

## Discussion

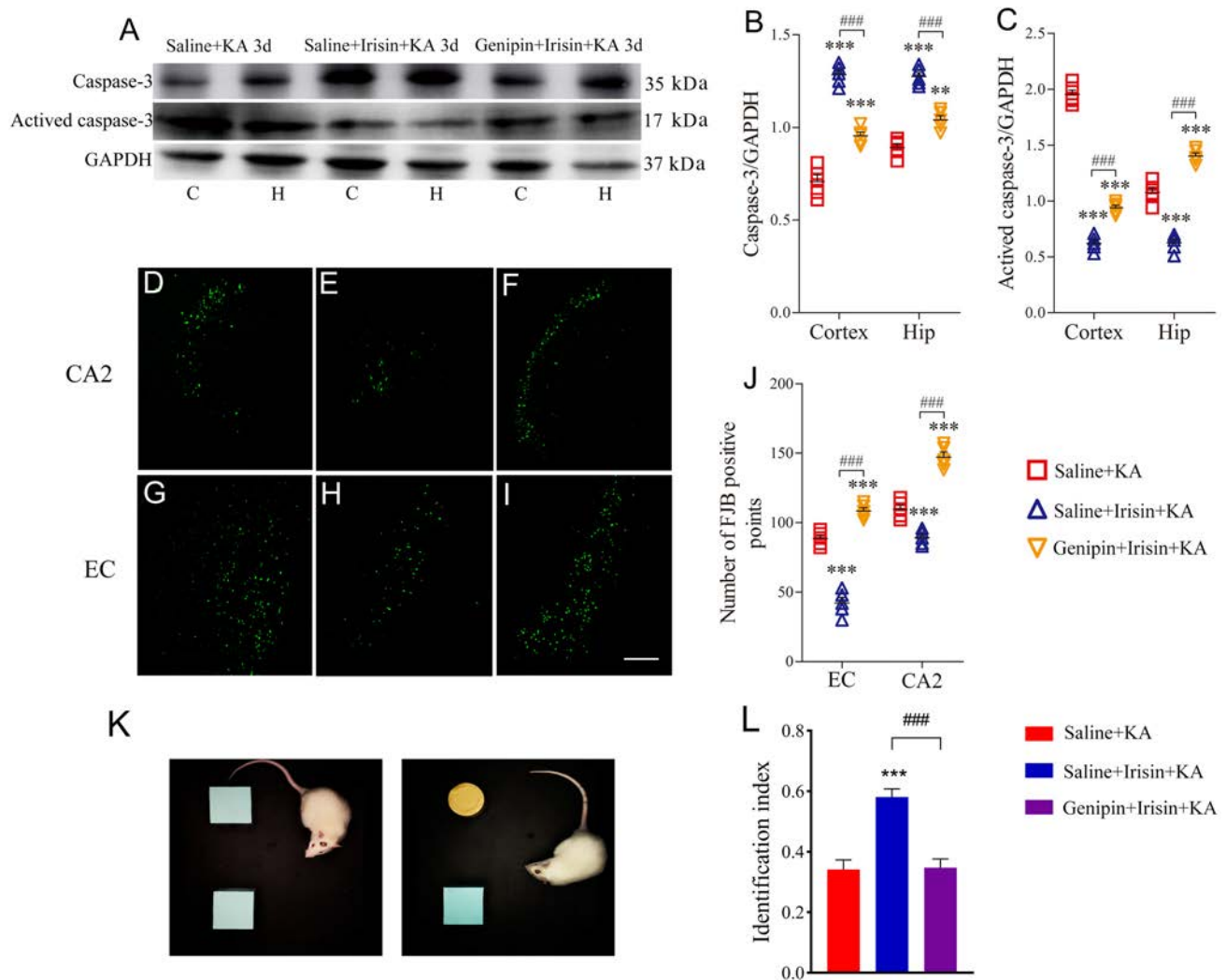
Irisin is mainly produced in skeletal muscle after exercise [35]. During exercise, the expression of FNDC5/irisin in the

CNS increases, in turn affecting a range of biological activities including mitochondrial biosynthesis, synaptic plasticity, mitochondrial  $\text{Ca}^{2+}$  homeostasis, and active oxygen generation [63, 64]. The above effects are closely associated



**Fig. 6** Genipin administration reverses the protective effect of irisin administration on seizures and the learning and memory defect. **A** Cumulative seizure duration of stage 1–5 seizures from day 30 to day 170 after KA injection (Saline+KA group,  $n = 12$ ; Irisin+KA group,  $n = 8$ ; Genipin+Irisin+KA group,  $n = 10$ ). **B** Cumulative time in stage 1–3 seizures. **C** Cumulative number of stage 1–3 seizures. **D–F** Representative electroencephalogram (EEGs) and corresponding analysis of frequency spectrum and power spectrum on

day 170. \* $P < 0.05$ , \*\* $P < 0.01$ , \*\*\* $P < 0.001$  vs Saline+KA group (one-way ANOVA). ## $P < 0.01$ , ### $P < 0.001$  vs each other (one-way ANOVA with Dunnett's T3 *post-hoc* test). **G** Latency to find the platform (Saline+Irisin+KA group,  $n = 8$ ; Genipin+Irisin+KA group,  $n = 10$ ). **H** Percentage of time in target quadrant. **I** Percentage of time in opposite quadrant. **J** Number of platform crossings. **K** Trajectories in Morris water maze. \* $P < 0.05$ , \*\* $P < 0.01$ , \*\*\* $P < 0.001$  vs Saline+Irisin+KA group (one-way ANOVA). KA, kainic acid.



**Fig. 7** Genipin reverses neuronal protection of exogenous irisin. **A–C** Levels of apoptosis-related proteins on day 3 ( $n = 5/\text{group}$ ). **D–J** FJB (Fluoro-Jade B) signal patterns in CA2 and EC on day 3 ( $n = 5/\text{group}$ ; scale bar, 100  $\mu\text{m}$ ). **K, L** The novel object recognition test (**K**) and identification index (**L**) of rats in each group ( $n = 10/\text{group}$ ,

on day 30).  $**P < 0.01$ ,  $***P < 0.001$  vs Saline+KA group (one-way ANOVA);  $###P < 0.001$  vs each other (one-way ANOVA with Dunnett's T3 *post-hoc* test). C, cortex; CA2, cornu ammonis 2; EC, entorhinal cortex; H/Hip, hippocampus; KA, kainic acid.

with epileptogenesis and seizures [65–67]. For example, ROS-induced oxidative stress injuries have been found along with epilepsy and seizures [68, 69]. Mitochondria are vulnerable to oxidative stress and ROS-induced mitochondrial injury leads to defects in energy metabolism, which play key roles in the initiation and development of epilepsy [18]. Irisin has been shown to reduce oxidative stress damage and increase free radical scavenging in various models [70, 71]. For example, irisin significantly reduces the excessive accumulation of the superoxide anion and the production of malondialdehyde (the final oxidation product of lipid peroxidation) after cerebral tissue infarction due to ischemic injury [72]. Intravenous administration of exogenous irisin protects the heart from ischemia-reperfusion injury by increasing

the expression of superoxide dismutase-1 and protecting mitochondrial function [29, 48]. Combined with the inhibitory effect of irisin on ROS production, the previous results led us to speculate that irisin might have a neuroprotective effect against epilepsy by reducing oxidative stress [73]. The results of our study confirmed our hypothesis. In the KA-induced chronic epilepsy model, irisin significantly attenuated the seizures and the learning and memory defect, as well as reducing neuronal injury and oxidative stress.

Interestingly, as irisin is mainly produced in skeletal muscle after exercise [35], over-excitation-induced contraction of skeletal muscle during the KA-induced seizures might lead to the increased irisin level. Indeed, an elevated irisin level has been reported in children with uncontrolled



epileptic seizures [74]. However, significant neuronal injury was found after KA administration. The results suggest that even if irisin might be produced by KA-induced seizures, it is not sufficient to resist the neuronal injury induced by KA administration. The detailed changes of endogenous irisin levels and the contribution in KA-induced chronic spontaneous epilepsy need further investigation.

The neuronal protection of irisin/FNDC5 through the regulation of BDNF has been confirmed. After endurance exercise, the level of FNDC5/irisin in the CNS is increased, further increasing the expression of BDNF in the brain [35]. Exogenous administration of irisin through the lateral ventricle leads to enhanced BDNF expression and reduced brain injury caused by ischemia-reperfusion [75]. Similarly, after intravenous injection of FNDC5, BDNF gene expression is increased in mouse cortical cell cultures and the hippocampus [35]. As the precursor of irisin, FNDC5 may regulate the expression of BDNF through hydrolyzing into irisin. As a neurotrophic factor, BDNF is closely associated with changes in cell survival and function [76], and epileptogenesis and seizures. Continuous release of BDNF in the epileptic hippocampus attenuates seizures, improves cognitive abilities, and reverses the histological and pathological changes in chronic epilepsy. In animal models of epilepsy induced by KA or pilocarpine, exogenous administration of BDNF reduces the toxic damage to neurons in the hippocampus [40]. Our results confirmed that exogenous irisin increased the expression of BDNF and significantly attenuated neuronal injury and seizure severity in KA-induced epilepsy, but there were almost no changes in the BDNF level with genipin pretreatment. These results indicated that irisin exerts its neuroprotective and anti-epileptic effects through the BDNF pathway.

However, there are two aspects of BDNF in epilepsy. According to previous studies, BDNF is closely associated with the growth of both normal and injured neurons and affects neurotransmitter synthesis and neuronal excitability [38, 77]. It has been reported that sharply elevated levels of BDNF could lead to temporal lobe epilepsy by activating tropomyosin receptor kinase B (TrkB) as well as other downstream signaling cascades [78, 79]. At the beginning of certain eclamptic events such as lesions and inflammation, the increased level of BDNF–TrkB in different regions of the brain may cause increased excitability of the limbic system [80]. Therefore, it was thought that high levels of this neurotrophin might promote epileptogenesis in epileptic or injured brains because it may participate in the establishment of an excitatory neural network (especially in the hippocampal region) during the latent period [79].

Nevertheless, some studies have reported that the elevated level of BDNF is one of the endogenous protective mechanisms in epilepsy: the increased expression of BDNF during a seizure protects neurons from further injury [81], and

the upregulated levels of BDNF within the normal range decrease neuronal excitability by combining with the TrkB receptor [82, 83]. Accordingly, a previous statistical analysis reported that the level of BDNF in normal human plasma is  $4289 \pm 1810$  pg/mL, which is significantly higher than that in the patients with epilepsy ( $977 \pm 565$  pg/mL) [84]. It has also been found that chronic injection of BDNF into the epileptic hippocampus reduces excitability, thus partly alleviating seizures [83]. Previous reports have suggested that the BDNF–TrkB pathway is an important factor in the occurrence of epilepsy and seizures, although the possible roles and mechanisms are controversial. Differences in BDNF levels and pathological states may explain its dual effects. More evidence is needed to establish the precise pathogenesis of BDNF–TrkB and its dual effects on epilepsy.

Downstream, the neuroprotective effect of BDNF is closely associated with UCP2, which has been shown to attenuate cell injury by inhibiting mitochondrial-mediated ROS production [66, 85, 86]. UCP2 is located in the inner membrane of the mitochondrion and belongs to a family of mitochondrial transporter proteins that are involved in energy production, apoptosis, and necrosis of cells [87]. In mitochondria, uncoupling of the respiratory chain and of oxidative phosphorylation converts the ADP of the proton gradient between the membrane space and the mitochondrial matrix into ATP. The energy destined to the ATP synthase disappears, it is consumed in the form of heat, and superoxide generation and energy storage are reduced [88]. The expression of mitochondrial UCP2 increases, followed by the uncoupling effect, and decreases cell death in animal models of acute brain injury [87] and Parkinson's disease [89]. Conversely, a decreased UCP2 level leads to a neurodegenerative process through mechanisms downstream from UCP2 [90, 91]. UCP2 stabilizes the mitochondrial inner membrane potential by changing the proton electrochemical concentration of the inner membrane, reduces the production of mitochondrial ROS and oxidative stress, and further protects myocardial cells from ischemia-reperfusion injury [85, 86]. Exogenous administration of BDNF upregulates UCP2 expression and reduces the nervous system damage caused by free radicals and oxidative stress [92]. As one of the BDNF regulators, exogenous irisin has also been reported to increase the expression of UCP2 [25]. Based on these results, we had reason to speculate that BDNF-regulated UCP2 might contribute to the anti-seizure and neuroprotective roles of irisin. Our results support this hypothesis. Increased expression of UCP2 and BDNF, and neuroprotective and anti-seizure effects were found after irisin treatment. Conversely, the UCP2 inhibitor genipin reversed the increase in UCP2 level, as well as attenuating the anti-seizure and neuroprotective effects of irisin.

Interestingly, irisin treatment 30 min before KA administration also attenuated the KA-induced acute seizures. The



results indicated an additional neuroprotective mechanism besides BDNF and UCP2 in the acute period, e.g. mitochondrial  $\text{Ca}^{2+}$  homeostasis and glutamate release [67]. Further, the less severe acute seizures may also contribute to the attenuated chronic spontaneous seizures. The detailed mechanisms need to be explored by further research.

The pathological hallmarks of epilepsy are neuronal apoptosis and brain injury, which are caused by epilepsy-induced excitotoxicity [93]. We used FJB staining to evaluate the neuronal damage caused by KA and the neuronal protection of irisin [54, 94]. The results showed that FJB-positive signals induced by KA were mainly located in the hippocampus and EC. Irisin reduced the FJB signals in the brain of epileptic rats. The hippocampus and EC are closely associated with seizures and cognition [95, 96]. Injury to the EC, which forms an epileptic network loop with the hippocampus, produces the recurrence of epileptic attacks, and further causes neuronal apoptosis [54, 96, 97]. Irisin can attenuate such neuronal damage [98]. Our experiments also showed that irisin protected against the neuroexcitatory damage in the hippocampus and EC induced by KA. Inhibiting the formation of the epileptic circuit by inhibiting neuronal damage in the hippocampus and EC may contribute to the anti-seizure effects of irisin, even though duality of the GABAergic signal on the excitability of neurons has been reported [28, 99].

In addition, in KA-induced chronic spontaneous epilepsy, increased levels of oxidative stress and neuronal injury were found as early as 24 h, which is much earlier than the occurrence of spontaneous seizures. The results indicated a possible contribution of early neuronal injury to the later seizures. Moreover, the early intervention in oxidative stress and neuronal injury by exogenous irisin treatment significantly attenuated the later spontaneous seizures. Consequently, the early neuropathy after epileptogenic stimulation may play a critical role in the subsequent epileptogenesis. The early protection against oxidative stress-induced neuronal injury may be a promising therapeutic strategy for epilepsy.

In conclusion, exogenous irisin treatment significantly increased the expression of BDNF and UCP2. Meanwhile, irisin treatment reduced oxidative stress, neuronal injury, learning and memory defects, and epileptic seizures. Administration of a UCP2 inhibitor confirmed the anti-seizure and neuroprotective effects of early irisin treatment in the KA-induced epilepsy model, and further indicated that the changed UCP2 level mediated by BDNF may be the underlying protective mechanism in this model.

**Acknowledgements** This work was supported by the National Natural Science Foundation of China (81573412 and 81803546), Key Research and Development Plan of Shandong Province (2018GSF121004), and Yantai Science and Technology Development Plan (2019xdhz098). We would like to thank Editage for English language editing.

**Conflict of interest** The authors claim that there are no conflicts of interest.

## References

1. Wurina S, Zang YF, Zhao SG. Resting-state fMRI studies in epilepsy. *Neurosci Bull* 2012, 28: 449–455.
2. Liu YQ, Yu F, Liu WH, He XH, Peng BW. Dysfunction of hippocampal interneurons in epilepsy. *Neurosci Bull* 2014, 30: 985–998.
3. Mishra CB, Kumari S, Prakash A, Yadav R, Tiwari AK, Pandey P. Discovery of novel Methylsulfonyl phenyl derivatives as potent human Cyclooxygenase-2 inhibitors with effective anticonvulsant action: Design, synthesis, in-silico, *in-vitro* and *in-vivo* evaluation. *Eur J Med Chem* 2018, 151: 520–532.
4. Ngugi AK, Bottomley C, Fegan G, Chengo E, Odhiambo R, Bauni E, *et al.* Premature mortality in active convulsive epilepsy in rural Kenya: Causes and associated factors. *Neurology* 2014, 82: 582–589.
5. Eid T, Lee TSW, Patrylo P, Zaveri HP. Astrocytes and glutamine synthetase in epileptogenesis. *J Neurosci Res* 2019, 97: 1345–1362.
6. Jin MM, Chen Z. Role of gap junctions in epilepsy. *Neurosci Bull* 2011, 27: 389–406.
7. Qi YB, Cheng HM, Wang Y, Chen Z. Revealing the precise role of calretinin neurons in epilepsy: We are on the way. *Neurosci Bull* 2022, 38: 209–222.
8. Kharatishvili I, Nissinen JP, McIntosh TK, Pitkänen A. A model of posttraumatic epilepsy induced by lateral fluid-percussion brain injury in rats. *Neuroscience* 2006, 140: 685–697.
9. Wang Y, Chen Z. An update for epilepsy research and antiepileptic drug development: Toward precise circuit therapy. *Pharmacol Ther* 2019, 201: 77–93.
10. Lee KI, Lin JW, Su CC, Fang KM, Yang CY, Kuo CY, *et al.* Silica nanoparticles induce caspase-dependent apoptosis through reactive oxygen species-activated endoplasmic reticulum stress pathway in neuronal cells. *Toxicol In Vitro* 2020, 63: 104739.
11. Lichota A, Gwozdziński L, Gwozdziński K. Therapeutic potential of natural compounds in inflammation and chronic venous insufficiency. *Eur J Med Chem* 2019, 176: 68–91.
12. Smilin Bell Aseervatham G, Abbirami E, Sivasudha T, Ruckmani K. Passiflora caerulea L. Fruit extract and its metabolites ameliorate epileptic seizure, cognitive deficit and oxidative stress in pilocarpine-induced epileptic mice. *Metab Brain Dis* 2020, 35: 159–173.
13. Xie NC, Wang C, Wu CJ, Cheng X, Gao YL, Zhang HF, *et al.* Mdivi-1 protects epileptic hippocampal neurons from apoptosis via inhibiting oxidative stress and endoplasmic reticulum stress *in vitro*. *Neurochem Res* 2016, 41: 1335–1342.
14. Li MM, Li X, Cao ZL, Wu YT, Chen J, Gao J, *et al.* Mitochondria-targeting BODIPY-loaded micelles as novel class of photosensitizer for photodynamic therapy. *Eur J Med Chem* 2018, 157: 599–609.
15. Pierce JD, Gupte R, Thimmesch A, Shen QH, Hiebert JB, Brooks WM, *et al.* Ubiquinol treatment for TBI in male rats: Effects on mitochondrial integrity, injury severity, and neurometabolism. *J Neurosci Res* 2018, 96: 1080–1092.
16. Wang C, Xie NC, Wang YL, Li YL, Ge XJ, Wang ML. Role of the mitochondrial calcium uniporter in rat hippocampal neuronal death after pilocarpine-induced status epilepticus. *Neurochem Res* 2015, 40: 1739–1746.
17. Waldbaum S, Patel M. Mitochondria, oxidative stress, and temporal lobe epilepsy. *Epilepsy Res* 2010, 88: 23–45.

18. Rowley S, Liang LP, Fulton R, Shimizu T, Day B, Patel M. Mitochondrial respiration deficits driven by reactive oxygen species in experimental temporal lobe epilepsy. *Neurobiol Dis* 2015, 75: 151–158.
19. Folbergrová J, Jesina P, Haugvicová R, Lisý V, Houstek J. Sustained deficiency of mitochondrial complex I activity during long periods of survival after seizures induced in immature rats by homocysteic acid. *Neurochem Int* 2010, 56: 394–403.
20. Folbergrová J, Ješina P, Kubová H, Otáhal J. Effect of resveratrol on oxidative stress and mitochondrial dysfunction in immature brain during epileptogenesis. *Mol Neurobiol* 2018, 55: 7512–7522.
21. Ng CSH, Wan S, Arifi AA, Yim APC. Inflammatory response to pulmonary ischemia-reperfusion injury. *Surg Today* 2006, 36: 205–214.
22. Chen K, Xu ZC, Liu YK, Wang Z, Li Y, Xu XF, *et al.* Irisin protects mitochondria function during pulmonary ischemia/reperfusion injury. *Sci Transl Med* 2017, 9: eaa06298.
23. Boström P, Wu J, Jedrychowski MP, Korde A, Ye L, Lo JC, *et al.* A PGC1- $\alpha$ -dependent myokine that drives brown-fat-like development of white fat and thermogenesis. *Nature* 2012, 481: 463–468.
24. Huh JY, Panagiotou G, Mougios V, Brinkoetter M, Vamvini MT, Schneider BE, *et al.* FNDC5 and irisin in humans: I. Predictors of circulating concentrations in serum and plasma and II. mRNA expression and circulating concentrations in response to weight loss and exercise. *Metabolism* 2012, 61: 1725–1738.
25. Erden Y, Tekin S, Sandal S, Onalan EE, Tektemur A, Kirbag S. Effects of central irisin administration on the uncoupling proteins in rat brain. *Neurosci Lett* 2016, 618: 6–13.
26. Zhang Y, Li R, Meng Y, Li SW, Donelan W, Zhao Y, *et al.* Irisin stimulates browning of white adipocytes through mitogen-activated protein kinase p38 MAP kinase and ERK MAP kinase signaling. *Diabetes* 2014, 63: 514–525.
27. Friedenreich CM, Neilson HK, Lynch BM. State of the epidemiological evidence on physical activity and cancer prevention. *Eur J Cancer* 2010, 46: 2593–2604.
28. Wang Y, Xu CL, Xu ZH, Ji CH, Liang J, Wang Y, *et al.* Depolarized GABAergic signaling in subicular microcircuits mediates generalized seizure in temporal lobe epilepsy. *Neuron* 2017, 95: 92–105.e5.
29. Wang H, Zhao YT, Zhang SY, Dubielecka PM, Du JF, Yano N, *et al.* Irisin plays a pivotal role to protect the heart against ischemia and reperfusion injury. *J Cell Physiol* 2017, 232: 3775–3785.
30. Wang Z, Chen K, Han Y, Zhu H, Zhou XY, Tan T, *et al.* Irisin protects heart against ischemia-reperfusion injury through a SOD2-dependent mitochondria mechanism. *J Cardiovasc Pharmacol* 2018, 72: 259–269.
31. Zhang WZ, Chang L, Zhang C, Zhang R, Li ZR, Chai BX, *et al.* Central and peripheral irisin differentially regulate blood pressure. *Cardiovasc Drugs Ther* 2015, 29: 121–127.
32. Abedpoor N, Taghian F, Ghaedi K, Niktab I, Safaiejad Z, Rabiee F, *et al.* PPAR $\gamma$ /Pgc-1 $\alpha$ -Fndc5 pathway up-regulation in gastrocnemius and heart muscle of exercised, branched chain amino acid diet fed mice. *Nutr Metab (Lond)* 2018, 15: 59.
33. Teufel A, Malik N, Mukhopadhyay M, Westphal H. Frcp1 and Frcp2, two novel fibronectin type III repeat containing genes. *Gene* 2002, 297: 79–83.
34. Wrann CD. FNDC5/irisin - their role in the nervous system and as a mediator for beneficial effects of exercise on the brain. *Brain Plast* 2015, 1: 55–61.
35. Wrann CD, White JP, Salogiannis J, Laznik-Bogoslavski D, Wu J, Ma D, *et al.* Exercise induces hippocampal BDNF through a PGC-1 $\alpha$ /FNDC5 pathway. *Cell Metab* 2013, 18: 649–659.
36. Dinda B, Dinda M, Kulsi G, Chakraborty A, Dinda S. Therapeutic potentials of plant iridoids in Alzheimer's and Parkinson's diseases: A review. *Eur J Med Chem* 2019, 169: 185–199.
37. Belviranlı M, Okudan N, Kabak B, Erdoğan M, Karanfilci M. The relationship between brain-derived neurotrophic factor, irisin and cognitive skills of endurance athletes. *Phys Sportsmed* 2016, 44: 290–296.
38. Kuipers SD, Bramham CR. Brain-derived neurotrophic factor mechanisms and function in adult synaptic plasticity: New insights and implications for therapy. *Curr Opin Drug Discov Devel* 2006, 9: 580–586.
39. Xia DY, Huang X, Bi CF, Mao LL, Peng LJ, Qian HR. PGC-1 $\alpha$  or FNDC5 is involved in modulating the effects of A $\beta$ <sub>1–42</sub> oligomers on suppressing the expression of BDNF, a beneficial factor for inhibiting neuronal apoptosis, A $\beta$  deposition and cognitive decline of APP/PS1 Tg mice. *Front Aging Neurosci* 2017, 9: 65.
40. Falcicchia C, Paolone G, Emerich DF, Lovisari F, Bell WJ, Fradet T, *et al.* Seizure-suppressant and neuroprotective effects of encapsulated BDNF-producing cells in a rat model of temporal lobe epilepsy. *Mol Ther Methods Clin Dev* 2018, 9: 211–224.
41. Wang CF, Bomberg E, Billington CJ, Levine AS, Kotz CM. Brain-derived neurotrophic factor (BDNF) in the hypothalamic ventromedial nucleus increases energy expenditure. *Brain Res* 2010, 1336: 66–77.
42. Bonet ML, Mercader J, Palou A. A nutritional perspective on UCP1-dependent thermogenesis. *Biochimie* 2017, 134: 99–117.
43. Hoang T, Smith MD, Jelokhani-Niaraki M. Toward understanding the mechanism of ion transport activity of neuronal uncoupling proteins UCP2, UCP4, and UCP5. *Biochemistry* 2012, 51: 4004–4014.
44. Binienda ZK, Ali SF, Virmani A, Amato A, Salem N, Przybyla BD. Co-regulation of dopamine D1 receptor and uncoupling protein-2 expression in 3-nitropropionic acid-induced neurotoxicity: Neuroprotective role of L-carnitine. *Neurosci Lett* 2006, 410: 62–65.
45. Diano S, Matthews RT, Patrylo P, Yang LC, Beal MF, Barnstable CJ, *et al.* Uncoupling protein 2 prevents neuronal death including that occurring during seizures: A mechanism for preconditioning. *Endocrinology* 2003, 144: 5014–5021.
46. Zhao BS, Sun LK, Jiang XR, Zhang Y, Kang JS, Meng H, *et al.* Genipin protects against cerebral ischemia-reperfusion injury by regulating the UCP2-SIRT3 signaling pathway. *Eur J Pharmacol* 2019, 845: 56–64.
47. Flori L, Testai L, Calderone V. The, “irisin system”: From biological roles to pharmacological and nutraceutical perspectives. *Life Sci* 2021, 267: 118954.
48. Zhu D, Wang HC, Zhang XT, Xin C, Zhang FY, *et al.* Irisin improves endothelial function in type 2 diabetes through reducing oxidative/nitrative stresses. *J Mol Cell Cardiol* 2015, 87: 138–147.
49. Ren YF, Qiu ML, Zhang J, Bi JB, Wang MZ, Hu LS, *et al.* Low serum irisin concentration is associated with poor outcomes in patients with acute pancreatitis, and irisin administration protects against experimental acute pancreatitis. *Antioxid Redox Signal* 2019, 31: 771–785.
50. Racine RJ. Modification of seizure activity by electrical stimulation. II. Motor seizure. *Electroencephalogr Clin Neurophysiol* 1972, 32: 281–294.
51. Liu T, Ma XR, Ouyang TX, Chen HP, Xiao Y, Huang YY, *et al.* Efficacy of 5-aminolevulinic acid-based photodynamic therapy against keloid compromised by downregulation of SIRT1-SIRT3-SOD2-mROS dependent autophagy pathway. *Redox Biol* 2019, 20: 195–203.
52. Zhang MD, Cui YR, Zhu W, Yu J, Cheng Y, Wu XD, *et al.* Attenuation of the mutual elevation of iron accumulation and oxidative stress may contribute to the neuroprotective and anti-seizure effects of xenon in neonatal hypoxia-induced seizures. *Free Radic Biol Med* 2020, 161: 212–223.

53. Zhang YR, Zhang MD, Zhu W, Yu J, Wang QY, Zhang JJ, *et al.* Succinate accumulation induces mitochondrial reactive oxygen species generation and promotes status epilepticus in the kainic acid rat model. *Redox Biol* 2020, 28: 101365.
54. Zhang YR, Zhang MD, Liu SH, Zhu W, Yu J, Cui YR, *et al.* Xenon exerts anti-seizure and neuroprotective effects in kainic acid-induced status epilepticus and neonatal hypoxia-induced seizure. *Exp Neurol* 2019, 322: 113054.
55. Morris R. Developments of a water-maze procedure for studying spatial learning in the rat. *J Neurosci Methods* 1984, 11: 47–60.
56. Vorhees CV, Williams MT. Morris water maze: Procedures for assessing spatial and related forms of learning and memory. *Nat Protoc* 2006, 1: 848–858.
57. Bromley-Brits K, Deng Y, Song W. Morris water maze test for learning and memory deficits in Alzheimer's disease model mice. *J Vis Exp* 2011: 2920.
58. Pereira LO, Arteni NS, Petersen RC, da Rocha AP, Achaval M, Netto CA. Effects of daily environmental enrichment on memory deficits and brain injury following neonatal hypoxia-ischemia in the rat. *Neurobiol Learn Mem* 2007, 87: 101–108.
59. Antunes M, Biala G. The novel object recognition memory: Neurobiology, test procedure, and its modifications. *Cogn Process* 2012, 13: 93–110.
60. Mathiasen JR, DiCamillo A. Novel object recognition in the rat: A facile assay for cognitive function. *Curr Protoc Pharmacol* 2010, Chapter 5: Unit5.59.
61. Lueptow LM. Novel object recognition test for the investigation of learning and memory in mice. *J Vis Exp* 2017, 126: 55718.
62. Zhang R, Xue GZ, Wang SD, Zhang LH, Shi CJ, Xie X. Novel object recognition as a facile behavior test for evaluating drug effects in A $\beta$ PP/PS<sub>1</sub> Alzheimer's disease mouse model. *J Alzheimers Dis* 2012, 31: 801–812.
63. Andrews ZB, Horvath B, Barnstable CJ, Elsworth J, Yang LC, Beal MF, *et al.* Uncoupling protein-2 is critical for nigral dopamine cell survival in a mouse model of Parkinson's disease. *J Neurosci* 2005, 25: 184–191.
64. Echtay KS. Mitochondrial uncoupling proteins—what is their physiological role? *Free Radic Biol Med* 2007, 43: 1351–1371.
65. Vaynman S, Ying Z, Gómez-Pinilla F. Exercise induces BDNF and synapsin I to specific hippocampal subfields. *J Neurosci Res* 2004, 76: 356–362.
66. Migliaccio V, Scudiero R, Sica R, Lionetti L, Putti R. Oxidative stress and mitochondrial uncoupling protein 2 expression in hepatic steatosis induced by exposure to xenobiotic DDE and high fat diet in male Wistar rats. *PLoS One* 2019, 14: e0215955.
67. Bannai H, Niwa F, Sherwood MW, Shrivastava AN, Arizono M, Miyamoto A, *et al.* Bidirectional control of synaptic GABAAR clustering by glutamate and calcium. *Cell Rep* 2015, 13: 2768–2780.
68. Yang XY, Tse MCL, Hu X, Jia WH, Du GH, Chan CB. Interaction of CREB and PGC-1 $\alpha$  induces fibronectin type III domain-containing protein 5 expression in C2C12 myotubes. *Cell Physiol Biochem* 2018, 50: 1574–1584.
69. Bhatti J, Nascimento B, Akhtar U, Rhind SG, Tien H, Nathens A, *et al.* Systematic review of human and animal studies examining the efficacy and safety of N-Acetylcysteine (NAC) and N-Acetylcysteine amide (NACA) in traumatic brain injury: Impact on neurofunctional outcome and biomarkers of oxidative stress and inflammation. *Front Neurol* 2017, 8: 744.
70. Askari H, Rajani SF, Poorebrahim M, Haghi-Aminjan H, Raeis-Abdollahi E, Abdollahi M. A glance at the therapeutic potential of irisin against diseases involving inflammation, oxidative stress, and apoptosis: An introductory review. *Pharmacol Res* 2018, 129: 44–55.
71. Batirel S, Bozaykut P, Mutlu Altundag E, Kartal Ozer N, Mantzoros CS. The effect of Irisin on antioxidant system in liver. *Free Radic Biol Med* 2014, 75(Suppl 1): S16.
72. Lu JY, Xiang GD, Liu M, Mei W, Xiang L, Dong J. Irisin protects against endothelial injury and ameliorates atherosclerosis in apolipoprotein E-Null diabetic mice. *Atherosclerosis* 2015, 243: 438–448.
73. Pearson-Smith JN, Patel M. Metabolic dysfunction and oxidative stress in epilepsy. *Int J Mol Sci* 2017, 18: E2365.
74. Elhady M, Youness ER, Gafar HS, Abdel Aziz A, Mostafa RSI. Circulating irisin and chemerin levels as predictors of seizure control in children with idiopathic epilepsy. *Neurol Sci* 2018, 39: 1453–1458.
75. Asadi Y, Gorjipour F, Behrouzifar S, Vakili A. Irisin peptide protects brain against ischemic injury through reducing apoptosis and enhancing BDNF in a rodent model of stroke. *Neurochem Res* 2018, 43: 1549–1560.
76. Greenberg ME, Xu BJ, Lu B, Hempstead BL. New insights in the biology of BDNF synthesis and release: Implications in CNS function. *J Neurosci* 2009, 29: 12764–12767.
77. Wu BW, Wu MS, Guo JD. Effects of microRNA-10a on synapse remodeling in hippocampal neurons and neuronal cell proliferation and apoptosis through the BDNF-TrkB signaling pathway in a rat model of Alzheimer's disease. *J Cell Physiol* 2018, 233: 5281–5292.
78. Lin TW, Harward SC, Huang YZ, McNamara JO. Targeting BDNF/TrkB pathways for preventing or suppressing epilepsy. *Neuropharmacology* 2020, 167: 107734.
79. Lu B, Nagappan G, Lu Y. BDNF and synaptic plasticity, cognitive function, and dysfunction. *Handb Exp Pharmacol* 2014, 220: 223–250.
80. Numakawa T, Suzuki S, Kumamaru E, Adachi N, Richards M, Kunugi H. BDNF function and intracellular signaling in neurons. *Histol Histopathol* 2010, 25: 237–258.
81. Kang DH, Choi BY, Lee SH, Kho AR, Jeong JH, Hong DK, *et al.* Effects of cerebrolisin on hippocampal neuronal death after pilocarpine-induced seizure. *Front Neurosci* 2020, 14: 568813.
82. Nieto-Gonzalez JL, Jensen K. BDNF depresses excitability of parvalbumin-positive interneurons through an M-like current in rat dentate gyrus. *PLoS One* 2013, 8: e67318.
83. Osehobo P, Adams B, Sazgar M, Xu Y, Racine RJ, Fahnstock M. Brain-derived neurotrophic factor infusion delays amygdala and perforant path kindling without affecting paired-pulse measures of neuronal inhibition in adult rats. *Neuroscience* 1999, 92: 1367–1375.
84. LaFrance WC Jr, Leaver K, Stopa EG, Papandonatos GD, Blum AS. Decreased serum BDNF levels in patients with epileptic and psychogenic nonepileptic seizures. *Neurology* 2010, 75: 1285–1291.
85. Safari F, Anvari Z, Moshtaghion S, Javan M, Bayat G, Forosh SS, *et al.* Differential expression of cardiac uncoupling proteins 2 and 3 in response to myocardial ischemia-reperfusion in rats. *Life Sci* 2014, 98: 68–74.
86. Safari F, Bayat G, Shekarforoush S, Hekmatimoghaddam S, Anvari Z, Moghadam MF, *et al.* Expressional profile of cardiac uncoupling protein-2 following myocardial ischemia reperfusion in losartan- and ramiprilat-treated rats. *J Renin Angiotensin Aldosterone Syst* 2014, 15: 209–217.
87. Bechmann I, Diano S, Warden CH, Bartfai T, Nitsch R, Horvath TL. Brain mitochondrial uncoupling protein 2 (UCP2): A protective stress signal in neuronal injury. *Biochem Pharmacol* 2002, 64: 363–367.
88. Guo XP, Zhang MM, Gao Y, Cao GZ, Lu D, Li WJ. Quantitative multi-omics analysis of the effects of mitochondrial dysfunction on lipid metabolism in *Saccharomyces cerevisiae*. *Appl Microbiol Biotechnol* 2020, 104: 1211–1226.
89. Horvath TL, Diano S, Leranath C, Garcia-Segura LM, Cowley MA, Shanabrough M, *et al.* Coenzyme Q induces nigral mitochondrial

- uncoupling and prevents dopamine cell loss in a primate model of Parkinson's disease. *Endocrinology* 2003, 144: 2757–2760.
90. Gupta RC, Milatovic D, Dettbarn WD. Depletion of energy metabolites following acetylcholinesterase inhibitor-induced status epilepticus: Protection by antioxidants. *Neurotoxicology* 2001, 22: 271–282.
  91. Gupta RC, Milatovic D, Dettbarn WD. Nitric oxide modulates high-energy phosphates in brain regions of rats intoxicated with diisopropylphosphorofluoridate or carbofuran: Prevention by N-tert-butyl-alpha-phenylnitron or vitamin E. *Arch Toxicol* 2001, 75: 346–356.
  92. Chan SHH, Wu CWJ, Chang AYW, Hsu KS, Chan JYH. Transcriptional upregulation of brain-derived neurotrophic factor in rostral ventrolateral medulla by angiotensin II: Significance in superoxide homeostasis and neural regulation of arterial pressure. *Circ Res* 2010, 107: 1127–1139.
  93. Bumanglag AV, Sloviter RS. No latency to dentate granule cell epileptogenesis in experimental temporal lobe epilepsy with hippocampal sclerosis. *Epilepsia* 2018, 59: 2019–2034.
  94. Wu J, Vogel T, Gao X, Lin B, Kulwin C, Chen JH. Neuroprotective effect of dexmedetomidine in a murine model of traumatic brain injury. *Sci Rep* 2018, 8: 4935.
  95. Tse K, Hammond D, Simpson D, Beynon RJ, Beamer E, Tymianski M, *et al.* The impact of postsynaptic density 95 blocking peptide (Tat-NR2B9c) and an iNOS inhibitor (1400W) on proteomic profile of the hippocampus in C57BL/6J mouse model of kainate-induced epileptogenesis. *J Neurosci Res* 2019, 97: 1378–1392.
  96. Basu J, Zaremba JD, Cheung SK, Hitti FL, Zemelman BV, Losonczy A, *et al.* Gating of hippocampal activity, plasticity, and memory by entorhinal cortex long-range inhibition. *Science* 2016, 351: aaa5694.
  97. Cheng HM, Wang Y, Chen JZ, Chen Z. The piriform cortex in epilepsy: What we learn from the kindling model. *Exp Neurol* 2020, 324: 113137.
  98. Jin Z, Guo PP, Li XY, Ke JJ, Wang YL, Wu HS. Neuroprotective effects of irisin against cerebral ischemia/reperfusion injury via Notch signaling pathway. *Biomed Pharmacother* 2019, 120: 109452.
  99. Chen C, Li H, Ding F, Yang LL, Huang PY, Wang S, *et al.* Alterations in the hippocampal-thalamic pathway underlying secondarily generalized tonic-clonic seizures in mesial temporal lobe epilepsy: A diffusion tensor imaging study. *Epilepsia* 2019, 60: 121–130.



REVIEW

# Unique Pharmacology, Brain Dysfunction, and Therapeutic Advancements for Fentanyl Misuse and Abuse

Ying Han<sup>1</sup> · Lu Cao<sup>3</sup> · Kai Yuan<sup>2</sup> · Jie Shi<sup>1</sup> · Wei Yan<sup>2</sup> · Lin Lu<sup>2,3</sup>

Received: 17 December 2021 / Accepted: 13 February 2022 / Published online: 15 May 2022

© Center for Excellence in Brain Science and Intelligence Technology, Chinese Academy of Sciences 2022

**Abstract** Fentanyl is a fully synthetic opioid with analgesic and anesthetic properties. It has become a primary driver of the deadliest opioid crisis in the United States and elsewhere, consequently imposing devastating social, economic, and health burdens worldwide. However, the neural mechanisms that underlie the behavioral effects of fentanyl and its analogs are largely unknown, and approaches to prevent fentanyl abuse and fentanyl-related overdose deaths are scarce. This review presents the abuse potential and unique pharmacology of fentanyl and elucidates its potential mechanisms of action, including neural circuit dysfunction and neuroinflammation. We discuss recent progress in the development of pharmacological interventions, anti-fentanyl vaccines, anti-fentanyl/heroin conjugate vaccines, and monoclonal antibodies to attenuate fentanyl-seeking and prevent fentanyl-induced respiratory depression. However, translational studies and clinical trials are still lacking. Considering the present opioid crisis, the development of effective pharmacological and

immunological strategies to prevent fentanyl abuse and overdose are urgently needed.

**Keywords** Fentanyl abuse · Neural mechanisms · Pharmacological interventions · Fentanyl vaccines

## Introduction

Fentanyl was initially designed and synthesized as a valuable therapeutic for anesthesia and severe pain management. It exerts analgesic and rewarding effects by binding to and activating  $\mu$ -opioid receptors (MORs). Fentanyl has unique pharmacological properties, including a rapid onset of action, high potency at activating MOR-associated signaling *in vivo* (100-fold more potent than morphine), high lipophilicity, and the induction of muscle rigidity. Fentanyl abuse and overdose are becoming increasingly more common [1, 2]. Moreover, fentanyl is commonly mixed with cocaine, methamphetamine, heroin, and other illicit drugs among addicts. Over 40% of opioid-dependent people who inject drugs report lifetime purposeful fentanyl use, which is independently correlated with younger age, recent daily injection, and moderate/severe depression [3]. In the United States, urine drug test data has shown that positivity rates for non-prescribed fentanyl increased 1850% (from 0.9% in 2013 to 17.6% in 2018) among cocaine-positive samples and increased 798% (from 0.9% in 2013 to 7.9% in 2018) among methamphetamine-positive samples [4]. Positivity rates of co-occurring methamphetamine, cocaine, and heroin have also increased since 2013 among fentanyl-positive urine drug test results [5]. Fentanyl abuse is rarely found in China, and its manufacture, consumption, and storage are strictly controlled [6–9]. All fentanyl-related substances have been

---

✉ Wei Yan  
weiyang@bjmu.edu.cn

✉ Lin Lu  
linlu@bjmu.edu.cn

<sup>1</sup> National Institute on Drug Dependence and Beijing Key Laboratory of Drug Dependence, Peking University, Beijing 100191, China

<sup>2</sup> Peking University Sixth Hospital, Peking University Institute of Mental Health, NHC Key Laboratory of Mental Health (Peking University), National Clinical Research Center for Mental Disorders (Peking University Sixth Hospital), Beijing 100191, China

<sup>3</sup> Peking-Tsinghua Center for Life Sciences and PKU-IDG/McGovern Institute for Brain Research, Peking University, Beijing 100871, China

included in the supplementary list of controlled narcotic drugs and psychotropic substances with non-medical use in China since May 1, 2019 [10] (<http://www.mps.gov.cn/n2254314/n2254487/c6473090/content.html>).

Before and during the COVID-19 pandemic, the misuse and abuse of fentanyl appear to have persistently increased in the United States and elsewhere [11]. Overdose deaths and infections among people who use drugs, including fentanyl, increased during the COVID-19 crisis [12–14]. A study in Ontario, Canada, showed that fentanyl use increased by 108% among patients who were treated with opioid receptor agonists [15]. These patients have a high risk of COVID-19 infection, and their treatment can be problematic under conditions of quarantine and isolation and considering the scarcity of healthcare resources during the pandemic [16]. Prescription fentanyl demand has increased in critically ill COVID-19 patients who require mechanical ventilation, resulting in a shortage of intravenous fentanyl. The combined use of intravenous and transdermal fentanyl may be an option [17, 18]. However, intravenous fentanyl administration can disrupt brainstem respiratory systems, trigger respiratory depression, and impair the microcirculatory compensatory response to hemorrhage in the brainstem and lungs. Therefore, COVID-19 patients who use fentanyl should be closely monitored to avoid the exacerbation of clinical outcomes [19–21].

The present review introduces the receptor pharmacology and behavioral effects of fentanyl and elucidates the potential neural mechanisms that underlie fentanyl abuse from different perspectives, including neural circuit dysfunction and neuroinflammation. We also discuss the progress in the development of pharmacological interventions and active immunopharmacotherapies to attenuate fentanyl abuse and its side-effects.

## Abuse Potential of Fentanyl

Despite its widespread use for chronic pain and severe cancer pain in the clinical setting, fentanyl and its analogs have been shown to produce hyperlocomotion and strong rewarding and reinforcing effects and have abuse potential.

## Fentanyl Abuse and Withdrawal

Fentanyl induces a strong rewarding and reinforcing effects, which is the main contributor to its abuse and overdose deaths [22, 23]. Similar to morphine, fentanyl and its analogs, including isobutyrylfentanyl, crotonylfentanyl, para-fluorobutyrylfentanyl,  $\beta$ -methylfentanyl, paramethoxyfentanyl, fentanyl carbamate, and 3-furanylfentanyl, have MOR agonist-like hyperlocomotor effects in mice

[24–26]. Self-administration models are commonly used to evaluate the reinforcing effects of drugs. Both male and female rats exhibit stable fentanyl self-administration, drug-primed reinstatement, and yohimbine (stress)- and cue-induced reinstatement [27]. When rats self-administer fentanyl with short access (ShA; 1 h are trained to duration daily) or long access (LgA; 6 h duration daily), both ShA and LgA rats exhibit an increase in craving during fentanyl-, yohimbine-, and cue-induced reinstatement [27], indicating strong fentanyl abuse potential. Monroe and Radke established an aversion-resistant fentanyl self-administration model in mice, and found that when quinine is added to the fentanyl solution, mice still robustly respond and consume the solution in both a home-cage two-bottle choice task and operant response task [28]. In addition, a fentanyl vapor self-administration model has been successfully established in mice. This model recapitulates key features of opioid addiction, including the escalation of fentanyl intake, somatic signs of withdrawal, punishment-resistant fentanyl intake, and relapse [29]. A study that combined fentanyl vapor self-administration and a behavioral economics approach found more inelastic demand for fentanyl and an increase in maximal response output in LgA (12 h) rats compared with ShA (1 h) rats [30]. These studies indicate that fentanyl is a powerful addictive drug with high abuse potential, which partially explain the sharp rise in fentanyl abuse in recent years.

Although chronic high-dose fentanyl administration reduces anxiety-like behavior, lowers sensitivity to painful stimuli, and decreases sensitivity to cocaine, fentanyl withdrawal increases anxiety-like behavior [31]. Spontaneous and naloxone-precipitated withdrawal from 2 weeks of intermittent fentanyl exposure also causes weight loss and increases signs of distress in both mice and rats [32]. States of opioid dependence and withdrawal can profoundly influence fentanyl reinforcement and the efficacy of therapeutic medications. The reinforcing effects of fentanyl increase in morphine-withdrawn rats, reflected by a rightward shift of the fentanyl dose-response curve with an increase in maximal effectiveness, whereas the reinforcing effects of fentanyl decrease in opioid-dependent rats [33]. However, no antinociceptive cross-tolerance occurs with repeated microinjections of morphine and fentanyl into the ventrolateral periaqueductal gray, which may be attributable to the different signaling mechanisms that mediate morphine- and fentanyl-induced antinociception [34, 35].

## Influential Factors

The behavioral effects of fentanyl administration are influenced by sex, animal strain, and genetic and environmental factors. Fentanyl potently induces an acute

locomotor response and behavioral sensitization in female rats but more potently induces contextual reward in a conditioned place preference paradigm in male rats [36]. Under a fixed-ratio 5 schedule of reinforcement and multi-day progressive-ratio schedule in a behavioral economics analysis, female rats exhibit greater reinforcing efficacy of fentanyl than male rats. In a fentanyl *versus*. food choice procedure, male rats are more sensitive to fentanyl than females [37]. Remifentanyl self-administration-induced neuroadaptations have been shown to differ between males and females, indicating that sex-specific interventions that target opioid-induced adaptations should be developed [38]. Species differences have been found in the expression of fentanyl withdrawal-associated pain. Spontaneous and ongoing pain is preferentially expressed in rats, whereas withdrawal-associated thermal hyperalgesia is found only in mice [32]. Genetic and environmental factors influence the risk of opioid use disorder. *Hnrnp1* mutant mice exhibit lower behavioral sensitivity to fentanyl, suggesting that the expression of this gene may be a biomarker that reflects addictive properties [39].

### Unique Pharmacology of Fentanyl Treatment

Fentanyl is known to be a strong MOR agonist, similar to other opioids, such as morphine. The structural assessment of agonist efficacy at MORs has revealed different patterns between fentanyl and morphine [40, 41]. Principal component analysis and computational functional analysis have identified differences in ligand binding, intracellular signaling events, and receptor conformational changes between fentanyl and morphine, which may contribute to the greater efficacy of fentanyl over morphine [40–42]. Chevalier *et al.* exploited the X-ray structure of the MOR in complex with fentanyl and elucidated detailed fentanyl-MOR interaction profiles, thus providing a structural basis for the binding affinity, ligand recognition, and abuse potential of fentanyl and its analogs [43]. Using molecular dynamics techniques to identify binding events of the MOR with fentanyl and its analogs carfentanil and lofentanil, a previous study found that fentanyl induces the unique rotameric conformation of M153, which is required for inducing  $\beta$ -arrestin coupling [44]. These studies provide structural and molecular insights into the detailed mechanisms by which fentanyl binds to MORs, which is helpful for the further optimization of fentanyl-based analgesics with fewer side-effects and improved safety and efficacy.

Fentanyl and its analogs can have serious side-effects, such as increases in brain and kidney levels of malondialdehyde, neuroadaptive changes in the brain, and acceleration of the onset of acute postoperative pain [45, 46].

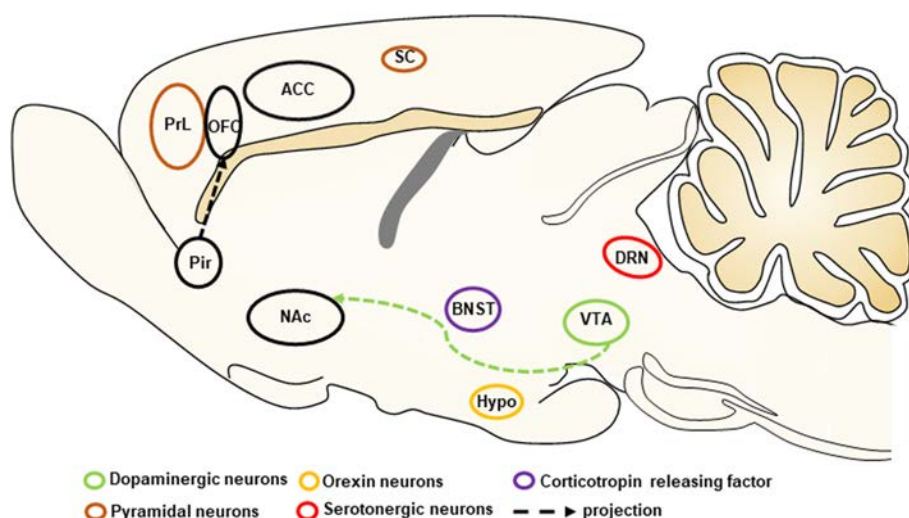
After exposure to fentanyl and its analogs in rats, the metabolite norfentanyl has been detected at high concentrations in urine and remains detectable for 3 days [47]. Fentanyl and its analogs have weak binding affinity for  $\kappa$ -opioid receptors,  $\delta$ -opioid receptors, and the  $\sigma 1$  receptor, which could contribute to the pharmacological actions and side-effects of these drugs [22, 48]. Fentanyl also interacts with non-opioid recombinant human neurotransmitter receptors and transporters, such as the  $\alpha 1A$  and  $\alpha 1B$  adrenoceptor subtypes and the dopamine  $D_1$  and  $D_4$  receptor subtypes [49]. Human ether-a-go-go-related gene channels have been associated with fentanyl-induced sudden death, and this is exacerbated by hypoxia, hypokalemia, or alkalosis [50, 51]. The complex receptor pharmacology of fentanyl contributes to the different clinical manifestations of fentanyl use, including respiratory and cardiothoracic side-effects and overdose deaths.

Recent studies have reported that fentanyl inhibits the viability and invasion of non-small-cell lung cancer cells by reversing the expression of microRNA-331-3p and histone deacetylase 5 [52]. Fentanyl has been shown to have anti-leukemia activity via suppression of the STAT5 and Ras pathways [53]. Fentanyl inhibits the progression, invasion, and migration of gastric cancer cells by suppressing activity of the phosphoinositide 3-kinase (PI3K)/protein kinase B (Akt)/matrix metalloproteinase-9 signaling pathway [54]. Fentanyl also stimulates tumor angiogenesis and promotes the migration of some but not all tested human lung cancer cells; this may be related to the activation of multiple pro-angiogenic signaling pathways, including vascular endothelial growth factor receptor 2/focal adhesion kinase/PI3K/Akt and small guanosine triphosphatases [55]. This study indicates that fentanyl use in cancer patients may have potential adverse effects and should be administered with caution. The  $\beta$ -arrestin 2 pathway plays an important role in recovery from opioid overdose [56], and ketamine may help attenuate some of the adverse physiological consequences of fentanyl use [21]. Li *et al.* found that ketamine combined with fentanyl and dexmedetomidine induces safer and more efficient anesthesia than ketamine alone [57]. These studies provide insights into the molecular basis and signaling pathways that mediate the multiple pharmacological effects of fentanyl and its analogs.

### Neural Circuit Dysfunction and Neuroinflammation Underlying Fentanyl Misuse and Abuse

Perinatal fentanyl exposure in newborn male and female mice leads to signs of spontaneous somatic withdrawal-related behavior, an increase in anxiety-like behavior, and impaired sensory function that lasts at least to adolescence

**Fig. 1** Schematic of potential neural mechanisms of fentanyl abuse. Specific types of neurons and neural circuits that are involved in fentanyl taking and seeking are shown in a sagittal cross-section of the brain. SC, somatosensory cortex; ACC, anterior cingulate cortex; VTA, ventral tegmental area; NAc, nucleus accumbens; Hypo, hypothalamus; BNST, bed nucleus of the stria terminalis; PrL, prelimbic cortex; OFC, orbitofrontal cortex; Pir, piriform cortex; DRN, dorsal raphe nucleus.



[58, 59]. Moreover, this exposure impairs synaptic transmission in the somatosensory cortex (SC) and anterior cingulate cortex (ACC), reduces ketamine-evoked cortical oscillations, and reduces the morphology of basal dendrites of pyramidal neurons in the SC [59]. Fentanyl binds to MORs in molecular-layer interneurons to reduce  $\gamma$ -aminobutyric acid (GABA)ergic neurotransmission to Purkinje cells, thus inhibiting sensory information processing [60]. In addition, fentanyl and morphine exposure during therapeutic hypothermia does not impair neurodevelopment and does not significantly affect cognition, language, or motor function in infants, but the long-term effects need further investigation [61]. Here, we describe the potential neural mechanisms that are involved in the pathophysiology of fentanyl abuse and fentanyl-related side-effects (Fig. 1).

## Reward and Stress Circuits

Drug addiction is viewed as a disorder of dopamine neurotransmission and the reward system in the brain, especially dopamine-releasing neurons in the ventral tegmental area (VTA) and its extensive projections [62, 63]. Previous studies have shown that fentanyl vapor self-administration causes long-lasting neuroadaptations of GABA<sub>B</sub> receptor-mediated currents in VTA dopamine neurons [29]. Both subcutaneous and intravenous fentanyl administration significantly increase dopamine release in the nucleus accumbens (NAc) and have reinforcing effects [64]. RNA sequencing has revealed that repeated fentanyl withdrawal elicits distinct transcriptional activity in the VTA and NAc in male and female rats [65]. In addition, fentanyl exhibits an affinity for, and effects on, recombinant human neurotransmitter transporters, including dopamine receptor subtypes [49]. These studies indicate that the

dopamine system mediates the rewarding and reinforcing effects of fentanyl abuse.

The orexin system is involved in the pathophysiology of opioid addiction, and orexin receptor antagonism attenuates drug-seeking behavior and relapse [66, 67]. Intermittent fentanyl self-administration induces a multifaceted addiction-like state and increases the number of orexin neurons in both the dorsomedial/perifornical hypothalamus and lateral hypothalamus [68]. The orexin receptor 1 antagonist SB-334867 decreases fentanyl intake, decreases motivation for fentanyl, and attenuates the cue-induced reinstatement of fentanyl-seeking [68, 69]. Intravenous fentanyl also decreases glutamate release and increases GABA release in the anterior hypothalamus, measured by the push-pull superfusion technique, and this is reversed by intrahypothalamic administration of the opioid receptor antagonist naloxone [70]. In addition, corticotropin-releasing factor (CRF) in the bed nucleus of the stria terminalis (BNST) is a critical driver of stress-induced relapse to drug-seeking. Intra-BNST microinjections of the CRF<sub>1</sub> receptor antagonist R121919 decreases cue-induced fentanyl-seeking and fentanyl-associated conditioned reinforcement in rats [71].

The SC and dorsal raphe nucleus (DRN) are critical regions involved in nociception and may also play a critical role in the process of fentanyl misuse. Fentanyl administration alters the firing activity of neurons and serotonin (5-hydroxytryptamine, 5-HT) efflux in the DRN, which may involve both opioid and 5-HT<sub>1A</sub> receptors [72, 73]. Autoradiographic mapping has shown that sufentanil tolerance is associated with the large-scale downregulation of MOR binding sites in various brain regions, including the DRN and SC [74]. Fentanyl decreases synaptic excitation and inhibits nociceptive stimulus-induced cortical activity in both the ACC and SC [59, 75]. Synchronization between the right SC and right hippocampus is



also impaired postoperatively after anesthesia with fentanyl and droperidol [76].

Chronic drug use is often accompanied by the loss of cognitive control, which is closely linked to the dysfunction of frontal cortex regions. Remifentanyl self-administration causes a long-lasting hypoactive basal state of pyramidal neurons in the prelimbic cortex (PrL) in females, and this is driven by a reduction of  $\alpha$ -amino-3-hydroxy-5-methyl-4-isoxazolepropionic acid receptor-mediated excitatory synaptic transmission [38]. In addition, remifentanyl self-administration has bidirectional effects on PrL layer 5/6 pyramidal neuron GABA<sub>B</sub>-G protein-coupled inwardly rectifying K<sup>+</sup> channel signaling in males [38]. Moreover, the chemogenetic activation of PrL pyramidal neurons reverses the deficits in cognitive flexibility, the basal hypoactive state, and remifentanyl-induced plasticity [38]. Reiner *et al.* developed a rat model of relapse to drug-seeking after food choice-induced voluntary abstinence and found that relapse to fentanyl-seeking is associated with an increase in activation in the orbitofrontal cortex (OFC) and its projection from the piriform cortex (Pir) but not in projections from the basolateral amygdala or thalamus. Using pharmacological inactivation and the anatomical disconnection of projections between the Pir and OFC, previous studies found that Pir–OFC projections play a critical role in relapse to fentanyl-seeking after voluntary abstinence [77, 78]. Future studies that use neural circuit-defined imaging and manipulation techniques may shed further light on the neurobiology of fentanyl relapse.

## Neuroinflammation

Opioid misuse, tolerance, and withdrawal have been reported to induce innate and adaptive neuroimmune dysfunction, affect neuronal function, and modulate the activation and phenotyping of microglial cells, thus producing proinflammatory effects in the brain [79]. Fentanyl self-administration profoundly alters innate immune proteins in the NAc and hippocampus. Fentanyl administration increases the expression of cytokines (e.g., tumor necrosis factor  $\alpha$  [TNF $\alpha$ ], interleukin-1 $\beta$  [IL-1 $\beta$ ], and IL5), chemokines (e.g., C-C motif chemokine 20), and interferon (IFN) proteins (e.g., IFN $\beta$  and IFN $\gamma$ ) in the NAc, decreases several interleukins (e.g., IL-4 and IL-7), chemokines (e.g., granulocyte-macrophage colony-stimulating factor, monocyte chemoattractant protein 1, and chemokine ligand 5), and interferons (e.g., IFN $\beta$  and IFN $\gamma$ ), and stimulates IFN gene protein expression in the hippocampus, which may initiate fentanyl misuse and perhaps the development of opioid use disorder [80, 81]. Fentanyl administration increases mechanical and thermal hyperalgesia, increases the expression of proinflammatory

cytokines (e.g., IL-1 $\beta$ , IL-6, and TNF- $\alpha$ ) in the spinal cord and dorsal root ganglia, and activates microglia in the spinal cord in rats [82]. Repeated fentanyl administration activates the NLRP3 inflammasome in astrocytes and serotonergic neurons and promotes NLRP3-dependent pyroptosis in the DRN. Furthermore, the antiinflammatory agent minocycline and the NLRP3 inhibitor MCC950 prevent fentanyl-induced antinociception and hyperalgesia [83]. Fentanyl has also been shown to reverse the lipopolysaccharide-induced release of TNF- $\alpha$ , IL-1 $\beta$ , and IL-10 by inhibiting Toll-like receptor-4 (TLR4) expression and glycogen synthase kinase-3 $\beta$  activation [84]. These studies indicate that neuroinflammation plays an important role in opioid-induced analgesia and fentanyl-induced hyperalgesia.

Gut microbiota and gut-brain communication also play a critical role in opioid use and opioid tolerance [85, 86]. Chronic opioid use alters fecal microbial diversity and composition and induces gut microbial dysbiosis in both rodents and humans, accompanied by increases in peripheral and central inflammation [87–89]. Moreover, microbial metabolites, such as short-chain fatty acids, are reduced, and intestinal and blood-brain barrier integrity is disrupted after opioid use, which could modulate the development, maturation, and function of microglia and exacerbate the neuroimmune responses [87, 89, 90]. Neuroinflammation that is induced by alterations of the microbiota can ultimately contribute to behaviors that are associated with opioid dependence [91, 92]. However, the effects of fentanyl use on the gut microbiota remain unknown. Future studies are needed to investigate the influence of alterations of the microbiota on brain immunity and function.

## Pharmacological Interventions to Prevent Fentanyl Abuse and Side-effects

Pharmacotherapies that target brain opioid receptors, including agonists (e.g., methadone and buprenorphine) and antagonists (e.g., naltrexone and naloxone), have been approved by the Food and Drug Administration (FDA) for the treatment of opioid use disorder. A meta-analysis has shown that these treatments can reduce mortality among opioid users [93]. A long-acting injection of extended-release buprenorphine has been shown to be feasible for users of heroin-containing fentanyl in an open-label trial [94]. However, these pharmacotherapies are limited by high relapse rates, a high risk of precipitating withdrawal in individuals who are exposed to fentanyl, and weak efficacy in preventing fentanyl overdose [95]. Thus, new approaches and novel medications are still needed for the treatment of opioid use disorder.

## Pharmacological Interventions to Prevent Fentanyl-Seeking

Here, we summarize the currently available pharmacological interventions to attenuate fentanyl taking and seeking in rodents and nonhuman primates (Table 1). These interventions mainly target opioid receptors and neurotransmitter and neuropeptide systems. Intravenous and subcutaneous administration of the long-lasting MOR antagonist methocinnamox reverses and prevents fentanyl-induced antinociception and respiratory depression in rats [96]. Methocinnamox attenuates heroin self-administration in rhesus monkeys, which continues to display efficacy even at very low plasma levels [97]. Contingent administration of the  $\kappa$ -opioid receptor agonists U50488 and nalfurafine decrease fentanyl choice, which is blocked by the selective  $\kappa$ -opioid receptor antagonist nor-binaltorphimine [98]. Levo-tetrahydropalmatine is an antagonist of dopamine receptors that suppresses the rewarding effects of fentanyl in the conditioned place preference paradigm by inhibiting the phosphorylation of extracellular signal-regulated kinase (ERK) and cyclic adenosine monophosphate response element binding protein (CREB) in the hippocampus, NAc, and prefrontal cortex in mice [99]. The acute stimulation of 5-HT<sub>2A</sub> receptors with the psychedelic 2,5-dimethoxy-4-iodoamphetamine decreases the economic demand for fentanyl and food after intermittent and continuous-access self-administration [100]. In a rat model of relapse, the glucagon-like peptide-1 receptor (GLP-1R) agonist exendin-4 reduces fentanyl self-administration in rats but causes malaise-like behavior. A novel dual agonist of GLP-1Rs and neuropeptide Y<sub>2</sub> receptors, GEP44, reduces fentanyl self-administration with fewer adverse effects compared with exendin-4 [101, 102]. The growth hormone secretagogue receptor antagonist JMV2959 reduces fentanyl-induced conditioned place preference and fentanyl self-administration [64]. The glucocorticoid receptor antagonist PT150 reduces footshock-induced fentanyl-seeking [103]. Intra-BNST injections of the CRF<sub>1</sub> receptor antagonist R121919 decreases cue-induced responding to fentanyl in both opioid-dependent and nondependent rats [71]. Compared with ShA and LgA to fentanyl, intermittent access increases the motivation for fentanyl and total intake, which is reversed by the orexin receptor-1 antagonist SB334867 [68].

## Pharmacological Interventions to Attenuate Fentanyl-Induced Respiratory Depression

Fentanyl overdose fatalities and the opioid crisis are mainly attributable to drug-induced respiratory depression. Fentanyl overdose induces hippocampal ischemia, accompanied by delayed leukoencephalopathy [104]. Fentanyl but not morphine alters mitochondrial morphology, depending

on the dosage and cell type, and this may be associated with neuronal apoptosis [105, 106]. Fentanyl-induced respiratory depression is associated with electrocortical changes, underscoring the importance of considering the activity of cortical and subcortical areas when evaluating fentanyl-induced respiratory depression [107]. Fentanyl and its analogs can rapidly produce airway closure and rigidity in the upper airway and diaphragm chest wall, which may involve  $\alpha$ -adrenergic and cholinergic receptor-mediated mechanical failure of the respiratory and cardiovascular systems [49, 108].

We summarize currently available pharmacological interventions to prevent fentanyl-induced respiratory depression in Table 2. D-amphetamine hastens the recovery of arterial pH and partial pressure of CO<sub>2</sub>, O<sub>2</sub>, and sO<sub>2</sub> in rats, promotes the alleviation of respiratory depression, and escalates the return of consciousness following high-dose fentanyl [109]. The G protein-biased cannabinoid CB<sub>2</sub> receptor agonist LY2828360 decreases fentanyl-induced respiratory depression in wildtype mice but not in G protein-biased CB<sub>2</sub> receptor knockout mice [110]. The acyclic cucurbit[n]uril molecular container calabadiol 1 reverses fentanyl-induced respiratory depression in rats [111]. The selective  $\alpha 4\beta 2$  nicotinic receptor agonist A85380 confers robust and rapid reversal of fentanyl-induced respiratory depression, without any obvious side effects. A85380 also significantly decreases respiratory depression and apnea when co-administered with fentanyl and remifentanyl [112]. Brackley *et al.* found that the peptide oxytocin receptor agonist oxytocin acetate and the non-peptide oxytocin receptor agonist WAY-267464 without vasopressin-1A receptor cross-activation rescues fentanyl-induced respiratory depression [113]. The clinically approved superoxide dismutase mimetic 4-hydroxy-2,2,6,6-tetramethylpiperidine-N-oxyl (Tempol) has also been reported to attenuate the cardiorespiratory depressant effects of fentanyl without affecting its analgesic effects [114].

Altogether, mounting preclinical data provide proof-of-concept of the efficacy of potential pharmacological interventions to attenuate fentanyl-seeking and prevent fentanyl-induced respiratory depression, demonstrating their potential for the treatment of fentanyl abuse and overdose. However, translational studies and clinical trials still need to be conducted.

## Progress in the Development of Anti-Fentanyl Conjugate Vaccines as Candidate Medications

The management and prevention of fentanyl-related overdoses are notable challenges. Anti-opioid vaccines may be a promising therapeutic approach to prevent opioid overdose and reduce opioid-induced behavior, including drug

**Table 1** Summary of recent findings on pharmacological interventions to attenuate fentanyl taking and seeking.

Drug	Route of administration	Pharmacological target	Subjects	Paradigm (fentanyl dose, model)	Main findings	References
SB-334867	IP	Orexin-1 receptor antagonist	Male Sprague-Dawley rats	Self-administration and behavioral economics procedure	SB-334867 decreases motivation for fentanyl without affecting drug consumption at null cost	Fragale <i>et al.</i> [69]
R121919	Intra-BNST injections	Corticotropin-releasing factor-1 receptor antagonist	Male Sprague-Dawley rats	2.5 mg/kg, infusion, self-administration	These patterns of responding with R121919 treatment result in less fentanyl-associated conditioned reinforcement during test	Gyawali <i>et al.</i> [71]
JMV2959	IP	Growth hormone secretagogue receptor antagonist	Male adult Wistar rats	20 or 30 µg/kg, SC; 10 µg/kg, IV	Pretreatment with JMV2959 significantly reduces the number of active lever presses and reduces fentanyl seeking/relapse-like behavior in rats on day 12 of forced abstinence	Sustkova-Fiserova <i>et al.</i> [64]
Methocinnamox	SC	µ-Opioid receptor antagonist	Male and female rhesus monkeys	0.00032 mg/kg, infusion, self-administration	Methocinnamox selectively reduces opioid self-administration and remains effective at times when its plasma levels are very low	Maguire <i>et al.</i> [97]
U50488 and nalfurafine	IV	κ-Opioid receptor agonists	Male and female Sprague-Dawley rats	0, 0.32–10 µg/kg, infusion, self-administration	Both U50488 and nalfurafine decrease fentanyl choice when administered contingently	Townsend [98]
PT150	IP	Glucocorticoid receptor antagonist	Male and female Sprague-Dawley rats	2.5 µg/kg, infusion, self-administration	Both footshock and yohimbine reinstate fentanyl-seeking; only footshock-induced reinstatement is decreased by PT150 (50 and 100 mg/kg)	Hammerslag <i>et al.</i> [103]
Levo-tetrahydropalmatine	IV	Dopamine receptor antagonist	Male C57BL/6 mice	0.05 mg/kg, conditioned place preference	Levo-tetrahydropalmatine suppresses the rewarding properties of fentanyl-induced conditioned place preference; the inhibitory effect may be related to the suppression of ERK and CREB phosphorylation in the hippocampus, nucleus accumbens, and prefrontal cortex in mice	Du <i>et al.</i> [99]
GEP44	SC	Novel dual agonist of glucagon-like peptide-1 receptors and neuropeptide Y Y <sub>2</sub> receptors	Male Sprague-Dawley rats	2.5 µg/kg, self-administration	GEP44 attenuates opioid taking and seeking at a dose that does not suppress food intake or produce adverse malaise-like effects in fentanyl-experienced rats	Zhang <i>et al.</i> [101]
2,5-Dimethoxy-4-iodoamphetamine (DOI)	IP	Psychedelic 5-HT <sub>2A</sub> receptor agonist	Male Sprague-Dawley rats	2.5 µg/kg, injection, self-administration, intermittent and continuous schedules	DOI acts through 5-HT <sub>2A</sub> receptors to alter economic demand for fentanyl; in economic food demand experiments, DOI (0.4 mg/kg) increases demand elasticity and reduces food consumption	Martin <i>et al.</i> [100]

**Table 1** continued

Drug	Route of administration	Pharmacological target	Subjects	Paradigm (fentanyl dose, model)	Main findings	References
SB334867	IP	Orexin-1 receptor antagonist	Male Sprague-Dawley male rats	Intermittent self-administration	Addiction-like behaviors induced by intermittent access to fentanyl are reversed by SB-334867	Fragale <i>et al.</i> [68]

IP, intraperitoneal; SC, subcutaneous; IV, intravenous; BNST, bed nucleus of the stria terminalis.

**Table 2** Summary of recent findings on pharmacological interventions to prevent fentanyl-induced respiratory depression.

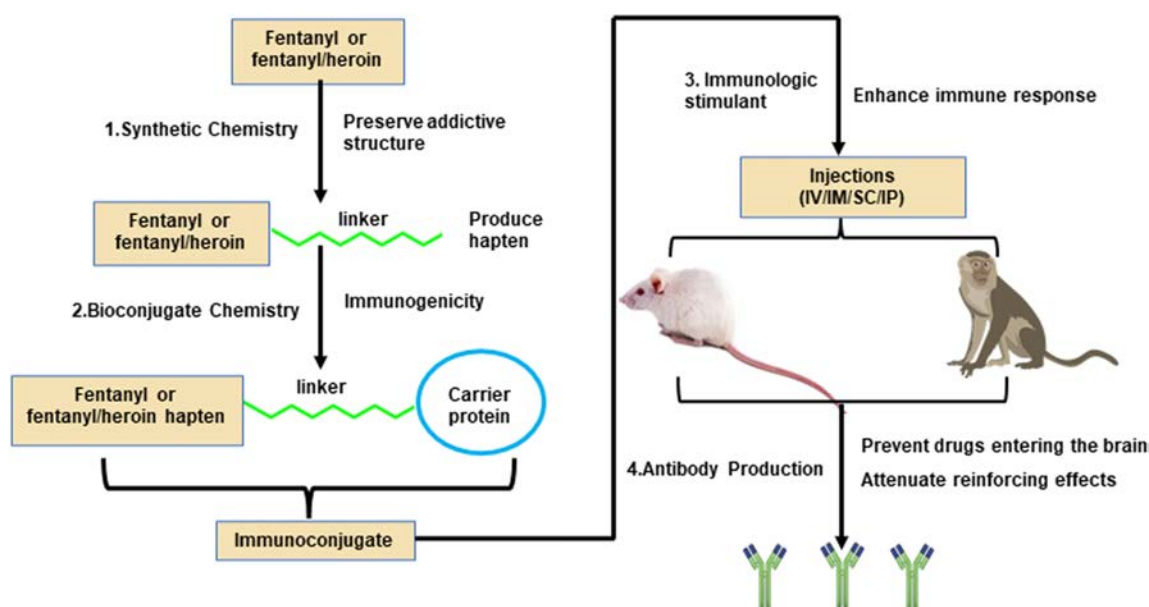
Drug	Route of administration	Pharmacological target	Subjects	Paradigm (fentanyl dose, model)	Main findings	References
A85380	SC	$\alpha 4\beta 2$ nicotinic acetylcholine receptor	Male and female Sprague-Dawley rats	20 $\mu\text{g/kg}$ , IV	Co-administration of A85380 (0.06 mg/kg) and fentanyl or remifentanyl markedly reduces respiratory depression and apnea and enhances fentanyl-induced analgesia	Ren <i>et al.</i> [112]
D-amphetamine	IV	Dopamine D <sub>1</sub> receptor	Male and female Sprague-Dawley rats	55 $\mu\text{g/kg}$ , IV	D-amphetamine attenuates respiratory acidosis, increases arterial oxygenation, and accelerates the return of consciousness in the setting of fentanyl intoxication	Moody <i>et al.</i> [109]
LY2828360	IP	G protein-biased cannabinoid CB <sub>2</sub> receptor	Wildtype and CB <sub>2</sub> knockout mice	0.2 mg/kg, IP	Combination of CB <sub>2</sub> agonist and fentanyl may represent a safer adjunctive therapeutic strategy compared with a narcotic analgesic alone by attenuating the development of opioid-induced respiratory depression	Zavala <i>et al.</i> [110]
Calabadion 1	IV	Acyclic cucurbit[n]uril molecular container	Male Sprague-Dawley rats	12.5 or 25 $\mu\text{g/kg}$ , IV	Calabadion 1 selectively and dose-dependently reverses the respiratory and central nervous system side-effects of fentanyl	Thevathasan <i>et al.</i> [111]
Oxytocin and WAY-267464	IP	Oxytocin receptor	Male Sprague-Dawley rats	60 nmol/kg, IV	Without vasopressin 1A receptor cross-activation, peptide and non-peptide agonist activation of oxytocin receptors (oxytocin and WAY-267464) rescue fentanyl-induced respiratory depression	Brackley <i>et al.</i> [113]
Methocinnamox	IV and SC	$\mu$ -Opioid receptor	Male Sprague-Dawley rats	0.0032–0.178 mg/kg, IV	Methocinnamox reverses and prevents fentanyl-induced antinociception and respiratory depression	Jimenez <i>et al.</i> [96]

IP, intraperitoneal; IV, intravenous; SC, subcutaneous.

self-administration in mice, rats, and nonhuman primates [14, 115]. Vaccines produce fentanyl-specific antibodies and sequester large amounts of these drugs in blood, thus reducing biodistribution in the brain and preventing binding to targeted receptors in the brain [116, 117]. Compared with FDA-approved small-molecule pharmacotherapies (e.g., methadone, buprenorphine, and naltrexone), fentanyl vaccines offer several potential clinical benefits, including prolonged protection because of the

relatively long serum half-life, fewer side-effects by directly binding and sequestering drugs in the periphery, high selectivity, and no abuse liability. Vaccines that target opioids (e.g., heroin, morphine, oxycodone, and hydrocodone) and psychostimulants (e.g., cocaine and methamphetamine) have shown promising results in animal models and are currently in various stages of preclinical development [118–121]. Anti-fentanyl vaccines are still in the early stages of development. Currently, several fentanyl





**Fig. 2** Design and production of fentanyl and fentanyl/heroin conjugate vaccines. Using synthetic chemistry, a specific linker is added to the fentanyl or fentanyl/heroin without affecting biological functionality to create a hapten. Linkage of the fentanyl or fentanyl/heroin hapten to the carrier protein occurs through bioconjugate chemistry, and subsequent adjuvating of the immunologic stimulant generates complete vaccines. These vaccines have been tested in

and fentanyl/heroin vaccines have been developed with different designs (Fig. 2), including the optimization of fentanyl-based haptens and linker chemistry, the choice of carrier proteins and adjuvants, delivery strategies, and the development of novel carriers and delivery platforms (Table 3).

### Fentanyl Vaccines in Mice and Rats

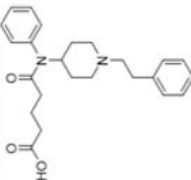

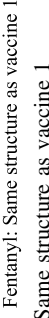

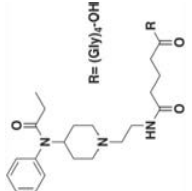
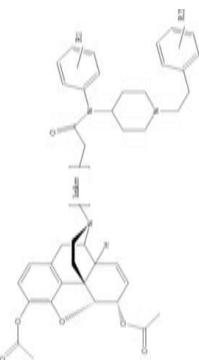
Considering the devastating opioid crisis worldwide, different carrier proteins, adjuvants, delivery strategies, and fentanyl-based haptens are being developed to improve fentanyl vaccine efficacy, shelf life, and safety. A vaccine that consists of a fentanyl-based hapten that is conjugated to the keyhole limpet hemocyanin (KLH) carrier protein or GMP-grade subunit KLH reduces fentanyl distribution in the brain and reduces fentanyl-induced antinociception and respiratory depression in mice and rats [122]. Fentanyl-tetanus toxoid (TT) conjugate vaccines elicit high anti-fentanyl antibody titers and ablate lethal doses of fentanyl and its analogs, including 3-methylfentanyl and  $\alpha$ -methylfentanyl [123]. A fentanyl-TT conjugate vaccine has also been reported to decrease fentanyl reinforcement, increase food reinforcement in a fentanyl *versus*. food choice procedure, and prevent the expression of opioid withdrawal-associated increases in fentanyl choice in male

mice, rats, and nonhuman primates, where they have been shown to enhance innate and adaptive immunity, produce fentanyl-specific antibodies, sequester opioid drugs in the periphery, and prevent them from entering the brain, thus attenuating the reinforcing effects of fentanyl or fentanyl-contaminated heroin. IV, intravenous; IM, intramuscular; SC, subcutaneous; IP, intraperitoneal.

and female rats [124, 125]. Carfentanil is  $\sim 100$ -fold more potent than fentanyl and can be lethal at extremely low doses. Pretreatment with the opioid receptor antagonist naltrexone decreases the seeking of fentanyl and heroin but not carfentanil [126]. Recently, two synthetic vaccines, Carfen-*ester*-TT and Carfen-*p-phenyl*-TT, have been shown to reduce carfentanil biodistribution in the brain and blunt carfentanil-induced antinociception and respiratory depression [127].

A recent study found that a fentanyl vaccine that is adjuvanted with a heat-labile toxin of *E. coli*, including dmLT and LTA1, elicits higher levels of anti-fentanyl antibodies than the traditional adjuvant alum. Vaccination with sublingual dmLT or intranasal LTA1 confers the robust blockade of fentanyl-induced analgesia and strong central nervous system penetration of anti-fentanyl antibodies [128]. This study also found that dmLT and LTA1 adjuvants and mucosal delivery enhance the immunogenicity and efficacy of fentanyl conjugate vaccines. A novel fentanyl vaccine, composed of a novel fentanyl hapten (para-AmFenHap), a safe and immunogenic carrier protein TT, and a potent liposomal adjuvant (ALF43A) that contains monophosphoryl lipid A, has also been synthesized and shown to prevent the side-effects of fentanyl [129]. The stimulation of TLR5 may also be an option to improve antibody production and enhance innate and adaptive immunity during active vaccination against

**Table 3** Summary of active immunopharmacotherapies developed for fentanyl abuse.

Vaccine	Hapten structure	Carrier protein	Adjuvant	Route of administration	Vaccinations/overall time	Subjects	Main findings	References
1		TT	Alum and CpG	SC	3 injections (0, 2, 4 weeks)	Male Swiss-Webster mice	Single conjugate vaccine elicits high levels of antibodies with cross-reactivity for a wide panel of fentanyl analogs and protects against lethal fentanyl doses	Bremer <i>et al.</i> [123]
2		TT or KLH	Alum and CpG	SC	3 injections (0, 2, 4 weeks)	Female BALB/c mice	Admixture vaccines sequester opioid drugs in blood and reduce fentanyl-induced antinociception	Hwang <i>et al.</i> [142, 143]
3		TT	CpG and alhydrogel	IV	3 injections (0, 3, 17 weeks)	Male and female Sprague-Dawley rats	Vaccination is very effective in preventing the binding of fentanyl to $\mu$ -opioid receptors in the central nervous system and reduces fentanyl-induced antinociception and its reinforcing effects	Townsend <i>et al.</i> [124]
4		TT	Alhydrogel	IM	6 injections (0, 2, 4, 9, 19, 44 weeks)	Adult male rhesus monkeys	The vaccine increases plasma fentanyl levels and reduces fentanyl-induced antinociception	Tenney <i>et al.</i> [133]
5		KLH	Alum	SC	3 injections (0, 2, 4 weeks)	Male BALB/c mice and male Holtzman rats	The vaccine reduces fentanyl-induced antinociception in hot-plate test, respiratory depression, and bradycardia over a range of cumulative subcutaneous fentanyl doses	Raleigh <i>et al.</i> [122]
6		KLH	Alum and CpG ODN 1826	IP	4 injections (0, 2, 4, 7 weeks)	Female BALB/c mice	New vaccines developed from chemically contiguous haptens composed of both heroin- and fentanyl-like domains; they confer robust protection against heroin but attenuate protection against fentanyl	Natori <i>et al.</i> [141]

**Table 3** continued

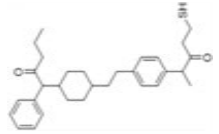
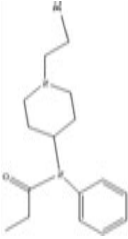
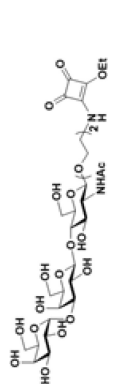

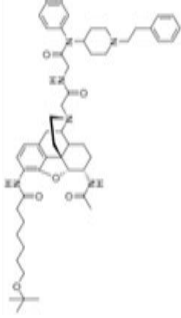
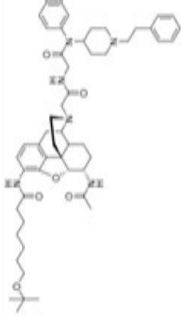
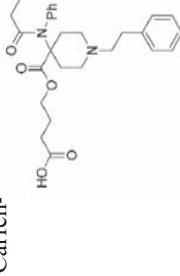
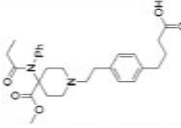
Vaccine	Hapten structure	Carrier protein	Adjuvant	Route of administration	Vaccinations/overall time	Subjects	Main findings	References
7	Same structure as vaccine 5	KLH	Alum	IP	3 injections (0, 3, 8 weeks)	Female A/J mice	Monoclonal antibodies generated in hybridomas from mice vaccinated with a fentanyl conjugate vaccine reverse fentanyl/carfentanil-induced antinociception	Smith <i>et al.</i> [135]
8		TT	ALF43A	IM	4 injections (0, 3, 6, 14 weeks)	Female BALB/c mice	The vaccine induces high-affinity antibodies against fentanyl and its highly potent analogs and protects mice against fentanyl-induced antinociceptive effects	Barrientos <i>et al.</i> [129]
9		KLH or CRM	Alum	IM	4 injections (0, 14, 28, 29 weeks)	Male BALB/c mice and male and female Sprague-Dawley rats	Prophylactic vaccination reduces fentanyl- and sufentanil-induced respiratory depression, antinociception, and bradycardia; therapeutic vaccination reduces intravenous fentanyl self-administration	Robinson <i>et al.</i> [131]
10		OVA	Alum	IP	3 injections (2 weeks)	$\alpha$ 1,3GalT knockout mice	The vaccine reduces psychoactive effects of fentanyl without addition of the immunostimulant CpG oligodeoxynucleotide	Wang <i>et al.</i> [132]
11		CRM or TT	Alhydrogel	IV	4 injections (0, 14, 42, 70 days)	Male and female Sprague-Dawley rats	The vaccine attenuates thermal antinociceptive effects of fentanyl/heroin but has no effects on fentanyl/heroin mixture self-administration	Townsend <i>et al.</i> [139]
12	Fentanyl: Same structure as vaccine 1 Same structure as vaccine 5	KLH	Alum	IP	3 injections (0, 2, 4 weeks)	Male and female BALB/c mice and male Sprague-Dawley rats	$\alpha$ -Fentanyl monoclonal antibodies generated from hybridomas via magnetic enrichment; passive immunization reduces fentanyl-induced antinociception, respiratory depression, and bradycardia	Baehr <i>et al.</i> [136]

Table 3 continued

Vaccine	Hapten structure	Carrier protein	Adjuvant	Route of administration	Vaccinations/overall time	Subjects	Main findings	References
13	Same structure as vaccine 1 	CRM	$\delta$ -Inulin	SC	3 injections (2 weeks) in mice 4 injections (0, 1, 2, 4 months) in monkeys	Male BALB/c mice and cynomolgus monkeys	A novel vaccine against heroin and fentanyl developed through the optimization of adjuvants and enhancing stability <i>via</i> lyophilization; it produces high-affinity antibodies and reduces fentanyl/heroin-induced antinociception	Blake <i>et al.</i> [137]
14		CRM	Alum	IP	4 injections (0, 2, 4, 7 weeks)	Female BALB/c mice	The vaccine with an optimized dual hapten produces antibodies with nanomolar affinities and blocks the analgesic effects of fentanyl-contaminated heroin	Park <i>et al.</i> [138]
15	Same structure as vaccine 1	TT	Liposomal	IM	4 injections (0, 3, 6, 14 weeks)	Female BALB/c mice	Combining TT-6-AmHap and TT-para-AmFen-Hap yielded an effective bivalent vaccine that ablates the effects of heroin and fentanyl	Barrientos <i>et al.</i> [140]
16	Same structure as vaccine 7	CRM	dmLT or LTA1	IM	2 injections (0, 4 weeks)	Female BALB/c mice	dmLT or LTA1 adjuvants and mucosal delivery may be attractive strategies for improving the efficacy of vaccines against fentanyl use disorder	Stone <i>et al.</i> [128]
17	Same structure as vaccine 1	CRM	Alum	IM	4 injections (0, 3, 8, 15 weeks)	Rhesus monkeys	Fentanyl vaccine effectively reduces fentanyl vs food choice in rhesus monkeys	Townsend <i>et al.</i> [133]
18	Carfen-  Carfen-p-phenyl: 	TT	alum and CpG	IP	4 injections (0, 2, 4, 9 weeks)	Female Swiss-Webster mice	The two synthetic vaccines reduce carfenamil-induced antinociception and respiratory depression	Eubanks <i>et al.</i> [127]

TT, tetanus toxoid; CpG, cytosine-phosphodiester-guanine oligodeoxynucleotide 1826; KLH, keyhole limpet hemocyanin; CRM, diphtheria toxin; OVA, ovalbumin; IV, intravenous; IM, intramuscular; SC, subcutaneous; IP, intraperitoneal.



fentanyl and its analogs [130]. Robinson *et al.* developed prophylactic vaccination and therapeutic vaccination that consists of novel fentanyl-based haptens that are conjugated to carrier proteins. Prophylactic vaccination reduces fentanyl- and sufentanil-induced respiratory depression, antinociception, and bradycardia in mice and rats, and therapeutic vaccination reduces fentanyl self-administration in rats [131]. Wang *et al.* developed a new fentanyl conjugate vaccine that is conjugated to the Gal $\alpha$ 1-3Gal epitope, which is based on preformed antibody-assisted antigen presentation, and this vaccine reduces fentanyl-associated side-effects [132].

### Fentanyl Vaccines in Nonhuman Primates and Monoclonal Antibodies against Fentanyl

In non-opioid-dependent rats and rhesus monkeys, fentanyl vaccine administration blunts fentanyl reinforcement and increases food reinforcement for a prolonged period [124, 133]. A fentanyl-CRM<sub>197</sub> conjugate vaccine produces anti-fentanyl antibodies and attenuates fentanyl *versus* food choice in male and female rhesus monkeys [133]. A fentanyl-TT conjugate vaccine increases plasma fentanyl levels ~6-fold and shifts fentanyl potency at least 10-fold in both schedule-controlled responding and thermal nociception assays in male rhesus monkeys [134]. Monoclonal antibodies (mAbs), especially 6A4, have been generated in hybridomas derived from mice vaccinated with a fentanyl conjugate vaccine. These mAbs have been reported to sequester large amounts of these drugs in blood, reverse fentanyl/carfentanil-induced antinociception, and prevent fentanyl-induced lethality, which could be a promising approach to treat opioid overdose and opioid use disorder [135].  $\alpha$ -Fentanyl mAbs have been generated from mice immunized with a fentanyl-sKLH conjugate vaccine. Pretreatment with these mAbs reduces fentanyl-induced antinociception, respiratory depression, and bradycardia in mice and rats [136]. These studies indicate that mAbs against fentanyl and its analogs have potential applications for the treatment of opioid use disorder and the prevention of overdose and toxicity.

### Fentanyl/Heroin Vaccines

Overdose deaths caused by opioids have increased substantially in recent years, attributable to the adulteration of these drugs with fentanyl. Many immunopharmacotherapeutic studies have focused on developing new vaccines that can effectively target dual haptens to produce antibodies that are able to sequester fentanyl and contaminated opioids in the periphery. Blake *et al.* developed a heroin/fentanyl combination vaccine that consists of inulin-based formulations

(Advax) that contain a CpG oligodeoxynucleotide and act as effective adjuvants when combined with a heroin conjugate. This vaccine produces high-opioid-affinity serum antibodies and reduces antinociception in both mice and cynomolgus monkeys [137]. By implementing an optimized dual hapten, a vaccine has been developed to produce antibodies that are able to bind fentanyl-contaminated heroin in the periphery, thus effectively blocking their analgesic effects [138]. A dual fentanyl/heroin vaccine generates high-affinity anti-fentanyl and anti-heroin antibodies and decreases the antinociceptive potency of a fentanyl/heroin mixture but does not attenuate combined fentanyl/heroin self-administration [139]. By combining TT-6-AmHap (a heroin monovalent vaccine) and TT-para-AmFenHap (a fentanyl monovalent vaccine) to formulate a bivalent vaccine that is adjuvanted with liposomes that contain monophosphoryl lipid A adsorbed on aluminum hydroxide, a study found that this bivalent conjugate vaccine induces dual immunogenic responses that ablate the effects of both heroin and fentanyl in mice [140]. A chemically contiguous heroin-fentanyl vaccine that uses a hapten with one epitope that has domains for both fentanyl and heroin has also been developed. This vaccine confers protection against heroin and fentanyl in an antinociception analysis [141]. Admixture vaccination strategies have also been applied to target two different drug species and combat fentanyl-adulterated heroin [142, 143]. These new fentanyl/heroin vaccines appear promising but need further testing for possible translation to clinical use.

### Conclusions and Perspectives

In conclusion, fentanyl and its analogs have complex receptor pharmacology and produce multifaceted behavioral effects and clinical characteristics, including analgesia, anesthesia, sedation, and respiratory and cardi thoracic side-effects. Fentanyl transdermal microneedles have a rapid onset of antinociceptive action, providing an effective mode of opioid delivery for immediate pain relief with limited side-effects [144]. Microneedles that are loaded with low doses of fentanyl may reduce the risk of overdose fatalities. Developing novel technologies to reduce the clinical dose of fentanyl may be useful for mitigating the opioid crisis. Mechanistically, the behavioral effects of fentanyl likely result from a combination of its chemistry, receptor pharmacology, receptor signaling, rapid distribution to the central nervous system, neural circuit dysfunction, and neuroinflammation. However, the detailed neurobiological mechanisms that contribute to fentanyl abuse and overdose remain largely unknown. Novel effective pharmacological and psychosocial treatments and vaccines are urgently needed.

Drug self-administration procedures and investigations of the choice between opioids and non-drug reinforcers are recommended to evaluate the effectiveness of candidate interventions in preclinical studies. States of opioid dependence and withdrawal should also be considered because such states can profoundly influence the results. The currently available small-molecule pharmacotherapies that mainly target MORs have limited efficacy to combat fentanyl abuse and overdose. Further elucidation of the molecular and structural bases of biased signaling and interactions between fentanyl and MORs is promising for optimizing fentanyl-based analgesics with fewer side-effects, a better safety profile, and higher efficacy. Future studies are needed to improve the effectiveness of opioid medications, such as G-protein biased MOR agonists, and develop novel non-opioid medications that target other systems, such as neurotransmitter and neuropeptide systems. Traditional Chinese medicine, including herbal therapy and acupuncture, has few side-effects and could also be considered for the treatment of fentanyl addiction [145–147].

Anti-fentanyl vaccines produce antibodies that sequester opioid drugs in the periphery and prevent them from entering the brain and activating reward circuits. They have high selectivity and long-lasting efficacy and do not interfere with endogenous opioids, thus providing safe and cost-effective interventions for the management of fentanyl abuse and overdose. However, although several fentanyl and fentanyl/heroin vaccines have been shown to be effective in rodents and nonhuman primates, these vaccines are still in preclinical stages and need to be translated to the clinical treatment of opioid use disorder and fentanyl overdose. To facilitate preclinical-to-clinical translation and increase the success of drug discovery, it is critical to develop clinically viable formulations and optimize rational vaccine designs to maximize efficacy, understand the immunological mechanisms that underlie drug-motivated behavior and vaccine-evoked immune responses, and identify biomarkers that are predictive of individual variability and support patient stratification.

**Acknowledgements** This review was supported by the National Key Research and Development Program of China (2019YFC0118604) and the National Natural Science Foundation of China (32071058).

**Conflict of Interest** The authors declare that they do not have any conflicts of interest.

## References

1. Volkow ND. The epidemic of fentanyl misuse and overdoses: Challenges and strategies. *World Psychiatry* 2021, 20: 195–196.
2. Di Trana A, Del Rio A. Fentanyl analogues potency: What should be known. *Clin Ter* 2020, 171: e412–e413.
3. Chandra DK, Altice FL, Copenhaver MM, Zhou X, Didomizio E, Shrestha R. Purposeful fentanyl use and associated factors among opioid-dependent people who inject drugs. *Subst Use Misuse* 2021, 56: 979–987.
4. LaRue L, Twillman RK, Dawson E, Whitley P, Frasco MA, Huskey A. Rate of fentanyl positivity among urine drug test results positive for cocaine or methamphetamine. *JAMA Netw Open* 2019, 2: e192851.
5. Twillman RK, Dawson E, LaRue L, Guevara MG, Whitley P, Huskey A. Evaluation of trends of near-real-time urine drug test results for methamphetamine, cocaine, heroin, and fentanyl. *JAMA Netw Open* 2020, 3: e1918514.
6. Fang YX, Wang YB, Shi J, Liu ZM, Lu L. Recent trends in drug abuse in China. *Acta Pharmacol Sin* 2006, 27: 140–144.
7. Lu L, Fang YX, Wang X. Drug abuse in China: Past, present and future. *Cell Mol Neurobiol* 2008, 28: 479–490.
8. Sun HQ, Bao YP, Zhou SJ, Meng SQ, Lu L. The new pattern of drug abuse in China. *Curr Opin Psychiatry* 2014, 27: 251–255.
9. Zhu WL, Zhang W, Li JL, Ding ZB, Huang YJ, Lu L. The abuse of anesthetic propofol: Associated with cognitive impairment. *Sci China Life Sci* 2018, 61: 1428–1431.
10. Bao YP, Meng SQ, Shi J, Lu L. Control of fentanyl-related substances in China. *Lancet Psychiatry* 2019, 6: e15.
11. Ciccarone D. The rise of illicit fentanyls, stimulants and the fourth wave of the opioid overdose crisis. *Curr Opin Psychiatry* 2021, 34: 344–350.
12. Striley CW, Hoefflich CC. Converging public health crises: Substance use during the coronavirus disease 2019 pandemic. *Curr Opin Psychiatry* 2021, 34: 325–331.
13. DiGennaro C, Garcia GGP, Stringfellow EJ, Wakeman S, Jalali MS. Changes in characteristics of drug overdose death trends during the COVID-19 pandemic. *Int J Drug Policy* 2021, 98: 103392.
14. Kosten TR, Petrakis IL. The hidden epidemic of opioid overdoses during the coronavirus disease 2019 pandemic. *JAMA Psychiatry* 2021, 78: 585–586.
15. Morin KA, Acharya S, Eibl JK, Marsh DC. Evidence of increased fentanyl use during the COVID-19 pandemic among opioid agonist treatment patients in Ontario, Canada. *Int J Drug Policy* 2021, 90: 103088.
16. Sun YK, Bao YP, Kosten T, Strang J, Shi J, Lu L. Editorial: Challenges to opioid use disorders during COVID-19. *Am J Addict* 2020, 29: 174–175.
17. Herndon KT, Claussen KS, Braithwaite JJ. A novel clinical consideration to conserve parenteral fentanyl during the COVID-19 pandemic. *Anesth Analg* 2020, 131: 1355–1357.
18. Kang N, Alrashed MA, Place EM, Nguyen PT, Perona SJ, Erstad BL. Clinical outcomes of concomitant use of enteral and intravenous sedatives and analgesics in mechanically ventilated patients with COVID-19. *Am J Health Syst Pharm* 2022, 79: S21–S26.
19. Blackwood CA, Cadet JL. COVID-19 pandemic and fentanyl use disorder in African Americans. *Front Neurosci* 2021, 15: 707386.
20. Tabatabai M, Kitahata LM, Collins JG. Disruption of the rhythmic activity of the medullary inspiratory neurons and phrenic nerve by fentanyl and reversal with nalbuphine. *Anesthesiology* 1989, 70: 489–495.
21. Xiang LS, Calderon AS, Klemcke HG, Scott LL, Hinojosa-Laborde C, Ryan KL. Fentanyl impairs but ketamine preserves the microcirculatory response to hemorrhage. *J Trauma Acute Care Surg* 2020, 89: S93–S99.
22. Comer SD, Cahill CM. Fentanyl: Receptor pharmacology, abuse potential, and implications for treatment. *Neurosci Biobehav Rev* 2019, 106: 49–57.

23. Han Y, Yan W, Zheng YB, Khan MZ, Yuan K, Lu L. The rising crisis of illicit fentanyl use, overdose, and potential therapeutic strategies. *Transl Psychiatry* 2019, 9: 282.
24. Varshneya NB, Walentiny DM, Moisa LT, Walker TD, Akinfiresoye LR, Beardsley PM. Fentanyl-related substances elicit antinociception and hyperlocomotion in mice via opioid receptors. *Pharmacol Biochem Behav* 2021; 173242.
25. Varshneya NB, Walentiny DM, Moisa LT, Walker TD, Akinfiresoye LR, Beardsley PM. Opioid-like antinociceptive and locomotor effects of emerging fentanyl-related substances. *Neuropharmacology* 2019, 151: 171–179.
26. Varshneya NB, Hassanien SH, Holt MC, Stevens DL, Layle NK, Bassman JR, *et al.* Respiratory depressant effects of fentanyl analogs are opioid receptor-mediated. *Biochem Pharmacol* 2022, 195: 114805.
27. Malone SG, Keller PS, Hammerslag LR, Bardo MT. Escalation and reinstatement of fentanyl self-administration in male and female rats. *Psychopharmacology (Berl)* 2021, 238: 2261–2273.
28. Monroe SC, Radke AK. Aversion-resistant fentanyl self-administration in mice. *Psychopharmacology (Berl)* 2021, 238: 699–710.
29. Moussawi K, Ortiz MM, Gantz SC, Tunstall BJ, Marchette RCN, Bonci A, *et al.* Fentanyl vapor self-administration model in mice to study opioid addiction. *Sci Adv* 2020, 6: eabc0413.
30. McConnell SA, Brandner AJ, Blank BA, Kearns DN, Koob GF, Vendruscolo LF, *et al.* Demand for fentanyl becomes inelastic following extended access to fentanyl vapor self-administration. *Neuropharmacology* 2021, 182: 108355.
31. Fujii K, Koshidaka Y, Adachi M, Takao K. Effects of chronic fentanyl administration on behavioral characteristics of mice. *Neuropsychopharmacol Rep* 2019, 39: 17–35.
32. Uddin O, Jenne C, Fox ME, Arakawa K, Keller A, Cramer N. Divergent profiles of fentanyl withdrawal and associated pain in mice and rats. *Pharmacol Biochem Behav* 2021, 200: 173077.
33. Seaman RW Jr, Collins GT. Impact of morphine dependence and withdrawal on the reinforcing effectiveness of fentanyl, cocaine, and methamphetamine in rats. *Front Pharmacol* 2021, 12: 691700.
34. Morgan MM, Tran A, Wescom RL, Bobeck EN. Differences in antinociceptive signalling mechanisms following morphine and fentanyl microinjections into the rat periaqueductal gray. *Eur J Pain* 2020, 24: 617–624.
35. Bobeck EN, Schoo SM, Ingram SL, Morgan MM. Lack of antinociceptive cross-tolerance with co-administration of morphine and fentanyl into the periaqueductal gray of male Sprague-Dawley rats. *J Pain* 2019, 20: 1040–1047.
36. Gaulden AD, Burson N, Sadik N, Ghosh I, Khan SJ, Brummelte S, *et al.* Effects of fentanyl on acute locomotor activity, behavioral sensitization, and contextual reward in female and male rats. *Drug Alcohol Depend* 2021, 229: 109101.
37. Townsend EA, Negus SS, Caine SB, Thomsen M, Banks ML. Sex differences in opioid reinforcement under a fentanyl vs. food choice procedure in rats. *Neuropsychopharmacology* 2019, 44: 2022–2029.
38. Anderson EM, Engelhardt A, Demis S, Porath E, Hearing MC. Remifentanyl self-administration in mice promotes sex-specific prefrontal cortex dysfunction underlying deficits in cognitive flexibility. *Neuropsychopharmacology* 2021, 46: 1734–1745.
39. Bryant CD, Healy AF, Ruan QT, Coehlo MA, Lustig E, Yazdani N, *et al.* Sex-dependent effects of an Hnrnp1 mutation on fentanyl addiction-relevant behaviors but not antinociception in mice. *Genes Brain Behav* 2021, 20: e12711.
40. Ricarte A, Dalton JAR, Giraldo J. Structural assessment of agonist efficacy in the  $\mu$ -opioid receptor: morphine and fentanyl elicit different activation patterns. *J Chem Inf Model* 2021, 61: 1251–1274.
41. Lipiński PFJ, Jarończyk M, Dobrowolski JC, Sadlej J. Molecular dynamics of fentanyl bound to  $\mu$ -opioid receptor. *J Mol Modeling* 2019, 25: 1–17.
42. Lipinski PFJ, Kosson P, Matalinska J, Roszkowski P, Czarnocki Z, Jaronczyk M, *et al.* Fentanyl family at the  $\mu$ -opioid receptor: uniform assessment of binding and computational analysis. *Molecules* 2019, 24.
43. Vo QN, Mahinthichaichan P, Shen J, Ellis CR. How  $\mu$ -opioid receptor recognizes fentanyl. *Nat Commun* 2021, 12: 984.
44. de Waal PW, Shi JJ, You EL, Wang XX, Melcher K, Jiang Y, *et al.* Molecular mechanisms of fentanyl mediated  $\beta$ -arrestin biased signaling. *PLoS Comput Biol* 2020, 16: e1007394.
45. Yadav SK, Nagar DP, Bhattacharya R. Effect of fentanyl and its three novel analogues on biochemical, oxidative, histological, and neuroadaptive markers after sub-acute exposure in mice. *Life Sci* 2020, 246: 117400.
46. Rupniewska-Ladyko A, Malec-Milewska M. A high dose of fentanyl may accelerate the onset of acute postoperative pain. *Anesth Pain Med* 2019, 9: e94498.
47. Li L, Yu X, Lyu L, Duan H, Chen Y, Bian J, *et al.* Determination of fentanyl, alpha-methylfentanyl, beta-hydroxyfentanyl, and the metabolite norfentanyl in rat urine by LC-MS/MS. *J Anal Toxicol* 2021, <https://doi.org/10.1093/jat/bkab021>.
48. Lipinski PFJ, Szucs E, Jaronczyk M, Kosson P, Benyhe S, Misicka A, *et al.* Affinity of fentanyl and its derivatives for the  $\sigma_1$ -receptor. *Med Chem Comm* 2019, 10: 1187–1191.
49. Torralva R, Eshleman AJ, Swanson TL, Schmachtenberg JL, Schutzer WE, Bloom SH, *et al.* Fentanyl but not morphine interacts with nonopioid recombinant human neurotransmitter receptors and transporters. *J Pharmacol Exp Ther* 2020, 374: 376–391.
50. Tschirhart JN, Li WT, Guo J, Zhang ST. Blockade of the human ether A-go-go-related gene (hERG) potassium channel by fentanyl. *Mol Pharmacol* 2019, 95: 386–397.
51. Tschirhart JN, Zhang ST. Fentanyl-induced block of hERG channels is exacerbated by hypoxia, hypokalemia, alkalosis, and the presence of hERG1b. *Mol Pharmacol* 2020, 98: 508–517.
52. Gong SK, Ying L, Fan YN, Sun ZT. Fentanyl inhibits lung cancer viability and invasion via upregulation of miR-331-3p and repression of HDAC5. *Oncotargets Ther* 2020, 13: 13131–13141.
53. Dai SB, Zhang XQ, Zhang P, Zheng XS, Pang QY. Fentanyl inhibits acute myeloid leukemia differentiated cells and committed progenitors via opioid receptor-independent suppression of Ras and STAT5 pathways. *Fundam Clin Pharmacol* 2021, 35: 174–183.
54. Li CL, Qin Y, Zhong Y, Qin YY, Wei Y, Li L, *et al.* Fentanyl inhibits the progression of gastric cancer through the suppression of MMP-9 via the PI3K/Akt signaling pathway. *Ann Transl Med* 2020, 8: 118.
55. Liu W, Chen Y, Xu W, Wang W, Tang L, Xia R, *et al.* Fentanyl stimulates tumor angiogenesis via activating multiple pro-angiogenic signaling pathways. *Biochem Biophys Res Commun* 2020, 532: 225–230.
56. Haouzi P, McCann M, Tubbs N. Respiratory effects of low and high doses of fentanyl in control and  $\beta$ -arrestin 2-deficient mice. *J Neurophysiol* 2021, 125: 1396–1407.
57. Li CZ, Peng JL, Hu R, Yan J, Sun Y, Zhang L, *et al.* Safety and efficacy of ketamine versus ketamine-fentanyl-dexmedetomidine combination for anesthesia and analgesia in rats. *Dose Response* 2019, 17: 1559325819825902.
58. Alipio JB, Brockett AT, Fox ME, Tennyson SS, deBettencourt CA, El-Metwally D, *et al.* Enduring consequences of perinatal fentanyl exposure in mice. *Addict Biol* 2021, 26: e12895.
59. Alipio JB, Haga C, Fox ME, Arakawa K, Balaji R, Cramer N, *et al.* Perinatal fentanyl exposure leads to long-lasting

- impairments in somatosensory circuit function and behavior. *J Neurosci* 2021, 41: 3400–3417.
60. Yang HM, Zhan LJ, Lin XQ, Chu CP, Qiu DL, Lan Y. Fentanyl inhibits air puff-evoked sensory information processing in mouse cerebellar neurons recorded in vivo. *Front Syst Neurosci* 2020, 14: 51.
  61. Gundersen JK, Chakkarapani E, Jary S, Menassa DA, Scull-Brown E, Frymoyer A, *et al.* Morphine and fentanyl exposure during therapeutic hypothermia does not impair neurodevelopment. *EClinicalMedicine* 2021, 36: 100892.
  62. Morales M, Margolis EB. Ventral tegmental area: Cellular heterogeneity, connectivity and behaviour. *Nat Rev Neurosci* 2017, 18: 73–85.
  63. Nutt DJ, Lingford-Hughes A, Erritzoe D, Stokes PRA. The dopamine theory of addiction: 40 years of highs and lows. *Nat Rev Neurosci* 2015, 16: 305–312.
  64. Sustkova-Fiserova M, Puskina N, Havlickova T, Lapka M, Syslova K, Pohorala V, *et al.* Ghrelin receptor antagonism of fentanyl-induced conditioned place preference, intravenous self-administration, and dopamine release in the nucleus accumbens in rats. *Addict Biol* 2020, 25: e12845.
  65. Townsend EA, Kim RK, Robinson HL, Marsh SA, Banks ML, Hamilton PJ. Opioid withdrawal produces sex-specific effects on fentanyl-vs.-food choice and mesolimbic transcription. *Biol Psychiatry Glob Open Sci* 2021, 1: 112–122.
  66. Han Y, Yuan K, Zheng YB, Lu L. Orexin receptor antagonists as emerging treatments for psychiatric disorders. *Neurosci Bull* 2020, 36: 432–448.
  67. Matzeu A, Martin-Fardon R. Targeting the orexin system for prescription opioid use disorder. *Brain Sci* 2020, 10: 226.
  68. Fragale JE, James MH, Aston-Jones G. Intermittent self-administration of fentanyl induces a multifaceted addiction state associated with persistent changes in the orexin system. *Addict Biol* 2021, 26: e12946.
  69. Fragale JE, Pantazis CB, James MH, Aston-Jones G. The role of orexin-1 receptor signaling in demand for the opioid fentanyl. *Neuropsychopharmacology* 2019, 44: 1690–1697.
  70. Pourzitaki C, Tsaousi G, Papazisis G, Kyrgidis A, Zacharis C, Kritis A, *et al.* Fentanyl and naloxone effects on glutamate and GABA release rates from anterior hypothalamus in freely moving rats. *Eur J Pharmacol* 2018, 834: 169–175.
  71. Gyawali U, Martin DA, Sulima A, Rice KC, Calu DJ. Role of BNST CRFR1 receptors in incubation of fentanyl seeking. *Front Behav Neurosci* 2020, 14: 153.
  72. Alojado ME, Ohta Y, Yamamura T, Kemmotsu O. The effect of fentanyl and morphine on neurons in the dorsal raphe nucleus in the rat: An in vitro study. *Anesth Analg* 1994, 78: 726–732.
  73. Tao R, Karnik M, Ma ZY, Auerbach SB. Effect of fentanyl on 5-HT efflux involves both opioid and 5-HT1A receptors. *Br J Pharmacol* 2003, 139: 1498–1504.
  74. Díaz A, Pazos A, Flórez J, Hurlé MA. Autoradiographic mapping of  $\mu$ -opioid receptors during opiate tolerance and supersensitivity in the rat central nervous system. *Naunyn Schmiedeberg's Arch Pharmacol* 2000, 362: 101–109.
  75. Peng YZ, Li XX, Wang YW. Effects of parecoxib and fentanyl on nociception-induced cortical activity. *Mol Pain* 2010, 6: 3.
  76. Xie P, Yu T, Fu XY, Tu Y, Zou Y, Lui S, *et al.* Altered functional connectivity in an aged rat model of postoperative cognitive dysfunction: A study using resting-state functional MRI. *PLoS One* 2013, 8: e64820.
  77. Reiner DJ, Lofaro OM, Applebey SV, Korah H, Venniro M, Cifani C, *et al.* Role of projections between piriform cortex and orbitofrontal cortex in relapse to fentanyl seeking after palatable food choice-induced voluntary abstinence. *J Neurosci* 2020, 40: 2485–2497.
  78. Everett NA, Baracz SJ. A piriform-orbitofrontal cortex pathway drives relapse to fentanyl-seeking after voluntary abstinence. *J Neurosci* 2020, 40: 8208–8210.
  79. Dominguini D, Steckert AV, Michels M, Spies MB, Ritter C, Barichello T, *et al.* The effects of anaesthetics and sedatives on brain inflammation. *Neurosci Biobehav Rev* 2021, 127: 504–513.
  80. Cisneros IE, Cunningham KA. Self-administered fentanyl profoundly impacts rat brain innate immune targets. *Neuropsychopharmacology* 2021, 46: 247.
  81. Ezeomah C, Cunningham KA, Stutz SJ, Fox RG, Bukreyeva N, Dineley KT, *et al.* Fentanyl self-administration impacts brain immune responses in male Sprague-Dawley rats. *Brain Behav Immun* 2020, 87: 725–738.
  82. Chang L, Ye F, Luo QH, Tao YX, Shu HH. Increased hyperalgesia and proinflammatory cytokines in the spinal cord and dorsal root ganglion after surgery and/or fentanyl administration in rats. *Anesth Analg* 2018, 126: 289–297.
  83. Carranza-Aguilar CJ, Hernández-Mendoza A, Mejias-Aponte C, Rice KC, Morales M, González-Espinosa C, *et al.* Morphine and fentanyl repeated administration induces different levels of NLRP3-dependent pyroptosis in the dorsal raphe nucleus of male rats via cell-specific activation of TLR4 and opioid receptors. *Cell Mol Neurobiol* 2022, 42: 677–694.
  84. Wang J, Jin YJ, Li JC. Protective role of fentanyl in lipopolysaccharide-induced neuroinflammation in BV-2 cells. *Exp Ther Med* 2018, 16: 3740–3744.
  85. Akbarali HI, Dewey WL. The gut-brain interaction in opioid tolerance. *Curr Opin Pharmacol* 2017, 37: 126–130.
  86. Ren M, Lotfipour S. The role of the gut microbiome in opioid use. *Behav Pharmacol* 2020, 31: 113–121.
  87. Cruz-Lebrón A, Johnson R, Mazahery C, Troyer Z, Joussef-Piña S, Quiñones-Mateu ME, *et al.* Chronic opioid use modulates human enteric microbiota and intestinal barrier integrity. *Gut Microbes* 2021, 13: 1946368.
  88. Wang FY, Meng JJ, Zhang L, Johnson T, Chen C, Roy S. Morphine induces changes in the gut microbiome and metabolome in a morphine dependence model. *Sci Rep* 2018, 8: 3596.
  89. Lee K, Vuong HE, Nusbaum DJ, Hsiao EY, Evans CJ, Taylor AMW. The gut microbiota mediates reward and sensory responses associated with regimen-selective morphine dependence. *Neuropsychopharmacology* 2018, 43: 2606–2614.
  90. Agirman G, Hsiao EY. SnapShot: The microbiota-gut-brain axis. *Cell* 2021, 184: 2524–2524.
  91. Hoffer RS, Russo SJ, Kiraly DD. Neuroimmune mechanisms of psychostimulant and opioid use disorders. *Eur J Neurosci* 2019, 50: 2562–2573.
  92. Wang Z, Chen WH, Li SX, He ZM, Zhu WL, Ji YB, *et al.* Gut microbiota modulates the inflammatory response and cognitive impairment induced by sleep deprivation. *Mol Psychiatry* 2021, 26: 6277–6292.
  93. Ma J, Bao YP, Wang RJ, Su MF, Liu MX, Li JQ, *et al.* Effects of medication-assisted treatment on mortality among opioids users: A systematic review and meta-analysis. *Mol Psychiatry* 2019, 24: 1868–1883.
  94. Mariani JJ, Mahony AL, Podell SC, Brooks DJ, Brezing C, Luo SX, *et al.* Open-label trial of a single-day induction onto buprenorphine extended-release injection for users of heroin and fentanyl. *Am J Addict* 2021, 30: 470–476.
  95. Varshneya NB, Thakrar AP, Hobelmann JG, Dunn KE, Huhn AS. Evidence of buprenorphine-precipitated withdrawal in persons who use fentanyl. *J Addict Med* 2021, <https://doi.org/10.1097/ADM.0000000000000922>.
  96. Jimenez VM Jr, Castaneda G, France CP. Methocinnamox reverses and prevents fentanyl-induced ventilatory depression in rats. *J Pharmacol Exp Ther* 2021, 377: 29–38.



97. Maguire DR, Gerak LR, Sanchez JJ, Javors MA, Disney A, Husbands SM, *et al.* Effects of acute and repeated treatment with methocinnamox, a mu opioid receptor antagonist, on fentanyl self-administration in rhesus monkeys. *Neuropsychopharmacology* 2020, 45: 1986–1993.
98. Townsend EA. Effects of kappa opioid receptor agonists on fentanyl vs. food choice in male and female rats: Contingent vs. non-contingent administration. *Psychopharmacology (Berl)* 2021, 238: 1017–1028.
99. Du KL, Wang ZY, Zhang HM, Zhang YF, Su HL, Wei ZW, *et al.* Levo-tetrahydropalmatine attenuates the acquisition of fentanyl-induced conditioned place preference and the changes in ERK and CREB phosphorylation expression in mice. *Neurosci Lett* 2021, 756: 135984.
100. Martin DA, Gyawali U, Calu DJ. Effects of 5-HT 2A receptor stimulation on economic demand for fentanyl after intermittent and continuous access self-administration in male rats. *Addict Biol* 2021, 26: e12926.
101. Zhang YF, Rahematpura S, Ragnini KH, Moreno A, Stecyk KS, Kahng MW, *et al.* A novel dual agonist of glucagon-like peptide-1 receptors and neuropeptide Y2 receptors attenuates fentanyl taking and seeking in male rats. *Neuropharmacology* 2021, 192: 108599.
102. Merkel R, Moreno A, Zhang YF, Herman R, Ben Nathan J, Zeb S, *et al.* A novel approach to treating opioid use disorders: Dual agonists of glucagon-like peptide-1 receptors and neuropeptide Y<sub>2</sub> receptors. *Neurosci Biobehav Rev* 2021, 131: 1169–1179.
103. Hammarslag LR, Denehy ED, Carper B, Nolen TL, Prendergast MA, Bardo MT. Effects of the glucocorticoid receptor antagonist PT150 on stress-induced fentanyl seeking in male and female rats. *Psychopharmacology (Berl)* 2021, 238: 2439–2447.
104. Switzer AR, Beland B, Sarna JR, Walzak A, Pfeffer G. Fentanyl overdose causing hippocampal ischaemia followed by delayed leukoencephalopathy. *Can J Neurol Sci* 2020, 47: 398–399.
105. Nylander E, Zellerroth S, Nyberg F, Grönbladh A, Hallberg M. The effects of morphine, methadone, and fentanyl on mitochondria: A live cell imaging study. *Brain Res Bull* 2021, 171: 126–134.
106. Finsterer J, Zarrouk-Mahjoub S. Fentanyl can be mitochondrion-toxic depending on dosage and cell type. *J Anaesthesiol Clin Pharmacol* 2019, 35: 570–571.
107. Montandon G, Horner RL. Electroconvulsive changes associating sedation and respiratory depression by the opioid analgesic fentanyl. *Sci Rep* 2019, 9: 14122.
108. Torralva R, Janowsky A. Noradrenergic mechanisms in fentanyl-mediated rapid death explain failure of naloxone in the opioid crisis. *J Pharmacol Exp Ther* 2019, 371: 453–475.
109. Moody OA, Zhang ER, Arora V, Kato R, Cotten JF, Solt K. D-amphetamine accelerates recovery of consciousness and respiratory drive after high-dose fentanyl in rats. *Front Pharmacol* 2020, 11: 585356.
110. Zavala CA, Thomaz AC, Iyer V, Mackie K, Hohmann AG. Cannabinoid CB 2 receptor activation attenuates fentanyl-induced respiratory depression. *Cannabis Cannabinoid Res* 2021, 6: 389–400.
111. Thevathasan T, Grabitz SD, Santer P, Rostin P, Akeju O, Boghosian JD, *et al.* Calabadiol 1 selectively reverses respiratory and central nervous system effects of fentanyl in a rat model. *Br J Anaesth* 2020, 125: e140–e147.
112. Ren J, Ding XQ, Greer JJ. Activating  $\alpha 4\beta 2$  nicotinic acetylcholine receptors alleviates fentanyl-induced respiratory depression in rats. *Anesthesiology* 2019, 130: 1017–1031.
113. Brackley AD, Toney GM. Oxytocin receptor activation rescues opioid-induced respiratory depression by systemic fentanyl in the rat. *J Pharmacol Exp Ther* 2021, 378: 96–107.
114. Baby S, Gruber R, Discala J, Puskovic V, Jose N, Cheng FX, *et al.* Systemic administration of tempol attenuates the cardiorespiratory depressant effects of fentanyl. *Front Pharmacol* 2021, 12: 690407.
115. Baehr C, Pravetoni M. Vaccines to treat opioid use disorders and to reduce opioid overdoses. *Neuropsychopharmacology* 2019, 44: 217–218.
116. Pravetoni M, Comer SD. Development of vaccines to treat opioid use disorders and reduce incidence of overdose. *Neuropharmacology* 2019, 158: 107662.
117. Olson ME, Janda KD. Vaccines to combat the opioid crisis: Vaccines that prevent opioids and other substances of abuse from entering the brain could effectively treat addiction and abuse. *EMBO Rep* 2018, 19: 5–9.
118. Banks ML, Olson ME, Janda KD. Immunopharmacotherapies for treating opioid use disorder. *Trends Pharmacol Sci* 2018, 39: 908–911.
119. Li QQ, Luo YX, Sun CY, Xue YX, Zhu WL, Shi HS, *et al.* A morphine/heroin vaccine with new hapten design attenuates behavioral effects in rats. *J Neurochem* 2011, 119: 1271–1281.
120. Liao F, Wang HX, Dao YK, Yuan K, Lu JZ, Shi J, *et al.* Synthesis and biological evaluation of a lipopeptide-based methamphetamine vaccine. *Chin Chem Lett* 2021, 32: 1575–1579.
121. Townsend EA, Banks ML. Preclinical evaluation of vaccines to treat opioid use disorders: How close are we to a clinically viable therapeutic? *CNS Drugs* 2020, 34: 449–461.
122. Raleigh MD, Baruffaldi F, Peterson SJ, Le Naour M, Harmon TM, Vigliaturo JR, *et al.* A fentanyl vaccine alters fentanyl distribution and protects against fentanyl-induced effects in mice and rats. *J Pharmacol Exp Ther* 2019, 368: 282–291.
123. Bremer PT, Kimishima A, Schlosburg JE, Zhou B, Collins KC, Janda KD. Combatting synthetic designer opioids: A conjugate vaccine ablates lethal doses of fentanyl class drugs. *Angew Chem Int Ed Engl* 2016, 55: 3772–3775.
124. Townsend EA, Blake S, Faunce KE, Hwang CS, Natori Y, Zhou B, *et al.* Conjugate vaccine produces long-lasting attenuation of fentanyl vs. food choice and blocks expression of opioid withdrawal-induced increases in fentanyl choice in rats. *Neuropsychopharmacology* 2019, 44: 1681–1689.
125. Tunstall BJ, Vendruscolo LF. Utility of fentanyl vaccines: Unique challenges posed by preventing opioid overdose and treating opioid use disorder. *Neuropsychopharmacology* 2019, 44: 1675–1676.
126. Flynn SM, France CP. Discriminative stimulus effects of carfentanil in rats discriminating fentanyl: Differential antagonism by naltrexone. *Drug Alcohol Depend* 2021, 221: 108599.
127. Eubanks LM, Blake S, Natori Y, Ellis B, Bremer PT, Janda KD. A highly efficacious carfentanil vaccine that blunts opioid-induced antinociception and respiratory depression. *ACS Chem Biol* 2021, 16: 277–282.
128. Stone AE, Scheuermann SE, Haile CN, Cuny GD, Velasquez ML, Linhuber JP, *et al.* Fentanyl conjugate vaccine by injected or mucosal delivery with dmlT or LTA1 adjuvants implicates IgA in protection from drug challenge. *NPJ Vaccines* 2021, 6: 69.
129. Barrientos RC, Bow EW, Whalen C, Torres OB, Sulima A, Beck Z, *et al.* Novel vaccine that blunts fentanyl effects and sequesters ultrapotent fentanyl analogues. *Mol Pharm* 2020, 17: 3447–3460.
130. Yang F, Kosten TR. Psychopharmacology: neuroimmune signaling in psychiatric disease-developing vaccines against abused drugs using toll-like receptor agonists. *Psychopharmacology* 2019, 236: 2899–2907.
131. Robinson C, Gradinati V, Hamid F, Baehr C, Crouse B, Averick S, *et al.* Therapeutic and prophylactic vaccines to counteract

- fentanyl use disorders and toxicity. *J Med Chem* 2020, 63: 14647–14667.
132. Wang JX, Ellis B, Zhou B, Eubanks LM, Blake S, Janda KD. A fentanyl vaccine constructed upon opsonizing antibodies specific for the Gal $\alpha$ 1-3Gal epitope. *Chem Commun (Camb)* 2020, 56: 6551–6554.
  133. Townsend EA, Bremer PT, Jacob NT, Negus SS, Janda KD, Banks ML. A synthetic opioid vaccine attenuates fentanyl-vs-food choice in male and female rhesus monkeys. *Drug Alcohol Depend* 2021, 218: 108348.
  134. Tenney RD, Blake S, Bremer PT, Zhou B, Hwang CS, Poklis JL, *et al.* Vaccine blunts fentanyl potency in male rhesus monkeys. *Neuropharmacology* 2019, 158: 107730.
  135. Smith LC, Bremer PT, Hwang CS, Zhou B, Ellis B, Hixon MS, *et al.* Monoclonal antibodies for combating synthetic opioid intoxication. *J Am Chem Soc* 2019, 141: 10489–10503.
  136. Baehr C, Kelcher AH, Khaimraj A, Reed DE, Pandit SG, AuCoin D, *et al.* Monoclonal antibodies counteract opioid-induced behavioral and toxic effects in mice and rats. *J Pharmacol Exp Ther* 2020, 375: 469–477.
  137. Blake S, Bremer PT, Zhou B, Petrovsky N, Smith LC, Hwang CS, *et al.* Developing translational vaccines against heroin and fentanyl through investigation of adjuvants and stability. *Mol Pharm* 2021, 18: 228–235.
  138. Park H, Lee JC, Eubanks LM, Ellis B, Zhou B, Janda KD. Improvements on a chemically contiguous hapten for a vaccine to address fentanyl-contaminated heroin. *Bioorg Med Chem* 2021, 41: 116225.
  139. Townsend EA, Bremer PT, Faunce KE, Negus SS, Jaster AM, Robinson HL, *et al.* Evaluation of a dual fentanyl/heroin vaccine on the antinociceptive and reinforcing effects of a fentanyl/heroin mixture in male and female rats. *ACS Chem Neurosci* 2020, 11: 1300–1310.
  140. Barrientos RC, Whalen C, Torres OB, Sulima A, Bow EW, Komla E, *et al.* Bivalent conjugate vaccine induces dual immunogenic response that attenuates heroin and fentanyl effects in mice. *Bioconjug Chem* 2021, 32: 2295–2306.
  141. Natori Y, Hwang CS, Lin L, Smith LC, Zhou B, Janda KD. A chemically contiguous hapten approach for a heroin-fentanyl vaccine. *Beilstein J Org Chem* 2019, 15: 1020–1031.
  142. Hwang CS, Smith LC, Natori Y, Ellis B, Zhou B, Janda KD. Improved admixture vaccine of fentanyl and heroin hapten immunoconjugates: Antinociceptive evaluation of fentanyl-contaminated heroin. *ACS Omega* 2018, 3: 11537–11543.
  143. Hwang CS, Smith LC, Natori Y, Ellis B, Zhou B, Janda KD. Efficacious vaccine against heroin contaminated with fentanyl. *ACS Chem Neurosci* 2018, 9: 1269–1275.
  144. Maurya A, Rangappa S, Bae J, Dhawan T, Ajjarapu SS, Murthy SN. Evaluation of soluble fentanyl microneedles for loco-regional anti-nociceptive activity. *Int J Pharm* 2019, 564: 485–491.
  145. Liu TT, Shi J, Epstein DH, Bao YP, Lu L. A meta-analysis of acupuncture combined with opioid receptor agonists for treatment of opiate-withdrawal symptoms. *Cell Mol Neurobiol* 2009, 29: 449–454.
  146. Shi J, Liu YL, Fang YX, Xu GZ, Zhai HF, Lu L. Traditional Chinese medicine in treatment of opiate addiction. *Acta Pharmacol Sin* 2006, 27: 1303–1308.
  147. Sun HQ, Chen HM, Yang FD, Lu L, Kosten TR. Epidemiological trends and the advances of treatments of amphetamine-type stimulants (ATS) in China. *Am J Addict* 2014, 23: 313–317.

# Lighting Up Neural Circuits by Viral Tracing

Liyao Qiu<sup>1,2</sup>  · Bin Zhang<sup>1,2</sup>  · Zhihua Gao<sup>1,2</sup> 

Received: 12 January 2022 / Accepted: 23 February 2022 / Published online: 16 May 2022  
© The Author(s) 2022

**Abstract** Neurons are highly interwoven to form intricate neural circuits that underlie the diverse functions of the brain. Dissecting the anatomical organization of neural circuits is key to deciphering how the brain processes information, produces thoughts, and instructs behaviors. Over the past decades, recombinant viral vectors have become the most commonly used tracing tools to define circuit architecture. In this review, we introduce the current categories of viral tools and their proper application in circuit tracing. We further discuss some advances in viral tracing strategy and prospective innovations of viral tools for future study.

**Keywords** Viral tracing · Neural circuit · Anterograde · Retrograde · Transsynaptic

## Introduction

The human brain, consisting of nearly 86 billion highly interwoven neurons, is the most complex and sophisticated organ that instructs versatile physiological functions and behaviors. Each neuron contacts or is contacted by tens of thousands of other neurons *via* synapses, by which neurons

transmit information from one to another. These neurons connect with each other to constitute intricate functional networks, namely neural circuits, to precisely transmit and process information in the brain. Unraveling the complex organization of these circuits is crucial to decipher how information is processed and how instructions are executed to generate thoughts and guide versatile behaviors.

A number of techniques have been developed to define the architecture of neural circuits. Fifty years have passed since the first use of horseradish peroxidase as a retrograde tracer in 1971 [1, 2]. Over the past half century, many new chemical tracers have been developed, for example, the anterograde tracer *Phaseolus vulgaris*-leucoagglutinin [3] and dextran-amine [4], and the retrograde tracers Fluoro-Gold [5] and cholera toxin B subunit [6], which did help to characterize the overall architecture of neural circuits. However, labeling strategies using these chemical tracers are usually transient with no cell-type-specificity. In recent years, the development of viral tracers has rapidly moved forward the dissection of the neural circuit. Since the first use of Herpes simplex virus (HSV) in neuroanatomical tracing in 1974 [7], engineered viral vectors have become the most commonly-used tools in neural circuit mapping, due to reduced cytotoxicity, long-term expression of reporter genes, efficient axonal transport or transsynaptic transport, cell-type-specific access and spatiotemporal transduction in a genetically modified background. Combined with the Cre/Flp-mediated recombination strategy, viruses containing fluorescent protein expression cassettes can selectively trace neuronal somas, their projections, and their synaptically connected neurons, thus lighting up the neural circuits in the brain.

Viruses that are routinely used in neural tracing differ in tropism, axonal or transsynaptic transport, and transgene expression (Table 1). Therefore, it is important to

✉ Zhihua Gao  
zhihuagao@zju.edu.cn

<sup>1</sup> Department of Neurobiology and Department of Neurology of the Second Affiliated Hospital, NHC and CAMS Key Laboratory of Medical Neurobiology, Zhejiang University School of Medicine, Hangzhou 310058, China

<sup>2</sup> The MOE Frontier Science Center for Brain Research and Brain-Machine Integration, School of Brain Science and Brain Medicine, Zhejiang University, Hangzhou 310058, China

understand the characteristics of different viruses in order to choose the right tools for different purposes. In this review, we introduce the key features of commonly used viral vectors and their appropriate application for different experimental needs, along with recent progress and prospects in the development of advanced viral tracers to meet more needs and resolve complicated problems.

## Viral Tools in Neural Tracing

A century ago, people suffered from a disease characterized by blisters in the oral and genital regions. The arch-criminal of this disease was unknown until the identification of HSVs in 1923 [8]. HSVs infect skin epithelial cells, spread through the sensory nerves, and finally reach the neuronal perikarya in the central nervous system [9]. These discoveries inspired scientists to test the possibility of applying HSVs to circuit tracing in the 1980s [10, 11]. Since then, more types of viruses have been identified and their genomes further genetically modified in the lab to generate recombinant viruses. These viruses have been widely used in neural tracing and promoted the dissection of neural circuits.

Several types of viral tracer are routinely used, including the HSV, adeno-associated virus (AAV) [12], canine adenovirus-2 (CAV-2) [13], rabies virus (RV) [14], pseudorabies virus (PRV) [15]. In general, based on their ability to cross the synapses, viral tracers can be categorized into two classes: non-transsynaptic and transsynaptic. The non-transsynaptic viruses are unable to span synapses to other

neurons and are restricted to infected neurons, whereas the latter can cross synapses and spread to other synaptically-connected neurons. Both classes contain viruses that are transported in the anterograde or retrograde direction along axons. Detailed information regarding the different properties and applications of viruses has been extensively reviewed [16–20]. Here, we summarize the features of widely-used viruses in neural tracing (Fig. 1).

## Non-transsynaptic Tracing Virus

As noted above, non-transsynaptic viruses are unable to cross synapses and are restricted to locally infected neurons. Based on the directionality of viral transport along axons, non-transsynaptic viruses are further divided into anterograde and retrograde viruses. Anterograde viruses generally infect neuronal somas and viral transgene products such as fluorescent proteins are transported from neuronal somas to the axonal terminals, whereas retrograde viruses usually infect nerve terminals and are transported from the terminals to the somas.

## Anterograde Viral Tracers

Non-transsynaptic anterograde tracing requires viruses to infect neuronal somas and fully label their axonal terminals either by the anterograde transport of viral particles or their passive diffusion along axonal processes. With the expression of reporter genes from the virus and subsequent filling throughout the neuronal soma and processes with

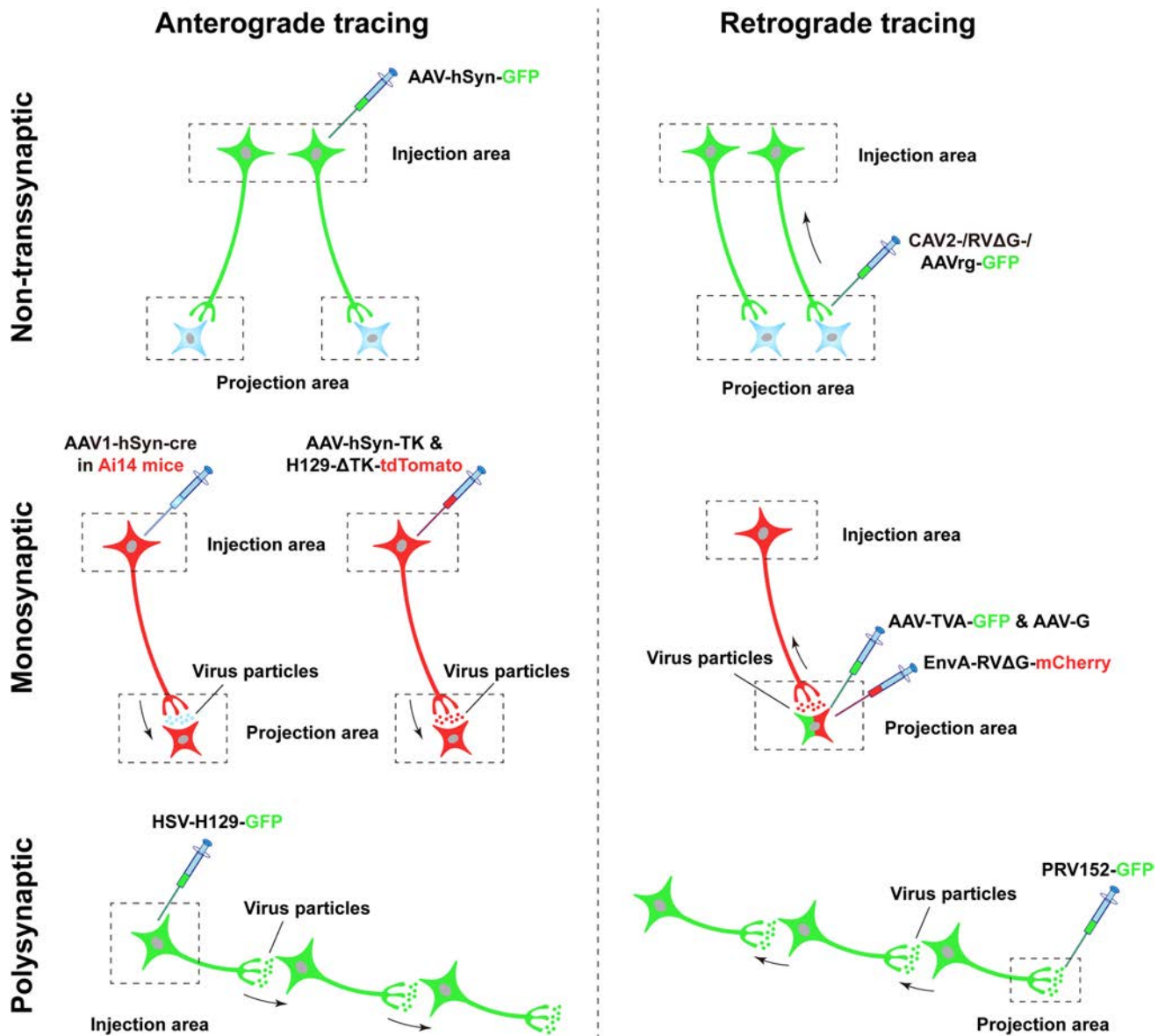
**Table 1** Key characteristics of viruses commonly used in viral tracing.

Virus	Genome type and size	Payload capacity (kb)	Spread direction	Transsynaptic	Integration into genome	Onset and duration of expression
HSV	dsDNA ~ 152 kb	30–40	Anterograde Retrograde	Yes	No	Onset: hours Duration: 5–7 days
AAV <sup>#</sup>	ssDNA ~ 4.7 kb	~ 4.7	Anterograde (except AAVrg)	No (except AAV1 and AAV9)	No	Onset: ~1 week Duration: months
CAV-2	dsDNA 32 kb	~ 30	Retrograde	No	No	Onset: days to weeks Duration: months
RV	(–) ssRNA ~ 12 kb	3.7–4	Retrograde	Yes	No	Onset: ~2 days Duration: months
PRV	dsDNA ~ 142 kb	30–40	Retrograde	Yes	No	Onset: hours Duration: variable

dsDNA, double-stranded DNA; ssDNA, single-stranded DNA; ssRNA, single-stranded RNA; (–), negative sense; HSV, Herpes simplex virus; AAV, adeno-associated virus; AAVrg, rAAV2-retro; CAV-2, canine adenovirus 2; RV, rabies virus; PRV, pseudorabies virus; kb, kilobase.

<sup>#</sup>AAV has many serotypes including AAV1, AAV2, AAV5, AAV8, and AAV9. All AAV types are anterogradely transported except AAVrg, which is retrogradely transported. Only AAV1 and AAV9 can spread transsynaptically, whereas the other AAVs cannot





**Fig. 1** Schematic of different viral-tracing strategies. Viral-tracing strategies can be divided into three classes based on their ability to cross synapses: non-transsynaptic (upper), monosynaptic (middle), and polysynaptic (lower). Each class contains both anterograde (left panels) and retrograde (right panels) approaches based on the transport direction of viruses. In anterograde tracing, viruses are often injected into the somal region (injection area), infecting the somas and fully labeling the axonal terminals by expression of fluorescent proteins, thus tracing the terminal regions (projection area). The non-transsynaptic viruses are unable to cross synapses (upper left), whereas the monosynaptic or polysynaptic viruses can transfer to the downstream neurons spanning one (middle left) or multiple synapses (lower left). In non-transsynaptic retrograde tracing, viruses are usually injected into the terminal region, in which they infect the axon terminals and spread retrogradely to the somas (upper right). In monosynaptic or polysynaptic retrograde tracing,

viruses are injected into the postsynaptic neuronal areas, are transferred to the presynaptic terminals, and spread retrogradely to the somas (middle right) or to further upstream synaptically-connected neurons (lower right). The neurons that are in both green and red indicate the co-expression of GFP and mCherry, while blue neurons are not infected by viruses (the same convention is used in the following figures). The black arrows indicate the spread direction of viral particles. AAV, adeno-associated virus; AAV1, one subtype of AAV; AAVrg, a retrograde-tracing variant of AAV; CAV, canine adenovirus; hSyn, human Synapsin I; TK, thymidine kinase; HSV, Herpes simplex virus; H129-ΔTK, a TK-deleted anterograde-tracing recombinant of HSV; G, rabies glycoprotein; RVΔG, G-deleted rabies virus; EnvA, avian ASLV type A envelope protein; TVA, avian receptor for EnvA; PRV152, a retrograde-tracing recombinant of the pseudorabies virus.

fluorescent proteins, anterograde tracing is able to determine the output of a certain neural pathway and delineate neuronal morphology. While many types of viruses meet this need, AAVs are the most extensively used anterograde tracing tools [21]. AAVs are non-enveloped single-stranded DNA viruses with a gene payload capacity limited to ~ 4.7 kb. Several advantages make AAVs the most popular tools in neural tracing. First, AAVs cannot self-replicate without a helper, therefore their expression is generally restricted to the injected neurons. Second, AAVs are rarely integrated into the host genome and their immunogenicity is low, with rare immune responses or toxicity [22]. Third, transgenes in AAVs are persistently and stably expressed for several months [23].

AAVs have multitudes of serotypes, defined as viral capsids with diverse antigenicity. Different AAV serotypes bind to different receptors expressed by different cell populations, resulting in species-, tissue- and cell-specific tropisms [24]. The most commonly used recombinant AAV serotypes include AAV1, AAV2, AAV5, AAV8, and AAV9 [25]. Since the diffusion of AAV2 is limited and it is highly selective for neurons [26], recombinant AAV (rAAV) vectors currently in use are based on the framework of AAV2. rAAVs are constructed by packaging the genes of interest flanked by two inverted terminal repeat sequences of AAV2 with the capsids of other serotypes [27] such as AAV8 or AAV9 to make a hybrid AAV2/8 or AAV2/9. These engineered rAAVs combine the advantages of different serotypes and meet different needs in studies that require different degrees of viral diffusion.

Different AAV serotypes have different cell tropisms. For example, AAV5 appears to exhibit a glial tropism in primary cultures of rat cortical cells [28], while others are more selective for neurons. However, the serotype is not the main determinant of cell type-specific infection *in vivo*, because the brain regions and how the virus is administered also affect the tropism. Therefore, specific promoters are required for AAVs to express transgenes in particular cell types. For example, hSyn (human Synapsin I) is commonly used as a pan-neuronal promoter and gfaABC<sub>1</sub>D as an astrocyte-specific promoter [29]. The most common way to selectively target certain cell types is *via* the Cre-LoxP (locus of x-over P1 site) and the Flp-FRT (Flp recombination target site) system-based genetic approaches, by which transgene expression is allowed in the presence of Cre or Flp recombinases [30, 31].

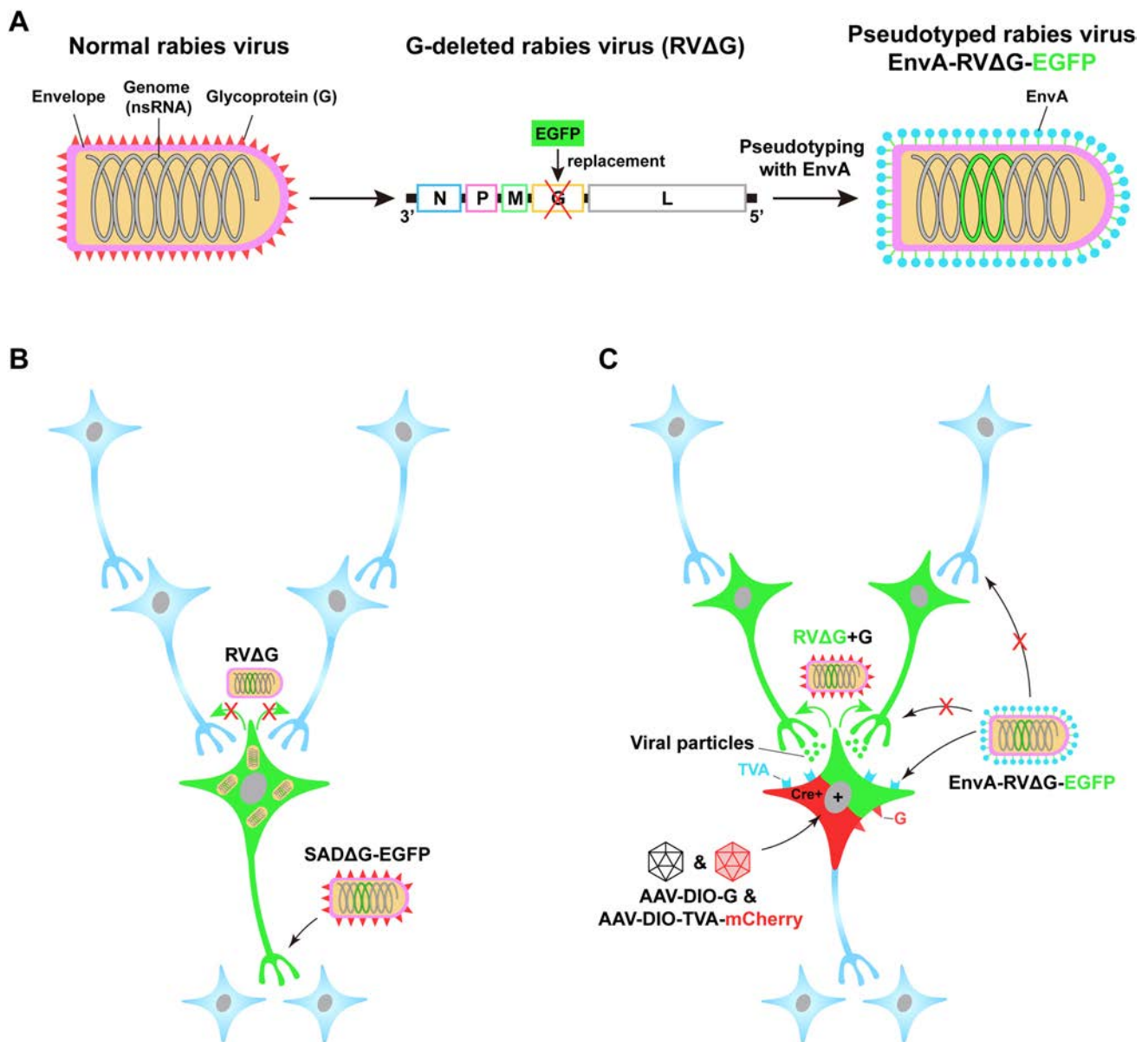
### Retrograde Viral Tracers

When studying the function of a certain brain region in neural circuits, it is indispensable to identify the source of upstream inputs, and this can be achieved by retrograde tracing. Retrograde tracing is based on viral entry from the

axonal terminals and retrograde transport of the viral particles to the neuronal somas. In contrast to anterograde tracing, retrograde tracing requires viral binding with surface receptors expressed at the axonal terminals. Several types of virus exhibit the properties of terminal entry and retrograde spread, including CAV-2, RV, PRV, and some specific strains of HSV. Among these viruses, only CAV-2 cannot be transmitted across synapses while the last three can (see below). CAV-2 is a double-stranded DNA adenovirus with many advantages such as little immunogenicity, a relatively large gene payload of up to 30 kb, high selectivity for neurons, enduring gene expression, and efficient retrograde transport [13, 32, 33]. However, the drawback that limits its application is cell tropism. The binding and endocytosis of CAV-2 require the coxsackie adenovirus receptor (CAR), which is predominantly localized at presynaptic terminals and mediates viral entry and retrograde transport [34, 35]. In other words, CAV-2 exclusively infects axon terminals that express CAR. Therefore, retrograde tracing using CAV-2 may fail to label neurons with low or no CAR expression.

Although RV naturally exhibits the property of transsynaptic transport and is most commonly used in retrograde monosynaptic tracing (see below), a newly-engineered RV with glycoprotein (G)-deleted (SADΔG-EGFP) is also an excellent tool for non-transsynaptic retrograde tracing (Fig. 2A). In this RV, the gene encoding the glycoprotein is substituted by the gene encoding the enhanced green fluorescent protein (EGFP) [36]. As the envelope glycoprotein is essential for the RV to cross synapses, the recombinant RV loses the ability to spread to other synaptically-connected neurons and is confined to the initially infected cells (Fig. 2B). However, since the recombinant virus retains the ability to replicate, the amplified virus contributes to enhanced fluorescent signals, making it suitable for delineating the morphology of retrogradely-labeled neurons.

Another powerful tool for non-transsynaptic retrograde tracing is rAAV2-retro, a recently developed AAV variant that exhibits a much higher efficacy of retrograde transport than other AAV serotypes and CAV-2 [37]. This variant contains a mutant capsid generated by error-prone PCR that demonstrates the highest potency of retrograde transport after several rounds of selection. The rAAV2-retro has highly-efficient retrograde transportability with stable transgene expression and has become the most commonly used retrograde viral tracer in dissecting projection-specific neural pathways. Recently, by injecting this powerful viral tracer into the posterior pituitary (PPI), we successfully labeled the neuroendocrine cell ensemble projecting to the PPI and reconstructed the three-dimensional architecture of the hypothalamo-neurohypophyseal system [38]. Other than rAAV2-retro, additional engineered AAVs with high



**Fig. 2** Pseudotyped rabies virus for retrograde tracing. **A** Engineering rabies virus (RV) by glycoprotein deletion and EnvA pseudotyping. Normal RV (left) contains a negative-strand RNA genome consisting of five genes and an envelope that is coated with the glycoprotein (G), which is coded by one of the five genes. RV can be engineered by replacing the G gene with an enhanced green fluorescent protein (EGFP) and pseudotyping this G-deleted RV with EnvA, the envelope protein of an avian virus (middle and right). **B** Non-transsynaptic retrograde tracing using SADΔG-EGFP. The recombinant RV SADΔG-EGFP, in which the G-coding gene is deleted, has been coated with G but loses the ability to produce G. This virus can infect axon terminals (shown by the black arrows without red crosses) and retrogradely spread to the somas. It retains the ability to replicate and produce a large amount of virus, thereby enhancing the EGFP fluorescent signal. Unable to synthesize G, however, the newly produced offspring fail to spread to synaptically-connected neurons (shown by the green arrows with red crosses). **C** Monosynaptic

retrograde tracing using EnvA-pseudotyped RV. Due to the absence of endogenous receptors for EnvA, EnvA-RVΔG is unable to infect neurons in the mammalian brain (shown by the black arrows with red crosses). When the EnvA receptor, TVA, is exogenously expressed in the Cre<sup>+</sup> neurons via Cre-dependent (DIO) AAV helper vectors, EnvA-RVΔG can selectively infect the TVA-harboring cells (neurons in green plus red), which is shown by the black arrows without red crosses. With the complementation of G in the same cells, the newly generated virus, RVΔG+G regains the ability to transsynaptically spread (shown by the green arrows) to presynaptic neurons (green). Due to the absence of G expression in these presynaptic neurons, however, the virus is unable to further spread out of these cells (blue). The red cross means inability. ns, negative strand; N, nucleoprotein, P, phosphoprotein; M, matrix protein; G, glycoprotein; L, the polymerase of rabies virus; DIO, double-floxed inverse open reading frame; SADΔG, a G-deleted RV strain.

efficiency of retrograde transport, including AAV MNM008 [39], AAV2 R585/R588 [40], and AAV-TT [41], have been developed. Among these viruses, AAV MNM008 appears to exhibit improved retrograde infectivity of dopaminergic neurons [39]. The ability to carry fluorescent protein expression cassettes, along with the properties of efficient retrograde transport and low toxicity make rAAV2-retro an ideal tool for retrograde tracing in modern neuroscience research.

## Transsynaptic Tracing Virus

Transsynaptic tracing viruses cross synapses and spread to other neurons in neural circuits mostly owing to their self-replication. Based on their spreading direction between pre- and post-synaptic neurons, transsynaptic viruses are also divided into anterograde (from pre- to post-synaptic neurons) and retrograde (from post- to pre-synaptic neurons) viruses.

### Anterograde Transsynaptic Viral Tracers

Neurons are intricately connected with each other *via* synapses, constituting a complex hierarchical network. To fully understand the architecture of the neural circuits, it is necessary to dissect the anatomical organization of synaptic pathways. Although AAVs are wonderful tools for delineating neuronal morphology and projection areas, they do not reveal synaptic connections between neurons in different regions. Neither do they provide information regarding the molecular identity of the downstream innervated neurons. Therefore, anterograde transsynaptic viral tracers are required to resolve these problems.

Several types of the virus naturally exhibit transsynaptic transduction, due to their self-replication in the initially infected neurons and spread to the downstream neurons. One of them is HSV, an enveloped double-stranded DNA virus with a quite large capacity for transgene packages compared with other viruses, with a gene payload ~ 30–40 kb. HSV has many strains that exhibit different properties of anterograde and retrograde transsynaptic transport with distinct cytotoxicity [42, 43]. H129, one strain of HSV type 1, has been widely used in anterograde multisynaptic neural tracing [44], especially in studies that define the peripheral afferent or efferent pathways of some brain regions [45]. However, since H129 is a replication-competent virus, it is able to continuously spread across multiple levels of synapses. This leads to uncontrollable infection in the brain, which may exacerbate cytotoxicity and eventually lead to the death of the animal. Moreover, it is difficult to distinguish the neurons with monosynaptic

and polysynaptic connections. Another limitation is that native HSV cannot selectively label specific neuronal populations, but this has recently been resolved by engineering the HSV genome. In the engineered virus, the thymidine kinase (*TK*) gene, required for viral replication, is replaced by a cassette including *loxP-STOP-loxP* with downstream *tdTomato* and a codon-modified *TK* gene [46]. This recombinant HSV, namely H129 $\Delta$ TK-TT, is unable to express the *TK* gene and loses the ability of replication and transsynaptic spread in the absence of Cre recombinase. The virus restores the replication competence and drives the expression of the reporter gene only in the Cre-containing neurons and their postsynaptic neurons, thereby making it a good tool for anterograde tracing in combination with Cre-based genetic animal strains. Another recombinant H129 (H129- $\Delta$ TK-tdT) has been generated by replacing the viral *TK* gene with the cytomegalovirus (CMV) promoter-driven *tdTomato* gene, to allow reporter gene expression but disrupt the ability to replicate and spread across synapses [47]. When an AAV helper vector carrying the *TK* cassette is present in H129- $\Delta$ TK-tdT infected cells, H129- $\Delta$ TK-tdT restores the ability to replicate and transduce the postsynaptic neurons. However, H129- $\Delta$ TK-tdT cannot continue to spread into downstream neurons due to the lack of *TK* expression in the second-order neurons, making the anterograde tracing strictly monosynaptic. In combination with Cre-dependent AAV helpers, this H129- $\Delta$ TK virus has been successfully used to identify a population of neurons in the Edinger-Westphal nucleus that is directly innervated by Htr2c neurons in the ventral CA1 [48].

Although HSV1 is a powerful tool in anterograde transsynaptic tracing, its high toxicity limits its applicability in the functional dissection of specific neuronal connections for prolonged periods. In addition, HSV is also taken up by axon terminals and exhibits delayed retrograde transport [46]. Recently, a live attenuated vaccine for yellow fever (YFV), YFV-17D, has been engineered for anterograde transsynaptic tracing with low cytotoxicity [49]. This YFV-17D contains three structural protein-encoding genes (C, prM, and E) and five genes (NS1–NS5) that are crucial for viral replication. By deleting the NS1 gene, YFV <sup>$\Delta$ NS1</sup> loses the ability to replicate. After complementing NS1 in the starter neurons and postsynaptic neurons, YFV <sup>$\Delta$ NS1</sup> recovers the ability to spread transsynaptically and label the postsynaptic neurons. Similar to HSV, however, the YFV virus also exhibits delayed retrograde transport. To limit its retrograde transport, the authors used the inducible Tet-ON strategy to temporally restrict the complementation of NS1 by intermittent doxycycline induction to minimize viral replication, thereby reducing the retrograde transport and



cytotoxicity. Moreover, by deleting the structural protein-encoding genes (C, prM, and E), the new variant, YFV<sup>ΔCME</sup>, is unable to package itself, thus losing the ability to infect neurons. YFV<sup>ΔCME</sup> viruses recover the packaging ability in the starter cells when the structural proteins are provided and possess the ability to spread to postsynaptic neurons. However, due to the absence of the structural proteins in the downstream neurons, the viruses fail to transfer further, thereby achieving monosynaptic anterograde tracing. Also, since the YFV<sup>ΔCME</sup> variant contains the complete NS1 gene, there is no need to supplement NS1 in downstream areas. This YFV<sup>ΔCME</sup> variant can be used to map the whole monosynaptic projections (projectome) of a specific neuronal cell type [49].

Another effective monosynaptic anterograde tracer is the AAV1 vector, which was recently found to exhibit anterograde transneuronal spread at high titers [50]. AAV9 also exhibits similar properties, though at an even higher titer than AAV1. Other AAV serotypes, such as AAV5, AAV6, and AAV8, have not shown such properties. It is worth noting that the efficiency of AAV1-mediated transsynaptic tracing is relatively low compared to HSV. Therefore, this strategy requires the application of Cre or Flp recombinase to amplify the expression of downstream reporter genes, allowing a clearer identification and more efficient manipulation of postsynaptic neural pathways. Another caveat is that AAV1 can also retrogradely label presynaptic neurons (albeit at low efficiency) [50–52], which may confound the identification of postsynaptic neurons.

### Retrograde Transsynaptic Viral Tracers

Retrograde transsynaptic tracing is well-established and widely used in modern neuroscience research, benefiting from the development of the PRV and pseudotyped RV. It should be noted that PRV is not a rabies virus. Instead, similar to HSV, it belongs to the herpesviridae. It is an enveloped double-stranded DNA virus with a large payload for gene packages. The direction of PRV transport differs between distinct strains. The wild-type virulent strain, namely PRV-Becker, spreads bidirectionally (both anterogradely and retrogradely) between connected neurons, whereas another attenuated strain, PRV-Bartha, exhibits selective retrograde transport [53]. PRV-152, an engineered strain of PRV-Bartha by adding the *CMV-EGFP* cassette to the viral genome to allow GFP expression, is widely used for retrograde polysynaptic tracing [54, 55]. It should be cautioned that PRV is highly virulent and lethal to animals, usually leading to death in 3–4 days after intracerebral injection [56]. Even though PRV-Bartha is an attenuated strain, it only prolongs the life of the animals for

several days [54]. Therefore, investigators should be careful and take security precautions when using PRV. Due to the nature of polysynaptic transport, PRV is an excellent tool for short-term retrograde tracing of multi-level neural circuits that terminate at the periphery.

Similar to HSV, however, it is difficult to differentiate the monosynaptic or polysynaptic connections of PRV-labeled neurons, owing to its uncontrollable transsynaptic spread. Another powerful vector, the engineered RV, came on stage to circumvent this limitation [57]. RV is an enveloped virus with a negative-sense single-stranded RNA genome that consists of only five genes [14]. Among the five genes, one encodes rabies glycoprotein (RG), the envelope protein that mediates the entry of RV into cells. Actually, wild-type RV spreads across multiple levels of synapses [58]; however, different from HSV, it naturally exhibits exclusively retrograde transport without inducing cytopathy or leakage to local glia [58, 59]. Retrograde monosynaptic tracing has been achieved by replacing the native G gene of RV with fluorescent reporter genes and pseudotyping this G-deleted RV with EnvA (EnvA-RVΔG), an avian virus envelope protein (Fig. 2). This pseudotyped EnvA-RVΔG loses the ability to infect mammalian cells and transfer to synaptically-connected neurons. When mammalian cells express exogenous tumor virus receptor A (TVA), a cognate avian receptor of EnvA, EnvA-RVΔG is able to selectively enter the neurons. However, it is unable to synaptically transfer unless the glycoprotein is exogenously complemented. Therefore, with helper AAVs expressing TVA and G in selected cell subpopulation in a Cre-dependent manner, EnvA-pseudotyped RVΔG is able to infect TVA-harboring cells, also known as starter cells. Moreover, with the complementation of G in these cells, RVΔG recovers the ability to transsynaptically spread to the upstream neurons that directly innervate the starter cells. Once the virus reaches the upstream (presynaptic) neurons, it fails to further spread to the second-order presynaptic neurons due to the absence of G, thus achieving monosynaptic retrograde tracing [60].

### Advances and Prospects in Viral Tracing

Recombinant neurotropic viruses have become the most potent and common tools in modern neuroscience research, regardless of neuronal morphology delineation and neural-circuit tracing. Since their initial discovery and application, each type of virus has been developed rapidly with much amazing progress during the past decades. In the following, we introduce some cutting-edge applications of the current recombinant viruses in neural-circuit tracing.

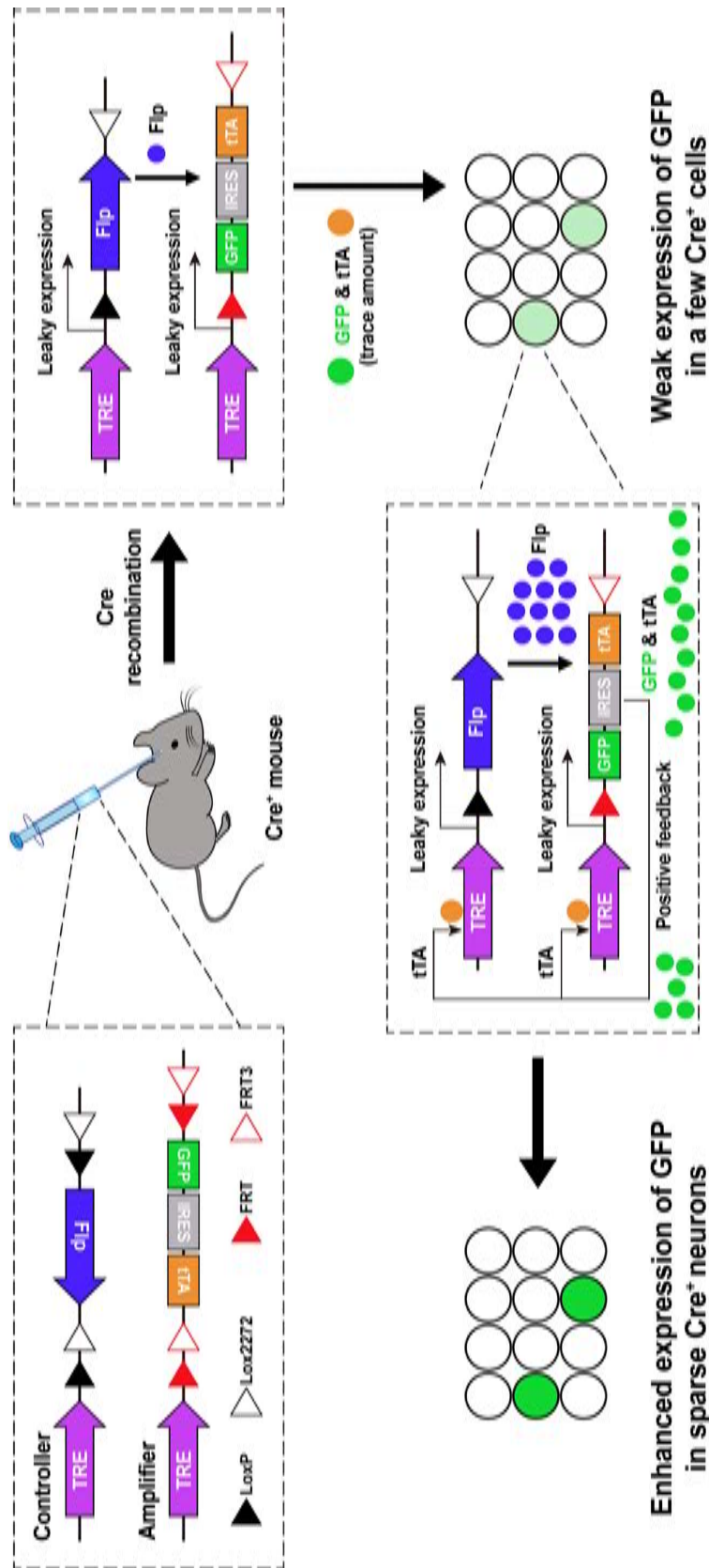
Among so many types of viruses, AAV is the most commonly used tool for transgene delivery into the host. It enables the labeling of local somas and distant axon terminals, which is indicative of the downstream projections of certain neuron populations. In addition, with the expression of the fluorescent reporter gene, AAVs delineate the neuronal morphology including soma, dendrites, and axon terminals. However, some neurons project distally to downstream regions to form long axonal tracts. The routinely used AAVs, due to the low intensity and non-uniformity of the fluorescence signals along long axons, are unable to provide a full view of the axon projection routes. Moreover, due to the high efficiency of AAV infection at the local injection site, it is difficult to differentiate individual neuronal morphology. A recently-developed dual-AAV system overcomes this limitation and achieves sparse and bright labeling of single neurons in a cell-type-specific manner [61]. This system includes a “controller” AAV vector which contains a tetracycline response element (TRE) promoter-driven, Cre-dependent, FLP expression cassette; and an “amplifier” vector, which contains a TRE promoter followed by an FLP-dependent *GFP-IRES-tTA* cassette. Since TRE is a bit leaky [62], it is able to drive low-level expression of downstream gene cassettes in the absence of the tetracycline trans-activator (tTA). When the “controller” and “amplifier” vectors are co-injected into the brain in a Cre-expressing mouse line, TRE-driven weak FLP expression (from the controller) only occurs stochastically in a few Cre-expressing neurons. It is in these neurons that FLP drives the recombination of the gene cassette in the amplifier, leading to minimal expression of the tTA protein due to the leakage of TRE. tTA subsequently binds to the TRE promoter and further potentiates the expression of FLP and tTA. This cascade reaction forms a positive feedback loop to enhance the GFP expression in only a few neurons, thereby resulting in sparse but bright labeling of single neurons (Fig. 3). The degree of labeling efficiency is tunable by adjusting the titer of the controller vector. Combined with fluorescent micro-optical sectioning tomography, a whole-brain reconstruction technology [63], this sparse labeling enables the complete exhibition of the morphology of cell-type-specific single neurons including their long axonal arborizations.

The retrograde tracer CAV-2 is usually used in combination with other vectors to achieve projection-specific tracing. For example, an AAV vector containing Cre-dependent gene cassettes, e.g., a fluorescent reporter gene, is injected into the candidate source region, while the CAV-2 carrying a Cre recombinase is injected into the putative downstream area. When the retrogradely transported CAV-2 reaches the neuronal soma, Cre recombinase drives the expression of the reporter gene, thereby

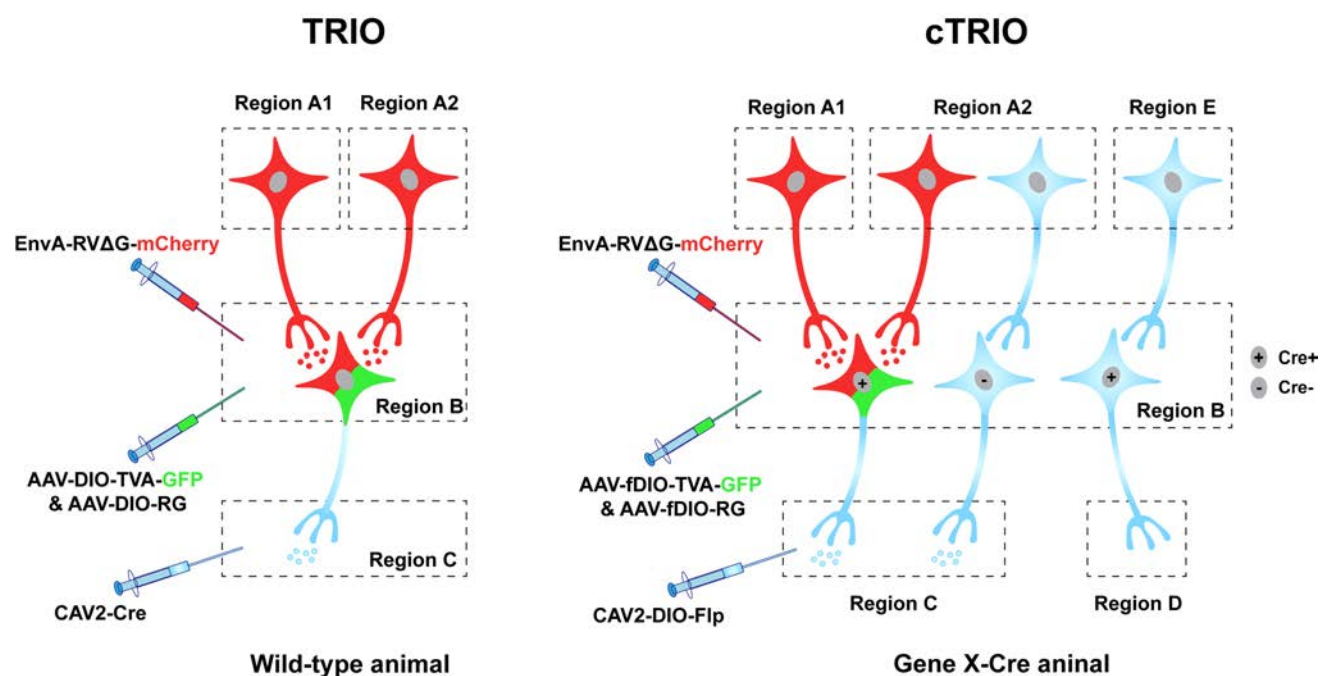
selectively labeling neurons projecting to the downstream area [64]. However, the applicability of CAV-2 is limited by the restricted expression of CAR in the nervous system. A recent study overcame this limit using a receptor-complementation strategy by expressing CAR in the candidate projection neurons [65]. This leads to a substantially increased retrograde-labeling efficiency of CAV-2. Moreover, by designing Cre-dependent CAR deletion (Cre-OFF) along with simultaneous expression of fluorescent reporters or channelrhodopsin (Cre-ON), this strategy not only removes CAR from retrogradely-labeled neurons to avoid potential interference with normal neuron function, but also provides a way to structurally and functionally characterize the neural circuits.

The EnvA-coated RVΔG system is widely used, not only to trace the monosynaptic inputs to specific neuronal populations [66, 67], but also to manipulate the neural circuits in combination with other viral tools expressing elements such as channelrhodopsin and designer receptors exclusively activated by designer drugs (DREADDs) [68]. Recently, ingenious tracing strategies combining the application of CAV-2 and RVΔG, called TRIO (tracing the relationship between input and output) and cTRIO (cell-type-specific TRIO), which are able to achieve three-node (e.g. A–B–C) circuit tracing, have been developed [69] (Fig. 4). In TRIO, AAV helpers carrying Cre-dependent TVA receptors and RG are delivered into region B, while CAV-2 expressing Cre recombinase is injected into the downstream region C. CAV2-Cre virus retrogradely spreads to region B and drives the expression of TVA and RG only in the neurons projecting to region C. EnvA-pseudotyped RVΔG is then allowed to infect these projection-specific neurons and is transsynaptically transported to the presynaptic neurons in upstream region A. In cTRIO, this three-node tracing approach has been applied in transgenic mice and enables the identification of the inputs and outputs of specific cell types in region B. Specifically, AAV helpers injected into region B are replaced by FLP-dependent TVA and RG, while CAV-2 expressing FLP recombinase in a Cre-dependent manner is delivered into the downstream region C. In this way, in region B, only neurons that contain Cre and innervate region C can express TVA and RG, allowing the subsequent RVΔG-mediated transsynaptic labeling of neurons in region A.

Although this intersectional strategy is now commonly used for circuit mapping between multilevel neurons, it still has some limitations [70]. First, the widely used RV strain SAD-B19 is an attenuated strain with relatively low efficiency of synaptic transfer [71]. Second, despite reduced cytotoxicity of the attenuated strain, RV infection leads to cell death within 1–2 weeks, thereby hindering its



**Fig. 3** A dual-AAV system for sparse labeling of cell-type-specific neurons. Schematic of the design of the dual-AAV system for sparse labeling, comprising a “controller” and an “amplifier” AAV vector (upper left). When these two vectors are mixed and injected into the Cre-expressing mouse, leakage of TRE drives the weak expression of Flp in a few Cre<sup>+</sup> neurons. Flp subsequently flips the GFP-IRES-tTA cassettes in the amplifier and drives the low level of GFP and tTA expression in these sparsely-labeled neurons (right panel). The small amount of tTA further binds to the TRE and potentiates the expression of Flp and GFP (lower middle), thereby triggering positive feedback to enhance GFP expression in sparse neurons (lower left). TRE, tetracycline response element; Flp, flippase; IRES, internal ribosome entry site; tTA, tetracycline trans-activator.



**Fig. 4** Viral strategies of TRIO and cTRIO. TRIO combines the application of CAV-2 and RV, thus allowing projection-specific retrograde tracing within three-node neural circuits (from regions A to C *via* B). cTRIO further combines genetic approaches to allow

use in the long-term functional manipulation of neural networks. Fortunately, recent studies have generated a new G-deleted RV strain (CVS-N2CΔG) with enhanced transsynaptic transfer and reduced cytotoxicity, which partly overcome these two limitations [72, 73]. Another study has also developed a self-inactivating RVΔG (SiR), which switches off in primary infected cells *via* proteasomal degradation that disrupts the viral transcription-replication cycle. Since SiR also carries a Cre element, it allows permanent genetic access to the traced cells but prevents neuronal toxicity [74].

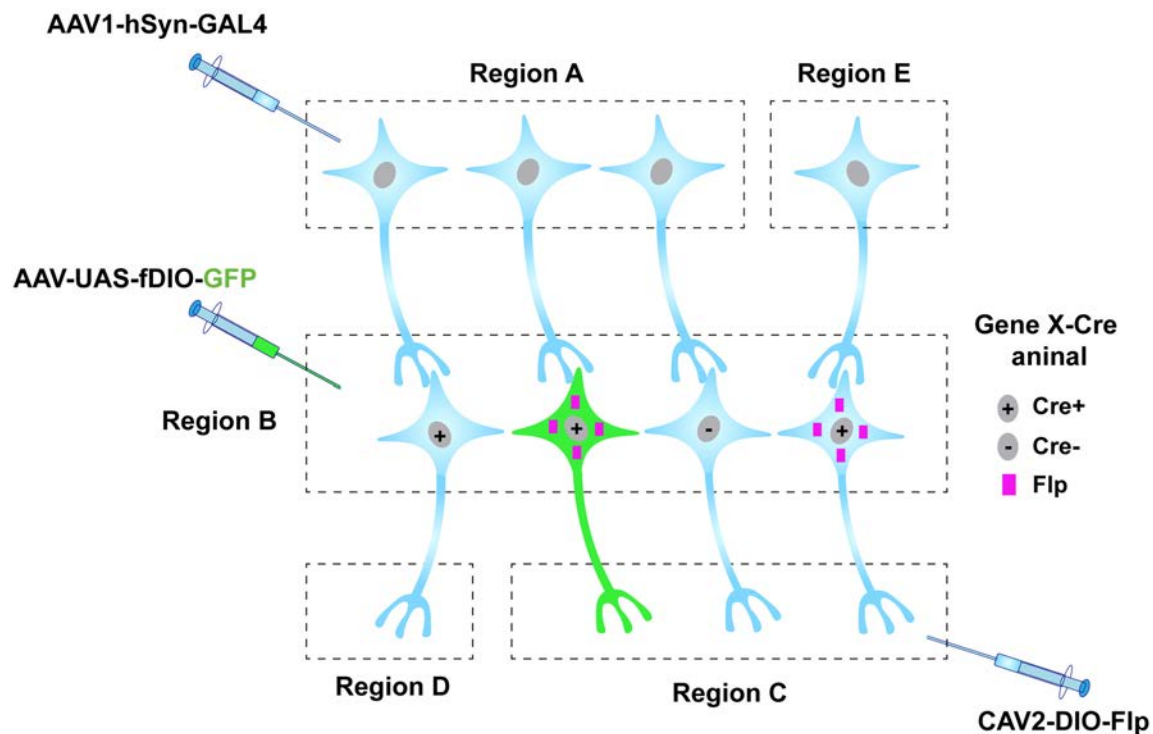
While current viral tools still have limitations in different aspects, the combinatorial use of viruses with diverse genetic strategies would expand their application. As described above, engineered viruses can label the neural circuits of interest in a cell type-specific and projection-specific manner, in combination with different recombinase systems. However, it is insufficient to define and get access to a function-specific neuronal subset based on one marker gene, as neurons are diverse with hundreds of subcategories. Intersectional strategies using multiplex recombinase systems allow viruses to get genetic and functional access to a more specific cell subtype [75]. In a recent study, a Cre- and Flp-dependent virus was delivered to a double transgenic mouse, in which Tac1-positive neurons expressed Cre and GABAergic neurons expressed Flp, thereby specifically labeling and manipulating the Vgat and Tac1 double-positive neurons [76]. Another study used

mapping cell type- and projection-specific neural circuits (from regions A to C *via* Cre<sup>+</sup> cells in B). TRIO, tracing the relationship between input and output; cTRIO, cell-type-specific TRIO; DIO, double-floxed inverse open reading frame; fDIO, Flp-controlled DIO.

viruses expressing recombinases driven by cell subclass-specific enhancers in new three-color reporter mice, Ai213, allowing specific and simultaneous labeling of three distinct cell subsets in the mouse cortex [77]. In the future, by virtue of versatile recombinases and viral systems, we may be able to label even more specific subsets of neurons (Region B in Fig. 5) based on input- and projection-tagging strategies (Fig. 5). For example, there are two different cell populations (Cre<sup>+</sup> and Cre<sup>-</sup>) in region B. By injecting CAV2-DIO-Flp in B's putative downstream area (Region C), Cre<sup>+</sup> cells projecting to C express Flp recombinase. However, this particular population of cells is usually innervated by multiple upstream inputs. After injecting the anterograde transsynaptic AAV1 vector carrying GAL4 into a presynaptic region (A), neurons (in B) innervated by region A express GAL4. By further injecting the UAS (upstream activating sequence)-driven AAV vector expressing Flp-dependent GFP into the local region (B), we are able to specifically label Cre<sup>+</sup> cells (shown in green) innervated by region A but projecting to C. By this means, a more specific subset of neurons, characterized by their specific input, output, and molecular identity, can be genetically accessed (Fig. 5).

Currently, viral tracers are mostly delivered through an invasive craniotomy or injection into peripheral tissue. For intersectional labeling strategies, several different types of viruses are injected into different target regions, which unavoidably leads to damage or trauma. Systemic delivery,





**Fig. 5** Intersectional strategies to define and access more specific cell types. With the combination of multiplex recombinase systems, including GAL4-UAS, Cre-LoxP, and Flp-FRT, a more specific subset of neurons can be defined by their input, output, and molecular identity. The schematic shows that neurons expressing Cre and projecting to region C contain Flp. However, only neurons that

receive input from region A (shown in green) can express GAL4, which binds to the UAS promoter and initiates the downstream expression of the virus injected into region B. In this case, a specific cell type expressing Cre, which is innervated by certain inputs and projects to putative downstream targets, can be accessed.

mostly *via* intravenous injection, provides a simpler and non-invasive alternative for virus delivery to the central and peripheral nervous systems [78, 79]. The newly-developed AAV variant AAV.CAP-B10 exhibits high specificity and efficiency to target neurons in the brain after intravenous delivery, with rare accumulation in the liver [80]. Although intravenous injection is more commonly used for gene therapy, it is plausible to suppose that systemic delivery could also be used in viral tracing to access specific cell types. For example, by locally applying focused ultrasound to open the blood-brain barrier, systemically-delivered viruses are able to enter this target region [81]. Moreover, adding cell-type-specific promoters into the viral genome, using the recombinase systems, or engineering the viral capsids according to the cell and tissue tropism, also helps to achieve the cell-type-specific entry of systemically-delivered viruses.

## Conclusions

Engineered viruses have become the most powerful tools in the technical arsenal of modern neuroscience. The ideal viral tools would be avirulent with a larger capacity for

transgene packaging, easier and non-invasive delivery, and greater specificity to target cells but wider applicability across species [82]. In addition to the traditional modification of the viral genome and capsid/envelope, new methods, including M-CREATE (multiplexed Cre recombination-based AAV targeted evolution) [83] and machine learning-guided design [84], have been developed to screen and engineer new recombinant viruses with wider applicability. As the unknown mechanisms of the virus are gradually unveiled, we believe that more suitable viral tools will be developed in the near future and accelerate the advances of neuroscience.

**Acknowledgments** This review was supported by the National Key Research and Development Program of China (2021ZD0202700 and 2021ZD0202703), and the National Natural Science Foundation of China (32070974).

**Conflict of interest** The authors claim that there are no conflict of interest.

**Open Access** This article is licensed under a Creative Commons Attribution 4.0 International License, which permits use, sharing, adaptation, distribution and reproduction in any medium or format, as long as you give appropriate credit to the original author(s) and the source, provide a link to the Creative Commons licence, and indicate

if changes were made. The images or other third party material in this article are included in the article's Creative Commons licence, unless indicated otherwise in a credit line to the material. If material is not included in the article's Creative Commons licence and your intended use is not permitted by statutory regulation or exceeds the permitted use, you will need to obtain permission directly from the copyright holder. To view a copy of this licence, visit <http://creativecommons.org/licenses/by/4.0/>.

## References

- Kristensson K, Olsson Y. Uptake and retrograde axonal transport of peroxidase in hypoglossal neurones. *Acta Neuropathol* 1971, 19: 1–9.
- Kristensson K, Olsson Y. Retrograde axonal transport of protein. *Brain Res* 1971, 29: 363–365.
- Gerfen CR, Sawchenko PE. An anterograde neuroanatomical tracing method that shows the detailed morphology of neurons, their axons and terminals: Immunohistochemical localization of an axonally transported plant lectin, Phaseolus vulgaris-leucoagglutinin (PHA-L). *Brain Res* 1984, 290: 219–238.
- Glover JC, Petrusdottir G, Jansen JK. Fluorescent dextran-amines used as axonal tracers in the nervous system of the chicken embryo. *J Neurosci Methods* 1986, 18: 243–254.
- Schmued LC, Fallon JH. Fluoro-Gold: a new fluorescent retrograde axonal tracer with numerous unique properties. *Brain Res* 1986, 377: 147–154.
- Trojanowski JQ, Gonatas JO, Gonatas NK. Conjugates of horseradish peroxidase (HRP) with cholera toxin and wheat germ agglutinin are superior to free HRP as orthogradely transported markers. *Brain Res* 1981, 223: 381–385.
- Kristensson K, Ghatti B, Wiśniewski HM. Study on the propagation of *Herpes simplex* virus (type 2) into the brain after intraocular injection. *Brain Res* 1974, 69: 189–201.
- Lanciego JL, Wouterlood FG. Neuroanatomical tract-tracing techniques that did go viral. *Brain Struct Funct* 2020, 225: 1193–1224.
- Goodpasture EW, Teague O. Transmission of the Virus of *Herpes* Febrilis along Nerves in experimentally infected Rabbits. *J Med Res* 1923, 44(139–184): 7.
- Kristensson K, Nennesmo L, Persson L, Lycke E. Neuron to neuron transmission of herpes simplex virus. Transport of virus from skin to brainstem nuclei. *J Neurol Sci* 1982, 54: 149–156.
- Bak IJ, Markham CH, Cook ML, Stevens JG. Intraaxonal transport of Herpes simplex virus in the rat central nervous system. *Brain Res* 1977, 136: 415–429.
- Peel AL, Zolotukhin S, Schrimsher GW, Muzyczka N, Reier PJ. Efficient transduction of green fluorescent protein in spinal cord neurons using adeno-associated virus vectors containing cell type-specific promoters. *Gene Ther* 1997, 4: 16–24.
- Junyent F, Kremer EJ. CAV-2—why a canine virus is a neurobiologist's best friend. *Curr Opin Pharmacol* 2015, 24: 86–93.
- Conzelmann KK, Cox JH, Schneider LG, Thiel HJ. Molecular cloning and complete nucleotide sequence of the attenuated rabies virus SAD B19. *Virology* 1990, 175: 485–499.
- Aston-Jones G, Card JP. Use of pseudorabies virus to delineate multisynaptic circuits in brain: Opportunities and limitations. *J Neurosci Methods* 2000, 103: 51–61.
- Cong W, Shi Y, Qi YQ, Wu JY, Gong L, He M. Viral approaches to study the mammalian brain: Lineage tracing, circuit dissection and therapeutic applications. *J Neurosci Methods* 2020, 335: 108629.
- Sarno E, Robison AJ. Emerging role of viral vectors for circuit-specific gene interrogation and manipulation in rodent brain. *Pharmacol Biochem Behav* 2018, 174: 2–8.
- Callaway EM. Transneuronal circuit tracing with neurotropic viruses. *Curr Opin Neurobiol* 2008, 18: 617–623.
- Li JM, Liu TA, Dong Y, Kondoh K, Lu ZH. Trans-synaptic neural circuit-tracing with neurotropic viruses. *Neurosci Bull* 2019, 35: 909–920.
- Xu XM, Holmes TC, Luo MH, Beier KT, Horwitz GD, Zhao F. Viral vectors for neural circuit mapping and recent advances in trans-synaptic anterograde tracers. *Neuron* 2020, 107: 1029–1047.
- Chamberlin NL, Du B, de Lacalle S, Saper CB. Recombinant adeno-associated virus vector: Use for transgene expression and anterograde tract tracing in the CNS. *Brain Res* 1998, 793: 169–175.
- Samulski RJ, Muzyczka N. AAV-mediated gene therapy for research and therapeutic purposes. *Annu Rev Virol* 2014, 1: 427–451.
- McCown TJ, Xiao X, Li J, Breese GR, Samulski RJ. Differential and persistent expression patterns of CNS gene transfer by an adeno-associated virus (AAV) vector. *Brain Res* 1996, 713: 99–107.
- Murlidharan G, Samulski RJ, Asokan A. Biology of adeno-associated viral vectors in the central nervous system. *Front Mol Neurosci* 2014, 7: 76.
- Watakabe A, Ohtsuka M, Kinoshita M, Takaji M, Isa K, Mizukami H, *et al.* Comparative analyses of adeno-associated viral vector serotypes 1, 2, 5, 8 and 9 in marmoset, mouse and macaque cerebral cortex. *Neurosci Res* 2015, 93: 144–157.
- Castle MJ, Turunen HT, Vandenberghe LH, Wolfe JH. Controlling AAV tropism in the nervous system with natural and engineered capsids. *Methods Mol Biol* 2016, 1382: 133–149.
- Burger C, Gorbatyuk OS, Velardo MJ, Peden CS, Williams P, Zolotukhin S, *et al.* Recombinant AAV viral vectors pseudotyped with viral capsids from serotypes 1, 2, and 5 display differential efficiency and cell tropism after delivery to different regions of the central nervous system. *Mol Ther* 2004, 10: 302–317.
- Howard DB, Powers K, Wang Y, Harvey BK. Tropism and toxicity of adeno-associated viral vector serotypes 1, 2, 5, 6, 7, 8, and 9 in rat neurons and glia *in vitro*. *Virology* 2008, 372: 24–34.
- Lee Y, Messing A, Su M, Brenner M. GFAP promoter elements required for region-specific and astrocyte-specific expression. *Glia* 2008, 56: 481–493.
- He M, Huang ZJ. Genetic approaches to access cell types in mammalian nervous systems. *Curr Opin Neurobiol* 2018, 50: 109–118.
- Luo LQ, Callaway EM, Svoboda K. Genetic dissection of neural circuits: A decade of progress. *Neuron* 2018, 98: 256–281.
- Soudais C, Laplace-Builhe C, Kissa K, Kremer EJ. Preferential transduction of neurons by canine adenovirus vectors and their efficient retrograde transport *in vivo*. *FASEB J* 2001, 15: 2283–2285.
- Soudais C, Skander N, Kremer EJ. Long-term *in vivo* transduction of neurons throughout the rat CNS using novel helper-dependent CAV-2 vectors. *FASEB J* 2004, 18: 391–393.
- Salinas S, Bilsland LG, Henaff D, Weston AE, Keriell A, Schiavo G, *et al.* CAR-associated vesicular transport of an adenovirus in motor neuron axons. *PLoS Pathog* 2009, 5: e1000442.
- Salinas S, Zussy C, Loustalot F, Henaff D, Menendez G, Morton PE, *et al.* Disruption of the coxsackievirus and adenovirus receptor-homodimeric interaction triggers lipid microdomain- and dynamin-dependent endocytosis and lysosomal targeting. *J Biol Chem* 2014, 289: 680–695.

36. Wickersham IR, Finke S, Conzelmann KK, Callaway EM. Retrograde neuronal tracing with a deletion-mutant rabies virus. *Nat Methods* 2007, 4: 47–49.
37. Tervo DGR, Hwang BY, Viswanathan S, Gaj T, Lavzin M, Ritola KD, *et al.* A designer AAV variant permits efficient retrograde access to projection neurons. *Neuron* 2016, 92: 372–382.
38. Zhang B, Qiu LY, Xiao W, Ni H, Chen LH, Wang F, *et al.* Reconstruction of the hypothalamo-neurohypophysial system and functional dissection of magnocellular oxytocin neurons in the brain. *Neuron* 2021, 109: 331–346.e7.
39. Davidsson M, Wang G, Aldrin-Kirk P, Cardoso T, Nolbrant S, Hartnor M, *et al.* A systematic capsid evolution approach performed *in vivo* for the design of AAV vectors with tailored properties and tropism. *Proc Natl Acad Sci U S A* 2019, 116: 27053–27062.
40. Gorbatyuk OS, Warrington KHJR, Gorbatyuk MS, Zolotukhin I, Lewin AS, Muzyczka N. Biodistribution of adeno-associated virus type 2 with mutations in the capsid that contribute to heparan sulfate proteoglycan binding. *Virus Res* 2019, 274: 197771.
41. Tordo J, O’Leary C, Antunes ASLM, Palomar N, Aldrin-Kirk P, Basche M, *et al.* A novel adeno-associated virus capsid with enhanced neurotropism corrects a lysosomal transmembrane enzyme deficiency. *Brain* 2018, 141: 2014–2031.
42. Zemanick MC, Strick PL, Dix RD. Direction of transneuronal transport of *Herpes simplex* virus 1 in the primate motor system is strain-dependent. *Proc Natl Acad Sci U S A* 1991, 88: 8048–8051.
43. Dix RD, McKendall RR, Baringer JR. Comparative neurovirulence of herpes simplex virus type 1 strains after peripheral or intracerebral inoculation of BALB/c mice. *Infect Immun* 1983, 40: 103–112.
44. Sun N, Cassell MD, Perlman S. Anterograde, transneuronal transport of herpes simplex virus type 1 strain H129 in the murine visual system. *J Virol* 1996, 70: 5405–5413.
45. Han WF, Tellez LA, Perkins MH, Perez IO, Qu TR, Ferreira J, *et al.* A neural circuit for gut-induced reward. *Cell* 2018, 175: 665–678.e23.
46. Lo L, Anderson DJ. A Cre-dependent, anterograde transsynaptic viral tracer for mapping output pathways of genetically marked neurons. *Neuron* 2011, 72: 938–950.
47. Zeng WB, Jiang HF, Gang YD, Song YG, Shen ZZ, Yang H, *et al.* Anterograde monosynaptic transneuronal tracers derived from herpes simplex virus 1 strain H129. *Mol Neurodegener* 2017, 12: 38.
48. Li XY, Chen WT, Pan K, Li H, Pang P, Guo Y, *et al.* Serotonin receptor 2c-expressing cells in the ventral CA1 control attention *via* innervation of the Edinger-Westphal nucleus. *Nat Neurosci* 2018, 21: 1239–1250.
49. Li E, Guo J, Oh SJ, Luo Y, Oliveros HC, Du WQ, *et al.* Anterograde transneuronal tracing and genetic control with engineered yellow fever vaccine YFV-17D. *Nat Methods* 2021, 18: 1542–1551.
50. Zingg B, Chou XL, Zhang ZG, Mesik L, Liang FX, Tao HW, *et al.* AAV-mediated anterograde transsynaptic tagging: Mapping corticocollicular input-defined neural pathways for defense behaviors. *Neuron* 2017, 93: 33–47.
51. Hollis Ii ER, Kadoya K, Hirsch M, Samulski RJ, Tuszynski MH. Efficient retrograde neuronal transduction utilizing self-complementary AAV1. *Mol Ther* 2008, 16: 296–301.
52. Rothermel M, Brunert D, Zabawa C, Díaz-Quesada M, Wachowiak M. Transgene expression in target-defined neuron populations mediated by retrograde infection with adeno-associated viral vectors. *J Neurosci* 2013, 33: 15195–15206.
53. Card JP, Levitt P, Enquist LW. Different patterns of neuronal infection after intracerebral injection of two strains of pseudorabies virus. *J Virol* 1998, 72: 4434–4441.
54. Card JP, Enquist LW. Transneuronal circuit analysis with pseudorabies viruses. *Curr Protoc Neurosci* 2014, 68: 1.5.1–1.539.
55. Pickard GE, Smeraski CA, Tomlinson CC, Banfield BW, Kaufman J, Wilcox CL, *et al.* Intravitreal injection of the attenuated pseudorabies virus PRV Bartha results in infection of the hamster suprachiasmatic nucleus only by retrograde transsynaptic transport *via* autonomic circuits. *J Neurosci* 2002, 22: 2701–2710.
56. Card JP, Rinaman L, Schwaber JS, Miselis RR, Whealy ME, Robbins AK, *et al.* Neurotropic properties of pseudorabies virus: Uptake and transneuronal passage in the rat central nervous system. *J Neurosci* 1990, 10: 1974–1994.
57. Callaway EM, Luo LQ. Monosynaptic circuit tracing with glycoprotein-deleted rabies viruses. *J Neurosci* 2015, 35: 8979–8985.
58. Ugolini G. Rabies virus as a transneuronal tracer of neuronal connections. *Adv Virus Res* 2011, 79: 165–202.
59. Ugolini G. Specificity of rabies virus as a transneuronal tracer of motor networks: Transfer from hypoglossal motoneurons to connected second-order and higher order central nervous system cell groups. *J Comp Neurol* 1995, 356: 457–480.
60. Wickersham IR, Lyon DC, Barnard RJO, Mori T, Finke S, Conzelmann KK, *et al.* Monosynaptic restriction of transsynaptic tracing from single, genetically targeted neurons. *Neuron* 2007, 53: 639–647.
61. Lin R, Wang RY, Yuan J, Feng QR, Zhou YT, Zeng SQ, *et al.* Cell-type-specific and projection-specific brain-wide reconstruction of single neurons. *Nat Methods* 2018, 15: 1033–1036.
62. Mizuno H, Luo WS, Tarusawa E, Saito YM, Sato T, Yoshimura Y, *et al.* NMDAR-regulated dynamics of layer 4 neuronal dendrites during thalamocortical reorganization in neonates. *Neuron* 2014, 82: 365–379.
63. Gong H, Xu DL, Yuan J, Li XN, Guo CD, Peng J, *et al.* High-throughput dual-colour precision imaging for brain-wide connectome with cytoarchitectonic landmarks at the cellular level. *Nat Commun* 2016, 7: 12142.
64. Eliava M, Melchior M, Knobloch-Bollmann HS, Wahis J, da Silva Gouveia M, Tang Y, *et al.* A new population of parvocellular oxytocin neurons controlling magnocellular neuron activity and inflammatory pain processing. *Neuron* 2016, 89: 1291–1304.
65. Li SJ, Vaughan A, Sturgill JF, Kepecs A. A viral receptor complementation strategy to overcome CAV-2 tropism for efficient retrograde targeting of neurons. *Neuron* 2018, 98: 905–917.e5.
66. Sun QT, Li XN, Ren M, Zhao MT, Zhong QY, Ren YQ, *et al.* A whole-brain map of long-range inputs to GABAergic interneurons in the mouse medial prefrontal cortex. *Nat Neurosci* 2019, 22: 1357–1370.
67. Watabe-Uchida M, Zhu LS, Ogawa SK, Vamanrao A, Uchida N. Whole-brain mapping of direct inputs to midbrain dopamine neurons. *Neuron* 2012, 74: 858–873.
68. Wu XT, Morishita W, Beier KT, Heifets BD, Malenka RC. 5-HT modulation of a medial septal circuit tunes social memory stability. *Nature* 2021, 599: 96–101.
69. Schwarz LA, Miyamichi K, Gao XJ, Beier KT, Weissbourd B, DeLoach KE, *et al.* Viral-genetic tracing of the input-output organization of a central noradrenaline circuit. *Nature* 2015, 524: 88–92.
70. Saleeba C, Dempsey B, Le S, Goodchild A, McMullan S. A student’s guide to neural circuit tracing. *Front Neurosci* 2019, 13: 897.

71. Schnell MJ, McGettigan JP, Wirblich C, Papaneri A. The cell biology of rabies virus: Using stealth to reach the brain. *Nat Rev Microbiol* 2010, 8: 51–61.
72. Reardon TR, Murray AJ, Turi GF, Wirblich C, Croce KR, Schnell MJ, *et al.* Rabies virus CVS-N2cΔG strain enhances retrograde synaptic transfer and neuronal viability. *Neuron* 2016, 89: 711–724.
73. Zhu XT, Lin KZ, Liu Q, Yue XP, Mi HJ, Huang XP, *et al.* Rabies virus pseudotyped with CVS-N2C glycoprotein as a powerful tool for retrograde neuronal network tracing. *Neurosci Bull* 2020, 36: 202–216.
74. Ciabatti E, González-Rueda A, Mariotti L, Morgese F, Tripodi M. Life-long genetic and functional access to neural circuits using self-inactivating rabies virus. *Cell* 2017, 170: 382–392.e14.
75. Fenno LE, Ramakrishnan C, Kim YS, Evans KE, Lo M, Vesuna S, *et al.* Comprehensive dual- and triple-feature intersectional single-vector delivery of diverse functional payloads to cells of behaving mammals. *Neuron* 2020, 107: 836–853.e11.
76. Wu YE, Dang J, Kingsbury L, Zhang MM, Sun FM, Hu RK, *et al.* Neural control of affiliative touch in prosocial interaction. *Nature* 2021, 599: 262–267.
77. Graybuck LT, Daigle TL, Sedeño-Cortés AE, Walker M, Kalmbach B, Lenz GH, *et al.* Enhancer viruses for combinatorial cell-subclass-specific labeling. *Neuron* 2021, 109: 1449–1464.e13.
78. Foust KD, Nurre E, Montgomery CL, Hernandez A, Chan CM, Kaspar BK. Intravascular AAV9 preferentially targets neonatal neurons and adult astrocytes. *Nat Biotechnol* 2009, 27: 59–65.
79. Chan KY, Jang MJ, Yoo BB, Greenbaum A, Ravi N, Wu WL, *et al.* Engineered AAVs for efficient noninvasive gene delivery to the central and peripheral nervous systems. *Nat Neurosci* 2017, 20: 1172–1179.
80. Goertsen D, Flytzanis NC, Goeden N, Chuapoco MR, Cummins A, Chen YJ, *et al.* AAV capsid variants with brain-wide transgene expression and decreased liver targeting after intravenous delivery in mouse and marmoset. *Nat Neurosci* 2022, 25: 106–115.
81. Szablowski JO, Lee-Gosselin A, Lue B, Malounda D, Shapiro MG. Acoustically targeted chemogenetics for the non-invasive control of neural circuits. *Nat Biomed Eng* 2018, 2: 475–484.
82. Nectow AR, Nestler EJ. Viral tools for neuroscience. *Nat Rev Neurosci* 2020, 21: 669–681.
83. Ravindra Kumar S, Miles TF, Chen XH, Brown D, Dobrev T, Huang Q, *et al.* Multiplexed Cre-dependent selection yields systemic AAVs for targeting distinct brain cell types. *Nat Methods* 2020, 17: 541–550.
84. Ogden PJ, Kelsic ED, Sinai S, Church GM. Comprehensive AAV capsid fitness landscape reveals a viral gene and enables machine-guided design. *Science* 2019, 366: 1139–1143.



REVIEW

# CRISPR-Based Genome-Editing Tools for Huntington's Disease Research and Therapy

Yiyang Qin<sup>1</sup> · Shihua Li<sup>1</sup> · Xiao-Jiang Li<sup>1</sup> · Su Yang<sup>1</sup>

Received: 2 December 2021 / Accepted: 17 March 2022 / Published online: 24 May 2022

© Center for Excellence in Brain Science and Intelligence Technology, Chinese Academy of Sciences 2022

**Abstract** Huntington's disease (HD) is an autosomal dominantly-inherited neurodegenerative disease, which is caused by CAG trinucleotide expansion in exon 1 of the Huntingtin (*HTT*) gene. Although HD is a rare disease, its monogenic nature makes it an ideal model in which to understand pathogenic mechanisms and to develop therapeutic strategies for neurodegenerative diseases. Clustered regularly-interspaced short palindromic repeats (CRISPR) is the latest technology for genome editing. Being simple to use and highly efficient, CRISPR-based genome-editing tools are rapidly gaining popularity in biomedical research and opening up new avenues for disease treatment. Here, we review the development of CRISPR-based genome-editing tools and their applications in HD research to offer a translational perspective on advancing the genome-editing technology to HD treatment.

**Keywords** Huntington's disease · CRISPR · Animal models

## Introduction

Huntington's disease (HD) is an autosomal dominant neurodegenerative disease caused by a mutation in the Huntingtin (*HTT*) gene, which is localized on the short arm of chromosome 4 (4p16.3). The mutation is caused by the expansion of CAG trinucleotide repeats in exon 1 of *HTT*.

In unaffected individuals, the number of CAG trinucleotide repeats in *HTT* varies from 6 to 35, whereas HD patients typically carry 40 or more CAG repeats [1–4]. The expanded CAG trinucleotide repeats are translated into a polyglutamine (polyQ) tract near the N-terminal region of the *HTT* protein, which renders the protein prone to misfold and aggregate. The mutant *HTT* protein confers gains of function that are neurotoxic, and the medium spiny neurons in the striatum are particularly vulnerable to such insults [5]. Therefore, the striatum is the most affected brain region in HD, but other regions, such as the cerebral cortex, globus pallidus, thalamus, subthalamic nucleus, substantia nigra, hypothalamus, and cerebellum can also be affected as the disease progresses. HD is a devastating disease, as most patients display characteristic symptoms such as chorea, motor dysfunction, psychiatric disturbance, and cognitive decline during middle age, which eventually leads to death in 15 to 20 years after the onset of symptoms [6]. Currently there is no effective treatment to halt or reverse the course of HD.

Since the *HTT* gene was identified as the causative gene for HD in 1993 [7], extensive efforts have been devoted to understanding HD pathogenesis, with the hope to eventually develop effective treatment options. Despite being a rare neurodegenerative disease, the monogenic background of HD makes it an ideal fit for such a challenging task: it is relatively easy to manipulate a single mutant gene to establish cellular and animal models; it is also quite straightforward that lowering *HTT* products should be able to alleviate neurotoxicity. Therefore, genome-editing technologies that can effectively manipulate individual genes, such as zinc finger nuclease (ZFN) and transcription activator-like effector nuclease (TALEN) [8–10], greatly facilitate HD-related research. This effect is much greater with the emergence of the latest technology, clustered

✉ Su Yang  
syang33@jnu.edu.cn

<sup>1</sup> Guangdong Key Laboratory of Non-human Primate Research, Guangdong-Hongkong-Macau Institute of CNS Regeneration, Jinan University, Guangzhou 510632, China

regularly-interspaced short palindromic repeats (CRISPR) [11]. Here, we briefly review the development of CRISPR-based genome-editing technology. We also summarize the use of CRISPR in HD research from three aspects: generating animal models, studying disease mechanisms, and developing HD treatment strategies. Finally, we list the major innovations in CRISPR technology, and preview how to take advantage of such innovations in future HD research and treatment.

## The Development of CRISPR Technology

The nucleotide sequence of the CRISPR system was first discovered by Ishino *et al.* in *Escherichia coli* in 1987 [12]. Since then, many similar sequences have been identified and given different names [13]. To avoid confusion related to the different nomenclatures, the acronym CRISPR was proposed in 2002 [14]. Although abundant CRISPR sequences have been identified, their biological function remained elusive. Subsequently, many studies have explored the potential function of CRISPR in cells. Most of the work has centered around adaptive immunity, as multiple research groups have independently reported that the spacers in CRISPR elements have high sequence homology with extrachromosomal elements [15–18]. These results triggered speculation that CRISPR may function as a protective mechanism against foreign genetic substances, such as phages and plasmids [19]. Indeed, most bacteria and archaea can incorporate the short invading DNA sequences into their own genome as CRISPRs [20–22], which helps them to acquire adaptive immunity to defend against the invading viruses [20]. In 2010, Garneau *et al.* revealed that the CRISPR-associated (Cas) protein, guided by short CRISPR RNAs, can specifically cleave bacteriophage and plasmid DNAs in a sequence-specific manner *in vivo* [23], thereby showing the great potential of the CRISPR/Cas system in genome editing. Two years later, the milestone study by Jinek *et al.* showed for the first time that the CRISPR/Cas9 system can be programmed to cut specific DNA sequences to generate double-stranded DNA breaks [24]. Since then, CRISPR-based genome-editing technology has begun to take off.

To date, more than 30 Cas proteins have been identified from different bacterial strains, and the number is rapidly expanding [25, 26], while CRISPR/Cas9 remains the major workhorse for genome editing in today's research community. CRISPR/Cas9 consists of two parts, the Cas9 endonuclease and a synthetic single guide RNA (sgRNA). The sgRNA contains an ~20-nucleotide protospacer that pairs with the target DNA sequence, and a 3 to 6-nucleotide protospacer adjacent motif (PAM), which is indispensable for sgRNA-DNA hybridization [11]. In

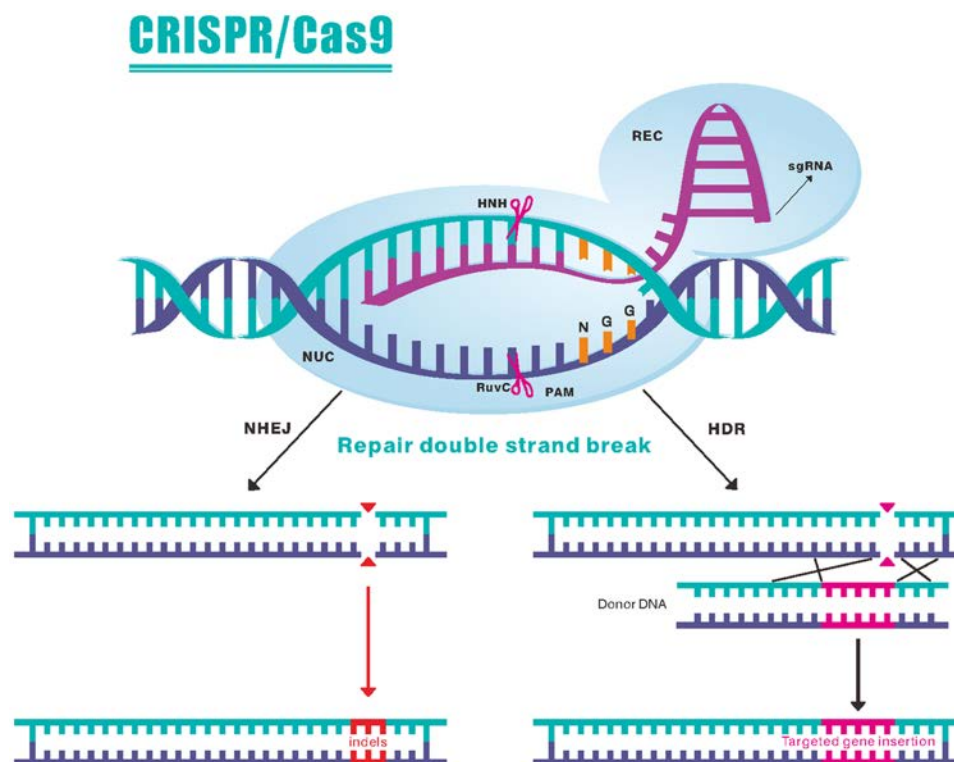
theory, CRISPR/Cas9 can edit any target DNA sequence by designing a proper protospacer sequence. Once the sgRNA recognizes the complementary sequences of the target gene, Cas9 binds to the sgRNA-DNA complex and cuts the DNA 3–4 nucleotides upstream of the correct PAM sequence. In eukaryotic cells, the cutting leads to a double-strand DNA break (DSB), which can be repaired by either homology-directed repair (HDR) or non-homologous end-joining (NHEJ). In most cases, the DSB is repaired by NHEJ, as it is a highly efficient but error-prone process. The random insertions or deletions caused by NHEJ can lead to frame-shift mutations or premature stop codons, so that a specific gene can be knocked out *via* this approach. Alternatively, HDR can precisely repair the DSB with a homologous DNA template. As a result, specific mutations can be introduced by providing a designed template to achieve gene knock-in (Fig. 1). Nonetheless, HDR efficiency is very low, especially in postmitotic cells, such as neurons [27, 28].

## Using CRISPR Technology in HD Research

In the most common neurodegenerative diseases, such as Alzheimer's disease (AD) and Parkinson's disease (PD), ~90% of the cases are sporadic [29, 30], making it difficult to use genetic tools to model them. In contrast, HD is purely genetic, and is caused by a monogenic mutation. Early generations of genome-editing tools, such as ZFN and TALEN, have been successfully used in HD research [31–33]. Nonetheless, designing such tools requires special techniques, and is time-consuming and expensive. After the seminal work showing that CRISPR works in mammalian cells [34], CRISPR rapidly replaced ZFN and TALEN and became the favorite genome-editing tool in HD research. The major applications of CRISPR technology in HD research can be categorized into three aspects (Fig. 2).

## Establishing Cellular and Animal Models

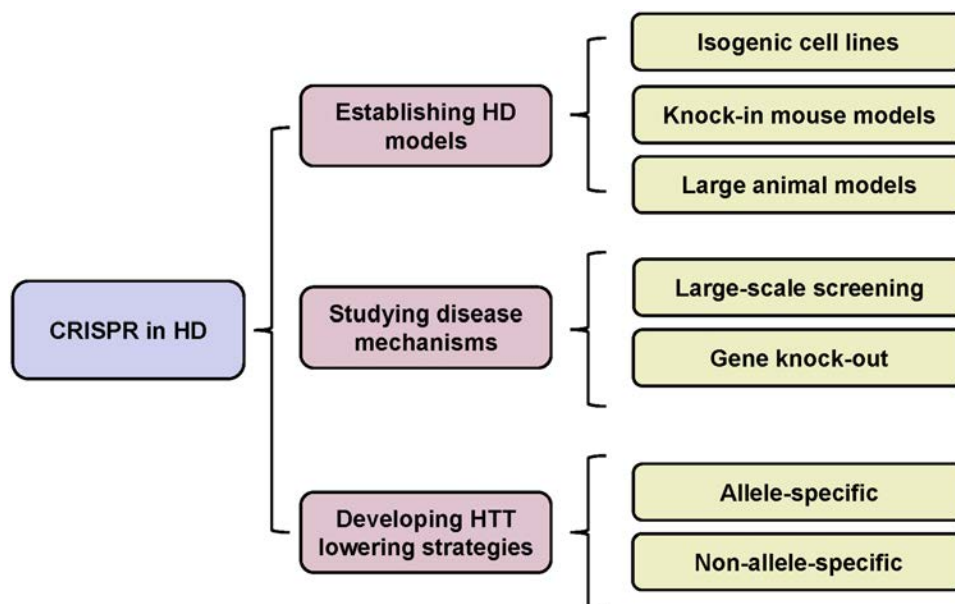
Disease models are essential for studying HD. Since *HTT* is a large gene spanning 180 kilobases and consisting of 67 exons, the conventional transgenic approach can only express DNA fragments that correspond to the neurotoxic N-terminal HTT proteins, which does not faithfully recapitulate HD conditions. In addition, overexpression of mutant proteins associated with the transgenic approach can lead to artificial or exaggerated pathological effects. Therefore, it is preferable to use a gene knock-in approach, so that mutant HTT toxicity can be studied under physiologically relevant conditions. CRISPR/Cas9, as a



**Fig. 1** Schematic showing the genome-editing mechanism of CRISPR/Cas9. The designed single guide RNA (sgRNA) binds to its complementary sequence in the genome and recruits the Cas9 protein to that region. Cas9 utilizes its two distinct active motifs, RuvC and HNH, to generate site-specific nicks (3–4 nucleotides upstream of the PAM sequence) on the opposite DNA strands, causing a double-strand break (DSB). This DSB is repaired by two

cellular mechanisms. The first is non-homologous end joining (NHEJ), which is efficient but error-prone. During the repair process, random nucleotide insertions or deletions are introduced near the DSB site, causing frame-shift mutations and gene knock-out. The other mechanism is homology directed repair (HDR), in which a donor DNA is used as a template to precisely repair the DSB. The donor DNA is specifically designed to achieve gene knock-in.

**Fig. 2** Summary of the major applications of CRISPR-based genome editing in Huntington's disease (HD) research. CRISPR-base genome-editing technology is currently used in three areas of HD research: (1) establishing HD models, including isogenic cell lines, knock-in mouse models, and large animal models; (2) studying disease mechanisms, such as large-scale genetic screening and gene knock-out; (3) developing mutant HTT-lowering strategies.



highly efficient genome-editing tool, greatly facilitates this process.

In 2014, CRISPR/Cas9 was first used to generate isogenic HD cellular models. By using CRISPR/Cas9 to

induce DNA cutting in the region of exon 1 *HTT* and supplying a donor construct containing 97 CAG repeats, the researchers established human induced pluripotent stem cells (iPSCs) harboring 21, 72, or 97 CAG repeats in *HTT* [35]. Since then, several groups have used similar approaches to generate isogenic HD human iPSCs, and reported phenotypic abnormalities in such cells, including impaired neuronal differentiation, increased sensitivity to growth factor withdrawal, mitochondrial defects, and gene expression changes [36, 37]. These results suggest that isogenic HD cellular models are promising resources for mechanistic studies and drug screening.

Mouse models remain the primary platforms for HD-related research. Multiple lines of HD knock-in mice have already been established by different research groups [38–41]. Nonetheless, CRISPR/Cas9 offers more versatility in creating novel knock-in mouse models to test hypotheses related to HD pathogenesis. For example, a prevailing theory in HD research is the toxic fragment hypothesis, which means that full-length mutant HTT protein is proteolytically cleaved to generate N-terminal HTT fragments of different lengths that are neurotoxic [42, 43]. However, which N-terminal fragment(s) confers the most toxicity remains unknown. By using CRISPR/Cas9 to edit the *HTT* gene in the embryos of HD140Q knock-in mice, two knock-in mouse lines expressing different N-terminal HTT fragments (the first 96 or 571 amino-acids) have been established. Compared with full-length HD140Q mice, these two lines show similar neuropathology and disease progression, and they all contain a stable N-terminal mutant HTT fragment equivalent to exon 1 HTT, suggesting that exon 1 HTT is the key pathological form [44]. Another provocative hypothesis is that CAG repeat expansion in the *HTT* gene leads to repeat-associated non-AUG (RAN) translation to produce toxic peptides [45]. *Via* CRISPR/Cas9-mediated genome editing, a knock-in mouse model that expresses mutant *HTT* mRNA but not mutant HTT protein was established. RAN-translated products were not detected in this mouse model, nor were HD-related pathological changes, indicating that RAN translation does not play a major role in HD pathogenesis [46].

Knock-in mouse models are valuable resources for HD research, but they lack the overt neurodegeneration in the striatum, which is a typical hallmark in HD patients [47, 48]. In 2018, an HD knock-in pig model was established. By using CRISPR/Cas9 and a donor vector carrying human exon1 *HTT* with 150 CAG repeats, the researchers successfully knocked in mutant *HTT* in fetal pig fibroblasts. Somatic cell nuclear transfer was later applied to generate newborn HD knock-in pigs. This pig model displayed striking HD-like phenotypes and selective neurodegeneration in the striatum [49], supporting the

rationale of using large animals to investigate HD pathogenesis and to explore potential therapeutics. Compared with the conventional method of homologous recombination, genome editing using CRISPR/Cas9 makes generating knock-in or knock-out animals much easier and faster, thereby turning the above research ideas into actual work.

## Studying Disease Mechanisms

The plethora of disease models enabled extensive research on the pathogenic mechanisms of HD. A great number of biological pathways and individual genes have been linked to HD pathogenesis. In addition, as a large protein consisting of more than 3000 amino-acids, HTT is believed to interact with numerous proteins. Studies using different methods have identified hundreds of potential HTT-interacting proteins [50–52]. However, there are two major challenges to clarify HD pathogenic mechanisms: first, how to efficiently and reliably perform screening and second, how to find the key targets that are most relevant to HD pathogenesis. Because CRISPR/Cas9 can easily and efficiently knock out genes of interest, it has been rapidly adopted to address these issues.

Large-scale genetic screening is a powerful way to identify essential genes for HD toxicity. In 2020, an unbiased genome-wide genetic screening was performed in the mouse central nervous system, using CRISPR and shRNA lentivirus [53]. In wild-type mice, the researchers found that neurons are vulnerable to perturbations of synaptic function, autophagy, proteostasis, mRNA processing, and mitochondrial function. The same approach was later used to identify genes that are essential for neuronal viability in the presence of mutant HTT. Screening results using one HD transgenic mouse model and one HD knock-in mouse model revealed that genes involved in methylation-dependent chromatin silencing, dopamine signaling, and members of the *Nme* gene family are genetic modifiers of mutant HTT toxicity, suggesting these genes could be new targets for therapeutic interventions.

Manipulating the expression level of an individual gene and examining its influence on the neuropathology in HD models remain the gold standard to verify the large screening results. For example, several genes, including *FAN1*, *RRM2B*, and *MLH1*, have been identified as genetic modifiers through genome-wide association studies [54, 55]. CRISPR/Cas9 was used to generate knock-out mice for each gene. These knock-out mice were then crossed with HD knock-in mice so that the genetic modifying effect of an individual gene could be tested *in vivo* [56]. HAP1 was the first discovered protein that interacts with HTT [57]. Deletion of HAP1 *via* CRISPR/Cas9 in adult HD knock-in mice leads to selective neuronal



loss in the striatum, and the neurotoxicity is mediated by Rhes, another HTT binding protein [58]. HspBP1 is an inhibitor of the carboxyl terminus of Hsp70-interacting protein, and functions as a regulator of protein quality control. Adeno-associated virus (AAV) carrying CRISPR/Cas9 was delivered to the striatum of HD knock-in mice to silence the expression of the HspBP1 gene, which reduced mutant HTT aggregates and attenuated neuropathology [59]. These are just a few examples of how CRISPR/Cas9 is enabling in-depth investigations of HD pathogenic mechanisms.

### Developing Mutant HTT-lowering Strategies

Through more than 20 years of research, it is apparent that HD pathogenesis is quite complex. Mutant HTT causes abnormalities in a myriad of cellular functions [2], including dysregulation of transcription, impairment of protein homeostasis, mitochondrial dysfunction, defective vesicle transport, disrupted  $\text{Ca}^{2+}$  signaling, epigenetic-chromatin deregulation, and excitotoxicity (Fig. 3). It would be very challenging to rely on traditional chemical approaches to rectify most of these abnormalities. However, as a monogenic disease, eliminating mutant HTT products serves as the most straightforward therapeutic option. Substantial efforts have been devoted to developing mutant HTT-lowering therapies. Methods targeting mutant *HTT* mRNA, such as antisense oligonucleotide (ASO) and RNA interference (RNAi), are being actively pursued in both preclinical and clinical studies [60, 61]. Another promising approach is to use small-molecule compounds that specifically tether mutant HTT protein to the autophagosome for clearance [62]. By targeting mRNA or protein, these methods have successfully reduced mutant HTT production in an allele-specific or non-allele-specific manner, and have achieved therapeutic benefits in animal models of HD. Compared with these methods, CRISPR/Cas9 has one unique advantage: it targets the genome, so that one treatment should permanently inactivate mutant HTT expression.

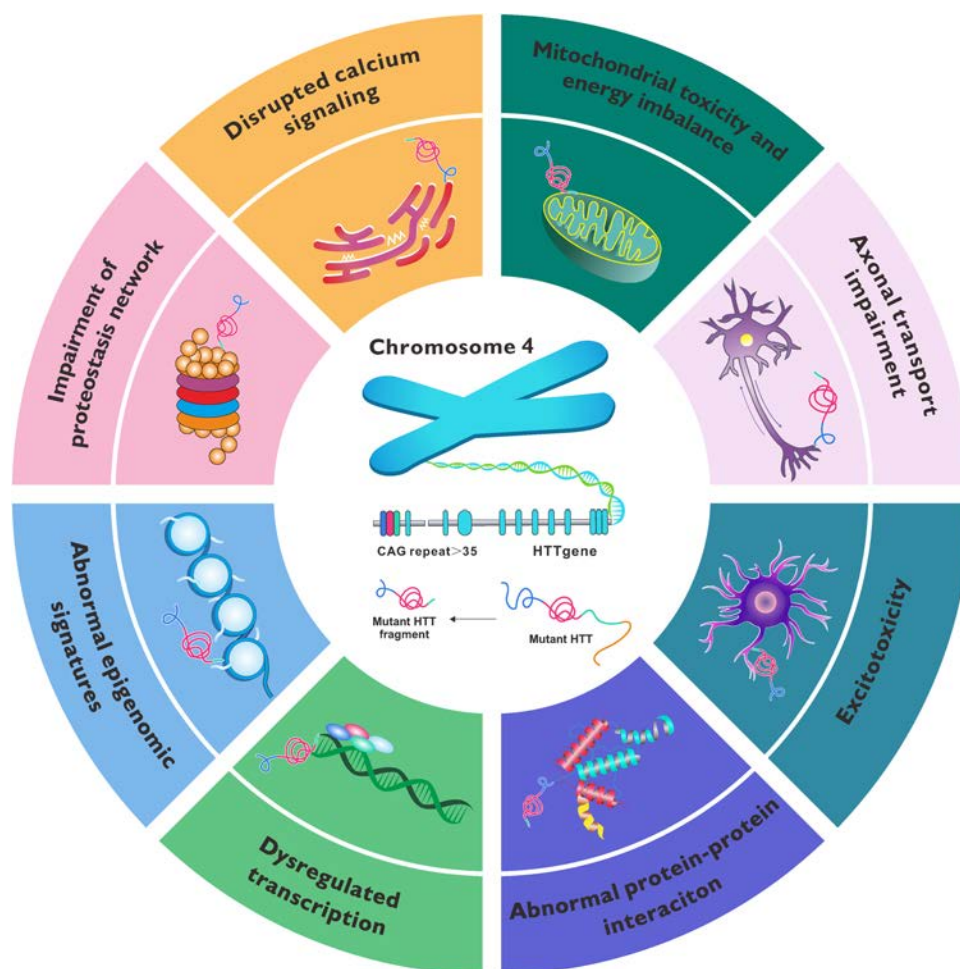
Multiple groups have already tested CRISPR/Cas9 genome editing in HD models (Table 1). Mutant *HTT* allele-specific deletion has been achieved by designing gRNAs targeting single nucleotide polymorphisms (SNPs) that only exist in the promoter region of the mutant allele [63, 64]. Because HD patients carry different SNPs in their genome, an array of sgRNAs needs to be designed, but they still cannot cover 100% of HD cases. Alternatively, sgRNAs spanning the CAG repeat were designed to remove the HTT protein in a non-allele-specific manner (Fig. 4). This strategy is backed by the findings that permanent removal of wild-type Htt in the mouse brain and temporary reduction of wild-

type HTT in the non-human primate brain are well tolerated [65–67]. Indeed, non-allele-specific reduction of HTT by CRISPR/Cas9 AAV injection ameliorates neurotoxicity and behavioral deficits in an HD knock-in mouse model [68]. These studies provide proof-of-concept that CRISPR/Cas9 could be a potential therapy for HD. In addition, several groups have further optimized this process. For example, a smaller version of Cas9 (SaCas9) has been used in the R6/2 mouse model of HD and prolonged its lifespan [69]. Virus-mediated expression of the bacterial Cas9 protein alters the transcription of genes involved in neuronal functions. Tagging Cas9 with a fragment of the cell-cycle protein Geminin reduces Cas9 protein stability in neurons, and significantly alleviates the neurotoxicity of Cas9 [70]. A self-destructive version of Cas9 (KamiCas9) has also been designed to limit the duration of expression of Cas9 protein, which reduces off-target effects [71]. CRISPR/Cas9 has also been used to reduce mutant HTT expression in HD patient iPSCs and differentiated neural stem cells, and this approach ameliorated mitochondrial and redox modifications [72].

Nonetheless, major concerns need to be addressed before CRISPR can be used as a therapeutic approach for HD. It remains technically challenging to effectively deliver CRISPR to the HD patient's brain, so that better delivery vehicles that can cross the blood-brain barrier and diffuse to a broad brain region are highly desirable. The off-target effects of CRISPR, which means that CRISPR induces DNA-cutting in unwanted chromosomal locations, need to be carefully examined using more stringent sequencing methods. Moreover, the long-term cellular reactions to HTT removal and the abnormal responses caused by the exogenous Cas9 protein, such as immune activation [73, 74], need to be tested, preferably in non-human primates. It is noteworthy that recently two highly-anticipated *HTT*-lowering candidates based on ASO failed in late-stage clinical trials. What is more confounding is that one of the candidates even worsened patient outcome measures compared with the placebo [61]. Such failure highlights the importance of correct dosage and timing for using ASOs to treat HD. Considering the effect of CRISPR is permanent, there would be less concern about timing, as CRISPR could be delivered to pre-symptomatic patients. Nonetheless, dosage remains a major issue. Given that *HTT*-lowering caused by CRISPR is irreversible, extra precautions need to be exercised in advancing CRISPR-based therapeutic methods for HD.

### Innovations of CRISPR Technology

In recent years, CRISPR technology has evolved so fast that novel innovations are published almost daily. Many of these innovations have yet been tested in HD research but



**Fig. 3** Summary of the major pathogenic mechanisms of Huntington's disease (HD) currently identified. Multiple cellular functions are believed to be affected by the presence of mutant Huntingtin (HTT): (1) the N-terminal fragments of mutant HTT enter the nucleus, interact with selected transcription factors, such as specificity protein 1 (Sp1) and tumor protein P53, and disrupt their transcriptional activity; (2) mutant HTT causes epigenetic abnormalities and chromatin structural changes, possibly by directly binding to methyl-CpG binding protein 2 (MeCP2); (3) mutant HTT impairs

the function of the proteasome ubiquitin system (UPS), which is the major mechanism for degrading misfolded proteins; (4) mutant HTT disrupts  $\text{Ca}^{2+}$  homeostasis and causes cytosolic  $\text{Ca}^{2+}$  overload; (5) mutant huntingtin triggers mitochondrial fragmentation and alters the mitochondrial proteome; (6) wild-type HTT is essential for axonal transport, whereas mutant HTT causes axonal transport defects; (7) mutant HTT inhibits glutamate uptake in glia, which leads to excitotoxicity; (8) mutant HTT has abnormal protein-protein interactions and affects the functions of individual proteins.

hold great promise (Table 2). For instance, Cpf1 or Cas12a was identified from *Francisella novicida* U112, and belongs to the Class 2, type V CRISPR system [75]. Compared with the commonly-used Cas9 (SpCas9), Cpf1 possesses some unique features. First, it is smaller, making it easier to package into viral vectors. Second, Cpf1 recognizes the TTN or TTTN PAM sequence, which is different from the NGG PAM sequence of Cas9, thereby offering more flexibility in targeting different genetic loci. Third, Cpf1 cleaves DNA and introduces a staggered DSB with 4- to 5-nucleotide overhangs, allowing for the incorporation of designed sequences, whereas Cas9 generates a blunt-ended DSB. Last, Cpf1 allows for multiplexed

genome editing, as a single crRNA (crRNA) array can target multiple loci in the genome [76]. These features make Cpf1 an ideal alternative to Cas9 to satisfy specific research needs.

SpCas9 and SaCas9 are large proteins consisting of 1368 and 1053 amino-acids, respectively. A constant endeavor is to find smaller Cas9 orthologues that offer more flexibility in viral packaging. For example, CjCas9, derived from *Campylobacter jejuni*, is composed of 984 amino-acid residues [77]; Cas12f (also known as Cas14), identified from uncultivated archaea, is a family of nucleases that are composed of 400–700 amino-acids [78–80]. These variants have been tested in human cells or

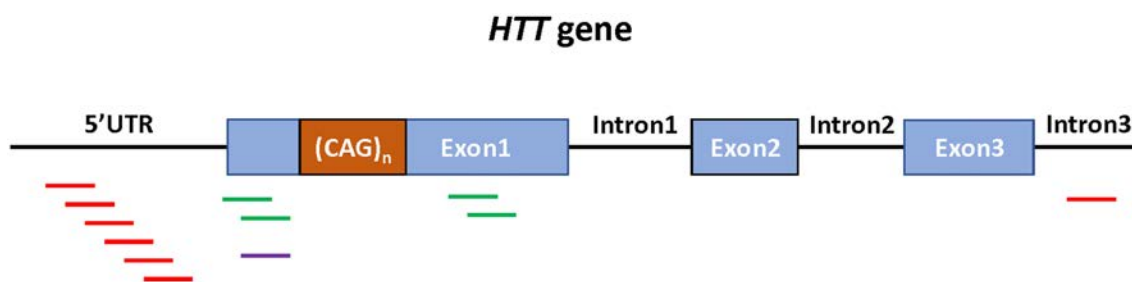
**Table 1** Mutant HTT-lowering studies using CRISPR/Cas9-based genome-editing tools

Allele specificity	Model system	Delivery vehicle	Major findings	References
Allele specific	HD patient fibroblasts and neural precursors from an HD patient induced pluripotent stem cell line	Lentivirus	Identified 1003 NGG PAM-altering SNPs that collectively account for ~90% of disease chromosomes in HD patients of European ancestry  A dual sgRNA approach with PAM-altering SNPs completely inactivated the mutant allele without impacting the normal allele	[63]
Allele specific	HEK293 cells, HD patient fibroblast, and an HD transgenic (BachHD) mouse model	Adeno associated virus	Designed sgRNAs targeting 6 prevalent SNP-dependent PAMs upstream of <i>HTT</i> exon1 and two common PAMs within <i>HTT</i> intron1  Achieved mutant allele-specific cleavage of <i>HTT</i> in cultured cells and in mouse brain  Identified SNPs located within the specific PAM positions that are suitable for other CRISPR systems, including SaCas9 and Cpf1	[64]
Non-allele specific	Mesenchymal stem cells from the bone marrow of an HD transgenic (YAC128) mouse model	Lentivirus	Designed sgRNAs targeting the 5' untranslated region (UTR) and the exon1-intron boundary of the <i>HTT</i> gene  Targeting 5'UTR or the exon1-intron boundary resulted in 79% or 58% reduction in mutant <i>HTT</i> mRNA levels	[100]
Non-allele specific	HEK293 cells and the HD140Q knock-in mouse model	Adeno associated virus	Designed sgRNAs targeting the flanking sequences of the CAG repeats in exon 1 of the human <i>HTT</i> gene  Reducing HTT expression in the striatum was sufficient to ameliorate behavioral deficits in the HD140Q knock-in mouse model	[68]
Non-allele specific	HEK293 cells and an HD transgenic (R6/2) mouse model	Adeno associated virus	Used SaCas9 and one sgRNA targeting exon 1 of the human <i>HTT</i> gene  Reducing HTT expression in the striatum ameliorated neuronal death and prolonged lifespan of R6/2 mice	[69]
Non-allele specific	HEK293 cells, mouse primary cortical neurons and astrocytes, neurons from an HD patient induced pluripotent stem cell line, an HD mouse model by lentivirus transduction in the striatum, and the HD140Q knock-in mouse model	Lentivirus	Designed an sgRNA targeting the region close to the translation start site of the human <i>HTT</i> gene  CRISPR/Cas9 successfully edited the <i>HTT</i> gene in different cellular and murine models  The off-target effect of CRISPR/Cas9 is low, and the self-inactivating KamiCas9 system has an even lower off-target effect	[71]
Non-allele specific	HD patient induced pluripotent stem cells and differentiated neural stem cells	Transfection	Designed sgRNAs targeting the flanking sequences of the CAG repeats in exon 1 of the human <i>HTT</i> gene  Successfully reduced mutant HTT expression and ameliorated mitochondrial defects	[72]

mouse models, with editing efficiency and specificity similar to SpCas9 [81–84], thereby paving the way to test their uses in the central nervous system.

CRISPR/Cas9 does not have to cleave DNA. Instead, nuclease-null Cas9 (dCas9) has been engineered to fuse with various elements to further expand its applications. In 2016, RNA-targeting Cas9 (RCas9) was created by fusing

dCas9 with GFP, together with a modified sgRNA scaffold that preferentially targets RNA but not the encoding DNA. RCas9 does not affect mRNA abundance or protein translation, but enables the tracking of endogenous mRNAs of interest in living cells [85]. In 2017, the same group further modified RCas9 by fusing dCas9 with the PIN RNA endonuclease domain from *SMG6* (PIN-dCas9). PIN-



**Fig. 4** Schematic showing sgRNAs targeting the *HTT* gene used in previous studies. Different sgRNA designs have been adopted in previous studies. To allele-specifically silence mutant *HTT*, sgRNAs covering HD patient-specific SNPs are located either in the 5'UTR

[64] or in intron 3 [63] (red). In the non-allele-specific approach, dual sgRNAs are designed to target sequences spanning the CAG repeats in exon 1 *HTT* [68, 69, 72] (green), or a single sgRNA upstream of exon 1 *HTT* is used [71] (purple).

dCas9 was directed to target mRNAs containing repeat expansions, including CUG, CCUG, CAG, and GGGGCC; it successfully cleaved and eliminated all the repeat expansion mRNAs [86]. Because CUG, CCUG, CAG, and GGGGCC repeat expansions are responsible for myotonic dystrophy type 1, myotonic dystrophy type 2, polyglutamine diseases, and frontotemporal dementia/amyotrophic lateral sclerosis (c9FTD/ALS) respectively, PIN-dCas9 has the potential to treat many genetic diseases caused by microsatellite expansions in different genomic loci. Nonetheless, it remains to be tested whether PIN-dCas9 can effectively work *in vivo*, and how long the effects last, considering PIN-dCas9 targets RNA, not DNA.

Gene expression can also be controlled by modulating transcriptional activity. To this end, a myriad of transcription regulators have been fused with dCas9 to achieve transcriptional activation or repression [87]. For example, the VP64 transcriptional activation domain has been used to activate the transcription of endogenous human genes, whereas fusion of the KRAB transcriptional repression domain from human KOX1 to dCas9 has been shown to silence transcription [88, 89]. Epigenetic editors such as DNA methyltransferase 3 alpha has been fused to dCas9 to achieve site-specific DNA methylation and transcriptional repression at several human promoters [90]. Likewise, fusion of ten-eleven translocation methylcytosine dioxygenase 1 leads to DNA demethylation and targeted upregulation of gene transcription [91]. In addition, many histone modifiers, including histone acetyltransferase p300 and histone deacetylase HDAC3, have been used to change the histone landscape at selected genomic loci, and resulted in gene activation or repression, respectively [92, 93]. These efforts created a full CRISPR arsenal to alter gene expression, which can be readily tested in HD to lower mutant *HTT* transcription. Indeed, a zinc finger-KRAB fusion protein (ZFP-TF) has already been created to specifically repress mutant *HTT* transcription. Treatment with ZFP-TF successfully ameliorates the neuropathology

and behavioral deficits in multiple lines of HD mice [94]. It is possible that a similar approach using CRISPR technology could achieve comparable or even better outcomes.

The CRISPR system has also been designed to precisely edit the genome through the invention of base editors, which are chimeric dCas9 proteins fused with DNA deaminase enzymes. To date, two types of base editor have been widely used: one is cytosine base editors (CBEs), which use the rat APOBEC1 cytidine deaminase domain to catalyze the conversion of C-G base-pairs to T-A base-pairs; the other one is adenine base editors, which use the TadA adenine deaminase to convert A-T base-pairs to G-C base-pairs [95, 96]. The base editors rely on base excision and DNA mismatch repair to achieve genome editing. More importantly, these repair mechanisms are active in post-mitotic cells such as neurons [97], thereby making these editors suitable for applications in the brain. By substituting single nucleotides, the base editors can create stop codons to terminate protein translation [98]. In 2020, this approach was tested in a mouse model of ALS. Intrathecal injection of AAVs encoding CBE significantly reduced the expression of mutant *SOD1*, a causative gene for ALS, leading to protection of motor neurons and reduction of muscle atrophy [99].

The above innovations could potentially push CRISPR-based therapies further into clinical applications. First, the large size of SpCas9 has always been a headache for viral packaging, and is known to elicit a myriad of cellular responses in mammalian cells. These more compact variants of nucleases could easily fit into the small AAV genome and potentially cause fewer host responses after delivery. Second, the permanent inactivation of gene expression by genome editing is a major safety concern. In contrast, transcriptional repressors or epigenetic modulators can silence gene expression without cutting chromosomes. Third, another drawback of CRISPR/Cas9 is the random mutations introduced by DNA DSB and NHEJ. Base editors that precisely change the genetic sequence enable genome editing in a controllable fashion.



**Table 2** CRISPR innovations that can potentially be used in HD research

CRISPR system	PAM sequence	Origin	Application	References
Cpf1	TTN or TTTN	Identified from <i>Francisella novicida</i> U112	Smaller than SpCas9. Complements SpCas9 due to PAM sequence differences. Introduces a staggered double-strand break with- 4 to 5-nucleotide overhangs, rather than blunt ends Suitable for multiplexed genome editing.	[75]
CjCas9	NNNVRYM	Identified from <i>Campylobacter jejuni</i>	A smaller variant of Cas9. Shows comparable editing efficiency, but better specificity than SpCas9.	[77]
Cas12f	Varies	Identified from uncultivated archaea	Smallest variants of Cas9 identified to date (400–700 amino-acids). Similar editing efficiency and specificity to SpCas9.	[78]
PIN-dCas9	Not required	A chimeric protein by fusing nuclease-null dCas9 to the PIN RNA endonuclease domain from <i>SMG6</i>	Specifically targets RNA but not DNA. Efficiently eliminates microsatellite repeat expansion RNAs (CUG, CCUG, CAG, GGGGCC) when exogenously expressed and in patient cells	[86]
dCas9-VP64	NGG	A chimeric protein by fusing nuclease-null dCas9 to the VP64 transcriptional activation domain	Increases transcription of selected human genes ( <i>VEGFA</i> and <i>NTF3</i> ) by targeting the promoter sequences.	[88]
dCas9-KRAB	NGG	A chimeric protein by fusing nuclease-null dCas9 to the KRAB domain of Kox1	Stably suppresses the expression of endogenous eukaryotic genes by targeting the promoter sequences.	[89]
dCas9-DNMT3A dCas9-DNMT3L	NGG	Chimeric proteins by fusing nuclease-null dCas9 to DNA methyltransferase 3 alpha or DNA methyltransferase 3 like	Transiently expressed in combinations to achieve long-term gene-silencing by modulating DNA methylation.	[90]
dCas9-Tet1	NGG	A chimeric protein by fusing nuclease-null dCas9 to the Tet1 enzymatic domain.	Activates transcription of selected genes ( <i>BDNF</i> and <i>MyoD</i> ) by targeted DNA demethylation.	[91]
dCas9 <sup>p300</sup> Core	NGG	A chimeric protein by fusing nuclease-null dCas9 to the catalytic histone acetyltransferase core domain of the human E1A-associated protein p300.	Activates transcription of endogenous genes from promoters and enhancers by catalyzing acetylation of histone.	[92]
dCas9-HDAC3	NGG	A chimeric protein by fusing nuclease-null dCas9 to full-length human HDAC3.	Modulates histone deacetylation and gene expression, which is critically dependent on the location of endogenous histone acetylation.	[93]
Adenine base editor (ABE)	NGG	A chimeric protein by fusing nuclease-null dCas9 to the TadA adenine deaminase.	Converts A-T base-pairs to G-C base-pairs, without causing DNA double-strand breaks.	[95]
Cytosine base editor (CBE)	NGG	A chimeric protein by fusing nuclease-null dCas9 to the rat APOBEC1 cytidine deaminase domain.	Converts C-G base-pairs to T-A base-pairs, without causing DNA double-strand breaks.	[96]

N, any nucleotide base; V, either A, G, or C; R, either A or G; Y, either T or C; M, either A or C.

## Concluding Remarks

Technological advancement has always been essential to biological and biomedical research. Former technological breakthroughs, such as molecular biology techniques and

large-scale sequencing, have profoundly changed the ways of conducting scientific research. CRISPR-based genome editing has the potential to play a similar role. The rapid development of CRISPR technology has particularly benefited HD research. Being a rare, monogenic

neurodegenerative disease, HD can serve as a vanguard in testing these innovative technologies, and such experiences can bring valuable insights to understand or even treat other diseases as well. We are hopeful that CRISPR, together with other technological advances, will bring a cure for the devastating HD in the near future.

**Acknowledgements** This review was supported by the National Key R&D Program of China (2021YFA0805200), the National Natural Science Foundation of China (31970954, 81901289 and 31872779) and the Guangdong Key Laboratory of Non-human Primate Research (2020B121201006).

**Conflict of interest** The authors declare no competing financial interests.

## References

- Lieberman AP, Shakkottai VG, Albin RL. Polyglutamine repeats in neurodegenerative diseases. *Annu Rev Pathol* 2019, 14: 1–27.
- Zuccato C, Valenza M, Cattaneo E. Molecular mechanisms and potential therapeutical targets in Huntington's disease. *Physiol Rev* 2010, 90: 905–981.
- Lu SY, Lu BX. Degeneration versus development: Hunting-out the D-unit of Huntington's disease. *Neurosci Bull* 2021, 37: 757–760.
- Cheng HR, Li XY, Yu HL, Xu M, Zhang YB, Gan SR. Correlation between CCG polymorphisms and CAG repeats during germline transmission in Chinese patients with Huntington's disease. *Neurosci Bull* 2020, 36: 811–814.
- Orr HT, Zoghbi HY. Trinucleotide repeat disorders. *Annu Rev Neurosci* 2007, 30: 575–621.
- Bates GP, Dorsey R, Gusella JF, Hayden MR, Kay C, Leavitt BR, *et al.* Huntington disease. *Nat Rev Dis Primers* 2015, 1: 15005.
- A novel gene containing a trinucleotide repeat that is expanded and unstable on Huntington's disease chromosomes. The Huntington's Disease Collaborative Research Group. *Cell* 1993, 72: 971–983. doi: [https://doi.org/10.1016/0092-8674\(93\)90585-e](https://doi.org/10.1016/0092-8674(93)90585-e).
- Carroll D. Genome engineering with targetable nucleases. *Annu Rev Biochem* 2014, 83: 409–439.
- Hockemeyer D, Soldner F, Beard C, Gao Q, Mitalipova M, DeKelver RC, *et al.* Efficient targeting of expressed and silent genes in human ESCs and iPSCs using zinc-finger nucleases. *Nat Biotechnol* 2009, 27: 851–857.
- Gaj T, Gersbach CA, Barbas CF III. ZFN, TALEN, and CRISPR/Cas-based methods for genome engineering. *Trends Biotechnol* 2013, 31: 397–405.
- Vachey G, Déglon N. CRISPR/Cas9-mediated genome editing for Huntington's disease. *Methods Mol Biol* 2018, 1780: 463–481.
- Ishino Y, Shinagawa H, Makino K, Amemura M, Nakata A. Nucleotide sequence of the iap gene, responsible for alkaline phosphatase isozyme conversion in *Escherichia coli*, and identification of the gene product. *J Bacteriol* 1987, 169: 5429–5433.
- Mojica FJ, Ferrer C, Juez G, Rodríguez-Valera F. Long stretches of short tandem repeats are present in the largest replicons of the Archaea *Haloferax mediterranei* and *Haloferax volcanii* and could be involved in replicon partitioning. *Mol Microbiol* 1995, 17: 85–93.
- Jansen R, Embden JD, Gaastra W, Schouls LM. Identification of genes that are associated with DNA repeats in prokaryotes. *Mol Microbiol* 2002, 43: 1565–1575.
- Horvath P, Barrangou R. CRISPR/Cas, the immune system of bacteria and Archaea. *Science* 2010, 327: 167–170.
- Bolotin A, Quinquis B, Sorokin A, Ehrlich SD. Clustered regularly interspaced short palindrome repeats (CRISPRs) have spacers of extrachromosomal origin. *Microbiology (Reading)* 2005, 151: 2551–2561.
- Pourcel C, Salvignol G, Vergnaud G. CRISPR elements in *Yersinia pestis* acquire new repeats by preferential uptake of bacteriophage DNA, and provide additional tools for evolutionary studies. *Microbiology (Reading)* 2005, 151: 653–663.
- Mojica FJM, Díez-Villaseñor C, García-Martínez J, Soria E. Intervening sequences of regularly spaced prokaryotic repeats derive from foreign genetic elements. *J Mol Evol* 2005, 60: 174–182.
- Makarova KS, Grishin NV, Shabalina SA, Wolf YI, Koonin EV. A putative RNA-interference-based immune system in prokaryotes: Computational analysis of the predicted enzymatic machinery, functional analogies with eukaryotic RNAi, and hypothetical mechanisms of action. *Biol Direct* 2006, 1: 7.
- Barrangou R, Fremaux C, Deveau H, Richards M, Boyaval P, Moineau S, *et al.* CRISPR provides acquired resistance against viruses in prokaryotes. *Science* 2007, 315: 1709–1712.
- Andersson AF, Banfield JF. Virus population dynamics and acquired virus resistance in natural microbial communities. *Science* 2008, 320: 1047–1050.
- Brouns SJJ, Jore MM, Lundgren M, Westra ER, Slijkhuys RJH, Snijders APL, *et al.* Small CRISPR RNAs guide antiviral defense in prokaryotes. *Science* 2008, 321: 960–964.
- Garneau JE, Dupuis MÈ, Villion M, Romero DA, Barrangou R, Boyaval P, *et al.* The CRISPR/Cas bacterial immune system cleaves bacteriophage and plasmid DNA. *Nature* 2010, 468: 67–71.
- Jinek M, Chylinski K, Fonfara I, Hauer M, Doudna JA, Charpentier E. A programmable dual-RNA-guided DNA endonuclease in adaptive bacterial immunity. *Science* 2012, 337: 816–821.
- Makarova KS, Wolf YI, Koonin EV. Classification and nomenclature of CRISPR-cas systems: Where from here? *CRISPR J* 2018, 1: 325–336.
- Adli M. The CRISPR tool kit for genome editing and beyond. *Nat Commun* 2011, 2018: 9.
- Nishiyama J, Mikuni T, Yasuda R. Virus-mediated genome editing via homology-directed repair in mitotic and postmitotic cells in mammalian brain. *Neuron* 2017, 96: 755–768.e5.
- Mao ZY, Bozzella M, Seluanov A, Gorbunova V. DNA repair by nonhomologous end joining and homologous recombination during cell cycle in human cells. *Cell Cycle* 2008, 7: 2902–2906.
- Bekris LM, Yu CE, Bird TD, Tsuang DW. Genetics of Alzheimer disease. *J Geriatr Psychiatry Neurol* 2010, 23: 213–227.
- Klein C, Westenberger A. Genetics of Parkinson's disease. *Cold Spring Harb Perspect Med* 2012, 2: a008888.
- Mittelman D, Moye C, Morton J, Sykoudis K, Lin YF, Carroll D, *et al.* Zinc-finger directed double-strand breaks within CAG repeat tracts promote repeat instability in human cells. *Proc Natl Acad Sci U S A* 2009, 106: 9607–9612.
- Garriga-Canut M, Agustín-Pavón C, Herrmann F, Sánchez A, Dierssen M, Fillat C, *et al.* Synthetic zinc finger repressors reduce mutant huntingtin expression in the brain of R6/2 mice. *Proc Natl Acad Sci U S A* 2012, 109: E3136–E3145.

33. Fink KD, Deng P, Gutierrez J, Anderson JS, Torrest A, Komarla A, *et al.* Allele-specific reduction of the mutant huntingtin allele using transcription activator-like effectors in human Huntington's disease fibroblasts. *Cell Transplant* 2016, 25: 677–686.
34. Cong L, Ran FA, Cox D, Lin SL, Barretto R, Habib N, *et al.* Multiplex genome engineering using CRISPR/Cas systems. *Science* 2013, 339: 819–823.
35. An MC, O'Brien RN, Zhang NZ, Patra BN, de la Cruz M, Ray A, *et al.* Polyglutamine disease modeling: Epitope based screen for homologous recombination using CRISPR/Cas9 system. *PLoS Curr* 2014, <https://doi.org/10.1371/currents.hd.0242d2e7ad72225efa72f6964589369a>
36. Malankhanova T, Suldina L, Grigor'eva E, Medvedev S, Minina J, Morozova K, *et al.* A human induced pluripotent stem cell-derived isogenic model of Huntington's disease based on neuronal cells has several relevant phenotypic abnormalities. *J Pers Med* 2020, 10: 215.
37. Xu XH, Tay Y, Sim B, Yoon SI, Huang YH, Ooi J, *et al.* Reversal of phenotypic abnormalities by CRISPR/Cas9-mediated gene correction in Huntington disease patient-derived induced pluripotent stem cells. *Stem Cell Reports* 2017, 8: 619–633.
38. Menalled LB, Kudwa AE, Miller S, Fitzpatrick J, Watson-Johnson J, Keating N, *et al.* Comprehensive behavioral and molecular characterization of a new knock-in mouse model of Huntington's disease: zQ175. *PLoS One* 2012, 7: e49838.
39. Menalled LB, Sison JD, Dragatsis I, Zeitlin S, Chesselet MF. Time course of early motor and neuropathological anomalies in a knock-in mouse model of Huntington's disease with 140 CAG repeats. *J Comp Neurol* 2003, 465: 11–26.
40. Lin CH, Tallaksen-Greene S, Chien WM, Cearley JA, Jackson WS, Crouse AB, *et al.* Neurological abnormalities in a knock-in mouse model of Huntington's disease. *Hum Mol Genet* 2001, 10: 137–144.
41. Heng MY, Duong DK, Albin RL, Tallaksen-Greene SJ, Hunter JM, Lesort MJ, *et al.* Early autophagic response in a novel knock-in model of Huntington disease. *Hum Mol Genet* 2010, 19: 3702–3720.
42. Lee CYD, Cantle JP, Yang XW. Genetic manipulations of mutant huntingtin in mice: New insights into Huntington's disease pathogenesis. *FEBS J* 2013, 280: 4382–4394.
43. Ross CA, Tabrizi SJ. Huntington's disease: From molecular pathogenesis to clinical treatment. *Lancet Neurol* 2011, 10: 83–98.
44. Yang HM, Yang S, Jing L, Huang LX, Chen LX, Zhao XX, *et al.* Truncation of mutant huntingtin in knock-in mice demonstrates exon1 huntingtin is a key pathogenic form. *Nat Commun* 2020, 11: 2582.
45. Bañez-Coronel M, Ayhan F, Tarabochia AD, Zu T, Perez BA, Tusi SK, *et al.* RAN translation in Huntington disease. *Neuron* 2015, 88: 667–677.
46. Yang S, Yang HM, Huang LX, Chen LX, Qin ZH, Li SH, *et al.* Lack of RAN-mediated toxicity in Huntington's disease knock-in mice. *Proc Natl Acad Sci U S A* 2020, 117: 4411–4417.
47. Crook ZR, Housman D. Huntington's disease: Can mice lead the way to treatment? *Neuron* 2011, 69: 423–435.
48. Levine MS, Cepeda C, Hickey MA, Fleming SM, Chesselet MF. Genetic mouse models of Huntington's and Parkinson's diseases: Illuminating but imperfect. *Trends Neurosci* 2004, 27: 691–697.
49. Yan S, Tu ZC, Liu ZM, Fan NN, Yang HM, Yang S, *et al.* A huntingtin knockin pig model recapitulates features of selective neurodegeneration in Huntington's disease. *Cell* 2018, 173: 989–1002.e13.
50. Culver BP, Savas JN, Park SK, Choi JH, Zheng SQ, Zeitlin SO, *et al.* Proteomic analysis of wild-type and mutant huntingtin-associated proteins in mouse brains identifies unique interactions and involvement in protein synthesis. *J Biol Chem* 2012, 287: 21599–21614.
51. Goehler H, Lalowski M, Stelzl U, Waelter S, Stroedicke M, Worm U, *et al.* A protein interaction network links GIT1, an enhancer of huntingtin aggregation, to Huntington's disease. *Mol Cell* 2004, 15: 853–865.
52. Shirasaki DI, Greiner ER, Al-Ramahi I, Gray M, Boontheung P, Geschwind DH, *et al.* Network organization of the huntingtin proteomic interactome in mammalian brain. *Neuron* 2012, 75: 41–57.
53. Wertz MH, Mitchem MR, Pineda SS, Hachigian LJ, Lee H, Lau V, *et al.* Genome-wide *in vivo* CNS screening identifies genes that modify CNS neuronal survival and mHTT toxicity. *Neuron* 2020, 106: 76–89.e8.
54. Genetic Modifiers of Huntington's Disease (GeM-HD) Consortium. Identification of genetic factors that modify clinical onset of Huntington's disease. *Cell* 2015, 162: 516–526.
55. Lee JM, Chao MJ, Harold D, Abu Elneel K, Gillis T, Holmans P, *et al.* A modifier of Huntington's disease onset at the MLH1 locus. *Hum Mol Genet* 2017, 26: 3859–3867.
56. Loupe JM, Pinto RM, Kim KH, Gillis T, Mysore JS, Andrew MA, *et al.* Promotion of somatic CAG repeat expansion by Fan1 knock-out in Huntington's disease knock-in mice is blocked by Mlh1 knock-out. *Hum Mol Genet* 2020, 29: 3044–3053.
57. Li XJ, Li SH, Sharp AH, Nucifora FC, Schilling G, Lanahan A, *et al.* A huntingtin-associated protein enriched in brain with implications for pathology. *Nature* 1995, 378: 398–402.
58. Liu Q, Cheng SY, Yang HM, Zhu LY, Pan YC, Jing L, *et al.* Loss of Hap1 selectively promotes striatal degeneration in Huntington disease mice. *Proc Natl Acad Sci U S A* 2020, 117: 20265–20273.
59. Zhao T, Hong Y, Yin P, Li SH, Li XJ. Differential HspBP1 expression accounts for the greater vulnerability of neurons than astrocytes to misfolded proteins. *Proc Natl Acad Sci U S A* 2017, 114: E7803–E7811.
60. Drouet V, Ruiz M, Zala D, Feyeux M, Auregan G, Cambon K, *et al.* Allele-specific silencing of mutant huntingtin in rodent brain and human stem cells. *PLoS One* 2014, 9: e99341.
61. Kingwell K. Double setback for ASO trials in Huntington disease. *Nat Rev Drug Discov* 2021, 20: 412–413.
62. Li ZY, Wang C, Wang ZY, Zhu CG, Li J, Sha T, *et al.* Allele-selective lowering of mutant HTT protein by HTT-LC3 linker compounds. *Nature* 2019, 575: 203–209.
63. Shin JW, Kim KH, Chao MJ, Atwal RS, Gillis T, MacDonald ME, *et al.* Permanent inactivation of Huntington's disease mutation by personalized allele-specific CRISPR/Cas9. *Hum Mol Genet* 2016, 25: 4566–4576.
64. Monteys AM, Ebanks SA, Keiser MS, Davidson BL. CRISPR/Cas9 editing of the mutant huntingtin allele *in vitro* and *in vivo*. *Mol Ther* 2017, 25: 12–23.
65. Grondin R, Kaytor MD, Ai Y, Nelson PT, Thakker DR, Heisel J, *et al.* Six-month partial suppression of Huntingtin is well tolerated in the adult rhesus striatum. *Brain* 2012, 135: 1197–1209.
66. McBride JL, Pitzer MR, Boudreau RL, Dufour B, Hobbs T, Ojeda SR, *et al.* Preclinical safety of RNAi-mediated HTT suppression in the rhesus macaque as a potential therapy for Huntington's disease. *Mol Ther* 2011, 19: 2152–2162.
67. Wang GH, Liu XD, Gaertig MA, Li SH, Li XJ. Ablation of huntingtin in adult neurons is nondeleterious but its depletion in young mice causes acute pancreatitis. *Proc Natl Acad Sci U S A* 2016, 113: 3359–3364.

68. Yang S, Chang RB, Yang HM, Zhao T, Hong Y, Kong HE, *et al.* CRISPR/Cas9-mediated gene editing ameliorates neurotoxicity in mouse model of Huntington's disease. *J Clin Invest* 2017, 127: 2719–2724.
69. Ekman FK, Ojala DS, Adil MM, Lopez PA, Schaffer DV, Gaj T. CRISPR-Cas9-mediated genome editing increases lifespan and improves motor deficits in a Huntington's disease mouse model. *Mol Ther Nucleic Acids* 2019, 17: 829–839.
70. Yang S, Li SH, Li XJ. Shortening the half-life of Cas9 maintains its gene editing ability and reduces neuronal toxicity. *Cell Rep* 2018, 25: 2653–2659.e3.
71. Merienne N, Vachey G, de Longprez L, Meunier C, Zimmer V, Perriard G, *et al.* The self-inactivating KamiCas9 system for the editing of CNS disease genes. *Cell Rep* 2017, 20: 2980–2991.
72. Lopes C, Tang Y, Anjo SI, Manadas B, Onofre I, de Almeida LP, *et al.* Mitochondrial and redox modifications in Huntington disease induced pluripotent stem cells rescued by CRISPR/Cas9 CAGs targeting. *Front Cell Dev Biol* 2020, 8: 576592.
73. Chew WL, Tabebordbar M, Cheng JKW, Mali P, Wu EY, Ng AHM, *et al.* A multifunctional AAV-CRISPR-Cas9 and its host response. *Nat Methods* 2016, 13: 868–874.
74. Wang D, Mou HW, Li SY, Li YX, Hough S, Tran K, *et al.* Adenovirus-mediated somatic genome editing of pten by CRISPR/Cas9 in mouse liver in spite of Cas9-specific immune responses. *Hum Gene Ther* 2015, 26: 432–442.
75. Zetsche B, Gootenberg JS, Abudayyeh OO, Slaymaker IM, Makarova KS, Essletzbichler P, *et al.* Cpf1 is a single RNA-guided endonuclease of a class 2 CRISPR-Cas system. *Cell* 2015, 163: 759–771.
76. Zetsche B, Heidenreich M, Mohanraju P, Fedorova I, Kneppers J, DeGennaro EM, *et al.* Multiplex gene editing by CRISPR-Cpf1 using a single crRNA array. *Nat Biotechnol* 2017, 35: 31–34.
77. Kim E, Koo T, Park SW, Kim D, Kim K, Cho HY, *et al.* *In vivo* genome editing with a small Cas9 orthologue derived from *Campylobacter jejuni*. *Nat Commun* 2017, 8: 14500.
78. Harrington LB, Burstein D, Chen JS, Paez-Espino D, Ma EB, Witte IP, *et al.* Programmed DNA destruction by miniature CRISPR-Cas14 enzymes. *Science* 2018, 362: 839–842.
79. Xiao RJ, Li Z, Wang SK, Han RJ, Chang LF. Structural basis for substrate recognition and cleavage by the dimerization-dependent CRISPR-Cas12f nuclease. *Nucleic Acids Res* 2021, 49: 4120–4128.
80. Takeda SN, Nakagawa R, Okazaki S, Hirano H, Kobayashi K, Kusakizako T, *et al.* Structure of the miniature type V-F CRISPR-Cas effector enzyme. *Mol Cell* 2021, 81: 558–570.e3.
81. Koo T, Lu-Nguyen NB, Malerba A, Kim E, Kim D, Cappellari O, *et al.* Functional rescue of dystrophin deficiency in mice caused by frameshift mutations using *Campylobacter jejuni* Cas9. *Mol Ther* 2018, 26: 1529–1538.
82. Lee JY, Jang YJ, Bae JH, Lee YH, Bae HS, Kim S, *et al.* Efficient and specific generation of knockout mice using *Campylobacter jejuni* CRISPR/Cas9 system. *Biochem Biophys Rep* 2020, 22: 100752.
83. Bigelyte G, Young JK, Karvelis T, Budre K, Zedaveinyte R, Djukanovic V, *et al.* Miniature type V-F CRISPR-Cas nucleases enable targeted DNA modification in cells. *Nat Commun* 2021, 12: 6191.
84. Kim DY, Lee JM, Moon SB, Chin HJ, Park S, Lim Y, *et al.* Efficient CRISPR editing with a hypercompact Cas12f1 and engineered guide RNAs delivered by adeno-associated virus. *Nat Biotechnol* 2022, 40: 94–102.
85. Nelles DA, Fang MY, O'Connell MR, Xu JL, Markmiller SJ, Doudna JA, *et al.* Programmable RNA tracking in live cells with CRISPR/Cas9. *Cell* 2016, 165: 488–496.
86. Batra R, Nelles DA, Pirie E, Blue SM, Marina RJ, Wang H, *et al.* Elimination of toxic microsatellite repeat expansion RNA by RNA-targeting Cas9. *Cell* 2017, 170: 899–912.e10.
87. Goell JH, Hilton IB. CRISPR/cas-based epigenome editing: Advances, applications, and clinical utility. *Trends Biotechnol* 2021, 39: 678–691.
88. Maeder ML, Linder SJ, Cascio VM, Fu YF, Ho QH, Joung JK. CRISPR RNA-guided activation of endogenous human genes. *Nat Methods* 2013, 10: 977–979.
89. Gilbert LA, Larson MH, Morsut L, Liu ZR, Brar GA, Torres SE, *et al.* CRISPR-mediated modular RNA-guided regulation of transcription in eukaryotes. *Cell* 2013, 154: 442–451.
90. Amabile A, Migliara A, Capasso P, Biffi M, Cittaro D, Naldini L, *et al.* Inheritable silencing of endogenous genes by hit-and-Run targeted epigenetic editing. *Cell* 2016, 167: 219–232.e14.
91. Liu XS, Wu H, Ji X, Stelzer Y, Wu XB, Czauderna S, *et al.* Editing DNA methylation in the mammalian genome. *Cell* 2016, 167: 233–247.e17.
92. Hilton IB, D'Ippolito AM, Vockley CM, Thakore PI, Crawford GE, Reddy TE, *et al.* Epigenome editing by a CRISPR-Cas9-based acetyltransferase activates genes from promoters and enhancers. *Nat Biotechnol* 2015, 33: 510–517.
93. Kwon DY, Zhao YT, Lamonica JM, Zhou ZL. Locus-specific histone deacetylation using a synthetic CRISPR-Cas9-based HDAC. *Nat Commun* 2017, 8: 15315.
94. Zeitler B, Froelich S, Marlen K, Shivak DA, Yu Q, Li D, *et al.* Allele-selective transcriptional repression of mutant HTT for the treatment of Huntington's disease. *Nat Med* 2019, 25: 1131–1142.
95. Gaudelli NM, Komor AC, Rees HA, Packer MS, Badran AH, Bryson DI, *et al.* Programmable base editing of A·T to G·C in genomic DNA without DNA cleavage. *Nature* 2017, 551: 464–471.
96. Komor AC, Kim YB, Packer MS, Zuris JA, Liu DR. Programmable editing of a target base in genomic DNA without double-stranded DNA cleavage. *Nature* 2016, 533: 420–424.
97. Iyama T, Wilson DM III. DNA repair mechanisms in dividing and non-dividing cells. *DNA Repair* 2013, 12: 620–636.
98. Kescu C, Parlak M, Tufan TR, Yang JK, Szlachta K, Wei XL, *et al.* CRISPR-STOP: Gene silencing through base-editing-induced nonsense mutations. *Nat Methods* 2017, 14: 710–712.
99. Lim CKW, Gapinske M, Brooks AK, Woods WS, Powell JE, *et al.* Treatment of a mouse model of ALS by *in vivo* base editing. *Mol Ther* 2020, 28: 1177–1189.
100. Kolli N, Lu M, Maiti P, Rossignol J, Dunbar GL. CRISPR-Cas9 mediated gene-silencing of the mutant huntingtin gene in an *in vitro* model of Huntington's disease. *Int J Mol Sci* 2017, 18: 754.



# Progress in Modeling Neural Tube Development and Defects by Organoid Reconstruction

Peng Li<sup>1,2</sup> · Yongchang Chen<sup>1,2</sup>

Received: 25 January 2022 / Accepted: 26 March 2022 / Published online: 26 June 2022

© Center for Excellence in Brain Science and Intelligence Technology, Chinese Academy of Sciences 2022

**Abstract** It is clear that organoids are useful for studying the structure as well as the functions of organs and tissues; they are able to simulate cell-to-cell interactions, symmetrical and asymmetric division, proliferation, and migration of different cell groups. Some progress has been made using brain organoids to elucidate the genetic basis of certain neurodevelopmental disorders. Such as Parkinson's disease and Alzheimer's disease. However, research on organoids in early neural development has received insufficient attention, especially that focusing on neural tube precursors. In this review, we focus on the recent research progress on neural tube organoids and discuss both their challenges and potential solutions.

**Keywords** Neural tube · Organoid · Neural tube defect

## Introduction

The nervous system regulates the functions of tissues and organs of the whole body so that humans are able to cope with environmental stress and pressure. The development of the nervous system determines whether it can perform such functions [1]. This system originates from the neuroectoderm which further forms the neural tube (NT) [2]. During this complex process, the morphological changes of

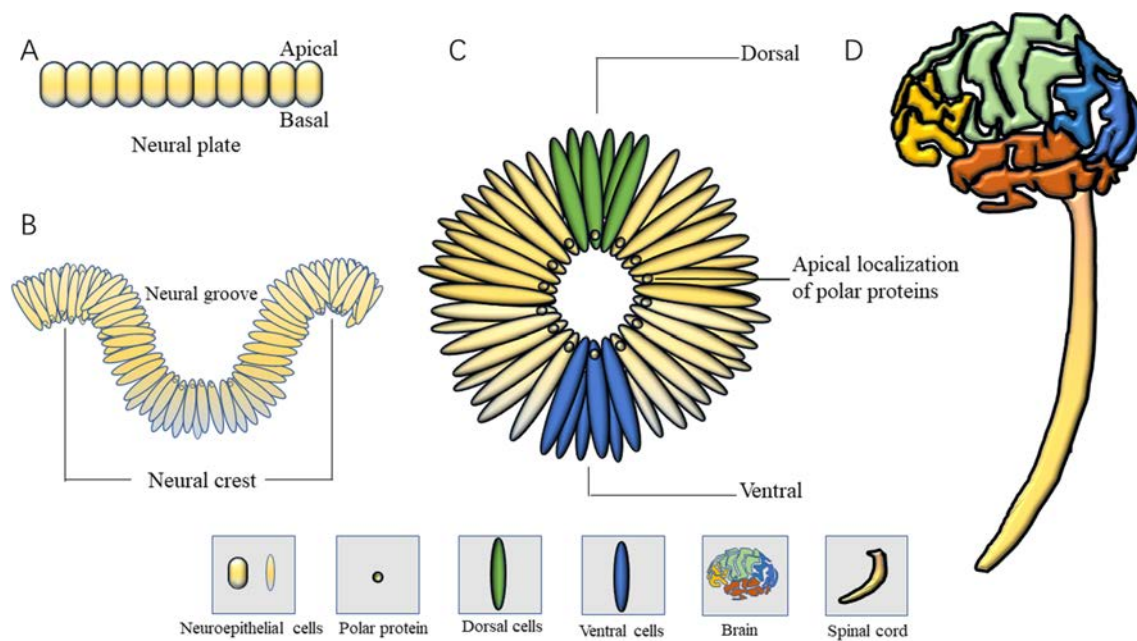
cells and the morphogenesis of the whole neural plate play key roles. Among them, the selective localization of polar proteins and the establishment of polarity are the internal driving forces. Cell polarity protein guides the positioning of the spindle axis and centrosome, thereby affecting the polarization from mesenchymal cells into neuroepithelial cells [3, 4]. In the process of NT closure, the polar protein complex acts as a bridge between cells, extracellular matrix, and cytoskeletal organization signals. This complex controls both the formation of the NT and the expansion of the coelom. Meanwhile, polarity-related proteins are clearly involved in the planar cell polarity (PCP) pathway during early neural development [5, 6]. The PCP pathway regulates the localization of polarity-related proteins (such as ZO-1, N-CAD, F-actin, and Shroom3) in the apical and basal regions, resulting in the morphology of neuroepithelial cells becoming spindle-shaped. On this basis, convergent extension occurs in the neural plate. The tissue folds and then bends at the dorsolateral hinge point, and neuroepithelial cells gradually fuse to form the NT by building a “zipper”-like structure in the dorsal mid-line. Later, the development of the nervous system is completed (Fig. 1).

During NT development, the PCP pathway has substantial effects on regulating the occurrence of cell polarity, in addition to the polarity-related proteins [7, 8]. Cell-to-cell interactions are also a crucial link. After polarized mesenchymal cells become neuroepithelial cells, they are tightly packed. This tight arrangement produces cell-to-cell interactions. The mechanism of NT development is a complex and delicate regulatory network. The interactions between these neuroepithelial cells often include information exchange and material transfer. For example, the physical force between the neuroepithelial cells affects their tight arrangement [9]. The inflow and outflow of ions across the cell membrane impact the transmission of action potentials, which in turn

✉ Yongchang Chen  
chenyc@lpbr.cn

<sup>1</sup> State Key Laboratory of Primate Biomedical Research and Institute of Primate Translational Medicine, Kunming University of Science and Technology, Kunming 650500, China

<sup>2</sup> Yunnan Key Laboratory of Primate Biomedical Research, Kunming 650500, China



**Fig. 1** Schematic diagrams of neural tube closure. **A** The neural plate. **B** The neural groove and neural crest. **C** The dorsal-ventral distribution of the neural tube and the localization of polarity-related proteins. **D** The neural tube eventually develops into the brain and spinal cord

influences the information exchange between neuroepithelial cells [10]. Therefore, the normal development of the NT is inseparable from the regulation of cell-to-cell interactions. However, there have been few studies on cellular interactions during early neural development, mainly due to the limitations of imaging techniques and the difficulty in performing *in-vivo* studies of early neural development. Based on the comprehensive study of NT development in experiment animals, this research still needs to overcome the bottleneck of technical limitations. Then the dynamic development of the NT in rodents and non-human primates will also be studied, which will provide the researcher with a better understanding of early neurodevelopment.

## Wide Use of Organoids in Biomedical Research

The concept of organoids can be traced back to the research on the self-assembly phenomenon of the sponge [11], but their application has to meet numerous conditions. The emerging technologies of artificially-established embryonic stem cells and *in vitro*-induced pluripotent stem cells offer the possibility of such application [12]. Based on the broad adoption of stem cells with the developmental characteristics of various organs, the research on organoids has advanced (Table 1). Therefore, we also summarize the research progress that has had a significant influence in the field (Fig. 2). As a result, current organoid research is mainly focused on organ diseases, neurodevelopment, and cancers [13–15].

The basis of all these studies depends on the functions of organoids, which can better simulate the three-dimensional status of the human body and facilitate designing personalized models of diseases. Simultaneously, it can also partially replace the breeding of experimental animals and overcome some limitations of human research and material acquisition [16]. These advantages of organoids will facilitate research in both fundamental medicine and the application of precision medicine.

The development of the nervous system is finely regulated by multiple factors, among which the endogenous regulation of genes plays a leading role. Under the co-regulation of signaling pathways such as bone morphogenic protein (BMP), transforming growth factor-beta (TGF- $\beta$ ), and Wnt, the ectoderm begins to transform into the neural plate. This process virtually turns on a developmental switch of the nervous system. The neural plate bends and closes to form the NT and finalizes this development process [2]. However, due to unfavorable hereditary and environmental factors, the normal developmental routine of the nervous system can already be interrupted, causing serious problems in nervous system development and certain diseases. Among these are the NT defects (NTDs) of closure at an incidence rate of 0.1% [17]. In clinical reports, these defects are most likely to cause malformation of the spinal cord and anencephaly. Although the phenotype is evident, the pathogenesis of NTDs and their effective treatment remain elusive. Although folic acid has been widely applied to prevent

**Table 1** Basic elements and examples of organoid formation**1. Activation or inhibition of key signaling pathways**

The development of different organs is regulated by complex signaling pathways. Only by activating or inhibiting the development-related pathways at specific times can embryoid bodies develop into specific organoids. This is extremely important in their cultivation.

**2. Medium configuration suitable for organoid culture**

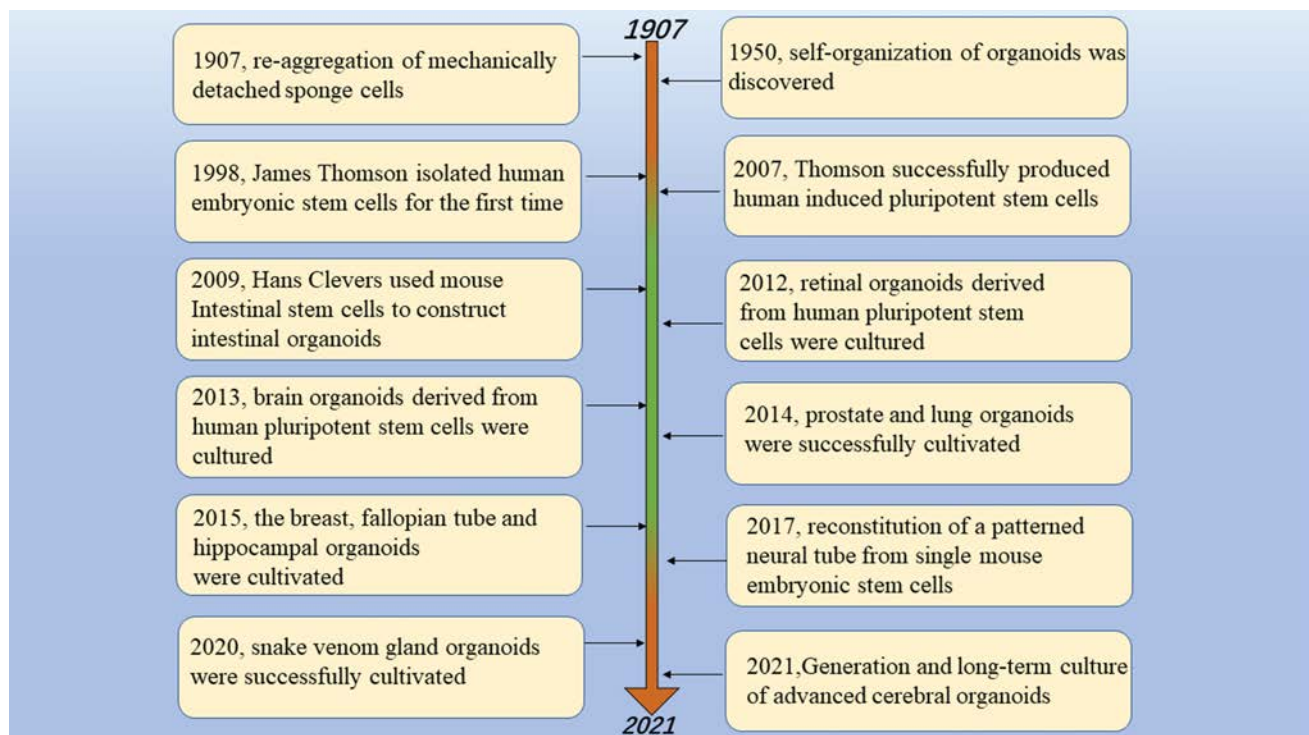
The organoid media vary according to the cultures. Among them, small chemicals, and small protein molecules both play key roles. They produce various differentiation results due to differences in the added amounts or concentrations. The development and regulation of organoids is a complex and delicate process, making it necessary to accurately quantify the configuration of media.

**3. Set up a culture environment other than the culture medium**

The transition from a 2D to a 3D culture system has resulted in more complex culture media for organoids. In a 3D culture system, biological Matrigel polymerizes to form a 3D matrix with biological activity simulating the structure, composition, physical properties, and functions of the cell basement membrane *in vivo*. Then, the 3D structure of neural tube organoids (NTOs) is fixed and various factors such as laminin, nestin, and collagen are provided, so that the environment of NTOs is closer to that in the body. This environment is very important for the cultivation of NTOs.

**4. Examples**

Before NTOs are cultured, human stem cells are first cultured in suspension to form spherical embryoid bodies, and then Matrigel is used to wrap the embryoid bodies and provide a suitable growth environment. We use Neurobasal medium (N2B27) in combination with factors such as CHIR, RA, SB, and LDN (refer to Table 2 and Fig. 3). The average culture period of human NTOs is ~ 10 days. After that, the status of NTOs can be confirmed by verifying their transcript levels and analyzing their immunohistochemistry.

**Fig. 2** Schematic of major progress in organoid research

NTDs, there are still numerous cases in which this disease cannot be effectively inhibited [18, 19]. As far as the research methods are concerned, the current method mainly uses mouse models. However, the huge differences among species, the limited effectiveness of drugs, and

the difficulty of *in-vivo* manipulation lead to the consideration of whether there are better solutions. With the continual breakthroughs in the recent research on diverse new organoids, the studies related to NT organoids has also developed quite rapidly.

## Research Progress on Neural Tube Organoids (NTOs)

### The Transition from Two-dimensional to Three-dimensional Culture Improves the Maturity of NTOs

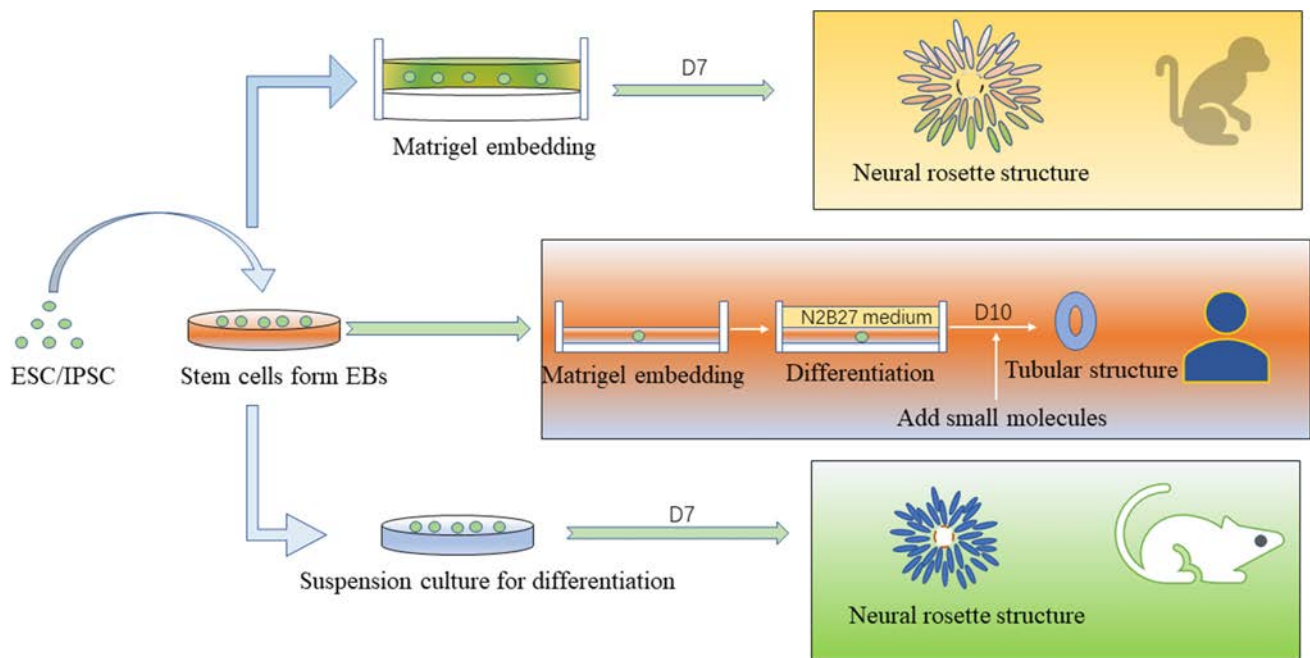
Before organoids were widely applied in neuroscience research, neural tissue from experimental animals were commonly used to reveal the morphology of the nervous system. Although this method greatly promoted the development of early neuroscience, its limitations were also noteworthy, such as the difficulty in accurately obtaining material and the inability to observe dynamic developmental processes. The emergence of embryonic stem cells and induced pluripotent stem cells just offset these shortcomings and offered researchers the capability to explore the differentiation of specific cells and tissues *in vitro* [12], effectively facilitating the study of NT development. Both NTOs and brain organoids are derived from stem cells, but NTOs develop relatively early and mimic earlier neurodevelopmental events as closely as possible. Compared with NTOs, the development of brain organoids is later and the development time is longer, but the maturity is better. This developmental routine is also consistent with the neurodevelopmental pattern *in vivo* (the NT closes and further develops into the brain and spinal cord). During the development from the neural plate to the NT, the polar proteins migrate to specific locations. The *in vitro* neural rosette mimics this process in terms of polarity [20]. In the two-dimensional (2D) neural rosette, the morphology of neuroepithelial cells has changed, and inside it, the polar proteins form a dense luminal structure. These phenomena have provided an illustrative model for studying the occurrence of polarity that affects NT development. With its simple operation and mature cultivation methods, the 2D system became very popular in the initial studies of NT development. However, to further study the development of different parts of the NT, the 2D culture system does not suffice. Therefore, the concept of three-dimensional (3D) training naturally arose. This novel system focuses on the 3D structure of NT development. Compared to 2D, this enables the researcher to reproduce the invisible dynamic processes of NT development. But the cultivation is also quite complicated. Biological Matrigel and synthetic hydrogel have both been used as support materials in 3D NT culture. Keisuke *et al.* used Matrigel to culture 3D mouse NTOs, and further developed a new type of extracellular matrix hydrogel. This series of attempts has led to the development of new materials for embedding organoids. Coupled with the oriented differentiation of culture components, NT-related structures with dorsal or ventral sides can be obtained, showing that the 3D systems are more feasible for revealing both developmental phenomena and defects [21, 22]. The current

experimental materials commonly used to study early neural development are mouse stem cells and human embryonic stem cells. Both the 2D and 3D culture systems of these cells have been reported [23]. NTOs must form spherical embryoid bodies before being cultured, and Matrigel wraps the embryoid bodies to provide a suitable growth environment for them. Neurobasal medium is then used in coordination with small-molecule factors that regulate signaling pathways to promote the formation of NTOs. In particular, the presence of key features such as the transformation of cells from round to spindle-shaped, the directed migration of polar proteins, the formation of luminal structures, and the strong expression of neuroepithelial marker genes are helpful to clarify the formation of NTOs. Although the culture methods for NTOs of different species are similar, there remain differences in their development durations. The NT closure time in humans is ~ 4 weeks, while the NT closure cycles in non-human primates and rodents are shorter, which is reflected in the culture duration of NTOs (the differentiation time of human NTOs is ~ 10 days, while the differentiation cycles in non-human primates and mice are 7 days). This is also a common phenomenon in the cultivation of NTOs (Fig. 3). In summary, it is important to choose the appropriate differentiation system corresponding to the type of problem to be studied. Only in this way can they be effectively applied.

### The Emergence of Various Technologies Promoting Research on NTOs

To culture NTOs, the *in vivo* developmental environment must first be simulated within high precision. The construction of a suitable growth environment for a complex organoid requires the support of new technologies and methods. The application of biological materials such as Matrigel and other extracellular matrix materials can facilitate the embedding of organoids and effectively support the culture environment [24, 25], assisting the organoids in forming a 3D structure. However, the extracellular matrix alone far from satisfies the directed cultivation of organoids. The composition of the medium is another crucial element that determines the direction of organoid development. Therefore, it is essential to simulate the microenvironment of the internal development in NTO cultures. We here summarize the significant progress in research on NTOs and the specific culture systems during the past decade (Table 2). In addition, the differentiation of various parts of organoids also needs to be further stimulated. The NT presents both a dorsal and a ventral side, which requires precise regulation by microfluidic technology during the directed differentiation of organoids [26, 27]. Quake *et al.* made a breakthrough in the large-scale integration of microfluidic chips, which play an important role in biomedical research [28, 29]. Since the





**Fig. 3** Schematic of the differentiation of NTOs in different species. Both experimental rodents and primates play important roles in NTO research. Their stem cells are used to form embryoid bodies and differentiate in different culture systems

development of the NT is regulated by PCP, TGF- $\beta$  signaling pathways, and Sonic hedgehog (SHH), bone morphogenetic protein (BMP), Activin receptor-like kinase 5 inhibitor (SB), and Morphogenetic protein type I receptor inhibitor (LDN), multiple factors must be fully considered when constructing the *in vitro* microenvironment.

Not only does NTO cultivation need the support of advanced technology and methods, but also requires relevant data analysis afterward. For example, because the dynamic process of NT development cannot be directly observed by the naked eye, *in vivo* imaging technology is needed. In 1999, Weissleder *et al.* of Harvard University proposed the concept of molecular imaging—the application of imaging methods to quantitatively study biological processes at the cellular and molecular levels *in vivo* [40, 41]. Nowadays, this technology can be implemented in both qualitative and quantitative studies of the developmental process without damaging the organoids [42]. Therefore, the NT development, cell proliferation, migration and morphogenesis can all be observed by means of fluorescence or bioluminescence [43]. Therefore, NT development, cell proliferation, migration, and morphogenesis can all be recorded by means of fluorescence or bioluminescence [44], providing a clearer and deeper understanding of the dynamic processes during NT development. Super-resolution technology further facilitates exploring the developmental mechanisms of the NT. In 2006, Hess *et al.* made significant progress in Fluorescence Photoactivation Localization Microscopy (FPALM). And they further demonstrated that FPALM can effectively

distinguish protein clusters on cell membrane lipid rafts [45], which laid a solid foundation for the development and application of organoids. Super-resolution technology enables the researcher to view the distribution and localization of intracellular proteins more clearly [46, 47]. In the research on pathogenic mechanisms, this technology is more helpful for studying specific features of pathogenesis. To summarize, studying the development of NTOs requires the integration of diverse disciplines and technologies. Only in this way can the application value of organoids be fully tapped.

## Potential Application Directions for NTOs

### NTOs Can Be Used to Study Early Neuropathogenesis and Drug Screening

Organoids have also been put to good use to study the pathogenesis of NTDs. Studies have shown that multiple mutations of a single gene can cause NTDs. At present, the mutant genes that have received much attention include Vangl2, Wnt5a, Shroom3, serine hydroxy methyltransferase 1 (SHMT1), and thymidylate synthetase (TYMS) [48]. However, the pathogenic mechanism of NTDs caused by these mutations is still unclear. Using animal models to study the pathogenic mechanism of these mutations have encountered many problems like high costs and complicated operations, while organoids present outstanding advantages in this aspect of research. Mutant stem cells can be obtained

**Table 2** The development of neural tube organoids

Year	Species	Dimensionality	Cell type	Differentiation factor	Matrigel used	Differen- tiation time (days)	Contribution	Author
2011	Human	3D	ESC	SB, BFGF, activin, DKK1	No	7	Demonstration that human organs can be induced <i>in vitro</i> and paves the way for the study of pattern formation	Nadav Sharon [30]
2013	Human	3D	ESC	N2, B27, heparin, insulin, BFGF	Yes	22	Demonstration that 3D organoids can recapitulate development and disease even in the most complex human tissue	Madeline A. Lancaster [31]
2014	Mouse	3D	ESC	N2, B27, noggin, RA, SAG	Yes	7	Development of a system for studying the mechanism of action of morphogens in a 3D environment and providing a source of patterned spinal cord tissue	Andrea Meinhardt [32]
2016	Monkey	2D	ESC	N2, B27, CHIR, SB, LDN, HLIF	No	7	System developed to help reveal the molecular mechanism of primate NTC and NTD and the self-renewal mechanism of NESC's	Xiaoqing Zhu [33]
2016	Mouse	3D	ESC	SHH, PM, RA, BMP4	Yes	9	Versatile microfluidic platform that mimicks the spatial and temporal chemical environments during NT development	Christopher J. Demers [34]
2016	Mouse	3D	ESC	RA, BFGF, BMP4, SHH, WNT	Yes	7	Method to discover and analyze the unique microenvironment that controls the morphogenesis of various organoid systems	Adrian Ranga [35]
2018	Human	2D-3D	ESC	BFGF, CHIR, RA, SHH, PM	Yes	10	The morphology of neural tissue is a key biophysical parameter that controls neural tissue <i>in vitro</i>	Gavin T Knight [20]
2019	Human	3D	ESC	RA, SHH, SAG, CHIR, LDN, SB	Yes	9	Development of the NE cyst system in the DV model to help understand the principles of self-organization that guide NT patterning	Y Zheng [36]
2020	Human	3D	ESC	N2, B27, insulin, BFGF, BSAV	Yes	21	First evidence that DDR gene mutations are risk factors for human NTD	X Cao [37]
2020	Human	2D-3D	IPSC	N2, B27, LDN, SB, bFGF	Yes	20	Demonstration that the NUAK2-Hippo signal axis regulates the cytoskeletal process that controls cell shape during neural tube closure	Carine Bonnard [38]
2021	Human	3D	ESC	N2, B27, Na pyruvate MEM	Yes	11	Demonstration that active mechanical forces increase growth and result in an enhanced pattern in a neural tube organoid model of HPSC	Abdel Rahman Abdel Fattah [39]

BFGF, Basic fibroblast growth factor; BMP, Bone-morphogenetic proteins; RA, Retinoic acid; SAG, Smoothed agonist; DKK1, Dickkopf 1; LIF, Leukemia inhibitory factor; LDN, BMP signaling inhibitor; CHIR, Glycogen synthase kinase-3 inhibitors; BSAV, Bovine serum albumin fraction V; PM, Purmorphamine

by gene knockout and this is followed by directed culture and *in-vitro* differentiation. These can be further combined with analyses of phenotypic differences and gene-expression differences to explore pathogenesis. This is an important application scenario of NTOs.

The NT grows in the early stage of neural development, and the dynamic processes in this period are difficult to capture. New drugs for preventing certain types of NTD still need to be further researched and developed. Fortunately, NTOs can be applied as a valid platform for the high-throughput screening of drugs. Disease-causing genes can be knocked out using a mature gene-editing system (CRISPR/Cas9, a single-base editing system), and then stem cell lines with specified mutations can be obtained. Mutant somatic cells can also be acquired directly from patients, and then the transcription factors Oct4, Sox2, Klf4, and c-Myc can be introduced into them through viral or plasmid vectors to reprogram the somatic cell nucleus to induce developmental pluripotency [12]. In this way, patient-derived-induced pluripotent stem cells have been obtained and then combined with the differentiation system of NTOs for *in vitro* studies. This is also the usual means of personalizing treatment. In early neurodevelopment, NTOs can be used to compare various effects of mutated genes on NT development (polarity phenomena, changes in cell morphology, type of cell differentiation, and cell size) and identify pathogenic mechanisms. On this basis, effective drugs for patients can be screened. NTOs [49, 50], compared with animal models, provide more experimental samples at a lower cost. This plays a significant role in the early testing of drug toxicity and effectiveness. In NT development, closure disorders caused by genetic mutations can have serious consequences. Screening platforms built by organoids are expected to identify effective drugs for completely preventing NTDs. Therefore, NTOs continue to be promising for drug screening.

### NTOs are More Maneuverable

Most of the early neurodevelopmental research data were obtained by animal dissection and further analysis. It can be said that this approach has greatly promoted the development of neuroscience. However, it is sometimes difficult to identify the precise sampling site and the specific development time, which causes the research to be quite complex. While NTOs are manipulated and analyzed *in vitro*, this approach can effectively assist *in vivo* research methods to assess the phenomena of interest more rapidly and more intuitively (e.g., polarity and cell morphology changes during NT closure). This is an effective strategy to help us better understand neural development. In general, the research on organoids in the life sciences is full of prospects. Its unique advantages have made organoid research quite popular in recent years. Not only does it play a role in neuroscience

but is also prominent in cancer research and immunology research. Equipped with such a useful research tool, investigators will further offset research shortcomings and tap its potential value, improving it to serve the life sciences and human health more efficiently.

## Major Challenges

After organoids have been applied to study neurodevelopment, the resulting progress in studying many diseases has demonstrated their effectiveness for such fundamental scientific studies. At present, organoids are already being widely applied in early neurodevelopmental research on NTDs and a variety of neurodegenerative diseases, such as Parkinson's and Alzheimer's diseases. This provides the researcher with more references for further analyses of neurodevelopment and pathogenic mechanisms. Even so, the challenges within the organoid field are still worthy of in-depth consideration [51, 52].

### The Complexity of NTO Development

NTOs are derived from the differentiation of stem cells. For example, neural rosettes can be induced by inhibiting the dual SMAD pathway [33, 53]. The NTOs obtained through the artificial regulation of such small molecules are different from the tissues naturally developed in the microenvironment inside the human body. In terms of neurodevelopment, early neuroectoderm and mesoderm are closely interconnected. However, the developmental stage from ectoderm to an NT is the joint result of multi-organization and multi-factor regulation. As for this stage, many developmental mechanisms have not yet been studied, while the organoids are just a single product that mimics the occurrence of one single factor of the neuroepithelium. This is not comprehensive enough to study all the factors and mechanisms affecting NT development. In recent years, researchers have applied Matrigel to embed embryoid bodies and provide NTOs with a three-dimensional developmental environment that is closer to the microenvironment inside the human body. However, the microenvironment established by Matrigel is sometimes far from satisfying the requirements of development. This has a major impact on the maturity of NTO development. Furthermore, the dorsal and ventral development of the NT is regulated by different combinations of various factors, which are extremely difficult to simulate *in vitro*. Although the emergence of microfluidic technology has improved the simulation of the natural microenvironment, it remains far from ideal. This complexity of organoid development occurs not only in neurodevelopment but also in cancer and other organoid studies. Certainly, this is also a

technical limitation, while the development of technology needs to be promoted by the challenges of scientific problems. Therefore, the complexity of organoid development determines the direction of organoid cultivation. This is also one of the problems faced by the NTO research organizations. If we want to solve these problems, we need to elaborately analyze the physiological environment in which early neurodevelopment occurs (such as the partial pressures of gases, the types and specific concentrations of nutritional factors, and the pressure and temperature of the surrounding environment), before accurately simulating the physiological environment of neural development *in vivo*, so that organoids can develop better.

### Accurately Modelling the Developmental Timeline of NTOs

The developmental timeline and links of mammals are relatively fixed. This may be the result of long-term evolution. Therefore, the timeline of neurodevelopment is also relatively fixed. The period of complete closure of the NT in the body is ~ 4 weeks, during which neurons are also created. However, within current NTO cultures, the developmental cycle is far from the time required for *in vivo* development. This is worth consideration in terms of organ developmental maturity. The timeline of NTO development does not completely match that of bodily development, causing organoids to be insufficient to simulate the real organic development of the body. Whether this difference in duration of development affects the research on developmental mechanisms is worthy of further discussion. This is not only a question for NTOs in the nervous system, but also applies to other research fields using organoids. Because the specific duration of organ development is more like a constant, this fixed pattern may affect the number of cells contained in the organ and the interactions between the cells. This is extremely important for organ development, and therefore is another major challenge. In the study of NTOs, the occurrence of polarity and the formation of a cavity structure can be investigated [20, 54]. But in terms of NT developmental maturity, this is not enough. Is this difference in maturity caused by insufficient cultivation time or insufficient cultivation environment? This problem still requires resolution. Meanwhile, neural tube closure is a continuous and dynamic process. It is also difficult to accurately capture this process *in vitro*. If the developmental timeline of NTOs is closer to the developmental process *in vivo*, perhaps further studies of neural tube development and related diseases will be more convincing. In other words, a thorough analysis of the developmental timelines of different species is needed, and meanwhile, the developmental environment *in vivo* can be simulated as realistically as possible, which may solve the above challenges.

### Construction of Vascularized NTOs

As is well known, blood vessels also play a key role in transporting nutrients and removing metabolites [55]. More importantly, various organs form a unified organism by connecting blood vessels, thereby ensuring the normal demand for oxygen and nutrients inside cells. In the study of NTOs, there is no mature method yet for simulating blood vessels. The avascular NTOs have low levels of internal nutrients and oxygen, which limits their normal growths and development. Therefore, *Shi* and colleagues ran some exploratory experiments to solve the blood vessel construction problem of organoids. They co-cultured human embryonic stem cells and human umbilical vein endothelial cells, and constructed blood vessels by regulating the related signal pathways [56]. Their results showed that, in the constructed vascularization system, the number of cell deaths was significantly reduced, therefore the organoids developed more steadily. *Cakir et al.* also subcutaneously transplanted vascularized human cortical organoids into mice [57]. The outcome showed that the transplanted organoids in the hindlimbs of immunodeficient mice could form a locally functioning system. Their work has inspired further exploration of the construction of vascularized organoids. However, few studies yet have reported on the vascularized construction of neural organoids [25, 58]. The development of an NT is inseparable from nutrients and oxygen, and the cultivation methods of NTOs currently applied are mainly embedded culture and suspension culture. This *in vitro* nutrient delivery method is completely different from the vascular delivery of nutrients. Furthermore, the development of different parts of the NT are subject to complex and precise regulation. And this difference in the means of nutrient delivery may affect the normal development of the NT, which also needs to be further verified. Therefore, the successful construction of a mature vascular system could determine that researchers can further study more organoids at maturity. In summary, blood vessels significantly affect the normal growth and development of organs. In the study of NTOs, this type of problem is worthy of further research.

### Conclusions and Future Perspectives

The application of tissue engineering technology is also one of the developmental directions for organoids. The micro-environment constructed by this technology makes organoid culture more feasible. This will enable the organoids to further stabilize in differentiation and assist in solving the problems of organoid maturity. It is also of competitive advantage in organoid hypoxia treatment and volume simulation. Specifically, the vascularization system constructed by tissue engineering technology enables the organoid center



**Table 3** Outstanding questions of NTOs research

1. The lack of a functional vascular system, nervous system, or immune system is one of the challenges to organoid research. These shortcomings cause the organoids to be far less effective than *in-vivo* models. Organoids can only express a limited number of the features of real organs, and their application scenarios are also limited. More importantly, most organoids are currently restricted in size. If the volume is too large, internal hypoxia and a lack of nutrients leads to the death of internal cells. Therefore, the construction of organoids with mature vascularization is one of the prospects. The nervous system also plays an irreplaceable role by innervating and regulating the organs. Non-neuronal organoids generally lack a nervous system, which is quite different from real organs inside the body. This is a challenge as well as an opportunity. If future research can achieve real simulations of internal organs, then animal experiments will be greatly reduced. Stem cells also serve as a steady source of donors for organoids to support disease research. On the other hand, this can also avoid ethical restrictions and provide a more convenient platform for drug research and development.
2. The maturity of organoids has also attracted the attention of numerous researchers. This determines the functions of an organ. However, most of the organoids studied at present are immature, and there are still many differences from real organs developed inside the body. This problem prevents organoids from fully reflecting the phenotype of a disease. At the same time, the microenvironment of organ development is extremely complicated. This increases the difficulty for researchers to artificially simulate this environment in an effective way.

to supply sufficient nutrients to address both the problems of hypoxia and volume. In the latest research on NT organs, the value of tissue engineering has proven significant [54]. Stem cells could be applied to effectively simulate the dynamic development of the NT. Simultaneously, the application prospects of organoids also depend to a certain extent on the development and application of novel technologies. In the current research on organoids, many challenges are due to the limitations of technology. Therefore, there remains a need to develop advanced technologies essential for further organoid research.

Secondly, studies of the co-cultivation and interaction of organoids is also a direction of future research. Organoid co-culture can be applied to study the interactions between different tissues. However, the effect of interactions between organs remains unknown. Inside the body, the major event of NT closure is the physical squeezing of the tissues around the nerve plate and the morphological variations of the individual cells. This is a complex process affected by multiple factors. Compared with the development of the NT inside the body, NTOs develop from the proliferation and differentiation of stem cells, without the intervention of other tissues. Thus, NTO simulation cannot fully imitate the actual situation inside the body. Therefore, the study of organoids should also approach multiple tissue co-cultivation, and simulate neural development in more detail. The advancement of these studies will surely provide more information and references for research on diseases related to NT development.

In conclusion, breakthroughs in neurobiological research have usually been led by innovative techniques and methods. From the discovery of the self-organization phenomenon of sponge cells, organoid research has experienced decades of development from concept to application. Gradually maturing culture systems and advancing analysis technologies have strengthened the application of organoids in bio-medicine. Moreover, the emergence of single-cell sequencing technology has facilitated the organoid researcher to better

understand the pathogenesis of various diseases. In addition, the construction of NTO disease models for specific gene mutations through gene-editing technology has allowed the researcher to intuitively understand the progression of diseases, and simultaneously enabled investigators to redefine their understanding of the diseases with new research ideas. Although problems in organoid research still need to be solved (see Table 3), their potential value for future research is undeniable. We should also take a positive attitude to evaluating organoid research for its effective application in the field of neuroscience.

**Acknowledgements** We would like to thank KetengEdit ([www.ketengedit.com](http://www.ketengedit.com)) for linguistic assistance during the preparation of this manuscript. This review was supported by the National Natural Science Foundation of China (81930121 and 82125008), the National Key Research and Development Program of China (2018YFA0107902 and 2018YFA0801403), and the Major Basic Research Project of Science and Technology of Yunnan Province, China (202001BC070001).

**Conflict of interest** The authors declare that there is no conflict of interest regarding the publication of this article.

## Reference

1. Zhang Y, Cui DH. Evolving models and tools for microglial studies in the central nervous system. *Neurosci Bull* 2021, 37: 1218–1233.
2. Nikolopoulou E, Galea GL, Rolo A, Greene NDE, Copp AJ. Neural tube closure: Cellular, molecular and biomechanical mechanisms. *Development* 2017, 144: 552–566.
3. Laumonerie C, Solecki DJ. Regulation of polarity protein levels in the developing central nervous system. *J Mol Biol* 2018, 430: 3472–3480.
4. Tepass U. The apical polarity protein network in *Drosophila* epithelial cells: Regulation of polarity, junctions, morphogenesis, cell growth, and survival. *Annu Rev Cell Dev Biol* 2012, 28: 655–685.
5. Gao B. Wnt regulation of planar cell polarity (PCP). *Curr Top Dev Biol* 2012, 101: 263–295.
6. Ueno N, Greene NDE. Planar cell polarity genes and neural tube closure. *Birth Defects Res C Embryo Today* 2003, 69: 318–324.

7. de Marco P, Merello E, Piatelli G, Cama A, Kibar Z, Capra V. Planar cell polarity gene mutations contribute to the etiology of human neural tube defects in our population. *Birth Defects Res A Clin Mol Teratol* 2014, 100: 633–641.
8. Mayor R, Theveneau E. The role of the non-canonical Wnt-planar cell polarity pathway in neural crest migration. *Biochem J* 2014, 457: 19–26.
9. Jussila M, Ciruna B. Zebrafish models of non-canonical Wnt/planar cell polarity signalling: Fishing for valuable insight into vertebrate polarized cell behavior. *Wiley Interdiscip Rev Dev Biol* 2017, 6(3): e267.
10. Chovancova B, Liskova V, Babula P, Krizanov O. Role of sodium/calcium exchangers in tumors. *Biomolecules* 2020, 10: 1257.
11. Lavrov AI, Kosevich IA. Sponge cell reaggregation: Cellular structure and morphogenetic potencies of multicellular aggregates. *J Exp Zool Ecol Genet Physiol* 2016, 325: 158–177.
12. Takahashi K, Tanabe K, Ohnuki M, Narita M, Ichisaka T, Tomoda K. Induction of pluripotent stem cells from adult human fibroblasts by defined factors. *Cell* 2007, 131: 861–872.
13. Rossi G, Manfrin A, Lutolf MP. Progress and potential in organoid research. *Nat Rev Genet* 2018, 19: 671–687.
14. Huch M, Knoblich JA, Lutolf MP, Martinez-Arias A. The hope and the hype of organoid research. *Development* 2017, 144: 938–941.
15. Bleijs M, van de Wetering M, Clevers H, Drost J. Xenograft and organoid model systems in cancer research. *EMBO J* 2019, 38: e101654.
16. Huang M, Yang J, Li P, Chen YC. Embryo-engineered nonhuman primate models: Progress and gap to translational medicine. *Research (Wash D C)* 2021, 2021: 9898769.
17. Botto LD, Moore CA, Khoury MJ, Erickson JD. Neural-tube defects. *N Engl J Med* 1999, 341: 1509–1519.
18. Botto LD, Lisi A, Robert-Gnansia E, Erickson JD, Vollset SE, Mastroiacovo P, *et al.* International retrospective cohort study of neural tube defects in relation to folic acid recommendations: Are the recommendations working? *BMJ* 2005, 330: 571.
19. van Gool JD, Hirche H, Lax H, de Schaepdrijver L. Folic acid and primary prevention of neural tube defects: a review. *Reprod Toxicol* 2018, 80: 73–84.
20. Knight GT, Lundin BF, Iyer N, Ashton LM, Sethares WA, Willett RM, *et al.* Engineering induction of singular neural rosette emergence within hPSC-derived tissues. *eLife* 2018, 7: e37549.
21. Adhya D, Chennell G, Crowe JA, Valencia-Alarcón EP, Seythoud J, Hosny NA, *et al.* Application of Airy beam light sheet microscopy to examine early neurodevelopmental structures in 3D hiPSC-derived human cortical spheroids. *Mol Autism* 2021, 12: 4.
22. Ishihara K, Ranga A, Lutolf MP, Tanaka EM, Meinhardt A. Reconstitution of a patterned neural tube from single mouse embryonic stem cells. *Methods Mol Biol* 2017, 1597: 43–55.
23. Chandrasekaran A, Avci HX, Ochalek A, Rösingh LN, Molnár K, László L, *et al.* Comparison of 2D and 3D neural induction methods for the generation of neural progenitor cells from human induced pluripotent stem cells. *Stem Cell Res* 2017, 25: 139–151.
24. Kaur S, Kaur I, Rawal P, Tripathi DM, Vasudevan A. Non-matrigel scaffolds for organoid cultures. *Cancer Lett* 2021, 504: 58–66.
25. Pham MT, Pollock KM, Rose MD, Cary WA, Stewart HR, Zhou P, *et al.* Generation of human vascularized brain organoids. *Neuroreport* 2018, 29: 588–593.
26. Aboulkheir Es H, Montazeri L, Aref AR, Vosough M, Baharvand H. Personalized cancer medicine: An organoid approach. *Trends Biotechnol* 2018, 36: 358–371.
27. Bein A, Shin W, Jalili-Firoozinezhad S, Park MH, Sontheimer-Phelps A, Tovaglieri A, *et al.* Microfluidic organ-on-a-chip models of human intestine. *Cell Mol Gastroenterol Hepatol* 2018, 5: 659–668.
28. Thorsen T, Maerkl SJ, Quake SR. Microfluidic large-scale integration. *Science* 2002, 298: 580–584.
29. Groisman A, Enzelberger M, Quake SR. Microfluidic memory and control devices. *Science* 2003, 300: 955–958.
30. Sharon N, Mor I, Golan-Lev T, Fainsod A, Benvenisty N. Molecular and functional characterizations of gastrula organizer cells derived from human embryonic stem cells. *Stem Cells* 2011, 29: 600–608.
31. Lancaster MA, Renner M, Martin CA, Wenzel D, Bicknell LS, Hurler ME, *et al.* Cerebral organoids model human brain development and microcephaly. *Nature* 2013, 501: 373–379.
32. Meinhardt A, Eberle D, Tazaki A, Ranga A, Niesche M, Wilsch-Bräuninger M, *et al.* 3D reconstitution of the patterned neural tube from embryonic stem cells. *Stem Cell Rep* 2014, 3: 987–999.
33. Zhu XQ, Li B, Ai ZY, Xiang Z, Zhang KS, Qiu XY, *et al.* A robust single primate neuroepithelial cell clonal expansion system for neural tube development and disease studies. *Stem Cell Reports* 2016, 6: 228–242.
34. Demers CJ, Soundararajan P, Chennampally P, Cox GA, Briscoe J, Collins SD, *et al.* Development-on-chip: *in vitro* neural tube patterning with a microfluidic device. *Development* 2016, 143: 1884–1892.
35. Ranga A, Girgin M, Meinhardt A, Eberle D, Caiazzo M, Tanaka EM, *et al.* Neural tube morphogenesis in synthetic 3D microenvironments. *Proc Natl Acad Sci U S A* 2016, 113: E6831–E6839.
36. Zheng Y, Xue X, Resto-Irizarry AM, Li Z, Shao Y, Zheng Y, *et al.* Dorsal-ventral patterned neural cyst from human pluripotent stem cells in a neurogenic niche. *Sci Adv* 2019, 5: eaax5933.
37. Cao XY, Tian T, Steele JW, Cabrera RM, Aguiar-Pulido V, Wadhwa S, *et al.* Loss of RAD9B impairs early neural development and contributes to the risk for human spina bifida. *Hum Mutat* 2020, 41: 786–799.
38. Bonnard C, Navaratnam N, Ghosh K, Chan PW, Tan TT, Pomp O, *et al.* A loss-of-function NUA2 mutation in humans causes anencephaly due to impaired Hippo-YAP signaling. *J Exp Med* 2020, 217: e20191561.
39. Abdel Fattah AR, Daza B, Rustandi G, Berrocal-Rubio MÁ, Gorissen B, Poovathingal S, *et al.* Actuation enhances patterning in human neural tube organoids. *Nat Commun* 2021, 12: 3192.
40. Weissleder R, Tung CH, Mahmood U, Bogdanov A. *In vivo* imaging of tumors with protease-activated near-infrared fluorescent probes. *Nat Biotechnol* 1999, 17: 375–378.
41. Bogdanov A Jr, Marecos E, Cheng HC, Chandrasekaran L, Kruttsch HC, Roberts DD, *et al.* Treatment of experimental brain tumors with trombospondin-1 derived peptides: An *in vivo* imaging study. *Neoplasia* 1999, 1: 438–445.
42. Liu YV, Sodhi SK, Xue G, Teng D, Agakishiev D, McNally MM, *et al.* Quantifiable *in vivo* imaging biomarkers of retinal regeneration by photoreceptor cell transplantation. *Transl Vis Sci Technol* 2020, 9: 5.
43. Wendt M, Schiemann W. Longitudinal bioluminescent quantification of three dimensional cell growth. *Bio Protoc* 2013, 3: e993.
44. Gould TJ, Verkhusha VV, Hess ST. Imaging biological structures with fluorescence photoactivation localization microscopy. *Nat Protoc* 2009, 4: 291–308.
45. Fang HB, Yao SK, Chen QX, Liu CY, Cai YQ, Geng SS, *et al.* De novo-designed near-infrared nanoaggregates for super-resolution monitoring of lysosomes in cells, in whole organoids, and *in vivo*. *ACS Nano* 2019, 13: 14426–14436.
46. Turco MY, Moffett A. Development of the human placenta. *Development* 2019, 146: 163428.
47. Luo ZG, Peng J, Li T. Single-cell RNA sequencing reveals cell-type-specific mechanisms of neurological diseases. *Neurosci Bull* 2020, 36: 821–824.

48. Lemay P, Guyot MC, Tremblay É, Dionne-Laporte A, Spiegelman D, Henrion É, *et al.* Loss-of-function de novo mutations play an important role in severe human neural tube defects. *J Med Genet* 2015, 52: 493–497.
49. Nychyk O, Galea GL, Molè M, Savery D, Greene NDE, Stanier P, *et al.* Vangl2-environment interaction causes severe neural tube defects, without abnormal neuroepithelial convergent extension. *Dis Model Mech* 2022, 15: dmm049194.
50. Yang W, Garrett L, Feng D, Elliott G, Liu XL, Wang N, *et al.* Wnt-induced Vangl2 phosphorylation is dose-dependently required for planar cell polarity in mammalian development. *Cell Res* 2017, 27: 1466–1484.
51. Marotta N, Kim S, Krainc D. Organoid and pluripotent stem cells in Parkinson's disease modeling: An expert view on their value to drug discovery. *Expert Opin Drug Discov* 2020, 15: 427–441.
52. Zhao J, Fu Y, Yamazaki Y, Ren YX, Davis MD, Liu CC, *et al.* APOE4 exacerbates synapse loss and neurodegeneration in Alzheimer's disease patient iPSC-derived cerebral organoids. *Nat Commun* 2020, 11: 5540.
53. Zhu XQ, Li B, Ai ZY, Xiang Z, Zhang KS, Qiu XY, *et al.* A robust single primate neuroepithelial cell clonal expansion system for neural tube development and disease studies. *Stem Cell Rep* 2016, 6: 228–242.
54. Karzbrun E, Khankhel AH, Megale HC, Glasauer SMK, Wyle Y, Britton G, *et al.* Human neural tube morphogenesis *in vitro* by geometric constraints. *Nature* 2021, 599: 268–272.
55. Segarra M, Aburto MR, Hefendehl J, Acker-Palmer A. Neurovascular interactions in the nervous system. *Annu Rev Cell Dev Biol* 2019, 35: 615–635.
56. Shi YC, Sun L, Wang MD, Liu JW, Zhong SJ, Li R, *et al.* Vascularized human cortical organoids (vOrganoids) model cortical development *in vivo*. *PLoS Biol* 2020, 18: e3000705.
57. Cakir B, Xiang YF, Tanaka Y, Kural MH, Parent M, Kang YJ, *et al.* Engineering of human brain organoids with a functional vascular-like system. *Nat Methods* 2019, 16: 1169–1175.
58. Mansour AA, Gonçalves JT, Bloyd CW, Li H, Fernandes S, Quang D, *et al.* An *in vivo* model of functional and vascularized human brain organoids. *Nat Biotechnol* 2018, 36: 432–441.

# Dual Effects of Light on Regulating *Aedes aegypti* Heat-Seeking Behavior

Haonan Zhou<sup>1,2</sup> · Kai Shi<sup>1,2</sup> · Fengming Wu<sup>1,2</sup> · Bingcai Wang<sup>1,2</sup> · Jing Li<sup>1,2,4</sup> · Bowen Deng<sup>3,4</sup> · Chuan Zhou<sup>1,2,4</sup> 

Received: 9 December 2021 / Accepted: 16 March 2022 / Published online: 24 May 2022  
© Center for Excellence in Brain Science and Intelligence Technology, Chinese Academy of Sciences 2022

## Dear Editor,

Mosquitoes, as important arthropod disease vectors, efficiently transmit pathogens such as dengue virus, Zika virus, yellow fever virus, and malaria. To find their host, female mosquitoes use multiple sensory systems to detect host-associated cues such as CO<sub>2</sub>, volatile odorants, visual signals, and temperature. Recent genetic studies have identified several sensory molecules that are required for detecting those host-associated cues. Gustatory receptor (*Gr3*) is required for *Aedes aegypti* to sense CO<sub>2</sub> produced by the host and to activate flight [1]. Olfactory receptor (*Or4*) is responsible for sensing sulcatone from the human body and might be required for the host preference of *Ae. aegypti* [2]. Female mosquitoes are also attracted to host body heat, and recent studies have found that the cooling receptor ionotropic receptor (*Ir21a*) is required for heat-seeking [3]. Mosquitoes are attracted to high-contrast

visual cues after sensing CO<sub>2</sub>, which indicates that visual signals also play an important role in host localization [4]. A recent study demonstrated that vision-guided target attraction requires opsin1 (*Op1*) and opsin2 (*Op2*) in *Ae. aegypti* [5].

Mosquitoes are distributed worldwide, and their vectorial capacity is dramatically affected by different environmental conditions. Despite that many studies have revealed the importance of host-associated cues during mosquito host-seeking, fewer investigations have investigated other environmental factors such as light, humidity, and temperature in regulating host-seeking. Light modulates a wide range of mosquito behaviors such as flight activity, mating, oviposition, and biting time [6]. Light also serves as a strong *zeitgeber* to entrain the circadian clock, and mosquito light preference and blood-sucking behaviors have been reported to be under circadian control [7]. A recent study in *Anopheles gambiae* showed that brief light exposure during night-time decreases the biting activity [8]. These studies strongly suggest that ambient light signals play important roles in regulating mosquito host-seeking behavior and might impact their vectorial capacity. Thus, examining how light regulates mosquito host-seeking behavior might lead to new measures to control mosquito-borne diseases.

In this study, we designed experiments to explore the effects of ambient light on *Ae. aegypti* host-seeking behavior as well as the underlying molecular mechanisms. Heat-seeking behavior serves as an excellent model to study mosquito host-seeking in the laboratory [1]. We established a heat-seeking behavior assay (Figs 1A, S1, and Supplementary Methods) and asked whether heat-seeking behavior is modulated by different ambient light conditions. Female mosquito heat-seeking activity was recorded under either ambient infrared light or ambient high-

**Supplementary Information** The online version contains supplementary material available at <https://doi.org/10.1007/s12264-022-00882-1>.

Haonan Zhou and Kai Shi contributed equally to this work.

✉ Chuan Zhou  
zhouchuan@ioz.ac.cn

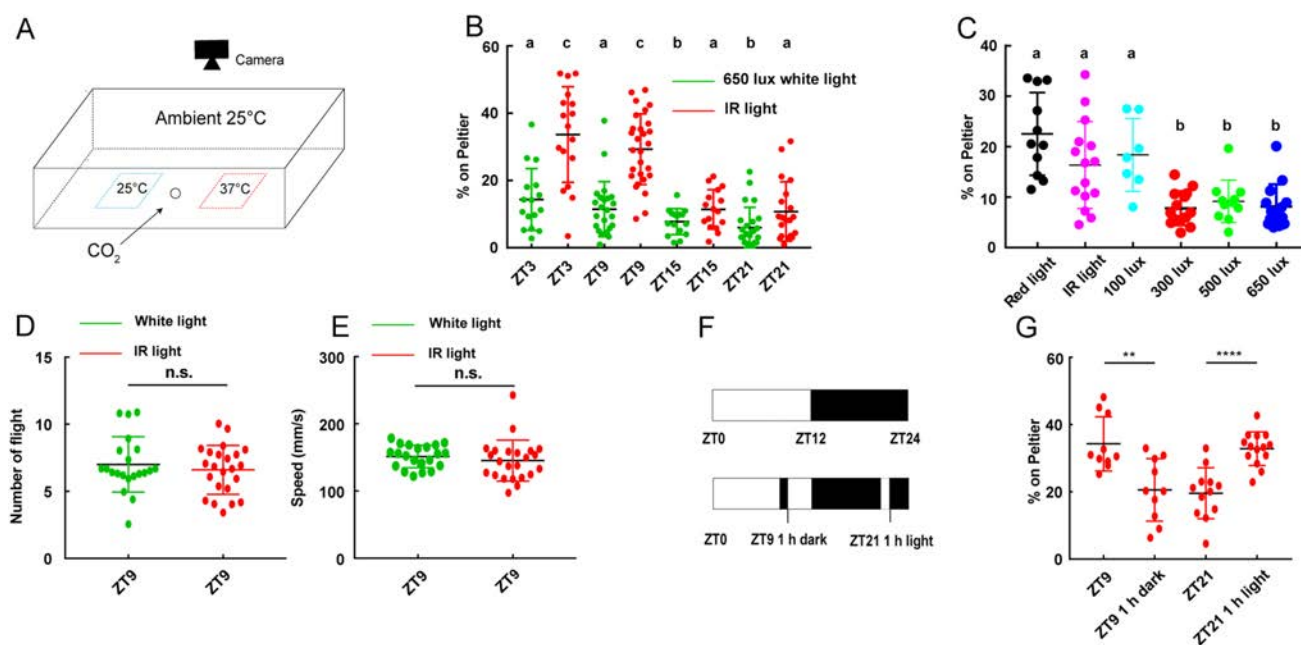
<sup>1</sup> State Key Laboratory of Integrated Management of Pest Insects and Rodents, Institute of Zoology, Chinese Academy of Sciences, Beijing 100101, China

<sup>2</sup> University of Chinese Academy of Sciences, Beijing 100049, China

<sup>3</sup> Chinese Institute for Brain Research, Beijing 102206, China

<sup>4</sup> Institute of Molecular Physiology, Shenzhen Bay Laboratory, Shenzhen 518132, China





**Fig. 1** Dual effects of light on mosquito heat-seeking. **A** Schematic of the behavioral assay for heat-seeking. Each chamber has 20 female mosquitoes. **B** Heat-seeking is stronger during the day and is suppressed by strong ambient light. “% on Peltier” means the the number of mosquitoes that land on zone 37°C minus the number of mosquitoes on zone 25°C then divided by the total number of mosquitoes (mean  $\pm$  SD,  $n = 16$ –28 trials per experiment; letters denote distinct categories; between a and b,  $P < 0.05$ , between b and c,  $P < 0.0001$ ; Kruskal-Wallis and *post hoc* Mann-Whitney *U* tests). **C** Heat-seeking is suppressed by white light >300 lux (mean  $\pm$  SD,  $n = 7$ –15 trials for each experiment; letters denote distinct categories;  $P < 0.05$ ; Kruskal-Wallis and *post hoc* Mann-Whitney *U* tests). **D**, **E**

intensity white light conditions ( $\sim 650$  lux). Since *Ae. aegypti* is a diurnal species that might display changing heat-seeking activity with the time of day, we measured the heat-seeking activity in both day-time (zeitgeber time ZT3 and ZT9) and night-time (ZT15 and ZT21). We found that heat-seeking activity under the white light condition was significantly weaker than that under the infrared light condition, suggesting that light acutely suppresses *Ae. aegypti* heat-seeking (Fig. 1B). On the other hand, consistent with previous studies on *Ae. aegypti* biting [9], mosquitoes displayed significantly stronger heat-seeking during the day (Fig. 1B). Since *Ae. aegypti* displays strong host-seeking during dawn and dusk, we hypothesized that mosquito heat-seeking might only be suppressed by strong light. Therefore, we further studied the heat-seeking behavior under different light conditions: infrared, red, and white light at different intensities from 100 lux to 650 lux. We found that the heat-seeking was greatly suppressed when the light intensity was stronger than 300 lux (Fig. 1C). To investigate whether the decrease in heat-seeking is attributable to the suppression of locomotion by light, the CO<sub>2</sub> activation rate and locomotor behavior at

Light does not decrease locomotion and CO<sub>2</sub> activation rate. The locomotion of wild-type mosquitoes was activated by CO<sub>2</sub> under 650 lux white light or infrared light. The number of mosquitoes that took off in response to the CO<sub>2</sub> and the speed at which they flew was recorded (mean  $\pm$  SD,  $n = 21$ –23 trials for each experiment; n.s., no significant; Student’s *t*-test). **F** Schematic of ZT time and light-dark switching. **G** Heat-seeking behavior at ZT9, ZT21, and the same times after 1 h of dark or light treatment in the incubator. The index increases after light treatment and decreases after dark treatment under the ambient infrared light condition (mean  $\pm$  SD,  $n = 10$ –14 trials for each experiment; \*\* $P < 0.01$ , \*\*\*\* $P < 0.0001$ ; Kruskal-Wallis and *post hoc* Mann-Whitney *U* tests).

ZT9 under 650 lux white or infrared light were measured, and no difference was found (Fig. 1D, E), indicating that the heat-seeking behavior suppression by light is not caused by a decrease of locomotion or the CO<sub>2</sub> activation rate.

Meanwhile, together with previous studies [5, 10], our finding that *Ae. aegypti* mosquitoes showed much stronger heat-seeking during the day (Fig. 1B) strongly suggested that light might regulate mosquito heat-seeking behavior through light entrainment of the biological clock. So, we switched the light condition 1 h ahead of the behavioral test to investigate whether prior light experience could entrain mosquito behavior (Fig. 1F, G). We found that turning on the light for 1 h during the night significantly facilitated heat-seeking, while turning off the light during the day for 1 h significantly decreased heat-seeking (Fig. 1G), indicating that light might also act as an entraining signal for heat-seeking behavior in *Ae. aegypti*. Thus, these results suggested that light plays dual roles in heat-seeking behavior: while light serves as an entraining signal to promote heat-seeking during the day, strong light also inhibits heat-seeking in *Ae. aegypti*.

Light is primarily detected through the visual system [11], and histamine is an essential neurotransmitter for visual signal transduction in *Drosophila melanogaster* [12]. To determine whether the visual system is required for light to regulate mosquito heat-seeking behavior, we generated blind mosquitoes by mutating histidine decarboxylase (*Hdc*) that is required for histamine synthesis. Two *Hdc* (AAEL009593) mutant alleles of *Ae. aegypti* were generated *via* the CRISPR/Cas9 (clustered regularly interspaced short palindromic repeats/CRISPR-associated protein 9) system (Fig. S2A). Electroretinogram (ERG) recording showed that the depolarization voltages in the *Hdc* mutant mosquitoes were significantly weaker than in the wild-type, and this was rescued by feeding *Hdc* mutant mosquitoes with histamine (Fig. S2C–E). These results demonstrated that histamine is required for a normal ERG potential, suggesting that the *Hdc* mutant mosquitoes were blind. To test if these mutants are truly blind, we further performed a flight simulator experiment (Fig. S2B and Supplementary Methods). The yaw of the mutant's flight indicated that they could not see moving objects. In contrast, the yaw of the wild-type and mutant fed with histamine was normal (Fig. S2F–K). These experiments indicate that *Hdc* mutant mosquitoes are indeed blind.

Using these *Hdc* mutant mosquitoes, we investigated whether white light suppresses mosquito heat-seeking through the visual system. Compared to wild-type mosquitoes whose heat-seeking was strongly suppressed by white light (650 lux) (Fig. 2A), the *Hdc* mutant mosquitoes showed no light-induced suppression such that they performed similar heat-seeking behavior under both white and red light conditions (Figs 2B, S3). The light-suppression defect of *Hdc* mutant mosquitoes was rescued by feeding 2‰ histamine (Figs 2C, S3). No locomotor defect was found in *Hdc* mutant mosquitoes (Fig. S4). We also used a pharmacological strategy to inhibit histamine synthesis and found that the heat-seeking of mosquitoes fed with histamine inhibitors was no longer suppressed by strong light, which is consistent with the findings in *Hdc* mutant mosquitoes (Fig. S5). These results demonstrated that *Hdc*-dependent visual transduction is required for light to suppress *Ae. aegypti* heat-seeking behavior.

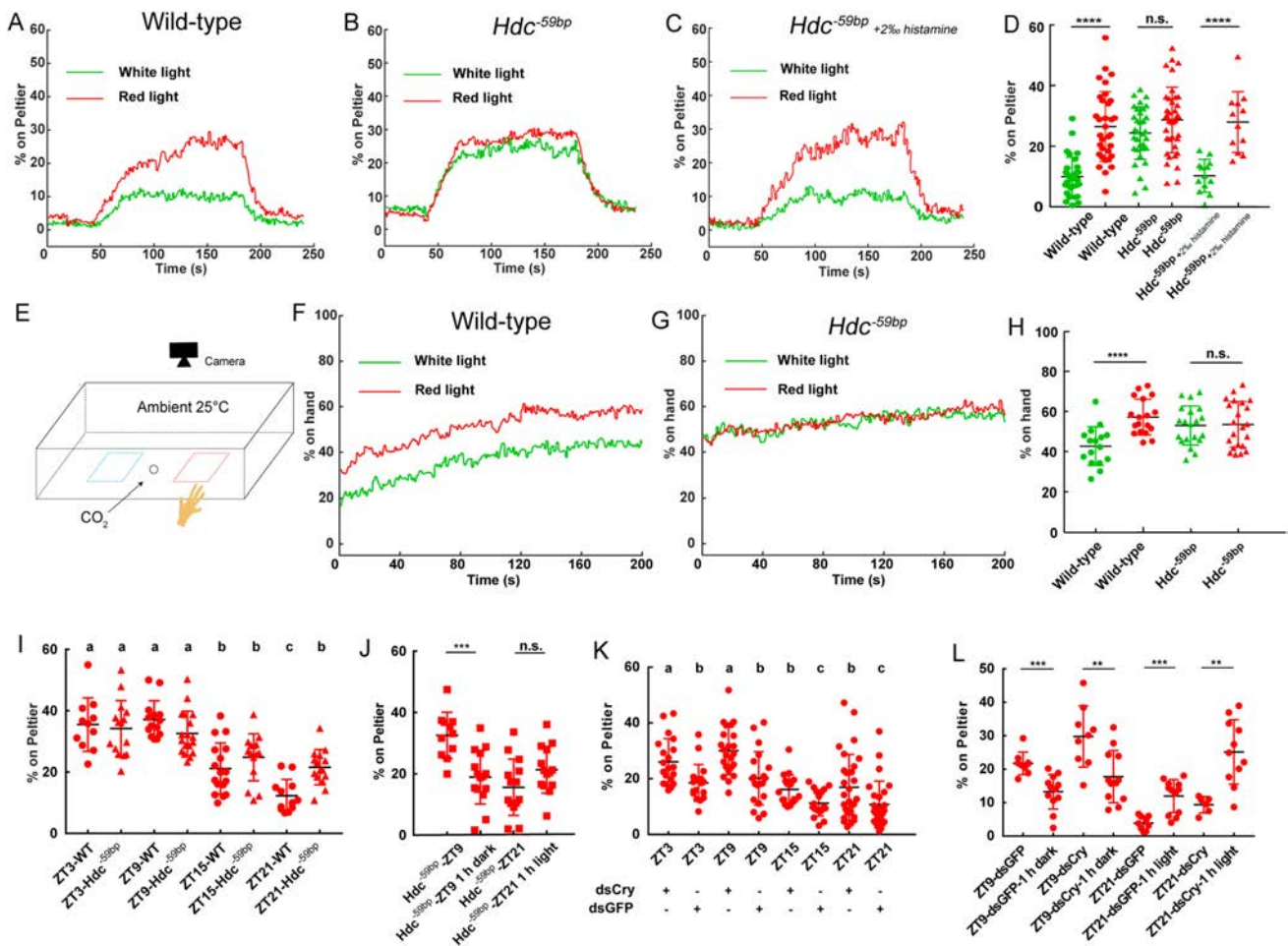
We further investigated whether light suppresses host-seeking using human hands as targets (Fig. 2E). We found that, similar to heat-seeking behavior, bright light (650 lux) strongly suppressed host-seeking behavior in wild-type mosquitoes but not in *Hdc* mutant mosquitoes, and feeding the *Hdc* mutants with 2‰ histamine rescued the light-suppression effect (Figs 2F–H, S3). Thus, light suppresses both heat-seeking and host-seeking behaviors through *Hdc*-dependent visual transduction in *Ae. aegypti*.

Animals synchronize their behavior to light/dark cycles through photoentrainment of the circadian clock [13, 14].

The visual system has been reported to mediate the photoentrainment in *D. melanogaster*, and we asked whether the mosquito visual system also contributes to the light/dark cycle of heat-seeking activity in *Ae. aegypti*. Using *Hdc* mutant mosquitoes in heat-seeking experiments, we found that these mutants still showed stronger heat-seeking during the day than they did during the night, which is similar to wild-type mosquitoes (Fig. 2I). When we turned off the light for 1 h during the day, the heat-seeking of *Hdc* mutant mosquitoes decreased significantly, which is also similar to wild-type mosquitoes. However, light treatment during the night was less effective in facilitating heat-seeking in *Hdc* mutant mosquitoes (Figs 2J, S3H). These results suggested that *Hdc*-dependent visual transduction only partially mediates the circadian-dependent heat-seeking behavior (Fig. 2I, J), indicating that other light transduction pathways might be involved. Cryptochrome (*Cry*) is a blue light-sensitive protein that mediates light-dependent degradation of the clock protein Timeless and plays an important role in circadian light entrainment in *D. melanogaster* [15]. We hypothesized that exposure to light might lead to the degradation of *Cry* to facilitate heat-seeking behavior in *Ae. aegypti*. So, we knocked down the *Cry* gene (AAEL004146) using RNA interference (RNAi) and conducted heat-seeking experiments at different ZTs under infrared light conditions. The expression of *Cry* significantly decreased after double-stranded RNA (dsRNA) injection into *Ae. aegypti* (Fig. S6). After *Cry* knockdown, mosquitoes showed stronger heat-seeking at all ZTs tested, while still maintaining the difference in heat-seeking activity between day and night (Fig. 2K), suggesting that *Cry* functions as a heat-seeking suppressor but does not significantly affect the rhythm of heat-seeking behavior. The light switch experiments also showed that mosquitoes were still able to respond to the light switch after the knockdown of *Cry* (Fig. 2L).

Taken together, our results revealed dual effects of light on heat- and host-seeking in *Ae. aegypti*. On one hand, strong light inhibits heat-seeking and host-seeking behaviors, which requires *Hdc*-dependent visual transduction. On the other hand, light serves as an entraining signal to promote heat-seeking during the day. The latter effect does not only depend on the visual system or the light-dependent circadian regulator CRY and possibly requires both or additional pathways.

Our results also indicated that light is able to regulate host-seeking behavior by mosquitoes through CRY. In *Drosophila*, *Cry* is expressed in a subset of clock neurons [15], which might be similar in mosquitoes. Further study of the *Cry*-expressing neural circuit in host-seeking behavior might provide new insights to understand the central neural mechanism of host-seeking behavior in mosquitoes.



**Fig. 2** Function of *Hdc* and *Cry* in mediating light effects on heat-seeking and host-seeking. **A–C** Heat-seeking behavior under 650 lux white light and red light. **D** Heat-seeking is no longer suppressed by white light in *Hdc* mutants. Wild-type and *Hdc* mutant mosquitoes fed histamine show reduced heat-seeking under white light (mean  $\pm$  SD,  $n = 12$ –39 trials for each experiment). **E** Schematic of host-seeking behavior using human hands. **F, G** Host-seeking behavior under red light and 650 lux white light conditions. **H** Host-seeking is no longer suppressed by white light in *Hdc* mutants (mean  $\pm$  SD,  $n = 17$ –22 trials for each experiment; n.s., not significant). **I** Similar to wild-type (WT) mosquitoes, *Hdc* mutant mosquitoes show strong heat-seeking during the day and weak heat-seeking at night under the

ambient infrared light condition (mean  $\pm$  SD,  $n = 11$ –17 trials per experiment; letters denote distinct categories; between a and b,  $P < 0.01$ , between b and c,  $P < 0.001$ ). **J** Heat-seeking of *Hdc* mutant mosquitoes with light-dark switching (mean  $\pm$  SD,  $n = 11$ –15 trials per experiment). **K** Heat-seeking behavior of mosquitoes after injection of *Cry* dsRNA is significantly enhanced (mean  $\pm$  SD,  $n = 18$ –29 trials per experiment; letters denote distinct categories; between a and b,  $P < 0.01$ , between b and c,  $P < 0.05$ ). **L** Heat-seeking of *Cry* knockdown mosquitoes with light-dark switching (mean  $\pm$  SD,  $n = 6$ –12 trials per experiment; \*\* $P < 0.01$ , \*\*\* $P < 0.001$ , \*\*\*\* $P < 0.0001$ ; Kruskal-Wallis and *post hoc* Mann-Whitney *U* tests).

*Ae. aegypti* has been found to be a diurnal mosquito that sucks blood almost exclusively during the day [9]. This might be controlled by the circadian clock. Here, we found that the heat-seeking of *Ae. aegypti* was stronger during the day, and light exposure during the night could facilitate heat-seeking, which might be a result of light entrainment of the mosquito's circadian clock. We studied the function of *Hdc* and *Cry* in mediating the light entrainment effects and found that loss-of-function of either pathway did not disrupt the diurnal heat-seeking activity in *Ae. aegypti*, suggesting the involvement of both pathways and potentially other unidentified pathways. Studies in *Drosophila*

have also found that the light signal is transduced through multiple pathways to entrain the circadian clock, and it would be of great interest to identify those pathways in both flies and mosquitoes, which might help to understand the evolutionary mechanisms of how different mosquito species adapted to be either diurnal or nocturnal and lead to new measures for mosquito control as well.

**Acknowledgements** We thank Zhen Zou, Yufeng Pan, and Chenzhu Wang for comments on the manuscript, and Yan Zhu and Xiaonan Li for providing experimental apparatus. This work was supported by the National Natural Science Foundation of China (Y711181133) and the State Key Laboratory of Integrated Management of Pest Insects

and Rodents, Institute of Zoology, Chinese Academy of Sciences (Y952824103).

**Conflict of interest** The authors have no financial conflicts of interest.

## References

- McMeniman CJ, Corfas RA, Matthews BJ, Ritchie SA, Vosshall LB. Multimodal integration of carbon dioxide and other sensory cues drives mosquito attraction to humans. *Cell* 2014, 156: 1060–1071.
- McBride CS, Baier F, Omondi AB, Spitzer SA, Lutomiah J, Sang R. Evolution of mosquito preference for humans linked to an odorant receptor. *Nature* 2014, 515: 222–227.
- Greppi C, Laursen WJ, Budelli G, Chang EC, Daniels AM, van Giesen L, *et al.* Mosquito heat seeking is driven by an ancestral cooling receptor. *Science* 2020, 367: 681–684.
- van Breugel F, Riffell J, Fairhall A, Dickinson MH. Mosquitoes use vision to associate odor plumes with thermal targets. *Curr Biol* 2015, 25: 2123–2129.
- Zhan YP, Alonso San Alberto D, Rusch C, Riffell JA, Montell C. Elimination of vision-guided target attraction in *Aedes aegypti* using CRISPR. *Curr Biol* 2021, 31: 4180–4187.e6.
- Farnesi LC, Barbosa CS, Araripe LO, Bruno RV. The influence of a light and dark cycle on the egg laying activity of *Aedes aegypti* (Linnaeus, 1762) (Diptera: Culicidae). *Mem Inst Oswaldo Cruz* 2018, 113: e170362.
- Baik LS, Nave C, Au DD, Guda T, Chevez JA, Ray A, *et al.* Circadian regulation of light-evoked attraction and avoidance behaviors in daytime- versus nighttime-biting mosquitoes. *Curr Biol* 2020, 30: 3252–3259.e3.
- Sheppard AD, Rund SSC, George GF, Clark E, Aciri DJ, Duffield GE. Light manipulation of mosquito behaviour: Acute and sustained photic suppression of biting activity in the *Anopheles gambiae* malaria mosquito. *Parasit Vectors* 2017, 10: 255.
- Corbet PS, Smith SM. Diel periodicities of landing of nulliparous and parous *Aedes aegypti* (L.) At Dar Es Salaam, Tanzania (Diptera, Culicidae). *Bull Entomol Res* 1974, 64: 111–121.
- Rund SSC, Labb LF, Benefiel OM, Duffield GE. Artificial light at night increases *Aedes aegypti* mosquito biting behavior with implications for arboviral disease transmission. *Am J Trop Med Hyg* 2020, 103: 2450–2452.
- Helfrich-Förster C. Light input pathways to the circadian clock of insects with an emphasis on the fruit fly *Drosophila melanogaster*. *J Comp Physiol A Neuroethol Sens Neural Behav Physiol* 2020, 206: 259–272.
- Montell C. *Drosophila* visual transduction. *Trends Neurosci* 2012, 35: 356–363.
- Allada R, Chung BY. Circadian organization of behavior and physiology in *Drosophila*. *Annu Rev Physiol* 2010, 72: 605–624.
- Mei Y, Teng HJ, Li ZG, Zeng C, Li YY, Song W, *et al.* Restricted feeding resets endogenous circadian rhythm in female mice under constant darkness. *Neurosci Bull* 2021, 37: 1005–1009.
- Emery P, So WV, Kaneko M, Hall JC, Rosbash M. CRY, a *Drosophila* clock and light-regulated cryptochrome, is a major contributor to circadian rhythm resetting and photosensitivity. *Cell* 1998, 95: 669–679.



# Release of Endogenous Brain-derived Neurotrophic Factor into the Lateral Entorhinal Cortex from the Paraventricular Thalamus Ameliorates Social Memory Deficits in a Mouse Model of Alzheimer's Disease

Yun-Long Xu<sup>1,2</sup> · Lin Zhu<sup>3</sup> · Zi-Jun Chen<sup>1</sup> · Xiao-Fei Deng<sup>1</sup> · Pei-Dong Liu<sup>4</sup> · Shan Li<sup>3</sup> · Bing-Chun Lin<sup>3,5</sup> · Chuan-Zhong Yang<sup>3</sup> · Wei Xu<sup>1</sup> · Kui-Kui Zhou<sup>1</sup> · Ying-Jie Zhu<sup>1,2,6,7,8</sup>

Received: 9 January 2022 / Accepted: 7 April 2022 / Published online: 28 June 2022

© Center for Excellence in Brain Science and Intelligence Technology, Chinese Academy of Sciences 2022

## Dear Editor,

Alzheimer's disease (AD) is one of the most devastating neurodegenerative disorders and the most common form of dementia. Synaptic loss is a hallmark of AD pathology and exacerbates cognitive impairment [1]. Synaptic loss, unlike neuronal loss, is reversible due to the highly dynamic properties of synapses. Thus, therapeutics targeting synaptic loss and dysfunction are practical and beneficial for treating neurodegenerative diseases. Most importantly, the window for the treatment of synapses is longer than that of clearing toxic proteins and preventing neuronal death. Treatment targeting synapses delivered at a relatively late stage still slows the progression of AD [2]. Evidence supporting a hypothesis for targeting the excitation-inhibition (EI) synaptic balance provides a therapeutic approach for preventing neurodegeneration in patients with AD [3].

Brain-derived neurotrophic factor (BDNF), a neurotrophic factor family member, has prominent effects on synaptic development and function, neuronal survival and differentiation, and cognition. As a synaptogenic modulator that improves synaptic function and plasticity, BDNF is sufficient to induce synapse formation and enhance synaptic transmission [4]. In patients with AD, the level of BDNF protein in the entorhinal cortex is reduced [5]. BDNF has an extensive protective action in AD animal models, aged rats, and adult primates. The TrkB (tropomyosin-related kinase B, BDNF receptor) agonist, AS86, reverses the cognitive function deficit in the amyloid- $\beta$  precursor protein/pre-senilin 1 (APP/PS1) mouse model [6], implying that BDNF is a beneficial therapy for AD [2]. However, the development of BDNF-based drugs is still challenging. Due to its intrinsic biochemical properties, exogenous BDNF protein

Yun-Long Xu, Lin Zhu, and Zi-Jun Chen contributed equally to this work.

**Supplementary Information** The online version contains supplementary material available at <https://doi.org/10.1007/s12264-022-00900-2>.

✉ Wei Xu  
freefresh2000@163.com

✉ Kui-Kui Zhou  
kk.zhou@siat.ac.cn

✉ Ying-Jie Zhu  
yj.zhu1@siat.ac.cn

<sup>1</sup> Shenzhen Key Laboratory of Drug Addiction, Shenzhen Neher Neural Plasticity Laboratory, the Brain Cognition and Brain Disease Institute (BCBDI), Shenzhen Institute of Advanced Technology, Chinese Academy of Sciences (CAS), Shenzhen-Hong Kong Institute of Brain Science-Shenzhen Fundamental Research Institutions, Shenzhen 518055, China

<sup>2</sup> University of Chinese Academy of Sciences, Beijing 100049, China

<sup>3</sup> Department of Neonatology, Shenzhen Maternity & Child Healthcare Hospital, The First School of Clinical Medicine, Southern Medical University, Shenzhen 518055, China

<sup>4</sup> The First Affiliated Hospital, Sun Yat-sen University, Guangzhou 510080, China

<sup>5</sup> Cheeloo College of Medicine, Shandong University, Jinan 250012, China

<sup>6</sup> Faculty of Life and Health Sciences, Shenzhen Institute of Advanced Technology, CAS, Shenzhen 518055, China

<sup>7</sup> CAS Center for Excellence in Brain Science and Intelligence Technology, CAS, Shanghai 200031, China

<sup>8</sup> CAS Key Laboratory of Brain Connectome and Manipulation, BCBDI, Shenzhen Institute of Advanced Technology (SIAT), CAS, Shenzhen 518055, China

directly delivered into the blood or cerebrospinal fluid is quickly metabolized, making it difficult to reach the target region. Diffusion of exogenous BDNF protein in the brain parenchyma is difficult due to the binding of BDNF to its high-affinity receptor TrkB. Previous findings indicate that BDNF release is dependent on neuronal activity and high-frequency stimulation is sufficient to induce BDNF release [7]. Therefore, it is urgent to develop novel therapies to increase endogenous BDNF levels in the target location by stimulating BDNF-secreting neurons.

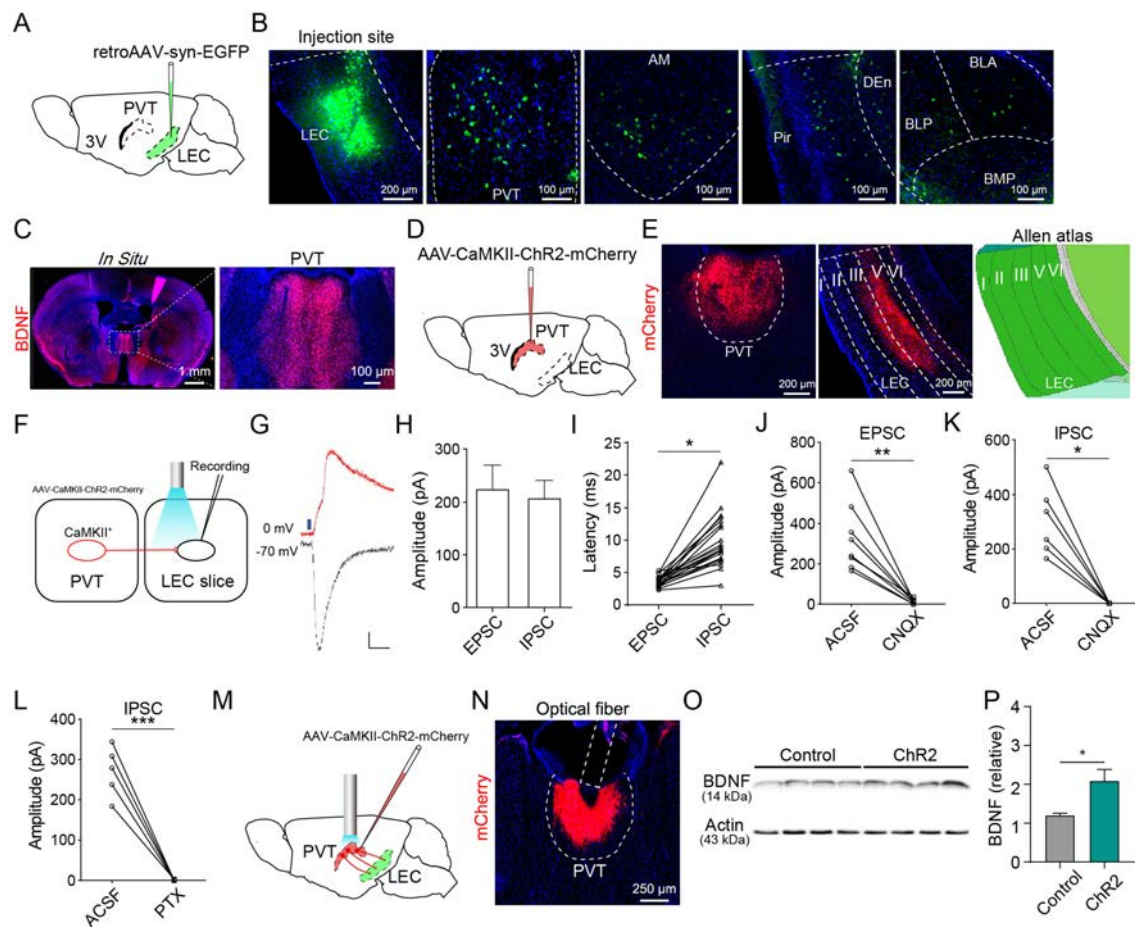
Several studies have suggested that the entorhinal cortex (EC) is a key region in the pathophysiology of the early stages of AD [8, 9]. Metabolic dysfunction in the EC has been reported using cerebral blood volume-functional magnetic resonance imaging (CBV-fMRI) in patients and mice [10]. AD is characterized by a series of pathological susceptibilities, the most prominent of which are amyloid and tau protein abnormalities in the EC in the early stage, resulting in short-term memory impairment [11]. A reduction in interneurons and inhibitory axon terminals has also been reported in the EC; this is consistent with synaptic dysfunction, and suggests that resolving synaptic imbalance in the EC may provide therapeutic benefit in the early stages of AD [3]. EC also relays and processes social signals associated with social cognition in human and animal models. A study has shown that optogenetic stimulation of the lateral entorhinal cortex (LEC) to the dentate gyrus (DG) facilitates social memory, providing insight into the improvement of social memory in brain diseases [12]. Thus, in the 5×FAD (familial Alzheimer's disease) mouse model, the LEC could serve as a potential area for the treatment of social memory deficits.

Based on the evidence above, we hypothesized that endogenous BDNF release into the LEC *via* stimulation of a source region could protect against AD-related pathological changes and ameliorate cognitive impairments. To determine the regions upstream of the LEC, we injected retroAAV-syn-EYFP into the LEC of adult wild-type (WT) mice. Retrogradely-labeled cells were found in the paraventricular thalamus (PVT) [13, 14], anteromedial thalamic nucleus (AM), piriform cortex (Pir), and amygdala (Fig. 1A, B), suggesting that these regions send monosynaptic inputs to the LEC. Fluorescent *in situ* hybridization revealed the presence of BDNF messenger RNA (mRNA) in the PVT (Fig. 1C), implying that it is a source of BDNF delivery into the LEC. We confirmed this connection by using another retrograde tracer CTB (cholera toxin subunit B)-488 and found that CTB-labeled neurons were distributed from anterior to posterior in the PVT. Careful examination revealed that the number of CTB<sup>+</sup> neurons in the anterior PVT was higher than that in the posterior PVT (Fig. S1A) and CTB<sup>+</sup> neurons were co-localized with BDNF in the PVT (Fig. S1B). Therefore, we focused on the PVT-LEC circuit.

To characterize the synaptic connection between the PVT and the LEC, we injected AAV-CaMKII-ChR2-mCherry into the PVT and made patch-clamp recordings from LEC neurons in slices prepared 4 weeks later (Fig. 1D). Dense mCherry fluorescent signals were detected in layers III and V of the LEC (Fig. 1E), suggesting that the PVT mainly innervates deep layers of the LEC. In acute LEC slices containing ChR2-expressing terminals from the PVT (Fig. 1F), brief blue light stimulation (1 ms) elicited reliable excitatory postsynaptic currents (EPSCs) and inhibitory postsynaptic currents (IPSCs) in LEC neurons (Fig. 1G, H). The latency of the picrotoxin-sensitive IPSCs was significantly longer than that of the EPSCs, and extended beyond the duration of monosynaptic transmission (Fig. 1I, L). Because most PVT neurons are glutamatergic, we suspected that the light-evoked IPSCs were mediated by multisynaptic feedforward inhibition. Indeed, both EPSCs and IPSCs were blocked by the  $\alpha$ -amino-3-hydroxy-5-methyl-4-isoxazole propionic acid (AMPA) receptor antagonist CNQX (10  $\mu$ mol/L) (Fig. 1J, K), suggesting that PVT sends feedforward inhibition *via* local LEC interneurons. To examine the LEC cell types that were directly innervated by PVT, we made targeted patch-clamp recordings from glutamatergic neurons in the LEC of vGluT1::Ai14 mice in which glutamatergic neurons were labeled with the red fluorescence protein tdTomato. Brief light stimulation evoked robust EPSCs in 90% (9/10) of tdTomato<sup>+</sup> glutamatergic neurons in the LEC (Fig. S1C). To determine whether PVT terminals also synapse on gamma-aminobutyric acid-ergic (GABAergic) neurons in the LEC, we made targeted recordings from GABAergic neurons in the LEC after labeling GABAergic neurons by injecting AAV2-dlx5/6-GFP into the LEC of WT mice [15]. We found that light-evoked EPSCs could be recorded from 40% (2/5) of GABAergic neurons (Fig. S1C). Overall, these results suggest that PVT neurons make synaptic connections with both glutamatergic and GABAergic neurons in the LEC, and the connection probability is higher with glutamatergic neurons.

To determine the activity-dependent release of BDNF from the PVT neurons into the LEC, we optogenetically activated PVT neurons (Fig. 1M, N) for 15 min (20 Hz, 15 mW) and collected LEC tissue for Western blotting to measure the BDNF protein. The BDNF protein level in the LEC was significantly higher in the ChR2 group than in the control group (Fig. 1O, P), indicating that the activation of PVT neurons is sufficient to release BDNF into the LEC.

Massive synaptic loss is a hallmark of the early stages of AD. To determine whether endogenous BDNF could rescue synaptic loss in AD, we applied chemogenetic tools to chronically activate the PVT neurons in 5×FAD mice. The utility of the chemogenetic approach in activating PVT and LEC neurons were validated by c-fos immunostaining (Fig. S2A–D). We then transduced PVT neurons with Gq-coupled



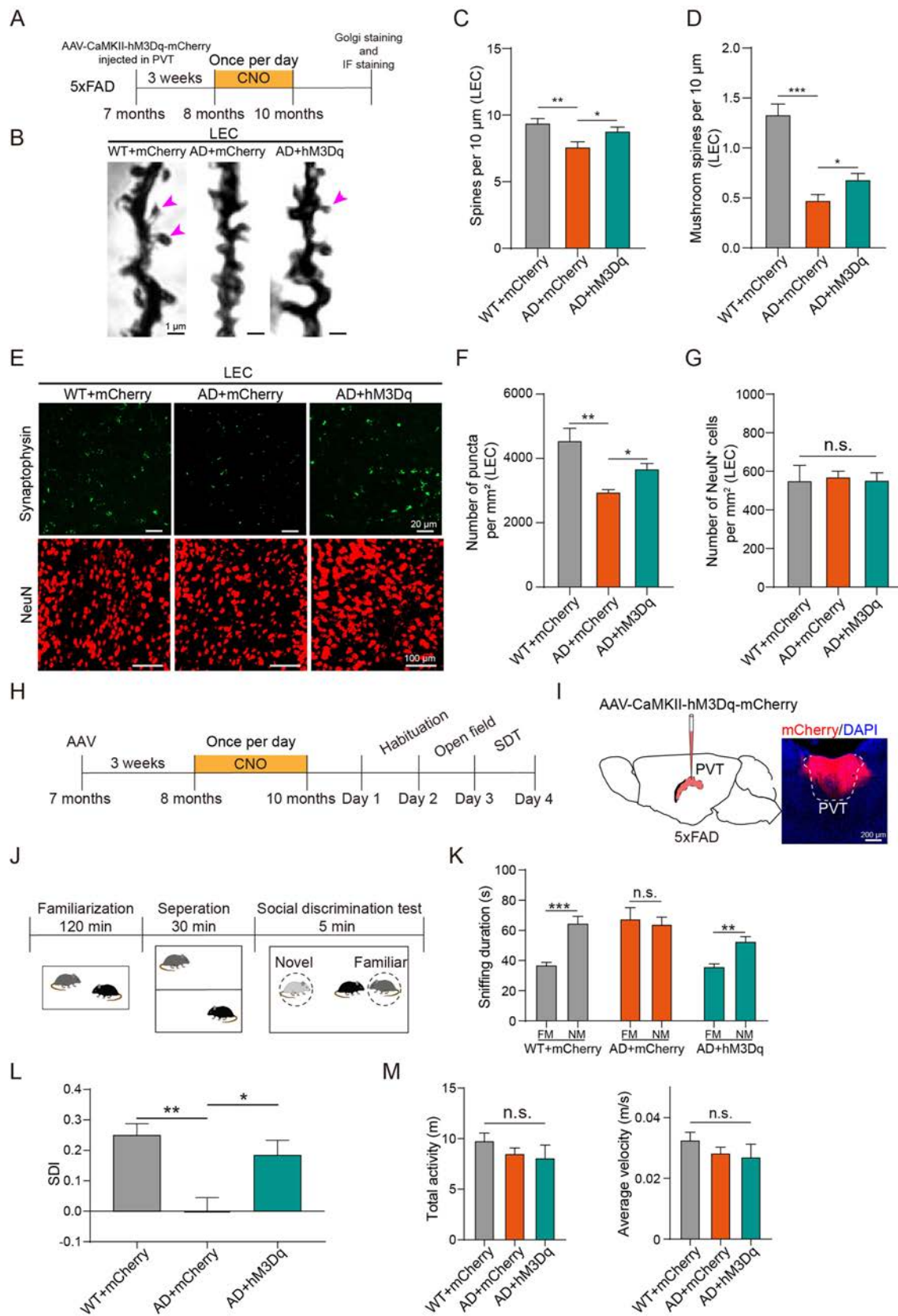
**Fig. 1** Excitatory neurons in the PVT release BDNF into the LEC. **A** Schematic of retroAAV injection into the LEC. **B** Location of an injection site and fluorescence images of EYFP-labeled neurons in the PVT, AM, Pir, and BLA. **C** Fluorescent *in situ* hybridization for BDNF mRNA in the PVT. **D** Schematic of AAV-CaMKII-ChR2-mCherry injection to the PVT. **E** Fluorescence images of viral expression in the PVT and the distribution of axonal fibers in the LEC. **F** Procedures for optogenetic manipulation and electrophysiological recording. **G** Example traces of light-induced EPSCs and IPSCs (scale bars, 50 pA, 50 ms). **H** Amplitudes of EPSCs and IPSCs recorded in the LEC ( $n = 21$  cells). **I** Latency of EPSCs and IPSCs recorded in the LEC ( $n = 21$  cells;  $*P < 0.05$ , paired Student's *t*-test). **J** Amplitude of EPSCs recorded in the LEC after application of CNQX (10  $\mu\text{mol/L}$ ;  $n = 8$  cells;  $**P < 0.01$ , paired Student's *t*-test). **K** Amplitude of IPSCs recorded in the LEC after applica-

tion of CNQX (10  $\mu\text{mol/L}$ ;  $n = 6$  cells;  $*P < 0.05$ , paired Wilcoxon test). **L** Amplitude of IPSCs recorded in the LEC after application of picrotoxin (100  $\mu\text{mol/L}$ ;  $n = 5$  cells;  $***P < 0.001$ , paired Student's *t*-test). **M** Procedure for optogenetic manipulation. **N** Location of viral expression and optic fiber placement. **O**, **P** Western blots and quantification of BDNF protein levels in the LEC ( $n = 4/\text{group}$ ;  $*P < 0.05$ , unpaired Student's *t*-test). 3V, 3rd ventricle; ACSF, artificial cerebrospinal fluid; AM, anteromedial thalamic nucleus; BDNF, brain-derived neurotrophic factor; BLA, basolateral amygdaloid nucleus, anterior part; BLP, basolateral amygdaloid nucleus, posterior part; BMP, basomedial amygdaloid nucleus, posterior part; CaMKII, calmodulin-dependent protein kinase II; DEn, dorsal endopiriform nucleus; EPSC, excitatory postsynaptic current; IPSC, inhibitory postsynaptic current; LEC, lateral entorhinal cortex; Pir, piriform cortex; PTX, picrotoxin; PVT, paraventricular thalamus.

human M3 muscarinic receptor (hM3Dq) in 5xFAD mice at 7 months old and chronically activated PVT neurons by daily injections of clozapine-N-oxide (CNO) (0.6 mg/kg) for 2 months (Fig. 2A). The animals were sacrificed at 10 months of age, and Golgi-Cox staining was used to evaluate the density and morphology of spines in the LEC. We found that the reduction in the density of all spines and mushroom spines in the AD mice was largely rescued by the chemogenetic activation of PVT neurons (Fig. 2B–D). Moreover, immunostaining of the presynaptic marker

synaptophysin also showed a significant increase in the number of synaptophysin<sup>+</sup> puncta in the hM3Dq group of AD mice compared to that of mCherry controls (Fig. 2E, F). Nonetheless, we found no difference in the number of NeuN<sup>+</sup> cells in the LEC among the three groups, hinting that neuronal loss was not reversed by the activation of PVT neurons (Fig. 2E, G). Overall, these results indicated that chronic activation of the PVT is sufficient to prevent synaptic loss in AD mice. Following that, amyloid  $\beta$  (A $\beta$ ) immunostaining in the LEC showed that there was no significant







**Fig. 2** Chronic activation of PVT neurons attenuates synaptic loss and ameliorates social memory in 5xFAD mice. **A** Experimental design for chemogenetic activation and staining. **B** Representative images of dendritic segments in the LEC (arrowheads represent mushroom spines). **C** Chronic activation of PVT neurons reduces total spine loss in the LEC (WT + mCherry:  $n = 43$ , AD + mCherry:  $n = 24$ , AD + hM3Dq:  $n = 24$ ;  $^{**}P < 0.01$ ,  $^{*}P < 0.05$ , one-way analysis of variance (ANOVA), Tukey's *post hoc* test). **D** Chronic activation of PVT neurons prevents mushroom spine loss in the LEC (WT + mCherry:  $n = 43$ , AD + mCherry:  $n = 24$ , AD + hM3Dq:  $n = 24$ ;  $^{***}P < 0.001$ ,  $^{*}P < 0.05$ , one-way ANOVA, Tukey's *post hoc* test). **E** Representative immunofluorescence staining of synaptophysin and NeuN in the LEC. **F** Numbers of synaptophysin-positive puncta per  $\text{mm}^2$  in the LEC of the WT + mCherry ( $n = 6$ ), AD + mCherry ( $n = 6$ ), and AD + hM3Dq groups ( $n = 8$ ) ( $^{**}P < 0.01$ ,  $^{*}P < 0.05$ , one-way ANOVA, Dunn's test). **G** Numbers of NeuN-positive cells per  $\text{mm}^2$  in the LEC of the WT + mCherry ( $n = 5$ ), AD + mCherry ( $n = 5$ ), and AD + hM3Dq groups ( $n = 5$ ) (n.s., no significant difference, one-way ANOVA, Tukey's *post hoc* test). **H** Experimental design for chemogenetic activation and behaviors. **I** Schematic of the injection of AAV-CaMKII-hM3Dq-mCherry into PVT (left) and the location of viral expression (right). **J** Protocol for the social discrimination test. **K** Total duration in the sniffing region during the social discrimination test (SDT) in the WT + mCherry ( $n = 28$ ), AD + mCherry ( $n = 17$ ), and AD + hM3Dq groups ( $n = 12$ ) ( $^{***}P < 0.001$ ,  $^{**}P < 0.01$ , n.s., no significant difference, paired Student's *t*-test). FM, familiar mouse; NM, novel mouse. **L** Comparison of social discrimination index (SDI) for the WT + mCherry ( $n = 28$ ), AD + mCherry ( $n = 17$ ), and AD + hM3Dq groups ( $n = 12$ ) ( $^{***}P < 0.001$ ,  $^{*}P < 0.05$ , one-way ANOVA, Tukey's *post hoc* test). **M** Total travel distance and speed in the open field for the WT + mCherry ( $n = 23$ ), AD + mCherry ( $n = 10$ ), and AD + hM3Dq groups ( $n = 9$ ) (n.s., no significant difference, one-way ANOVA, Tukey's *post hoc* test).

difference in the number of A $\beta$  plaques between the hM3Dq and mCherry groups (Fig. S2K, L), which suggests that chronic activation of the PVT has no effect on clearing A $\beta$ .

Next, we sought to determine whether chronic stimulation of the PVT is beneficial for the social memory deficits associated with AD. We transduced PVT neurons with hM3Dq in 5xFAD mice at 7 months old and chronically activated PVT neurons by daily injection of CNO (0.6 mg/kg) for different time periods. Control AD mice spent an equal amount of time sniffing the novel and familiar mice, which resulted in a low social discrimination index (SDI), indicating an impairment of social memory. Two months of CNO treatment (Fig. 2H, I) significantly increased the time spent in investigating the novel mice, and the SDI (Fig. 2J–L). To determine how long the CNO treatment is required for the improvement of social memory, we shortened the treatment duration to 1 month or 0.5 month. The one-month CNO treatment also significantly increased the time spent in sniffing novel mice and the SDI. The improvement effect was blocked by pretreatment with the TrkB antagonist K252a (1  $\mu\text{L}$  and 1  $\mu\text{mol}$  in 1% DMSO/artificial cerebrospinal fluid), demonstrating a crucial role of the BDNF–TrkB signaling pathway in mediating the memory improvement (Fig. S2H–J). AD mice with 0.5-month CNO treatment also exhibited a trend of increase in SDI, but this did not

reach the significance level (Fig. S2E–G). These results suggest that one month of CNO treatment is required for the improvement of social memory.

We further investigated whether the activation of PVT neurons alters the locomotor activity of AD mice using the open field test. There was no significant difference among the three groups in total distance traveled and speed (Fig. 2M), suggesting that chronic PVT stimulation does not influence locomotion.

In summary, we demonstrated that activating PVT neurons results in the endogenous release of BDNF into the LEC. In line with a previous study in which optogenetic stimulation of the LEC–DG restores social memory deficits [12], chronic activation of PVT prevented synaptic loss, and was sufficient to attenuate social memory deficits. Another study has demonstrated that in the early stages of AD, an excitatory–inhibitory imbalance occurs in the LEC, and allosteric modulators restore synaptic balance [3], implying that regulating synaptic function in the LEC is a promising target for treating AD. Furthermore, our results also showed that the endogenous release of BDNF by manipulating neural circuits, which prevented synaptic loss and attenuated social memory deficits, could be a potentially important strategy in treating the symptoms of AD. Because of the longer window of treatment for synapses, this therapeutic strategy has a unique advantage over traditional treatments such as the clearance of toxic proteins.

**Acknowledgements** This work was supported by the Frontier Research Program of Bioland Laboratory (Guangzhou Regenerative Medicine and Health Guangdong Laboratory) (2018GZR110105006), the National Natural Science Foundation of China (31900735, 82171492, and 81922024), and the Science, Technology and Innovation Commission of Shenzhen Municipality (RCJC20200714114556103 and ZDSYS20190902093601675).

**Conflict of interest** The authors declare no conflict of interest in this work.

## References

1. Zhang XM, Zhao F, Wang CF, Zhang J, Bai Y, Zhou F. AVP(4–8) improves cognitive behaviors and hippocampal synaptic plasticity in the APP/PS1 mouse model of Alzheimer's disease. *Neurosci Bull* 2020, 36: 254–262.
2. Lu B, Nagappan G, Guan XM, Nathan PJ, Wren P. BDNF-based synaptic repair as a disease-modifying strategy for neurodegenerative diseases. *Nat Rev Neurosci* 2013, 14: 401–416.
3. Petrache AL, Rajulawalla A, Shi AQ, Wetzel A, Saito T, Saido TC, *et al.* Aberrant excitatory-inhibitory synaptic mechanisms in entorhinal cortex microcircuits during the pathogenesis of Alzheimer's disease. *Cereb Cortex* 2019, 29: 1834–1850.
4. Ji YY, Lu Y, Yang F, Shen WH, Tang TTT, Feng LY, *et al.* Acute and gradual increases in BDNF concentration elicit distinct signaling and functions in neurons. *Nat Neurosci* 2010, 13: 302–309.

5. Phillips HS, Hains JM, Armanini M, Laramée GR, Johnson SA, Winslow JW. BDNF mRNA is decreased in the hippocampus of individuals with Alzheimer's disease. *Neuron* 1991, 7: 695–702.
6. Wang SD, Yao HY, Xu YH, Hao R, Zhang W, Liu H, *et al.* Therapeutic potential of a TrkB agonistic antibody for Alzheimer's disease. *Theranostics* 2020, 10: 6854–6874.
7. Figurov A, Pozzo-Miller LD, Olafsson P, Wang T, Lu B. Regulation of synaptic responses to high-frequency stimulation and LTP by neurotrophins in the hippocampus. *Nature* 1996, 381: 706–709.
8. Dai ZJ, He Y. Disrupted structural and functional brain connectomes in mild cognitive impairment and Alzheimer's disease. *Neurosci Bull* 2014, 30: 217–232.
9. Ying Y, Wang JZ. Illuminating neural circuits in Alzheimer's disease. *Neurosci Bull* 2021, 37: 1203–1217.
10. Khan UA, Liu L, Provenzano FA, Berman DE, Profaci CP, Sloan R, *et al.* Molecular drivers and cortical spread of lateral entorhinal cortex dysfunction in preclinical Alzheimer's disease. *Nat Neurosci* 2014, 17: 304–311.
11. Kordower JH, Chu Y, Stebbins GT, DeKosky ST, Cochran EJ, Bennett D, *et al.* Loss and atrophy of layer II entorhinal cortex neurons in elderly people with mild cognitive impairment. *Ann Neurol* 2001, 49: 202–213.
12. Leung C, Cao F, Nguyen R, Joshi K, Agrabawi AJ, Xia ST, *et al.* Activation of entorhinal cortical projections to the dentate gyrus underlies social memory retrieval. *Cell Rep* 2018, 23: 2379–2391.
13. Zhu YJ, Nachtrab G, Keyes PC, Allen WE, Luo LQ, Chen XK. Dynamic salience processing in paraventricular thalamus gates associative learning. *Science* 2018, 362: 423–429.
14. Zhu YJ, Wienecke CFR, Nachtrab G, Chen XK. A thalamic input to the nucleus accumbens mediates opiate dependence. *Nature* 2016, 530: 219–222.
15. Dimidschstein J, Chen Q, Tremblay R, Rogers SL, Saldi GA, Guo LH, *et al.* A viral strategy for targeting and manipulating interneurons across vertebrate species. *Nat Neurosci* 2016, 19: 1743–1749.

RESEARCH HIGHLIGHT

# ***UNC13A* Gene Brings New Hope for ALS Disease-Modifying Drugs**

Xi Chen<sup>1</sup>  · Heling Chu<sup>2</sup> · Yi Dong<sup>1</sup> 

Received: 23 March 2022 / Accepted: 9 June 2022 / Published online: 30 July 2022

© Center for Excellence in Brain Science and Intelligence Technology, Chinese Academy of Sciences 2022

Amyotrophic lateral sclerosis (ALS) is an idiopathic and fatal neurodegenerative disorder leading to progressive muscle atrophy, dysarthria, dysphagia, and respiratory failure [1]. More than 80 different drugs have been tested since the 1980s, but only two, riluzole and edaravone, have been approved for ALS treatment. Riluzole is an anti-excitotoxic drug that may moderately prolong ALS patients' survival by 2–3 months, and edaravone is an antioxidant that could suppress neurodegeneration in early-stage patients. But neither can significantly prevent the rapid disease progression [2]. Therefore, searching for effective disease-modifying treatment for ALS remains essential.

Aberrant phosphorylation, ubiquitination, cleavage, or nuclear depletion of TDP-43 (TAR DNA-binding protein 43) is the predominant pathological feature in ~97% of ALS and 45% of frontotemporal dementia (FTD) patients, suggesting that ALS-causing mechanisms converge on this central pathological axis. TDP-43, encoded by the *TARDBP* gene, plays a critical role in messenger RNA (mRNA) splicing, RNA transport, translation, and microRNA biogenesis. The loss of TDP-43 nuclear function may decrease alternative splicing, such that some cryptic exons (CEs) are incorrectly included in the mature mRNAs of many genes, leading to the dysregulation of these genes [3].

The *UNC13A* gene has been identified as a shared risk locus for ALS and FTD by genome-wide association studies, but the association between *UNC13A* and disease risk has not been elucidated. Recently, two striking studies [4, 5] in *Nature* concerning a functional link between the *UNC13A* gene and the TDP-43 protein offer new thinking on the development of ALS disease-modifying treatment. Ma *et al.* and Brown *et al.* found that TDP-43 depletion leads to a CE in *UNC13A* mRNA, resulting in nonsense-mediated decay (NMD) and decreased UNC13A protein. Single-nucleotide polymorphisms (SNPs) with ALS or FTD risk in *UNC13A* exacerbate the CE inclusions when TDP-43 function is lost (Fig. 1).

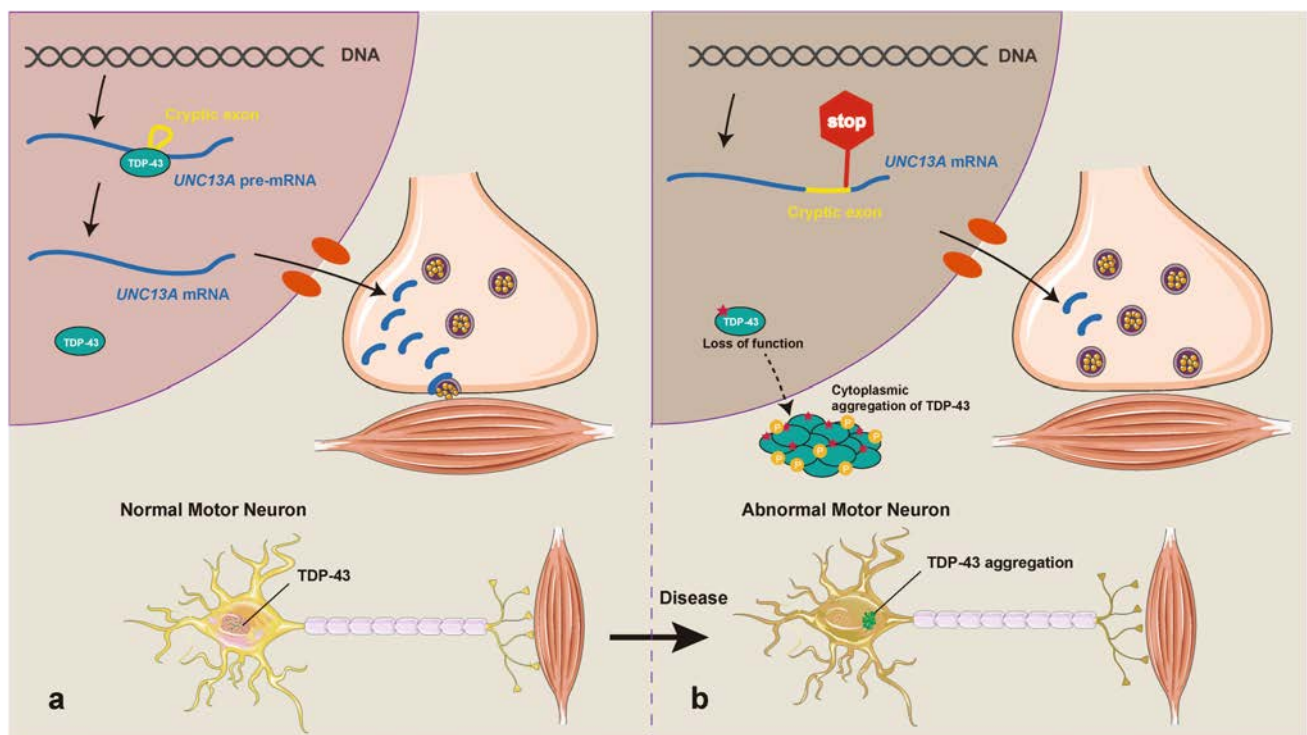
These two groups started their work by identifying CEs upon TDP-43 depletion using RNA sequencing (RNA-seq). Ma *et al.* obtained data from FTD and ALS (FTD-ALS) patients' brain tissue, while Brown *et al.* used human induced pluripotent stem cell (iPSC)-derived cortical neurons. They both identified the CE inclusion of *UNC13A* mRNA between exons 20 and 21 that was associated with nuclear depletion of TDP-43. Next, in order to determine that TDP-43 directly repressed the splicing of CE, both groups downregulated the TDP-43 level and then confirmed the *UNC13A* CE in different cell models. Furthermore, the UNC13A protein was also decreased because of premature stop codons and NMD. Using patients' samples, they both found the mRNA splicing variants containing *UNC13A* CE exclusively in neuronal nuclei from ALS or FTD patients' tissue with TDP-43 pathology (ALS-TDP or FTD-TDP), but neither in those with other pathology (RNA-binding protein FUS, Microtubule-associated protein tau, or Superoxide dismutase 1) nor control samples. Moreover, they found that the level of *UNC13A* CE was related to the level of TDP-43 pathology.

✉ Heling Chu  
chuheling85@163.com

✉ Yi Dong  
drdongyi@yeah.net

<sup>1</sup> Department of Neurology, National Center for Neurological Disorders, Huashan Hospital, Fudan University, Shanghai 200040, China

<sup>2</sup> Department of Gerontology, Shanghai Jiao Tong University Affiliated Sixth People's Hospital, Shanghai 200233, China



**Fig. 1** Incorrect splicing of *UNC13A* with a loss of TDP-43 function. **A** In normal neurons, TDP-43 is mainly present in the nucleus and plays an important role in alternative splicing. It represses the cryptic exon in *UNC13A* mRNA and guarantees the normal function of UNC13A protein. UNC13A bridges synaptic vesicles and the plasma membrane, and so contributes to synaptic vesicle docking, priming,

and neurotransmitter release [8]. **B** Under pathological conditions, phosphorylation of TDP-43 occurs in the cytoplasm. Upon loss of nuclear TDP-43, the cryptic exon is spliced into *UNC13A* mRNA, often disrupting the translation of UNC13A protein by nonsense-mediated decay. Hence, the impairment of UNC13A bridging function leads to abnormal neurotransmitter release.

To determine whether risk SNPs promote CE inclusions in the *UNC13A* mRNA upon TDP-43 nuclear depletion, they analyzed RNA-seq data from patients and RT-PCR products from motor neurons derived from patients' iPSCs with risk variants. The risk alleles contributed to a higher ratio of CE inclusions than reference alleles. Ma *et al.* revealed a strong positive correlation between the number of risk haplotypes and the level of CE inclusions. By using minigene reporters, these two groups found that different risk alleles enhanced CE upon TDP-43 nuclear depletion in an additive way. Lastly, by using TDP-43 RNA-recognition motifs (RRMs), Brown *et al.* discovered that risk SNPs of CE reduced the TDP-43 binding affinity to the mRNA. However, Ma *et al.* only found a diminished TDP-43 binding affinity to risk SNPs within introns and repeat sequences, but not to SNPs within CE sequences of *UNC13A*, by using full-length TDP-43.

Together, these results concluded that the formation of *UNC13A* CE and the downregulated UNC13A protein due to splicing defects are caused by nuclear TDP-43 dysfunction. Risk alleles in *UNC13A* could promote this abnormal splicing. However, there are some differences between these two articles. First, the Brown group also reported the inclusion

of a frameshift exon (FSE) of *UNC13B* and increased intron retention (IR) in both *UNC13A* and *UNC13B*. However, they did not detect an increase of *UNC13B* FSE and the IR of *UNC13A* and *UNC13B* in the tissues from ALS-TDP or FTD-TDP patients. Second, these groups both tested the TDP-43 binding affinity of risk variants to explore the mechanisms that underlie the exacerbated CE inclusions in *UNC13A*, but they had partially different results, which may be attributed to the different lengths of TDP-43 that they used. Thus, these controversial results still need to be further studied.

The *UNC13A* gene plays an essential role in the disease onset and progression of ALS. Previous studies have identified *UNC13A* as a susceptibility gene for ALS and FTD [6]. Furthermore, the minor allele of *UNC13A* is strongly linked with shorter survival in ALS patients [7]. These two articles establish a causal linkage between the TDP-43 loss and UNC13A downregulation, and reveal its underlying mechanisms. Therefore, *UNC13A* is identified as a genetic modifier of ALS survival mediated by nuclear TDP-43 loss, and might be a promising therapeutic target to slow disease progression, which may work in most ALS patients, about half of FTD patients, and other TDP-43 proteinopathies.



The UNC13A protein is widely expressed in the nervous system and is essential in efficient synchronous neurotransmission. UNC13A bridges the synaptic vesicles and plasma membrane, then leads to the docking, priming, and fusion of synaptic vesicles [8]. Loss of UNC13A drastically reduced ~90% of vesicular release and ~50% the number of docked vesicles at the *Drosophila* larval neuromuscular junction (NMJ) [9]. Previous research found that synaptic vesicle priming is defective in UNC13-deficient *Caenorhabditis elegans*, *Drosophila*, and mouse models. The morphology of the NMJ in mutant mice also shows distinct abnormality due to the vital function of UNC13A in neurotransmitter release and synaptogenesis [10]. Moreover, *C. elegans* with *UNC13* mutations have a severe disability in motility at an early stage [11]. UNC13A-deficient mice are completely paralyzed and die within hours of birth. However, Vérièpe *et al.* demonstrated that blocking UNC13-dependent neurosecretion suppresses motor neuron degeneration using mutant TDP-43<sup>A315T</sup> *C. elegans*, which is contradictory to the above studies [11]. Thus, the pathophysiological effect and mechanism of UNC13A downregulation in ALS-related motor neurons and disease models are still unknown. Furthermore, as the *UNC13A* CE had a TDP-43 loss-of-function-dependent disease-modifying effect, we are curious about when and how the *UNC13A* CE appears in ALS patients with various disease durations. Therefore, there are still many mysteries about *UNC13A* to be solved before its development as a disease-modifying target.

As for the targeted therapy of *UNC13A* CE, exon-skipping therapeutics, gene replacement, and small molecule treatment might be reasonable methods. Antisense oligonucleotides (ASOs) are single-stranded nucleotide analogs that modify gene expression. ASO-mediated exon-skipping has already been applied to several diseases, including Duchenne muscular dystrophy (DMD). With ASO-based splice-switching therapy, an out-of-frame exon can be deleted from *DMD* pre-mRNA, thereby producing functional dystrophin [12]. Therefore, ASO drugs carefully designed to induce skipping of the *UNC13A* mRNA CE, may restore the protein expression and slow the disease progression in ALS patients. Of note, the efficient delivery of ASOs to the targeted organs or cells remains a major obstacle, and most ASO therapies are designed to be delivered locally or into highly vascularized organs. In addition to intrathecal injection, chemical modification, covalent attachment, and nanoparticle formulations are common ways to allow oligonucleotide drug delivery to cross the blood-brain barrier. More advanced methods like exosome loading, spherical nucleic acids, and nanotechnology applications are still on the way [13]. In addition, a CRISPR-mediated exon-skipping approach can be an attractive way to skip the targeted CE, by using SpCas9-mediated non-homologous end joining at 5' or 3' splice sites containing the 5'-NAG-3' or 5'-NGG-3'

protospacer adjacent motif. However, CRISPR therapy is still in pre-clinical studies, and its off-target effects, the lack of efficient delivery methods, and the immunogenicity of this treatment also need caution [14]. Also, using lentivirus to rescue the expression of UNC13A protein and thereby attenuate the disease phenotype might be an alternative choice. Besides, some small molecules such as ataluren can promote ribosomal read-through to pass the termination codon and thereby generate the full-length and functional dystrophin protein in DMD; this could be applied to treat ALS patients with TDP-43 dysfunction [15].

Given that the phosphorylation, ubiquitination, and truncation of TDP-43 are the main hallmarks of most ALS and FTD diseases, a gain-of-function process and a loss-of-function mechanism might contribute equally to the pathology of TDP-43 proteinopathies. Therefore, some may wonder why TDP-43 mRNA or protein could not be therapeutic targets. Much evidence can answer this question. On the one hand, TDP-43 plays a critical role in the early development and normal neural function in the mouse, *Drosophila*, and zebrafish [16]. Forebrain-specific TDP-43 knockout mice exhibit a spectrum of age-dependent FTD-like behavioral disorders [17]. On the other hand, mammalian models with TDP-43 overexpression display a range of motor and non-motor phenotypes. And TDP-43 transgenic mice with modestly elevated wild-type TDP-43 expression show late-onset neurodegeneration and ALS-like phenotypes [18]. Thus, it is not favorable to directly target TDP-43 protein or mRNA; instead, targeting the RNAs or proteins regulated by TDP-43 may be a better and safer choice.

*UNC13A* is not the only gene with CEs upon nuclear TDP-43 loss. TDP-43 has two RRM domains, which preferentially bind the UG dinucleotide repeats. TDP-43 represses CE inclusions by binding to UG-rich sequences in distal intronic regions. Using a database from mice, Ling *et al.* revealed that TDP-43 loss induces many mis-splicing events that contribute to cell death, and CE repression protects TDP-43 knockout cells. In addition, they found that human CE data are entirely different from mouse CE data, but the CE repression function of TDP-43 is maintained across evolution. Therefore, it is recommended that future research of genes affected by CEs after TDP-43 loss should be conducted on the human background [3]. The results from the Ma and Brown groups showed that TDP-43 depletion promotes hundreds of splicing events in the human context and several CEs are associated with ALS or FTD. Among them, *STMN2* and *POLDIP3* have been widely studied. *STMN2* harbors a CE (exon 2a) after TDP-43 knockdown, resulting in reduced *STMN2* mRNA and STATHMIN-2 expression in the motor cortex and spinal motor neurons from ALS patients and iPSC-derived motor neurons. STATHMIN-2 is a microtubule regulator that is essential for neurite outgrowth and axon regeneration. Moreover, researchers have

found that restoring STATHMIN-2 rescues neurons, providing valuable experience for the development of methods of restoring UNC13A [19, 20]. And the loss of TDP-43 function leads to decreased wild-type POLDIP3 (variant-1) and increased POLDIP3-lacking exon 3 (variant-2), and the dysfunctional POLDIP3 has a low ability to maintain the size of SH-SY5Y cells. The amount of POLDIP3 variant-2 mRNA increase in the motor cortex, spinal cord, and spinal motor neurons in ALS, indicating that variant-2 might be a biomarker for TDP-43 dysfunction [21, 22]. But the links between most CEs and disease pathogenesis remain unknown. Furthermore, recently, more and more CE-associated mechanisms have been reported in central nervous system diseases, and these abnormal CEs could be promising targets for future disease-modifying therapy.

To sum up, pathologic TDP-43 features in the majority of ALS and approximately half of FTD patients. Considering the crucial role of TDP-43 in mRNA metabolism, dysfunctional TDP-43 may lead to a mass of dysregulated mRNAs. It is probably not favorable to target TDP-43 protein or mRNA directly due to its essential physiological function. Hence, targeting alternatively-spliced genes, such as *UNC13A*, might be an effective therapeutic strategy for ALS disease. Further clarification of the pathophysiological effects and mechanisms for *UNC13A* dysregulation in ALS may require continuous exploration. In this marathon, these two studies prove a novel linkage between two risk genes of ALS and provide a new target for its treatment.

**Conflict of interest** There is no conflict of interest.

## References

- Wen X, An P, Li H, Zhou Z, Sun Y, Wang J. Tau accumulation via reduced autophagy mediates GGGGCC repeat expansion-induced neurodegeneration in *Drosophila* model of ALS. *Neurosci Bull* 2020, 36: 1414–1428.
- Petrov D, Mansfield C, Moussy A, Hermine O. ALS clinical trials review: 20 years of failure. Are we any closer to registering a new treatment? *Front Aging Neurosci* 2017, 9: 68.
- Ling JP, Pletnikova O, Troncoso JC, Wong PC. TDP-43 repression of nonconserved cryptic exons is compromised in ALS-FTD. *Science* 2015, 349: 650–655.
- Ma XR, Prudencio M, Koike Y, Vatsavayi SC, Kim G, Harbinski F, *et al.* TDP-43 represses cryptic exon inclusion in the *FTD-ALS* gene *UNC13A*. *Nature* 2022, 603: 124–130.
- Brown AL, Wilkins OG, Keuss MJ, Hill SE, Zanovello M, Lee WC, *et al.* TDP-43 loss and ALS-risk SNPs drive mis-splicing and depletion of *UNC13A*. *Nature* 2022, 603: 131–137.
- van Es MA, Veldink JH, Saris CGJ, Blauw HM, van Vught PWJ, Birve A, *et al.* Genome-wide association study identifies 19p13.3 (*UNC13A*) and 9p21.2 as susceptibility loci for sporadic amyotrophic lateral sclerosis. *Nat Genet* 2009, 41: 1083–1087.
- Chiò A, Mora G, Restagno G, Brunetti M, Ossola I, Barberis M, *et al.* *UNC13A* influences survival in Italian amyotrophic lateral sclerosis patients: A population-based study. *Neurobiol Aging* 2013, 34: 357.e1–357.e5.
- Quade B, Camacho M, Zhao X, Orlando M, Trimbuch T, Xu J, *et al.* Membrane bridging by Munc13-1 is crucial for neurotransmitter release. *eLife* 2019, 8: e42806.
- Böhme MA, Beis C, Reddy-Alla S, Reynolds E, Mampell MM, Grasskamp AT, *et al.* Active zone scaffolds differentially accumulate *Unc13* isoforms to tune  $\text{Ca}^{2+}$  channel-vesicle coupling. *Nat Neurosci* 2016, 19: 1311–1320.
- Varoqueaux F, Sons MS, Plomp JJ, Brose N. Aberrant morphology and residual transmitter release at the Munc13-deficient mouse neuromuscular synapse. *Mol Cell Biol* 2005, 25: 5973–5984.
- Vérière J, Fossouo L, Parker JA. Neurodegeneration in *C. elegans* models of ALS requires TIR-1/Sarm1 immune pathway activation in neurons. *Nat Commun* 2015, 6: 7319.
- Matsuo M. Antisense oligonucleotide-mediated exon-skipping therapies: Precision medicine spreading from Duchenne muscular dystrophy. *JMA J* 2021, 4: 232–240.
- Roberts TC, Langer R, Wood MJA. Advances in oligonucleotide drug delivery. *Nat Rev Drug Discov* 2020, 19: 673–694.
- Choi E, Koo T. CRISPR technologies for the treatment of Duchenne muscular dystrophy. *Mol Ther* 2021, 29: 3179–3191.
- McDonald CM, Campbell C, Torricelli RE, Finkel RS, Flanigan KM, Goemans N, *et al.* Ataluren in patients with nonsense mutation Duchenne muscular dystrophy (ACT DMD): A multicentre, randomised, double-blind, placebo-controlled, phase 3 trial. *Lancet* 2017, 390: 1489–1498.
- Kim G, Gautier O, Tassoni-Tsuchida E, Ma XR, Gitler AD. ALS genetics: Gains, losses, and implications for future therapies. *Neuron* 2020, 108: 822–842.
- Wu LS, Cheng WC, Chen CY, Wu MC, Wang YC, Tseng YH, *et al.* Transcriptopathies of pre- and post-symptomatic frontotemporal dementia-like mice with TDP-43 depletion in forebrain neurons. *Acta Neuropathol Commun* 2019, 7: 50.
- Yang C, Qiao T, Yu J, Wang H, Guo Y, Salameh J, *et al.* Low-level overexpression of wild type TDP-43 causes late-onset, progressive neurodegeneration and paralysis in mice. *PLoS One* 2022, 17: e0255710.
- Klim JR, Williams LA, Limone F, Guerra San Juan I, Davis-Dusenbery BN, Mordes DA, *et al.* ALS-implicated protein TDP-43 sustains levels of STMN2, a mediator of motor neuron growth and repair. *Nat Neurosci* 2019, 22: 167–179.
- Melamed Z, López-Erauskin J, Baughn MW, Ouyang Z, Drenner K, Sun Y, *et al.* Premature polyadenylation-mediated loss of stathmin-2 is a hallmark of TDP-43-dependent neurodegeneration. *Nat Neurosci* 2019, 22: 180–190.
- Fiesel FC, Weber SS, Supper J, Zell A, Kahle PJ. TDP-43 regulates global translational yield by splicing of exon junction complex component SKAR. *Nucleic Acids Res* 2012, 40: 2668–2682.
- Shiga A, Ishihara T, Miyashita A, Kuwabara M, Kato T, Watanabe N, *et al.* Alteration of POLDIP3 splicing associated with loss of function of TDP-43 in tissues affected with ALS. *PLoS One* 2012, 7: e43120.

RESEARCH HIGHLIGHT

# The Lung Microbiome: A Potential Target in Regulating Autoimmune Inflammation of the Brain

Luoman Yang<sup>2</sup> · Shu Feng<sup>1</sup> · Chongyun Wu<sup>1</sup> ·  
Luodan Yang<sup>3</sup>

Received: 15 April 2022 / Accepted: 17 May 2022 / Published online: 12 July 2022

© Center for Excellence in Brain Science and Intelligence Technology, Chinese Academy of Sciences 2022

Under normal conditions, the immune system protects the brain from outside invaders, including viruses, bacteria, toxins, and fungi. However, an abnormal immune response within the brain affects its function and contributes to the progression of neurological diseases. For example, the immune system attacks the myelin sheath surrounding the nerve fibers in multiple sclerosis, causing nerve signal transmission problems [1], and excessive glial activation exacerbates Alzheimer's disease and contributes to its progression [2]. The discovery of the gut-brain axis indicates that the immune system in the central nervous system is also regulated by peripheral organ systems [3]. Numerous studies have demonstrated that the microbiome in the gastrointestinal tract is one of the critical regulators of the brain's immune response [4]. However, the roles of the microbiomes in other peripheral organs in regulating the brain's immune systems remain unclear.

In a recent study, Hosang *et al.* elucidated the role of the lung microbiome in regulating the brain's immune reactivity [5]. Hosang *et al.* first analyzed whether the lung microbiota affects the lung autoimmune process in a rat model

of experimental autoimmune encephalomyelitis (EAE). The EAE model is a well-established animal model of T-cell-mediated autoimmune disease of the central nervous system (CNS) [6]. This animal model has been established in various animals and is induced by administering CNS-derived antigens. Myelin basic protein (MBP) peptide fragment-induced EAE is a widely used model of multiple sclerosis. In the study by Hosang *et al.*, lung EAE was established by intravenous administration of MBP-specific T cells (T<sub>MBP</sub> cells) followed by intratracheal administration of MBP. They found that daily application of intratracheal neomycin completely blocks the lung EAE and regulates the diversity and abundance of the lung microbiome. To exclude the possibility that the improvement of lung EAE was due to the changes in gut microbiota, Hosang *et al.* analyzed the gut microbiota after intratracheal neomycin treatment. They did not detect any significant changes in abundance or diversity of the gut bacterial strains. Moreover, direct neomycin application in the gastrointestinal tract at the dose used in the intratracheal treatment or 10-fold-higher doses does not ameliorate clinical EAE, suggesting the improvement of lung EAE has no relationship with the microbiome diversity of the gut. Furthermore, they found that subcutaneous neomycin injection that lacks a microbial environment did not affect the lung EAE, indicating that the lung microbiota is necessary for the effect of neomycin in lung EAE. Interestingly, the number of T cells within the CNS was significantly reduced following local neomycin treatment. However, no significant changes were detected in the proliferation and migration of T cells into the blood following intratracheal neomycin treatment. This finding suggests the disease-suppressing effects of the intratracheal neomycin treatment is not due to the changes in T-cell activation within the lung tissue and further confirms that local microbiota dysregulation plays a vital role in the disease-suppressing effects of intratracheal neomycin.

Luoman Yang and Shu Feng contributed equally to this work.

✉ Chongyun Wu  
2017010064@m.scnu.edu.cn

✉ Luodan Yang  
luodan.yang@lsuhs.edu

<sup>1</sup> Laboratory of Regenerative Medicine in Sports Science, School of Physical Education and Sports Science, South China Normal University, Guangzhou 510006, China

<sup>2</sup> Department of Anesthesiology, Peking University Third Hospital, Beijing 100083, China

<sup>3</sup> Department of Neurology, Louisiana State University Health Sciences Center, Shreveport, LA 71103, USA

Hosang *et al.* next asked whether peripheral EAE induced by subcutaneous immunization or transfer EAE by the transfer of effector T cells could also be affected by changes in the lung microbiome [5]. Interestingly, the authors found that the peripheral EAE and transfer EAE induced outside the lung were significantly impaired after treatment with intratracheal neomycin. Next, lung microbiota transfer experiments were conducted to further confirm the role of the lung microbiota in the peripheral EAE model. Intriguingly, animals that received lung microbiota from the neomycin-treated rats showed significant improvement in the clinical symptoms of transfer EAE but not in the animals that received microbiota isolated from control animals without neomycin treatment. Similarly, in both peripheral and transfer EAE, neomycin treatment did not influence T cell numbers and migration in the periphery but rather it reduced T cell numbers within the CNS.

The authors also analyzed changes in the autoimmune process within the CNS following neomycin treatment [5]. They found that CNS inflammation was significantly decreased following the neomycin treatment. However, the reduced CNS inflammation could not be explained by the changes in T<sub>MBP</sub> cells. Therefore, the authors speculated that the changes in CNS inflammation might be due to changes in the microglia, the brain's primary resident immune cells. To confirm the role of microglia in EAE pathogenesis following neomycin treatment, the authors treated transfer EAE animals with minocycline, a microglial activation inhibitor. Interestingly, the transfer EAE was significantly inhibited, and pretreatment with neomycin did not show any additional disease-dampening effect. Similar results were found when the microglial depletion strategy was applied, suggesting that microglia mediate the altered autoimmune response after neomycin-induced lung microbiome changes. However, morphological changes of microglia were seen after intratracheal neomycin treatment. In addition, global transcriptome analyses of total tissue and microglia found that the gene changes in microglia and whole tissue had considerable overlap, suggesting that microglial changes play a crucial role in the lung-microbiota-induced changes in CNS tissue.

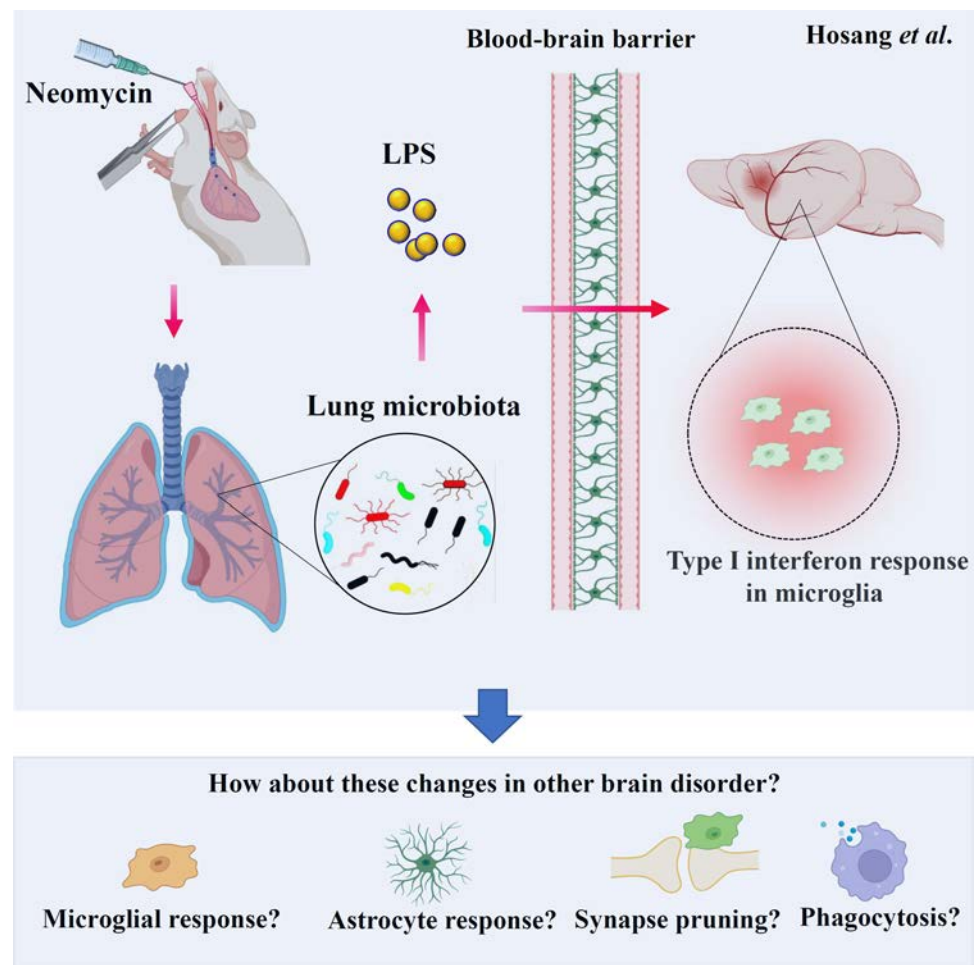
The authors next investigated the lung microbiome changes after intratracheal neomycin treatment to determine the relationship between microglial reactivity and lung microbiome changes. First, they found that Bacteroidetes were the most affected species of bacteria. Next, they transferred *Prevotella melaninogenica*, an inactivated strain of the Bacteroidetes phylum, to examine whether Bacteroidetes contributes to the clinical effects following neomycin treatment. Intriguingly, the intratracheal transfer of *P. melaninogenica* significantly improved clinical EAE rather than transfer by gastrointestinal gavage. This finding further

supports the hypothesis that the lung microbiome regulates the immune reactivity of the CNS. Because lipopolysaccharide (LPS) is the main component of the bacterial cell wall and 80% of the LPS production in the gut is attributed to Bacteroidetes, the authors then measured its levels in bronchoalveolar lavage fluid. Interestingly, they found a significant increase of LPS in neomycin-treated rats, and antibiotic treatment that did not affect LPS did not affect microglial and had no effect in regulating EAE. In contrast, an antibiotic peptide that neutralizes LPS in the bronchoalveolar lavage fluid significantly exacerbates the severity of EAE. These results confirmed that LPS is a regulator of CNS immune functions and plays a vital role in regulation of brain autoimmunity by the lung microbiome.

In summary, Hosang *et al.* confirmed that the lung microbiome regulates the autoimmune responses in the CNS. Moreover, they found that LPS-producing bacterial taxa play a central role in this process (Fig. 1). Although they could not rule out the effects of microbial metabolites and the changes of peripheral or recruited immune cells on the CNS autoimmunity, their study provides a new concept for the peripheral organ system controlling the CNS. It offers novel mechanisms underlying lung and CNS connections. Several intriguing questions arise based on these critical findings and are worth further investigation. First, although the astrocyte may not be involved in the lung-microbiota-induced CNS tissue changes [5], astrocyte changes may also be detected at a later stage or other brain disease models because of the crosstalk between astrocytes and microglia. Therefore, the role of astrocytes in the lung microbiome-regulated autoimmune inflammation of the brain deserves further investigation. Second, because microglia play an essential role in many processes in the brain, including microglia-mediated synaptic pruning, microglial phagocytosis, and neuroinflammation [7, 8], treatments influencing the lung microbiome may be able to regulate these processes. Further studies may examine the effect of the lung microbiome on microglia-mediated synaptic pruning during early brain development and microglial phagocytosis in neurological disorders. Third, more studies are needed to explore new avenues and possible therapeutic approaches targeting the lung microbiome. For example, is it possible to use inhaled probiotics to treat brain disorders? Finally, it would be interesting to explore whether other lung microbe-derived products influence CNS autoimmunity and whether chronic lung diseases are risk factors for neurodegenerative diseases. Looking deeper into the effects and the underlying mechanisms of the regulation of the lung microbiome in regulating brain autoimmunity in various brain diseases may provide a possible way to prevent or slow the progression of these brain disorders.



**Fig. 1** The lung microbiome regulates brain microglia. Intratracheal neomycin administration shifts the lung microbiota towards LPS-enriched types. The released LPS can cross the blood-brain barrier and target the brain, where the increased LPS in neomycin-treated rats induces a microglial type I interferon response within the CNS, resulting in the alleviation of EAE. Several intriguing questions arise and are worth further investigation, including the role of the lung microbiome in regulating the microglial response, the long-term astrocyte response, microglial pruning, and microglial phagocytosis in other brain disorders.



**Acknowledgements** This highlight was supported by the National Natural Science Foundation of China (32100918), and the project was funded by the China Postdoctoral Science Foundation (2021M690060), and the Sigma Xi Grants in Aid of Research program (G03152021115804390).

**Conflict of interest** The authors declare no competing financial interests.

## References

- Shaharabani R, Ram-On M, Talmon Y, Beck R. Pathological transitions in myelin membranes driven by environmental and multiple sclerosis conditions. *Proc Natl Acad Sci USA* 2018, 115: 11156–11161.
- Yang LD, Wu CY, Parker E, Li Y, Dong Y, Tucker L. Non-invasive photobiomodulation treatment in an Alzheimer Disease-like transgenic rat model. *Theranostics* 2022, 12: 2205–2231.
- Rutsch A, Kantsjö JB, Ronchi F. The gut-brain axis: How microbiota and host inflammasome influence brain physiology and pathology. *Front Immunol* 2020, 11: 604179.
- Carabotti M, Scirocco A, Maselli MA, Severi C. The gut-brain axis: Interactions between enteric microbiota, central and enteric nervous systems. *Ann Gastroenterol* 2015, 28: 203–209.
- Hosang L, Canals RC, van der Flier FJ, Hollensteiner J, Daniel R, Flügel A, *et al.* The lung microbiome regulates brain autoimmunity. *Nature* 2022, 603: 138–144.
- Baxter AG. The origin and application of experimental autoimmune encephalomyelitis. *Nat Rev Immunol* 2007, 7: 904–912.
- Wu CY, Yang LD, Youngblood H, Liu TCY, Duan R. Microglial SIRP $\alpha$  deletion facilitates synapse loss in preclinical models of neurodegeneration. *Neurosci Bull* 2022, 38: 232–234.
- Yang LD, Tucker D, Dong Y, Wu CY, Lu YJ, Li Y, *et al.* Photobiomodulation therapy promotes neurogenesis by improving post-stroke local microenvironment and stimulating neuroprogenitor cells. *Exp Neurol* 2018, 299: 86–96.

## Brief Instructions to Authors

*Neuroscience Bulletin* (NB) aims to publish research advances in the field of neuroscience and promote exchange of scientific ideas within the community. The journal publishes original papers of various topics on neuroscience and focuses on potential disease implications on the nervous system. NB welcomes research contributions on molecular, cellular, or developmental neuroscience using multidisciplinary approaches and functional strategies.

### Manuscript Submission

Manuscripts should be submitted through our online submission system, ScholarOne Manuscripts, at <http://mc03.manuscriptcentral.com/nsb> or <http://www.neurosci.cn>.

Manuscript file types that we accept for online submission include Word and WordPerfect. For Figure submission, we accept JPEG, TIFF, or AI files. Required items differ for each article type and are specified during the submission process.

The submitted manuscript should be accompanied with a signed “*Neuroscience Bulletin* copyright transfer statement and submission form”.

### Manuscript Preparation

**Original Article:** An original article contains original research materials and presents compelling data on conceptual advances in any area of neuroscience. The total character count of all sections of the main text (including references and figure legends but excluding supplemental data) should not exceed 80,000, including spaces. Up to 8 figures and/or tables are allowed for the entire manuscript. The minimum requirement of a submitted research article is 40,000 characters in total (or 5000 words excluding the references) and at least 6 display items (figures and tables). The submitted manuscript should be a substantial novel research study in all aspects of neuroscience organizing a complete story with complex mechanisms elucidated using multiple techniques or approaches. NB also welcomes clinical research investigating the pathogenesis or diagnostic markers of a disease. Please note that for clinical trials, an Informed Consent should be provided as supplemental material and stated in the main text. NB no longer accepts clinical research that lack insightful mechanistic implications. References are limited to 100.

**Review:** Authoritative reviews contribute greatly to our journal and we are interested in comprehensive articles well-written to describe recent development in any field of neuroscience for a general audience. Authors are expected to cover controversies in the field and propose their own viewpoints in an unbiased and justifiable way. In particular, the scope of the review should not be dominated by the authors' own work. Review is usually 5,000 to 8,000 words in length (including an abstract of no more than 150 words, excluding the references and title) and 3–6 schematic illustrations are strongly encouraged. Reviews are often contributed by leaders in the field and solicited by the editors. The authors are encouraged to submit a letter of inquiry before the submission.

**Insight:** For Insight, the article should contain discussion on recent primary research literature similarly as Review. Yet, Insight is shorter in length (no more than 2,000 words, excluding the reference and title) and focuses on a narrower scope. It is possible

that in Insight authors advocate a position over a controversial issue or a speculative hypothesis. One schematic illustration is allowed to make the Insight more comprehensive. References are limited to 20.

**Method:** NB welcomes Method article on novel experimental techniques in any field of basic neuroscience. The Method can be written in the Research Article format yet the content should follow the criteria described below. The description of the method must be accompanied by its validation, its application to an important biological question, and results illustrating its performance in comparison to available approaches. The manuscript will be judged on its novelty, general interest, through assessments of methodological performance and comprehensive technical descriptions that facilitate immediate application. The detailed step-by-step procedure must be described in the form of flow charts for readers to comprehend easily. Additional annotation for key procedures and special treatments will be encouraged. In addition, please note that NB no longer accepts Method on neurosurgery pathway, surgical techniques, or any other clinical related technical studies.

**Letter to the Editor:** The Letter to the Editor reports a short but exciting finding in a particular field of neuroscience with high quality and of broad interest. The letter should be brief yet concise, and no specific subsections are required. No Materials and Methods section is needed, but any technical information which the authors think is important should be submitted as supplementary materials. The total words count should not exceed 2500 (exclude references and title) and the display items should be limited to 2. References are limited to 15. No abstract and subsections are needed.

**Research Highlight:** The Research Highlight describes recent research advances by articles published in NB or other journals. It highlights the main results of the research, emphasizes the significance and provides further discussion on the topic. The main text of a Research Highlight is up to 1,500 words (excluding references and title) with no more than 10 references and one or two figures. Research Highlights are usually by editor invitation, but submitted manuscript with high quality will also be considered. No abstract and subsections are needed.

Submitted manuscripts should be divided into the following sections:

(1) Title Page; (2) Abstract; (3) Introduction; (4) Materials and Methods; (5) Results; (6) Discussion; (7) Acknowledgements; (8) References; (9) Figures, legends, and tables; (10) Supplementary information.

### Manuscript Revision

Upon peer-reviews, the authors may be asked to revise the manuscript. If the authors have substantial reasons to believe that their manuscript was treated unfairly, they may appeal for reconsideration. Revision should be completed within four (minor revision) or eight weeks (major revision). The authors should provide a cover letter and a point-to-point response for addressing the reviewers' comments. The editor will notify the corresponding author upon the acceptance of the manuscript. Accepted papers will be processed to advanced online publication as soon as possible.

**Proofs**

A PDF proof will be sent to the authors for them to correct last minute errors on the manuscript.

**Page Charges**

Page charges for the printed form are as follows: 500 CNY (80 USD) for each text page, 800 CNY (120 USD) for each page containing black-and-white figures, 1500 CNY (250 USD) for each page containing color figures. The corresponding author will receive an invoice on all the publication-related charges once the manuscript is accepted for publication and enters the editing process.

**Make checks or money orders payable to:**

Center for Excellence in Brain Science and Intelligence  
Technology, Chinese Academy of Sciences  
(中国科学院脑科学与智能技术卓越创新中心)

The bank account number is 4585 4835 7666,  
Shanghai Jianguo West Road Subbranch, Bank of China  
(中国银行上海市建国西路支行).

Address of Editorial Office of Neuroscience Bulletin:

319 YueYang Road, Room 612, Building 8, Shanghai 200031,  
China.

Phone: +86-21-64032273; 64170853; 64032696;

E-mail: nsb@ion.ac.cn

<http://www.neurosci.cn>

(Updated January 2021)

## Neuroscience Bulletin Copyright Transfer Statement and Submission Form

We submit this type of article (✓):

- Original Article
- Review
- Research Highlight
- Insight
- Letter to the Editor
- Method

**Title of article:**

Words:                      Figures:                      (Color figures:                      );                      Tables:

**A signature below certifies compliance with the following statements**

**Copyright Transfer Statement:** The copyright to this article is transferred to *Neuroscience Bulletin*, Center for Excellence in Brain Science and Intelligence Technology, CAS and Springer Nature (respective to owner if other than Center for Excellence in Brain Science and Intelligence Technology, CAS and Springer Nature and for U.S. government employees: to the extent transferable) effective if and when the article is accepted for publication. The author warrants that his/her contribution is original and that he/she has full power to make this grant. The author signs for and accepts responsibility for releasing this material on behalf of any and all co-authors. The copyright transfer covers the exclusive right and license to reproduce, publish, distribute and archive the article in all forms and media of expression now known or developed in the future, including reprints, translations, photographic reproductions, microform, electronic form (offline, online) or any other reproductions of similar nature. An author may self-archive an author-created version of his/her article on his/her own website. He/she may also deposit this version on his/her institution's and funder's (funder designated) repository at the funder's request or as a result of a legal obligation, including his/her final version, provided it is not made publicly available until after 12 months of official publication. He/she may not use the publisher's PDF version which is posted on [www.springerlink.com](http://www.springerlink.com) for the purpose of self-archiving or deposit. Furthermore, the author may only post his/her version provided acknowledgement is given to the original source of publication and a link is inserted to the published article on Springer's website. The link must be accompanied by the following text: "The original publication is available at [www.springerlink.com](http://www.springerlink.com)". The author is requested to use the appropriate DOI for the article. Articles disseminated via [www.springerlink.com](http://www.springerlink.com) are indexed, abstracted and referenced by many abstracting and information services, bibliographic networks, subscription agencies, library networks, and consortia.

After submission of this agreement signed by the corresponding author, changes of authorship or in the order of the authors listed will not be accepted by *Neuroscience Bulletin*, Center for Excellence in Brain Science and Intelligence Technology, CAS and Springer Nature.

### Authorship responsibilities

I/We confirm that:

- (1) The work described has not been published before in any language or in any journal or media; that it is not under consideration for publication elsewhere; that its publication has been approved by all co-authors, if any, as well as (tacitly or explicitly) by the responsible authorities at the institution where the work was carried out.
- (2) We also give an assurance that the material will not be submitted for publication elsewhere until a decision has been made as to its acceptability for *Neuroscience Bulletin* in 2 months, then declare this statement becomes null and void.
- (3) I am/We are responsible for obtaining permission for the use of any material in the manuscript that may be under copyright to my/our employer(s) or other party(ies).
- (4) I have read the complete manuscript and accept responsibility for the content and completeness.
- (5) I have made a significant contribution to this work and am familiar with the contents.

Author (1) signed:                      Date:                      Author (2) signed:                      Date:

Author (3) signed:                      Date:                      Author (4) signed:                      Date:

Author (5) signed:                      Date:                      Author (6) signed:                      Date:

Author (7) signed:                      Date:                      Author (8) signed:                      Date:

Author (9) signed:                      Date:                      Author (10) signed:                      Date:

Corresponding author signed:                      Date:

Corresponding author address:

Tel:                      E-mail:



# Neuroscience Bulletin

## Editors-in-Chief

**Shumin Duan**, Zhejiang University, Hangzhou, China  
**Ru-Rong Ji**, Duke University, Durham, USA

## Deputy Editors

**Julin Du**, Center for Excellence in Brain Science and Intelligence Technology, CAS, Shanghai, China  
**Zuoren Wang**, Center for Excellence in Brain Science and Intelligence Technology, CAS, Shanghai, China

## Executive Associate Editors

**Iain C. Bruce**, Zhejiang University, Hangzhou, China  
**Guangyin Xu**, Institute of Neuroscience, Soochow University, Suzhou, China

## Associate Editors

**Shiqing Cai**, Center for Excellence in Brain Science and Intelligence Technology, CAS, Shanghai, China  
**Renjie Chai**, Southeast University, Nanjing, China  
**Zhong Chen**, Zhejiang University, Hangzhou, China  
**Yiru Fang**, Shanghai Mental Health Center, Shanghai, China  
**Tianming Gao**, South Medical University, Guangzhou, China  
**Yong-Jing Gao**, Nantong University, Nantong, China  
**Yong Gu**, Center for Excellence in Brain Science and Intelligence Technology, CAS, Shanghai, China  
**Shihui Han**, Peking University, Beijing, China  
**Cheng He**, Naval Medical University, Shanghai, China  
**Tianzi Jiang**, Institute of Automation, CAS, Beijing, China  
**Weidong Le**, Sichuan Academy of Medical Science/ Sichuan Provincial Hospital, Chengdu, China  
**Tao Li**, Zhejiang University School of Medicine Affiliated Mental Health Center, Hangzhou, China  
**Chengyu Li**, Center for Excellence in Brain Science and Intelligence Technology, CAS, Shanghai, China  
**Chun-Feng Liu**, Second Affiliated Hospital of Soochow University, Suzhou, China  
**Minmin Luo**, National Institute of Biological Sciences, Beijing, China  
**Mengsheng Qiu**, Hangzhou Normal University, Hangzhou, China  
**Zilong Qiu**, Center for Excellence in Brain Science and Intelligence Technology, CAS, Shanghai, China  
**Fu-Dong Shi**, Tianjin Medical University General Hospital, Tianjin, China  
**Yangang Sun**, Center for Excellence in Brain Science and Intelligence Technology, CAS, Shanghai, China

**You Wan**, Peking University, Beijing, China  
**Jian-Zhi Wang**, Huazhong University of Science and Technology, Wuhan, China  
**Kai Wang**, Anhui Medical University, Hefei, China  
**Liping Wang**, Shenzhen Institute of Advanced Technology, CAS, Shenzhen, China  
**Liping Wang**, Center for Excellence in Brain Science and Intelligence Technology, CAS, Shanghai, China  
**Yanjiang Wang**, Daping Hospital, Army Medical University, Chongqing, China  
**Zheng Wang**, Peking University School of Psychological and Cognitive Sciences, Beijing, China  
**Longjun Wu**, Mayo Clinic, Rochester, USA  
**Sheng-Xi Wu**, The Fourth Military Medical University, Xi'an, China  
**Si Wu**, Peking University, Beijing, China  
**Zhi-Ying Wu**, The Second Affiliated Hospital Zhejiang University School of Medicine, Hangzhou, China  
**Ninglong Xu**, Center for Excellence in Brain Science and Intelligence Technology, CAS, Shanghai, China  
**Tianle Xu**, Shanghai Jiao Tong University School of Medicine, Shanghai, China  
**Yun Xu**, Nanjing Drum Tower Hospital, Nanjing, China  
**Tian Xue**, University of Science and Technology of China, Hefei, China  
**Dai Zhang**, Peking University, Beijing, China  
**Hanting Zhang**, Qingdao University School of Pharmacy, Qingdao, China  
**Jie Zhang**, Xiamen University, Xiamen, China  
**Yongqing Zhang**, Institute of Genetics and Developmental Biology, CAS, Beijing, China  
**Chunjiu Zhong**, Fudan University, Shanghai, China

## Editorial Board

**Goran Angelovski**, Center for Excellence in Brain Science and Intelligence Technology, CAS, Shanghai, China  
**George Baillie**, Institute of Cardiovascular and Medical Sciences, University of Glasgow, UK  
**Guo-Qiang Bi**, University of Science and Technology of China, Hefei, China

**Junli Cao**, Xuzhou Medical College, Xuzhou, China  
**L. Judson Chandler**, Medical University of South Carolina, USA  
**Jun Chen**, The Fourth Military Medical University, Xi'an, China  
**Qing-Hui Chen**, Michigan Technological University, Houghton, USA

**Xiaoke Chen**, Stanford University, Stanford, USA  
**Isaac M. Chiu**, Harvard Medical School, Boston, USA  
**He Cui**, Center for Excellence in Brain Science and Intelligence Technology, CAS, Shanghai, China  
**Jun Ding**, Stanford University, Stanford, USA  
**Aaron Gitler**, Stanford University, Stanford, USA  
**Xiaosong Gu**, Nantong University, Nantong, China  
**Junhai Han**, Southeast University, Nanjing, China  
**Gregg E. Homanics**, University of Pittsburgh, USA  
**Zhi-An Hu**, Army Medical University, Chongqing, China  
**Peter Illes**, University of Leipzig, Leipzig, Germany  
**Pierre Lavenex**, University of Fribourg, Fribourg, Switzerland  
**Juan Lerma**, Instituto de Neurociencias de Alicante, Alicante, Spain  
**Wolfgang Liedtke**, Duke University School of Medicine, Durham, USA  
**Stuart A. Lipton**, Sanford-Burnham Medical Research Institute and University of California at San Diego, San Diego, USA  
**Jingyu Liu**, Center for Excellence in Brain Science and Intelligence Technology, CAS, Shanghai, China  
**Tong Liu**, Nantong University, Nantong, China  
**Lin Lu**, Peking University Sixth Hospital, Beijing, China  
**Benyan Luo**, Zhejiang University School of Medicine, Hangzhou, China  
**Ceng Luo**, The Fourth Military Medical University, Xi'an, China  
**Jian-Hong Luo**, Zhejiang University School of Medicine, Hangzhou, China  
**Zhen-Ge Luo**, ShanghaiTech University, Shanghai, China  
**Lan Ma**, Fudan University, Shanghai, China  
**Qiufu Ma**, Dana-Farber Cancer Institute, Boston, USA  
**Quanhong Ma**, Soochow University, Suzhou, China  
**Robert C. Malenka**, Stanford University, Stanford, USA  
**Manuel S. Malmierca**, Universidad de Salamanca, Salamanca, Spain  
**John H.R. Maunsell**, Harvard Medical School, Boston, USA  
**Earl K. Miller**, Massachusetts Institute of Technology, Cambridge, USA  
**Hideyuki Okano**, Keio University, Tokyo, Japan  
**Vladimir Parpura**, University of Alabama at Birmingham, Birmingham, USA  
**Jos Prickaerts**, School for Mental Health and Neuroscience, Maastricht University, The Netherlands  
**Joshua R. Sanes**, Harvard University, Boston, USA  
**Michael N. Shadlen**, Columbia University, New York, USA  
**Yousheng Shu**, Fudan University, Shanghai, China  
**Bai-Lu Si**, Beijing Normal University, Beijing, China  
**Sangram S. Sisodia**, The University of Chicago, Chicago, USA

**Peter Somogyi**, University of Oxford, Oxford, UK  
**Ron Stoop**, Lausanne University, Lausanne, Switzerland  
**Feng-Yan Sun**, Fudan University, Shanghai, China  
**Dick F. Swaab**, Netherlands Institute for Neuroscience, Amsterdam, The Netherlands  
**Yong Tang**, Chengdu University of TCM, Chengdu, China  
**Makoto Tsuda**, Kyushu University, Fukuoka, Japan  
**Alexei Verkhratsky**, The University of Manchester, Manchester, UK  
**Guanghui Wang**, Soochow University, Suzhou, China  
**Yun Wang**, Neuroscience Research Institute, Peking University, Beijing, China  
**Xu-Chu Weng**, South China Normal University, Guangzhou, China  
**William Wisden**, Imperial College London, London, UK  
**Jun-Xia Xie**, Qingdao University, Qingdao, China  
**Zhiqi Xiong**, Center for Excellence in Brain Science and Intelligence Technology, CAS, Shanghai, China  
**Lin Xu**, Kunming Institute of Zoology, CAS, Kunming, China  
**Xiao-Hong Xu**, Center for Excellence in Brain Science and Intelligence Technology, CAS, Shanghai, China  
**Jun Yan**, Center for Excellence in Brain Science and Intelligence Technology, CAS, Shanghai, China  
**Hui Yang**, Center for Excellence in Brain Science and Intelligence Technology, CAS, Shanghai, China  
**Tianming Yang**, Center for Excellence in Brain Science and Intelligence Technology, CAS, Shanghai, China  
**Haishan Yao**, Center for Excellence in Brain Science and Intelligence Technology, CAS, Shanghai, China  
**Shanping Yu**, Emory University School of Medicine, Atlanta, USA  
**Hong Zhang**, The Second Affiliated Hospital of Zhejiang University School of Medicine, Hangzhou, China  
**Xiaohui Zhang**, Beijing Normal University, Beijing, China  
**Xu Zhang**, Shanghai Advanced Research Institute, CAS, Shanghai, China  
**Yong Zhang**, Peking University, Beijing, China  
**Yu-Qiu Zhang**, Fudan University, Shanghai, China  
**Zhi-Jun Zhang**, Zhongda Hospital, Southeast University, Nanjing, China  
**Ping Zheng**, Fudan University, Shanghai, China  
**Jiang-Ning Zhou**, University of Science and Technology of China, Hefei, China  
**Jiawei Zhou**, Center for Excellence in Brain Science and Intelligence Technology, CAS, Shanghai, China  
**Jingning Zhu**, Nanjing University, Nanjing, China



Impact Factor

5.271

2021 Journal Citation Reports: Q2  
(CLARIVATE ANALYTICS, 2022)

---

NEUROSCIENCE BULLETIN 神经科学通报 (Monthly)

Vol. 38 No. 11 November 15, 2022

---

**Administrated by:** Chinese Academy of Sciences

**Sponsored by:** Center for Excellence in Brain Science and Intelligence Technology, Chinese Academy of Sciences  
Chinese Neuroscience Society

**Editors-in-Chief:** Shunmin Duan, Ru-Rong Ji

**Edited by:** Editorial Board of *Neuroscience Bulletin*

319 Yueyang Road, Building 8, Room 612, Shanghai 200031, China

Phone: +86-21-64032273; 64170853; 64032696

E-mail: nsb@ion.ac.cn; <http://www.neurosci.cn>

**Editors:** Bin Wei, Fei Dong, Ting Lyu

**Published by:** Center for Excellence in Brain Science and Intelligence Technology, Chinese Academy of Sciences

**Printed by:** Shanghai Shengtong Times Printing Co., Ltd (A6, No. 2888, Caolang Highway, Jinshan District, Shanghai)

**Overseas Distributed by:** Springer Nature

**Home Distributed by:** Local Post Offices

---

ISSN 1673-7067

CN 31-1975/R

Post Office Code Number: 4-608

Permit of Ad. Number: 3100420130051

Price: ¥ 100.00

ISSN 1673-7067





# APEXVIEW

## APX 100

### 一体化智能成像解决方案

持续专注于您的研究

几次点击即可获得出版级质量的图像

快速、高效的数据管理功能



## 轻松获得高质量图像

### 一体式封闭显微镜设计

无需暗室也能获取极致荧光图像

### “智能样品导航”

助您轻松找到感兴趣区，并立即开始拍摄

### 全新“Gradient Contrast”观察方式

立体成像即刻呈现

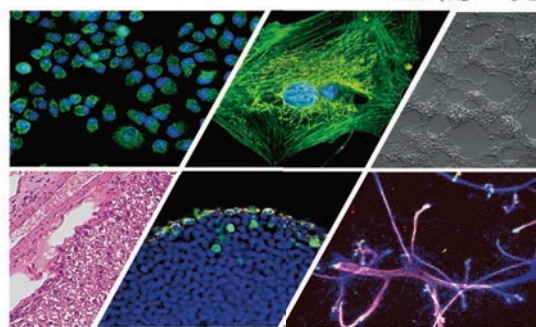
### 智能“抗漂白模式”

大幅降低光毒性和光漂白，活细胞友好

### 浩瀚数据的收纳专家

用清晰、统一的索引方式管理您的数据

显而E见



仪景通光学科技(上海)有限公司  
EVIDENT (Shanghai) Co. Ltd.

更多详情请咨询: 400-969-0456 / SSBD.Marketing@olympus.com.cn

[www.olympus-lifescience.com.cn](http://www.olympus-lifescience.com.cn)